Advanced laboratory studies to explore the axial cyclic behaviour of driven piles

By

Amin Aghakouchak

A thesis submitted to Imperial College London in partial fulfilment for the degree of Doctor of Philosophy and Diploma of Imperial College London

Department of Civil and Environmental Engineering

2015

Abstract

Importance of addressing cyclic behaviour when designing piled foundations has been emphasised in recent years. Instrumented full scale field and model pile tests have revealed key features of pile's axial cyclic response in recent years. Along with those, laboratory tests may be conducted to provide site specific cyclic soil characteristics, but questions arise concerning how to: (i) take into account the pile installation process and (ii) apply the results to assess pile capacity and deformation responses under cyclic loads. This thesis describes an investigation into the cyclic behaviour of Dunkerque and NE34 Fontainebleau sands, performed to support and help analyse field-scale and model pile cyclic loading tests on the same soils. Series of triaxial and HCA cyclic and static tests were performed, following testing schemes developed that reflect the conditions applying adjacent to the pile shafts. Assessments were made of how the cyclic variations of stresses imposed during installation and the period allowed for the sands to creep following such 'installation' effects, affect the response to subsequent cycling. Constant-volume cyclic tests involving up to 4500 cycles were imposed from alternative sets of initial conditions that revealed the relationships between the cyclic amplitude, the changes in effective stress and number of cycles as well as the permanent strain accumulation and cyclic stiffness characteristics. Monotonic compression and extension tests were also performed for both sands to help frame their strength, stiffness and critical state properties. Finally, methods are introduced to compare the laboratory results with field and model pile tests.

Declaration

The work presented in this thesis is result of experiments and analyses of Author which was performed at the Soil Mechanics section of Imperial College London, Civil and Environmental Department between 2011 to 2015. Any material, idea or data presented which is not my own is referenced and indicated.

The work presented here is original and is not the same as any submitted for any degree, diploma or other qualification at any other university

The copyright of this thesis rests with the author and is made available under a Creative Commons Attribution Non-Commercial No Derivatives licence. Researchers are free to copy, distribute or transmit the thesis on the condition that they attribute it, that they do not use it for commercial purposes and that they do not alter, transform or build upon it. For any reuse or redistribution, researchers must make clear to others the licence terms of this work.

Amin Aghakouchak

London, 2015

Acknowledgments

Successful completion of this thesis could not be possible without the help many supportive people whom I like to thank here.

I would like to thank my supervisors, Prof. Richard Jardine and Dr. Way Way Sim for their continuous support and guidance throughout this project. Their guidance not only helped me to finish this project successfully but also gave me valuable lessons regarding right approaches in scientific thinking and research.

I would also like to thank the laboratory technical support team: Mr. Steven Ackerley, Mr. Alan Bolsher, Mr. Graham Keefe and Mr. Duncan Parker, for their assistance. Advanced laboratory tests performed in this research would not be possible without their continuous help and their expertise which is the result of years of professional experience. I also like to thank Dr. Amandine Brosse who took time to teach me how to work with the HCA apparatus. Her help throughout this research is much appreciated.

I would also like to extend my gratitude to Atkins, Imperial College's Dixon Scholarship Fund and JAMM Design and Development Engineering Co. for their sponsorship and support of this project.

And finally I would like to thank my family and friends whom without their support and encouragement I could never go through these challenging years. I hope one day I can pay their unconditional help and support back.

Table of contents

CHAPTER 1 1

1.1 Objectives 3

1.2 Thesis layout 4

CHAPTER 2 Monotonic and cyclic behaviour of sands 7

2.1 Pre-failure behaviour 7

2.1.1 Stiffness of sands 11

2.2 Critical state soil mechanics for sands and state parameter 12

2.2.1 State parameter 14

2.3 Cyclic behaviour of sands 15

2.3.1 Definition and modes of cyclic loading 15

2.3.2 Sand cyclic loading response 17

2.3.3 Modelling field cyclic loading in laboratory experiments 26

2.4 High cycle accumulation model 27

2.5 Summary and conclusions 31

CHAPTER 3 Monotonic and cyclic behaviour of pile foundations in sand 47

3.1 Axial static capacity of single piles in sands 47

3.1.1 Base resistance 49

3.1.2 Pile shaft resistance 54

3.2 Experience of cyclic loading in field 65

3.3 Axial cyclic loading study in field and model piles 67

3.3.1 Field pile tests 67

3.3.2 Model pile tests 70

3.4 Framework for laboratory modelling of axial cyclic pile response 72

3.4.1 Cyclic CNL and CNS simple and direct shear tests 75

3.4.2 Critical assessment of practiced cyclic shear tests 77
3.4.3 Other laboratory tests for investigating pile axial cyclic response 79
3.5 Summary and conclusions 80
CHAPTER 4 Apparatus description and sample preparation technique 105
4.1 Triaxial Stress Path Apparatus 105
4.1.1 General structure of apparatus 105
4.1.2 Transducers 107
4.1.3 Data Analysis 110
4.1.4 Ability to perform cyclic tests 112
4.2 Hollow Cylinder apparatus 113
4.2.1 Apparatus general structure 114
4.2.2 Instrumentation: 116
4.2.3 Analysis of stress and strain data 118
4.2.4 Sources for possible errors 122
4.2.5 Modifications for cyclic tests 124
4.3 Resonant column system 125
4.4 Sample preparation method 129
4.4.1 Sample preparation 129
4.4.2 Saturation 131
4.5 Conclusion and remarks 132
CHAPTER 5 Index properties and monotonic behaviour of test sands 146
5.1 Description of test sands 146
5.1.1 Dunkerque sand 147
5.1.2 NE34 sand 148
5.2 Monotonic behaviour of test sands 149
5.2.1 Drained normally consolidated K_0 tests 149
5.2.2 Undrained tests 163

5.3 Summary and conclusions 167
CHAPTER 6 Design of the "standard" testing procedure 202
6.1 Field conditions 203
6.1.1 Soil element stress regime and failure mechanism 203
6.1.2 Soil element stress history adjacent to pile 205
6.1.3 Cyclic loads 206
6.2 Cyclic tests 206
6.2.1 Effect of stress history on cyclic response 207
6.2.2 Effect of pre-cycling 210
6.2.3 Effects of ageing 215
6.3 Standard test procedure 217
6.4 Conclusion and remarks 218
CHAPTER 7 Main triaxial cyclic series to evaluate the axial cyclic response of piles 232
7.1 Undrained "standard" cyclic tests 232
7.1.1 Pre-conditioning 233
7.1.2 Undrained cyclic response 234
7.2 Undrained "standard" cyclic tests at other void ratios 239
7.2.1 Pre-conditioning 239
7.2.2 Undrained cyclic response 241
7.3 Drained cyclic tests with "standard" pre-conditioning 242
7.4 Comparison between drained and undrained tests 244
7.5 Conclusions and remarks 244
CHAPTER 8 HCA undrained tests using the "standard" test procedure 273
8.1 Modelling the simple shear conditions adjacent to pile in HCA tests 274
8.2 "Standard" test procedure for HCA tests 274
8.2.1 Consolidation-swelling 274
8.2.2 Creep and ageing 275

8.2.3 Pre-cycling 276
8.2.4 Main cycling stage 277
8.3 Monotonic simple shear tests with "standard" pre-conditioning 278
8.3.1 Small strain behaviour 278
8.3.2 Stiffness measurements 279
8.3.3 Behaviour moving towards the critical state line 280
8.4 "Standard" HCA cyclic tests 281
8.4.1 Pre-conditioning 282
8.4.2 Undrained simple shear cycling at Point D 283
8.5 Relation between σ'_r and p' degradation 291
8.6 Conclusions and remarks 291
CHAPTER 9 Comparison of testing results with field and model pile tests 323
9.1 Outcomes of single element testing program 323
9.2 Interpretation of pile behaviour based on laboratory tests 326
9.2.1 Cyclic HCA tests 330
9.2.2 Cyclic Triaxial tests 332
9.2.3 Shaft friction degradation relation with N 334
9.3 Conclusions 335
CHAPTER 10 Conclusions, remarks and recommendations for future work 349
10.1 Apparatus and sample set-up 349
10.2 Test sands and their monotonic behaviour 350
10.3 Development of the "standard" testing procedure 351
10.4 "Standard" triaxial and HCA cyclic results 352
10.5 Comparison with pile tests 354
10.6 Recommendations for future works 355

Abbreviations

A_p Pile end area

A_{si} Pile shaft area

b Intermediate principal stress factor

CSR Cyclic stress ratio in triaxial tests

$CSR_{pre\text{-}cyc}$ Cyclic stress ratio at pre-cycling stage in triaxial tests

CSR_τ Cyclic stress ratio in HCA tests

$CSR_{\tau\ pre\text{-}cyc}$ Cyclic stress ratio at pre-cycling stage in HCA tests

d_{50} Diameter for which 50% (by mass) of the particles in a **soil** sample are finer

D_{pile} Pile diameter

D_r Relative density

e_{cs} Void ratio at critical state line

E'_h Horizontal (radial) drained Young's modulus

E_u Undrained Young's modulus

$E_u{}^v$ Undrained cyclic secant vertical stiffness

E'_v Vertical (axial) drained Young's modulus

F_a Axial load in triaxial cell

G Sand shear stiffness

G_{hh} Shear modulus in horizontal plane for a cross anisotropic material

G_{vh} Shear modulus in any vertical plane for a cross anisotropic material

H Sample height

I_G Grading index

K Coefficient of earth pressure at rest

K_{CNS} Constant normal stiffness value

M_T Applied torque in HCA

N Number of cycles

N_f	Number of cycles to failure
N_q	Dimensionless bearing capacity factor
OCR	Over-consolidation ratio
p'	Mean effective stress
P_{cell}	Cell pressure in triaxial tests
P_i	Inner cell pressure in HCA
p_{lim}	Limit pressure at pile base
p'_{mean}	Mean effective stress
P_o	Outer cell pressure in HCA
P_r	Atmospheric pressure
q	Deviatoric stress
Q_{avg}	Average load applied to pile
q_b	Cone resistance
Q_b	End bearing capacity
Q_{cyc}	Cyclic load applied to pile
q_{cyc}	Cyclic deviatoric amplitude stress
Q_{max}	Maximum applied load to pile $Q_{cyc}+Q_{avg}$
q_{max}	Cyclic deviatoric mean stress
q_{mean}	Mean deviatoric stresses
q_s	Ultimate shaft friction capacity
q_s	Pile shaft friction
R	Sample radius
R	Pile radius
r	Radial coordinate in cylindrical coordinate system
R_i	Inner radius HCA
R_o	Outer cell pressure
S_{hh}	horizontally propagating horizontally polarised shear wave

S_{vh} Vertically propagating horizontally polarised shear wave

U_c Uniformity coefficient

z Vertical coordinate in cylindrical coordinate system

α Angle of major principal stress with vertical direction

γ_{zh} Shear strain

$\gamma_{z\theta}$ Shear strain

δ' Pile soil interface friction angle

δ'_f Interface friction angle

ε_{cyc} Cyclic shear strain

ε_r Radial strain

ε_r Radial Strains

ε_s Invariant shear strain ε_1-ε_3

ε_v Volumetric strain $\varepsilon_1+ \varepsilon_2+ \varepsilon_3$

ε_z Vertical strains

ε_z Vertical strains

ε_θ Circumferential strains

ε_θ Circumferential strains

θ Angular coordinate in cylindrical coordinate system

λ Slope of CSL in e_c-ln(σ_m) space for semi-log idealization

σ'_1 Major principle stress

σ'_2 Intermediate principle stress

σ'_3 Minor principle stress

σ'_r Radial effective stress

σ'_{rc} Equilibrium radial effective stress adjacent to pile shaft surface

σ'_{rf} Radial effective stress at failure acting on pile shafts

σ'_v Vertical effective stress in-situ

σ'_z Vertical effective stress

σ'_θ Circumferential effective stress

σ'_θ Circumferential effective stress

τ_{cyc} Cyclic shear stress

τ_f Ultimate shaft shear stress at failure

$\tau_{max\ static}$ Maximum pile shaft friction

τ_{rz} Shear stresses on the pile shaft

υ Specific volume 1+e

ϕ'_{cs} Critical state angle of shearing resistance

ψ State parameter

ω Circular frequency of the oscillation

Γ Reference void ratio on CSL, conventionally defined at p≒1kPa

CHAPTER 1

Introduction

The potential impact of cyclic loading on soil shear strength and stiffness properties has been widely appreciated since the work of Seed & Lee (1966) and there is a growing appreciation of the need to address the impact of cyclic loading generated by operating plant, seasons, tides or storms particularly in offshore applications: Erbrich (2010); Jardine *et al.* (2012); Andersen *et al.* (2013). Cyclic loading is addressed routinely in offshore Gravity Base Structure (GBS) foundation design (Andersen *et al.*, 1994) but is only recently being addressed with piled installations. In recent years, along with improvements in static driven pile design (for example Jardine *et al.*, 2005), Field and laboratory tests with instrumented piles have provided powerful insights into how driven piles behave during installation, equalisation and axial and cyclic loading. Imperial College has actively been involved in a series of research projects including works by Lehane *et al.* (1993), Chow (1997), Yang *et al.* (2010), Tsuha *et al.* (2012) and Jardine *et al.* (2013a, b) who reported results from their field and model piles tests.

The earliest cyclic tests on piles driven in sands known to the author are reported Lehane (1992) and Chow (1997) along with their more extensive static tests. The first comprehensive

full scale cyclic test series in dense marine sands were reported by Jardine & Standing (2000, 2012) at Dunkerque. These experiments proved that low level *Stable* cyclic loading could lead to shaft capacity growth and little accumulation of displacement over 1000 or more cycles, whereas high level *Unstable* cyclic loading led to heavy losses in shaft capacity and failure within 100 or fewer cycles. An intermediate *Metastable* zone was also identified where displacements accumulated at moderate rates and piles could sustain cycling for some hundreds of cycles.

Better understanding of the pile response was achieved using the 'Imperial College Instrumented Piles' (ICPs) that offered accurate local measurements of shaft shear and normal stresses. They showed that the shaft capacities developed under both static and cyclic loading are controlled by the evolution of the local shaft radial effective stresses. The cyclic tests with "mini-ICP" piles in pressurised calibration chambers filled with relatively dense sand supported the field categorisation of cyclic response into the *Stable*, *Metastable* and *Unstable* categories. These tests gave new insights into the main processes that lead to cyclic degradation. Following the effective stress paths developed at the pile soil interface showed that different modes of behaviour can be understood using the kinematic multi yield surface framework. While *Stable* tests kept the local effective stresses within the sand's Y_2 kinematic yield surfaces (Jardine, 1992; 2013), *Metastable* cycling led to failure through a negative (leftward) drift in the local radial effective stresses that continued until local interface failure ensued. *Unstable* cycling led rapidly to sharp drops in σ'_r interface phase transformation and local slip. These key features explain the pile-soil response and suggest how the pile response to cyclic loading might be addressed in cyclic design.

Jardine *et al.* (2012) proposed a cyclic design flow chart for axially loaded piles in which in-situ testing, laboratory testing and large scale field experiments offered routes for assessing

cyclic response and capacity degradation. This proposed a range of approaches including simple semi-empirical methods for assessing stability and predict possible shaft degradation through calibration against field or model pile tests. Noting that such tests may be hard to apply generally, laboratory element tests were also proposed as a potential means of developing site-specific assessments. To be successful, such tests must be able to model representatively both the stress history of soil elements adjacent to displacement piles and the field cyclic loading conditions.

1.1 Objectives

The aim in this project is to assess whether it is possible with sands to capture the key axial cyclic behavioural features observed in field and model pile tests in laboratory single element tests that model the key features of the stress history and loading conditions applying to a soil element located adjacent to driven pile. The critical aspects of the behaviour that need to be matched include: modest effective stress gains under low level cycling, abrupt losses of effective stress leading to failure in high level cycling and gradual losses of effective stresses at intermediate levels of cycling.

To achieve this, key features of the stress history and kinematic conditions of a single element of soil adjacent to a driven pile surface must be studied and properly modelled in laboratory single element tests. These features are:

- Matching the pile installation stresses.
- Applying conditioning pre-loading cycles.
- Allowing for creep and ageing.
- Considering a range of final cyclic loading conditions.

The aim will be to assess the effect of each of these features on the subsequent cyclic response and to design a “testing strategy” that models these features as closely as possible. The designed testing strategy will then be used to assess the cyclic response in a wide range

of cyclic loads and soil states. Obtained results will then be compared with field and model pile tests reported by Tsuha *et al.* (2012) and Jardine & Standing (2000, 2012) to assess whether they were able to replicate the results obtained from pile tests.

The other aim will be to study whether the cyclic response can be understood within the small strain frameworks available for sands behaviour. It was mentioned earlier that instrumented ICP model pile tests revealed that different modes of cyclic response can be understood using the kinematic multi-yield surface model. To do this, a series of monotonic tests will be performed to capture the small strain data of the tests sands along with their large strain ultimate behaviour. The results will then be used on an attempt to describe the cyclic responses obtained.

1.2 Thesis layout

This thesis is divided into ten Chapters, the first being this introductory chapter.

Chapter 2 presents a review of the current knowledge on the behaviour of sands under static and cyclic loading. The focus is on the small strain behaviour and kinematic multi-yield surface model along with critical state behaviour. In addition, results from a wide range of laboratory cyclic tests on sands are presented. These tests are performed using different laboratory apparatuses and have studied different modes of cyclic loading under wide range of soils states.

Chapter 3 presents a review of the current knowledge on the behaviour of driven piles in sands. It begins with monotonic behaviour of driven piles and presents methods presented to calculate the shaft and base capacity of piles. Later current knowledge on the behaviour of driven piles under axial cyclic loading is studied. The main focus is on the two specific projects supervised by Imperial College which are field pile tests on Dunkeruqe, France reported by Jardine & Standing (2000, 2012) and model pile tests reported by Tsuha *et al.*

(2012) and Rimoy (2013). Finally, a review on laboratory techniques and tests that aimed to replicate the conditions adjacent to pile shaft under axial cyclic loading is presented. These methods are then critically assessed.

Chapter 4 describes the laboratory equipment used for testing. It first presents the properties of the modified Bishop & Wesley triaxial apparatus used for monotonic and some of cyclic tests. It also gives an assessment on the capability of the triaxial equipment to apply accurate cyclic loads. It later move on to ICRCHCA apparatus which is an HCA apparatus equipped with resonant column system. A full description of the apparatus is given and also theoretical background on the interpretation of HCA tests and the drawbacks link to the presence of non-uniformities in the sample are presented. Finally adjustments made to enable the system to apply fast and accurate cyclic loads are discussed.

Chapter 5 presents a description of tests sands (Dunkerque and Fontainebleau NE34) and also gives results from extensive series of monotonic tests. Results from series of drained and untrained triaxial monotonic tests are presented and their small strain behaviour and ultimate critical state behaviour are studies. Special attention is given to the kinematic multi-yield surface framework since as discussed earlier it is believed that this framework can explain he cyclic response of test sands.

The aim in Chapter 6 is to develop a testing strategy that replicates the stress history and kinematic conditions of a single element of soil adjacent to a driven pile. Results from previous works reported (Chapter 3) are used to capture the key features that might have an impact on the cyclic behaviour of sand including stress history, ageing an pre-cycling. Effects of each of these features are then assessed in separate series of triaxial tests. Results are then used to design a “standard” testing procedure which will be tested extensively in cyclic triaxial and HCA tests in later chapters.

Chapter 7 presents results from triaxial cyclic tests using the "standard" testing procedure developed. First results from triaxial tests on a wide range of cyclic loads on both test sands are presented. Degradation of mean effective stresses, accumulation of permanent strains and degradation of cyclic stiffness values are studied in these undrained tests. It later presents results from "standard" tests that assessed the effect of initial void ratio on cyclic response using results from tests on specimens with initial void ratios ranging from relatively loose to dense specimens. Finally it presents results of drained triaxial cyclic tests with "standard" pre-conditioning procedure.

Chapter 8 presents results from HCA cyclic tests using the "standard" testing procedure developed on both test sands. It first discusses the adjustment made to the "standard" testing procedure to fit it for HCA tests since it was originally developed based on triaxial test on Chapter 6. It later presents results from HCA cyclic tests with special focus of effective stress and cyclic stiffness degradations.

In Chapter 9 attempts will be made to compare the soil element tests' behaviour with the cyclic field pile tests reported by Jardine & Standing (2000, 2012) and the model pile tests of Tsuha *et al.* (2012). The aim is to assess the applicability of the laboratory stress path element tests predicting the cyclic behaviour of piles.

Finally Chapter 10 gives the conclusions made and offers suggestions for further works.

CHAPTER 2
Monotonic and cyclic behaviour of sands

Introduction

The small strain and yielding characteristics of sands have been studied extensively over the last few decades. Advancements in testing techniques have led to a greater understanding of sand response especially at very small strains and different frameworks have been proposed to capture the key features obtained from experimental tests. The behaviour of sands under cyclic loading also been researched extensively in recent years. Sand's cyclic responses are particularly important in seismic studies where cyclic loading might lead to liquefaction. It is also important for the design of foundation of structures that experience cyclic loading during their working life. This chapter reviews, current understanding of sand's monotonic and cyclic response aiming to help understand the behaviour of sand elements located adjacent to pile shaft undergoing monotonic or cyclic loading.

2.1 Pre-failure behaviour

It is now well know that soil behaviour is largely in-elastic when loaded from small strains to ultimate failure or large volume strains. Traditionally, the term 'yielding' referred to the first

onset of plastic behaviour and in most cases, the break from a linear to non-linear stress-strain relationship. Historically the region of stress space within which sand behaviour could be considered elastic was considered to be extensive. Improved laboratory testing techniques (see for example Jardine *et al.* (1984) and Tatsuoka & Shibuya (1992)) have demonstrated that the "elastic" region of stress space is in fact very small for uncemmented sands and that their yielding is a progressive process in which first particle contacts yield, then inter-grain contact force chains buckle and finally large scale particle rotation takes place (Jardine, 1992). Progressive elastic-plastic models are now proposed that capture and predict this behaviour more accurately. These include multiple kinematic yield surface models such as those proposed by Mroz (1967) and Puzrin & Burland (1998) that aim to describe the non-linear behaviour of soils.

High-resolution laboratory tests with clays led Jardine (1992) to propose a multiple kinematic surface framework consisting of two kinematic surfaces (Y_1 and Y_2) inside the conventional yield surface (Y_3). Kuwano (1999), Kuwano & Jardine (2002) and Kuwano & Jardine (2007) later showed that a similar framework can be applied to sand. Figure 2-1 from Kuwano & Jardine (2007) shows the main features of this framework. The characteristics of each zone of behaviour are defined as:

Y_1 Surface: The Y_1 surface identifies the boundary to the region of effective stress space within which Tatsuoka & Shibuya (1992) and later Kuwano & Jardine (2002) identified a linear fully reversible stress-strain response. However, even this elastic range did not appear to satisfy fully the symmetry requirements of an elastic continuum. Jardine *et al.* (1999) and Kuwano & Jardine (2002) argued that this might be due to the discontinuous nature of granular materials. Another feature noted within the Y_1 elastic range was its cross-anisotropic and effective stress dependent nature. Kuwano (1999) and Kuwano & Jardine (2002) reported results from numerous axial and radial triaxial probing and bender element tests that

propagated and polarised shear waves in vertical and horizontal directions, combined with small amplitude axial or radial effective stress cycles to study the elastic response. Their results proved that partially elastic behaviour was confined to a very small strain range within which behaviour could be highly anisotropic. They found that the size and shapes of the Y_1 surfaces of Ham River (Thames Valley) and Dunkerque sands, as well as glass Ballotini were functions of void ratio, stress history (OCR), current effective stress and degree of creep ageing. Figure 2-2 shows the stress-strain diagram from one of the small stress cyclic tests on lightly overconsolidated (OCR=1.3) loose (Dr=25%) Ham river sand (HRS) reported by Kuwano & Jardine (2002). The boundaries of the Y_1 elastic surface were located at points where the initially linear stress-strain curves changed slope and became curved developing also finite irreversible plastic strains.

Y_2 Surface: This surface marks a boundary beyond which the pattern of straining as expressed by the strain increment vectors ($\delta\varepsilon_s/\delta\varepsilon_v$) can change and in which plastic strains develop much more rapidly leading to more significant energy dissipation. This surface can also be correlated with the thresholds beyond which a) permanent strains start to accumulate in cyclic tests (Kuwano & Jardine, 2002) and b) creep straining becomes important. Kuwano & Jardine (2007) identified their Y_2 surfaces primarily from changes in direction of the $d\varepsilon_s/d\varepsilon_v$ strain increment.

Y_3 Surface: This surface is the conventional geotechnical yield point associated with onset of marked loss of stiffness, contraction, dilation or abrupt failure. The Y_3 surface is identified as a point where the effective stress path direction changes sharply in undrained tests or where the strain increment direction changes direction markedly in drained tests. Another method to identify Y_3 yield points in either drained or undrained tests is to find abrupt change in tangent stiffness.

Y_4 Surface: Ishihara *et al.* (1975) identified an important feature of post-yield behaviour in granular materials when tested in states that are neither extremely loose nor very dense. Their shearing response often manifests contractive behaviour at moderate strains which changes abruptly at a certain stage to show a dilatant response. They termed this "yield point" the Phase Transformation Point (PTP). Ideal tests on granulate media should continue to dilate post PTP until they develop ultimate Stable critical states. In fact though most practical experiments develop shear bifurcations and form shear bands that truncate this process before uniform critical state are reached. Jardine *et al.* (2001) considered this behaviour to correlate with the micro-mechanical response of granular material after the buckling of the strong force network. Kuwano & Jardine (2007) proposed that the PTP points could be considered as Y_4 yield points within their kinematic multi-yield framework.

Kuwano & Jardine (2007) assessed the effects of factors such as OCR ratio and consolidation procedure on general shape of yield surfaces with triaxial tests on Ham river sand (HRS) and made the following conclusions:

1) The location, shape, alignment and size of the Y_1 surface depends on the stress history and current effective stress levels. The elongated shape of the kinematic surface is dragged behind the effective stress path during any large strain process such as consolidation or shearing.
2) The location of the Y_2 surface is affected by the relative location of the current stress point in relation to the Y_3 surface as well as the recent stress history.
3) The Y_2 andY_3 surfaces size increase with the current p′and are affected by K_0. Void ratio also has a significant effect and denser samples show bigger Y_3 surfaces.

Figure 2-3a shows the location of the Y_1, Y_2,Y_3 and Y_4 yield surfaces for lightly over consolidated loose HRS sand samples while Figure 2-3b shows the evolution of the Y_2

surfaces for loose HRS at OCRs between 1.0 and 4.0, after consolidation to p′=200 and 400kPa.

2.1.1 Stiffness of sands

Non-linear stress-strain response of sands leads to stiffness values falling rapidly with strain post Y_1 yielding. Kuwano (1999) and Kuwano & Jardine (2007) reported stiffness degradation curves from triaxial tests on HRS and Dunkerque sands (as well as glass Ballotini) and plotted the relative position of kinematic yield surfaces as shown in Figure 2-4. While extension and compression tests gave similar pseudo-elastic initial stiffness values, their curves diverged considerably post Y_1 yielding.

Stiffness anisotropy is another aspect of soil response that has been investigated by recent researchers. A soil mass that is deposited vertically and is subjected to equal horizontal stresses can be expected to possess cross-anisotropic properties, unless disturbed by other non-axial systematic loading. A generalised form of Hooke's law can be applied to relate the stress and strain increments for linear small strain range. Zdravkovic & Jardine (1997) investigated the post-Y_1 anisotropy of angular rock flour silt (HPF4) at low OCRs by HCA testing and concluded that the compliance matrix for these materials is non-symmetrical in the non-linear range (even at relatively small stresses) and its terms depend on the current effective stresses, the stress history (over consolidation ratio) and loading stress path (with different stiffness values achieved when the principal stress axes are rotated). Moreover, their results showed that the cross-coupling terms of compliance matrix are different in the non-linear range from the conventional form proposed by Love (1927). In particular shear straining could affect the normal strain components (causing vertical compression) while the inverse did not apply.

Kuwano & Jardine (1998) and Kuwano (1999) used triaxial apparatus equipped with multi-axial bender elements to study the cross-anisotropy of sand samples within the Y_1 yield surface. Kuwano argued that anisotropic elastic parameters could be obtained from axial and radial probing tests along with bender element S_{hh} (horizontally propagated and polarised) and S_{vh} (vertically propagated and horizontally polarised) shear wave velocity measurements by assuming a symmetrical compliance and rate independent response within the pseudo-elastic range. Results from hundreds of stress probing and bender element tests showed that cross-anisotropic moduli depend principally on void ratio and effective stress conditions, leading to the following empirical equations for estimation of individual cross anisotropic stiffness parameters for sands:

$$E_u = f(e).C_u.(p'/p_r)^{b_u} \quad \text{Equation 2-1}$$

$$E'_v = f(e).C_v.(\sigma'_v/p_r)^{a_v} \quad \text{Equation 2-2}$$

$$E'_h = f(e).C_h.(\sigma'_h/p_r)^{b_h} \quad \text{Equation 2-3}$$

$$G_{vh} = f(e).C_{vh}.(\sigma'_v/p_r)^{a_{vh}}.(\sigma'_h/p_r)^{b_{vh}} \quad \text{Equation 2-4}$$

$$G_{hh} = f(e).C_{hh}.(\sigma'_v/p_r)^{a_{hh}}.(\sigma'_h/p_r)^{b_{hh}} \quad \text{Equation 2-5}$$

Where C_u, C_v, C_h, C_{vh}, C_{hv}, b_u, a_v, b_h, a_{vh}, b_{vh}, a_{hh} and b_{hh} are material constants and p_r is the atmospheric pressure. The stiffness curves for HRS were nearly parabolic with a+b=0.5 while the stress dependency was higher in Dunkerque sand with a+b=0.6.

2.2 Critical state soil mechanics for sands and state parameter

The volume change behaviour of soil is different from that of most engineering materials. It is commonly known that when soils are sheared under drained conditions they change volume and that the volume change characteristics depend on the soil's state. These features are addressed in the critical state soil mechanics framework, first introduced by Schofield & Worth (1968) which is widely used for predicting the volumetric behaviour of clays. Several authors including Been & Jefferies (1986) and Coop & Lee (1993) have shown that the

critical state framework can be used to interpret sand behaviour and numerical critical state models for sands such as Jefferies (1993), Manzari & Dafalias (1997) and Taborda *et al.* (2014) have been proposed.

According to this framework, the volumetric behaviour of sand during shearing is highly non-linear and if the shearing is continued to high strains, it will reach a steady state were deviatoric stress (q) is constant and volumetric strains in drained tests and pore water pressure in undrained tests also become constant. This "critical state" depends only on the final void ratios and is independent of soil's initial density and structure. For each soil the locus of critical state points form a Critical State Line (CSL) which is usually presented in ν:Ln p′ space where ν=1+e and is classically (Coop & Lee, 1993; Papadimitriou & Bouckovalas, 2002) represented as a straight line parallel to assumed Normal Compression Lines (NCL) as:

$$\nu = \Gamma - \lambda . \ln p' \qquad \text{Equation 2-6}$$

Where Γ is the specific volume at p′=1 kPa and λ is the slope of the line in ν:Log p′ space. However, results from high pressure triaxial tests such as those on Leighton Buzzard sand presented by Been *et al.* (1991) or tests on Fontainebleau NE34 sand by Altuhafi & Jardine (2011) show a curved "overall" CSL mainly due to particle crushing at high pressures that change the sand's grading and grain shapes markedly, especially when p' >1MPa. It may be postulated that this "overall" curve reflects the locus of multiple CSLs, each one of which represents the current grading curve. However, Been *et al.* (1991) fitted multiple linear equations to their Leighton Buzzard sand data to account for the curved shape at higher pressures as shown in Figure 2-5a. While, Taborda *et al.* (2014) concluded that a better solution was the use of a power law relationship such as one proposed by Li & Wang (1998):

$$e_{cs} = e_{cs-ref} - \lambda\left(\frac{p'}{p'_{ref}}\right)^{\xi} \qquad \text{Equation 2-7}$$

Where ξ controls the curvature of the CSL and $e_{cs\text{-}ref}$ is the maximum void ratio under zero mean effective stress. Figure 2-5b shows the power law CSL fitted to the same Leighton Buzzard sand data.

Wood & Maeda (2008) studied the effect of change in grading during loading on sand properties using DEM analysis of two-dimensional assemblies. They proposed that changes in grading lead to asymptotic state appropriate to the current grading which will influence the critical state parameters. Results suggested that the location of critical state line moves lower in the specific volume:mean effective stress space as particle breakage progresses. Based on the results they proposed a new equation for critical state line to account for the effect of change in grading as:

$$\nu = \Gamma(I_G) - \lambda(I_G)\ln p' \qquad \text{Equation 2-8}$$

Where I_G is the grading index and varies from 0 (no crushing) to 1 (maximum crushing achievable). This equation leads into a series of critical state lines at different I_G values parallel to the virgin critical state line achieved from fresh sand with I_G=0.

2.2.1 State parameter

The combination of sand's density and its current effective stress level is known as its "state" and that state determines its volumetric behaviour under shearing. A state parameter may be defined as the relative distance of current location in volume:stress space from the CSL which is fixed for each soil.

Different parameters are proposed to quantify the soil state. The "state parameter" (ψ) proposed by Been & Jefferies (1985) is the most widely used, which is defined as the void ratio difference between the current location from the void ratio at CSL with equal p'.

$$\psi = e - e_{cs} \qquad \text{Equation 2-9}$$

Been & Jefferies (1986) showed that ψ can provide a useful normalisation for predicting sand response under shearing. Figure 2-6 shows results from tests on Kogyuk 359/10 sand with

different initial void ratios and mean effective stresses. It is shown that tests with similar ψ values exhibit similar normalised behaviours under shearing.

It has been argued that sand test specimens prepared in different ways develop different patterns of normalised behaviour. Konrad (1988) proposed a normalised state parameter to reduce the scatter in triaxial data and stated that the source for the scatter is due to difference in the fabrics of the sands tested. He normalised the data by diving the ψ by the difference between e_{max} and e_{min}.

$$\psi = \frac{\psi}{e_{max} - e_{min}} = \frac{\psi}{\psi_1} \qquad \text{Equation 2-10}$$

2.3 Cyclic behaviour of sands

The cyclic loading response of granular soils has been investigated extensively during the last few decades using triaxial, simple shear, HCA and ring shear tests. The following sections summarize key findings from some of the more significant studies.

2.3.1 Definition and modes of cyclic loading

The term 'cyclic loading' usually relates to a system of fluctuating loading that exhibits a degree of regularity in its magnitude variations and frequencies. Cyclic loads can be encountered in practice for example under highways, in foundations for rotary machinery or in offshore structures subjected to storms. While the periodic loads are rarely uniform, they are usually treated as uniform loads in both experiments and practical analysis to simplify test interpretation and design procedures.

The most common way to characterise and apply cyclic loads is to consider sinusoidal load variations and to set fixed cyclic amplitude, mean cyclic level load and frequency parameters for each suite of cycles. For example, for cyclic deviatoric triaxial tests the q_{mean}, q_{cyclic}, frequency and number of cycles, N, parameters defined in Figure 2-7 are sufficient to describe a suite of cyclic loads.

A soil element can experience different modes of cyclic loading in-situ and the soil response will vary depending on the imposed cyclic load. Table 2-1 offers an updated version of a schematic illustration presented by Jefferies & Been (2006) which summarises different modes of cyclic loading as:

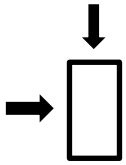
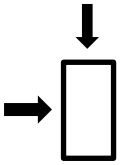
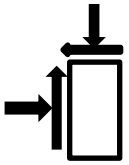
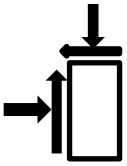
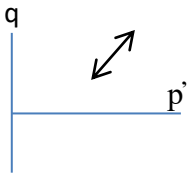
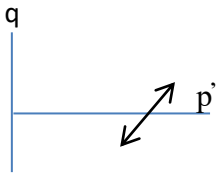
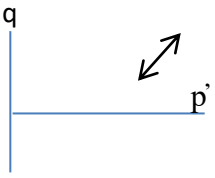
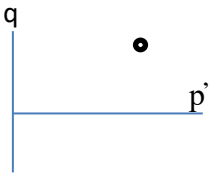
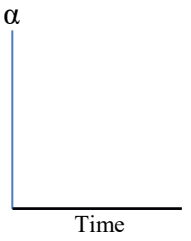
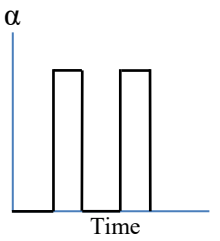
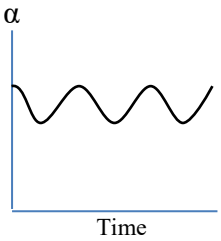
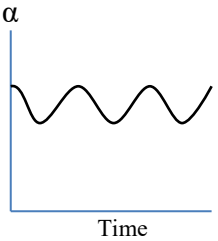
Type a: Asymmetrical loading that can be either one-way or two-way depending on the cyclic load amplitude that can model the in-situ response to axisymmetric triaxial cyclic loads accurately. In triaxial tests, the major principal stress direction changes if q_{cyc} exceeds q_{mean}.

Type b: Symmetrical loading around the isotropic axis, which is more common in triaxial laboratory tests, although it may not model in-situ ground conditions realistically because the soil state in-situ is often anisotropic. The major principal stress axis direction varies between 0 and 90° by jump rotations each time the cyclic stress point crosses the isotropic axis.

Type c: Moving away from purely axisymmetric triaxial cycling, cyclic shear tests can be performed in direct shear, simple shear or HCA apparatuses. The principal stress directions can be varied to follow a similar pattern to the cyclic pile shaft shear loading. However, it is not possible to define stress conditions fully unless such tests are performed in HCA apparatus

Type d: Cyclic rotation of major principal stress axis rotation without changing q-p′the co-ordinates. This special type of loading can be experienced under some forms of wave, earthquake or traffic loading (Ishihara & Towhata, 1983). This type of cycling can only be studied in advanced HCA apparatuses that have independent control of the q-p′, b and α parameters. This can only be achieved by having separate control over inner-cell and outer-cell pressures.

Table 2-1 Modes of single element cyclic loading (After Jefferies & Been, 2006)

Sample	 **Type a**	 **Type b**	 **Type c**	 **Type c**
Effective Stress Path				
Principal stress direction				

2.3.2 Sand cyclic loading response

The potential impact of cyclic loading on soil shear strength and stiffness properties of sands has been widely appreciated since the 1960s. Much attention has been given to seismic induced liquefaction of sands by authors such as Seed & Lee (1966), Castro (1975) and Ishihara (1993), who show that cyclic loading can lead to stress and stiffness degradation and potentially full failure in the form of complete loss of effective stresses in undrained tests, or loss of stiffness and accumulation of large strains in drained tests. In cyclic tests the aim has been to investigate the cyclic induced failure and to study the effects of different parameters that affect the cyclic resistance.

2.3.2.1 Cyclic failure

Cyclic behaviour of sands under drained and undrained conditions has been studied extensively. Drained cyclic tests have investigated on the accumulation of permanent strains and effective stiffness degradation, and are used for modelling relatively low frequency cyclic conditions where full pore pressure dissipation is possible, for example in the granular

layers placed beneath highways. In these tests the failure criteria has usually been defined as a certain level of accumulated permanent strains and in seismic studies it is usually set as 5% permanent strains. On the other hand, undrained cyclic tests have investigated the potential for effective stress drift and total stiffness degradation and liquefaction. They have been used in seismic studies where high rates of cyclic loading do not allow full pore pressure dissipation during shaking and special boundary conditions where response under constant volume conditions have been required. The conditions required to trigger undrained cyclic failure and liquefaction have been examined by many authors including Hyodo *et al.* (1994), De Gennaro *et al.* (2004), Georgiannou *et al.* (2008) who attempted to correlate the undrained cyclic response to monotonic behaviour. The following paragraphs summarises results from some of these studies:

Hyodo *et al.* (1994) reported results from monotonic and cyclic undrained tests on Toyoura sand to study the cyclic failure behaviour. Their correlation between monotonic and undrained cyclic tests showed that Unstable softening begins in a region between the CSR line (critical stress ratio line that connects q_{max} points from monotonic undrained shearing tests) and the failure line. They report that flow deformation occurs when $q_{max} = q_{mean} + q_{cyc}$ reaches the phase transformation line, as shown in Figure 2-8. De Gennaro *et al.* (2004) made similar conclusions from triaxial tests on Hostun quartz sand and concluded that liquefaction starts when the effective stress path engages the phase transformation line in compression or the extension monotonic failure line in extension as illustrated in Figure 2-9.

Georgiannou & Tsomokos (2008) investigated undrained cyclic failure under torsional loading using HCA apparatus to test Fontainebleau NE34 sand. Relatively loose samples (D_r ≈ 40-50%) were isotropically consolidated and cycled. Figure 2-10 shows results from one torsional undrained cyclic test where the sample was consolidated to $p' = 130$ kPa and cycled under stress controlled torsional sine waves with $\tau_{cyc} = 30$ kPa ($CSR=\tau_{cyc}/p'_0 = 23\%$). The pore

pressure response was most marked in the first cycle and pore pressures continued to increase steadily until the effective stress path reached the instability line (defined as a line connecting the peak points in monotonic shear tests). Further cycling from this point led to sudden increase in excess pore pressure and cyclic shear strains until the stress path eventually reached the phase transformation line (PTP) where contractive tendencies were replaced by dilative tendencies. At point 8 the specimen lost its strength and liquefied. The final two cycles developed large torsional shear strains, led to a butterfly shaped effective stress path. It was concluded that full instability was developed once the effective stress path reached the PTL line.

2.3.2.2 Cyclic resistance

The rates at which permanent strains and effective stiffnesses accumulate in drained tests or effective stresses and total stiffness degrade in undrained tests appear to depend on several factors including:

- The cyclic loading parameters and loading style
- Density/void ratio and effective stresses prior to cycling
- Stress history and preloading
- Specimen preparation method

Findings regarding each of the above parameters are summarised below.

- **Effect of cyclic amplitude on cyclic resistance (q_{cyc} in triaxial tests)**

Cyclic stress amplitude (composed to initial effective stress conditions) has been considered to be the most influential parameters in accumulation of strains in drained tests and effective stresses degradation rates in undrained tests. Numerous investigations have been reported on the effect of normalised cyclic amplitude on cyclic resistance of sands such as those by Silver & Seed (1971), Dobry *et al.* (1982), Vucetic & Dobry (1988) and Hsu & Vucetic (2004).

Dobry *et al.* (1982) investigated the effect of cyclic strain amplitude on several sands undergoing cyclic simple shear and concluded that a shear strain cyclic amplitude (ε_{cyc}) threshold exists below which soil shows no permanent volumetric strains in drained cyclic tests or no effective stress degradation in undrained cyclic tests as illustrated in Figure 2-11. They reported that the ε_{cyc} threshold for sands they investigated were around 0.01% strain in direction of axisymmetric cyclic loads. Vucetic (1994) expanded this concept to clayey soils and concluded that threshold value is higher in clays and roughly correlates with Plasticity Index (PI) of the soil. Hsu & Vucetic (2004) used results from cyclic drained and undrained tests with NGI Direct Simple Shear (DSS) apparatus to create a database for ε_{cyc} threshold for 7 sands and showed that at strain levels close to threshold ε_{cyc}, the behaviour becomes highly nonlinear with shear stiffness modulus (G) dropping to 55-80% of their maximum values.

The shear strain threshold concept can be understood using the kinematic multiyield surface model explained in previous sections. As noted, as long as the effective stress path is kept inside the Y_2 surface load-unload stress paths will not create permanents strains but once the Y_2 surface is engaged permanent strains start to accumulate and load-unload stress-strain loop opens. Therefore the shear strain ε_{cyc} threshold corresponds to engage the Y_2 surface. As shown by Kuwano & Jardine (2007), the size of the Y_2 surface in stress space depends on the stress history, effective stress level and void ratio. However, Dobry *et al.* (1982) reported that the strain threshold is independent of sand type, effective stress or initial state. The two sets of conclusions could be compatible if stiffness variations with sand type, state and effective stress level compensated for these factors. However, the simple shear tests suffer from several fundamental difficulties and give little information on the sands' detailed response at very small strains.

Dobry *et al.* (1982) reported that strain levels higher than the ε_{cyc} threshold lead to higher accumulated volumetric strains in drained tests and higher effective stress degradation rates in undrained tests.

- **Effect of stress anisotropy on cyclic resistance (q_{mean} in triaxial tests)**

Most triaxial studies into the cyclic response of sands have been performed under isotropic confining pressures. However, it is known that most sands in nature (either in undisturbed ground or adjacent to loaded structures) experience anisotropic stress conditions. The effects of stress anisotropy on cyclic resistance have been debated and some contradictory conclusions drawn in recent years. One group of authors have argued that existence of static shear stresses decreases strain accumulation rates in drained tests and reduce pore pressure generation rates in undrained tests (Seed, 1983). Others have pointed at that static shear stresses bring the initial effective stress states closer to failure envelope, leading to failure under smaller cyclic loading perturbations, as shown by Konrad (1993) in Figure 2-12.

Harder & Boulanger (1997) suggested that the effect of stress anisotropy on cyclic resistance depends on specimen relative density. They argue that the effect is positive for medium dense and dense sands (D_r = 55 to 70%) while it is negative for loose and relatively loose sands (below D_r = 50%). Yang & Sze (2011) investigated this proposal further by performing a series of cyclic triaxial tests with Toyoura sand in a wide range of relative densities and cyclic deviatoric mean stresses (q_{mean}) in undrained cyclic tests. Two different patterns of behaviour were observed in loose and dense specimens. For dense samples, cyclic resistance increased (larger q_{cyc} was required to reach liquefaction after 10 cycles) with increasing level of q_{mean} but in loose samples cyclic resistance initially increased with q_{mean} up to a threshold limit and decreased beyond that. Yang & Sze (2011) studied the q_{mean} threshold in critical state framework and pointed that this threshold value decreases with increasing values of ψ suggesting that the even for dense samples this q_{mean} threshold exists if the confining effective

stresses involved are sufficiently high. However, all their tests have been performed at relatively large levels of q_{cyc} and it has not been discussed how the q_{mean} value might affect the response under low level cycles. Moreover, effect of stress history on response has not been considered on these tests.

Tong *et al.* (2010) used a HCA apparatus to perform cyclic principal stress axis direction rotation tests at constant q-p′and b values to study the effect of stress anisotropy on drained cyclic response. Medium dense to dense Toyoura sand samples were anisotropically consolidated and subjected to drained cycles in which α cycled between 0 and 90°. Plastic deformations were induced during cyclic rotations and contractive volumetric strains accumulated as cyclic rotation continued while the rate of accumulation dropped as cycling continued. The rate of accumulation also depended on the intermediate principal stress parameter (b). The stress-strain hysteric loop was open in early cycles indicating clear plastic response and became closed and steeper as cycling continued, indicating that secant "stiffness" increased over the early cycles and tended to reach a steady state. Although most field cyclic conditions involve α changes combined with q and p′variations, these HCA tests emphasises the importance of principal stress axis rotation on sand's cyclic response.

- **Effect of relative density or state on cyclic resistance**

The effect of sand relative density on its cyclic response has been investigated since the early days of geotechnical cyclic testing. Authors such as Seed & Lee (1966), Ishihara (1975) and Tatsuoka *et al.* (1986) emphasised the positive effect of relative density on the cyclic resistance in both drained and undrained tests. For example, Tatsuoka *et al.* (1986) reported results from drained triaxial tests on Toyoura sand that showed the cyclic stress ratio ($CSR=q_{cyc}/p'_{mean}$) required to cause 5% double amplitude axial strain within 20 cycles increased with increasing relative density as shown in Figure 2-13. It was shown the cyclic

resistance increased sharply with D_r values and that when D_r<70% the cyclic stress ratio increased linearly with relative density.

The effects of relative density combined with effective stress level (state), on cyclic resistance have been investigated and interpreted with the critical state framework by Ruech (1997), Hyodo *et al.* (1998), Qadimi (2005), Qadimi & Coop (2006) and Yang & Sze (2011). According to this framework and considering that cyclic loads are larger than the "no effect threshold", loose samples with an initial state on the wet side (right) of the CSL should show contractive behaviour under cyclic loading. Provided a sufficient number of cycles are applied, a "flow failure" under undrained conditions should develop which is characterised with abrupt, runaway deformations is expected. On the other hand, a medium dense to dense sample whose state falls on the dry side (left) of the CSL is expected to show a "stronger" undrained response under similar loading conditions. If subjected to CSRs greater than the "no effect threshold" ratios, they should show a "cyclic mobility" response in which pore pressures accumulate at slower rates. This is because the rate of pore water pressure build-up in will be moderated by the dilative tendency applying under these "dry" states.

Qadimi & Coop (2006) performed undrained triaxial cyclic tests to assess the effect of specimen "state" on its cyclic resistance. As shown in Figure 2-14a, Three sets of samples were consolidated to reach initial states on the interpreted NCL line and also to fall to two lines parallel to the NCL, but positioned at different states to the left of the NCL. The specimens were then subjected to undrained cycles with q_{cyc}/p'_0 = 20%. Their normalised pore pressure trends (Figure 2-14b) indicated that samples tested at equal states gave similar pore pressure responses. Samples positioned on the NCL line showed the least resistance to cyclic loading while "dryer" specimens that were tested from "dry" states to the left of the NCL showed greater cyclic resistance and lower rates of pore pressure generation. Qadimi & Coop

(2006) did not identify any threshold condition. Even at their lowest cyclic amplitudes (q_{cyc}=5%p′), p′losses of up to 20% were recorded. Reviewing their testing procedure, it seems that non extended creep periods had been allowed prior to undrained cyclic loading. It is possible that ongoing compressive creep affected their low CSR experiments.

- **Effect of loading history on cyclic response**

Ovando-Shelley (1986) reported undrained cyclic triaxial tests on Ham River Sand (HRS) specimens. He showed that samples consolidated under approximately K_0 conditions and swelled to OCR=4 at on isotropic state (Path O-A-B as shown in Figure 2-15) could sustain a higher number of cycles than normally consolidated samples tested after consolidation on Path O-B under similar cyclic stress conditions.

Qadimi & Coop (2006) investigated the effect of over-consolidation on pore water pressure generation rates in undrained triaxial cyclic tests on crushable calcareous Dogs Bay sand. They found that isotropically consolidated samples that were swelled back to OCSRs of X and Y (C32i and C31i tests in Figure 2-14) generated far smaller pore pressures than tests that applied the same CSR=20% to normally consolidated samples.

- **Effect of Ageing in cyclic response**

The increase of sand stiffness and shear strength with time, which is known as the ageing effect, has been reported by several authors including Skempton (1986), Chow (1997) and Kuwano (1999). Increase in capacity of driven piles in sand has also been observed by Chow *et al.* (1997), Chow *et al.* (1998), Jardine *et al.* (2006) and Rimoy (2013). The effects of ageing on the cyclic response of sands are also significant. Seed (1979) reported results from undrained stress-controlled tests on sands aged between 1 day to 100 days prior to cycling. He reported that the liquefaction resistance of a specimen aged for 100 days was 25% higher

compared to one tested without aging. He extrapolated his data to larger aging periods to predict the liquefaction resistance of in-situ sand deposits.

- **Additional factors that influence the cyclic resistance**

The main factors that control cyclic resistance are known to be initial state, consolidation history and cyclic load characteristics. The following paragraphs consider two additional potential factors that have been investigated:

Loading frequency*:* Ideally laboratory cyclic testing frequencies should be similar to those experienced in-situ for the problem under consideration. However, in many cases apparatus (or time) constraints lead to the application of higher or lower than ideal frequencies.

Airey & Fahey (1991) reported results from triaxial tests on marine silica sand from the North-West shelf of Western Australia. Cyclic tests performed with frequencies between 0.05 to 10Hz that applied q_{cyc}=100kPa to specimens consolidated to p′ between 300 to 500kPa indicated no effect of frequency on the stress-strain response. However, higher pore pressures were measured in high frequency tests, although these are believed to reflect laboratory measurement errors rather than to be representative of the entire sample.

Salavati & Anhdan (2008) performed triaxial tests on dense Monterey sand with loading frequencies of 0.1 and 1.5 Hz under varying confining effective stresses. Their strain accumulation rates appeared greater under the higher loading frequency over the early cycles, but dropped to follow similar trends as cycling continued. Cyclic loading with different frequency on pre-cycled samples showed almost no difference in strain accumulation rates. In general the conclusion is that load frequency does not have major impact on cyclic resistance response.

Sample preparation method: Sand samples may be prepared by a range of techniques as “air pluviation” or “water pluviation” or “moist tamping”. Each results in a different formation fabric which affect their monotonic or cyclic strength and stiffness response.

Mulilis *et al.* (1977) reported results from a series of undrained triaxial cyclic tests with remoulded sand specimens from similar initial density levels (D_r=70%) but with different sample preparation procedures. Results from tests on Monterey No.0 sand showed variations in liquefaction resistance of up to 100% between the different specimens preparation procedures. However, results from similar tests on other sands showed lower variations. They concluded that the influence of sample preparation method on undrained cyclic resistance is a function of sand type and its angularity.

Mahmood *et al.* (1976) stated that the "water pluviation" method models the random orientation fabric of marine sands most closely since the grains come to rest gently under gravity and they take up positions that depend principally on their grain shapes. It appears advisable to follow this technique whenever possible

2.3.3 Modelling field cyclic loading in laboratory experiments

Field cyclic loading is usually irregular in terms of frequency and amplitude. For example, the wave and wind loading applied to offshore structures in storms is highly irregular in amplitude and presents a spread of frequencies. Although some authors (Tatsuoka *et al.,* 1986) have conducted irregular (random) cyclic loading in laboratory experiments, most researches have replaced the field event with packets of regular cyclic loading. Different methods have been proposed for how this should be undertaken. In the simplified methods proposed by Seed & Idriss (1971) irregular cyclic stresses are transformed into regular uniform cyclic loads of amplitude equal to 65% of the maximum irregular cycles' amplitude and having an "equivalent number" of cycles which means that same build-up of excess pore water pressure after cyclic loadings is applied.

In order to consider the total effect of packets of uniform amplitude cyclic loading, Miner's rule may be implemented. Miner's rule was developed from research into the fatigue of metals subjected to cyclic loading with varying amplitudes. According to Miner, if N_{fi} is the

number of cycles to failure at the i^{th} stress amplitude, $q_{cyc,i}$, the damage fraction imposed from varying amplitudes can be expressed as:

$$\sum_{i=1}^{n} \frac{n_i}{N_{fi}} = C \qquad \text{Equation 2-11}$$

Where n_i is the number of cycles applied with the amplitude $q_{cyc,i}$. C is the degree of damage ranging from 0 to 1. According to this rule, the sequence in which the amplitudes are applied is irrelevant.

Kaggwa *et al.* (1991) used drained triaxial tests to check the application of Miner's rule to their high amplitude (low number of cycle) tests on medium dense calcareous sand. A series of anisotropic triaxial cyclic tests with constant average p'_{mean}=266.7kPa and q_{mean}=200kPa and with three packets of 50 cycles with different amplitudes (q_{cyc}=100, 150 and 200kPa) were performed in different sequences. They considered that the sequence in which the three cyclic loading packets were applied hardly influenced the final values of the residual volumetric and shear strains. As detailed later, Wichtmann (2005) found that the sequence of cyclic loads has a modest, but not dominant effect on the overall rates of permanent strain accumulation.

2.4 High cycle accumulation model

Most of the research on the cyclic loading behaviour of sands has been focused on its behaviour under high amplitude cycles that lead to liquefaction failure in undrained tests or large strain accumulations in drained tests under low number of cycles (mostly below 50 cycles in most seismic studies). Behaviour under intermediate cyclic loading levels which exceed the no effect threshold, but are not high enough to cause failure within a few cycles has been studied in recent years. Gradual loss of effective stress in undrained tests or accumulation of permanent strains in drained tests under a large number of cycles ($N > 10^3$) can be problematic to model. Fully "implicit" numerical models that require multiple calculation increments over each cycle to predict the strain accumulation or effective stress

degradation are generally not yet suitable for modelling such intermediate cyclic loads because the accumulation of numerical errors and inaccuracies over the large numbers of cycles make it very hard to achieve reliable results. Therefore, implicit methods are generally limited to applications with N < 50. One solution applied in practice is to use "explicit" methods. In these methods only one cycle is modelled implicitly and cyclic degradation over the remaining cycles are predicted using empirical equations obtained from laboratory single element tests. Figure 2-16 illustrates the key features of implicit and explicit accumulation models.

Witchmann (2005) and Witchmann *et al.* (2005) reported results from several series of drained triaxial tests employing large numbers of cycles and small cyclic amplitudes. Their aim was to establish a comprehensive explicit predictive model that accounts for six factors that influence the cyclic response. Based on triaxial results they proposed an empirical equation to predict of the strain accumulation rate:

$$\dot{\varepsilon}^{acc} = f_{amp}\dot{f}_N f_e f_p f_Y f_\pi \qquad \text{Equation 2-12}$$

Where

$$\varepsilon^{acc} = \sqrt{(\varepsilon_1)^2 + 2(\varepsilon_3)^2}$$

f_{amp} Accounts for strain amplitude.

$\dot{f}_N$ Accounts for number of cycles and pre-cycling effects.

f_e Accounts for void ratio.

f_p Accounts for mean effective stress (p′).

f_Y Accounts for average stress ratio (q_{cyc}/p'_{mean})

f_π Accounts for direction of cyclic load applied in q-p′stress space.

The following paragraphs review the experiments that led to the above proposals and factors:

- **Influence of strain amplitude**

Witchmann *et al.* (2005) conducted drained constant stress amplitude tests to study how strain accumulation rates increase with stress amplitude. Figure 2-17a shows the accumulated strain ($\bar{\varepsilon} = \varepsilon^{acc} = \sqrt{{\varepsilon_1}^2 + 2({\varepsilon_3}^2)}$ trends after 10^5 cycles from tests on 8 different normally consolidated sands with d_{50}=0.1 to 0.52mm at q_{mean}=150 and p'_{mean}=200kPa, in specimens with D_r= 50 to 77%. Their results showed that strain accumulation increased with q^{amp} (q_{cyc}) and the rate of strain accumulation decreased with increasing mean grain size (d_{50}). The cyclic strain amplitudes generally decreased within the first 100 cycles under the lowest amplitude cycling, as shown in Figure 2-17b. The densification and contact distribution network developed under drained cycling increased the cyclic stiffness over these early cycles.

- **Influence of void ratio**

Witchmann *et al's.* trends for tests conducted at varying void ratios are shown in Figure 2-17. These experiments confirm that strain accumulation falls as relative density rises, which is also demonstrated in Figure 2-18a. The direction of the accumulated strains (ω as defined in Figure 2-18b) was found to be independent of both void ratio and strain amplitude as shown in Figure 2-18b.

- **Influence of mean effective stress (p′)**

Witchmann *et al's.* analysis of drained triaxial tests with constant cyclic stress ratio (η=CSR= q_{cyc}/p'_{mean}) and mean effective stresses between 50 and 500kPa showed strain accumulation trends were almost independent (in normally consolidated specimens) of p′over this range as shown in Figure 2-19. However, due to the non-linear effective stress dependency of stiffness, the strain amplitude in each cycle increased with increasing p′under constant CSR values. These results, suggest the sand "state" had little effect on cyclic response over this

stress range, which is in contrast with the earlier work reported in section 3.3.2.2. However, Witchmann *et al's* tests were performed over a modest p′ range. Tests at higher effective stress levels could show different trends.

- **Influence of mean cyclic stress** (q_{mean}/p'_{mean})

Drained triaxial experiments by Witchmann *et al.* employing with different q_{mean}/p'_{mean} ratios showed strain accumulation rates increasing with q_{mean}/p'_{mean} under constant q_{cyc} loading, as shown in Figure 2-20a. The mean stress ratio was found to influence the direction of strain accumulation strongly as shown in Figure 2-20b.

- **Influence of number of cycles and cyclic preloading**

The overall characteristic curves relating the accumulated strain $\bar{\varepsilon}$ with number of cycles (N) are illustrated in Figure 2-18 to 2-20a. Witchmann *et al.* (2009) suggested that for uniform sands ($1.3<U_c<1.9$), the $\bar{\varepsilon}$ curves are almost semi logarithmic, varying nearly linearly with ln(N) up to $N\approx10^4$, but become over-logarithmic at larger N values. For more non-uniform sands ($U_c>3.2$) $\bar{\varepsilon}$ grew at "faster than logarithmic" rates.

Effects of cyclic preloading: Witchmann (2005) studied the effects of pre-cycling by performing tests with four consecutive regular packages of cycles, each consisting of 25,000 cycles. Samples were tested at p'_{mean}=200kPa q_{mean}=150kPa at target D_r=60%. Each package had a different q_{cyc} (20kPa, 40kPa, 60kPa and 80kPa) and different q_{cyc} sequences were applied in each test. He showed that, for the sequences considered, the final $\bar{\varepsilon}$ values is only moderately (±10%) dependent on the sequence of cyclic load packages, as shown in Figure 2-21. Moreover, the directions of the accumulated strains were not influenced significantly by the consecutive packages of cyclic loading.

Witchmann (2005) proposed from his experiments, empirical equations for each of the factors considered above, as listed in equation 3-10. These factors are given in Table 2-2.

Table 2-2 Summary of functions and material constants from high cycle accumulation model by Whitchman (2005)

Influencing parameter	Function	Parameters
Strain amplitude	$f_{amp} = \min\{\left(\frac{\varepsilon_{cyc}}{\varepsilon_{cyc-ref}}\right)^2 ; 100\}$	ε_{cyc} = cyclic amplitude $\varepsilon_{cyc-ref} = 10^{-4}$
Cyclic preloading	$\dot{f_N} = \dot{f_N}^A + \dot{f_N}^B$ $\dot{f_N}^A = C_{N1}C_{N2}\exp[-\frac{g^A}{C_{N1}f_{amp}}]$ $\dot{f_N}^B = C_{N1}C_{N3}$	C_{N1}, C_{N2}, C_{N3} = material constants $g^A = \int f_{amp}\dot{f_N}^A dN$ N=Number of cycles
Average p′	$f_p = \exp[-C_P(\frac{p'_{mean}}{p'_{ref}} - 1)]$	C_p = material constant $p'_{ref} = 100\text{kPa}$
Average q_{cyc}/p'_{mean}	$f_Y = \exp(C_Y\overline{Y^{av}})$	C_Y = material constant
Void ratio	$f_e = \frac{(C_e - e)^2}{1+e}\frac{1+e_{ref}}{(C_e - e_{ref})^2}$	C_e = material constant $e_{ref} = e_{max}$

2.5 Summary and conclusions

This chapter offered a brief review of recent developments concerning the monotonic and cyclic behaviour of sands. The small strain behaviour and yielding characteristics of sand were discussed and the critical state framework for behaviour at larger strains summarised. The typical responses of the sands to cyclic loading were reviewed and factors influencing cyclic resistance discussed. Finally, an empirical high cyclic accumulation model for the volumetric behaviour at small strains was introduced. The following overall conclusions are made:

1- The Critical state framework, first introduced for clay also applies to the volumetric behaviour of sands at larger strains. The state of sands relative to the Critical State Line appears to control their behaviour under shearing.

2- Sand response is only linear and approximately elastic over a very small strain range within the yield surface defined in conventional critical state soil mechanics. Its behaviour is highly non-linear under stress or strain increments that are well within the conventional yield surface defined for granular material. Multiple kinematic yield surface models capture these features of behaviour in a more representative manner than conventional constitutive modelling.

3- Within the framework set out by Jardine (1992) the first kinematic yield surface Y_1 defines the elastic limit while the second Y_2 kinematic surface bounds the stress states within which load cycling can lead to permanent strains developing or, in undrained tests, mean effective stress changing.

4- The Initiation of cyclic induced failure in undrained tests is controlled by the third Y_3 yield surfaces boundaries that may be defined from monotonic tests.

5- The rates of cyclic pore pressure generation developed in undrained tests and strain accumulation under all conditions depend on sand state, cyclic loading parameters, stress history, ageing and testing techniques.

6- In general high relative densities or state parameters ψ, correlate with high cyclic resistance.

7- The effects of consolidation stress ratio $K_c=\sigma'_3/\sigma'_1$ have been debated in the literature. While some suggested that employing $K_c<1$ increases cyclic resistance, others have argued that initial deviatoric stresses bring the initial effective stress point closer to failure and therefore reduces cyclic resistance. Recent testing shows that the influence

of K_c depends on initial state. It appears beneficial, for dense (dry) states, but negative for looser (wet) conditions.

8- Stress history, creep ageing and pre-loading all have a major impact on cyclic resistance with over consolidated aged and pre-cycled samples showing greater resistances under similar loading conditions. These aspects allow more resistant contact grain fabrics to develop prior to cyclic loading and are critical to modelling the field response to cyclic loading adequately.

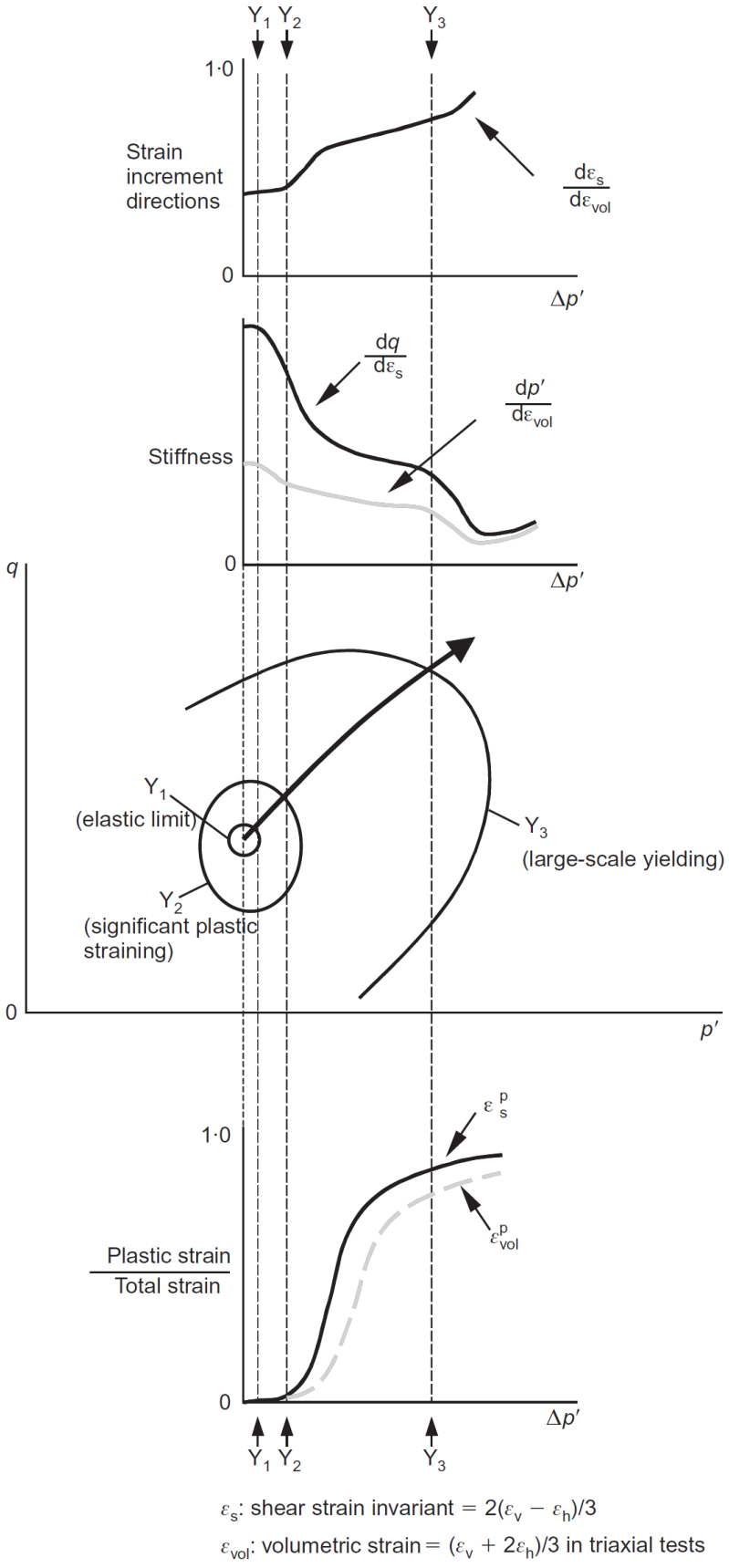


Figure 2-1 Scheme for multiple yielding surface framework after Kuwano & Jardine (2007)

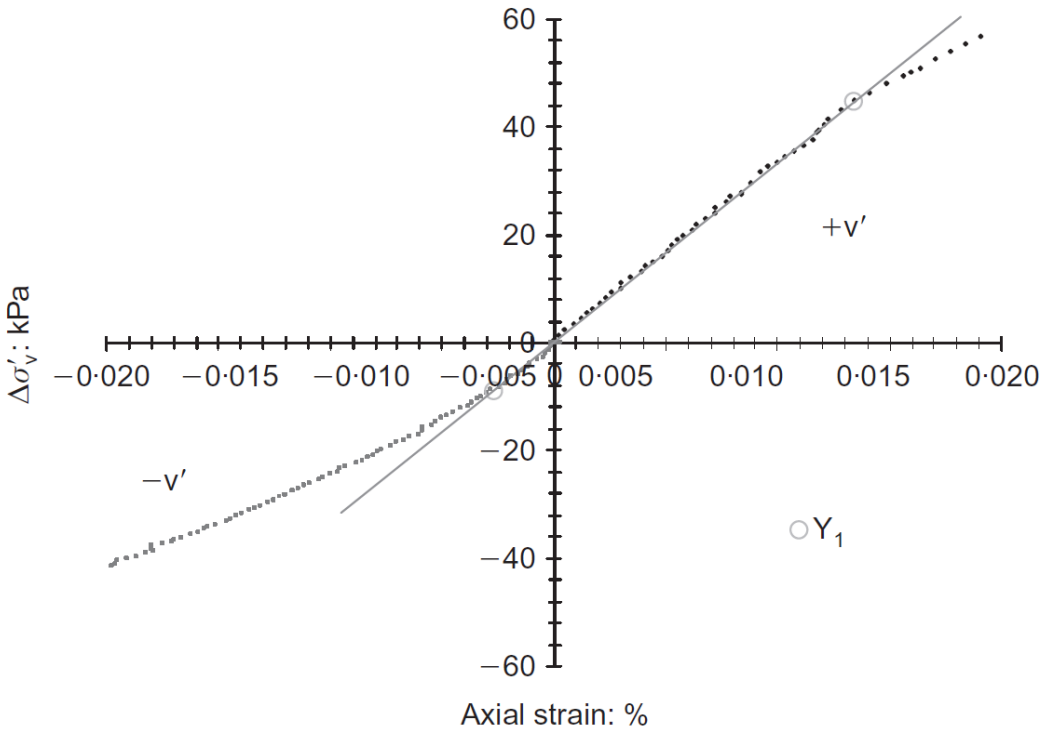


Figure 2-2 Stress-strain measurements at small strain in drained axial probing triaxial test to locate the boundary for Y1 surface (Kuwano & Jardine 2007) – HRS sand at D_r=25%, OCR=1.3 and σ'_v=243kPa.

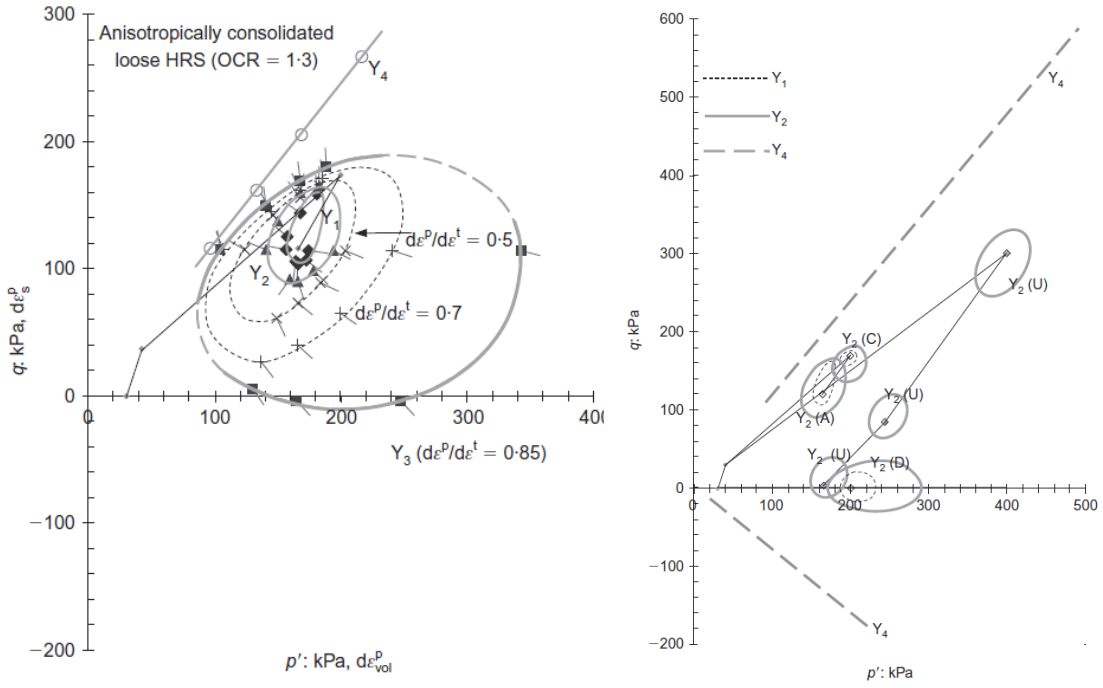


Figure 2-3 a) Location of yield surfaces in dense HRS sample and b) evolution of Y2 yield surface by stress history (Kuwano & Jardine, 2007)

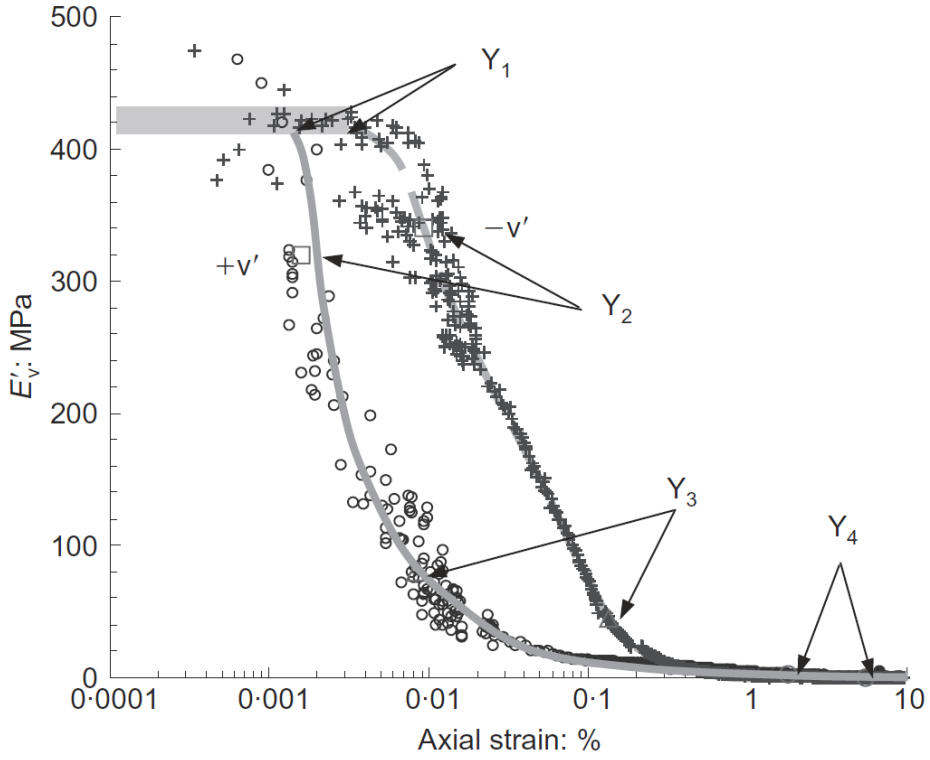


Figure 2-4 Tangent effective vertical stiffness of dense HRS sand on compression and extension tests shown in Figure 3-2 (Kuwano & Jardine , 2007). – HRS sand at D_r=25%, OCR=1.3 and σ'_v=243kPa.

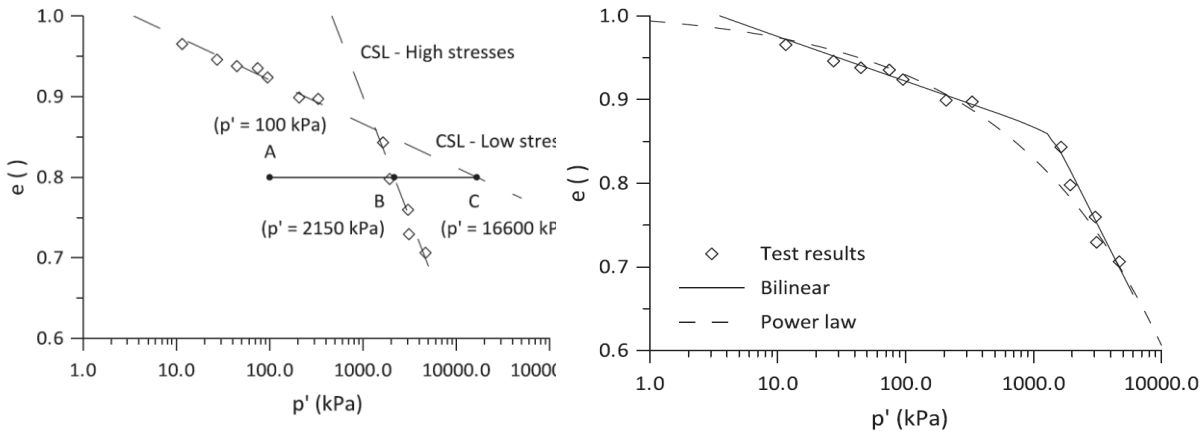


Figure 2-5 Fitting a) multiple linear lines and b) power law equations to critical state points in e-p′space (Taborda *et al.*, 2014).

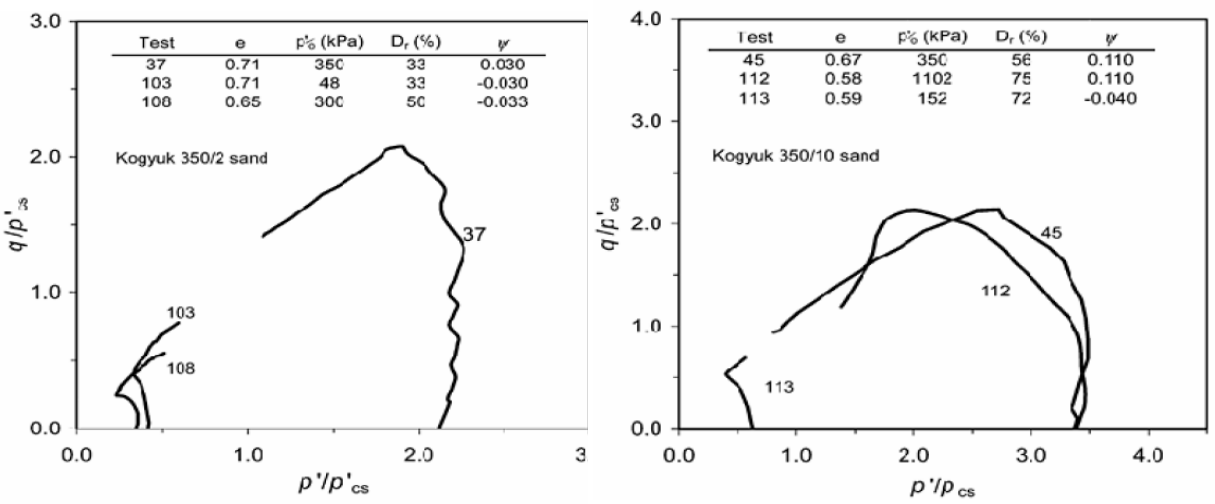


Figure 2-6 Comparison of behaviour as a function of state parameter for Kogyuk 350/2 and Kogyuk 350/10 sand (Jeffries & Been, 2006)

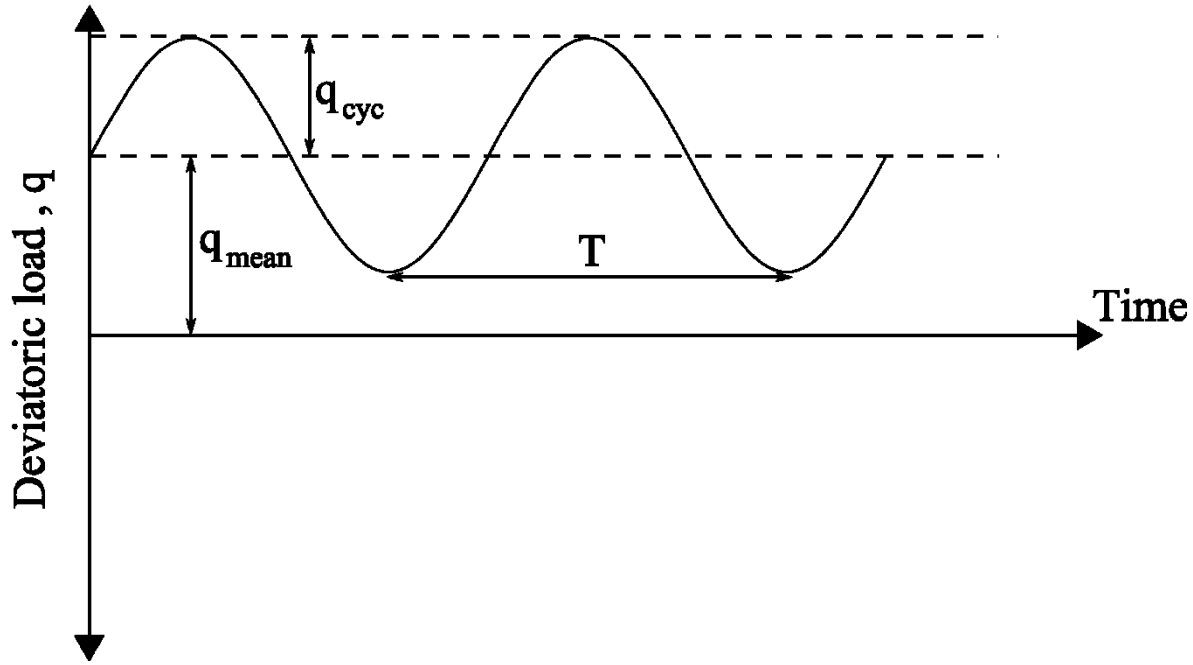


Figure 2-7 Cyclic parameters in triaxial conditions

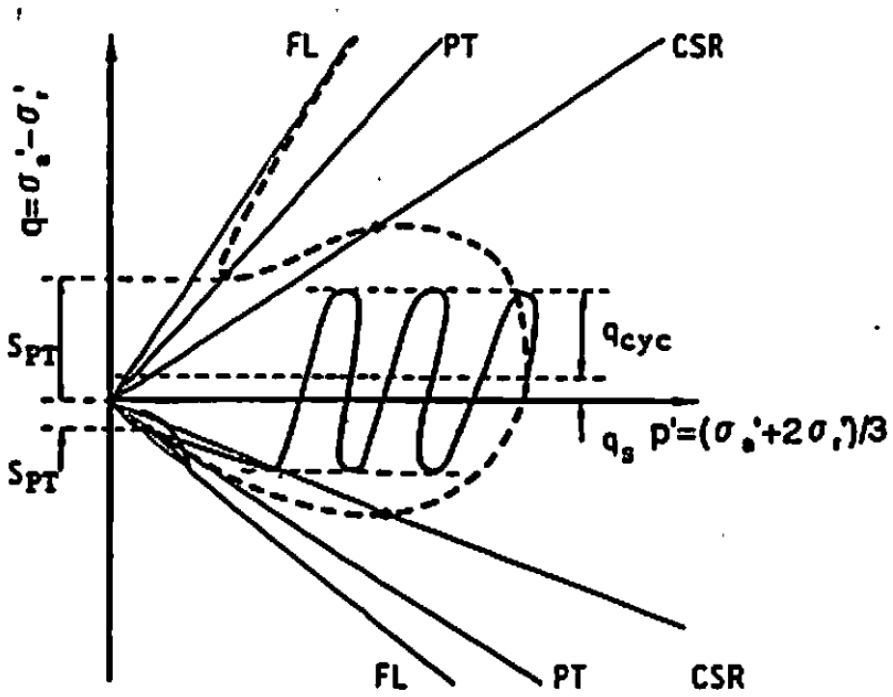
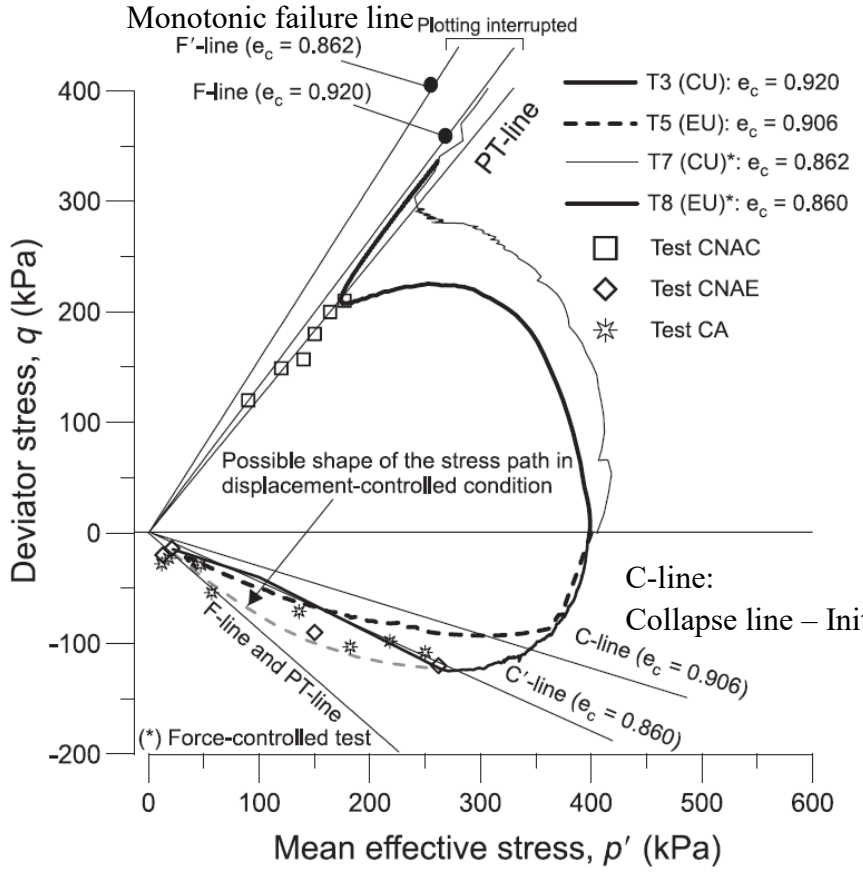


Figure 2-8 Schematic diagram for explaining the initiation of failure in effective stress path during cyclic loading (Hyodo *et al.*, 1994)



C-line:
Collapse line – Initiation of liquefaction

Figure 2-9 Comparison of points for initiation of instability and the monotonic stress path (De Gennaro *et al.*, 2004)

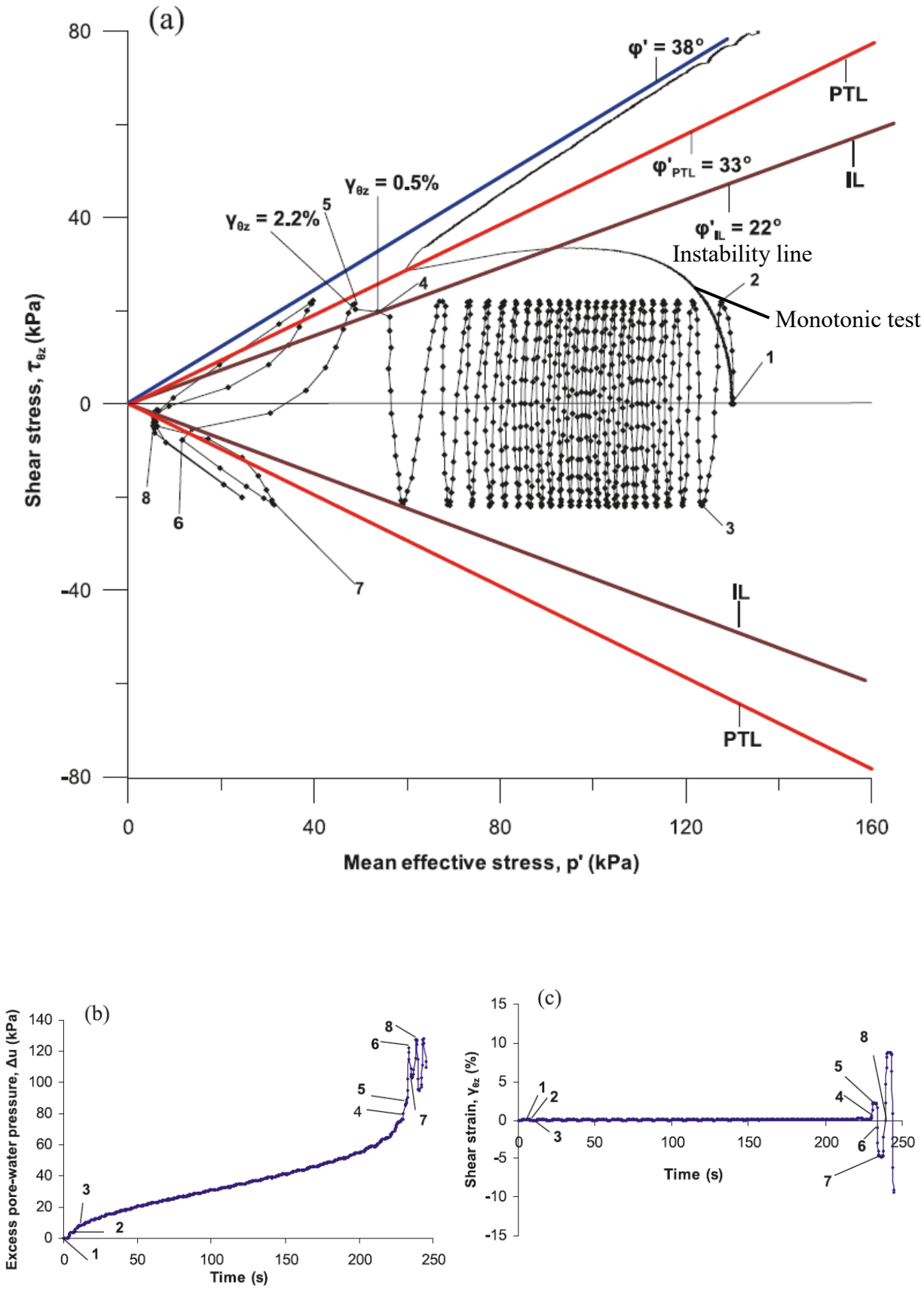


Figure 2-10 Undrained cyclic torsional HCA test on Fontainebleau sand a) Effective stress path b) excess PWP against time and c) shear strain against time (Georgiannou & Tsomokos, 2008)

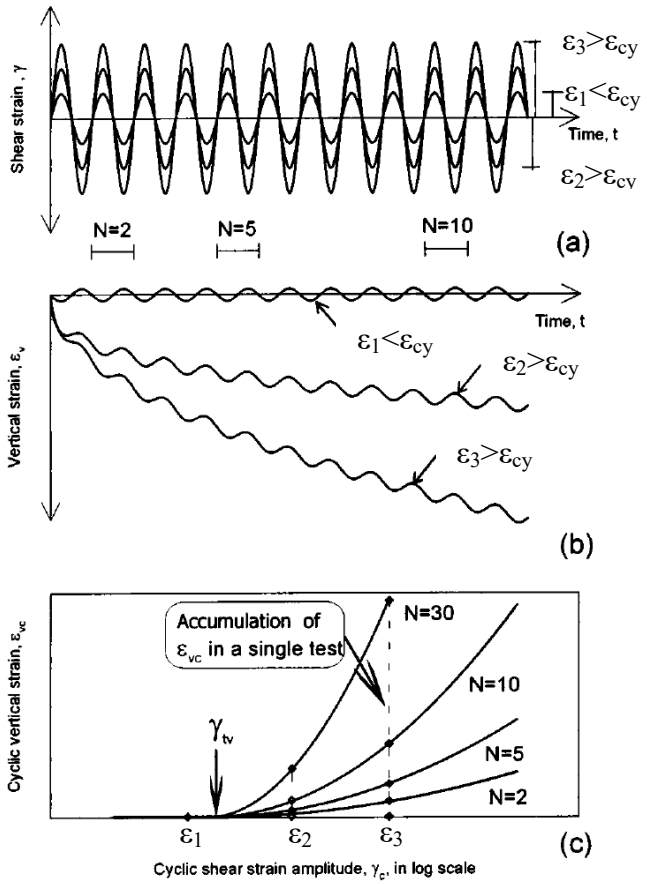


Figure 2-11 Illustrative sketches showing the definition of the no effect threshold in cyclic tests

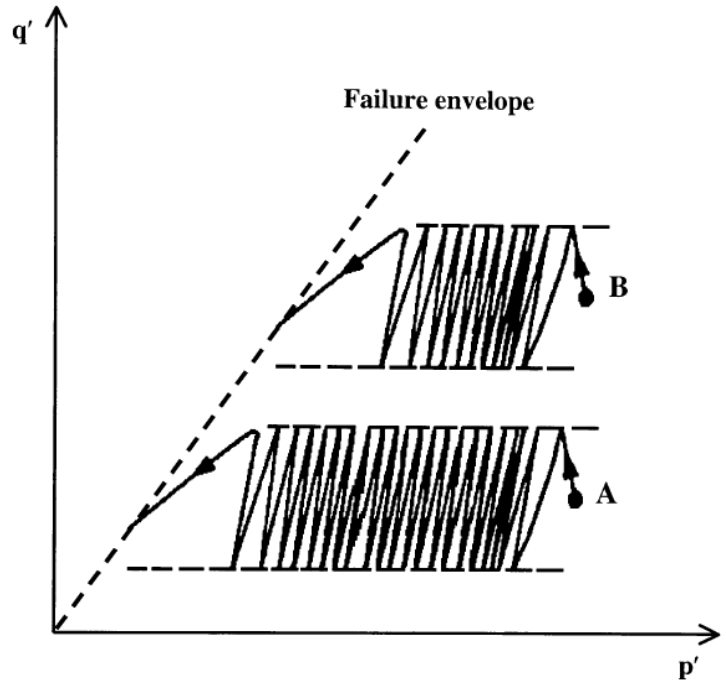


Figure 2-12 Schematic diagram illustrating the effect of initial stress anisotropy on the number of cycles needed for failure. (Konrad, 1993)

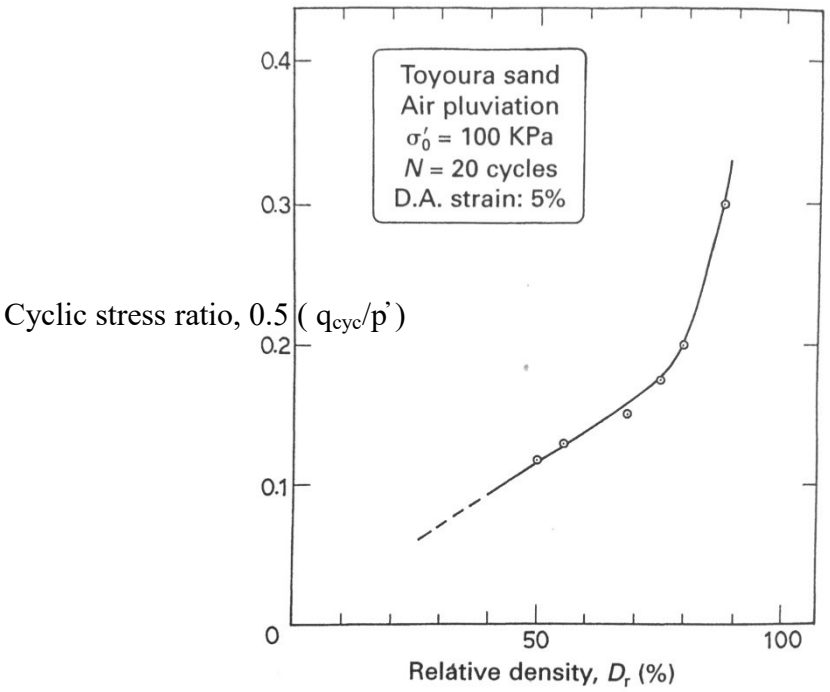


Figure 2-13 - Effect of relative density on cyclic strength (Tatsuoka *et al.*, 1986)

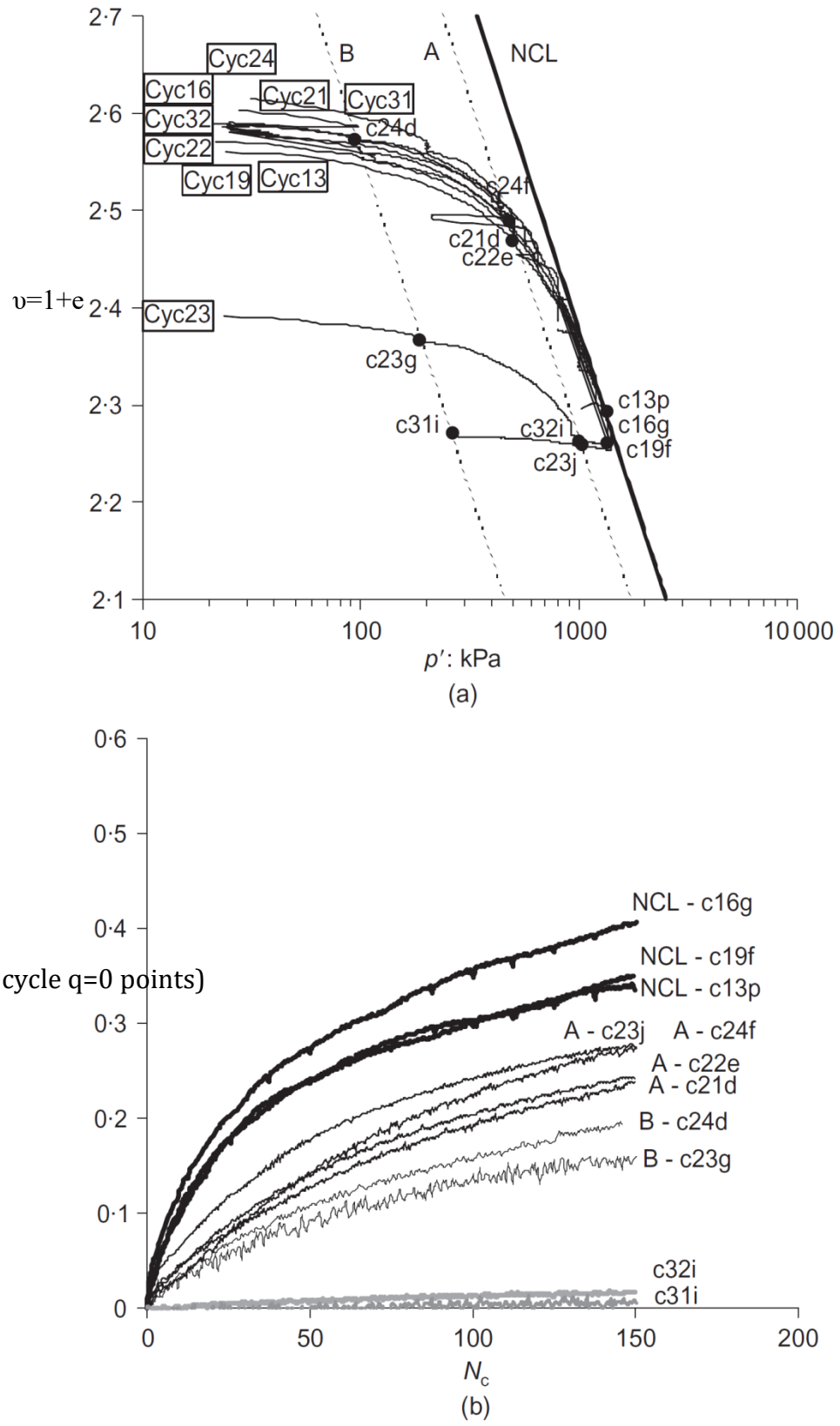


Figure 2-14 Pore pressure change for states on lines parallel to isotropic NCL line a) Initial states b) normalised PWP generated (Qadimi & Coop, 2006)

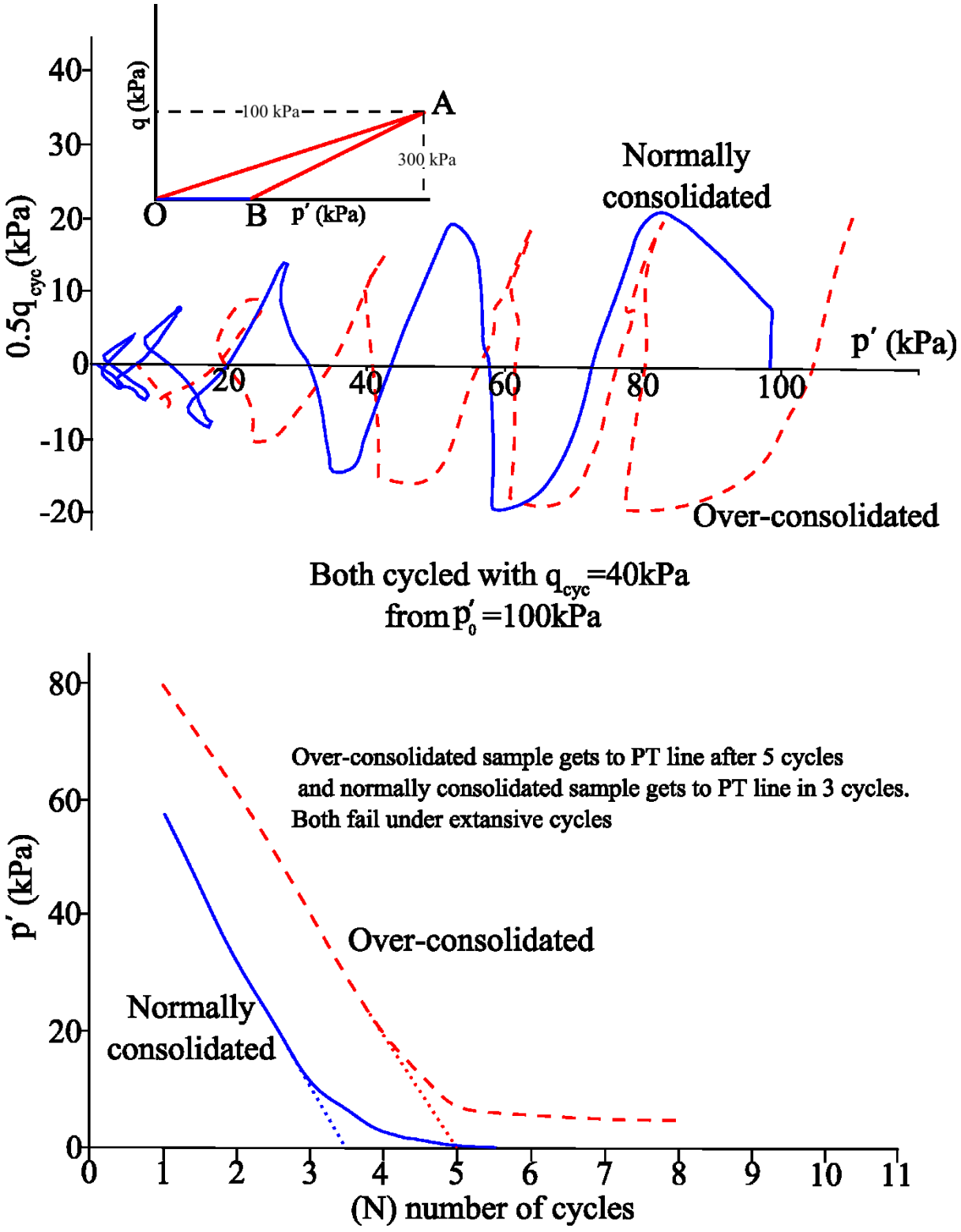


Figure 2-15 Undrained cyclic tests on HRS sand, samples with same initial stress state but different stress histories (Ovando-Shelley,1986)

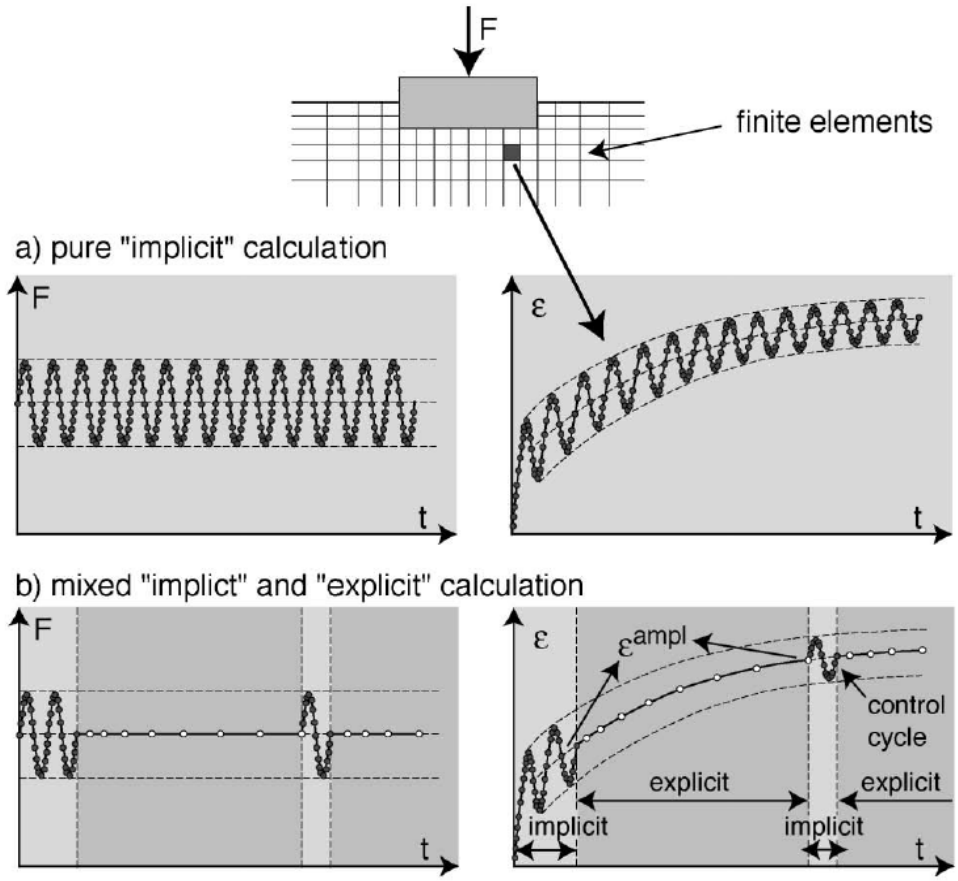


Figure 2-16 - illustration of implicit and explicit models (Witchmann *et al.* 2009)

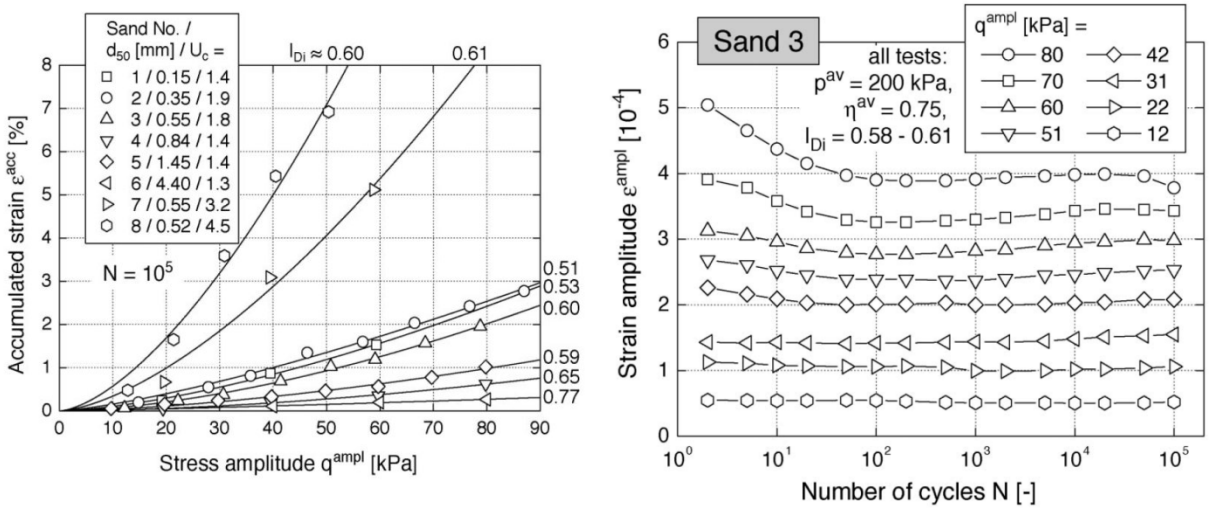


Figure 2-17 Accumulated strain after 10^5 cycles as a function of stress amplitude b) Development of strain amplitude with number of cycles. (Witchmann *et al.* 2009)

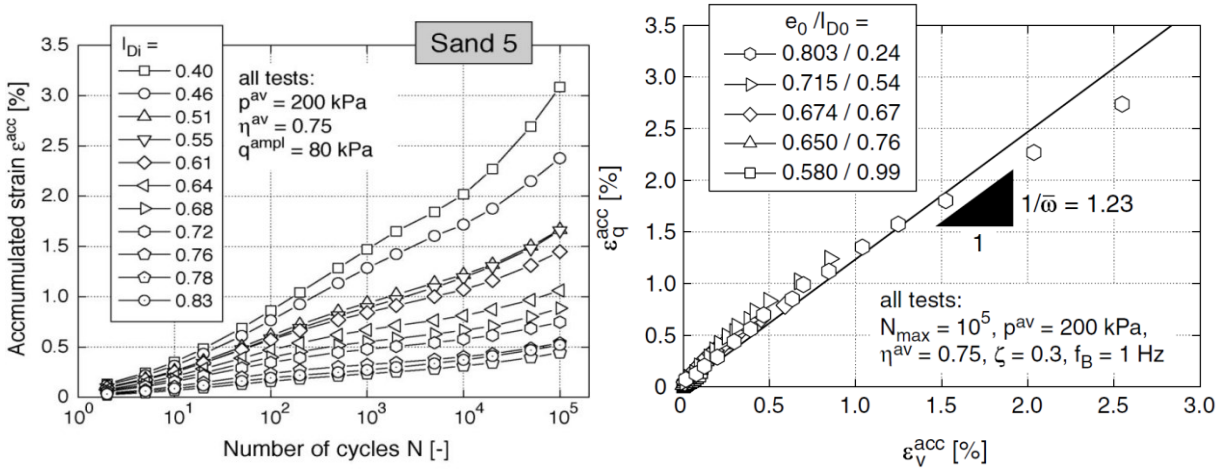


Figure 2-18 a) Accumulation of strains in tests with different relative densities b) direction of strain accumulation (Witchmann, 2005) ($\varepsilon^{acc}=\bar{\boldsymbol{\varepsilon}}$, η^{av}=CSR , $q^{amp}=q_{cyc}$, $p^{av}=p'_{mean}$)

\

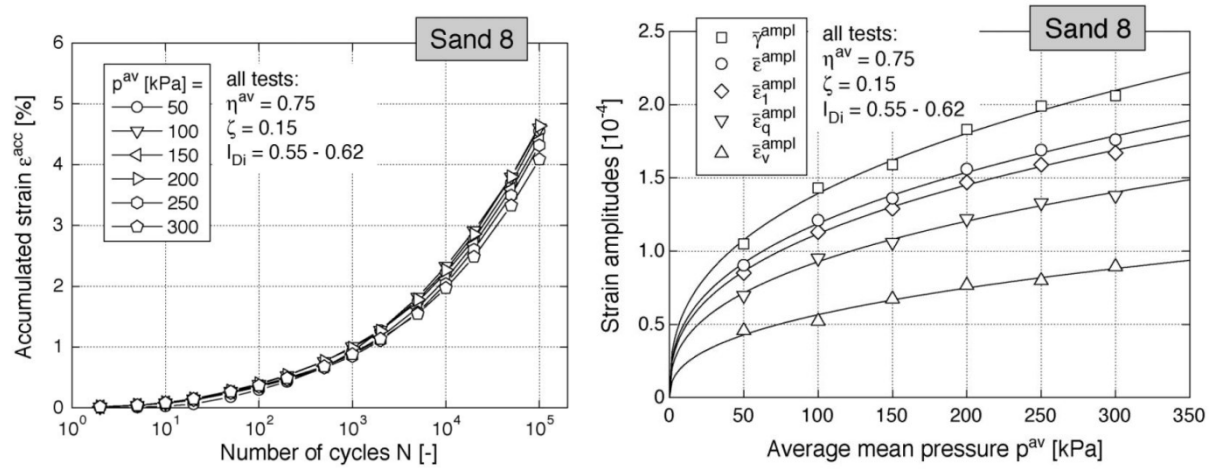


Figure 2-19 a) strain Accumulation curves in tests with different average pressures b) cyclic strain amplitude as a function of mean pressure (Witchmann *et al.* 2009)

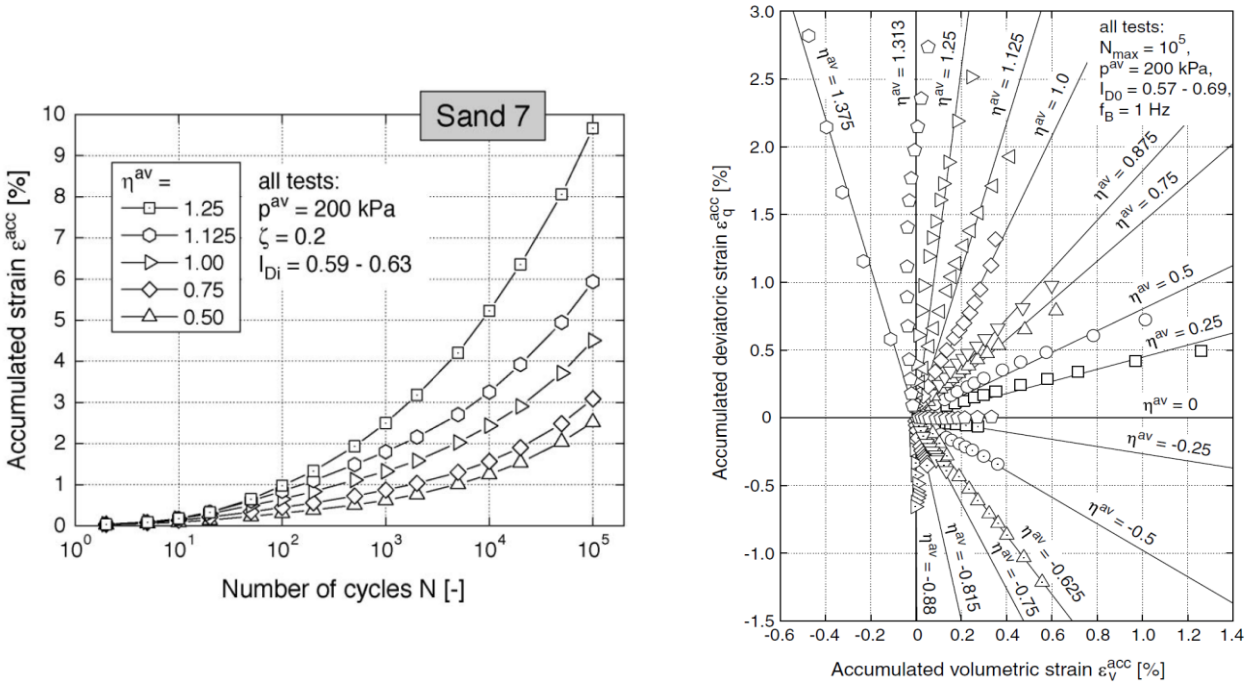


Figure 2-20 a) Accumulation of strains in tests with different average stress ratios b) Direction of strain accumulation with different average stress ratios (Witchmann, 2005)

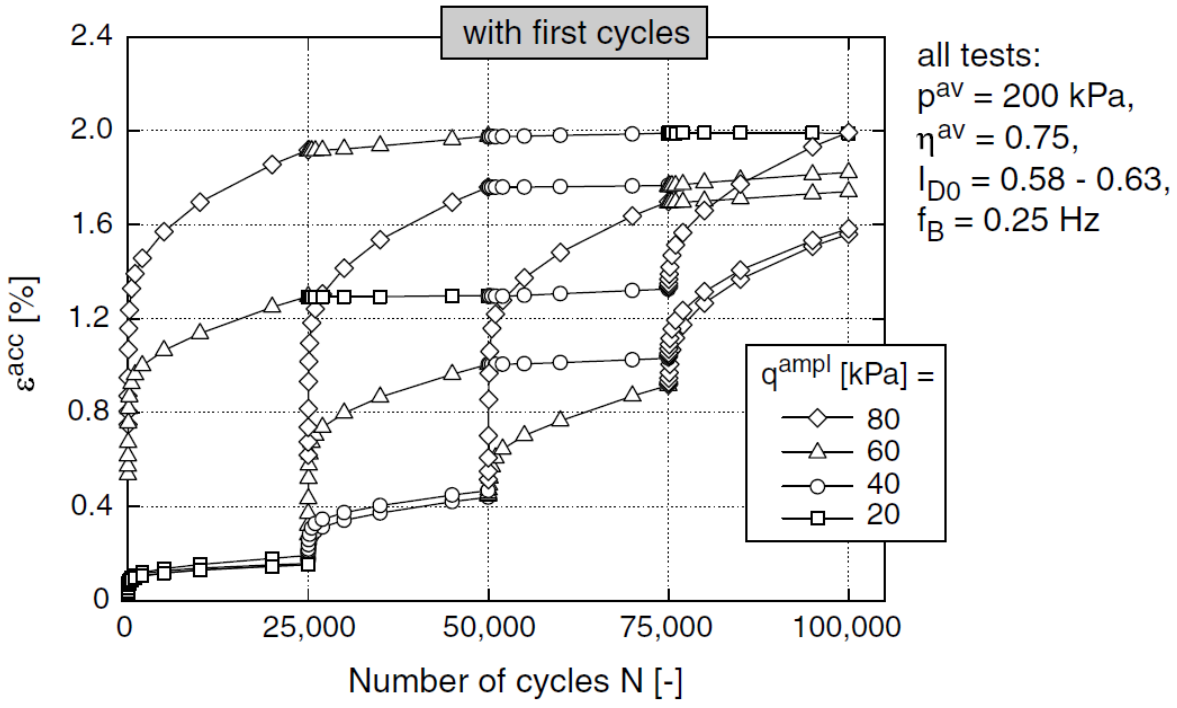


Figure 2-21Strain accumulation curves with different sequence of packets of cycles with different amplitude (Witchmann, 2005

CHAPTER 3
Monotonic and cyclic behaviour of pile foundations in sand

Introduction

Interest in the cyclic behaviour of offshore piles has grown in the recent decades as offshore platforms have become more efficient structurally and energy production has moved to deeper water and more dynamic environments. Offshore foundations experience a range of load cycles from intense storm loading to more gentle operating and tidal cycles. While axial cyclic loading effects were broadly considered negligible, from the 1960s onwards in most Gulf of Mexico and North Sea developments, investigation of the cyclic loading repose of piled foundations has become a growing topic in offshore geotechnical engineering research.

This chapter reviews current approaches for predicting the response of piles under axial monotonic and cyclic loading. Bearing in mind the topic of the thesis, a discussion is given on the role of laboratory tests designed to study the pile shaft load-displacement and capacity behaviour under such loads.

3.1 Axial static capacity of single piles in sands

The ultimate axial capacity of piles consists of two separate elements of shaft friction (Q_s) and end bearing capacity (Q_b). The end bearing capacity is the product of pile end area and

the unit end bearing and the friction capacity is the product of the outer pile shaft area and the unit skin friction. The ultimate capacity equation is therefore given as:

$$Q_u = \mathrm{Q_b} + \mathrm{Q_s} = \mathrm{q_p A_p} + \int f_p A_{si} \qquad \text{Equation 3-1}$$

Reliable, high quality pile load tests should be able to separately assess and measure the base resistance and shaft resistance distribution. To achieve this, the pile has to be equipped with on-pile strain gauges or other instrumentations. However, in practice most pile tests are not suitably instrumented. When instruments are provided they often fail during driving and if they survive beyond installation, they usually need to be re-zeroed carefully to overcome arbitrary shifts in readings that develop during driving.

Pile tests should involve sufficient displacements to mobilise the shaft and base capacities. Historically, the ultimate pile capacity is defined at a vertical pile head displacement of 10% of pile diameter (D_{pile}). However, piles driven in sands often require far larger displacements to develop their full base capacities (Chow, 1997). Fleming *et al.* (1992) proposed a hyperbolic relationship for bored piles that related end bearing pressure to the pile base displacement. With bored piles they expected end bearing pressures to reach only around 15-20% of the local CPT resistance, q_c, at a base displacement of 10% D_{pile}. However, for driven and jacked piles the base response is stiffer and significantly higher end-bearing stresses are generated at the same displacements (Chow, 1997; Randolph, 2003).

Historically, it has been difficult to predict the capacity of piles driven in sand accurately. Conventional methods based on earth pressure analysis (such as the API main text method) give relatively low reliability. Methods based on simple application of in-situ tests (such as the French cone method) can work better, but are still subject to considerable scatter and uncertainty (Lehane, 1992; Chow, 1997; Jardine *et al.*, 2005).

Over the past two decades there have been major improvements and advances in pile design approaches through field tests on instrumented piles by Lehane (1992) and Chow (1997) which revealed key features of stress regime adjacent to pile during pile installation, equalisation and loading to failure. These authors linked the base resistances to the sand state in-situ as represented by the CPT cone resistance q_b. The local shaft friction was also linked to q_c, the sand-shaft interface frictions angle, a geometrical factor relating to relative pile tip depth (h/R*) and the vertical effective stress σ'_v. New design methods were developed for estimating the base and shaft resistance for sands under axial loading as outlined below.

3.1.1 Base resistance

The conventional design approaches such as API RP2A (1969) for end-bearing resistance specifies empirical relationships that relate the ultimate end-bearing pressure to relative density, sand type and friction angle using a shallow foundation bearing capacity approach with a limiting bearing pressure as:

$$q_b = A_b \times N_q \times \sigma'_v \leq Q_{b-max} \qquad \text{Equation 3-2}$$

Where N_q is a dimensionless bearing capacity factor and varies from 12 to 50 depending on the grain size and relative density of the material. Table 3-1 shows a summary of different categories of sand and silt and recommended pile design parameters, as in the main text of API RP2 GEO (2014) documents.

Equation 3-2 predicts that end-bearing resistance increases linearly with depth under offshore conditions in uniform sands. However, the API rules specify a range of limiting maximum values that depend on the sand grading and density. Both of these outcomes have been challenged by experimental research in recent years:

- *Linear rate of increase in depth:* Field observations by Lehane (1992) and Chow (1997) showed that end bearing fluctuates markedly with depth, rising and falling with local cone resistance q_c. Randolph *et al.*, (1994) suggested that non-linear rates of end-bearing resistance increase with depth might be due to: a) reduction in ϕ′with σ'_v therefore reduction of N_q and b) confined failure beneath the pile tip which entails the end-bearing resistance being affected by the soil stiffness which is non-linear in nature as well as its shear strength. As a result, the bearing capacity will be a function of both ϕ′and the rigidity indices (G/p′) of the material. However, the variations found experimentally were far greater than might be anticipated from the two above factors. End bearing appears more directly related to q_c, which can vary by factors of ten or more over shaft depth ranges in sands.
- *Limiting end bearing resistance:* The assumptions of the conventional API method for a limiting end-bearing pressure to apply in the field was challenged by Vesic (1970), Kulhawy (1984). Lehane (1992) and Chow (1997) who demonstrated that the limiting pressures can easily be exceeded, especially in dense sands.

Table 3-1 API RP2 GEO (2014) recommended practice for pile base capacity design. Note: Cases for which method cannot be applied are indicated as NA.

Density index, D_r (%)	Soils description	Nq	$q_{b,lim}$ (Mpa)
Very loose (0-15)	Sand	N/A	N/A
Loose (15-35)	Sand		
Loose (15-35)	Sand-Silt		
Medium (35-65)	Silt		
Dense (65-85)	Silt		
Dense (65-85)	Gravel		
Medium (35-65)	Sand-Silt	12	3
Medium (35-65)	Sand	20	5
Dense (65-85)	Sand-Silt		
Dense (65-85)	Sand	40	10
Very dense (85-100)	Sand-Silt		
Very dense (85-100)	Sand	50	12

Noting the existing short comings of the proposed methods, several groups have proposed improvements that start from a range of perspectives. One theoretical solution is to apply an analogy between spherical cavity expansion and bearing failure and applying it to the case of a closed-ended (or fully plugged) flat-based pile by assuming a rigid cone beneath the pile tip with the angle α (Figure 3-1) which is determined by the friction angle of the soil (Gibson, 1950). By assuming that the soil beneath the pile tip has been sheared to its ultimate state and taking the angle α as $45+\phi'_{cs}/2$; the relationship between end-bearing pressure q_b and the limit pressure p_{lim} was given by Gibson (1950) as:

$$q_b=p_{lim}\,(\,1+\tan\phi'\tan\alpha) \qquad \text{Equation 3-3}$$

Spherical cavity expansion analysis are then undertaken to establish p_{lim} as a function of the sand's pressure dependent and non-linear stiffness, shearing resistance and dilatancy characteristics.

The method tends to predict a non-linear increase in end-bearing pressure with depth and so gives better predictions. Despite requiring a detailed list of elastic and plastic input parameters for analysis (Randolph, 1994), it is unlikely to be able to capture the marked fluctuations with depth in base resistance seen in field experiments.

An alternative approach is to relate end-bearing resistance directly to in-situ CPT tests. CPT cones have similar geometries to closed-ended piles and are able to record continuous or semi- continuous profiles under most conditions (provided suitable equipment is deployed). CPT based methods can be classified into two types as summarised by Cai (2008). First are direct approaches where the unit end bearing capacity of the pile (q_b) is evaluated directly from the cone tip resistance (q_c). The second type employs indirect approaches in which CPT results are used to evaluate parameters such as ϕ' that are then substituted into equations for

end bearing resistance. The direct approaches do not require intermediate parameters and are found to be more accurate compared to indirect methods and are used more common in practice.

The main challenge in direct CPT approach is to find the right relation between the q_b and q_c. Several methods such as ICP-05, FUGRO-05, NGI-05 and UWA-05 have been proposed to predict the base capacities based on CPT results. The range of ratios in these methods between q_b and q_c varies from 0.15 to 0.6 across a number of different methods and its dependence on scale effect has been a point of debate. Chow (1997) assembled a database of high quality pile load tests and added data from her tests on closed-ended piles driven into sand. A plot of q_b/q_c ratio against pile diameter from this database is shown in Figure 3-2 where the ultimate end-bearing resistance values (q_b) are mobilised at pile displacement of 10% D_{pile}. The design curve proposed by Jardine & Chow (1996) is also shown in Figure 3-2 that suggests the existence of scale effects on q_b/q_c for closed-ended piles. The ICP-05 design method by Jardine *et al.* (2005) recommended that the q_b/q_c ratio available for piles at displacements of 10% D_{pile} is less than 1 in sands and reduces with increasing pile diameter and suggested the following equation for base resistance for closed-ended piles:

$$q_{b,10\%D} = q_{c,average}(\max[1 - 0.5\log(D/D_{CPT}),0.3]) \quad \text{Equation 3-4}$$

For open-ended piles the base capacity was found to be contributed by small contribution from the pile internal skin-friction acting through the core soil column and the resistance beneath the area of the pipes. Chow (1997) suggested that piles with D_i>0.02 (I_D-30) and $D_i>0.083(q_{c,average}/p_a)D_{cpt}$, will core under axial loading where D_i is the internal diameter of the pile in meters and P_a=100kPa. The base capacity is then:

$$q_{b,0.1D} = A_r q_{c,average}\ , A_r = 1 - (\frac{D_i}{D})^2 \quad \text{Equation 3-5}$$

For other D_i values the base load capacity is given as:

$$q_{b,10\%D} = q_{c,average}(\max[0.5 - 0.25\log(D/D_{CPT}),0.15, A_r]) \quad \text{Equation 3-6}$$

Randolph (2003) questioned the existence of a link between pile diameter and q_b/q_c ratio for closed-ended piles by pointing that the data for small diameter piles in Chow's database are dominated by the jacked piles where the full cone resistance would be mobilised at each stroke and high residual stresses would be retained. By removing the small diameter pile data he suggested a value of 0.4 independent of pile diameter for q_b/q_c ratio. White & Bolton (2005) reassessed the same database and concluded that the outlying trend in Figure 3-2 for which $q_b/q_c < 0.5$ includes data from sites with SPT tests and pointed that by excluding sites which actual CPT data are not available the ratio can increase by almost the factor of two to 0.9 if the fully mobilised "plunging" large displacement capacity is considered and suggested that rather than the pile diameter, reduction factor should be linked to partial embedment and partial mobilisation. They argued that contained failure around the base does not cause shear bands to propagate along planes of slip-up in shallow foundations. However, Yang *et al.* (2010) later showed that shear bands did form around the mini-ICP piles in their calibration chamber experiments. Lehane *et al.* (2005) made a fresh interpretation of the pile test database and concluded that q_b/q_c could be taken as 0.4 for closed-ended piles. However, like Jardine *et al.* (2005), they found that the base resistance of open-ended piles tended to show q_b/q_c ratios that fell with increasing diameter, reaching a lower limit of q_b/q_c=0.15 for large open piles.

Another factor affecting the end-bearing resistance interpretation is the existence of residual loads during installation which are generated in driven piles. A schematic illustration of this phenomenon was illustrated by Alawneh & Malkawi (2000) as shown in Figure 3-3. Recording the residual loads requires continuous and separate recording of base and shaft

capacities during installation. However, the load cells in instrumented piles undergo high dynamic stresses and therefore are re-zeroed prior to pile testing. Randolph (2003) considered that end bearing interpretations would be non-conservative when high residual loads exist that are balanced by residual shaft shear stresses, leading to underestimation of shaft stresses and over estimation of base capacity.

3.1.2 Pile shaft resistance

The main focus in the Author's research is on the shaft friction response of pile under cyclic axial loading. The majority of early design methods for calculating static shaft resistance for piles in sand were derived by fitting to databases that comprised only a modest number of tests from a few sites (Gavin & Lehane, 2003). The most widely known and applied offshore pile design approach for ultimate shaft friction (q_s) in piles is the API approach that relates q_s to the radial effective stress indirectly using coefficient of earth pressure (K) and interface friction angle at failure between pile surface and soil mass adjacent to it using the following equation:

$$q_s = \sigma'_r \tan(\delta_f) = K\,\sigma'_v \tan(\delta_f)\,, \quad \text{now written as} \quad q_s = \beta\sigma'_v \qquad \text{Equation 3-7}$$

This method was first employed in the first edition of API RP2A and it did not consider the effect of sand density directly but instead the δ_f was estimated to be 5° less than ϕ' for medium-dense sands with the difference increasing with the grain size. Olson & Dennis (1982) emphasised the importance of relative density in addition to grain size in parameter estimation and edition of API RP2A (2014) addressed the effect of relative density on q_s by varying δ_f with both relative density and soil grain size while leaving K unchanged. The most recent API RP2 GEO (2014) still keeps the modified version of the earth pressure approach as its Main Text method, but adds more advanced methods its commentary section. The Main Text approach also imposes limiting shaft shear stress $\tau_{f,lim}$ values that lead, in uniform

sands, to shaft shear stresses increasing practically linearly with depth and reaching a fixed plateau below a certain depth.

Field research by Lehane (1992) and Lehane *et al.* (1993) with Imperial College ICP instrumented pile has revealed major shortcoming in different aspects of this approach which can be summarised as:

a) The values of $K=\sigma'_r/\sigma'_{v0}$ developed on pile shafts are far from constant with displacement piles. The shaft stresses are directly related to q_c.
b) Both field and laboratory tests show that δ does not depend on grain size and soil density as expected by the original API Main Text approach. Instead, the critical state δ' angle controls shaft resistance.

c) The ICP tests show that there is no limiting shear stress that acts as a cut off.

Research from Uesugi & Kishida (1986) and Jardine *et al.* (1992) revealed that there is no evidence that critical state δ_f should vary with the in-situ density of the sand. It was shown that interface friction angle is most strongly affected by the ratio of grain size to pile roughness and increases with decreasing grain size, employing the opposite trend to that suggested in the original Main Text API approach.

Fundamental improvements have been made in understanding the distribution of ultimate shaft friction with depth through field tests. These started with Vesic's (1970) observation that his field data was not constant with K being constant with depth or limiting values for τ_s applying. Further advances were made with the Imperial College instrumented pile tests (ICP) made in loose silica dune sand by Lehane (1992) at Labenne, and in dense silica marine sand by Chow (1997) at Dunkerque. Figure 3-4 shows profiles of shaft friction recorded by 3 instrument clusters in a 6m by 100mm diameter pile jacked into Dunkerque sand. It is clear

that interface shear stresses developed by the leading cluster are very weakly related to σ'_v, implying highly variable K values. Instead they correlate closely with the local CPT q_c profile. The two higher instruments (located further from the pile tip) show progressively reducing values of τ_f at any given depth. Lehane *et al.* (1993) referred to this reduction as 'h/R' effect with h being the relative depth of the pile below any given layer and R the pile radius. This feature also has been referred to as 'friction fatigue' by others such as Randolph *et al.* (1994). Jardine *et al.* (2005) suggested three main points that contributed to friction fatigue which are: a) The reduction due to geometrical effects in the radial stresses at any depth as the pile is driven past the point b) the effect of cyclic loading during installation and c) the creation of circumferential arching of conditions that prevented high radial effective stresses from acting on the pile. Lehane (1992) and Chow (1997) compared their field measurements with profiles estimated using Main Text API as illustrated in Figure 3-5 and concluded that the API method under-estimates the shaft stresses for short piles and over-estimates it for more slender piles. However, the API methods also suffer from systematic bias with relative density and tends to under-estimate unit shaft resistances in dense sands and over-estimated in loose sands.

Results from high quality pile tests showed the shortcomings of conventional methods and the need for new design proposals. Lehane *et al.* (1993) demonstrated that the ultimate shaft shear stress can be described by the simple Coulomb failure criterion:

$$\tau_f = \sigma'_{rf} \tan (\delta_f) \qquad \text{Equation 3-8}$$

However, σ'_r the radial effective stress on the shaft at failure is not constant during loading and the failure value σ'_{rf} differs from the equilibrium value (σ'_{rc}) by an amount $\Delta\sigma'_r$. The equilibrium radial effective stress (σ'_{rc}) is in turn controlled by the combination of the in-situ

soil conditions and the pile installation process. It is suggested that changes in radial effective stress during loading are generated from two independent components:

a) *Principal stress rotation*: principal stress rotation taken place as a result of pile loading that decreases σ'_r. Lehane *et al.* (1993) noted that these reductions are small for compression loading but were more significant under tension loading in their field tests.

b) *Dilation induced by interface shearing*: Lehane *et al.* (1993) reported marked increase in σ'_r at any depth as the pile approached local failure. It is suggested that the observed changes in σ'_r are caused by radial displacements that occur in a narrow shear band in the pile interface. Uesugi & Kishida's (1986) laboratory interface shear demonstrated that the volume changes induced by interface shearing develop within a narrow band positioned close to the interface.

Estimating the shaft friction resistances through Equation 3-8 requires accurate estimates for the stationary radial stresses (σ'_{rc}) and the changes in $\Delta\sigma'_r$ developed during loading stage. Lehane (1992) used results from the ICP pile tests in Labenne to propose an equation for predicting the stationary radial stresses which was updated by Chow (1997) after her Dunkerque tests to give, for closed-ended piles:

$$\sigma'_{rs} = 0.029\, q_c \left(\frac{\sigma'_{v0}}{p_r}\right)^{0.13} \left(\frac{h}{R}\right)^{-0.38} \qquad \text{Equation 3-9}$$

Where σ'_{v0} = vertical effective stress, p_r=atmospheric pressure and R=pile radius. A modified version of the equation is also proposed for open-ended pipe piles which substitutes an equivalent radius R^* for R where $R^* = (R_{outer}^2 - R_{inner}^2)^{0.5}$. In this equation q_c and σ'_v express the soil state and the 'h/R' term accounts for the effect of shear stress falling with *h* at points above the pile tip (i.e friction fatigue).

Considering the radial stress changes during loading stage ($\Delta\sigma'_r$), Boulon & Foray (1986) used the cavity expansion theory to estimate the increase in the radial effective stress caused by dilation. By assuming an elastic response under the small strains mobilised in the soil mass around the shaft, the changes in radial effective stress are equal to:

$$\Delta\sigma'_r = 2Gdr / R \qquad \text{Equation 3-10}$$

Where G is the shear modulus, dr is the dilatant radial displacement of soil at the interface and R is the pile radius. For model piles where R is small, the dilation effect can dominate the shaft capacity whereas with large diameter offshore piles the effect reduces considerably and the stationary radial effective stresses become dominant.

Chow (1997) and Jardine *et al.* (2005) showed that applying Equations 3-8 to 3-10 led to considerably greater predictive reliability and these and the related methods listed in the commentary section of the API RP2 (2014) are being applied widely. However; a number of important aspects including the "installation effects", "ageing behaviour" and the "cyclic loading" of driven piles in sand have required further investigation in recent years as discussed below:

3.1.2.1 Effect of installation method on shaft resistance

The "modern-CPT" methods proposed in API RP2 (2014) for estimating the shaft friction resistance do not consider explicitly the effects of the installation technique on the development of effective radial stresses acting on the surface of displacement piles in sands. The development of new pile installation techniques, such as large stroke hydraulic jacking and concerns over scale effects led to a need for research into the effects of installation mode on shaft resistance response.

White & Lehane (2004) used 9x9mm square instrumented closed-ended model piles to study the effect of installation mode through centrifuge tests. Three different installation methods were studied:

a) monotonic installation in which a continuous push with 0.2 mm/s penetration rate to half of the final depth was applied and was followed by a similar push to reach the final pile length.

b) Jacked installation which included cycles of fixed downward displacement followed by unloading to zero head load

c) "Pseudo-dynamic" installation where two-way cycles of fixed downward (2 mm at 0.2 mm/s) and upward (1.5 mm at 0.2 mm/s) displacement were applied.

The radial effective stresses White & Lehane measured (by relatively simple earth pressure cells) post-installation were greatest after monotonic installation and were lowest for pseudo-dynamic installation. Jacked piles showed intermediate σ_r' values. It was argued that the number of load cycles experienced at any depth during installation phase rather than the distance from the pile base might control σ_r'. Plots of normalised stationary radial effective stress did not produce a unique relationship with pile tip depth *h*; instead at any given h, the radial stresses depended on the number of load cycles during installation. However, Zhu *et al.* (2009) found that the earth pressure cells used for this research needed close cyclic calibrations in special cells that did not appear to have been made and suffered from marked cell-action effects in sands. In addition, a comprehensive study of tests on instrumented piles by Lehane *et al.* (2005) found that the ICP-05, UWA-05 and Fugro-05 design methods that assumed 'h/R' dependence provided better estimates for the shaft friction resistance of field tests than approaches based on the number of cycles experienced during installation. As noted later, calibration chamber tests with closely instrumented mini-ICP piles also suggested that

the effects of installation cycles were not as marked as had been interpreted from White & Lehane's centrifuge tests.

Gavin & O'Kelly (2007) used tubular stainless-steel tubular instrumented closed-ended 73mm diameter piles with L/D up to 40 in field tests on heavily over-consolidated, very dense, fine sand to study the effect of installation on stationary effective radial stresses and noticed that although greater values of σ'_r were mobilised after monotonic installation than jacking, the values were indistinguishable after the application of few number of load cycles.

Greater understanding in changes occurring in stress regime around the shaft during installation phase was achieved in a series of experiments reported by Jardine *et al.* (2013a, 2013b) and Rimoy (2013). Tests were performed using a closed-ended 36mm diameter stainless steel mini-Imperial College pile (mini-ICP) along with a standard CPT cone-tip ended pile in a calibration chamber (1.2 diameters by 1.5 deep) filled with medium dense pressurized NE-34 Fontainebleau sand. The effects of installation method, jacking style (and number of blows during driven installation) were investigated by comparisons between series of tests where jack loads were maintained between strokes and tests where full unloading between each stroke was employed. Their tests showed that the jacking style had relatively little effect on the stress regime, as exemplified by the σ'_r/q_c – h/R trends recorded by carefully calibrated soil stress sensors positioned at the 4.9R from the pile axis in Figure 3-6. Load-unload type of installation led to lower maximum values (at h/R = 0) at the end of push, but after unloading (pause stage) the maximum values at h/R = 0 came close to each other and the decay pattern above the tip did not show much difference between two methods of installation. Normalisation of the stationary soil mass radial effective stress decay curves (measured at r = 2R and 3R away from pile surface) between the maximum point at the pile tip and lower stresses remaining higher above the tip showed better convergence when the

data were normalised against h/R, rather than number of cycles as shown in Figure 3-7. Jardine *et al.* (2013a, 2013b) however speculated that a stronger dependence on number of cycles N could apply at lower r/R ratios closer to the pile interface, where two-way cycling is more intense during installation. Later driven pile installation did indeed lead to lower shaft capacities, Rimoy (2013).

Jardine *et al.* (2013b) summarized their measurements of stresses in the full depth of the soil mass out to r > R=33 away from the pile in contour plots of the cylindrical normal stress components developed in the soil mass. Radial (σ'_r), vertical (σ'_v) and circumferential (σ'_θ) contour plots normalised by the q_c values, were developed from "moving" and "stationary" conditions. The patterns found applying at the end of cyclic jacking pause phases are shown in Figure 3-8. The plots show intense stress concentrations around the pile tip with stresses generally reducing with distance from this "stress source". Interesting features can be found by considering the stresses further above the tip in more detail. Figure 3-9 shows radial profiles of the stationary σ'_r and σ'_θ values measured at h/R values between 5.6 to 40.6 after the end of the installation phase. The on-pile radial effective stress measurements are also shown and it is clear that at all points above the pile tip the final radial (and therefore circumferential) stresses developed their maxima away from the shaft between $2 < r/R < 4$. Jardine *et al.* (2013b) demonstrated this feature by applying the equation of cylindrical equilibrium.

Yang *et al.* (2010) report the use of same mini-ICP calibration chamber tests to study the micromechanical features and fabric changes in NE-34 Fontainebleau sand mass around the pile surface during the installation phase. They found three concentric fabric zones around the pile tip and measured the radial extent of each. Figure 3-10 shows the schematic development of Zones 1 to 3 around the pile tip. Zone 1 which was the closest to the pile surface consisted

of grey heavily fractured material that had been both crushed beneath the tip and augmented by intense surface abrasion. The pile's maximum surface roughness clearly reduced as a result of the intense interface shearing. The thickening of zone 1 above the pile tip showed that breakage and abrasion continued higher on the shaft as installation continued. Approximately 5% of the displaced sand converted into grey Zone 1 material which contained 20% of fines crushing products, while about 50% of the displaced sand experienced less significant breakage beneath the advancing tip and formed Zone 2. The rest of the altered material formed Zone 3 further away from pile interface where the degree of crushing was more moderate (developing 5% fines).

Yang *et al.* (2010) summarized the major processes that soil elements experience as the pile tip approaches and passes the soil element. As the pile tip approaches, particularly large stresses and strains develop in the active zone beneath the tip. As the pile advances the strain paths around the tip reverse due to the pile geometry and sharp unloading occurs. Significant creep straining (or stress relaxation) also occurs. The overall process of stress build-up, stress reversal, relaxation and creep generates apparently heavily over consolidated conditions in partially crushed sand around the pile surface with radial stress falling from maxima of around $q_c/3$ immediately beneath the tip to minima between to between 1.5 to 2.5% q_c on the shaft, albeit with higher values of $r/R>1$. The on-going stress relaxation and compressive creep act in combination with the geometrical factors and compaction caused by the shaft loading cycles to reduce the shaft radial stresses with increasing h/R.

It is vital to recognise the above features when designing experiments to replicate the sand's subsequent response to static or cyclic loading.

3.1.2.2 Ageing effect on pile shaft resistance

Another key finding regarding the shaft resistance of piles driven in sand is the effect of ageing on their shaft resistance post-installation. Full scale pile tests have shown that capacity increases sharply over the weeks and months that follow driving (See for example Chow *et al.*,1998; Axelsson, 2000; Jardine *et al.* 2006 and Rimoy *et al.*, 2015). This phenomenon is also referred to as "set-up" or "freeze".

Various hypotheses have been proposed to explain the set-up mechanism which can be summarised into three main categories:

a) *Increase in the radial effective stress (σ'_r) acting on pile surface linked to relaxation of circumferential stresses in sand arch formed around the pile during installation*: Chow *et al.* (1998) proposed that the increase in σ'_r is the most dominant process leading to pile set-up. A similar hypothesis that was suggested by Åstedt *et al.* (1992). The radial profiles reproduced in Figure 3-9 are compatible with this hypothesis.

b) *An increase in shear stiffness and dilatancy of the sand around the pile after the pile installation:* According to this hypothesis, the contribution to shaft resistance offered by the kinematically constrained dilatant radial stress changes that develop on pile leading increase with time due to either greater shear stiffness G or dilation (dr in equation 2-8). Axelsson (2000) measured a 60% increase in pile shaft capacity over a 22-month period and recorded a remarkable increase in horizontal (radial) stresses due to increased dilatancy over time. Bowman & Soga (2005) reported results from triaxial creep tests which showed that strong dilation follows the preconditioned samples after short period of contraction. It was also suggested that small cyclic perturbations might accelerate the dilative process.

c) *Increase in pile-sand interface friction angle due to the physiochemical action*: This effect can be dominant for clays. Chow *et al.* (1998) noted that rusting occurred over

steel piles in the presence of air and water but noted that ageing applied equally to concrete piles and steel piles below the water table. Baxter & Mitchel (2004) performed series of laboratory tests and concluded that chemical reactions are unlikely to be the dominant cause for set-up effects in piles.

Jardine *et al.* (2006) showed that any pre-testing of piles over their ageing periods had significant effect on their set-up behaviour. First-time tension tests gave the strongest gains in shaft capacity during set-up period, which could exceed 100% over a year, although the database for such tests is limited. Rimoy *et al.* (2015) added to Jardine et al's Dunkerque data tension tests reported by Gavin *et al.* (2013) and Karlsrud (2014). They normalised the static tension capacity-trends by time with ICP-05 tension capacity estimates and showed that all three sets of tests followed trends as shown in Figure 3-11.

Rimoy *et al.* (2015) also reported their ageing tests conducted in a calibration chamber with mini-ICP piles and simpler driven piles. While the model tests support the hypothesis of stress redistribution during set-up period, the pile loading tests showed only slight increases in σ'_r and total capacity. It was suggested that important scale effects could apply that relate to size of the grains in the interface shear zone. Pile installation method and physiochemical processes might also lead to differences in model and field ageing trends. A limited study of field test data supported the suggestion that ageing benefits increase with pile diameter. The later conclusion is in direct opposition to the inference from Hypothesis B that gains in capacity should fall with diameter.

The third area of intensive recent investigation into the axial behaviour of piles driven in sand, and the one that is the principal topic considered in this thesis, is their response to axial cyclic loading. The remaining sections of this chapter are devoted to reviewing the

background to relevant recent research, the research itself and its implications for the author's experimental laboratory soil element cyclic loading study.

3.2 Experience of cyclic loading in field

All foundations experience some cyclic loading during their service lifetime. These cyclic loads range from gentle temperature change cycles through to significant loads imposed by operation plants, tides or extreme environmental conditions (Jardine *et al.,* 2012). With moves to more extreme conditions in particularly offshore environments, there has been a growing appreciation of the need to address the impact of cyclic loading in design of foundations. The effects of cyclic loading on offshore Gravity Base Structure (GBS) foundations have been addressed since the early 1970s and have been a major part of GBS foundation design, as discussed by Andersen (2009). However, attention to axial cyclic loading effects on piled oil and gas installations and offshore wind turbines built on tripods or jackets has increased in recent years. Improvements in static driven pile design methods (for example ICP method reviewed above) must now extend to consider how stability and permanent displacements are affected by cyclic loading.

The cyclic loads experienced by foundations under critical storm conditions comprise a series of non-uniform irregular amplitude load cycles. These time-histories are usually transformed when considering cyclic loading assessments into idealized suites of uniform cycles, with each suite having a fixed load amplitude (Q_{cyc}) and average load (Q_{avg}) and specific number of cycles which is found by a "rainfall" analysis approach. Figure 3-12 shows a real field time-history for a tension pile and an idealised load cycle pattern.

Regular cyclic loading may be characterised in terms of average and cyclic load components and outcomes from experiments or analysis are often normalised by the static pile capacity Q_s as shown in Figure 3-13. Jardine *et al.* (2012) considered critical cyclic storm loading data

from 7 exemplar offshore foundation projects to show the indicative ranges for cyclic loading components under the 100 year return period design storms considered for oil or gas platforms and 50 year events for wind turbines. Table 3-2 shows the cyclic parameters applying to the worst single cycle expected at these sites. The average Q_{cyclic}/Q_{mean} ratio on the windward side is around 7.8 and 3.18 for the leeward side. The maximum compressive loads developed on the leeward side (Q_{max}) are usually considered critical in conventional design. The illustrative cases in Figure 3-14 were plotted by Jardine *et al.* (2012) assuring that the foundations were designed considering these load maxima with an FOS=1.5. The critical points are compared with interaction diagrams from Dunkerque field tests reported by Jardine & Standing (2000, 2012) that are discussed later. The illustration suggests that Cases A to G should plot above the "zero damage line", so cycles applied in these cases will experience some degradation that will reduce the factor of safety and could even lead to failure after a sufficient number of cycles. In particular, Case C plots above the N_f=100 contour, indicating a considerable potential impact on foundation under cyclic loading.

Table 3-2 Indicative range of critical cyclic loads from 7 offshore platform foundation cases (Jardine *et al.*, 2012)

Jacket code, Location and type	Water depth m	Leeward Q_{cyc}/Q_{mean}	Windward Q_{cyc}/Q_{mean}
A West of Shetland, oil/gas	140	0.36	6.69
B China sea, oil/gas	36	0.6	3
C China sea, oil/gas	49	3.18	4.68
D North sea, oil/gas	70	0.72	2.47
E North sea, Wind-turbine jacket	35	0.72	1.25
F North sea, Wind-turbine jacket	50	1.13	35
G North sea, Wind-turbine jacket	26 to 33	0.88	1.6

A key aim in cyclic loading assessments is to investigate how capacity may vary under cyclic loading and to predict the permanent induced by cycling displacements. The displacements accumulated under GBS foundations by cyclic loading have been separated in two major

parts: 1) displacements caused by the strains developed under cyclic loading and 2) subsequent straining caused by the dissipation of the cyclically induced pore pressures which are unlikely to be as significant except with very large diameter piles. The following sections summarize findings from field and model pile cyclic test studies.

3.3 Axial cyclic loading study in field and model piles

3.3.1 Field pile tests

Several full scale field cyclic testing programmes have been conducted on piles driven at clay sites as summarised by Jardine *et al.* (2012). However, surprisingly limited high quality pile cyclic testing has been conducted at sand sites. The earliest field cyclic tests on piles known to the author are the few reported by Lehane (1992) along with his more extensive static tests. Modest suites of one-way cyclic loads were applied in two ICP tests in Labenne and Dunkerque (Q_{cyc}= 0.15 Q_T, Q_{mean}= 0.55 Q_T and N =40 in Labenne) in which a fully drained response was achieved. Neither of the tests led to failure but modest reductions in local shaft capacity were recorded under limited local two-way failure at the upper parts of the pile. Chow (1997) ICP's testing at Dunkerque in medium dense marine silica sand included a cyclic series (with Q_{cyc}= 0.31 Q_T, Q_{mean}= 0.50 Q_T and N = 40) which also showed no cyclic failure and a slight improvement in shaft capacity (of 8%) was recorded. Chow (1997) noted that this gain in capacity under low level cyclic loading was due to local gains in the failure values of σ'_r.

The first comprehensive full scale test series focusing on the cyclic response of piles driven in sand were that reported by Jardine & Standing (2000, 2012) for dense marine sand at Dunkerque. Tests were conducted on six 19m long 457mm diameter open-ended steel pipe piles and one shorter (10m) similar pile. Their results led to the identification of three modes

of behaviour that depended on the average and cyclic normalised axial loads imposed. The styles of response were defined as:

a) *Stable* (S): This response was observed in a series of tests that showed slow pile head displacement accumulations (only 0.4 mm over 500 cycles in one test) throughout the tests. Subsequent static tension tests after cycling showed a gain of up to 20% over the estimated tension capacity.

b) *Metastable* (MS): Pile head displacement accumulated with moderate rates of ≈0.013mm/cycle up to around 50 cycles and after that the rates accelerated more sharply. Between 100 and 1000 cycles were required to induce failure. *Metastable* cycle tests involved significant tension capacity reductions. However, piles could sustain small numbers of Metab*Stable* cycles without sustaining significant displacements or significant damage.

c) *Unstable* (US): Permanent displacements were initially high (≈0.5mm/cycles) and accelerated progressively after first few cycles. Rapid development of displacements led to failure under 100 cycles. *Unstable* tests involved heavy losses in capacity.

Jardine & Standing (2000, 2012) produced interaction diagrams that identified the mode of behaviour based on the $Q_{cyclic}/Q_{max\ static}$, $Q_{mean}/Q_{max\ static}$ and N_f (number of cycles to failure). Figure 3-15 shows their boundaries for the *Stable*, *Metastable* and *Unstable* regions.

Jardine & Standing (2012) showed that the power-law equation proposed by Jardine *et al.* (2005) for the changes expected in local radial effective stress acting on pile shaft due to cyclic loading could be used to position the N_f lines in the *Unstable* and *Metastable* regions of the $Q_{cyclic}/Q_{max\ static}$, $Q_{mean}/Q_{maxstatic}$ diagram. According to this equation:

$$\Delta\sigma'_r / \sigma'_{rc} = A\,(B + \tau_{cyclic}/\tau_{max\ static})\,N^C \qquad \text{Equation 3-11}$$

Equation 3-11 can be incorporated into simplified T-Z analysis of simple piles under axial cyclic loading, Atkins (2000) incorporated the expression into their in-house soil-structure interaction code and were able to make good to fair prediction for the Dunkerque field tests, including the growth of permanent pile head displacements. In these methods pile is modelled by a string of beam elements and axial and lateral soil confinement is modelled by a series of springs attached to nodes on beam element end points.

Other computer programs that apply the beam-column methods to assess axial pile response under cyclic loading include RATZ (Randolph, 1994), PAXCY (Karlsrud *et al.*, 1986) and PAX2 (Nadim & Dahlberg, 1996). RATZ method utilizes a load-transfer scheme that consists of a linear range elastic stage that expands up to a fraction of the peak shear stress, a parabolic stage in which stiffness gradually drops from maximum value to zero and a softening stage where the current value of the shaft friction is related to the absolute pile displacement. In this model accumulation of permanent displacements under cyclic loading is controlled by the extent of the linear stage at small strains which defines a yield point that will be engaged on reloading. The post-yield plastic displacements are considered as equivalent to post-peak monotonic displacements which lead to gradual degradation of the shaft friction from peak to residual values. PAXCY and PAX2 methods are based on the cyclic assessment methods from NGI laboratory tests on clays. In these methods the t-z springs are established by intergrading with respect to radius the shear strains developed in the disk of soil surrounding the pile segment.

By assuming that the entire cyclic load is taken in shaft resistance and base cyclic loading is negligible, Jardine *et al.* (2005) applied the above equation to overall pile capacity and proposed the following equation for piles:

$$\Delta Q_{max\ static}/Q_{max\ static} = A\ (B + Q_{cyclic}/Q_{max\ static})\ N^{c}$$ Equation 3-12

Linear interpretations made by Jardine & Standing (2000) for N_f lines and predictions from above method are plotted in Figure 3-16. Poulos (1981) has also proposed power-law equations to fit the cyclic degradation trends of piles under axial cycling.

Meritt *et al.* (2012) report on the application of the above "A,B,C" approach in the design analysis of a major German offshore windfarm founded on piled tripods at a dense sand North sea site. Their analysis used an "equivalent number of cycles" approach to "curve-hop" from one cyclic loading level to another and so consider a full design storm. Critical to this study and the earlier work by Atkins (2000) was defining the lower limits below which cycling led to zero damage and possibly even beneficial effects.

3.3.2 Model pile tests

Model pile tests offer another way of studying axial cyclic behaviour. Since full scale pile tests are difficult and expensive to perform, models can provide cost effective insights, especially when instrumented appropriately. Model tests can be performed in 1-G self-weight tests, calibration chambers or in geotechnical centrifuges.

Van Weele (1979) and Chan & Hanna (1980) reported early cyclic studies on model piles installed in sand. Tests on a hydraulically jacked 36 mm diameter model pile in a 1.1m calibration chamber with medium dense silica sand under 100kPa vertical surcharge stress by Van Weele (1979) showed continuous accumulation of displacement even at low cyclic amplitudes although failure was not reached up to the number of cycles applied. He also reported on the effect of loading frequency on the acceleration of displacement accumulation due to potential progressive partial drainage. Chan & Hanna (1980) used 19 mm diameter aluminium alloy tubes in a pressurized chamber to test dry uniform sands. They studied the effect of cyclic loading amplitude and identified *Stable* response on low level cyclic loads

($Q_{cyclic}/Q_{max\ static} < 0.1$) and *Metastable* to *Unstable* response at higher amplitudes. Low-level tensile cyclic tests led to improvements in cyclic pile head stiffness while high level two-way loading led to progressive failure after a limited number of cycles.

Tsuha *et al.* (2012) conducted model pile tests in a 1.1m diameter pressurised calibration chamber using highly instrumented mini-ICP model piles to investigate the axial cyclic response of piles in Fontainebleau NE34 and GA39 sands. Tests were performed with a 36mm × 0.99mm 60° conical-tip ended mini-ICP pile that gave a $d_{chamber}/D_{ratio}$ ratio of 33. The mini-ICP allowed continuous recordings of the local shear (τ_{rz}) and radial effective (σ'_r) stresses developed during the installation, equalisation and cycling testing stages. *Stable*, *Metastable* and *Unstable* modes were observed, comparable to those seen in field pile tests by Jardine & Standing (2000, 2012) – although with lower critical displacement rates – with each mode developing a unique style of local effective stress path response in τ_{rz} - σ'_r space approach as shown in Figure 3-17a. Tsuha *et al.* (2012) used the kinematic multi-yielding surface approach proposed by Jardine (1992) and Kuwano & Jardine (2007) to describe the different responses under cyclic loading. In *Stable* tests the local effective stress loops kept inside the sand's local Y_2 yield surface and little or no changes were seen in effective stresses over thousands of cycles. In *Metastable* tests, effective stress paths engaged the Y_2 surfaces and cycling led to a progressive downward drift in the local radial effective stresses that, if continued for hundreds of cycles could lead to shaft failure. *Unstable* cycling led to more rapid degradation that resulted in interface phase transformation and local slip after less than 100 cycles. Tsuha *et al.* (2012) also used miniature stress sensors to measure the stresses developed in the sand mass during cycling and presented the results in q-p′ space as shown Figure 3-17b. Static tension tests to failure conducted after cyclic loading showed modest increases in shaft capacity after *Stable* cycling as shown in Figure 3-18. It was argued that gains in shaft capacity for *Stable* tests were due in this case to marginal densification near the

interface zone and development of an optimal soil fabric that enhanced dilation under later static loading. Interaction diagrams that identified the zones over which the three styles of behaviour applied were produced as functions of $Q_{cyclic}/Q_{max,static}$, $Q_{mean}/Q_{maxstatic}$ and N that are shown in Figure 3-19.

Rimoy (2013) extended the model pile cyclic testing, employing upgraded versions of the equipment used by Tsuha *et al.* (2012) to study the effect of parameters that could potentially influence the cyclic results. For example, tests on finer and looser GA39 sand showed greater susceptibility to cyclic loading with faster rates of displacement accumulation. The most significant effect was the reduced level of cycling below which no degradation was measured. Tests were also performed with different boundary conditions and it was concluded that the field condition is best modelled in tests where "active" radial chamber boundary conditions are applied to reproduce the action of the elastic strain energy stored at r/R>33 in the field. Rimoy (2013) also studied the axial cyclic pile stiffness degradation developed in his tests by defining secant stiffness (k_n) as $(Q_{max} - Q_{min})/d_{cyclic}$ as shown in Figure 3-20a. Results from *Stable*, *Metastable* and *Unstable* cyclic response of piles are shown in Figure 3-20b-d. It is shown that cyclic pile stiffness remained approximately constant in *Stable* tests, while *Unstable* tests showed substantial stiffness degradation from early cycles. *Metastable* tests showed only modest global stiffness degradation until local failure was approached and then showed considerable stiffness degradation over their final few cycles.

3.4 Framework for laboratory modelling of axial cyclic pile response

Instrumented field and model pile tests provide the most direct means of understanding the axial cyclic response of piles. However, they are usually expensive, time consuming and difficult to perform. It is usually impractical to perform such tests as part of a practical

offshore design. Laboratory element tests that are easier and cheaper to perform and yet provide representative predictions of how axial cyclic loading affects the shaft effective stresses and those in the surrounding soil would clearly be valuable. However, such tests could only be representative if they could model in the laboratory the stress regime and stress history of single elements of soil adjacent to the pile.

It has been discussed by numerous authors (Boulon & Foray, 1986; Airey 1992) that the decrease in skin friction adjacent to pile is linked with a decrease in normal stress resulting from compressive strain in the soil adjacent to the pile. Constant Normal Stiffness (CNS) direct shear test which is able to account for expansions or contractions at pile-soil interface is a suitable option for modelling the interface conditions in laboratory. This test procedure was first introduced by Johnston *et al.* (1987) to investigate the behaviour of rock joints and rock-socketed piles. Boulon & Foray (1986) suggested that CNS conditions are applicable to pile case in sands since it has been shown that most of soil deformation occurs in a narrow band close to pile interface with soil mass located outside the shear band behaving almost as an elastic material. Boulon *et al.* 1988 used results from monotonic CNS tests to predict the pile response under monotonic loading while Airey (1992) compared results from his cyclic CNS tests with cyclic model pile tests reported by Al-Douri (1992) as shown in Figure 3-22. Airey argued that CNS test results were able to predict the reduction of the shear stresses seen under constant strain (±1mm) cycles but to improve the accuracy of the prediction; more information was needed about the normal stresses acting on the pile surface as they are strongly dependent on the installation phase of the pile (as was shown earlier this was studied in more depth by Tsuha *et al.,* 2012 and Rimoy, 2013).

Johnston *et al.* (1987) and Boulon & Foray (1986) argued that the changes in local radial stresses developed in response to shaft shear stresses can be related to shear stiffness of the sand using the elastic expanding cylinder theory as:

$$\Delta\sigma'_r / dr = 2G/R = K_{CNS} \qquad \text{Equation 3-13}$$

The strains are expected to be very small with industrial piles, and as suggested by Jardine *et al.* (2005) are approximately equal to the peak-to-trough centreline average roughness of the pile surface under static loading to failure.

Boulon & Foray (1986) proposed an analogy for modelling the CNS conditions in laboratory simple shear or direct shear tests as shown in Figure 3-23. Choosing an appropriately realistic value for K_{CNS} and the subsequent boundary conditions is then the key issue. Fakharian & Evgin (1997) expressed three categories of boundary conditions and their relevant K_{CNS} values as:

Case 1: $K_{CNS} = 0 – d\sigma_n = 0 – dv \neq 0$: Constant normal load (CNL) as in standard shear box tests

Case 2: K_{CNS}=constant - $d\sigma_n \neq 0$ - $dv \neq 0$: Constant normal stress (CNS)

Case 3: $K_{CNS}=\infty$ - $d\sigma_n \neq 0$ - $dv=0$: Constant volume (CV)

Where $d\sigma_n$ is the normal load and dv is the normal displacement. Many authors have reported results from CNL and CNS cyclic shear tests on sands and results from some of these works are summarised in the following. However, Jardine (2013) and Sim *et al.* (2013) argued that since the shear stiffness of sand is non-linear, pressure dependent and anisotropic and K_{CNS} depends on pile radius, it is impossible to define a meaningful simple constant value for K_{CNS}. It was suggested that performing constant volume tests should provide an upper limit

(infinite) value for K_{CNS} that can be met by performing laboratory shear tests on saturated undrained samples.

3.4.1 Cyclic CNL and CNS simple and direct shear tests

Direct shear and simple shear (SS) soil-soil or soil-interface tests are sometimes considered as representing the shearing conditions around piles (Randolph & Wroth, 1981). Several testing programs aiming to model this response under different boundary conditions (CNL, CNS or CV tests) are reported in the literature. Findings from some of these programs are summarised below, before discussing possible short comings in these methods of testing.

Conventional interface experiments were mostly performed under CNL (Case 1) conditions. Figure 3-24 shows monotonic displacement controlled and cyclic CNL direct shear tests on loose and dense Toyoura sand reported by Mortara (2001) using rough and smooth interfaces. Both samples showed overall contracting interface behaviour during cyclic loading with dense sand showing contraction followed by considerable dilation at each high-level cyclic shear stress reversal, with contractive accumulation rates decreasing as cycling continued. The post cyclic shearing behaviour showed significantly dilation enhanced due to progressive densification during the cyclic loading.

CNS tests (Case 2) using a conventional shear box were reported by Airey *et al.* (1992) on dense calcareous sand under initial σ_n=250kPa. Figure 3-25 shows the evolution of shear stresses and normal effective stresses during a high level (±1mm) displacement-controlled cyclic loading soil-soil test employing K_{CNS}=1.6 MPa/mm which is equivalent to that expected for a pile with radius R=1m and a very high shear modulus of 800MPa. It can be seen that the shear stresses attained in each cycle decreased with number of cycles, associated with drops in normal vertical stresses. The cyclic stress paths followed in τ-σ'_n space manifested patterns similar to those of undrained cyclic triaxial tests. The normal stresses

developed over the first shear cycle showed an initial fall (up to phase transformation) followed by a steady increase up to the maximum shear displacement. However, the normal stress fell sharply on shear reversal. A similar pattern was noted with each subsequent cycle although with steady downward drifts in σ'_v and τ_{max}. Airey *et al.* (1992) proposed a procedure for relating results from CNL tests to CNS tests and compared shear stress reductions predicted from CNS tests with model piles, noting good agreement with calcareous sands.

Fakharian & Evgin (1997) reported results from CNS and CNL cyclic simple shear tests to investigate factors influencing the cyclic degradation rates. Figure 3-26 shows results from two displacement-controlled tests on dense silica sand employing CNS boundary conditions applying 200kPa/mm<K_{CNS}<1200kPa/mm. Their maximum shear stresses showed marked decreases over the first cycles and rates of degradation that decreased as cycling continued. Fakharian & Evgin (1997) concluded that the degradation was due to compression of the sand mass during shearing cycles which leads to a reduction in normal stresses and consequently a reduction in shear stresses. Results from tests with different cyclic displacement amplitudes showed that if the cyclic amplitudes are sufficiently large, the stress ratio τ/σ_n drops to low residual values as, shown in Figure 3-27a. Tests conducted under higher values of K_{CNS} produced steeper rates of shear and normal stress reduction as shown in Figure 3-27b. Mortara *et al.* (2002) reported similar sensitivities to K_{CNS} in the cyclic response of their tests on loose samples.

Oumarou & Evgin (2005) studied the effect of initial density (<22%D_r<92%) in constant volume cyclic simple shear tests on quartz sand using a simple shear apparatus. Results from strain-controlled tests under normal stresses σ_n=100, 200 and 300kPa with cyclic shear displacement amplitudes ranging from 1 to 3mm showed that as cycling continued the shear

stresses mobilised on the interface increased for loose samples and decreased for dense samples, until they eventually became independent of the initial density.

Mortara *et al.* (2007) investigated the effect of normalised roughness of the sand on cyclic response in a conventional direct shear box. Cyclic CNS tests with finer material (giving a relatively rough value of R_{CLA}/d_{50}) showed alternating phases of compression and dilation with an overall trend for compression which caused reduction in normal stresses, whereas coarser materials (which had lower "smooth" R_{CLA}/d_{50} ratios) showed a continuous compression during cyclic loading and showed less stress degradation in tests with similar conditions, as shown in Figure 3-28. Monotonic post-cyclic shear tests showed that the densification of coarse samples during the cyclic stage enhanced the dilation developed subsequently and allowed recovery of the shear stresses, whereas smooth surfaces showed no recovery due to lack of dilation. Mortara *et al.* (2007) argued that this difference in behaviour can be understood in terms of relative roughness, as shown in Figure 3-29. The relative scale of interface asperities enables the sand to dilate, whereas the geometry of the coarser sands limits the scope for dilation.

3.4.2 Critical assessment of practiced cyclic shear tests

Although simple and direct shear tests provide insights into the cyclic response under shear loading, they inherit implicit problems fundamental from the apparatus' design. Two of the main problems encountered are:

a) *Stress uniformity in sample:* It is well known that the direct shear apparatus suffers from severe stress non-uniformity. The simple shear apparatus originally aimed to create a more uniform shear strain within the soil (offering a marked improvement over conventional direct shear tests). However, it proved impossible to produce practical apparatuses that could provide the complimentary shear stresses required on

the vertical boundaries to keep uniform stresses during shearing. Simple shear apparatus is in fact subject to strong stress non-uniformity. Shen (2012) and Shen *et al.* (2011) used a numerical discrete element method (DEM) to model different types of simple shear apparatuses to study the level and mechanisms of possible stress non-uniformities during shearing of granular materials. Results from simulations of CNL shear tests on dense sands showed that the stress conditions are inhomogeneous inside the specimen and are highly non uniform along the boundaries. The principal stress axis rotation that is imposed is neither controllable nor recordable in the laboratory tests. Figure 3-30 shows results from Shen's Cambridge simple shear type simulations. Figure 3-30a shows the strain non-uniformities inside the sample and Figure 3-30b shows the rotation of contact forces after 20% shear strain.

b) *In-ability to record the stress tensor representatively*: Conventional simple shear apparatuses are at best only able to measure one global average normal stress and one global average shear stress component. Two more measurements are necessary to undertake a complete stress analysis in terms of Mohr's circle or stress invariants. Mohr's circle cannot be drawn and the magnitudes and directions of the principal stresses cannot be found without making extra assumptions such as the classical Columb, Davis or Josselyn de Jong hypotheses. Randolph & Wroth (1981) discussed the application of these methods and assumptions concerning the directions of potential failure planes in the soil to predict pile shaft friction capacity in clays. They suggested that the direction of any potential failure plane must coincide with a direction of a zero extension plane. Therefore, two possible modes of failure (horizontal or vertical) are possible for simple shear tests as shown in Figure 3-31.They argued that for normally consolidated samples the second Josselyn De Jong mode of failure will apply. These arguments can be invoked when using simple shear

tests to predict the pile shear strength under axial loading, although these are considerable variations in the predictions obtained from the two methods. Furthermore, as noted above, these theories only apply to the average stresses measured in tests that are in fact highly non-uniform.

Another way to overcome the problems associated with simple shear experiments is to perform them in an HCA apparatus. Although HCA samples inherit some non-uniformity due to the curved shape of their samples, their overall stress and strain uniformity is much better than in simple shear apparatus. Moreover, all four major stress components can be controlled and measured separately. Successful HCA simple shear tests have been conducted on a wide range of media in Imperial College Hight (1988), Porovic (1995), Nishimura (2006) and Brosse (2012).

3.4.3 Other laboratory tests for investigating pile axial cyclic response

Apart from conventional direct shear and simple shear tests, ring shear tests which develop for larger displacements during shearing can be used to model soil-pile interface behaviour in static or cyclic tests that match driven pile conditions. Jardine *et al.* (2005) recommended interface ring shear tests to model pile-soil interfaces for driven piles as providing design δ_{cv} values. The procedure includes a series of fast shear stages to model pile driving during installation followed by consolidation/creep pauses prior to a main slow shearing phase. Yang *et al.* (2010) and Ho *et al.* (2011) used ring shear equipment to study particle breakage in soil-pile interface at large strains and to measure changes in δ_{cv} during shearing and reported that measured δ_{cv} match closely with model and field pile measurements and can give good predictions for pile design. They also suggested that cyclic ring shear tests are likely to generate more particle breakage even though ring shear tests do not model the particle crushing that takes place ahead of advancing piles. Kelly (2001) performed cyclic ring shear tests using a large 1m diameter apparatus and reported contraction in “low level”

cyclic tests, while “high level” tests showed phase transformation within each cycle. He concluded that the cyclic effects will be most important in dense fine grained sands.

Dejong *et al.* (2003) used a micro-scale investigation technique to study interface shear during CNS cyclic loading by incorporating GeoPIV image processing in a cell made with a glass side. Their results showed three distinct zones of deformation within the interface zone as: 1) slip between the interface and the shear zone 2) a distinct interface shear zone and 3) a relatively inactive region above the shear. Under cyclic loading the thickness of the interface shear zones increased with cumulative displacements; and the secant shear modulus (G) stabilized after drops in early cycles. Figure 3-32 shows results from a stress controlled test on uncemmented silica sand. Figure 3-32a shows the stiffness reductions noted as cycling continued while Figure 3-32b shows the overall contraction of the soil due to cycling. Figure 3-32c shows the evolution of horizontal stresses and it can be seen that most of the horizontal displacement occurs in the soil layer closest to the interface and accumulates as cycling continues. Dejong *et al.* (2006) used the same GeoPIV image processing method to study the effect of different parameters influencing the thickness of the shear zone during cyclic loading. Their results showed that the thickness of shear zone increased with increasing relative density, particle angularity and surface roughness and decreased with increasing particle hardness, normal stress and normal stiffness. It was argued that increased particle angularity and surface roughness will increase the degree of particle interlocking with the interface and propagates the shear and volumetric straining further into the soil mass.

3.5 Summary and conclusions

This chapter has reviewed recent research into the axial monotonic and cyclic behaviour of single piles in sands. Attention has been given to the governing stress regime, boundary conditions and stress history experienced by the soil around the pile shaft during installation and under axial loading. A review of methods for estimating base and shaft capacity of piles

was presented and the frameworks available for studying pile shaft friction through laboratory testing were discussed. Finally, the results from laboratory tests aiming to study shaft friction were presented and a critical assessment of current direct and simple laboratory practices was given.

The following overall observations will be carried forward:

1) High quality instrumented model and field pile tests have allowed considerable progress to be made in understanding the stress regimes developed around pile shafts during installation and loading.
2) Shaft interface failure under shear loading is governed by the local radial effective stresses and a Coulomb criterion. The operational interface friction angles are soil properties that can be measured reliably in ring shear interface tests.
3) The importance of ageing time after driving and installation method on pile shaft capacity was reviewed and possible explanations for such effects explained.
4) Axial cyclic loading was considered in some detail. Field tests show that the ultimate static capacity of driven piles reduces significantly under high to moderate cyclic loading levels. Consideration of cyclic effect in design is required. Depending on the mean and cyclic amplitude values, cyclic repose are categorised into *Stable* (S), meta-*Stable* (MS) and *Unstable* (U) zones. While capacity can increase under *Stable* cycling, large capacity losses are recorded under *Unstable* conditions. Moderate degradation rate is recorded in *Metastable* tests.
5) Field and laboratory instrumented pile axial tests prove that local shaft capacity changes experienced under axial cyclic loading are governed by the evolution of the radial effective stress distributions acting over their shafts.
6) A framework for predicting the evolving radial effective stresses developed on pile shafts under axial loading using laboratory tests was set out. CNS simple shear tests

were considered potentially suitable for modelling such conditions provided representative K_{CNS} values can be estimated.

7) However, choosing simple representative K_{CNS} values may prove very difficult due to the anisotropic, nonlinear nature of the soil and the dependency of K_{CNS} on pile radius. Performing constant volume tests (K_{CNS} = infinity) offers a conservative solution to this problem.
8) Conventional types of simple shear apparatuses inherit implicit fundamental problems which create difficulties when modelling interface behaviour in laboratory testing. HCA simple shear tests can largely overcome these problems associated with lack of complimentary shear stresses and an incomplete description of the stress tensor.
9) Laboratory interface tests can predict aspects of the pile axial cyclic degradation. However, in order to get make representative predictions, it is necessary to apply the appropriate stress history, boundary conditions and ageing phases prior to applying load cycling.

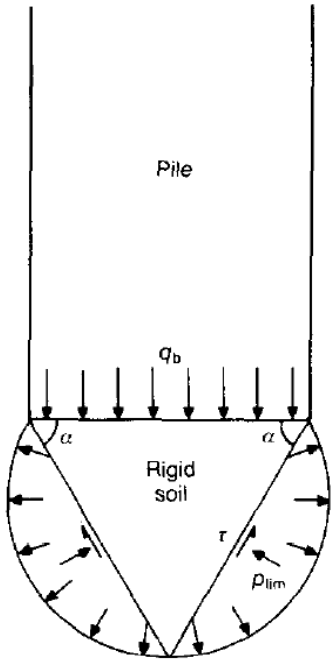


Figure 3-1 Relation of cavity expansion limit pressure and end-bearing capacity (Randolph *et al.*, 1994)

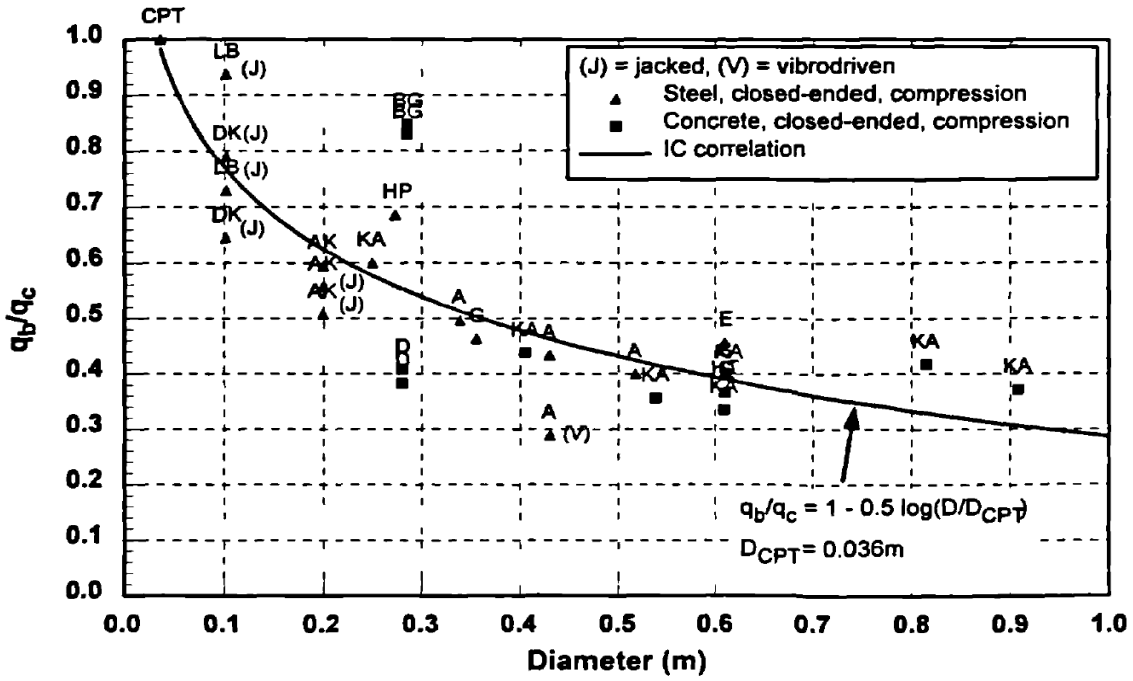


Figure 3-2 - Effect of pile diameter on pile base resistance (Chow, 1997)

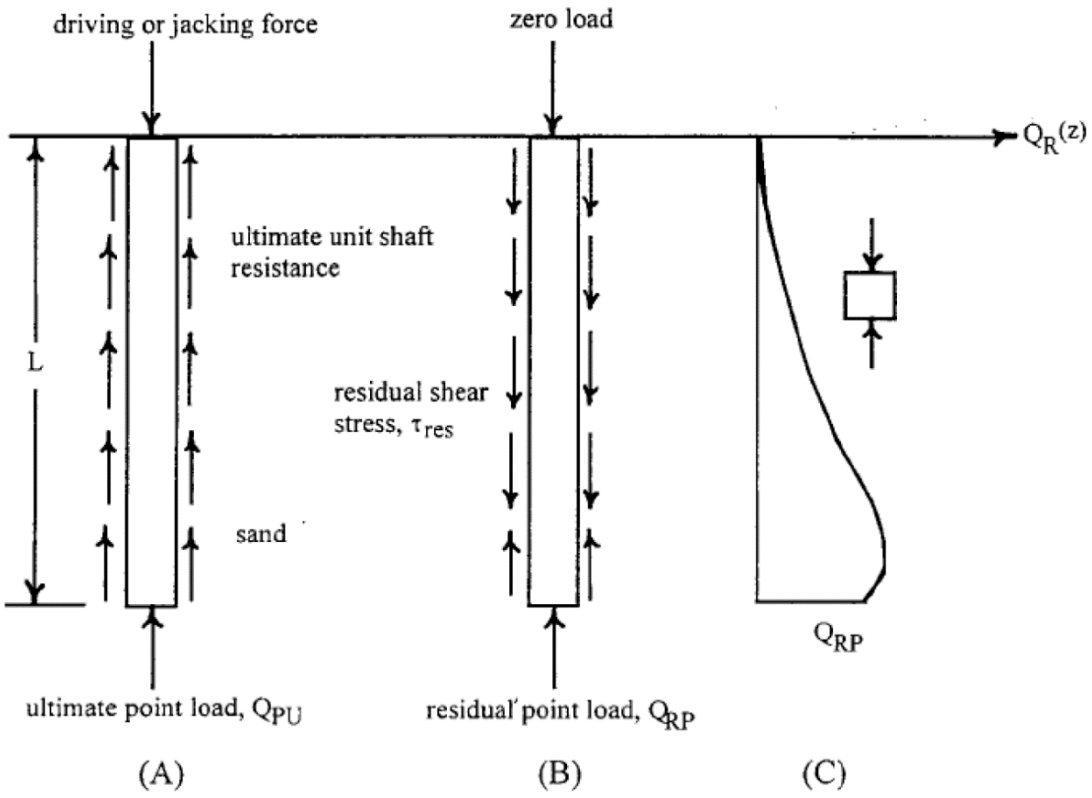


Figure 3-3 - Residual loads at the end of installation and their effect on base load (Alawneh & Malkawi, 2000)

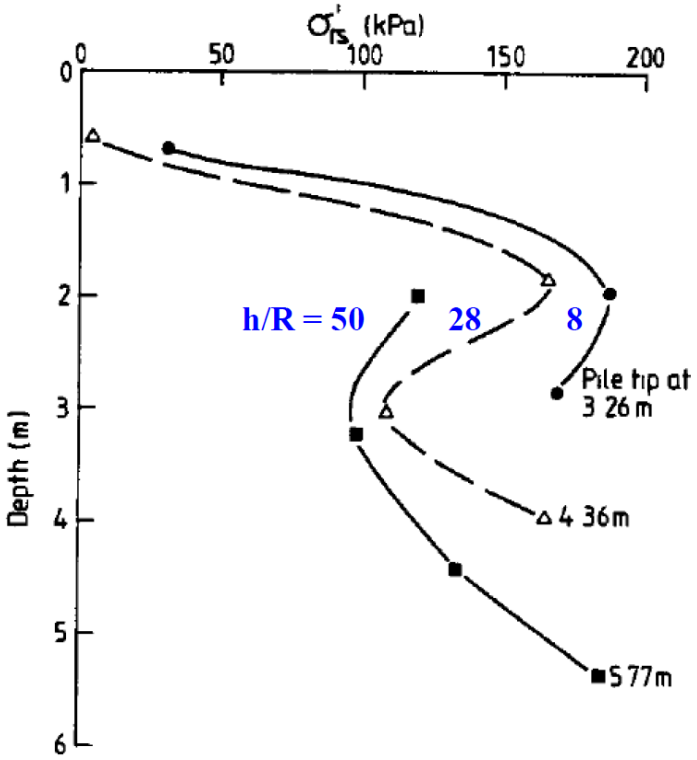


Figure 3-4 Stationary radial effective stresses during pile installation in medium dense Dunkerque sand (Chow, 1997)

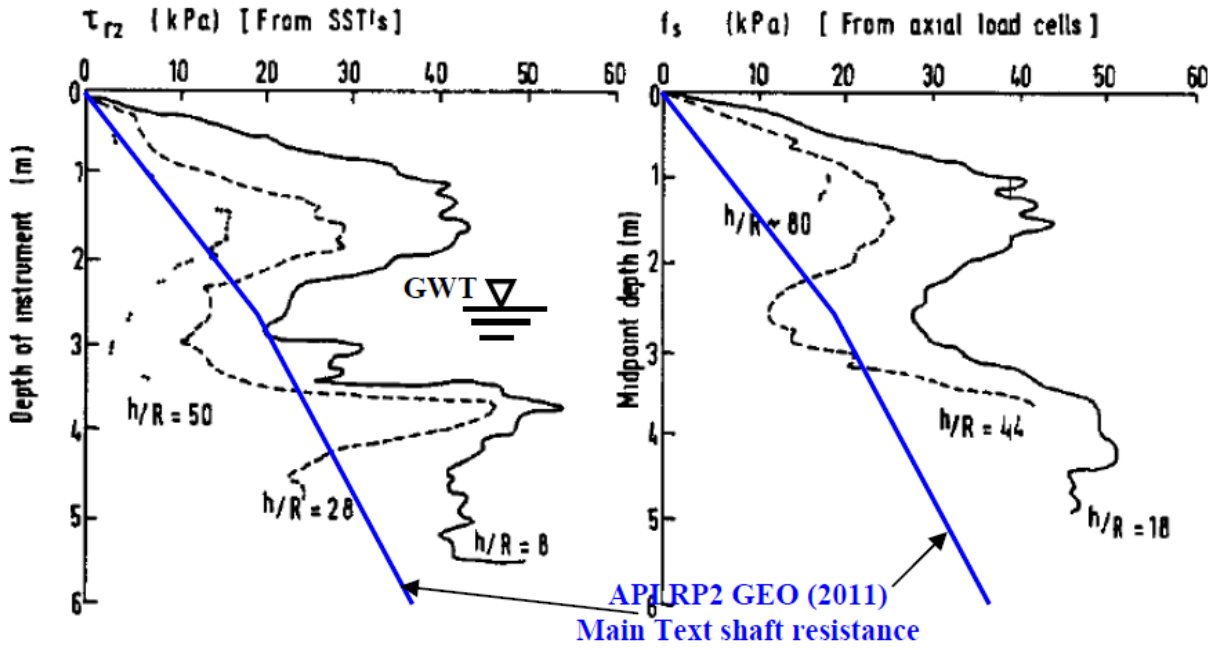


Figure 3-5 Comparison of shaft frictions measured during and after installation in Labenne sand with API RP2 GEO (2011) design method (Lehane, 1992 and Rimoy, 2012)

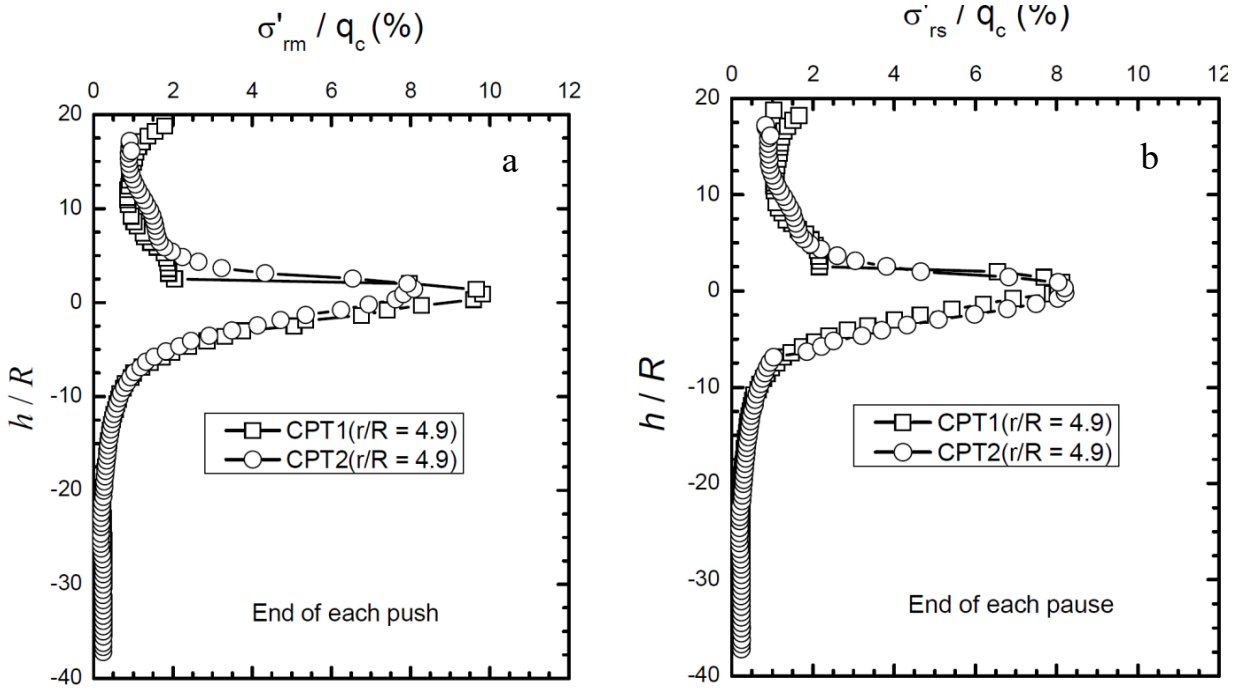


Figure 3-6 Effect of installation method on radial stresses at the end of each a) push; b) pause (Jardine *et al.,* 2013a) CPT1 test involved steady jacking, while CPT2 was installed by cyclic jacking with full unloading between each 20mm long jack stroke

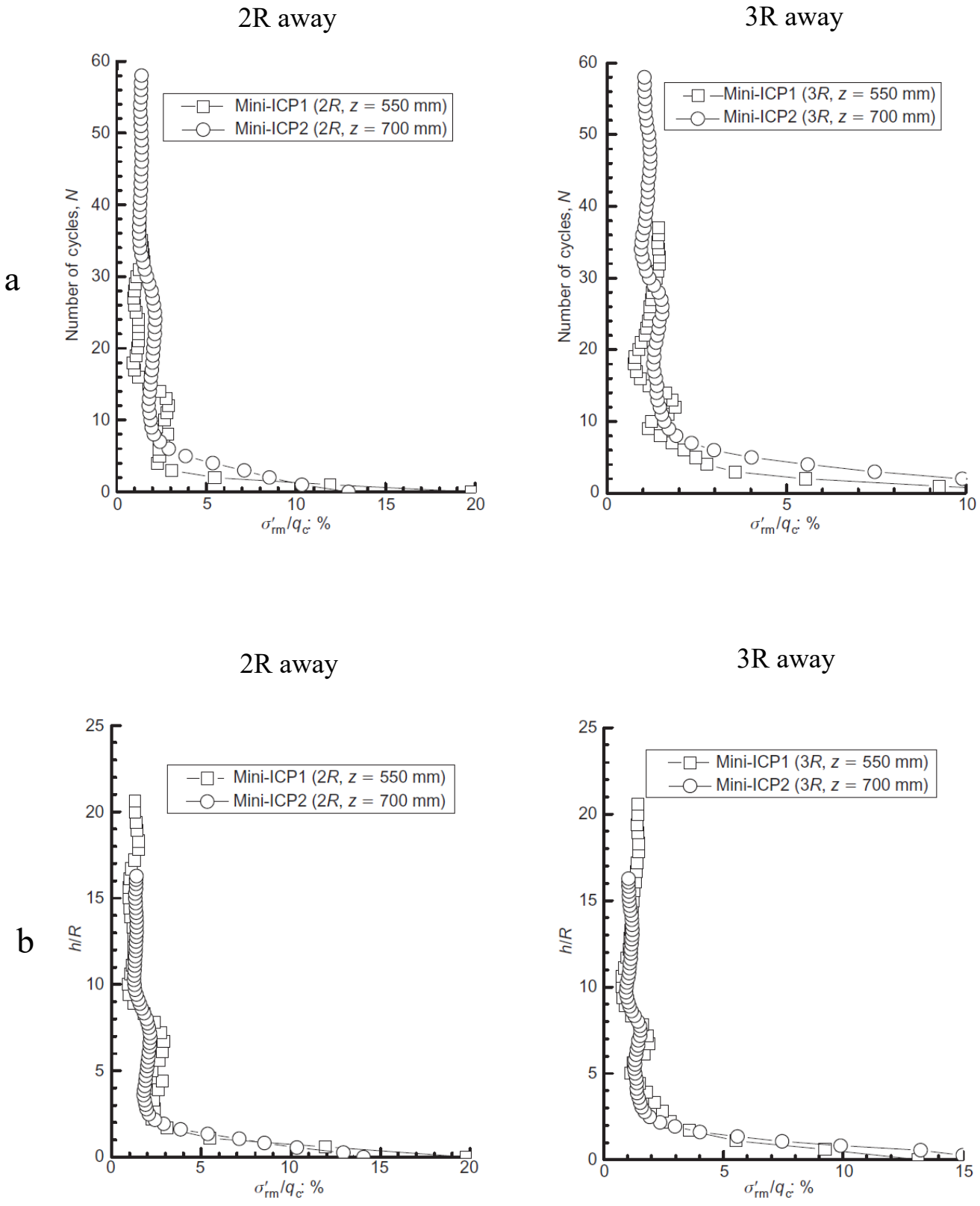


Figure 3-7 Normalisation of radial effective stresses by a) Number of cycles during installation b) h/R in 2R and 3R distances away from pile surface (Jardine *et al.,* 2013)

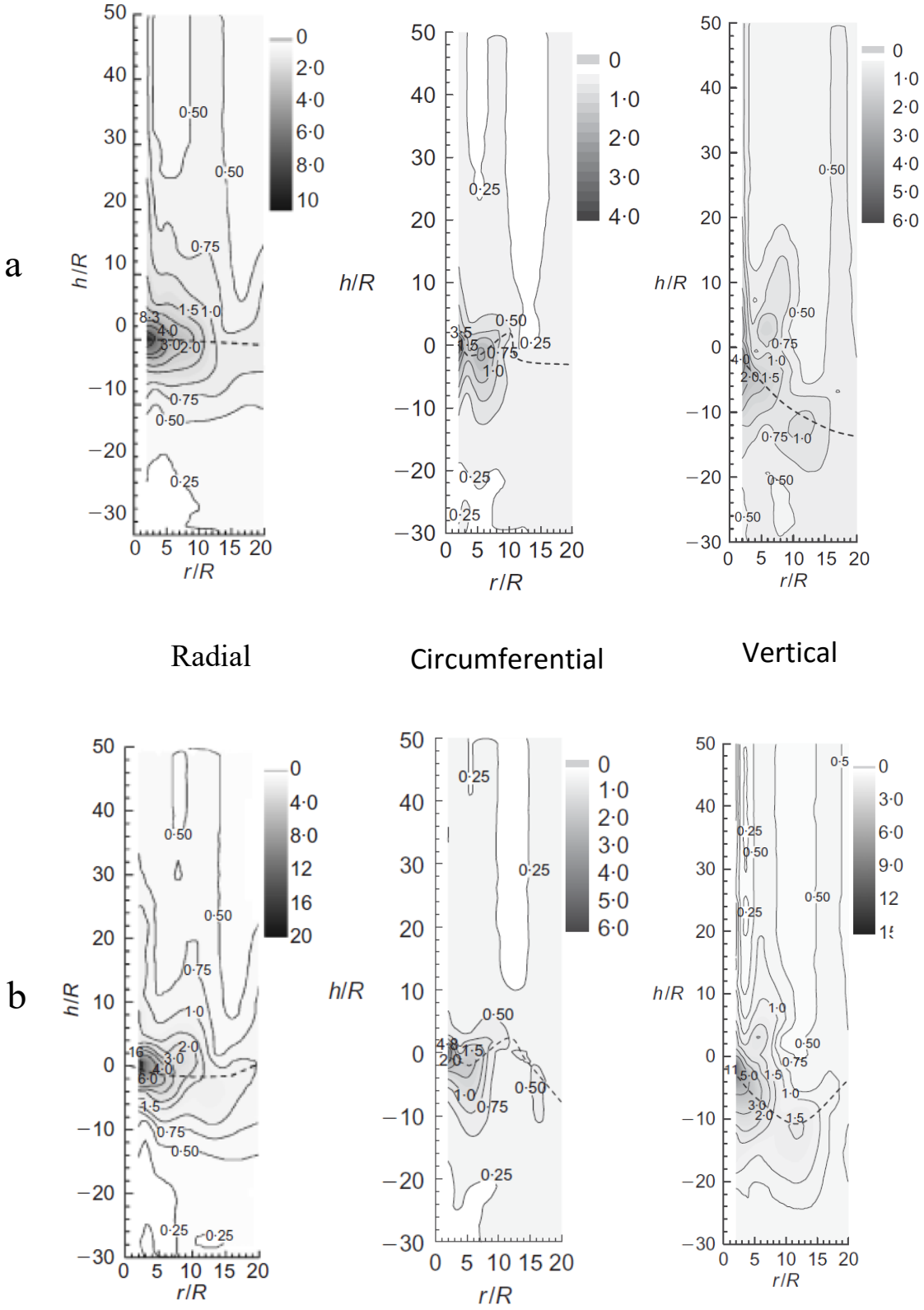


Figure 3-8 Radial, circumferential and vertical stresses at a) end of each pause and b) end of push in stationary conditions (Jardine *et al.*, 2013b) .

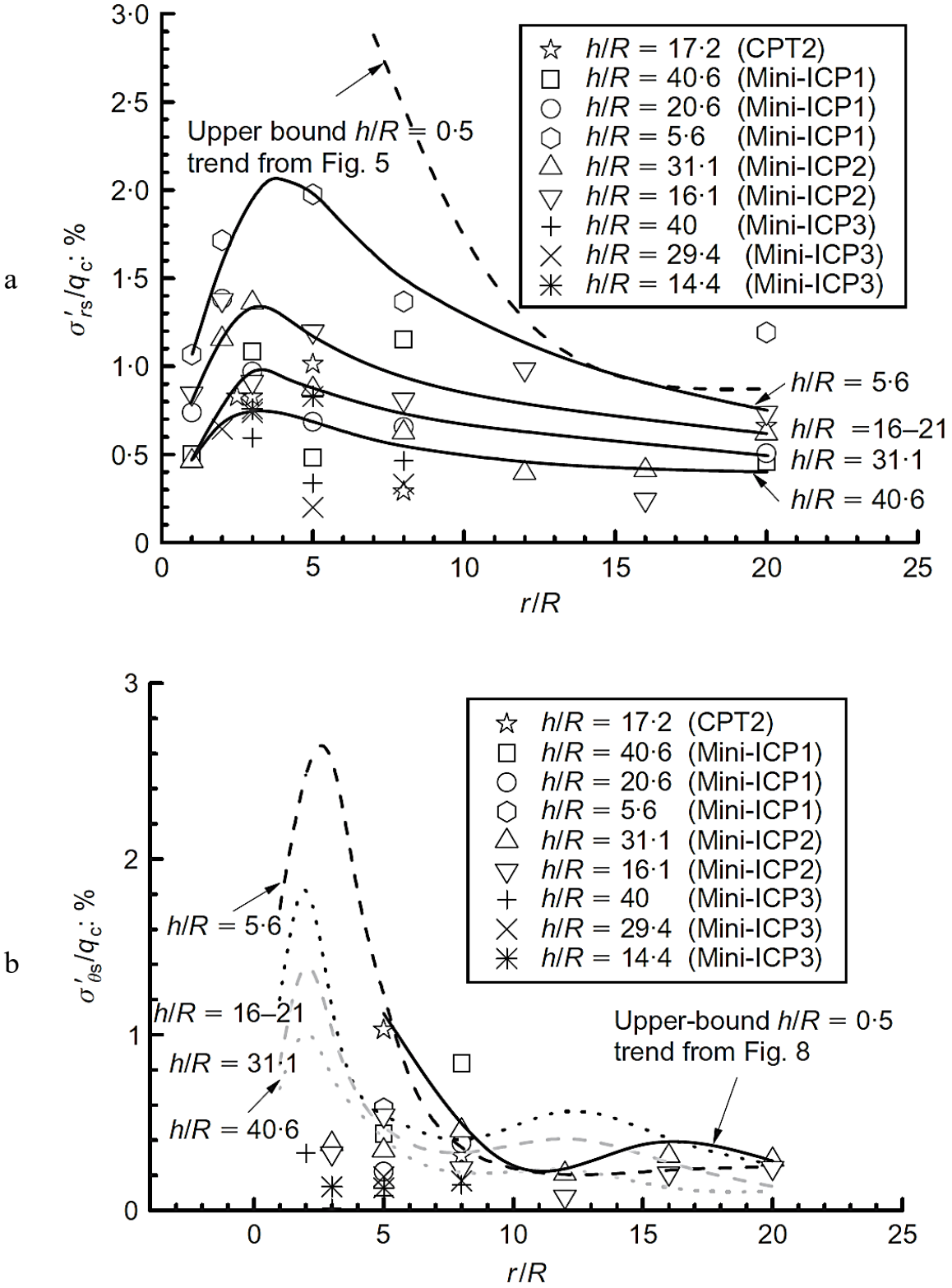


Figure 3-9 Stationary a) radial and b) circumferential stress at the end final jacking stroke during installation (Jardine *et al.,* 2013b)

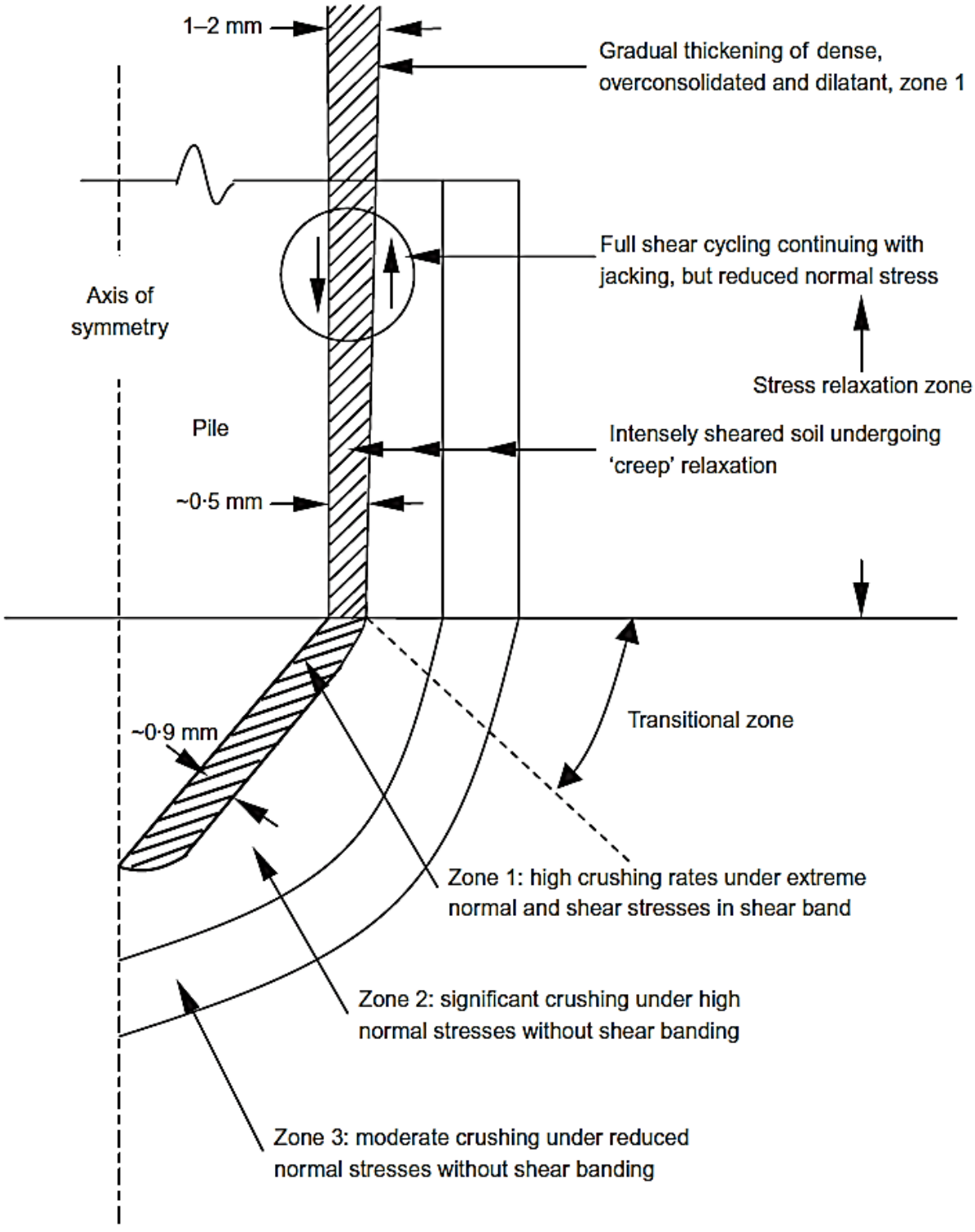


Figure 3-10 Schematic development of three zones of crushing and their stress level. (Yang *et al.,* 2013)

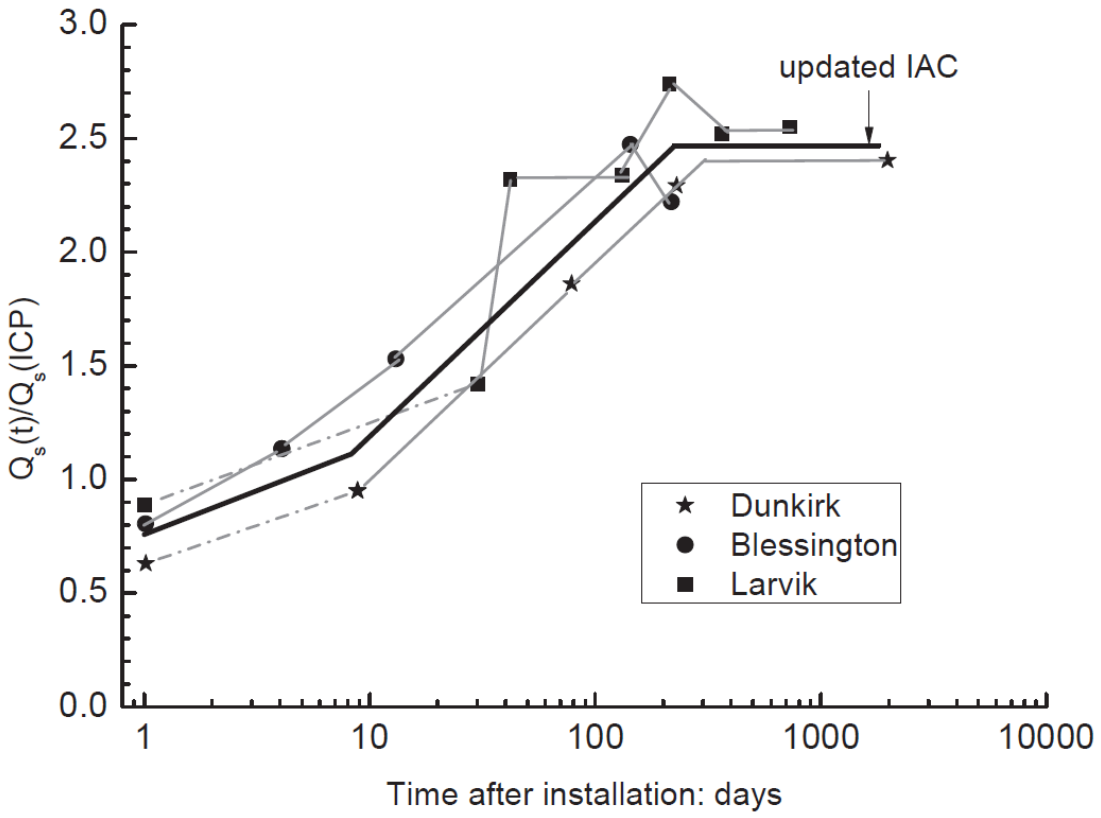
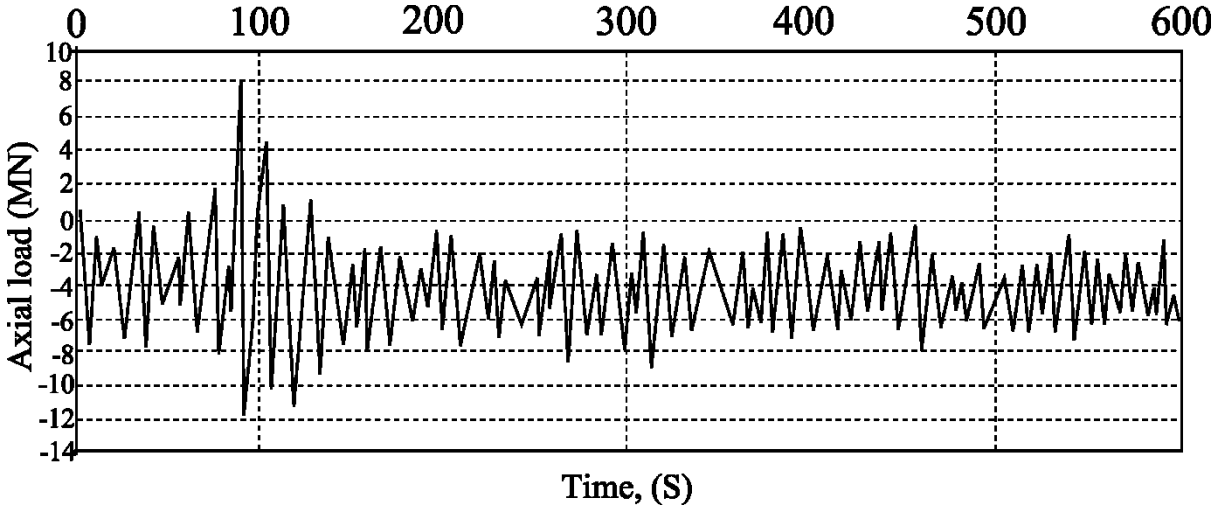


Figure 3-11 Static tension capacity-time tension capacity (Q_s) trends from tests on steel piles driven at three sand sites, normalised by ICP-05 tension capacities. (Q_s (ICP)) (Rimoy *et al.,* 2015)



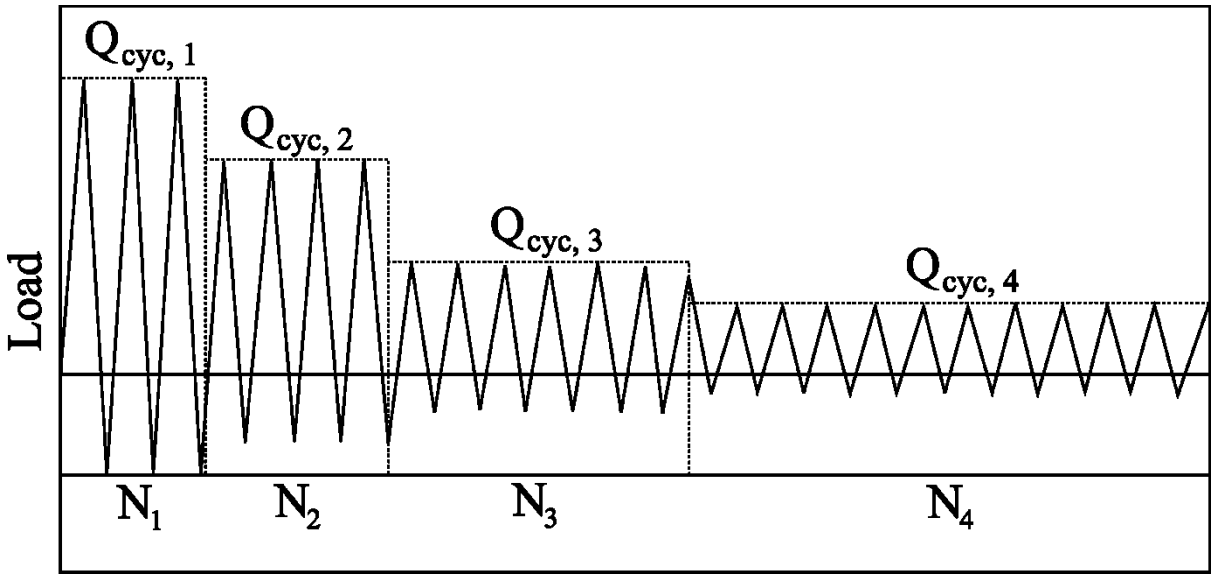


Figure 3-12 a)chart of 600s time history for worst tensile pile during peak of 35 hour design storm in Dunkerque b) Idealised series of uniform loads. (Meritt *et al.*, 2012)

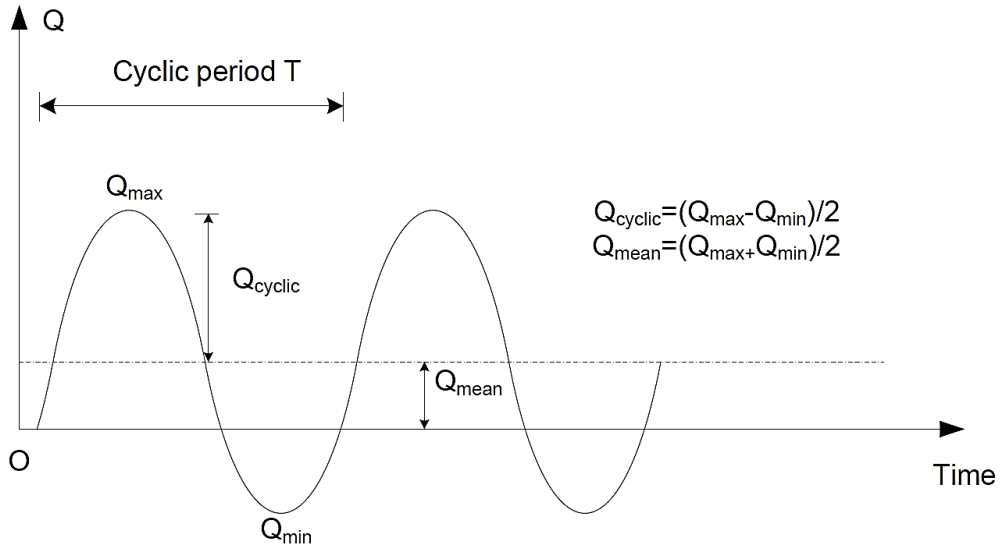


Figure 3-13 Schematic illustration of Q_{cyc} and Q_{mean} values (Tsuha *et al.,* 2012)

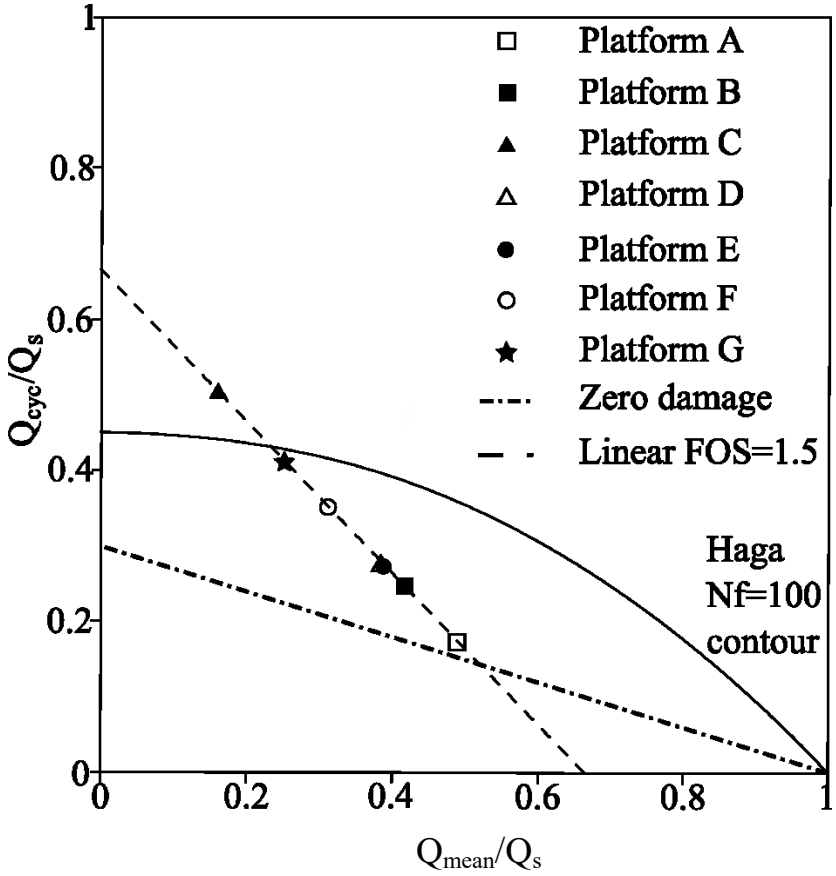


Figure 3-14 Illustration of potential cyclic effects; WSD, FOS=1.5 design conditions compared with Dunkerque zero damage and Haga Nf=100 contours in normalised interaction diagram

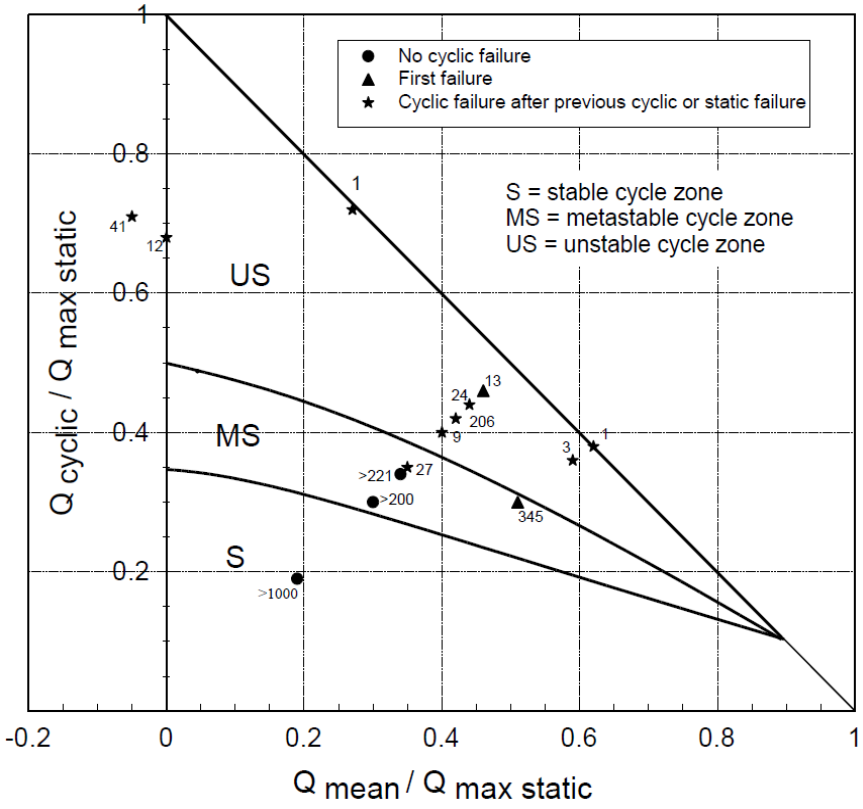


Figure 3-15 Interaction diagram indicating the influence of number of cycles (N) and Q_{cyc} and Q_{mean} on cyclic response with tentative *Stable*, *Metastable* and *Unstable* zones.

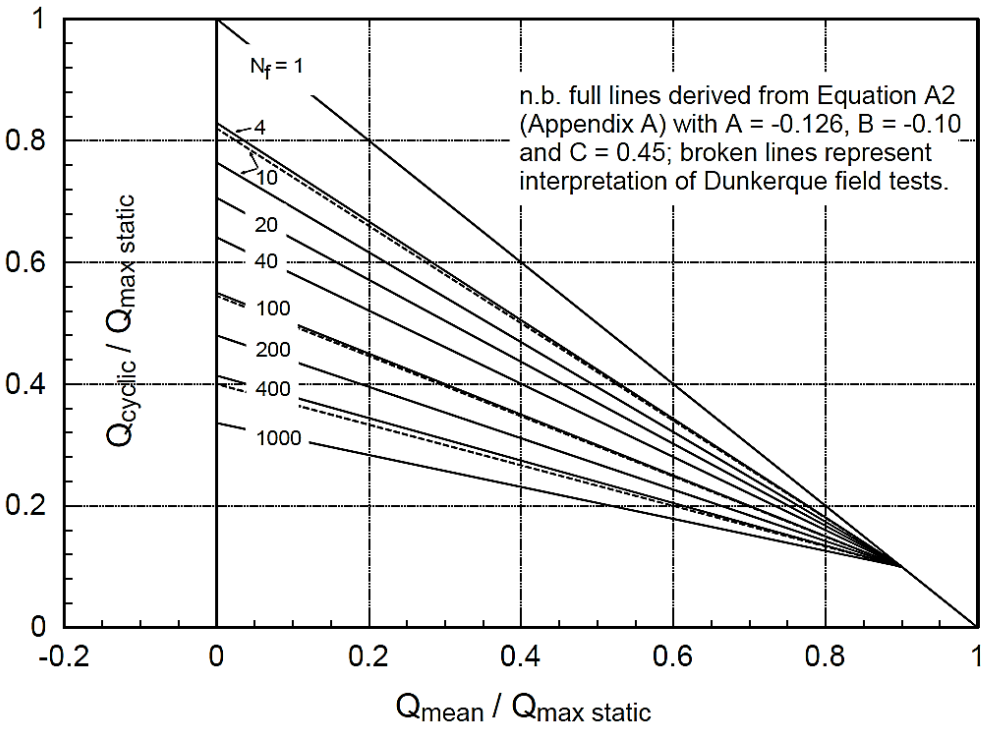


Figure 3-16 Interaction diagram based on methodology introduced by Jardine *et al.* (2005) to predict N_f in terms of Q_{cyc} and Q_{mean}

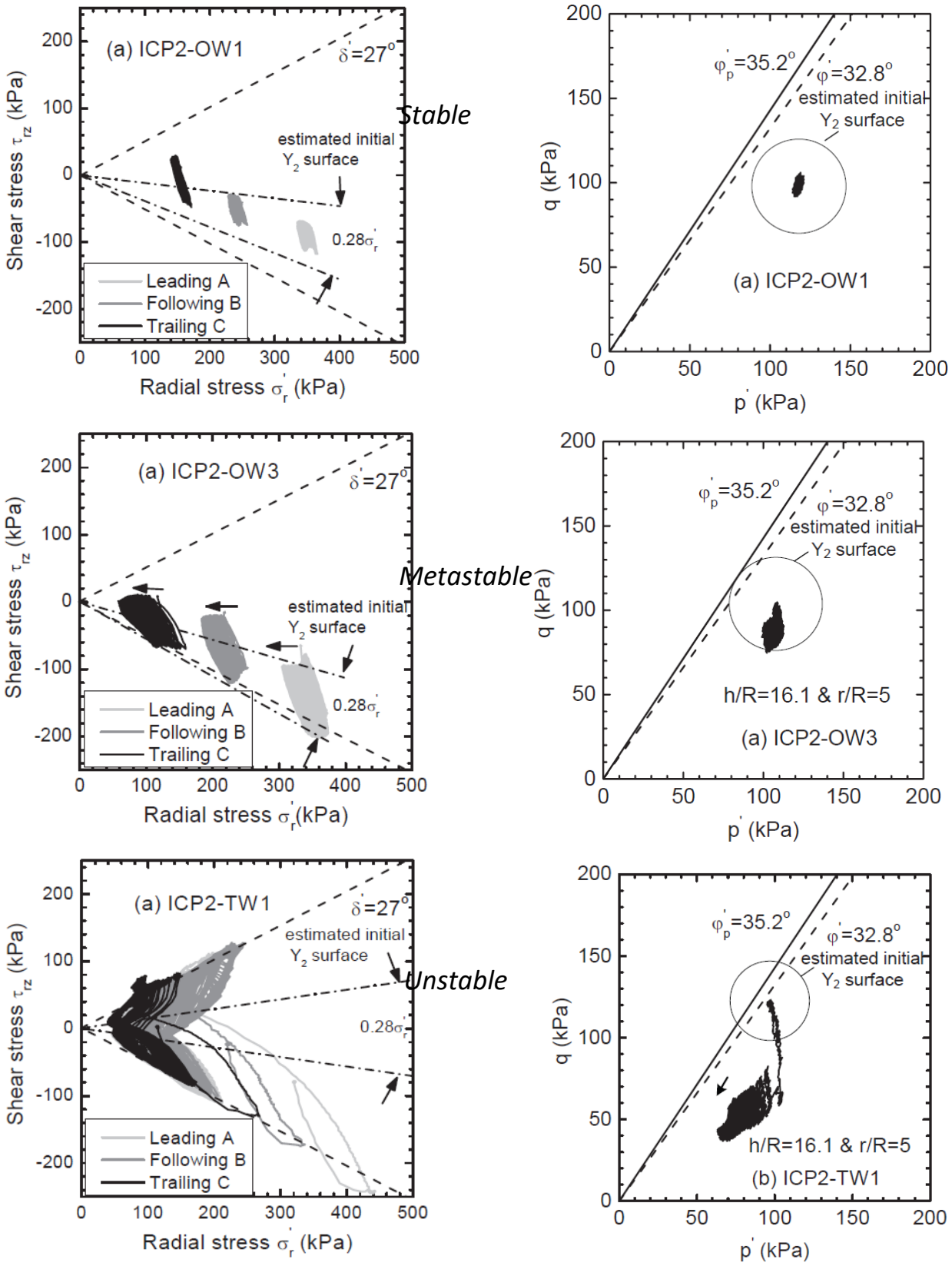


Figure 3-17 a) Effective stress paths recorded in ICP mini pile tests at three shaft levels (A, B, and C) and ultimate shaft failure interface envelope under *Stable*, *Metastable* and *Unstable* axial cyclic loading tests. b) Effective stress paths developed in sand mass at 5R, h/R≈15 during each test. (After Tsuha *et al.*, 2012)

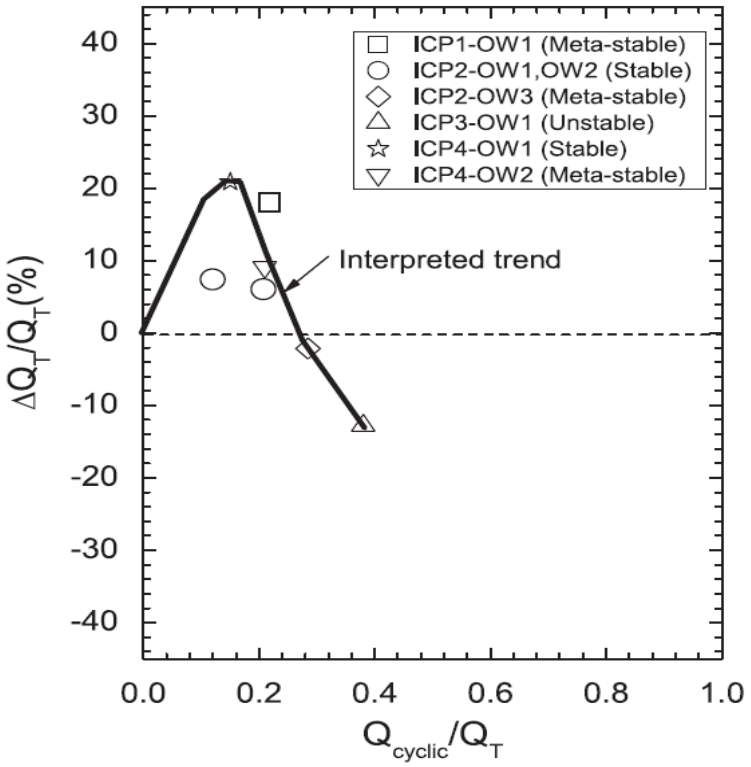


Figure 3-18 Effect of load cycling on tensile capacity in one-way model pile tests on NE34 sand. (Tsuha *et al.,* 2012) Q_T= Tensile capacity.

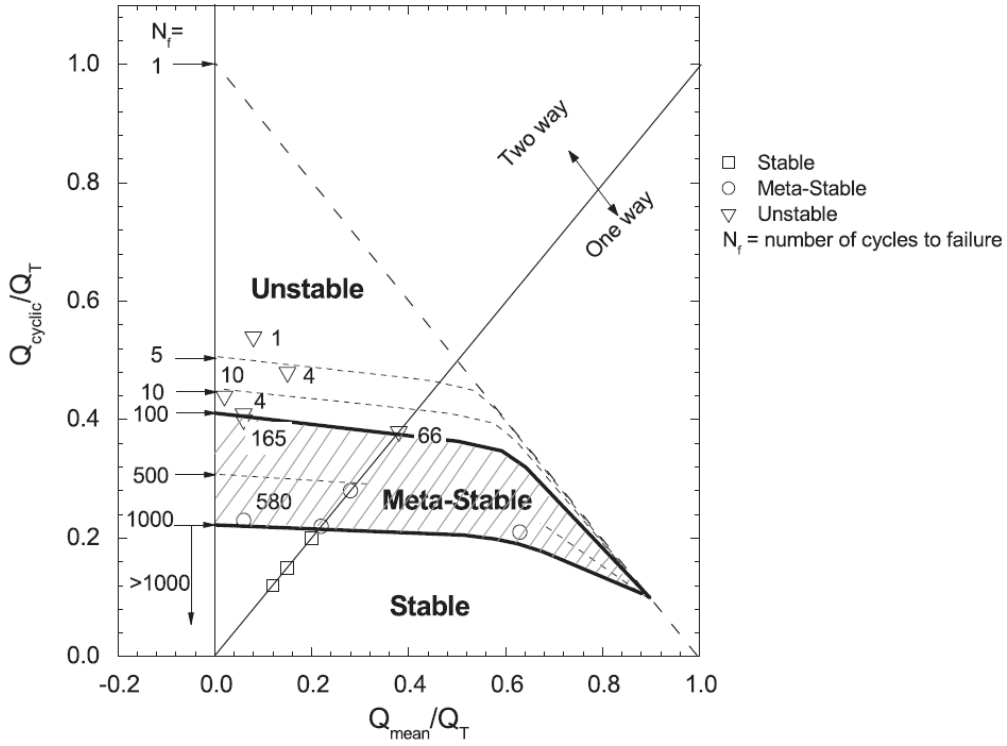


Figure 3-19 Interaction diagram indicating the influence of number of cycles (N) and Q_{cyc} and Q_{mean} on cyclic response with tentative *Stable*, *Metastable* and *Unstable* zones. (Tsuha *et al.,* 2012)

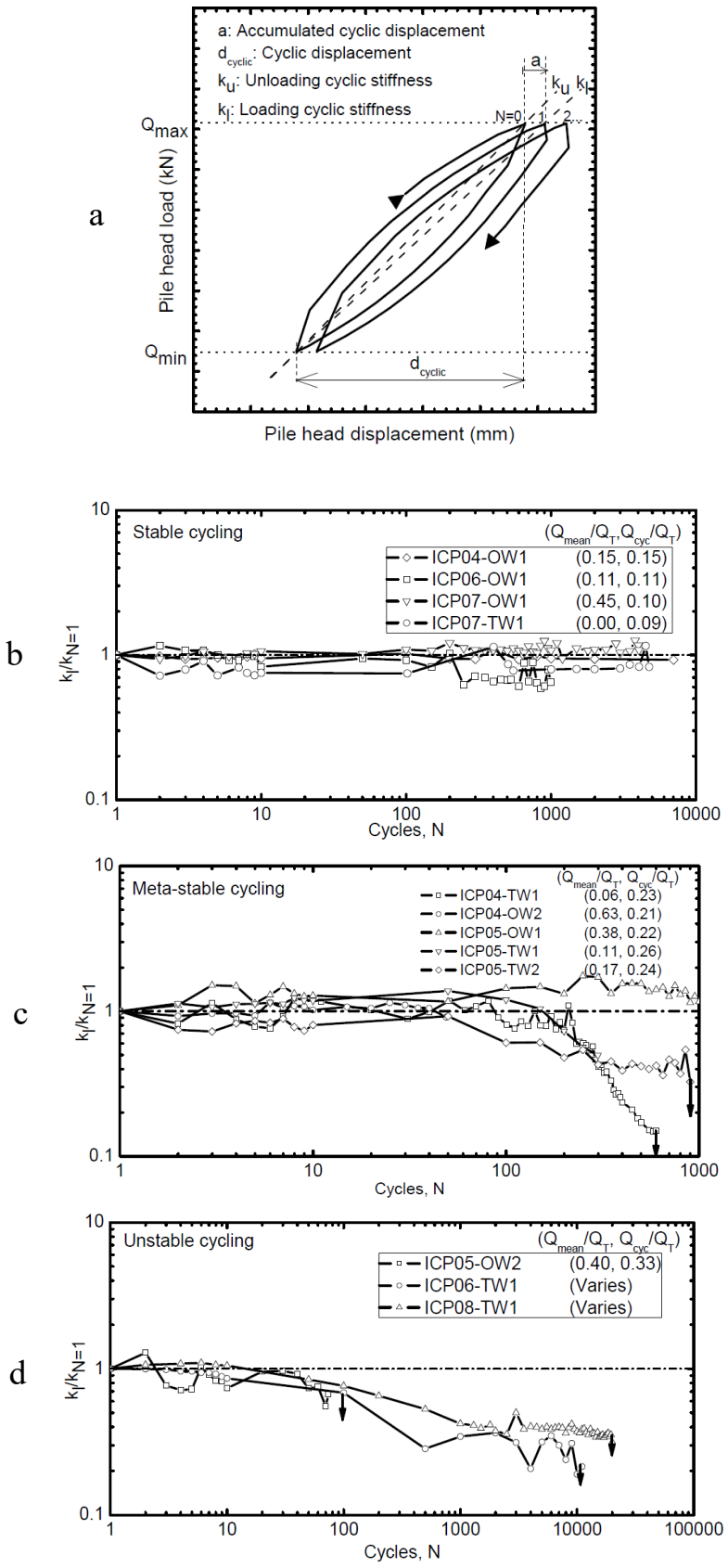


Figure 3-20 a) illustration of stiffness calculation. Normalised axial cyclic pile stiffness versus number of cycles applied in a) *Stable*, b) *Metastable* and c) *Unstable* cyclic model pile tests. (Rimoy, 2013). $K= (Q_{max}-Q_{min})/d_{cyc}$

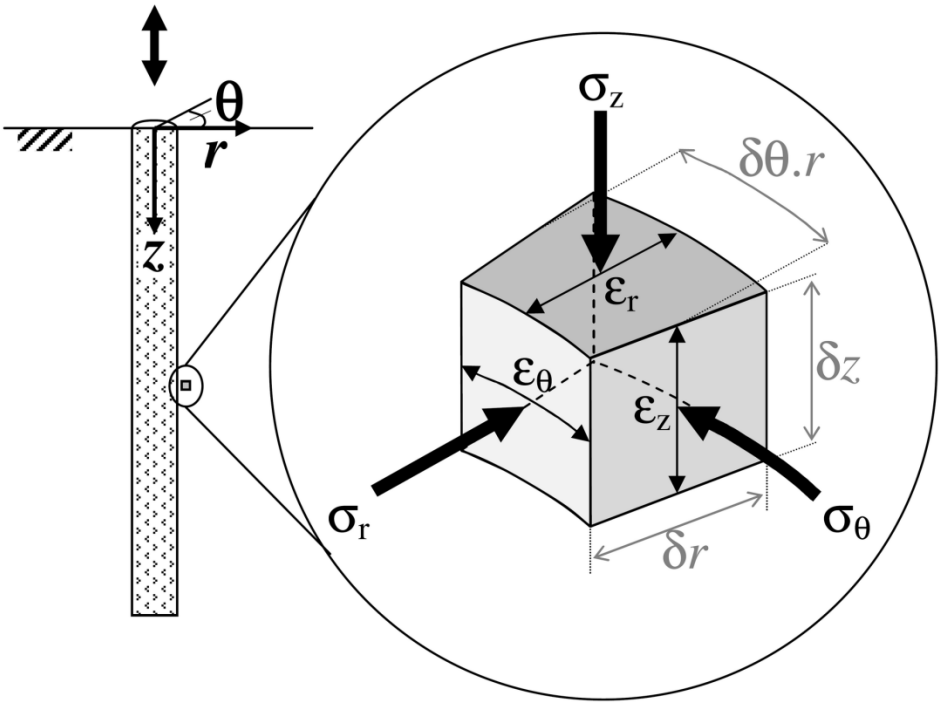


Figure 3-21 Stress and strain conditions for soil element adjacent to pile (Sim *et al.,* 2013)

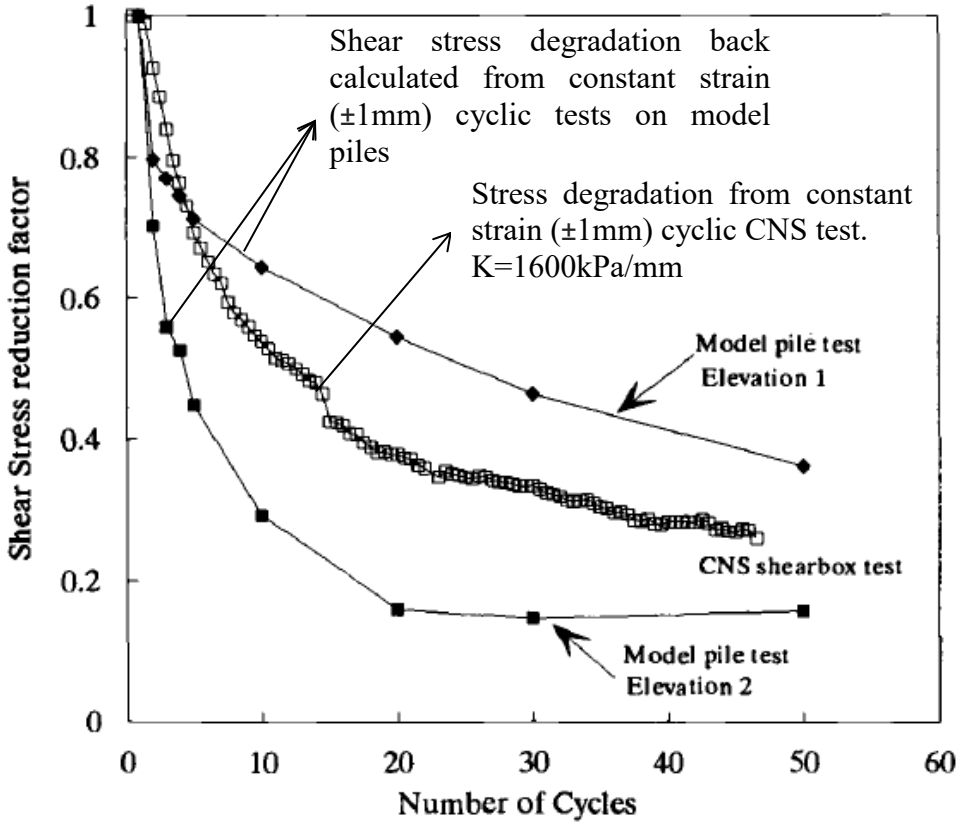


Figure 3-22 Comparison of shear stress degradation observed in model pile tests with prediction made from cyclic CNS tests.

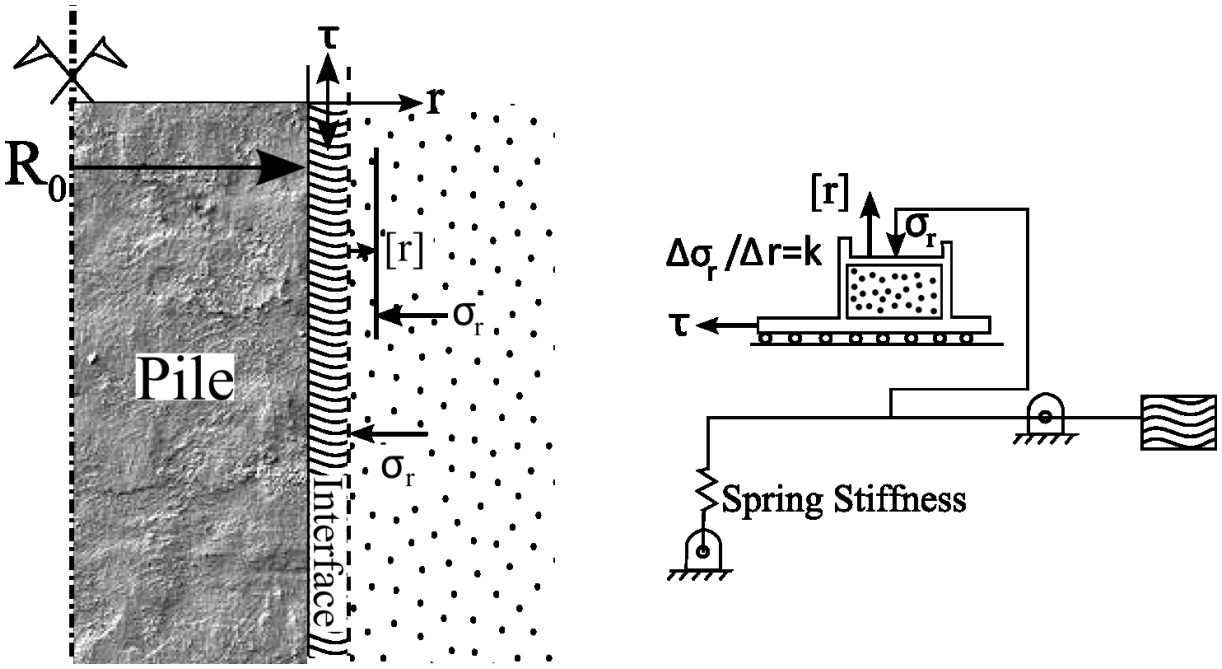
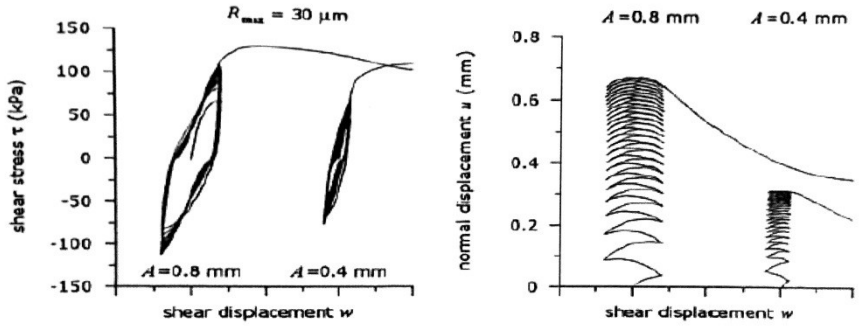


Figure 3-23 Analogy for modelling soil-pile interaction in laboratory testing (After Boulon & Foray, 1986)

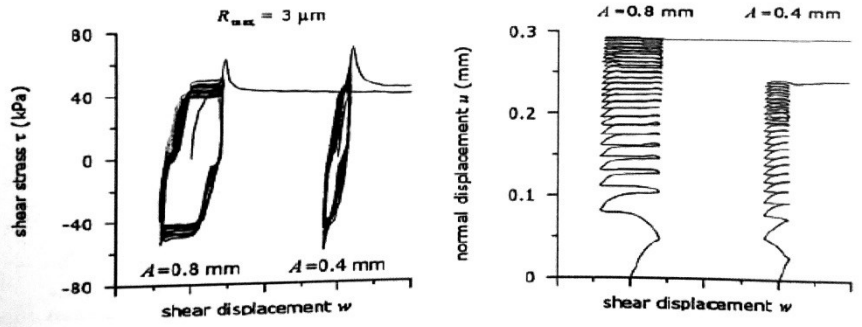
Loose

Smooth surface



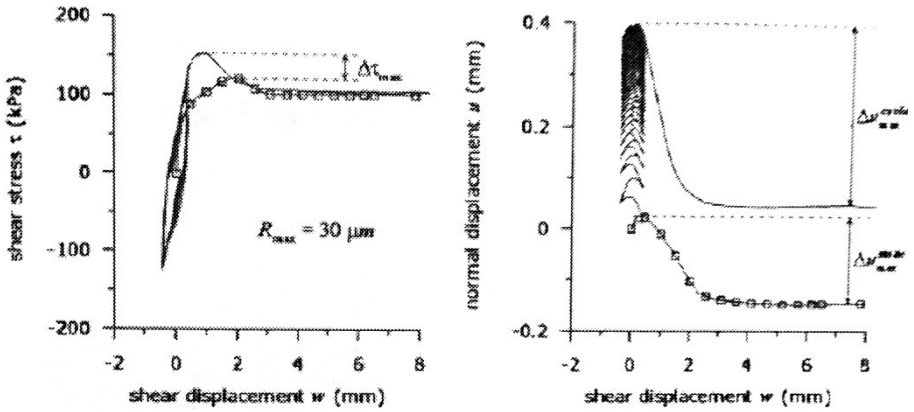
Loose

Rough surface



Dense

Loose surface



Dense

Rough surface

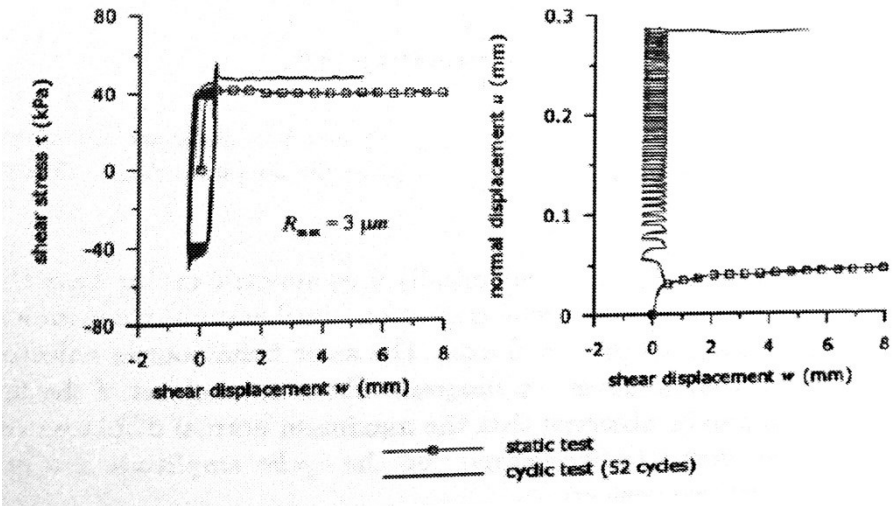


Figure 3-24 Cyclic CNL tests on loose and dense Toyoura sand in rough and smooth surfaces (Mortara, 2001)

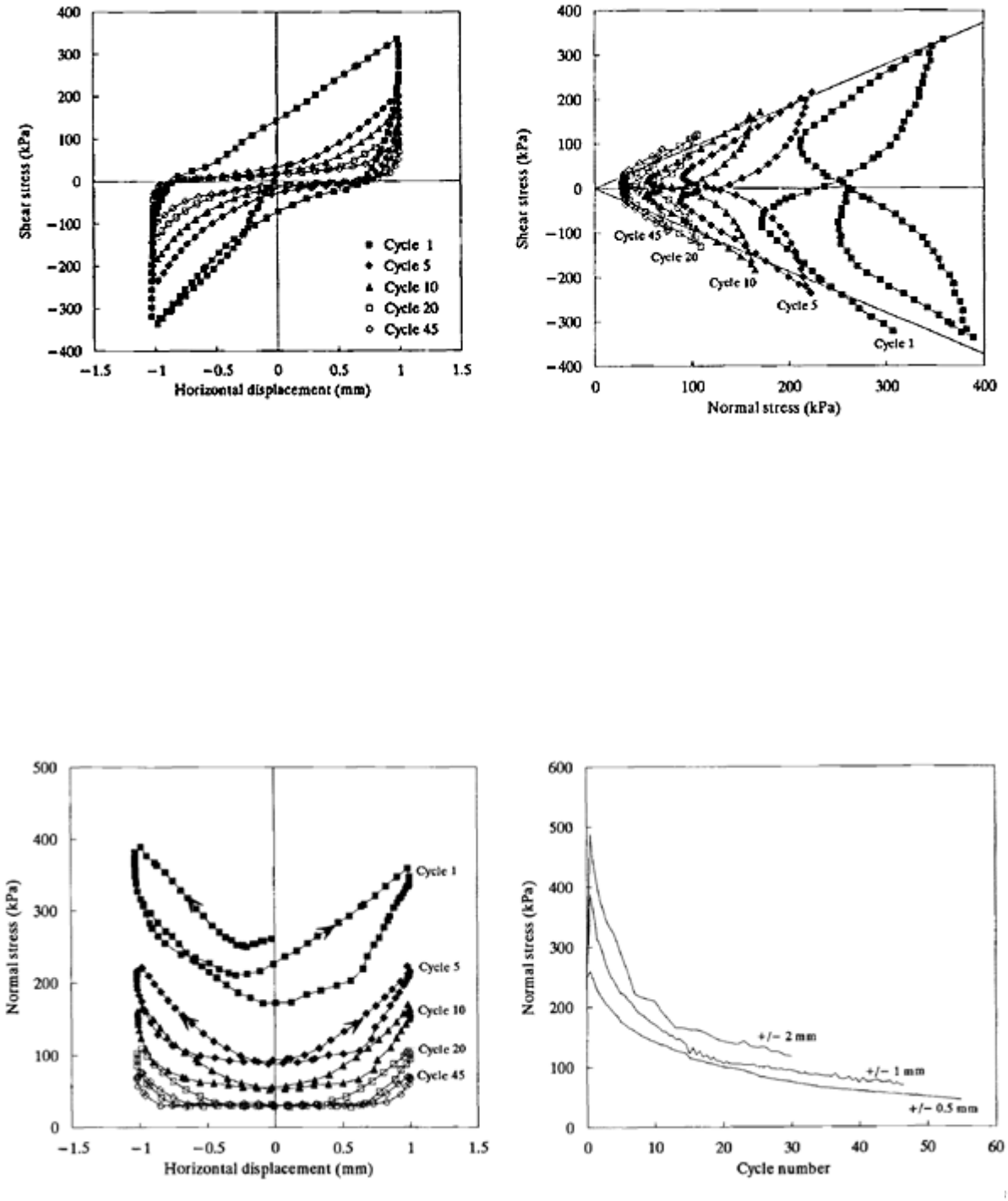


Figure 3-25 Evolution of shear and normal stresses during cyclic CNS soil-soil test (Airey 1992)

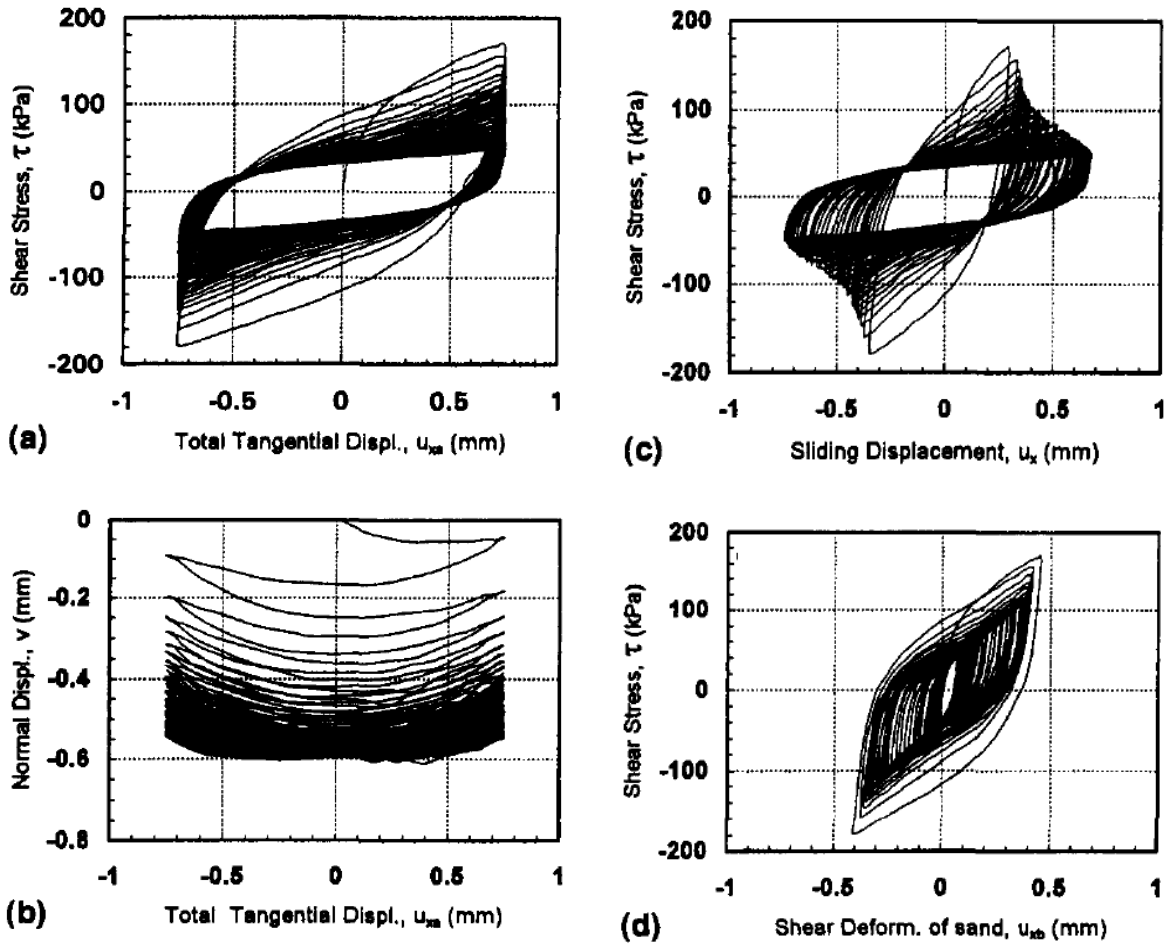


Figure 3-26 Two-way CNS tests on silica sand (Fakharian & Evgin, 1997)

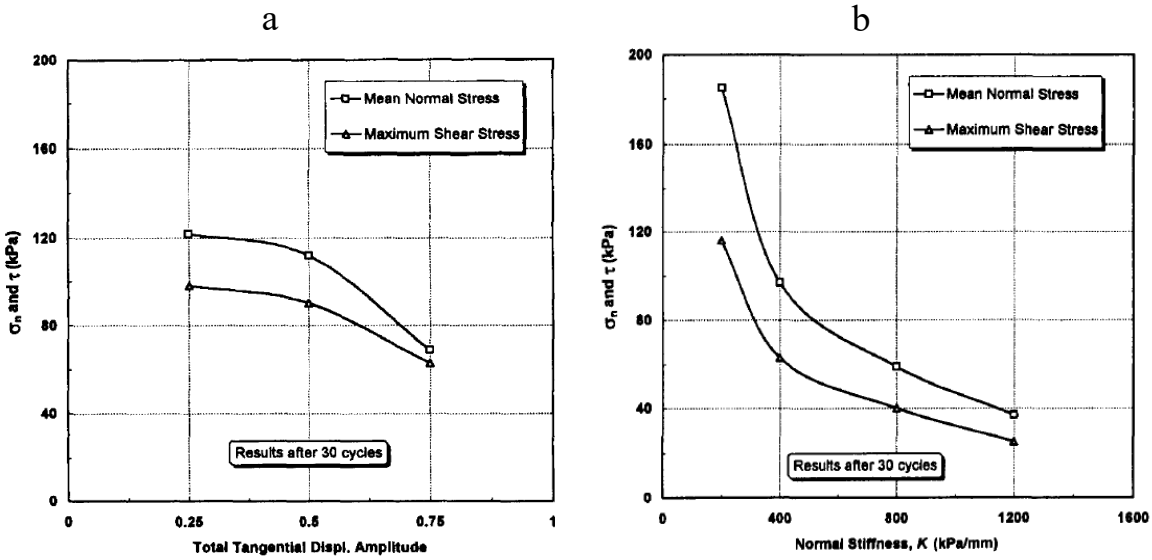


Figure 3-27 a) Effect of cyclic amplitude on normal and shear stresses b) Effect of K_{CNS} on normal and shear stresses (Fakharian & Evgin, 1997)

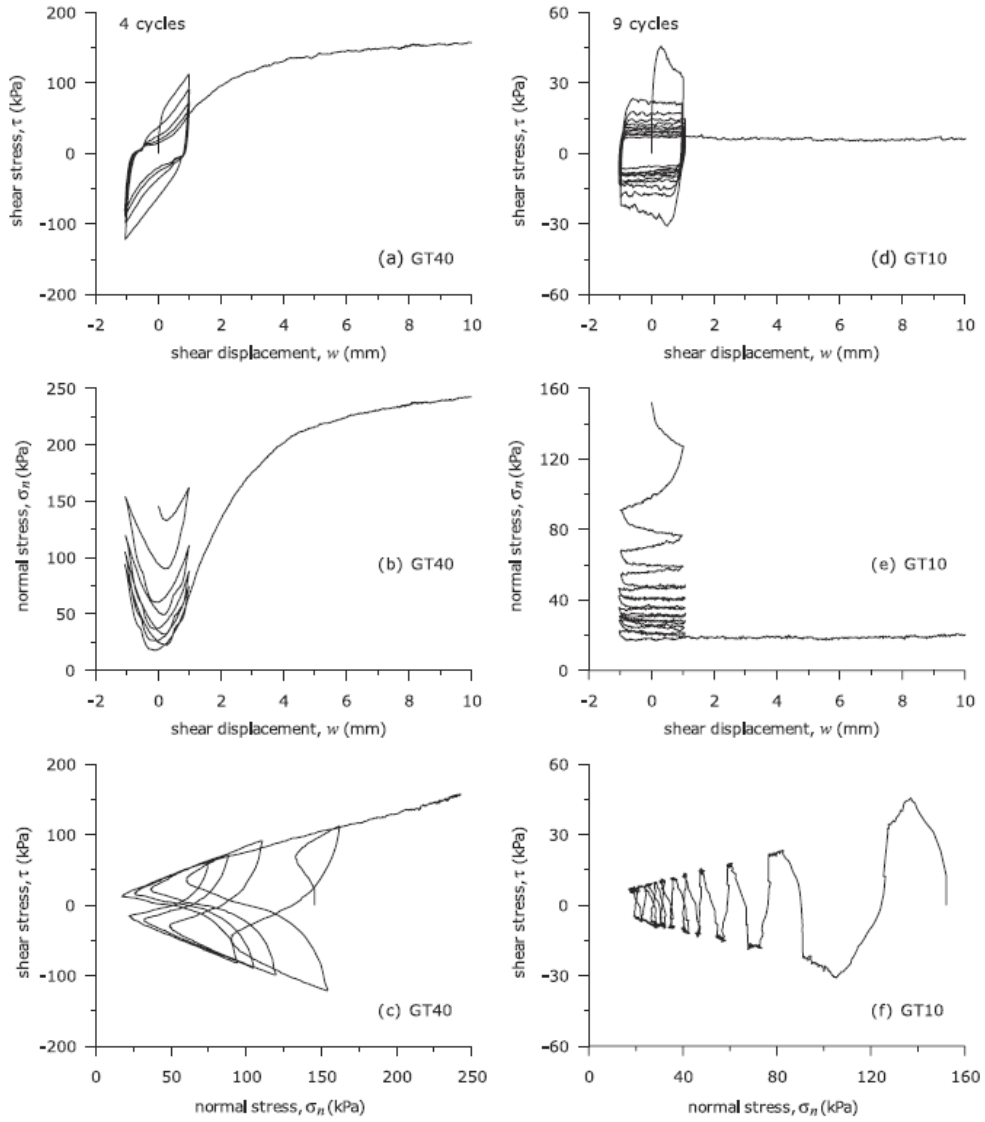


Figure 3-28 Comparison between CNS tests on rough and smooth surfaces (Mortara *et al.*, 2007)

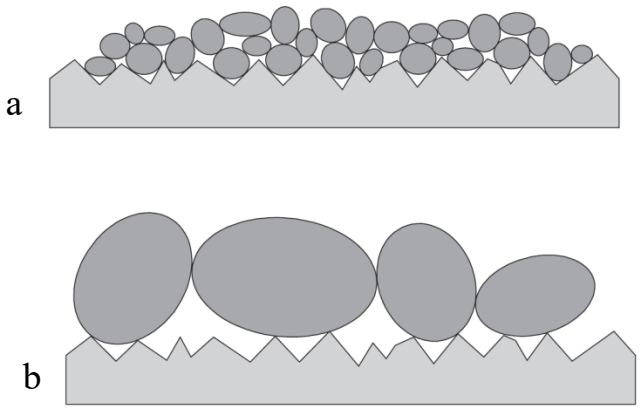
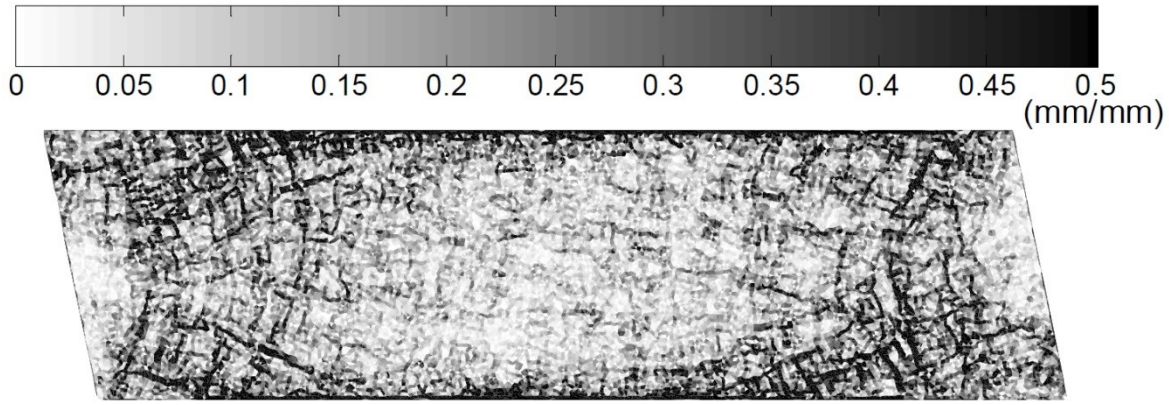


Figure 3-29 Interpretation of interface roughness a) rough interface b) smooth interface (Mortara *et al.*, 2007)

a



b

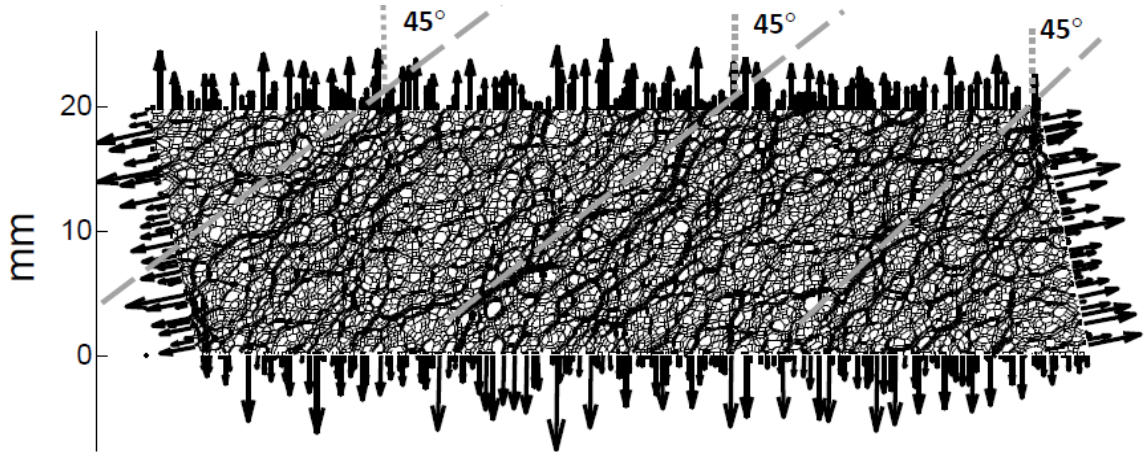
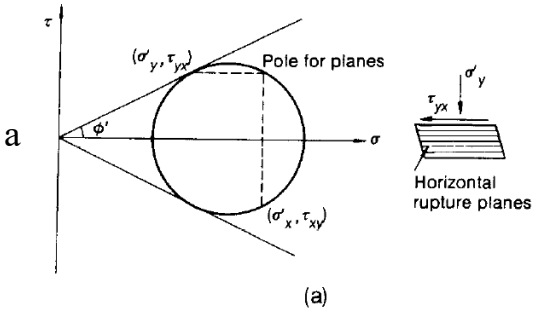


Figure 3-30 DEM analysis to simulate "Cambridge" style simple shear apparatus. a) incremental maximum deviatoric strains for frictional flat boundary specimen at 20% shear strain b) Plot of internal contact force chains and the force on the boundaries at20% shear strain from central portion (Shen ,2012)

a



b

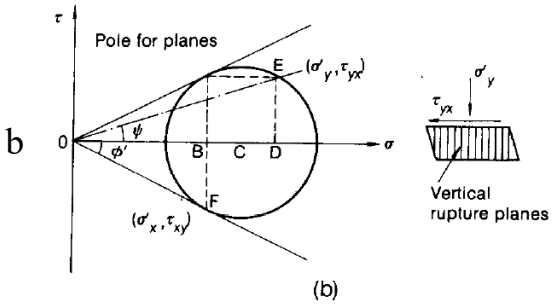


Figure 3-31 Possible modes of failure in simple shear tests (Randolph & Wroth, 1981)

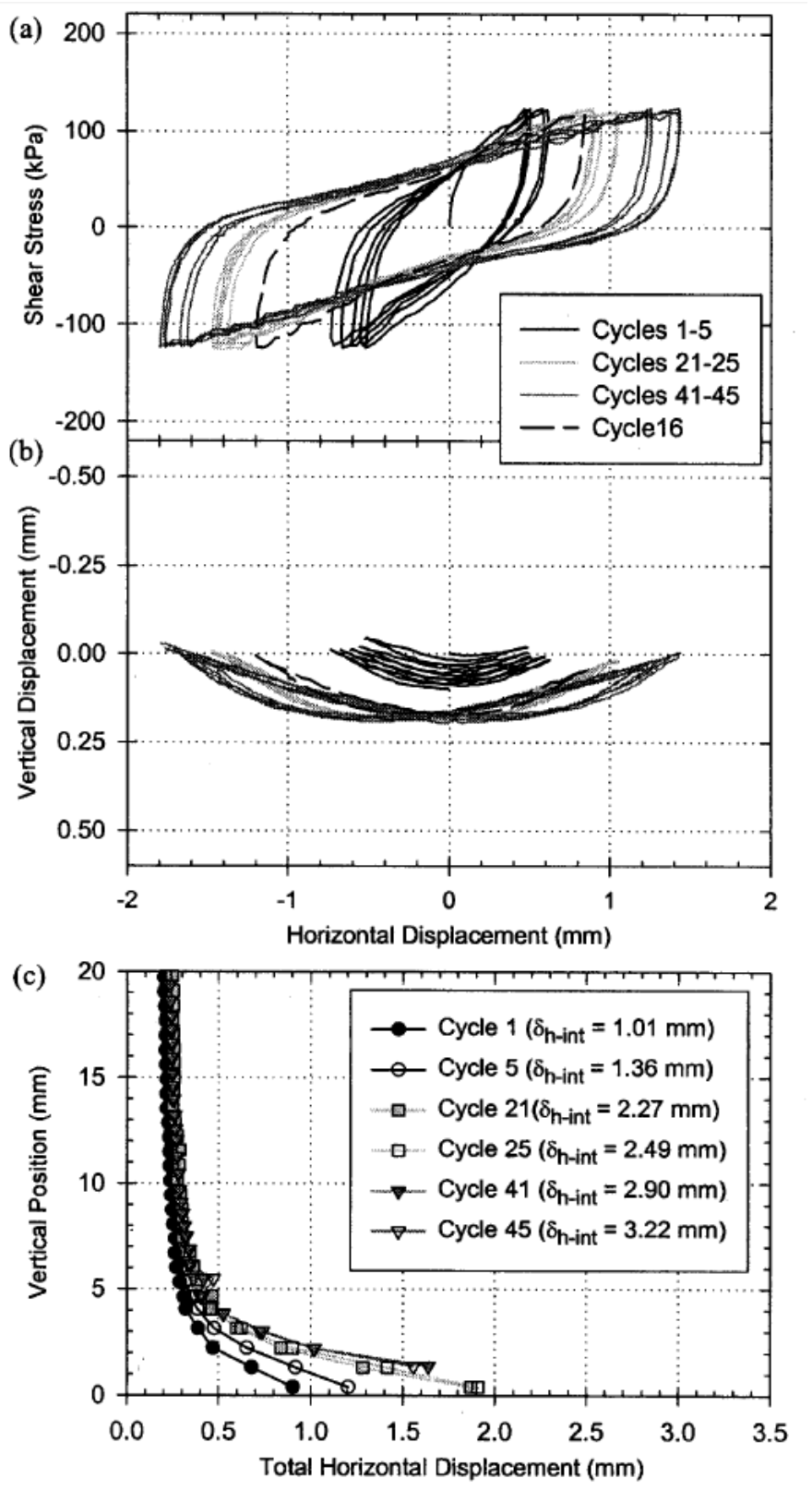


Figure 3-32 a) Shear stress vs horizontal displacements b) vertical displacement vs horizontal displacements and c) vertical position vs total horizontal displacement from cyclic tests monitored by GeoPIV image processing technique. (Dejong *et al.*, 2003)

CHAPTER 4
Apparatus description and sample preparation technique

Introduction

This chapter presents a detailed description of the two main apparatuses used, the triaxial stress path and Hollow Cylinder Apparatus (HCA). The methods for calculation of stresses, strains and their invariants are also discussed. In addition, limitations and systematic errors that exist in each apparatus are reviewed and the modifications made to perform cyclic tests are also summarized. Finally, the sample preparation procedure used to create the pluviated reconstituted sand specimens is presented.

4.1 Triaxial Stress Path Apparatus

4.1.1 General structure of apparatus

The triaxial stress path apparatus is commonly used in geotechnical engineering and research. Although the name suggests that the apparatus is able to control three principal stresses, it is only able to control and measure two axisymmetric principal stresses in vertical and horizontal directions. Therefore, the intermediate principal stress is equal to either σ_1 or σ_3, depending on whether the axial stress or radial stress is their higher of the two. The other limitation of the triaxial stress path apparatus is its inability to apply horizontal or vertical

shear stresses, or rotate the principal stress axes apart from 90 degree jump rotations. Both of these limitations can be overcome in hollow cylinder apparatus (HCA) apparatus, as described later in this chapter.

The Author employed two modified Bishop & Wesley (1975) 38mm diameter sample size stress path triaxial cells. A schematic representation is shown in Figure 4-1 and a photograph of one of the sets used is shown in Figure 4-2. The pressures required for controlling cell, back and ram pressures were supplied by a central air compressor system (which supplies 800 kPa air pressure) and were controlled by automatic electro-pneumatic controllers developed at Imperial College by Toll & Ackerley (1988) which allow very accurate air pressure changes (as small as 0.07 kPa) using a digitally controlled stepper motor. The controlled air pressure is then transferred to water pressure using an in-house air-water interface system.

The cell is filled with de-aired water and is connected to cell pressure line which controls radial stresses (σ_r) applied to the sample. The back pressure line is connected to an Imperial College volume gauge and applies the pressures to the sample through a line at the base of the piston where sample seats. The triaxial stress path cell can control either axial stress or axial strain via the ram pressure chamber at the base of the cell following the original design by Bishop & Wesley (1975). The stress control is provided by an air-water interface and strain control is provided by a constant rate of strain pump (CRSP) which is a piston controlled by a stepper motor. The CRSP system is able to apply pressures higher than the 800 kPa limit of the air pressure system. However, the speed of response of the CRSP is slower, making it unsuitable for fast cyclic tests.

The top of the sample is connected to the load cell that measures the deviatoric load using a suction cap. The suction cap is made from silicone rubber and allows extension loads to be applied. It also aligns the vertically to avoid eccentric loading and specimen tilting.

4.1.2 Transducers

Ten transducers are installed on or in the "38 mm cells" to measure:

- Deviatoric force: one submersible pressure compensated load cell
- Pressures: Cell pressure; Back pore pressure; Ram pressure
- Displacement: One external axial; Two local axial; One local radial strain sensors
- Volume change: One volume gauge
- Temperature: Cell water temperature

Further details of these devices are outlined below.

4.1.2.1 Deviatoric load cell

A submersible "Applied Measurements Ltd" STALC3 series load cell was placed at the top of each apparatus inside the cell to measure the deviatoric load (F_a). The load cell is able to measure up to ±5 kN compression and tension and incorporates an internal pressure compensation system that eliminates zero offset changes when it is subjected to cell pressure changes. Figure 4-3 shows the general appearance and the internal structure of these load cells.

The "Imperial College" load cells used since the early 1970s had a small "dead-spot" in their measurement ranges around the zero deviatoric load level. The dead-spot was caused by unrestrained deformation of the triangular webs that measured the loads through sensing their deflections under bending with strain gauges. The load cells used in this research have an internal structure that employs shear webs that are instrumented with four inclined strain gauges at connection points as shown in Figure 4-3. The system is far stiffer and no layer suffers from any "dead-spot" error.

The load cells were calibrated against a Budenberg dead-weight tester and gave a linear relation between output voltage and the imposed load.

4.1.2.2 Pressure transducers

Three Druck semiconductor pressure transducers were employed to measure the cell, back pore water and ram pressures. These transducers are able to measure positive pressure of up to 10 bar however at negative pressures less than -50 kPa cavitation occurs and pressure cannot be measured. Similar to load cells, pressure transducers were calibrated against a Budenberg dead-weight tester and gave a linear relation with output voltage and imposed pressure.

4.1.2.3 Temperature transducer

Tests were performed in a temperature controlled room with temperature kept at 20°C. However, temperature fluctuation of ±0.75C° during the day was possible. To monitor these changes, a temperature transducer was installed inside the cell to measure the temperature changes of the cell water.

4.1.2.4 Displacement transducers

An "Applied measurements Ltd" SGD series strain gauged displacement transducer was connected to the ram piston arm assembly to measure the axial displacement of the entire sample and its load cell. The transducer is able to measure up to 50 mm of displacement and gives linearly proportional output voltage in relation to the movement. However, data from this external displacement transducer is affected by system compliance including that due to the load cell and drainage disks and samples end's bedding and tilting under loading, as well as temperature fluctuations outside the cell. It is not possible to record small strain data accurately such external transducers (Jardine *et al.*; 1984).

Three RDP D5W/200W submersible LVDT transducers were used to improve the small strain measurements. Two axial and one radial LVDTs, with linear ranges of 10mm, were directly attached to the sample as proposed by Cuccovillo & Coop (1997) and shown in Figure 4-4. In this setup, the movement of the armature inside the transducer changes the

output voltage which is sent to the data logger. Axial LVDTs were located in two opposite sides of the sample at middle heights and the radial LVDT was placed in a radial belt at the middle height. The problem with the installation of a radial LVDT in the horizontal orientation was that at very small strains the armature stuck to the inner wall of the transducer under its own weight. However, this issue became less significant once radial strains exceeded 0.05%.

The effects on LVDT readings of small temperature fluctuations inside the cell were investigated with metal samples. Figure 4-5 shows the temperature-time trend and the readings from two LVDTs when logged over 5 hours. It can be seen that temperature and displacement readings correlate with each other, but that in this case each LVDT responds with a different sign of voltage change. This could be due to difference in the inner iron cores of each LVDT. The temperature effect on LVDT1 was +0.05mm/C° and for LVDT2 was -0.08mm/C°. The temperature controlled laboratory within which the tests were undertaken experienced relatively minor variations of ±0.75 per diurnal cycle. Nevertheless, corrections based on the measured ratios were used to reduce the effect of temperatures on local strain measurements.

4.1.2.5 Volume gauge

The volumes of water exiting or entering the sample were measured using a 50cc in-house designed volume gauge (de Campos, 1981) equipped with a linear displacement transducer (as in 4.1.2.3 above) mounted on the outside of its body. The volume gauge was calibrated by measuring the volume of the water entering the gauge using a Bishop ram under high pressure. This was considered better than making measurement under atmospheric pressure of volumes exiting gauge.

4.1.2.6 Data logger and software

The output signals from all the transducers were recorded using a data logger system connected to a PC. The software used for recording the data and controlling the pressures was Triax-V5.2. The software was originally developed at Imperial College (Toll, 1993) and was later updated by Durham University. Its flexibility in applying complicated stress paths makes it suitable for advanced testing and cyclic loading in both triaxial and HCA equipment.

4.1.2.7 Resolution of the transducers

The resolution and accuracy values for all the transducers are listed in Table 4-1. Due to higher resolution of the local LVDTs, it was better to use the local axial and radial LVDTs instead of the volume gauge to calculate volumetric strains. The external displacement transducer also had lower resolution compared to the local LVDTs and was only used at higher displacements where local transducers were dislodged and out of work due to the deformation of the specimen. Local LVDTs gave the best resolutions when output voltages were close to zero. Therefore, prior to starting the tests the voltages for all three local transducers were re-zeroed.

Table 4-1 Range, resolution and accuracy of transducers used for triaxial apparatus

Parameter	Units	Range	Resolution	Accuracy*
Axial load	N	±5.00E+03	0.4	1.7
Cell pressure	kPa	0-800	0.04	0.55
Back pressure	kPa	0-800	0.04	0.55
External LVDT	mm	±25	0.001	0.008
Local axial LVDT 1	mm	±5	0.0002	0.0005
Local axial LVDT 2	mm	±5	0.0002	0.0005
Radial LVDT	mm	±5	0.0002	0.0005
Volume gauge	cm3	0-50	0.0008	0.001
Temperature	C^o	0-100	0.02	0.07

*Accuracy is defined as the 95% confidence range (2 standard deviation from best fit line)

4.1.3 Data Analysis

Recorded data from tests were analysed using data processing MATLAB codes developed by the Author. The equations used for stress data analysis are:

- Radial stress: $\sigma_r = p_{cell}$ Equation 4-1
- Axial stress: $\sigma_z = p_{cell} + \frac{F_a}{\pi r^2}$ Equation 4-2

Where p_{cell} is the cell pressure and F_a is the axial load. For effective radial and axial stresses the PWP is subtracted from total stress values. For strain measurements equations are:

- Axial strain: $\varepsilon_a = \frac{\Delta H}{H}$ Equation 4-3
- Radial strain: $\varepsilon_r = \frac{\Delta r}{r}$ Equation 4-4
- Volumetric strain $\varepsilon_v = \varepsilon_z + 2\varepsilon_r$ Equation 4-5

Where H is the length in which the LVDT is measuring the strain changes. This value is equal to sample height for external LVDT and is equal to LVDTs opening for local transducers.

The state of the sample and its stress path is usually defined by independent stress invariants as:

- Mean stress: $q = \sigma_1 - \sigma_3$ Equation 4-6
- Deviatoric stress: $p = \frac{\sigma_1+\sigma_2+\sigma_3}{3}$ Equation 4-7

Where σ_1 and σ_3 are major and minor principal stresses. In triaxial conditions the higher value between radial and axial stresses is equal to σ_1 and the lower value is σ_3.

4.1.3.1 Corrections

Area correction: The axial stress is calculated by dividing the axial load by the cross sectional area of the sample and since the specimen deforms during consolidation and shearing stages, it is necessary to calculate the corrected area at any stage during the test, based on the initial area and displacements up to that stage. In order to do this, one must address the way sample deforms under axial loads. The most common assumption is that the

sample deforms as a right cylinder as shown in Figure 4-6a. Although this assumption is often suitable for lubricated platens, for tests with frictional ends the central portion of the specimen deforms more than both ends and forms a bulging or parabola shape as shown in Figure 4-6b-c. The following equations are proposed for different modes of deformation by Donaghe *et al.* (1988):

- Cylindrical: $A_c = A_0(\frac{1-\varepsilon_v}{1-\varepsilon_a})$ Equation 4-8
- Bulging: $A_c = A_0 \ (-\frac{1}{4} + \frac{\sqrt{25-20\varepsilon_a-5\varepsilon_a{}^2}}{4(1-\varepsilon_a)})^2$ Equation 4-9
- Parabolic: $A_c = A_0(\frac{1-\varepsilon_v}{1-a\varepsilon_a})$ Equation 4-10

Where A_0 is the area at zero strain and *a* is the ratio between length of the specimen to the bulging zone. To decide which deformation mode should be chosen for the individual sand samples prepared in this research, the specimen deformation developed during a compression monotonic shearing test was recorded by taking multiple photographs. Applying the image processing software allowed the evolution of sample shape during shearing to be measured as shown in Figure 4-7. It can be seen that mid-sample deformation behaviour could be best described as bulging over the middle 2/3(=*a*) of the specimen.

4.1.4 Ability to perform cyclic tests

Although the Bishop & Wesley triaxial apparatus was originally designed for monotonic tests, however, several researches such as Qadimi (2005) have also used the apparatus for cyclic triaxial tests. The important point to consider is to assess how fast and accurately the software and pressure control systems are able to apply cyclic loads. In order to do this, a series of trial triaxial tests were performed with sand specimens under different levels of cyclic loads and cyclic frequencies. The recorded data were used to determine the acceptable limits for cyclic frequency and cyclic amplitude. Figure 4-8 shows a comparison between

ideal deviatoric sinusoidal cyclic loading and applied cyclic loading achieved, considering a range from small amplitude to large amplitude cycles. Assessment of the results showed that applying cyclic amplitudes of up to 60 kPa with period of 1 cycle per minute gives acceptable response for medium dense NE34 specimens consolidated to p≒167. For cyclic tests with amplitudes higher than 60 kPa a period of 0.75 cycles per minute proved acceptable.

The accuracy of the applied stresses was gauged using the following equation:

$$\text{Accuracy} = \frac{A_{applied}}{A_{ideal}} \qquad \text{Equation 4-11}$$

Where $A_{applied}$ is the area beneath the applied q-time curve and is presentative of the applied energy and A_{ideal} is the area beneath the ideal q-time curve. Measured accuracy values are presented in Table 4-2.

Table 4-2 Accuracy of the applied cyclic loads at different cyclic amplitude ranges

q_{avg}	q_{cyc}	Period, S	Accuracy
50	8.35	60	98.1
50	25.05	60	99.5
50	41.75	60	97.3
50	58.45	60	99.8
50	71.15	60	99.3
50	91.85	60	99.7

4.2 Hollow Cylinder apparatus

Hollow cylinder apparatus was first used in soil mechanics by Cooling & Smith (1936). However, it became more commonly used in soil testing in the early 1980s with new designs including that proposed by Hight *et al.* (1983). While initially employed for advanced soil testing in research institutes, in recent years it has been used in advanced industrial laboratories.

For the present study the Imperial College Resonant Column HCA (ICRCHCA) was used. In the following, the apparatus structure is described and a discussion on analysis of results is

given as well. Finally, a discussion over modifications applied for performing cyclic simple shear tests is given.

4.2.1 Apparatus general structure

The ICRCHCA apparatus was first made in 1991 by Soil Dynamics Instruments (SDI), Inc of Kentucky USA in a joint project by Imperial College and since its development it has been modified several times at Imperial College by researchers working with it (Porovic, 1995; Nishimura, 2006; Brosse 2012). The apparatus is equipped with a resonant column system located at top of the sample which consists of a Hardin oscillator that measures the stiffness independently from the measurements made in static tests.

The general outline of the apparatus is presented in Figure 4-9. In its current modified set-up the apparatus is able to control four pressures and load invariants separately which are:

- Outer cell pressure
- Inner cell pressure
- Axial load
- Torque

4.2.1.1 Outer cell pressure

The outer cell pressure is provided by pressurized air directly to the cell water at top of the cell and is controlled by automatic electro-pneumatic controllers made in Imperial College. Due to the limited strength of the acrylic cylinder enclosing the pressurised cell, the maximum outer cell pressure is limited to 700 kPa. This safety limit is particularly important because the top part of the cell contains pressurised air, which is more potentially dangerous than pressurised water. The reason for this set-up is that the proximity transducers and Hardin Oscillator located at top of the cell cannot be submerged in water. However, applying direct air pressure at the top of the outer cell water causes an air diffusion problem, which will be discussed later in this Chapter.

4.2.1.2 Inner cell pressure

The inner cell chamber is filled with de-aired water and its pressure is controlled by automatic electro-pneumatic controllers connected to an air-water interface which is capable of applying up to 800 kPa pressure. The original (SDI) design of the apparatus had no sealing between the outer and inner cell pressure. Nishimura (2006) modified the apparatus to isolate the inner cell by using a sealing mechanism at the top and bottom of the sample as shown in Figure 4-10a. In both positions the seal was made using a two piece circular fitting of metal with a central rubber o-ring. The seal was made by tightening the metal pieces which squeeze the membrane against the wall of the stainless steel base or top cap. Brosse (2012) found that the seals could rotate vertically during installation and diminish the seal quality. To overcome this, she made further modifications by adding an extra o-ring to the top and bottom seals and screwing the bottom seal to base of the inner cell as shown in Figure 4-10b. Trial tests, by the Author, showed that Brosse's set-up is fully efficient for sealing the inner cell up to the maximum applicable pressures.

4.2.1.3 Axial load

The axial load is applied using a large double-acting Bellofram cylinder with an inner diameter of 58 cm. The pressure at top of the Bellofram is controlled by an electro-pneumatic stepper motor and at the base is controlled manually via a manostat/air pressure regulator. At the beginning of each test, the top and bottom pressures of the Bellofram chambers are increased simultaneously, keeping the net axial load zero. After reaching a bottom chamber pressure=100kPa, the base pressure is kept constant and the required loads are applied by controlling the top chamber pressure. This set-up allows extension loads to be applied by reducing the top pressure below the value of bottom pressure. The maximum air pressure in the Bellofram is 800 kPa and it can apply a maximum axial load of 4.6 kN.

4.2.1.4 Torque

A stepper motor connected to a metal rotary gear assembly is used to apply torque to the sample top cap. The gear assembly is connected to the load transmitting shaft via a gear reduction system and a metal chain drive as shown in Figure 4-11. The rotary gear is connected to a tension cylinder that consists of a metal wire which is tensioned using air pressure. The tension cylinder is used to remove backlash in the torque drive system at load reversal points. However, employing the system puts more loads on the stepper motor since it has to overcome the applied tension load as well as the torque loading.

The original SDI design included a cyclic loading system. However, this has not been deployed for cyclic loading up to 2013 and modifications were required to enable it to apply the desired, relatively fast, cyclic torsional loads. The modifications made are explained later in this chapter.

4.2.2 Instrumentation:

The eleven measuring instruments installed in and on the ICRCHCA comprise:

- Pressure transducers: For inner cell pressure, outer cell pressure and back pressure
- Displacement transducers: One external axial LVDT
- Volume gauge: For back pressure and inner cell pressure
- Double-axis load cell: For measuring axial and torque applied
- Proximity transducers: Two proximity transducers for angle of axial rotation measurement
- Temperature: Cell water temperature

The pressure transducers, displacement transducers and volume gauges used for this apparatus are similar to the ones employed in the stress path triaxial detailed in section 4.1.2.

4.2.2.1 Double-axis load cell

A specially designed double axis load cell was made by Maywoods Instruments in conjunction with Imperial College for the ICRCHCA. It is placed below the metal base seating of the sample which measures the applied axial force and torque. All dual axis transducers incorporate a degree of cross-sensitivity: changes in axial force influence to some degree the torque "readings" and vice versa. These cross-effect errors have linear trends and corrections are made during calibration to reduce their effect. The output voltages and input loads (Force, Torque) are related via a 2 by 2 matrix as:

$$\begin{bmatrix}\Delta F\\ \Delta T\end{bmatrix} = \begin{bmatrix}d_{ff} & d_{tf}\\ d_{ft} & d_{tt}\end{bmatrix} X \begin{bmatrix}\Delta F_{voltage}\\ \Delta T_{voltage}\end{bmatrix} \qquad \text{Equation 4-12}$$

Where F is the axial force, T is the torque and d_{ij} are calibration constants. For axial load calibration a Budenberg dead-weight system was used and for torque calibration, a lever arm was attached to the load cell and equal lead weight loads were placed at both ends to create a known amount of torque.

4.2.2.2 Proximity transducers

Two proximity transducers are placed diametrically opposite one another at top of the sample to measure the axial rotation of the specimen. Each proximity transducer measures the distance between the transducer and a specially shaped cam attached to top of the sample which has logarithmically curved sides to produce linear relation between angle of rotation and distance from the proximity transducer. Figure 4-12 shows the plan view of the proximity transducer set-up.

4.2.2.3 Resolution and accuracy

The resolutions and accuracies of all the transducers are given in Table 4-3

Table 4-3 Range, resolution and accuracy of transducers used for triaxial apparatus

Parameter	Units	Range	Resolution	Accuracy
Axial load	N	$-1\ 10^3+6\ 10^6$	0.4	1.7
Torque	N.m	±180	0.0002	0.55
PWP pressure	kPa	0-800	0.04	0.55
Outer cell pressure	kPa	0-800	0.04	0.34
Inner cell pressure	kPa	0-800	0.01	0.81
Axial LVDT	mm	0-50	0.0004	0.009
Sample VG	cm^3	0-50	0.0008	0.01
Inner cell VG	cm^3	0-50	0.0008	0.01
Proximity 1	Degree	±20	0.0007	0.008
Proximity 2	Degree	±20	0.0007	0.008
Temperature	Co	0-100	0.02	0.07

4.2.2.4 Data logger and software

The signal outputs from all the transducers were transmitted to a 16-bit data logger that is attached to the control and recording software. At the beginning of this research the data acquisition and control software consisted of a Q-basic program written by Nishimura (2006) based on subroutines developed by Zdravkovic (1996). However, the code did not have the ability to apply cyclic loads and was also unable to record large amounts of data from fast reading intervals in cyclic tests. Therefore, the control software was upgraded to Triax-V5.2 and the equations stored in the software were upgraded to suit the HCA apparatus.

4.2.3 Analysis of stress and strain data

Assessing the average stresses and strains developed in HCA samples, involves addressing the curved specimen geometry and boundary conditions. Figure 4-13 shows the external forces applied to a HCA sample and the corresponding stress state of an element of soil inside the HCA sample. Following Hight *et al.* (1983), Nishimura (2006) and Brosse (2012) summarised the stress and strain assumptions as:

4.2.3.1 Displacement assumptions:

- Symmetry around the vertical axis exists throughout the test, hence; all displacements are independent of θ.

$$\frac{\delta u_z}{\delta \theta} = 0, \quad \frac{\delta u_r}{\delta \theta} = 0, \quad \frac{\delta u_\theta}{\delta \theta} = 0 \qquad \text{Equation 4-13}$$

- A horizontal cross-section stays in a horizontal plane. Therefore, axial displacement is independent of r.

$$\frac{\delta u_z}{\delta r} = 0 \qquad \text{Equation 4-14}$$

- A vertical plane stays plannar during the rotation and the circumferential strain u_θ variation have linear relation with r and z.

$$\frac{\delta u_\theta}{\delta r} = \text{Constant}, \quad \frac{\delta u_\theta}{\delta z} = \text{Constant}, \qquad \text{Equation 4-15}$$

4.2.3.2 Stress assumptions

- No shear stress in radial and circumferential direction by assuming no end restraint effects.

$$\tau_{zr} = 0, \ \tau_{r\theta} = 0 \qquad \text{Equation 4-16}$$

- The axial stress is uniform in horizontal plane.

$$\frac{\delta \sigma_z}{\delta r} = 0, \quad \frac{\delta \sigma_z}{\delta \theta} = 0 \qquad \text{Equation 4-17}$$

- Circumferential stress does not vary with z and θ within central portion.

$$\frac{\delta \sigma_\theta}{\delta z} = 0, \quad \frac{\delta \sigma_\theta}{\delta \theta} = 0 \qquad \text{Equation 4-18}$$

- z and θ have no influence on variation of shear stresses.

$$\frac{\delta \tau_{z\theta}}{\delta z} = 0, \quad \frac{\delta \tau_{z\theta}}{\delta \theta} = 0 \qquad \text{Equation 4-19}$$

Further assumptions regarding the constitutive model and stress averaging scheme are also required for the stress and strain calculations.

4.2.3.3 Constitutive model

Previous researchers (Nishimura, 2006; Anh-Minh, 2007; Brosse, 2012) have used an implicitly isotropic linear elastic model to calculate the average stresses developed within specimens, except for the shear stress, which was treated as fully plastic. Some authors have

argued that using perfectly plastic response for shear stress is inconsistent with other assumptions made for other parameters, but Nishimura (2006) showed that using the proposed equations for shear strain (Equation 4-13 to 4-16) and perfect plasticity for shear stress satisfies the elastic energy equations. Although granular materials are often cross-anisotropic, Nishimura (2006) showed that the equations remain valid for cross-anisotropic linear elastic materials.

Averaging scheme: Average stresses and strains can be obtained by considering variations across either the sample wall or the volume of the sample. However, Sayao & Vaid (1991) showed that both methods give results that differ by no more than 2%. Maintaining consistency with previous work at Imperial College, the components are averaged across the wall.

In keeping with the above assumptions, the equations proposed by Hight *et al.* (1983) are:

Stress measurements:

Axial stress: $\sigma_z = \frac{\int_0^H \sigma_z dz}{\int_0^H dz} = \frac{F_a}{\pi(r_0^2 - r_0^2)} + \frac{p_0 r_0^2 - p_i r_0^2}{r_0^2 - r_0^2}$ Equation 4-20a

Radial stress: $\sigma_r = \frac{\int_{r_i}^{r_0} \sigma_r dr}{\int_{r_i}^{r_0} dr} = \frac{p_0 r_0 + p_i r_i}{r_0 + r_i}$ Equation 4-20b

Circumferential stress: $\sigma_\theta = \frac{\int_{r_i}^{r_0} \sigma_\theta dr}{\int_{r_i}^{r_0} dr} = \frac{p_0 r_0 - p_i r_i}{r_0 - r_i}$ Equation 4-20c

Shear stress: $\tau_{z\theta} = \frac{M_T}{\int_0^{2\pi} \int_{r_i}^{r_0} r^2 dr d\theta} = \frac{3M_T}{2\pi(r_0^3 - r_0^3)}$ Equation 4-20d

Where p_o and p_i are outer and inner cell pressure, r_o and r_i , are the outer and inner radius and H is the height of the sample.

Strain parameters:

Axial strain: $\varepsilon_z = \frac{\int_0^H \varepsilon_z dz}{\int_0^H dz} = \frac{-\Delta h}{H}$ Equation 4-21a

Radial strain: $\varepsilon_r = \frac{\int_{r_i}^{r_o} \varepsilon_r dr}{\int_{r_i}^{r_o} dr} = -\frac{\Delta r_o - \Delta r_i}{r_o - r_i}$ Equation 4-21b

Circumferential strain: $\varepsilon_\theta = \frac{\int_{r_i}^{r_o} \varepsilon_\theta dr}{\int_{r_i}^{r_o} dr} = -\frac{\Delta r_o + \Delta r_i}{r_o + r_i}$ Equation 4-21c

Shear strain: $\gamma_{z\theta} = \frac{\int_0^{2\pi}\int_{r_i}^{r_o} \gamma_{z\theta} r dr d\theta}{\int_0^{2\pi}\int_{r_i}^{r_o} r dr d\theta} = \frac{2\Delta\theta({r_o}^3 - {r_o}^3)}{3H({r_o}^2 - {r_o}^2)}$ Equation 4-21d

Values obtained from these equations are average values.

Using the Mohr's circle for general stress space, principal stress and strain values can be obtained as shown in Figure 4-14. (Assuming the σ_r stays as the intermediate principal stress)

Principal stresses:

$\sigma_1 = \frac{\sigma_z + \sigma_\theta}{2} + \sqrt{(\frac{\sigma_z - \sigma_\theta}{2})^2 + {\tau_{z\theta}}^2}$ Equation 4-22a

$\sigma_2 = \sigma_r$ Equation 4-22b

$\sigma_3 = \frac{\sigma_z + \sigma_\theta}{2} - \sqrt{(\frac{\sigma_z - \sigma_\theta}{2})^2 + {\tau_{z\theta}}^2}$ Equation 4-22c

Principal strains:

$\varepsilon_1 = \frac{\varepsilon_z + \varepsilon_\theta}{2} + \sqrt{(\frac{\varepsilon_z - \varepsilon_\theta}{2})^2 + {\gamma_{z\theta}}^2}$ Equation 4-23a

$\varepsilon_2 = \varepsilon_r$ Equation 4-23b

$$\varepsilon_3 = \frac{\varepsilon_z+\varepsilon_\theta}{2} - \sqrt{(\frac{\varepsilon_z-\varepsilon_\theta}{2})^2 + {\gamma_{z\theta}}^2}$$ Equation 4-23c

Using principal stresses, independent stress invariants can be defined as:

Mean stress: $q = \sqrt{\frac{(\sigma'_1-\sigma'_3)^2+(\sigma'_1-\sigma'_2)^2+(\sigma'_2-\sigma'_3)^2}{2}}$ Equation 4-24a

Deviatoric stress: $p' = \frac{\sigma'_1+\sigma'_2+\sigma'_3}{3}$ Equation 4-24b

Intermediate principal stress factor: $b = \frac{\sigma_2-\sigma_3}{\sigma_1-\sigma_3}$ Equation 4-24c

Angle of major principal stress with vertical direction: $\alpha = \frac{1}{2}\tan^{-1}(\frac{2\tau_{z\theta}}{\sigma_z-\sigma_\theta})$ Equation 4-24d

4.2.3.4 Area correction

Similar to triaxial tests, the area of HCA specimens change during consolidation and shearing. To calculate stress values, the dimensions applying at any point during the test are required. The equations proposed by Brosse (2012) have been used for area correction:

$$H = H_0 - \Delta H$$ Equation 4-25a

$$r_i = r_{i0}\sqrt{\frac{1-\Delta V_i/V_{i0}}{1-\Delta H/H_0}}$$ Equation 4-25b

$$r_0 = r_{o0}\sqrt{\frac{1-(\Delta V+\Delta V_i)/(V_0+V_{i0})}{1-\Delta H/H_0}}$$ Equation 4-25c

4.2.4 Sources for possible errors

Air diffusion: As mentioned previously, the cell pressure is controlled by the pressurised air supply fed to the top of the cell. This set-up is essential for the upper instrumentation, but generates air diffusion problem in the outer cell water. As Henry's law states, concentration of dissolved gas in liquid depends on the pressure of the air phase in equilibrium with the liquid. Since the outer cell pressure goes to pressures up to 700 kPa in HCA tests for several

days during each test, the cell water saturates with air. As the latex sample membranes are not impermeable to air, the dissolved air can diffuse into the sample voids, where air and water pressures are lower. The air forms bubbles within the pore space as it comes out of solution and reduces the degree of saturation in the specimen. This leads to pore water pressure measurement errors in undrained tests while in drained or consolidation stages the sample becomes apparently more compressible. The effects are more noticeable with higher permeability granular media than in finer grained clays.

All previous researchers working with ICRCHCA apparatus have highlighted this problem and have tested a variety of solutions. Nishimura (2006) concluded that replacing the cell water every few hours with fresh de-aired water was the best solution and used a small tank filled with pressurised de-aired water to achieve this. However, the small tank had to be refilled several times to fully change the cell water. Brosse (2012) replaced the tank with a bigger cell that could change the cell water with one single fill. The set-up used for this procedure is illustrated in Figure 4-15.

Although changing the cell water reduces the air diffusion rates, every time the water is being changed, it creates a stress disturbance inside the cell due to the exit line (see Figure 4-15) being open to atmospheric pressure which affects the stresses at top of the cell. In order to study the disturbance caused by the water change procedure and to find an optimum solution for the air diffusion problem, a series of trial undrained cyclic simple shear tests were performed. Samples subjected to similar preconditioning and loading levels with different procedures to tackle air diffusion problem were cycled under undrained simple shear conditions starting from p'_0=167kPa. Mean effective stress trends, as measured over 4500 cycles applied over almost 4.5 days, are shown in Figure 4-16. The test that involved with no water change generated high rates of pore pressure build-up or mean effective stress drop. The specimens that experienced daily water changes and a 350 kPa cell pressure showed

lower pre pressure build-up rates. However, every time the water was changed the build-up accelerated due to pore pressure relaxation at the top of the cell. However, increasing the cell pressure to 550 kPa and initial pore pressure to 400kPa practically eliminated the pore pressure accelerations noted during water changes and led to the least amount of pore pressure build-up during the cyclic simple shear tests. A further trial where the de-aired water was flushed through the specimen by creating a small head (2-3 kPa) difference between the top and bottom of the sample showed highest rates of pore pressure build-up, showing that flushing causes significant disturbance inside the sample. Based on the observed results, applying high cell and initial back pressures and a daily water change made using the larger re-fill tank was chosen as the optimum solution and implemented for the main run of experiments.

4.2.5 Modifications for cyclic tests

As the ICRCHCA apparatus had not been used previously for cyclic shear testing, a detailed assessment was required of its ability to perform relatively fast cyclic tests accurately. Early trial tests identified two main problems:

a) Significant backlash in the chain and gear system at stress reversal points.
b) A slow response in the torque stepper motor.

To solve the backlash problem the chain was initially tightened to the maximum possible level permitted by the tension cylinder. However, this added the load on the torque motor, making its response slower. Trials identified that the backlash problem could be solved by tightening the drive chain. To improve the torque motor response, a gear box was added to the system, as shown in Figure 4-11. The gear box had a 1 to 10 ratio and enabled the motor to send bigger rotation steps with every pulse sent.

Once the modifications were made, a series of trial tests were performed to measure the accuracy and establish how rapidly the shear loads could be cycled. Figure 4-17 shows a comparison between data obtained from a trial tests and ideal sinusoidal paths. Assessment of results showed that with medium dense NE34 samples tested at p'=167, amplitudes in $\tau_{z\theta}$ of up to 30 kPa could be applied at 1 cycle/min while for higher cyclic amplitudes period of 0.75 cycle/min is more suitable suitable.

4.3 Resonant column system

The ICRCHCA is equipped with a Hardin oscillator that enables it to perform resonant column (RC) testing. The RC configuration is a fixed-base-spring-top design with the bottom of the sample being connected to a rigid base while the top of the sample is coupled with the oscillator that generates torsional excitation. The sinusoidal input voltage is generated by a function generator and is amplified before being sent the Hardin oscillator. The output consists of voltage signals from an accelerometer placed inside the Hardin oscillator. These signals are also amplified and sent to a HAMEG oscilloscope. Figure 4-18 shows the schematic set-up of the RC system.

To obtain damping ratios and shear stiffness modulus, a sinusoidal torsional excitation is applied and the frequency is changed until resonance is achieved in a steady state from accelerometer output. The resonance occurs when the input and output signals have an angular phase difference of 90° degrees. In the oscilloscope this can be observed when in a "voltage input:voltage output" plot an ellipse forms with its axes pointing in the horizontal and vertical directions (Drenevich *et al.*, 1978; Brosse, 2012).

Calculating the elastic modulus and damping ratios from the RC measurements requires applying solutions to the RC boundary value problem. These solutions have been found by taking three main steps:

1- Constitutive model

The hollow HCA specimen can be modelled as a visco-elastic material, and the Kelvin-Voigt constitutive model can be applied to it as:

$$\tau_{z\theta} = G_{z\theta}\gamma_{z\theta} + \mu\frac{\delta\gamma_{z\theta}}{\delta t} \qquad \text{Equation 4-26}$$

Where $G_{z\theta}$ is the elastic shear modulus and μ is the coefficient of viscosity. The inviscid hysteretic behaviour is represented by either the μ or D parameters. The parameter D is defined as the ratio of the dissipated energy per cycle, ΔW, to the elastic energy, W, multiplied by 4π:

$$D = \frac{\mu\omega}{2G} \qquad \text{Equation 4-27}$$

Where ω is the circular frequency of the oscillation. According to this, if D is taken to be independent of the frequency, the stress-strain loop will also be independent from frequency and will be purely hysteretic.

2- Force equilibrium

The wave equation applying to the RC specimens is found by applying Newton's law of equilibrium of forces as:

$$\frac{\delta^2\theta}{\delta t^2} = \frac{G}{\rho}\frac{\delta^2\theta}{\delta z^2} + \frac{\mu}{\rho}\frac{\delta^3\theta}{\delta t\delta z^2} \qquad \text{Equation 4-28}$$

Where ρ is the mass density of the sample. The solution for this differential equation can be expressed as:

$$\theta(z,t) = (C_1 e^{aiz} + C_2 e^{-aiz})e^{i\omega t} \qquad \text{Equation 4-29}$$

Where i^2= -1 and C_1 and C_2 are complex constants that depend on the boundary conditions of the problem and *a* is defined as:

$$a^2 = \frac{\rho\omega^2}{G(1+2Di)} \qquad \text{Equation 4-30}$$

3- Boundary conditions

An ideal resonant column apparatus could conform to a 1 degree of freedom (DOF) system with a fixed base and single (resonator system) spring at the top. However, in practice the RC apparatus has various system compliances that act at different locations that make the 1DOF idealisation unrealistic. These compliances affect the resonant frequency of the specimen and if ignored could lead to errors in the G and D calculations. To overcome this, Nishimura (2006) and Brosse (2012) used a three degree of freedom system, as originally proposed by Ashmawy & Drnevich (1994), to account for the active, passive and reaction response induced by the apparatus boundary conditions as shown in Figure 4-19. The governing equation and boundary conditions for each system are:

At the base of the passive system, which represents the lower assembly including the dual axis load cell:

$$K_p\theta_p + C_p\frac{\delta\theta_p}{\delta t} + J_p\frac{\delta^2\theta_p}{\delta t^2} - GI\frac{\delta\theta}{\delta z}|z=0 \quad - \mu I\frac{\delta^2\theta}{\delta z\delta t}|z=0 \quad = 0 \qquad \text{Equation 4-31}$$

Within the reaction system provided by the cell and its top fixity:

$$K_r\theta_r + K_a(\theta_r - \theta_a) + C_r\frac{\delta\theta_r}{\delta t} + C_a(\frac{\delta\theta_r}{\delta t} - \frac{\delta\theta_a}{\delta t}) + J_r\frac{\delta^2\theta_r}{\delta t^2} = -T_0\sin(\omega t) \qquad \text{Equation 4-32}$$

And within the active resonator system:

$$K_a(\theta_a - \theta_r) + C_a(\frac{\delta\theta_a}{\delta t} - \frac{\delta\theta_r}{\delta t}) + J_a\frac{\delta^2\theta_a}{\delta t^2} + GI\frac{\delta\theta}{\delta z}|z=H \quad + \mu I\frac{\delta^2\theta}{\delta z\delta t}|z=H \quad = -T_0\sin(\omega t)$$

Equation 4-33

The rotation-time relationships developed in each element (Passive p, Reaction r, and Active, a) can be expressed in complex space by putting:

$$\theta_p = A_p e^{iwt},\ \theta_r = A_r e^{iwt},\quad \theta_a = A_a e^{iwt}$$

The equations can be written in matrix form as:

$$\begin{bmatrix} A_p \\ A_a \\ A_r \end{bmatrix} = \begin{bmatrix} y_{11} + iz_{11} & y_{12} + iz_{12} & y_{13} + iz_{13} \\ y_{21} + iz_{21} & y_{22} + iz_{22} & y_{23} + iz_{23} \\ y_{31} + iz_{31} & y_{32} + iz_{32} & y_{33} + iz_{33} \end{bmatrix} \begin{bmatrix} 0 \\ \frac{T_o}{J\omega^2} \\ -\frac{T_o}{J\omega^2} \end{bmatrix} \quad \text{Equation 4-34}$$

The values of y_{ij}, z_{ij} are given by Nishimura (2006).The accelerometer measures the rotational acceleration of the active mass and the Hardin oscillator give the input torque T_0. The solution can be expressed in terms of the transfer function H:

$$H = \frac{A_a J\omega^2}{T_o} = y_{22} + y_{23} + i(z_{22} + z_{23}) \quad \text{Equation 4-35}$$

$$MMF_a = |H| = \sqrt{(y_{22} + y_{23})^2 + (z_{22} + z_{23})^2} \quad \text{Equation 4-36}$$

$$\varphi_a = \arg(H) = \arctan\left(\frac{z_{22} + z_{23}}{(y_{22} + y_{23}}\right) \quad \text{Equation 4-37}$$

The factors of MMF_a and ϕ_a are dependent of G and D. Therefore, using these two functions, the resonant frequency and the magnification factor at resonance is expressed as functions of G and D:

$$f_{ares} = f_{ares}(G, D) \quad \text{Equation 4-38}$$

$$MMF_{ares} = MMF_{ares}(G, D) \quad \text{Equation 4-39}$$

Using the Newton-Raphson method to find roots of a non-linear equation system, values of G and D are calculated.

4.4 Sample preparation method

4.4.1 Sample preparation

Care is required when choosing preparation method for reconstituted sand specimens. The technique must be able to produce samples with uniform internal fabrics. Also, since the behaviour of sand strongly depends on its density and state, controllability and reproducibility of formation void ratio is an important point in sample preparation stage (Kuwano, 1999). The main techniques available for sample preparation are:

Air pluviation: The formation void ratios of air pluviated samples are controlled by the grain drop height and rate of pouring. To keep uniform samples it is essential that the drop height should be kept constant. Air pluviated samples reproduce the fabric for air blown deposits although the range of possible initial void ratios is limited. Additional densification can be achieved by tapping or vibration post-pluviation. However, applying vibration causes the grains to acquire a preferred orientation which will create a fabric that is not necessarily a replica of the sand's in-situ state (Mahmoud *et al.* 1976).

Moist placement: The moist placement technique is able to produce extremely loose samples, due to the capillary forces that apply between slightly moistened sand particles. This technique can model the fabric of poorly compacted fills (Kuwano, 1999).

Water pluviation: This method is most suited for generating dense samples. Uniform samples can be prepared with water pluviation because the grains achieve their terminal velocity after a relatively small fall distance in water. Water pluviation best simulates the fabrics of sand deposited under water. Therefore, it is often the most appropriate method for testing sands deposited in offshore environments. Similar to the air pluviation method, the density can be

increased by tapping and adjusted (marginally) by varying the drop height. This method also generates samples with the highest degrees of initial saturation when compared to other methods.

The water pluviation method was chosen for the Author's study as it is best able to generate dense uniform samples. The resulting fabric models the offshore deposits which are the main focus of this research. The Dunkerque sands in which the field pile tests were performed involved mainly marine sands while the laboratory calibration chamber pile tests were conducted in NE34 sand masses that were performed by air pluviation.

The set-up procedure adopted for triaxial and HCA tests are described in more detail below.

Triaxial sample preparation:

The Author's triaxial sample set-up procedure involved twelve main steps:

1- The mass of sand required was measured knowing the sample dimensions and the target void ratio.
2- The entire mass was submerged in a beaker of de-aired water.
3- The sand mass and the porous stone were placed in a vacuum chamber for 1-2 hours to remove dissolved air.
4- The porous stone was placed on the triaxial pedestal and the rubber membrane was fixed around it and was sealed with 2 O-rings at the bottom.
5- A split mould was assembled around the membrane and the membrane was stretched to conform with its inner wall by applying a small vacuum.
6- A small volume of de-aired water was placed in the base of the sample to depth of 5mm.

7- Using a funnel with a fixed drop height, the sand was allowed to fall through the water inside the mould. Occasional tapping was applied to adjust the target density. The aim was to place all the weighed sand and simultaneously reach the precise target height located at the top edge of the mould.
8- Once the entire sand mass had been was poured inside the mould, the top cap was placed and the sample was sealed using two O-rings at the top.
9- Prior to opening the split mould, suction was applied to the sample through the back pressure line in order to keep the sample in shape after removing the mould. For this research a -20 kPa suction was applied.
10- Once the mould was removed the local strain transducers were attached to the membrane with superglue and the sample dimension were measured.
11- The triaxial cell was closed and filled with de-aired water.
12- An initial cell pressure of 30 kPa and back pressure of 10 kPa were applied once the suction was disconnected.

The specimen was then ready for its saturation procedure.

HCA sample preparation:

For HCA samples the procedure was very similar. One main difference was that the HCA requires two moulds, one inner and one outer. Another was that the and connection for axial loading was made using a screw instead of a suction cap. Figure 4-20 shows an illustrative sketch of the sample preparation procedures for triaxial and HCA specimens while Figure 4-21 shows photographs taken during the sample set-up stages.

4.4.2 Saturation

Additional steps were taken in order to ensure that samples were fully saturated, with checks being made by the B test method after each experiments saturation phase.

Triaxial samples, were saturated by increasing both cell and back pressures simultaneously at a rate of 60 kPa/hour until the cell pressure=300 kPa and the back pressure=280 kPa. By increasing the pressures simultaneously, air bubbles trapped inside the sand structure were compressed and forced into solution. To assess the degree of saturation B tests were performed by closing the drainage line and applying 50kPa extra cell pressure. The pore pressure response was monitored and the resulting B value was calculated as:

$$B = \frac{\Delta U}{\Delta \sigma} \qquad \text{Equation 4-40}$$

Saturation stage B values above 94% were achieved in all tests on the two sands used for this research. These values are likely to have increased as the tests progressed through diffusion into the surrounding cell water.

For HCA Samples, a back pressure of 280 kPa could not be reached at the early stages of testing as it would have limited the maximum allowable effective stresses of the consolidation stage. Therefore, cell and back pressures were increased simultaneously to 200 kPa and 180 kPa, respectively. However, these pressures did not give B value high enough to ensure complete saturation; the B values were on average equal to 90%. The Author's main test series involved experiments conducted at OCR=4 and the level of saturation was increased by raising the cell and back pressures after the maximum effective stresses required for consolidation had been achieved, as the effective stresses were lowered over the swelling stages. The trial cell pressures allowed a back pressure of 460kPa and this led to samples with B values exceeding 93%. The high back pressures imposed prior to the undrained stages also reduced the rates and effects of air diffusion into the sample during shearing.

4.5 Conclusion and remarks

This chapter have presented a detailed description of the triaxial and HCA apparatuses used in the research, covering the general structure of the testing systems and the instrumentation

installed in both apparatuses. Assessments were reported of the apparatuses ability to perform cyclic loading and modifications made in the HCA apparatus were explained in detail. Finally, the sample preparation method used to create representative triaxial and HCA specimens was presented. The following remarks are made:

1- The modified Bishop & Wesley (1975) was able to apply relatively fast and accurate sine axial cyclic loads. Period of 1 cycle/min for q_{cyc} up to 60 kPa and 0.75 cycles/min, for amplitudes higher than 60 kPa could be employed for accurately controlled cyclic tests.
2- Assessments made with the ICRCHCA showed that the torque transmitting system and controlling software required changes to enable the system to apply relatively fast and accurate cyclic loads. To do this, a gear box was added to the torque motor and the metal chain assembly was tightened. In addition, the ICRCHCA control software was upgraded to TRIAX 5.2
3- A water pluviation technique was chosen for sample preparation because of its ability to produce dense samples with uniform internal fabrics similar to those of marine sand deposits.
4- Saturation stages were performed to ensure that air bubbles trapped inside the sand were dissolved in water. B tests performed after saturation showed that values above 93% saturation were achieved prior to final cycling using the saturation techniques practiced.

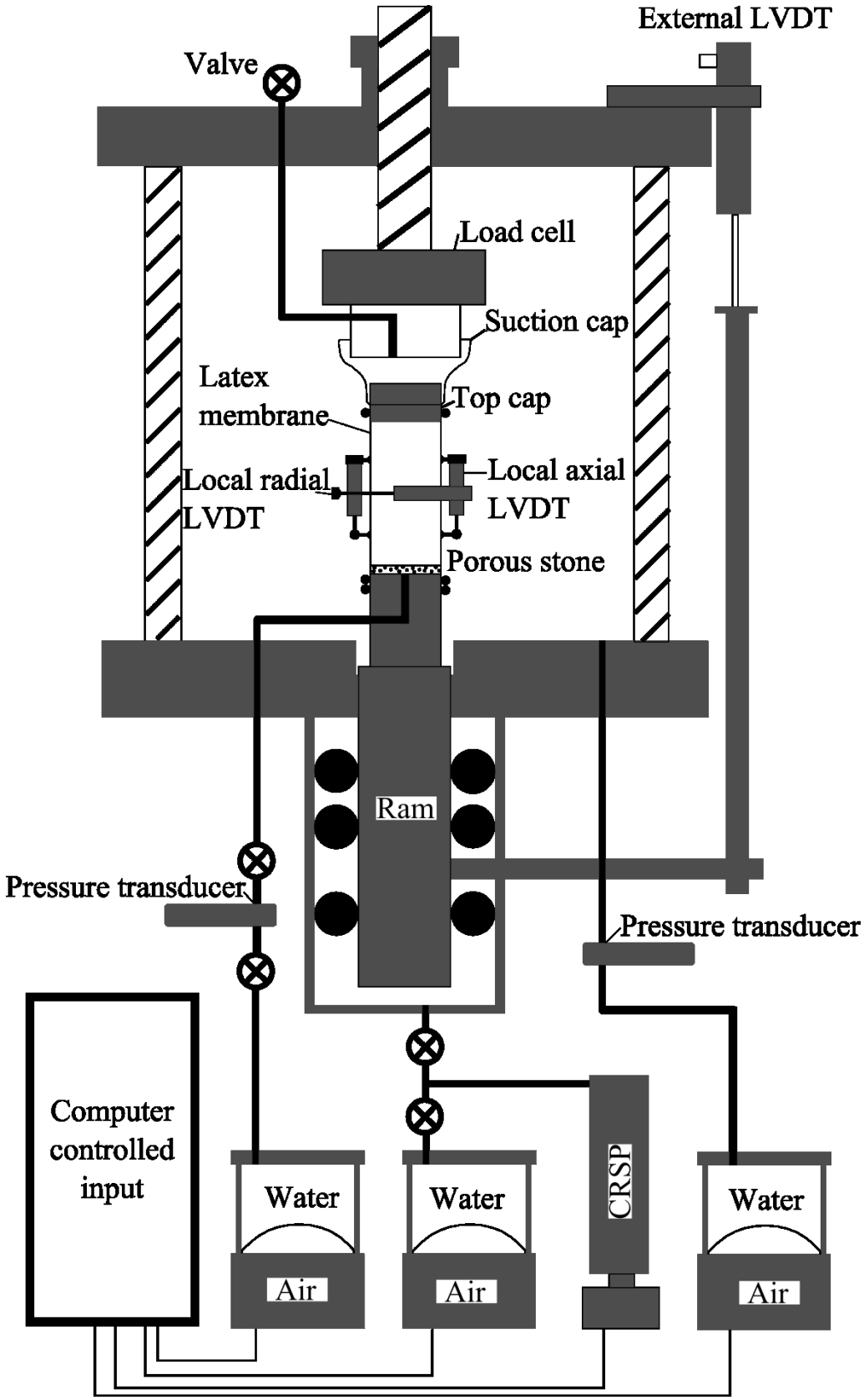


Figure 4-1 Schematic diagram of the modified Bishop & Wesley (1975) triaxial apparatus used

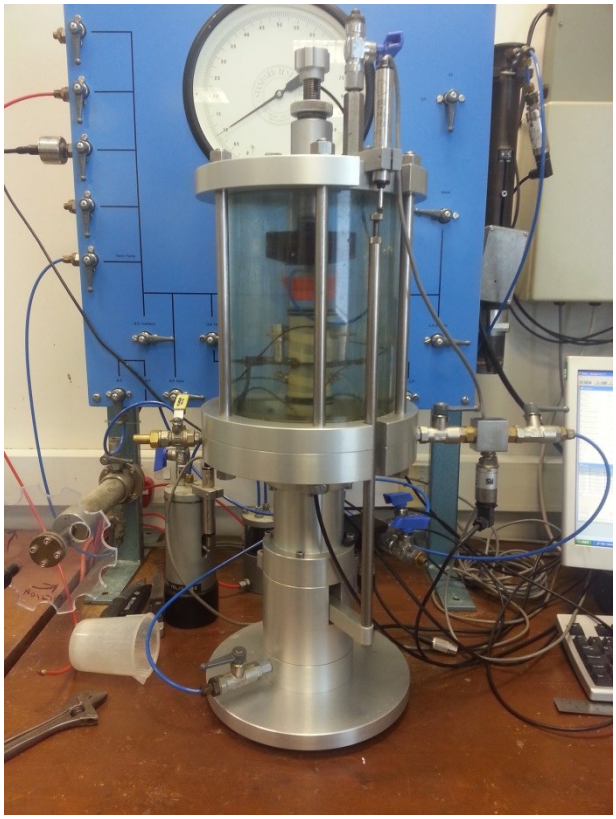


Figure 4-2 Photograph of the modified Bishop & Wesley (1975) triaxial apparatus used

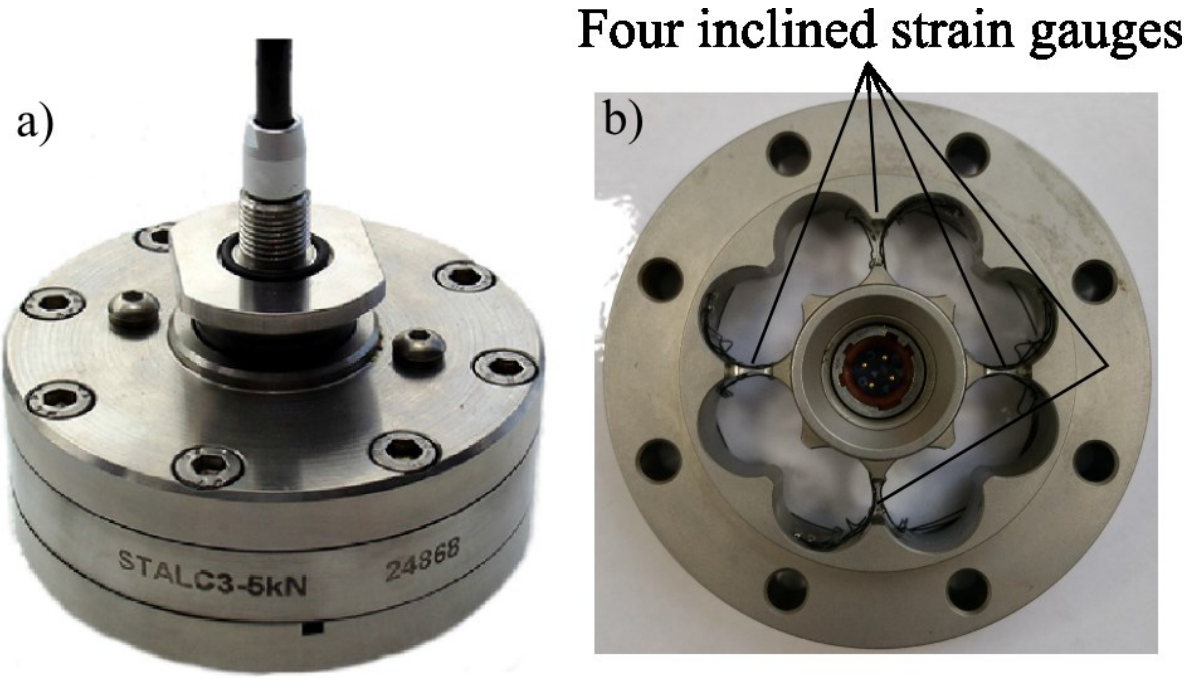


Figure 4-3 a) Photograph of the load cell used b) internal structure of the load cell, shearing its strain gauged shear webs.

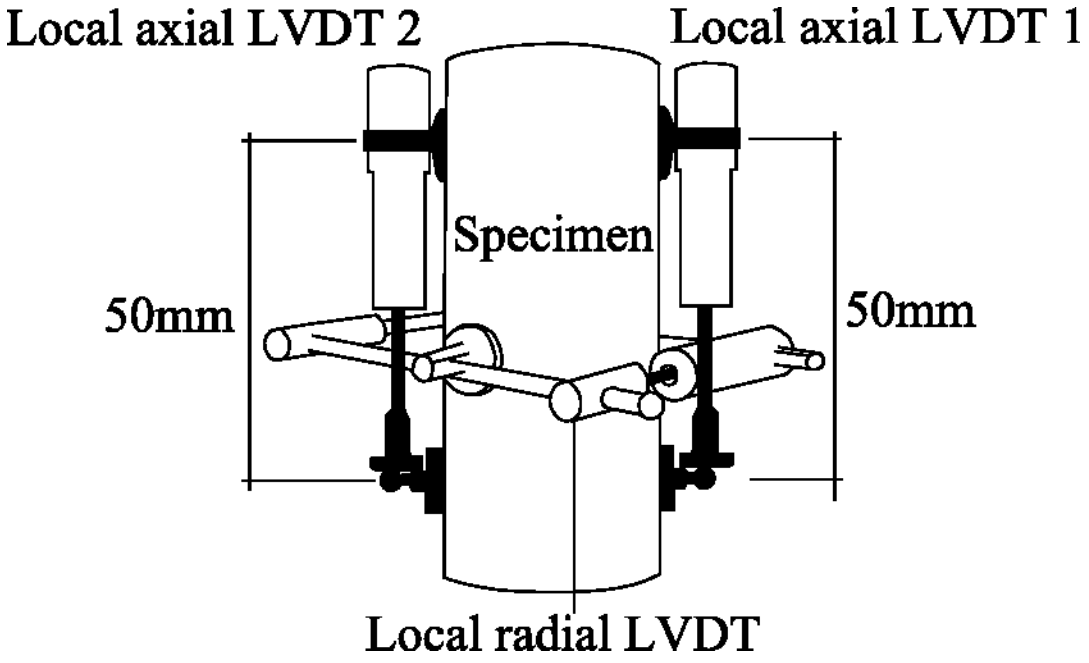


Figure 4-4 Illustrative sketch showing how local transducers were installed on the surface of the triaxial specimens.

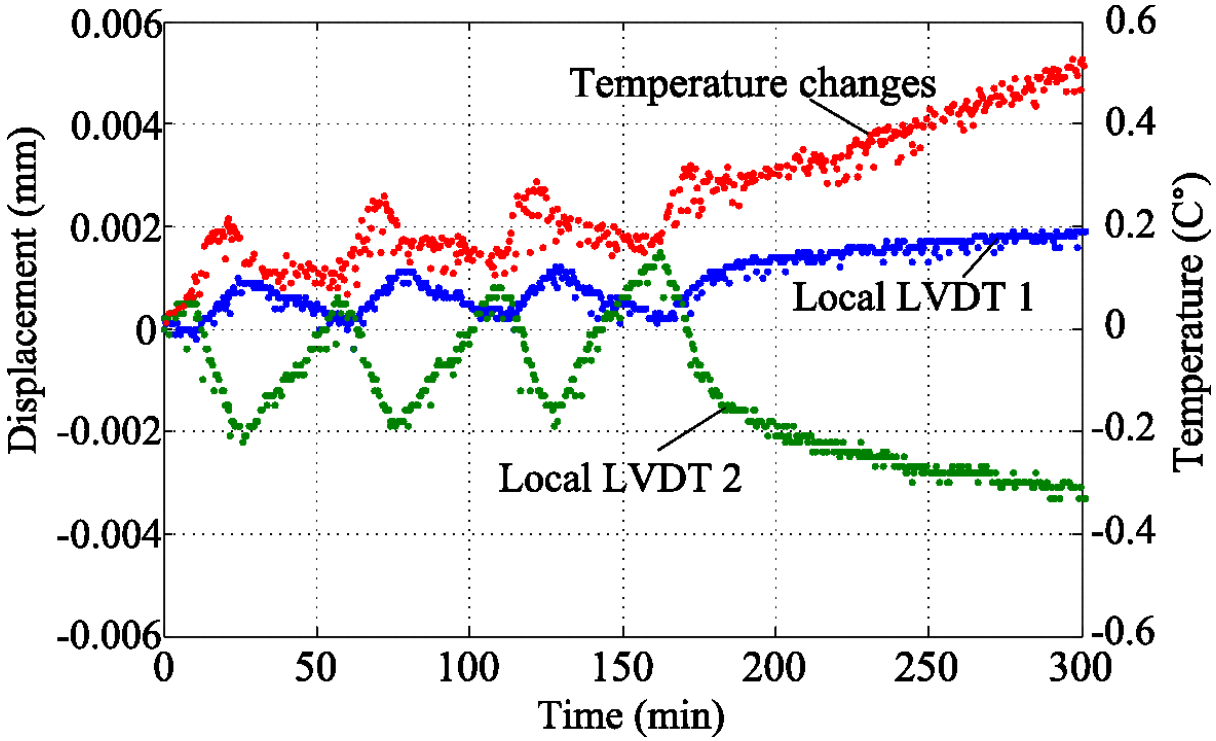


Figure 4-5 Effect of temperature fluctuations on local LVDT readings.

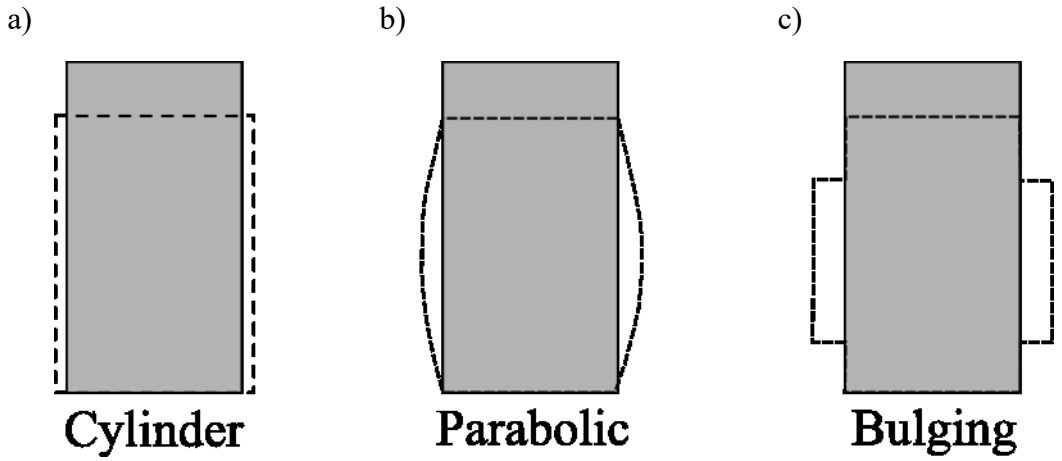


Figure 4-6 Different modes of sample deformation as suggested by Germaine et al (1988)

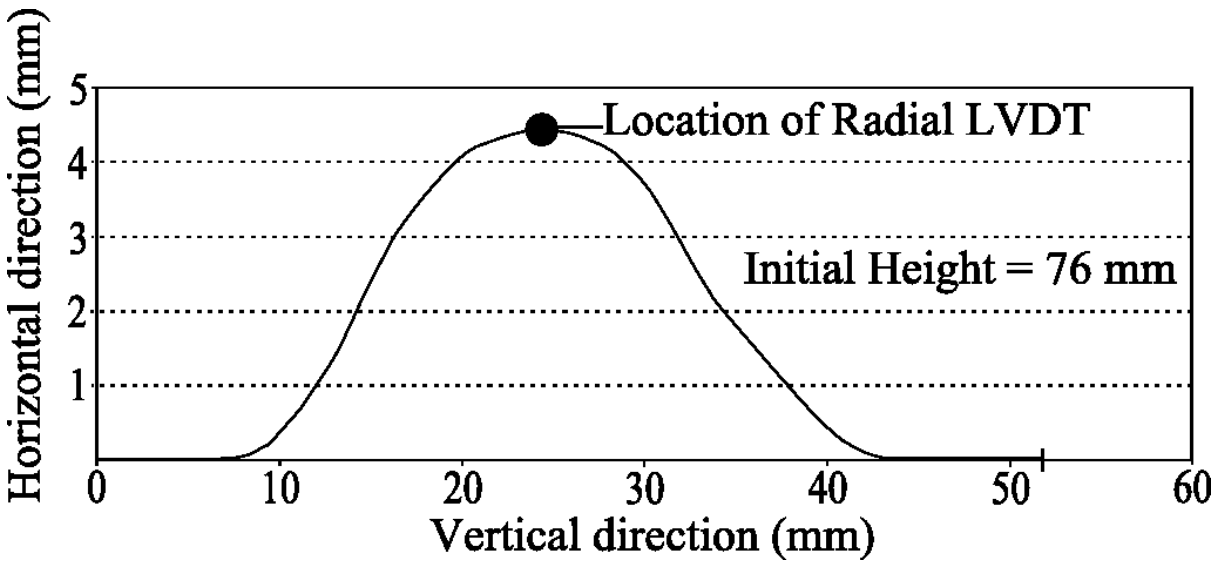


Figure 4-7 Deformation of a Dunkerque specimen under axial shearing to 20% axial strain as determined from digital analysis of photograph taken sequentially during compressive shearing.

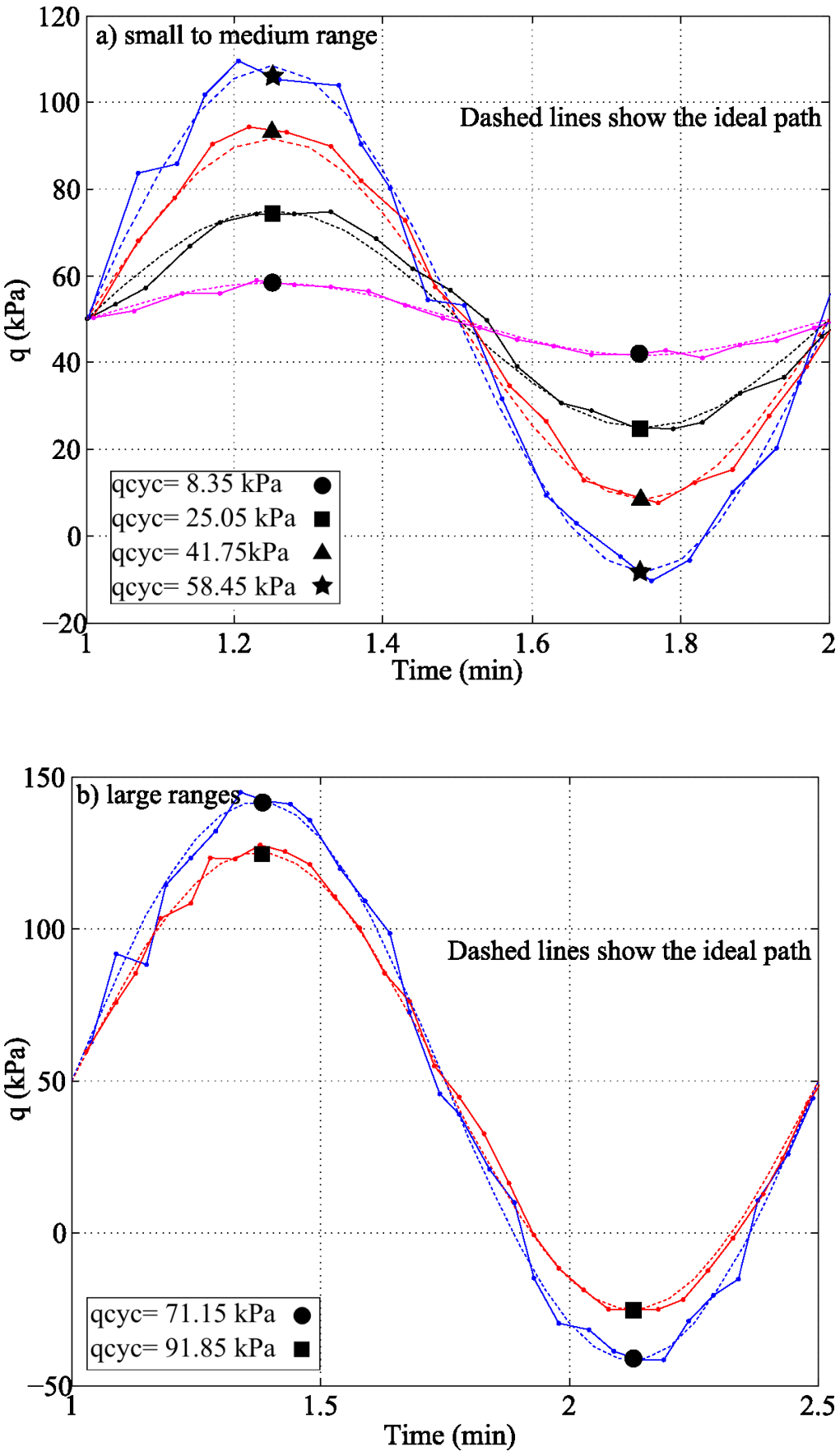


Figure 4-8 Comparison between applied and ideal sinusoidal cyclic loads in triaxial apparatus for a) small to medium amplitudes and b) large amplitudes.

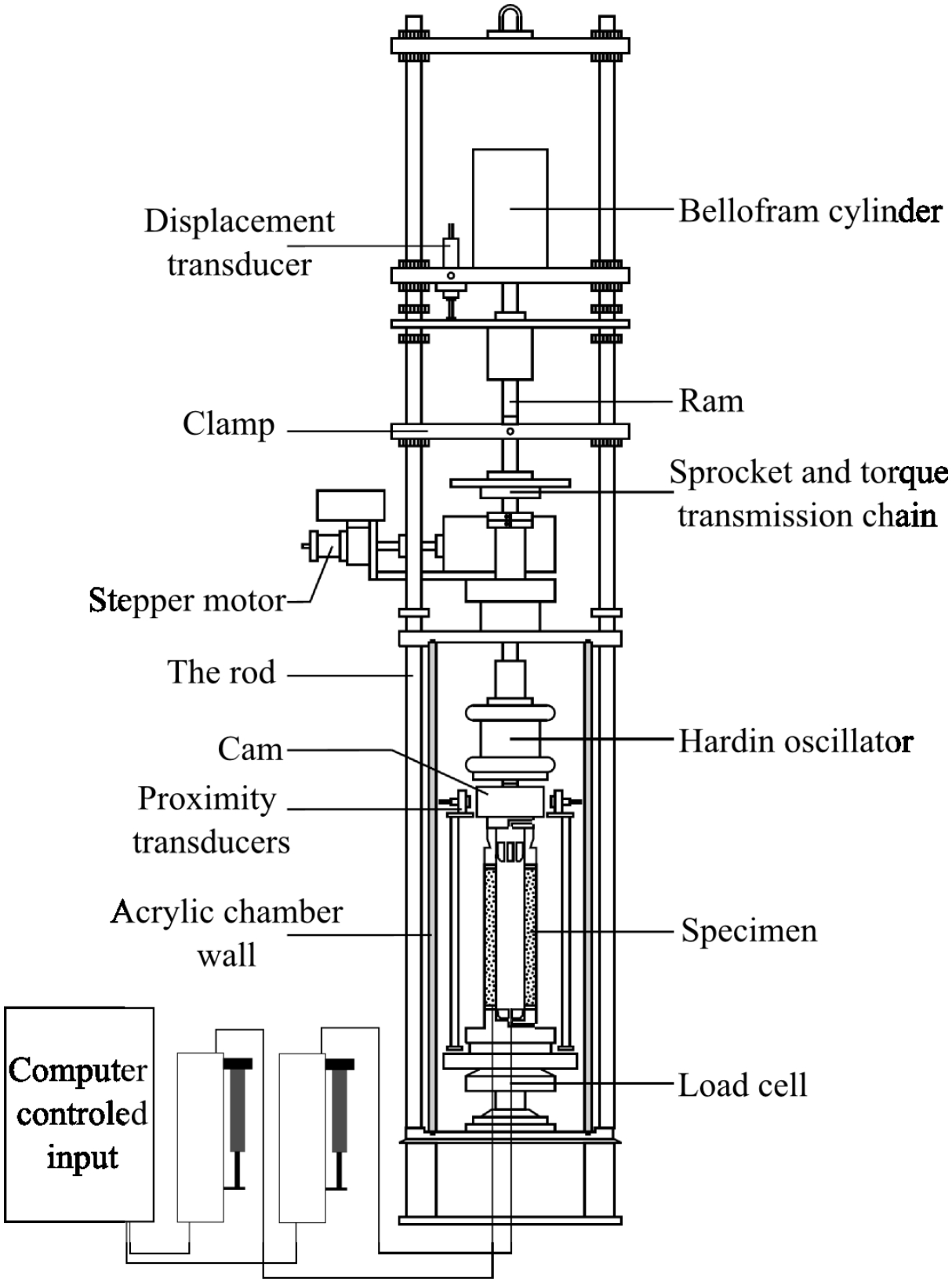


Figure 4-9 Schematic diagram of the ICRCHCA apparatus after Brosse (2012)

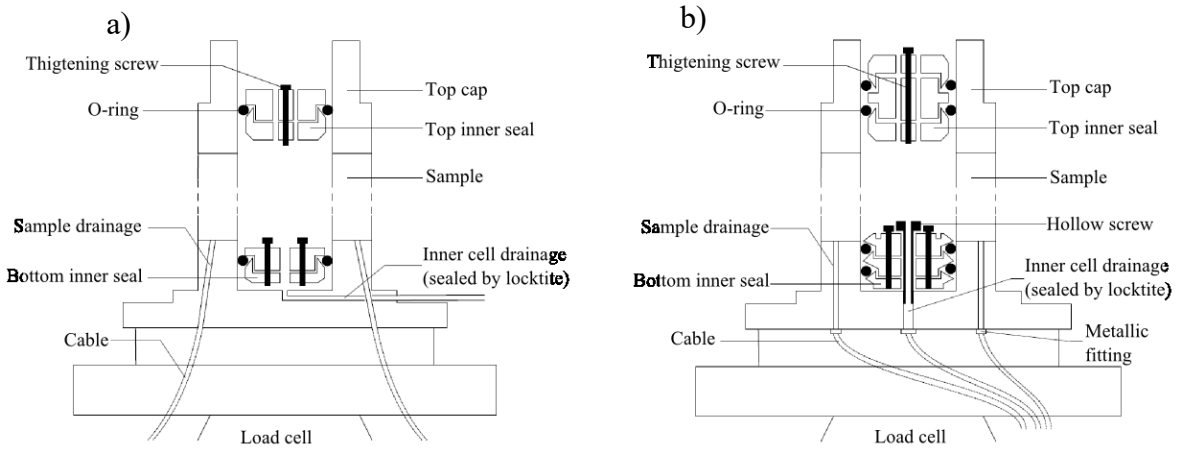


Figure 4-10 a) Inner cell sealing mechanism by Nishimura (2006) b) Modified inner cell mechanism by Brosse (2012)

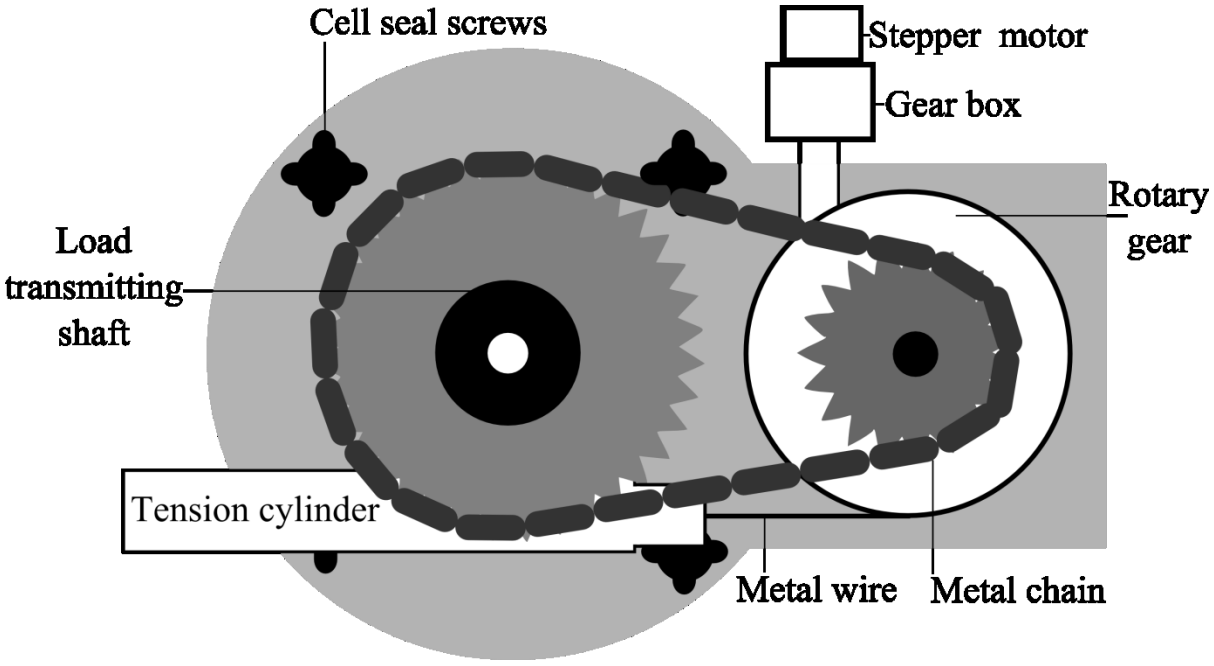


Figure 4-11 Schematic illustration of the torque transmitting system in ICRCHCA

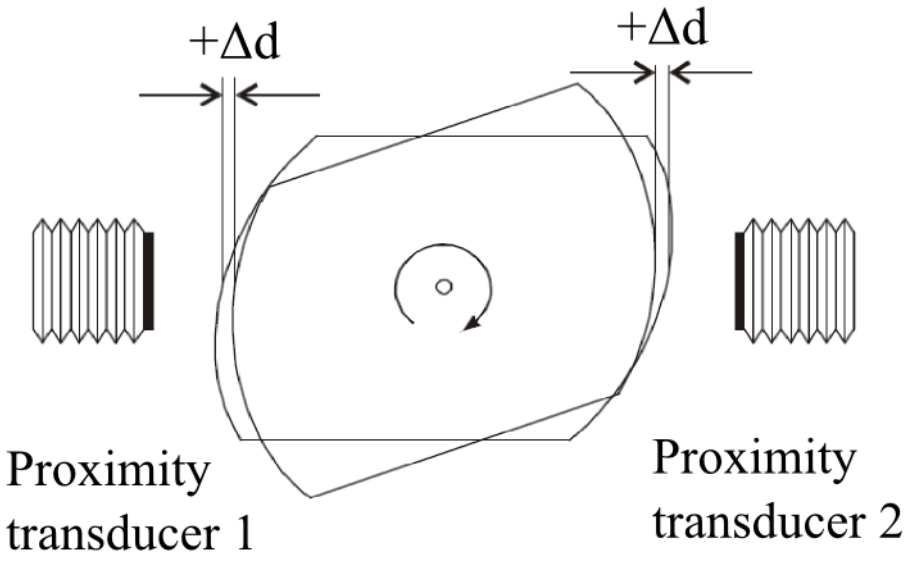


Figure 4-12 Schematic plan of the proximity transducers at top of the HCA specimen

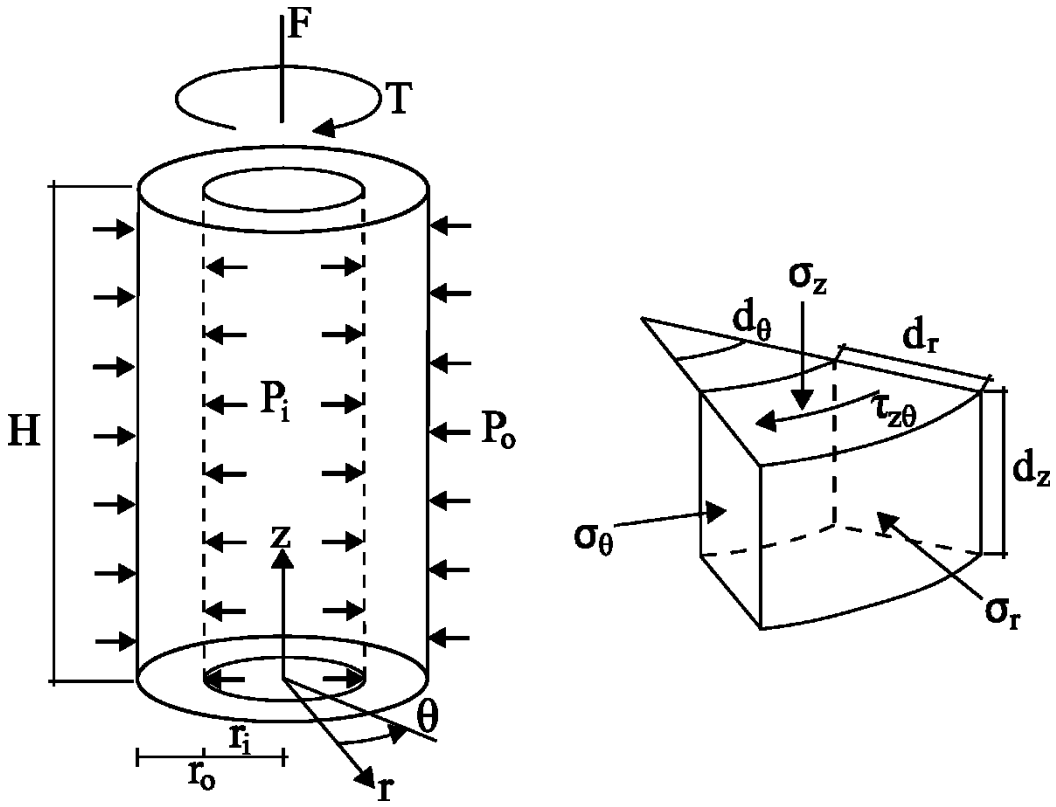


Figure 4-13 External forces applied to the specimen in the HCA and corresponding stress state of an element of soil.

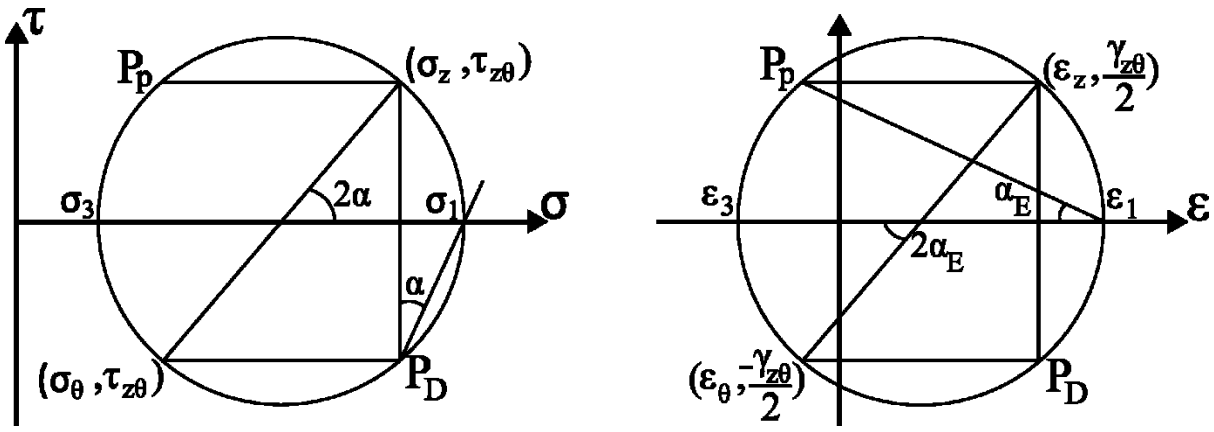


Figure 4-14 Stress and strain state in HCA specimen. Pp refers to pole in term of planes of stress orientation and PD in terms of stress axis direction.

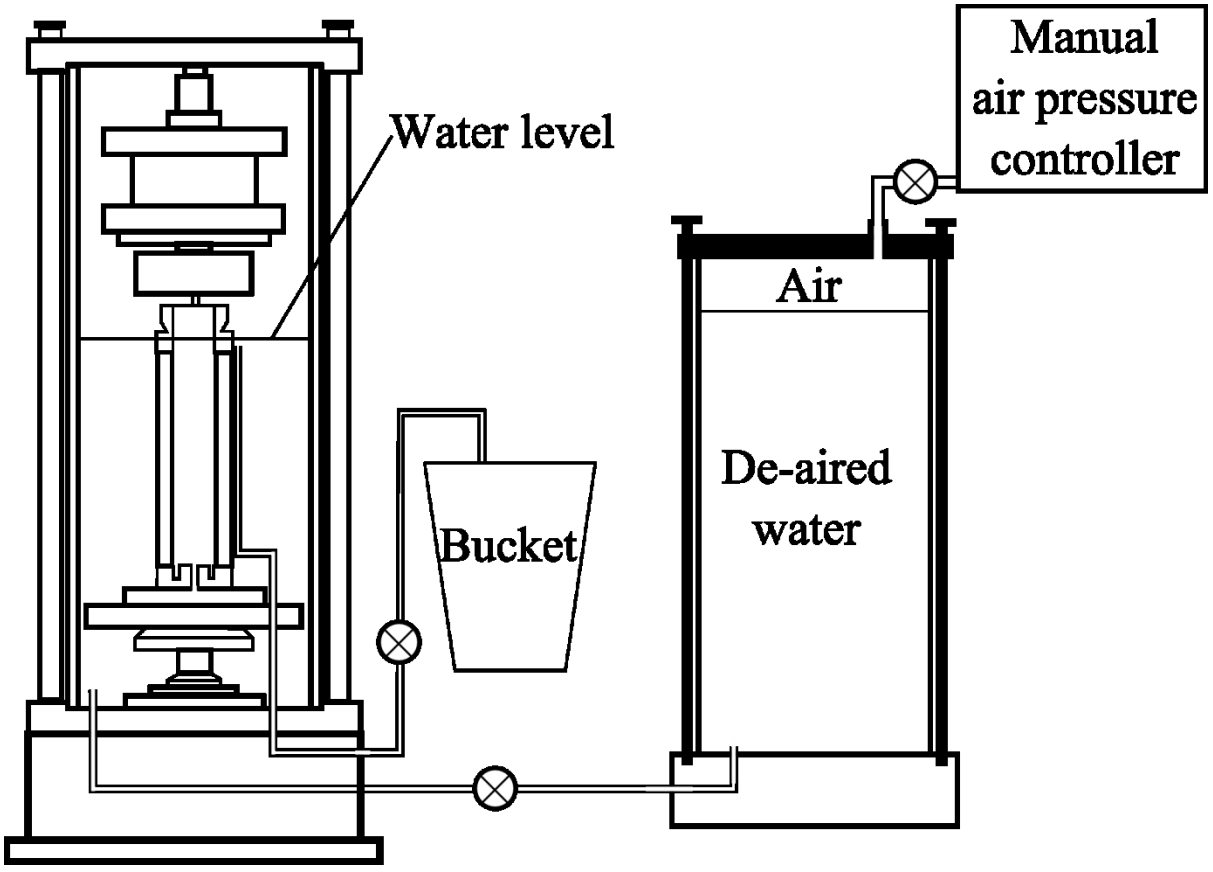


Figure 4-15 Schematic illustration of the water changing procedure in HCA apparatus

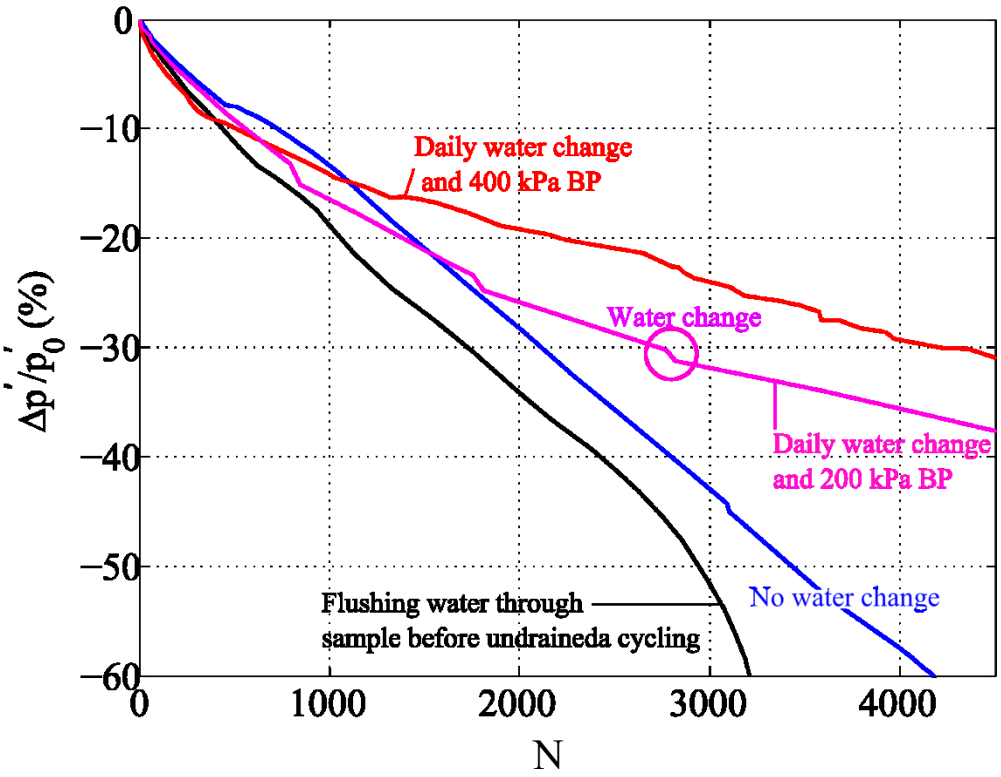


Figure 4-16 Comparison of response under undrained simple shear cyclic loading between tests with different water changing procedure. p'=167kPa, $\Delta\tau_{z\theta}$=41.75kPa

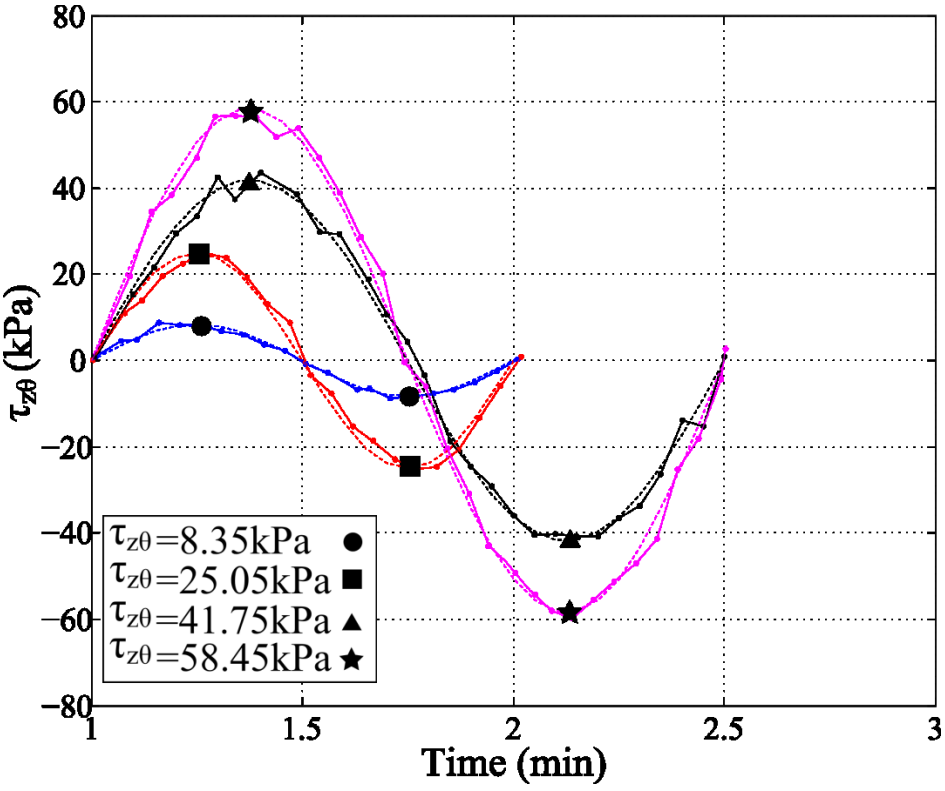


Figure 4-17 Comparison between applied and ideal sinusoidal cyclic loads in HCA apparatus

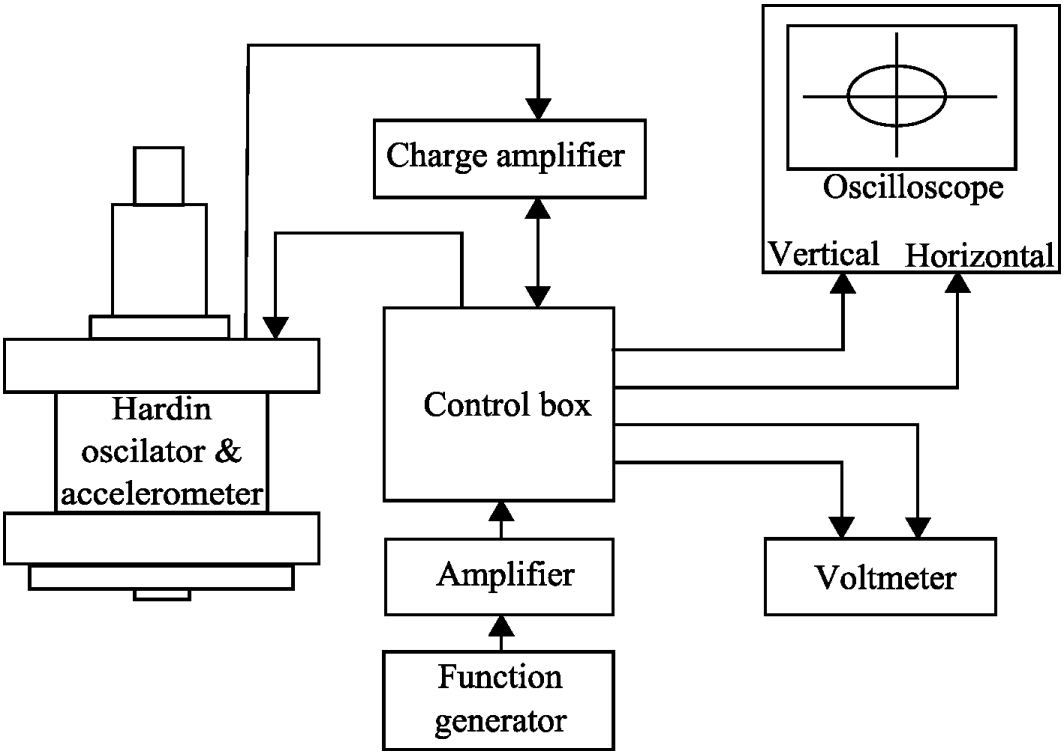


Figure 4-18 Schematic illustration of the electrical set-up of the RC system

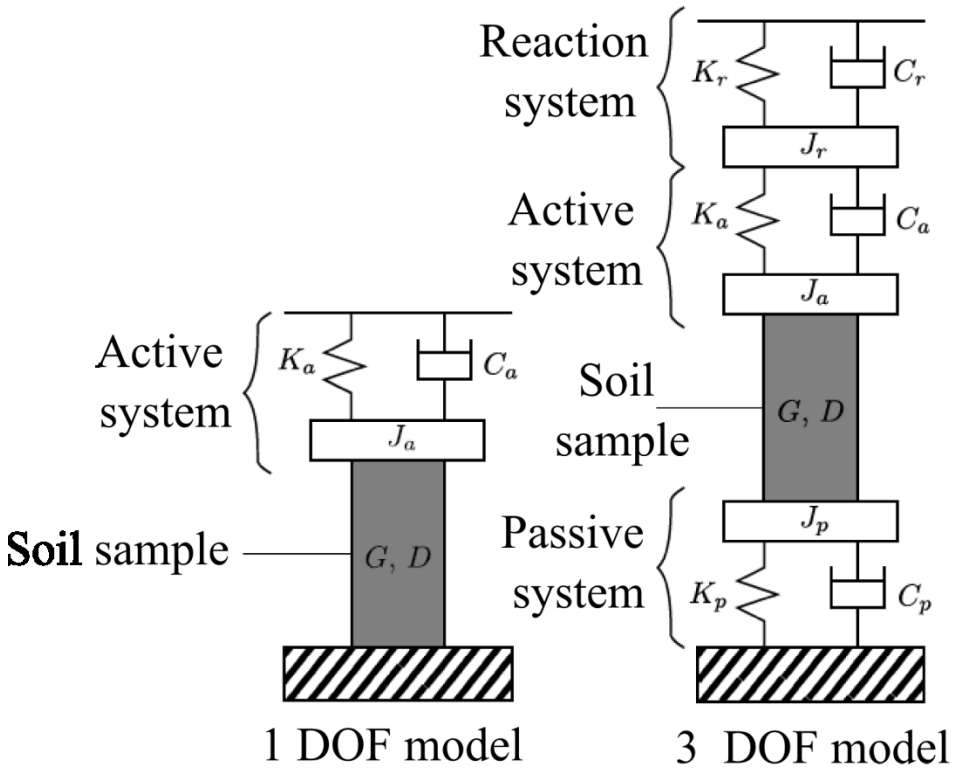


Figure 4-19 Schematic illustration of two possible boundary condition assumptions for HCA RC system

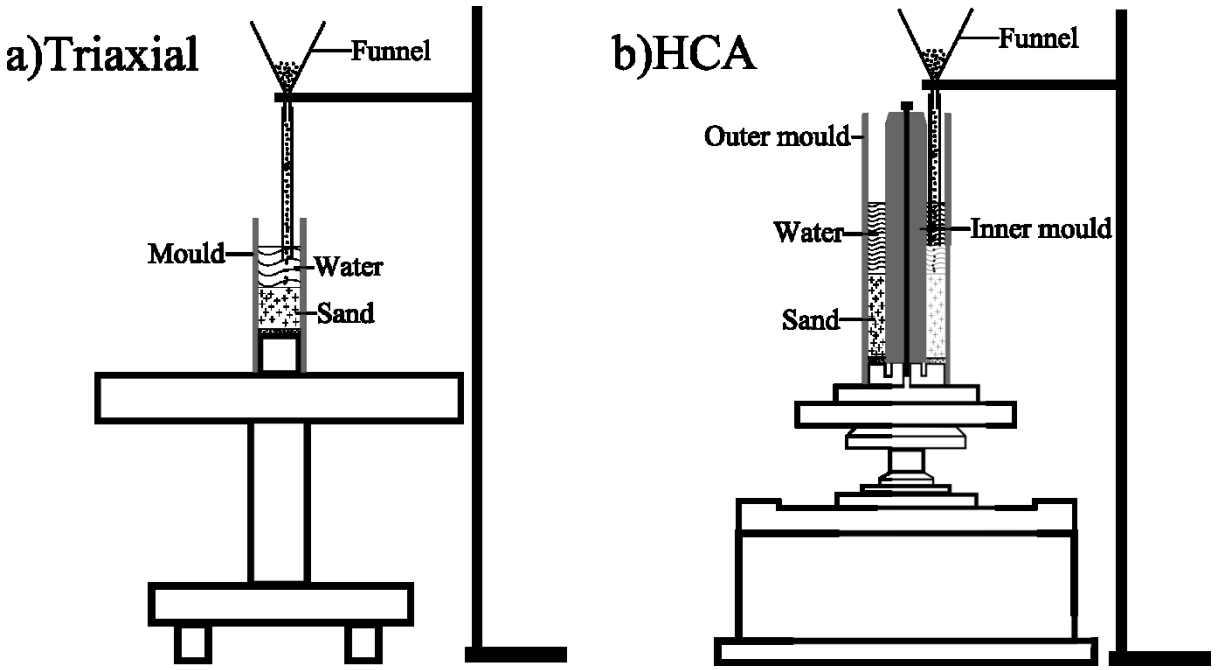


Figure 4-20 Schematic illustration of sample preparation procedure for triaxial and HCA samples.

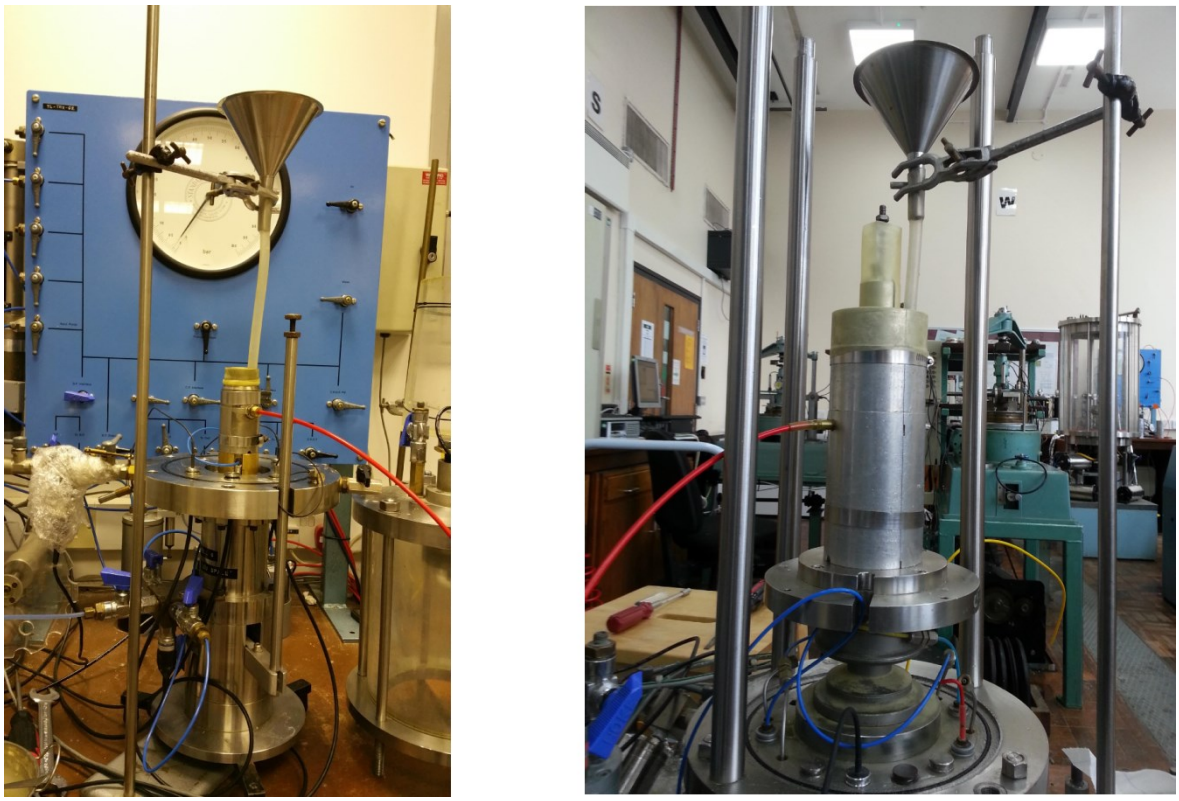


Figure 4-21 Photographs of sample preparation procedure for triaxial and HCA samples.

CHAPTER 5
Index properties and monotonic behaviour of test sands

Introduction

Dunkerque and Fontainebleau NE34 sands were chosen for this research in order that the laboratory cyclic tests could be related to the field pile tests reported by Jardine & Standing (2000, 2012) and model the pile tests described by Tsuha *et al.* (2012). This chapter presents descriptions of both sands' index properties and mechanical characteristics under static loading. Their behaviour under drained and undrained monotonic triaxial testing are reported, including information about their small strain stiffness behaviour and large strain, critical state, characteristics.

5.1 Description of test sands

The broad aim of the Author's research was to find laboratory models that capture the conditions generated around driven piles. The specific objectives were to model the Dunkerque field pile tests reported by Jardine & Standing (2000, 2012) and the laboratory model pile tests described by Tsuha *et al.* (2012). The tested specimens of Dunkerque sand were sampled from shallow depth (0 to 0.7m from surface) at Port-Quest, France - the Dunkerque site employed by Jardine & Standing (2000). Specimens of industrially mined and

processed NE34 sand obtained from the Nemours site, south Paris, France that had been used in the calibration chamber model pile tests of Tsuha *et al.* (2012) were also tested. Earlier testing on both sands has been reported by Chow (1997), Kuwano (1999), Jardine & Standing (2000, 2012), Tsuha *et al.* (2012) and Rimoy (2012). This chapter summarises the latters earlier work before describing the Author's experimental programme of static testing on the two sands.

5.1.1 Dunkerque sand

The Dunkerque site, whose location is shown in Figure 5-1, has a deep profile of dense marine sands similar to those found at many North Sea offshore oil and gas platform sites. It has been used as a site for driven pile research since the 1980's by the French CLAROM group (Brucy *et al.*, 1991) and later by Imperial College London by Chow (1997) and Jardine & Standing (2000, 2012). Chow (1997) reported results from borehole logging and CPT tests, summarised in Figure 5-2. The depth profile shows dense to medium-dense silica sand with some shell fragments and a thin layer of organic material found at 8m depth with average CPT tip resistance, q_c, around 20 MPa. The ground water level rests at around 4m depth. Chow reported relative density profiles derived from (i) bulk density measurements on rotary cores by the CLAROM group, and (ii) CPT tests, as shown in Figure 5-3. Chow's CPT relative density profile was interpreted using the Lunne & Christoffersen (1983) correlation for normally consolidated sands. Chow found that, on average $D_r = 75\%$, from a depth of 3m and below.

Chow (1997) reported the mineralogy of Dunkerque sand from X-ray diffraction tests, noting an average composition of 84% SiO_2 quartz, 8% Feldspar and 8% Calcium carbonate shell fragments. Samples tested by the CLAROM project team also indicated 9 to 18% shell fragments with an average value of 11.5% from all their test samples.

Sieve analyses of the near surface samples were performed by the Author using dry sieving and QicPic laser-based analysis apparatus and the results are shown in Figure 5-4. Sieve analyses by the Author on core samples taken at different depths of up to 25m by the CLAROM project are also shown. The distributions are generally similar down to 15m depth, but the deeper samples tend to become progressively finer. In order to keep consistency in the research, only the near surface samples were employed for the author's main laboratory test programme.

Maximum and minimum void ratios were obtained for the samples through the BS procedures (BS 1377-4:1990) and their values along with other index properties are given in Table 5-1. The QicPic laser-based analyses of particle grain shapes are given in Figure 5-5 and a microscope image obtained from Zeiss Optical Micrscope is presented in Figure 5-6.

5.1.2 NE34 sand

NE34 is a standard test sand mined and processed from quarries at Fontainebleau and Nemours, South of Paris, France. It was chosen for the Grenoble-Imperial College calibration chamber model pile research because of its similarity in grading to Dunkerque sand (Tsuha *et al.,* 2012; Rimoy, 2013).

The main difference between the Dunkerque and NE34 sands is the latters purity. NE34 sand is composed of 99.7% SiO_2 quartz particles and this avoids any potential physiochemical reactions the might develop with Dunkerque sand due to the presence of carbonate shell fragments, trace of minerals or salt (Rimoy, 2013).

Sieve analysis on NE34 sand is shown and compared with Dunkerque sand in Figure 5-7, and its main index properties are summarised in Table 5-1. Results from QicPic laser-based analysis of grain shapes are given in Figure 5-8 and a microscope image obtained from Zeiss Optical Microscope is presented in Figure 5-9.

It can be seen that Dunkerque sand is slightly coarser with particles possessing smoother edges due to their continuous re-working in their offshore environment, while NE34 is slightly more angular. NE34 sand has a marginally lower minimum void ratio e_{min}.

Table 5-1 Index characteristics of test sands

Parameter	Dunkerque	NE34
G_s	2.655	2.65
e_{max}	0.91	0.90
e_{min}	0.57	0.51
d_{50} -µm	268.8	234.5
Sphericity	0.89	0.89
Elongation	0.51	0.54

5.2 Monotonic behaviour of test sands

Some mechanical properties have been reported for Dunkerque sand by Chow (1997) and Kuwano (1999). Similar reports are available for NE34 sand in Yang *et al.* (2010) and Altuhafi & Jardine (2011). However, a more advanced and detailed programme of monotonic testing was required to assess the detailed mechanical characteristics of both sands and set the framework for interpreting the Authors' cyclic tests. A series of drained and undrained triaxial tests were performed to achieve this:

5.2.1 Drained normally consolidated K_0 tests

All samples were prepared using the sample set-up procedure described in Section 4.3. As mentioned earlier, the average D_r at Dunkerque was ≈75% over the depth range of interest and the calibration chamber tests reported by Yang *et al.* (2010) and Tsuha *et al.* (2012) adopted a target e_0=0.62, equivalent to D_r=72%. Aiming to have samples with states similar to the field and model pile tests, and also to maintain comparable conditions with the two sands, an initial e_0=0.64 was targeted for both sands, leading to D_r values of 79% and 70% for the Dunkerque and NE34 sands respectively.

By adjusting the laboratory pluviation drop height during sample formation and practicing the set-up procedure numerous times, multiple samples could be produced with initial D_r values to ± 0.003 to the target value of 0.64. The initial void ratios achieved for each sample are presented in Table 5-2.

The normally consolidated K_0 value of Dunkerque sand was estimated by Chow (1997) and Kuwano (1999) to vary between 0.35 to 0.40 (from triaxial tests) while Gaudin *et al.* (2005) have reported variations between 0.34 to 0.47 for NE34 sand being inferred from in-situ cone pressuremeter tests. Jaky's (1944) expression for the K_0 of normally consolidated sand based on ϕ'_{cs} obtained by Chow (1997) and Kuwano (1999) gives K_0 values of 0.47 and 0.45 for Dunkerque sand and NE34 respectively. Based on the above, a nominal K_0 = 0.45 was applied to both sands during their consolidation stages.

5.2.1.1 Consolidation and creep

The Authors' triaxial specimens were consolidated to 150, 300 and 500kPa initial p′ values (with σ'_v=232, 483 and 794 kPa respectively) at a $d\sigma'_r/dt$ rate of 60 kPa/hr. To assess the degree to which K_0 conditions were applied, radial strain changes were monitored, and the final values reached at the end of consolidation are summarised in Table 5-2. Generally the final radial strains were relatively small (<0.06% dilative) for p′ up to 500 kPa, indicating tolerably near K_0 conditions while also suggesting that K_0^{nc} may have been marginally over-estimated. Consideration was given to using the servo-control system to adjust the cell pressures to ensure that the radial strains were kept even closer to zero. However, even differences in initial internal structure and fabric could have led to different K_0 values and deviatoric stress (q) conditions prior to shearing therefore this procedure was not adopted.

Table 5-2 Initial void ratios and radial strains accumulated in K_0 consolidation stages of static tests at OCR=1

Material	shear direction	Sample	p′ (kPa)	q (kPa)	e_0	Final ε_r (%)
Dunkerque	$+\Delta\sigma'_v$	DK150C	150	138	0.639	0.018
		DK300C	300	276	0.637	0.035
		DK500C	500	460	0.637	0.045
	$-\Delta\sigma'_v$	DK150E	150	138	0.642	0.029
		DK300E	300	276	0.640	0.020
		DK500E	500	460	0.643	-
NE34	$+\Delta\sigma'_v$	NE150C	150	138	0.637	0.016
		NE300C	300	276	0.637	0.020
		NE500C	500	460	0.638	0.060
	$-\Delta\sigma'_v$	NE150E	150	138	0.639	0.020
		NE300E	300	276	0.639	0.030
		NE500E	500	460	0.640	-
		Average:			0.64±0.003	0.04±0.024

The void ratio changes developed during the consolidation and creep stages of all the above triaxial tests are shown in Figure 5-10 in e:log (p′) space. The consolidation curves did not follow the classical log-linear pattern and the compressibility values, λ, calculated using Equation 5-1 were pressure dependent for both sands, as shown in Table 5-3.

$$\lambda = \frac{\Delta e}{\Delta(\ln p')} \qquad \text{Equation 5-1}$$

Table 5-3 Compressibility values obtained from different pressure ranges

Material	λ		
	20-100 kPa	**100-300 kPa**	**300-500 kPa**
Dunkerque	6.1×10^{-4}	9.3×10^{-4}	1.2×10^{-3}
NE34	6.3×10^{-4}	9.0×10^{-4}	1.1×10^{-3}

Porovic (1995), Zdravkovic (1997) and Kuwano (1999) reported significant creep rates in their granular media. The Authors' aim was to extend the creep stages imposed after "consolidation" until the residual creep rates fell to below 1% of the subsequent shearing rate.

To achieve this, 48 hour creep stages were allowed at constant effective stresses prior to shearing. The axial strains accumulated during the creep stage are plotted against time in Figure 5-11, showing that the creep strain rates dropped from 0.03 and 0.015 %/day for Dunkerque and NE34 sand, respectively, to 0.008 and 0.002%/day over 48 hours. The Dunkerque sand generated higher creep rates at any given time under similar p′ and e values. This can be related to the existence of shell fragments in Dunkerque sand which increase its compressibility. The Dunkerque sands particles are less angular than those of NE34 sand, which would normally reduce both the creep rates and compressibility (Tatsuoka, 2011). Kuwano (1999) suggested that a power-law relation between creep rate and time, t, can describe the behaviour over such pauses:

$$\frac{d\varepsilon_{creep}}{dt} = A_{creep} t^{B_{creep}} \qquad \text{Equation 5-2}$$

Where ε_{creep} is the creep shear strain and A_{creep} and B_{creep} are fitting constants. Therefore, the strain accumulation relation can be derived by integrating the above equation as:

$$\varepsilon_{creep} = C + \frac{A_{creep}}{B_{creep}+1} t^{B_{creep}+1} \qquad \text{Equation 5-3}$$

In order to assess the applicability of the proposed equation with the Authors' tests, power-law equations were fitted to the data that gave a relatively good fit with an average regression of $R^2 = 0.92$. The fitting parameters obtained and regression values for power-law fitting are given in Table 5-4. While the A_{creep} values show some dispersion, the B_{creep} values are consistent.

Table 5-4 Constants obtained from power-law fitting to creep trends at end of K_0 drained stages

Material	shear direction	Sample	A_{creep}	B_{creep}
Dunkerque	$+\Delta\sigma'_v$	DK150C	0.00090	-0.64
		DK300C	0.00039	-0.70
		DK500C	0.00056	-0.63
	$-\Delta\sigma'_v$	DK150E	0.00203	-0.71
		DK300E	0.00078	-0.61
		DK500E	0.00090	-0.61
	Range	-	0.001±0.001	-0.66±0.05
NE34	$+\Delta\sigma'_v$	NE150C	0.00090	-0.70
		NE300C	0.00074	-0.75
		NE500C	0.00072	-0.80
	$-\Delta\sigma'_v$	NE150E	0.00083	-7.40
		NE300E	0.00089	-0.75
		NE500E	0.00091	-0.73
	Range	-	0.0008±0.0001	-0.75±0.05

For comparison, Kuwano (1999) reported A_{creep} = 0.0004 and B_{creep} = -0.70 and A_{creep} = 0.0012 and B_{creep} = -0.68 values from similar tests on dense and loose Ham River Sand (HRS) specimens respectively.

5.2.1.2 High pressure oedometer tests

The compressibility of test sands were measured at intermediate pressures (up to 506 kPa) during consolidation stage of triaxial tests. However, in order to obtain compressibility data at higher pressures where breakage becomes more important, two high-pressure oedometer tests were performed by Mr. T. Liu who worked closely with Author during this research and is currently working on a continuation of this research project. Results shown in Figure 5-12 show that Dunkerque sand becomes significantly more compressible at higher pressures which is due to higher breakage rates compared to NE34 sand.

5.2.1.3 Small strain and stiffness behaviour

The kinematic multi-yield surface model that was originally proposed by Jardine (1992), which was based on tests on clays, has also been employed to describe the small strain

behaviour of sand within its classical large-scale yield surface in earlier studies by Zdravkovic (1997), Kuwano (1999), Kuwano & Jardine (2002, 2007) and others as noted in Section 2.1.

High resolution local strain transducers were used to explore the behaviour of both sands at small strains in a programme that was informed by the kinematic multi-yield surface framework.

In all compression and extension tests, samples were sheared at an axial strain rate of 0.03 %/hr while the cell pressure was kept constant. Stress-strain measurements at small strains allowed a detailed examination of response at small strains.

5.2.1.4 Y_1 surface (Linear range)

As discussed in Chapter 2, within the Y_1 surface the soil response is linear elastic and the small load–unload loops should show no permanent strains. The maximum stiffness of the soil applies inside this surface and its value is a function of void ratio and current the effective stresses (see Section 2.1.1). The shape and size of the Y_1 locus is a function of the current stresses and stress history. The arrangement of particles and their contacts do not change under stress perturbations that remain within this zone (Kuwano, 1999).

In order to assess the elastic response within the Y_1 surface and to find the boundaries of the Y_1 loci, stress-strain measurements from all drained tests at strains up to ε_v=0.02% are plotted in Figure 5-13. Results from drained compression ($+\Delta\sigma'_v$) and extension ($-\Delta\sigma'_v$) tests show an initially linear relation between $\Delta\sigma'_v$ and ε_v until the Y_1 surface is engaged at a certain σ'_v or ε_v limit. Thereafter the stress-strain response becomes non-linear and stiffness falls with strain. The shear strain invariants and the length of strain vector ($\varepsilon = \sqrt{{\varepsilon_1}^2 + 2{\varepsilon_3}^2}$) at which the Y_1 yielding took place are given in Table 5-5. Locations of the Y_1 boundaries obtained in the direction of drained (and undrained) axial shearing are shown in q-p′space in Figure 5-15 at

p'_0=500kPa and their evolution in relation with the applied p'_0 is shown in Figure 5-16. In order, to obtain the full Y_1 locus, it is required to perform probing tests at different stress path directions as performed by Kuwano & Jardine (2007).

5.2.1.5 Y_2 Surface

According to the original yield surface framework proposed by Jardine (1992), once the Y_1 locus is engaged the behaviour is non-linear within the Y_2 surface but the hysteretic load-unload cycles may close on unloading, showing no permanent straining (Jardine, 1992; Smith *et al.*, 1992). However, Kuwano (1999) reported from her higher resolution tests on sand that small permanent strains did accumulate from load-unload loops applied within the Y_2 surface. The Y_2 surface definition was therefore modified to correspond to points where the strain increment direction $d\varepsilon_s/d\varepsilon_{vol}$ starts to change direction (Zdravkovic & Jardine, 1997; and Tatsuoka *et al.* 1997; and Kuwano, 1999). Additionally, Y_2 yielding was associated with sharp increase in the susceptibility of the soil element to the load cycling, leading to significant rates of strain accumulation. To locate the possible Y_2 boundary, the shear invariant strain (ε_s) were plotted against volumetric strain (ε_{vol}) for all tests (except for DK500E and NE500E specimens that had no local radial strain sensors) as shown in Figure 5-14. The traces show that $d\varepsilon_s/d\varepsilon_{vol}$ does not change significantly as the Y_1 locus is engaged. However, each test showed a subsequent point where the strain path clearly changed direction, which was identified as the boundary of the Y_2 surface. The shear strain invariants and the length of strain vector at which the Y_2 yielding took place are given in Table 5-5. Similar to Y_1 boundaries, the size of the Y_2 locus depends on the level of $p'$with a square root relation.

Table 5-5 Shear, volumetric and total strains at Y_1 and Y_2 surfaces

Material	Sample	Y_1			Y_2		
		ε_s (%)	ε_v (%)	ε (%)	ε_s (%)	ε_v (%)	ε (%)
Dunkerque	DK150C	0.0041	0.0045	0.0060	0.018	0.006	0.018
	DK300C	0.0033	0.0037	0.0049	0.010	0.008	0.012
	DK500C	0.0030	0.0032	0.0043	0.019	0.015	0.024
	DK150E	0.0041	0.0043	0.0059	-0.020	0.006	0.020
	DK300E	0.0040	0.0042	0.0058	-0.024	0.011	0.026
	DK500E	0.0031	0.0033	0.0045	-	-	-
NE34	NE150C	0.0036	0.0038	0.0052	0.010	0.009	0.013
	NE300C	0.0025	0.0026	0.0036	0.010	0.008	0.012
	NE500C	0.0030	0.0031	0.0043	0.006	0.007	0.009
	NE150E	0.0033	0.0034	0.0047	-0.02	-0.020	0.028
	NE300E	0.0045	0.0046	0.0064	-0.022	-0.015	0.026
	NE500E	0.0039	0.0040	0.0055	-	-	-

5.2.1.6 Y_3 Surface

Once the Y_1 locus is engaged, irrecoverable strains start to accumulate more markedly under both static and cyclic loading and the ratio of plastic strain increment to the total strain increment grows. This ratio increases markedly on Y_2 yielding and continues to grow as shearing continues. The ratio can be calculated as:

$$\frac{d\varepsilon^p}{d\varepsilon^t} = \frac{d\varepsilon^t - d\varepsilon^e}{d\varepsilon^t} = 1 - \frac{d\varepsilon^e}{d\varepsilon^t} \qquad \text{Equation 5-4}$$

Where $d\varepsilon^e$ is the elastic strain increment and can be calculated using the maximum elastic strain measured or the experimental equations (Equation 2-1 to 2-5) based on the void ratio and the current effective stress levels.

Kuwano (1999) found that the $d\varepsilon^p / d\varepsilon^t$ ratio was typically ≈50% when the Y_2 surface was engaged that the ratio gradually increased until the Y_3 surface was reached and behaviour became almost fully plastic. Y_3 correlates with the conventional soil mechanics definition of yielding and is classically determined as the point where sharp changes occur in the overall stress-strain curves. Kuwano (1999) reported that the Y_3 yield stresses obtained from the

Ham River Sand (HRS) corresponded to contours of $d\varepsilon^p / d\varepsilon^t = 0.95$ and proposed that Y_3 could be defined as the point where this ratio was reached in all tests. A similar definition was used for the Author's tests on Dunkerque and NE34 sands to locate the Y_3 locus in ε_s-ε_{vol} space as shown in Figure 5-17. The shear strain invariants and the length of the strain vectors at which Y_3 yielding took place are given in Table 5-6.

5.2.1.7 Y4 Surface

Kuwano & Jardine (2007) proposed that the phase transformation point proposed by Ishihara (1975) could be viewed as an extra Y_4 surface within the original kinematic multi-yield surface framework. Points where an initially contractive response becomes dilative as shearing continues are recorded under most loading conditions with medium dense sands. The current drained tests on relatively dense samples led to the phase transformation points shown in Figure 5-18. Drained shearing beyond the Y_4 surface induced dilation as the samples moved towards their critical state points.

Table 5-6 Shear, volumetric and total strains developed between K0 conditions points at Y3 and Y4 surfaces

Material	Sample	Y_3			Y_4		
		ε_s (%)	ε_v (%)	ε (%)	ε_s (%)	ε_v (%)	ε (%)
Dunkerque	DK150C	0.113	0.031	0.104	0.212	0.100	0.223
	DK300C	0.081	0.034	0.086	0.252	0.090	0.265
	DK500C	0.073	0.051	0.086	0.331	0.063	0.305
	DK150E	-0.013	0.031	0.033	-0.631	0.122	0.611
	DK300E	-0.122	-0.032	0.123	-1.335	0.172	1.311
	DK500E	-	-	-	-	-	-
NE34	NE150C	0.111	0.032	0.114	0.301	0.114	0.316
	NE300C	0.092	0.041	0.098	0.240	0.073	0.253
	NE500C	0.117	0.050	0.120	0.221	0.051	0.225
	NE150E	-0.121	-0.031	0.104	-0.853	0.156	0.863
	NE300E	-0.120	-0.005	0.120	-1.402	0.194	1.412
	NE500E	-	-	-	-	-	-

5.2.1.8 Stiffness measurements

The maximum soil stiffnesses obtained within the Y_1 elastic ranges of sands are known to be functions of the current effective stress tensor and the void ratio. Linear equations were fitted

to the data points obtained within the Y_1 surface and the best fitting slopes defined the maximum effective vertical Young's modulus ($E'_{v,max}$) values given in Table 5-7.

Maximum stiffness: Kuwano (1999) noted that the sign of the stress increment should have no influence on the maximum stiffness value within the elastic region, meaning that compression ($+\Delta\sigma'_v$) and extension ($-\Delta\sigma'_v$) tests stating from the same initial σ'_v values should give equal $E'_{v,max}$ values. The tabulated results show that there is indeed broad agreement between the $E'_{v,max}$ measurements made at similar σ'_v values in compression and extension, but that the extension tests ($-\Delta\sigma'_v$) tended to give values that are ≈5% lower. The difference cannot be due to any ongoing compressive creep since its effect on $E'_{v,max}$ should be to reduce compressive stiffness by adding to the compressive strains under same Δq values.

Table 5-7 Maximum effective vertical Young's modulus from K_0 drained tests on NC samples.

Material	Sample	E_v' (MPa)
Dunkerque	DK150C	430
	DK300C	640
	DK500C	820
	DK150E	395
	DK300E	600
	DK500E	795
NE34	NE150C	440
	NE300C	660
	NE500C	830
	NE150E	435
	NE300E	645
	NE500E	795

Stiffness degradation: Once the Y_1 surface has been engaged the stiffness values fall sharply with increasing strain. To measure the tangent E'_v, the stress-strain data were plotted in semi-log space and cubic equations were fitted to the data at small strain intervals to give the

tangent stiffness at any strain level. The obtained stiffness degradation curves for both sands are shown in Figure 5-19 and Figure 5-20.

Comparison of the stiffness degradation curves from compression and extension tests show that under compression, the stiffness dropped more rapidly once the Y_1 surface was reached. The reason for this is that since these OCR=1 samples were anisotropically consolidated, the initial effective stress point is closer to the compressive part of the Y_3 yield surface in q-p′ space and therefore the drop in stiffness is faster under compression loading than in the extension tests, which start with relatively *Stable* unloading down to the isotropic axis.

Effect of p′and e on stiffness values: Wroth & Houlsby (1985) proposed a power function relation between the shear stiffness and p′

$$\frac{G}{P_r} = A\left(\frac{p'}{P_r}\right)^n \qquad \text{Equation 5-5}$$

However, with anisotropic soils, such as sands, the individual stiffness components are related better individual components of the effective stress tensor. For example E'_v is related solely to σ'_v:

$$\frac{E'_v}{P_r} = f(e)A\left(\frac{\sigma'_v}{P_r}\right)^n \qquad \text{Equation 5-6}$$

Where p_r is the reference pressure equal to 1 kPa and the effect of void ratio on the stiffness is considered by one of the normalisation functions *f(e)* proposed by numerous authors. The most used function is the Hardin & Richart (1963) equation originally used for Ottawa sand and this has been retained by the Author

$$f(e) = \frac{(2.17-e)^2}{1+e} \qquad \text{Equation 5-7}$$

To assess the E'_{vtan}: σ'_v relation in K_0 drained tests performed, E'_{vtan} values measured at different strain levels are plotted against the σ'_v in a log-log space and power law equations are fitted to the data at every strain level as shown in Figure 5-21 and Figure 5-22. At strain levels within the Y_1 surface, the relation can best be described with n=0.63 and 0.51 for Dunkerque and NE34 sands respectively. However, as strain level increases, the n values increase until at strain levels of ≈0.01% the relations become almost linear (n≈1) under compression and extension for both sands.

Note that the effects of void ratio on E'_{vtan} were not be assessed directly in these set of tests since all specimens had similar targeted e_0 values and the difference in their actual obtained e_0 values were very small (±0.025).

5.2.1.9 Other parameters

Poisson's ratios: The drained Poisson's ratios were measured using the local axial and radial LVDTs under shearing. A feature observed was that the local radial transducer system fitted to the 38mm cells did not always show any clear trends within the sands' elastic ranges. This is maybe due to inner friction between the rod and inner wall of the LVDT, as discussed in chapter 4. As shown in Figure 5-23 little radial straining was seen up to 0.009% axial strains, although that the radial strains subsequently increased. The slope of the ε_a:ε_r gives υ_{vh}=0.27 and 0.33 over the $0<\varepsilon_a<0.05\%$ ranges for Dunkerque and NE34 specimens respectively. These values compare with Kuwano (1999) who reported υ_{vh}=0.33 for K_0 dense HRS. It is recognised that any LVDT errors would impact on the previously discussed Y_2 surface identification process.

Bulk modulus: The octahedral bulk modulus corresponding to $\Delta\sigma'_v$ conditions may be obtained from the following equation:

$$K'_{oct} = \frac{E'_v}{3(1-2\upsilon_{vh})}$$ Equation 5-8

However, it can also be calculated simply as $K=\Delta p'/\varepsilon_{vol}$ from tests that include flatter dq/dp′ gradients. Data from swelling path test stages are used for this purpose. This swelling stage is part of the pre-conditioning procedure in cyclic tests which will be discussed in more detail in upcoming chapters. However, here data are used to calculate the bulk modulus at different mean effective stress levels. Figure 5-24 shows the bulk modulus values measured for both test sands following the swelling stress path.

5.2.1.10 Strength and volumetric characteristics moving towards the critical state

Strength characteristics: Under shearing to large strains, both sands showed brittle behaviour with drops in q developing after reaching peak q/p′ratios. Figure 5-25 shows the q-ε_a plots for the drained compression tests and it can be seen that the peak q/p′ratios were reached at strain levels $\varepsilon_a \approx$ 2.5-4% before q fell towards supposed final critical state values. Previous research on sands has indicated that critical state points may be reached at strain levels of about $\varepsilon_a \approx$ 25% (Jefferies & Been, 2006). However, reaching such strain levels in the stress path triaxial apparatus used was difficult because of the physical limitations in the ram movement system. Shearing continued to $\varepsilon_a \approx$ 20% in most compression tests which brought the soil relatively close to critical state conditions as assessed from changes in deviator stress and void ratio stabilisation. In tests with p'_0=150 and 300 kPa the q values reached on almost steady state, but for the p'_0 = 500 kPa tests further shearing appeared to be required to reach critical states. To measure the final critical state strength, data extrapolation was used for tests that did not reach a fully Stable state.

When shearing in extension, sample necking typically developed at $\varepsilon_a \approx$ 10% which prevented the tests from reaching clear critical states. The extension tests shown in Figure 5-26 indicate at certain strain levels clear breaks in the slope of the q- ε_a graphs which correspond to the initiation of necking. The effect is clearer in the higher effective stress tests.

Peak and critical state M values and angles of shearing resistance (M_{cs}, M_{peak}, ϕ'_{peak} and ϕ'_{cs}) were measured by fitting straight lines between the origin and the respective q-p′ points as shown in Figure 5-27, which show ϕ'_{peak}=36.7° and ϕ'_{cs}=32.1° for Dunkerque sand and ϕ'_{peak}=37.1° and ϕ'_{cs}=32.6° for NE34 sand. These angles are comparable to those reported by Chow (1997), Kuwano (1999), Yang *et al.* (2010) and Altuhafi & Jardine (2011) for the same sands. Triaxial compression and direct shear box tests performed by Kuwano (1999) on Dunkerque sand gave values of ϕ'_{cs} of 32° and 31° respectively, while triaxial compression tests reported by Altuhafi & Jardine (2011) and direct shear box tests reported by Yang *et al.* (2010) gave ϕ'_{cs}=33° and 32.8° for NE34 sand respectively. Tests reported in the literature and values obtained from this work are summarised in Table 5-8.

Table 5-8 Summary of strength parameters obtained for both test sands

Dunkerque	Kuwano (1999)	K_0 consolidated undrained triaxial stress path tests	Compression ϕ'=37° Extension ϕ'=35° ϕ'_{cs}=32, Dr=75% ,
	Chow (1997)	Aged sand stainless steel direct shear tests	$\delta p'$=31° δ_{cv}'=26.8° D_r=85% σ'_n=300kPa
	Kuwano (1999)	Direct shear box	ϕ'_{peak}=39.4° ϕ'_{cs}=31.1°
	Author's results	K_0 consolidated drained triaxial stress path tests	ϕ'_{peak}=36.6° ϕ'_{cs}=32.1°
NE34	Yang *et al.* (2010)	Direct shear box	ϕ'_{peak} =35.2° ϕ'_{cs} =32.8°
	Gaudin *et al.* (2005)	Triaxial compression	ϕ'_{peak} =36.5° ϕ'_{cs} =29° D_r=68%, p'_0=60 kPa
	Yang *et al.* (2010) Ho *et al.* (2011)	High pressure triaxial compression	ϕ'_{peak} =33° D_r=85%
	Author's results	K_0 consolidated drained triaxial stress path tests	ϕ'_{peak}=37.1° ϕ'_{cs}=32.6°

***Volumetric behaviour*:** After reaching the phase transformation point (Y_4), all samples showed a dilative response moving towards critical state points as shown in Figure 5-28. As expected from the critical state parameter framework adopted in Chapter 2, samples tested at lower p'_0 showed more dilation at every strain level than equivalent specimens tested at higher pressures.

Although the q trends became almost steady at the maximum strain levels reached, the volumetric strains did not always stabilise fully. Therefore, it can be concluded that true critical states were not fully reached. Extrapolation suggests the ultimate void ratios at critical state estimated in Figure 5-29 in e-log(p′) space. As explained in Chapter 2, the critical state line is conventionally represented as a straight line in e-log(p′) space but more recently researchers have shown that power-law equations model the critical state line more accurately. Both linear (equation 2-6) and power-law equations (equation 2-7) are fitted to the critical state e-p′values estimated as shown in Figure 5-29. The tests were performed at over a restricted range of intermediate pressures, making it hard to assess which equation fits the data better. High pressure tests are required in order to confirm this question.

5.2.2 Undrained tests

A series of K_0 normally consolidated and over-consolidated undrained tests were performed to compliment the drained tests. The consolidation and swelling paths applied were chosen to match the undrained cyclic tests presented in following chapters. A complete discussion regarding the reasons for choosing such effective stress values is given later in Chapter 6. Table 5-9 summarises the undrained tests performed on both sands.

For K_0 normally consolidated tests, samples were prepared using the same setup procedure on the drained tests and were consolidated from q = 0, p′= 20 kPa to q = 440 kPa and p′= 506 kPa (σ'_r=360kPa and σ'_z=800kPa) with K_0 = 0.45 for both sands. 48 hours of creep were then

allowed prior to shearing and then samples were sheared undrained under axial compression ($+\Delta\sigma_v$) and extension ($-\Delta\sigma_v$) while the cell pressure was kept constant. Over-consolidated specimens were prepared following similar set-up and consolidation procedures. The final swelling path brought the effective stresses to q = 50 kPa and p′= 167 kPa (σ'_r = 150 kPa and σ'_z = 200 kPa) at a rate of -60 kPa/hr. A further 48 hours creep was allowed at these final points prior to undrained axial compression and extension shearing.

Table 5-9 initial void ratio and p'_0 and q_0 values prior to start of shearing

Sand	Sample	OCR	e_0	p'_0 (kPa)	q_0 (kPa)
Dunkerque	DK-NC-CP	1	0.635	506	440
	DK-NC-ET	1	0.633	506	440
	DK-OC-CP	4	0.641	167	50
	DK-OC-ET	4	0.639	167	50
NE34	NE-NC-CP	1	0.642	506	440
	NE-NC-ET	1	0.639	506	440
	NE-OC-CP	4	0.633	167	50
	NE-OC-ET	4	0.638	167	50

5.2.2.1 Small strain and stiffness behaviour

The kinematic multi-yield surface framework has also been employed in interpreting the author's undrained tests. Kuwano (1999) determined the Y_1 to Y_4 points for undrained tests as:

Y_1 The end of the linear portion in stress-strain curve

Y_2 A possible change in $du/d\sigma_v$, although these points may be hard to detect without performing additional cyclic or creep holding tests

Y_3 Distinct change of the slope in the stress-strain curve or a sharp rotation of the effective stress path

Y_4 Phase transformation point

However, Kuwano & Jardine (2007) argued that as Y_2 surfaces are hard to detect in static undrained tests, drained static or cyclic undrained experiments should be preferred.

Y_1 Surface: As with the drained tests, the small strain $\Delta q : \varepsilon_a$ data at were plotted to locate any linear range as shown in Figure 5-30 Figure 5-31 under normally consolidated conditions the linear ranges extended to ≈0.004% and 0.005% for Dunkerque and NE34 sands respectively in both compression and extension tests. The linear ranges of over-consolidated samples in compression were ≈0.02% for both Dunkerque and NE34 sands, while their respective linear ranges were 0.004% and 0.005% in extension.

It is clear that the linear range for over-consolidated samples under compression is 3-4 times larger than that of normally consolidated specimens. This is due to the effect of stress history on the size and orientation of the Y_1 locus, as explained in Chapter 2. The pre-straining experienced by over-consolidated samples sets up a system of inter-particle contacts that can carry higher vertical stresses more easily and allows a linear response up to higher strain levels. Locations of the Y_1 boundaries obtained in the direction of undrained axial shearing at $p'_0$506kPa are shown in q-p′ space in Figure 5-15. The Y_1 strain limits and maximum undrained stiffness $E_U{}^{max}$ values are given in Table 5-10.

All the undrained compression tests showed dilative (positive dq/dp′) behaviour from the beginning of their shearing stages and therefore no phase transformation point or Y_4 locus was identified. Two main reasons can be identified for this: one is the dense initial state of the samples and the other is the existence of initial deviatoric loads (q) which locate the initial effective stress close to compression yield surface. However, for extension where the initial effective stress points are further from yield surface the behaviour was contractive at early stages until they reached the phase transformation point (i.e. Y_4 points) and became dilative afterwards. Y_4 points for extension tests are located in Figure 5-34.The other reason is the initial relative dense state of test specimens.

Table 5-10 Maximum shear stiffness and strain levels for reaching Y_1 – Y_3 surfaces in undrained tests

Sand	sample	E_U^{max} (MPa)	Y_1 ε_v (%)
Dunkerque	DK-NC-CP	1111.11	0.003
	DK-NC-ET	1052.63	-0.003
	DK-OC-CP	571.43	0.019
	DK-OC-ET	532.00	-0.006
NE34	NE-NC-CP	1000.00	0.004
	NE-NC-ET	909.09	-0.005
	NE-OC-CP	625.00	0.018
	NE-OC-ET	525.00	-0.007

5.2.2.2 Undrained stiffness

Similar to drained tests, after reaching the Y_1 surface the tangent E_U values dropped rapidly (Figure 5-32 and Figure 5-33) as shearing continued. The drop was more rapid in compression tests since the initial stress point was closer to the compressive side of the yield surface.

Comparison between the normalised undrained E_U and drained E'_v values shows that E_U values are as expected significantly higher under comparable pressure ranges (Table 5-11), with the average ratio for Dunkerque being 1.33 and 1.23 for NE34 sand.

Table 5-11 Relation between E_U and E'_v values at close initial p'_0 values

Sand	Test	OCR	p'_0	Max E_U or E'_v	$(E_U/p'_0)/(E'_v/p'_0)$
Dunkerque	Drained - Compression	1	500	820	1.35
	Undrained - Compression	1	506	1111	
	Drained - Extension	1	500	795	1.32
	Undrained - Extension	1	506	1052	
NE34	Drained - Compression	1	500	830	1.21
	Undrained - Compression	1	506	1000	
	Drained - Extension	1	500	795	1.14
	Undrained - Extension	1	506	909	
Dunkerque	Drained - Compression	1	150	430	1.32
	Undrained - Compression	4	167	571	
	Drained - Extension	1	150	395	1.34
	Undrained - Extension	4	167	532	
NE34	Drained - Compression	1	150	440	1.42
	Undrained - Compression	4	167	625	
	Drained - Extension	1	150	435	1.20
	Undrained - Extension	4	167	525	

5.2.2.3 Behaviour moving towards the critical state

The dilative response of all samples at higher strain levels led to continuous reductions in pore pressures. Since the pressure transducers could not read values below around 50 kPa below atmospheric pressure, the maximum possible initial back pressures were applied to the samples to retain pore pressure measurements for as long as possible. However, all tests ended with negative pore pressure values and therefore the ultimate critical state points could not be defined. Higher pressure apparatuses would be required to reach critical states. The q versus ε_a plots are shown in Figure 5-35. As shown, in compression tests the q values continued to increase with a relatively steady slope over the 1 to 2%, axial strain levels, while the extension tests slopes became flatter after $\varepsilon_a \approx$-0.3%.

5.3 Summary and conclusions

This chapter has presented description of both test sands. The first Section presented the index characteristics including e_{max}, e_{min} and PSD curves. Additional information from more advanced QicPic apparatus and 3D image processing facilities were also reported. The second Section of this chapter outlined drained and undrained triaxial tests conducted under static loading. These data characterise behaviour from small to large strains as shearing progressed towards critical states. The following summary points apply:

1- The Dunkerque and NE34 sands are fine predominantly silica sands. While Dunkerque sand consists of ≈ 10% shell fragments, NE34 is processed pure silica sand.
2- The shapes of the clean quarried NE34 particles are more angular than those of the Dunkerque sand which have been subject to recent weathering in a dynamic marine environment.
3- The sand's small strain behaviours can be interpreted within the kinematic multi-yield surface framework proposed by Jardine (1992) and Kuwano & Jardine (2007).

4- Inside the Y_1 surface response was elastic and stiff. Once the Y_1 surface was engaged, the tangent stiffness values fall sharply and plastic strains started to accumulate. However, marked changes in $d\varepsilon_s/d\varepsilon_v$ were delayed in drained tests until the effective stress paths engaged the second Y_2 kinematic surface.

5- The Y_3 surfaces were located at points where the incremental straining first became predominantly plastic. The later Phase Transformation Points (PTP) were identified as Y_4 yield points.

6- Shearing at large strains moved the sands towards critical state where deviatoric stresses became steady. Although the critical void ratios were not fully reached at strain levels of around 20%, the sand specimens were clearly tending towards *Stable* states.

7- The stiffness, stress-dilatancy and shear strength data obtained from the static tests provide valuable benchmarks that aid the interpretation of the subsequent cyclic triaxial and HCA testing.

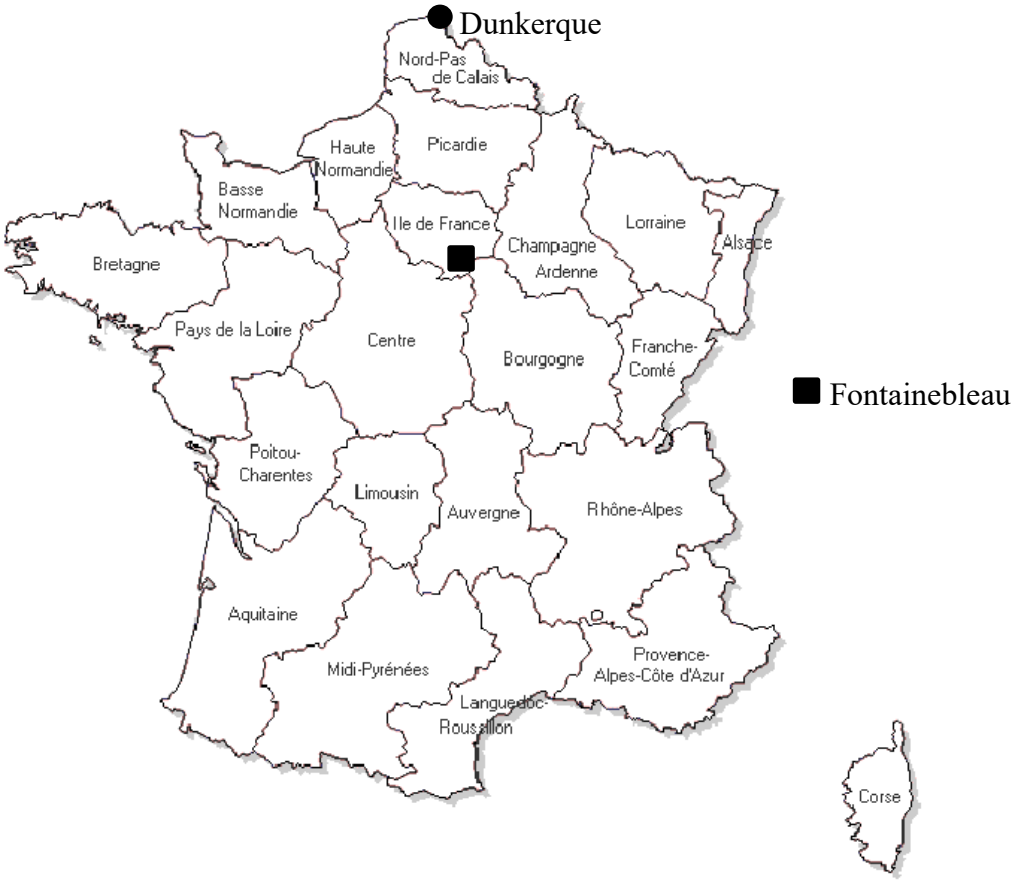


Figure 5-1 Location of Dunkerque and Fontainebleau sites in France

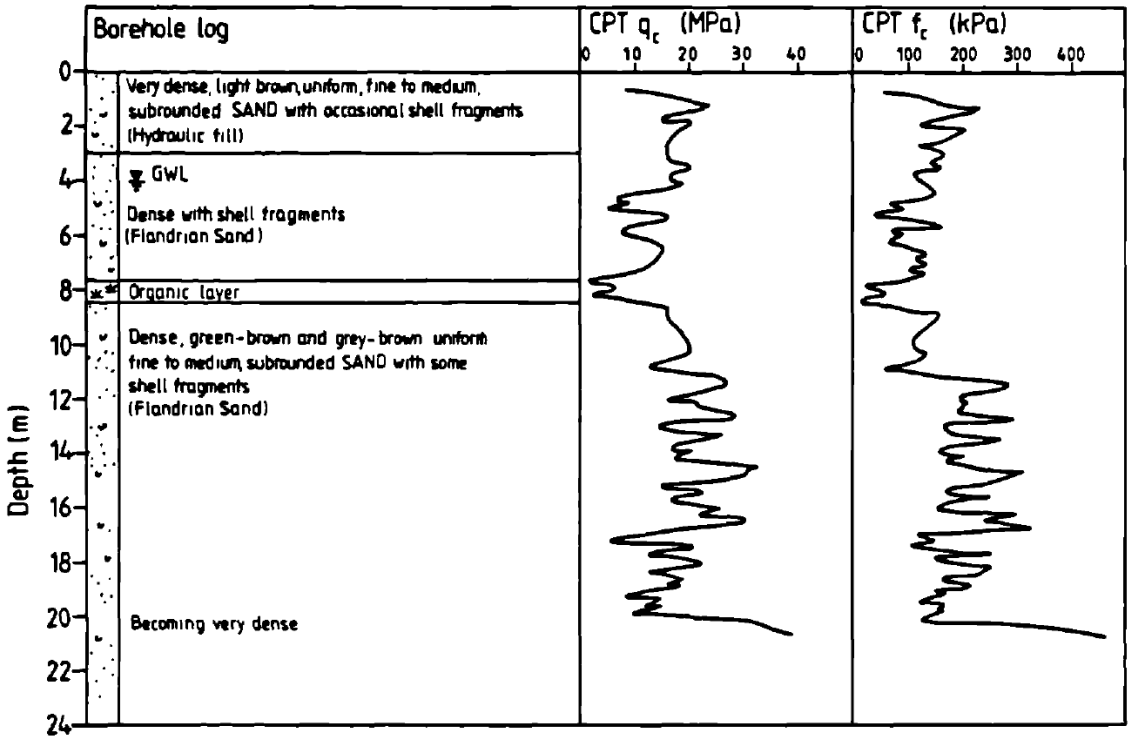


Figure 5-2 Summary of geotechnical profile for Dunkerque site from Chow (1997)

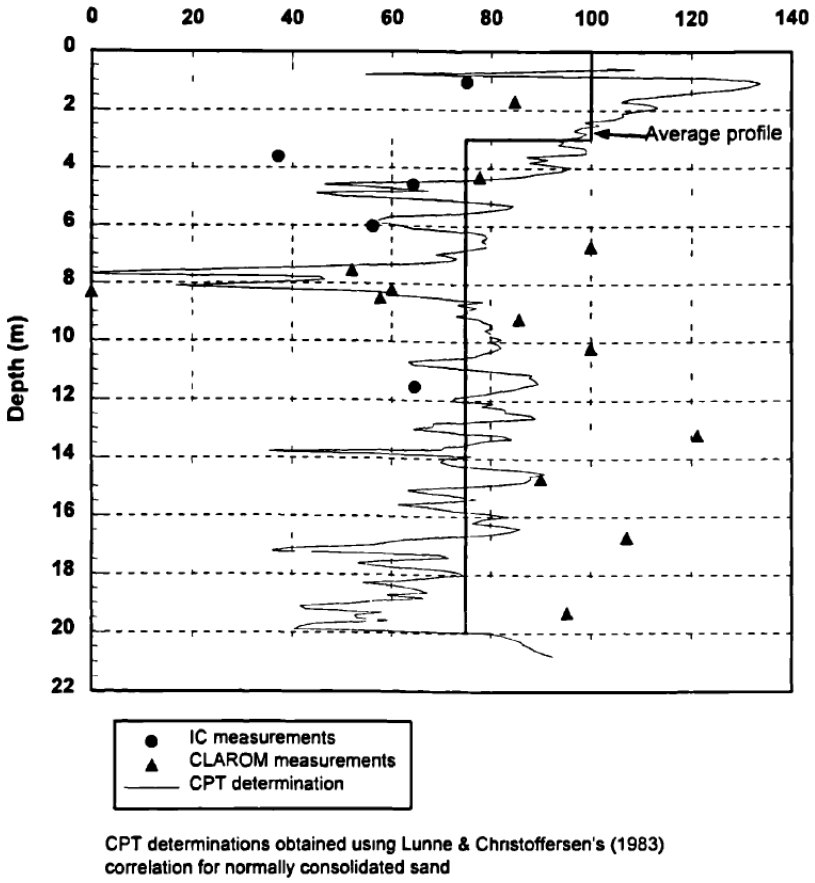


Figure 5-3 Relative density profile in Dunkerque site reported by Chow (1997)

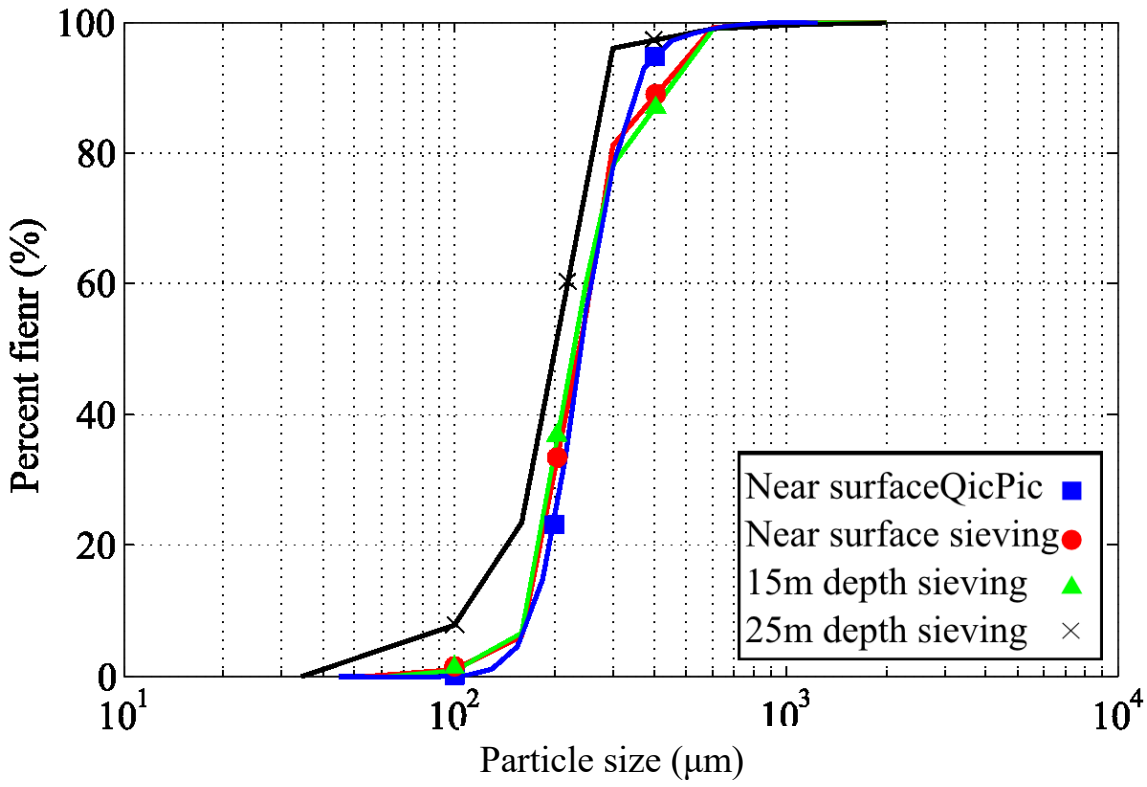


Figure 5-4 PSD graph for Dunkerque samples at surface and higher depths

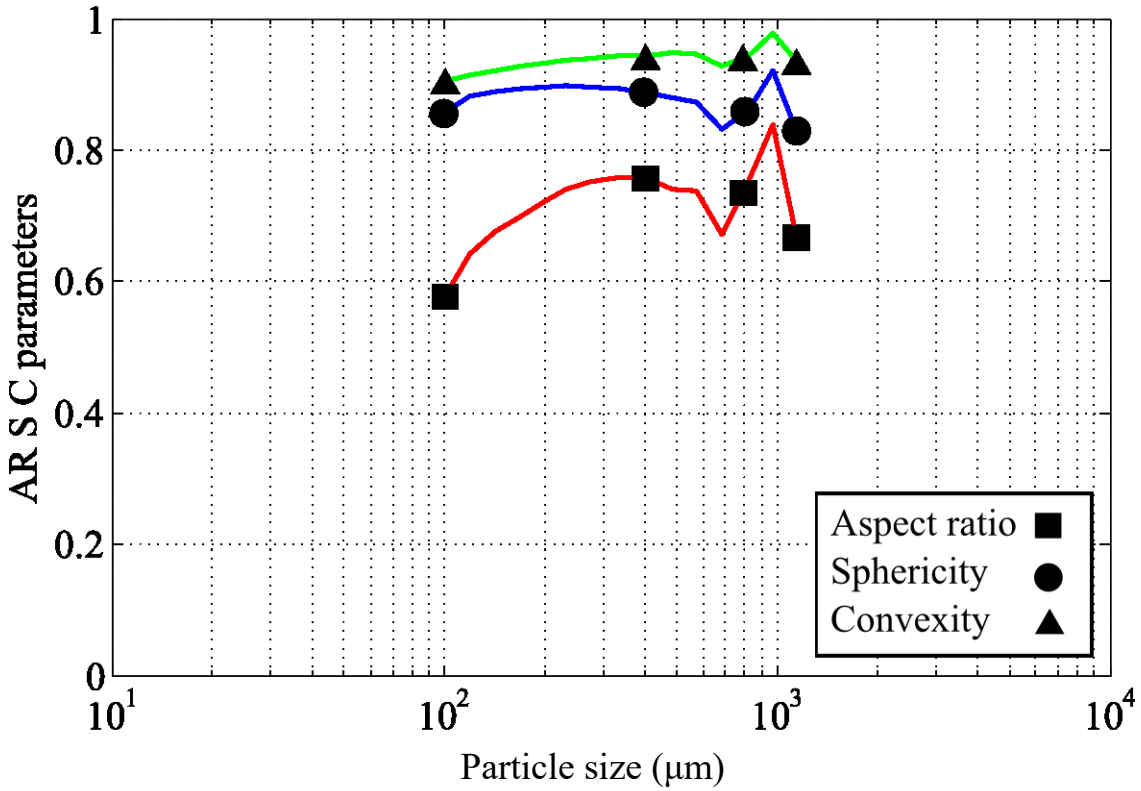


Figure 5-5 Aspect ratio (AR), sphericity (S) and convexity (C) parameters for Dunkerque sand obtained from QicPic.



Figure 5-6 Microscope image of Dunkerque sand using nanotech Microsurf 3D optical profiler by Nanotech

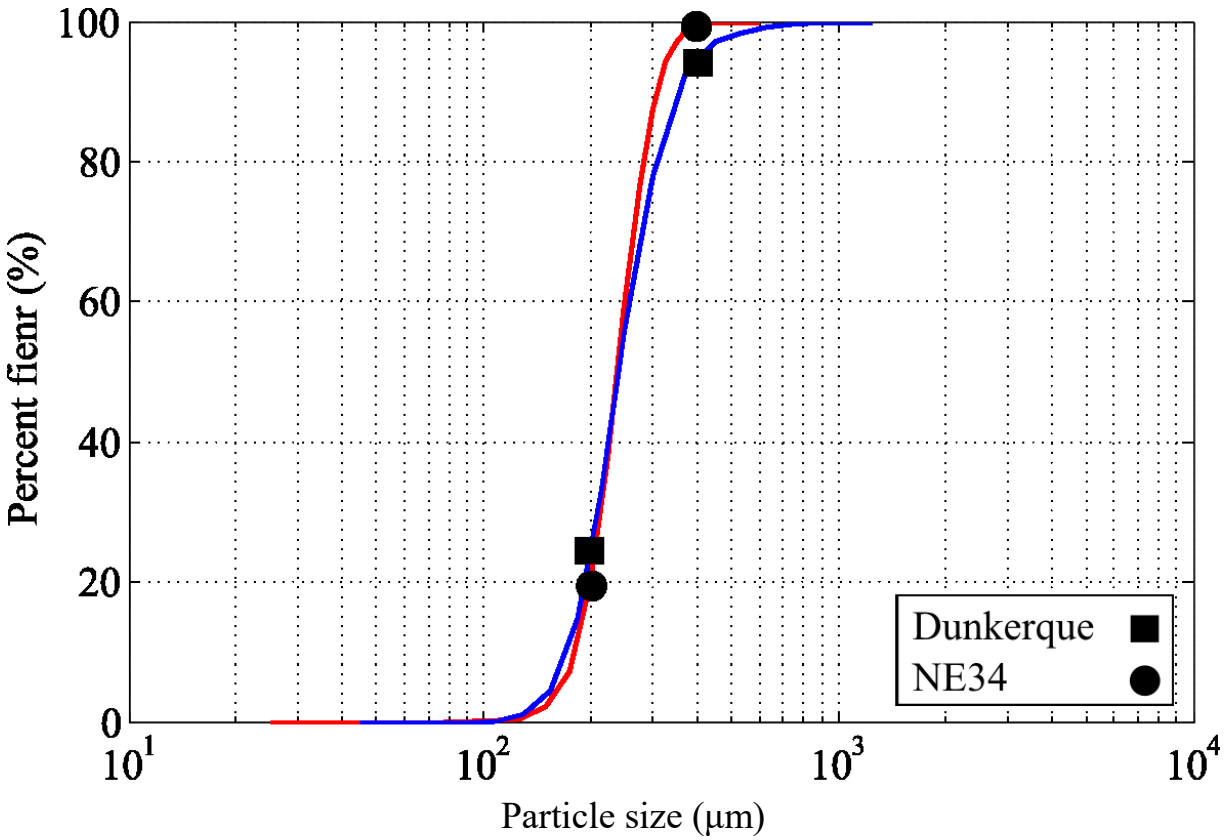


Figure 5-7 PSD Graphs for NE34 and Dunkerque sand from QicPic tests

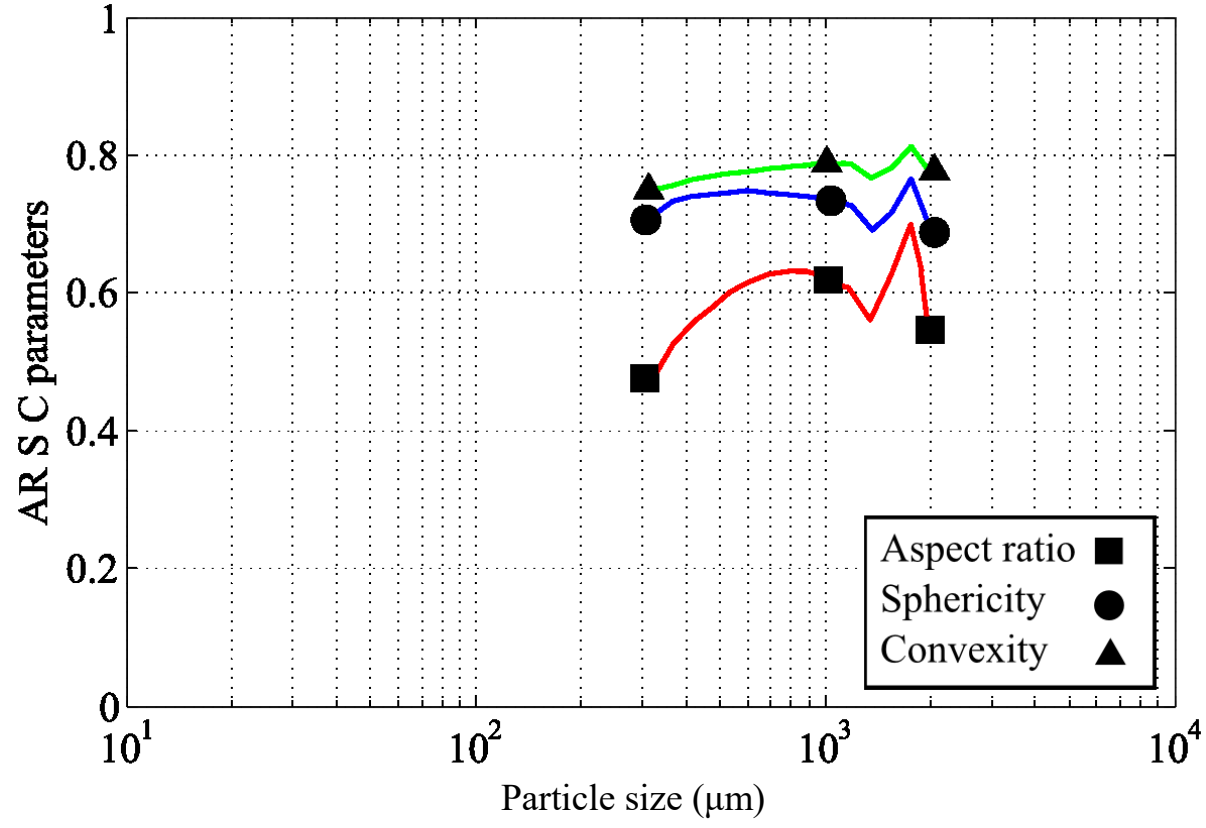


Figure 5-8 Aspect ratio (AR), sphericity (S) and convexity (C) parameters for NE34 sand obtained from QicPic.

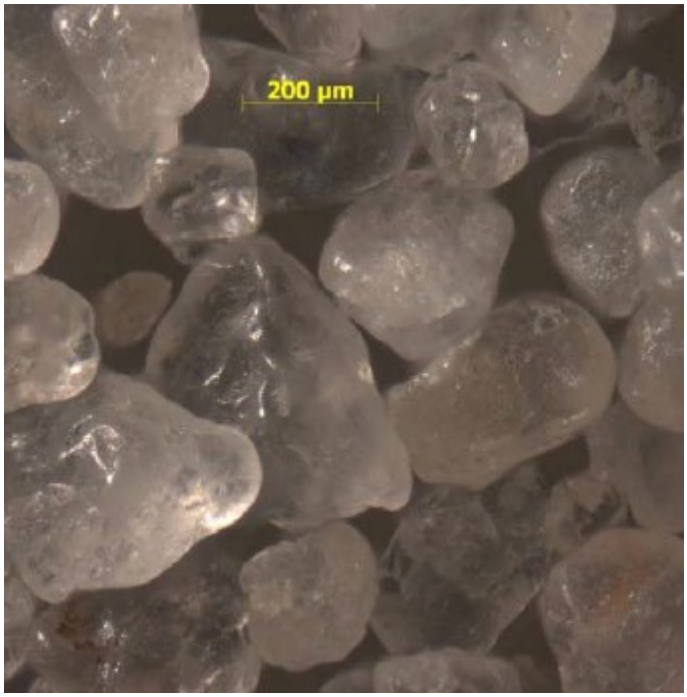


Figure 5-9 Microscope image of NE34 sand using nanotech Microsurf 3D optical profiler by Nanotech

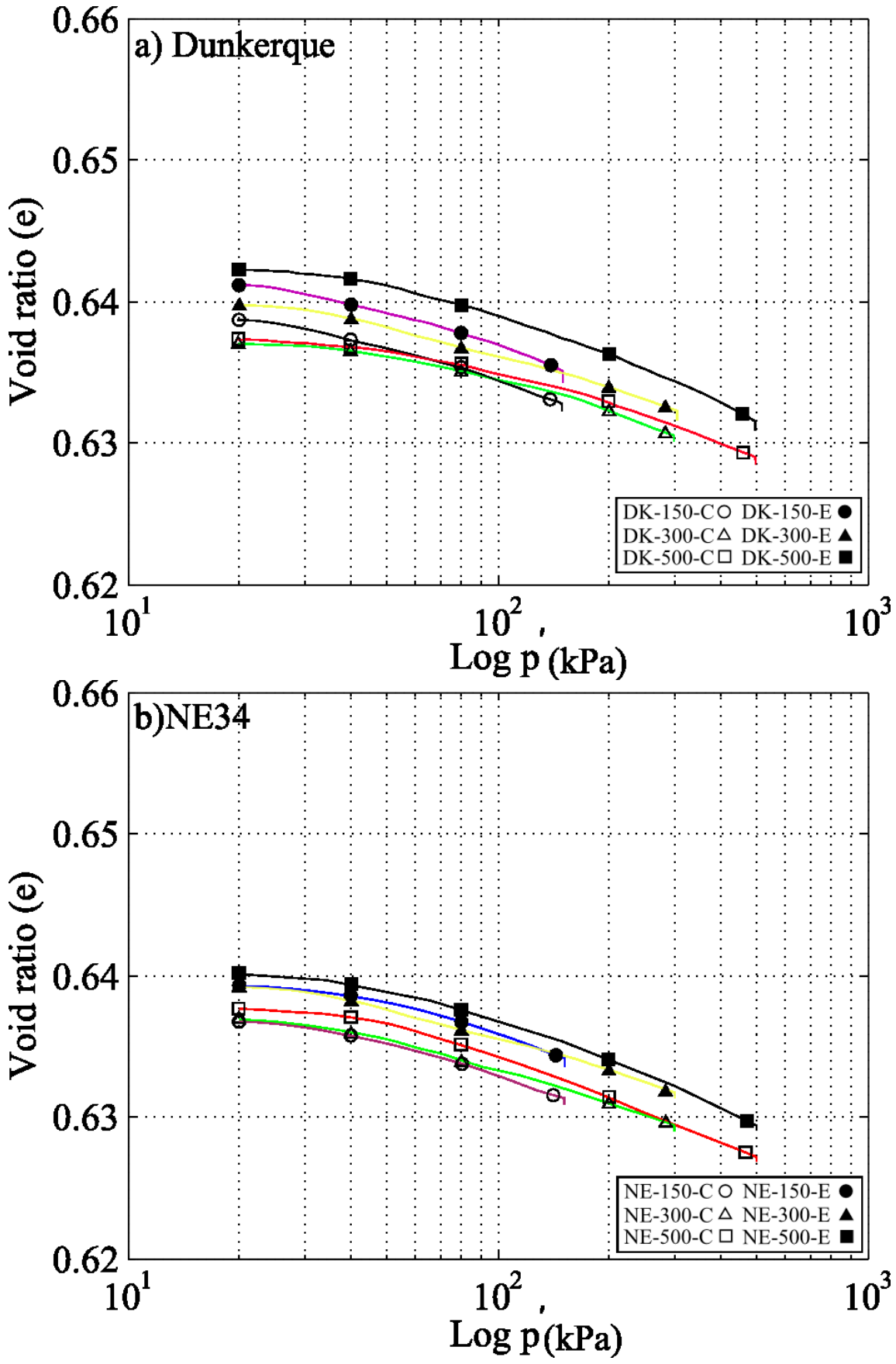


Figure 5-10 Void ratio changes during consolidation and creep stage for K_0 drained tests on a) Dunkerque, b) NE34. e_0=0.64

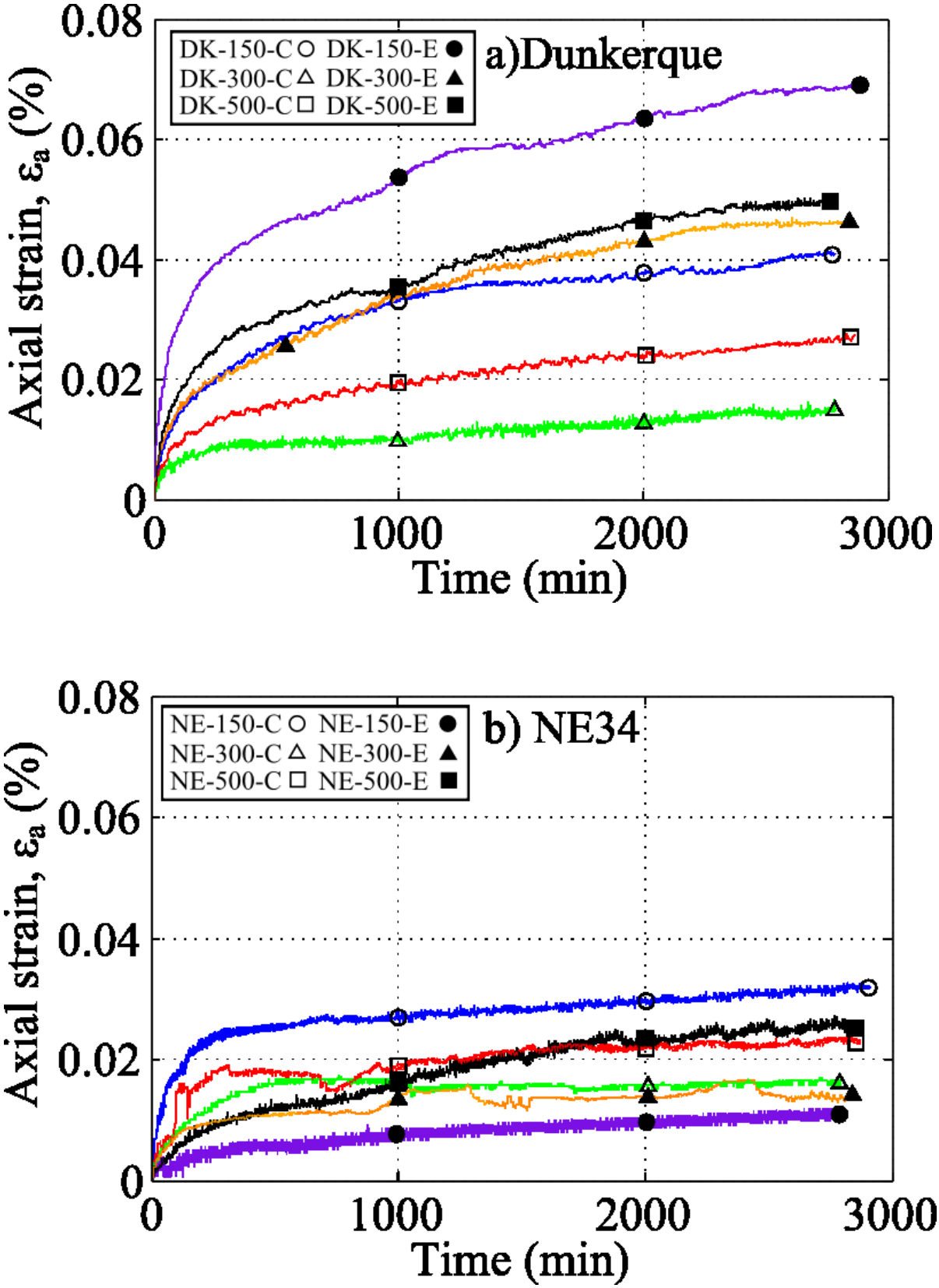


Figure 5-11 Axial strain accumulation in creep stage prior to shearing for K_0 drained tests on a) Dunkerque, b) NE34. e_0=0.64

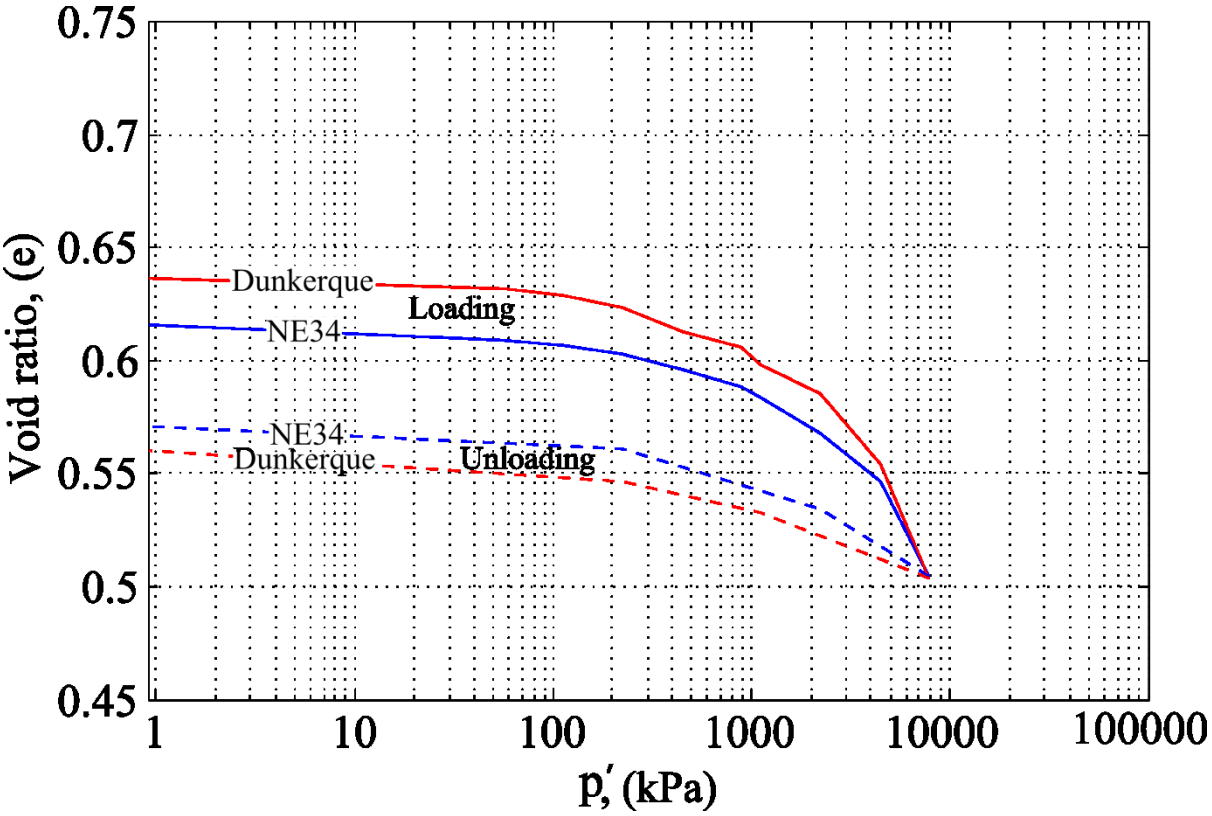


Figure 5-12 void ratio changes in high-pressure Oedometer test performed on Dunkerque and NE34 sands.

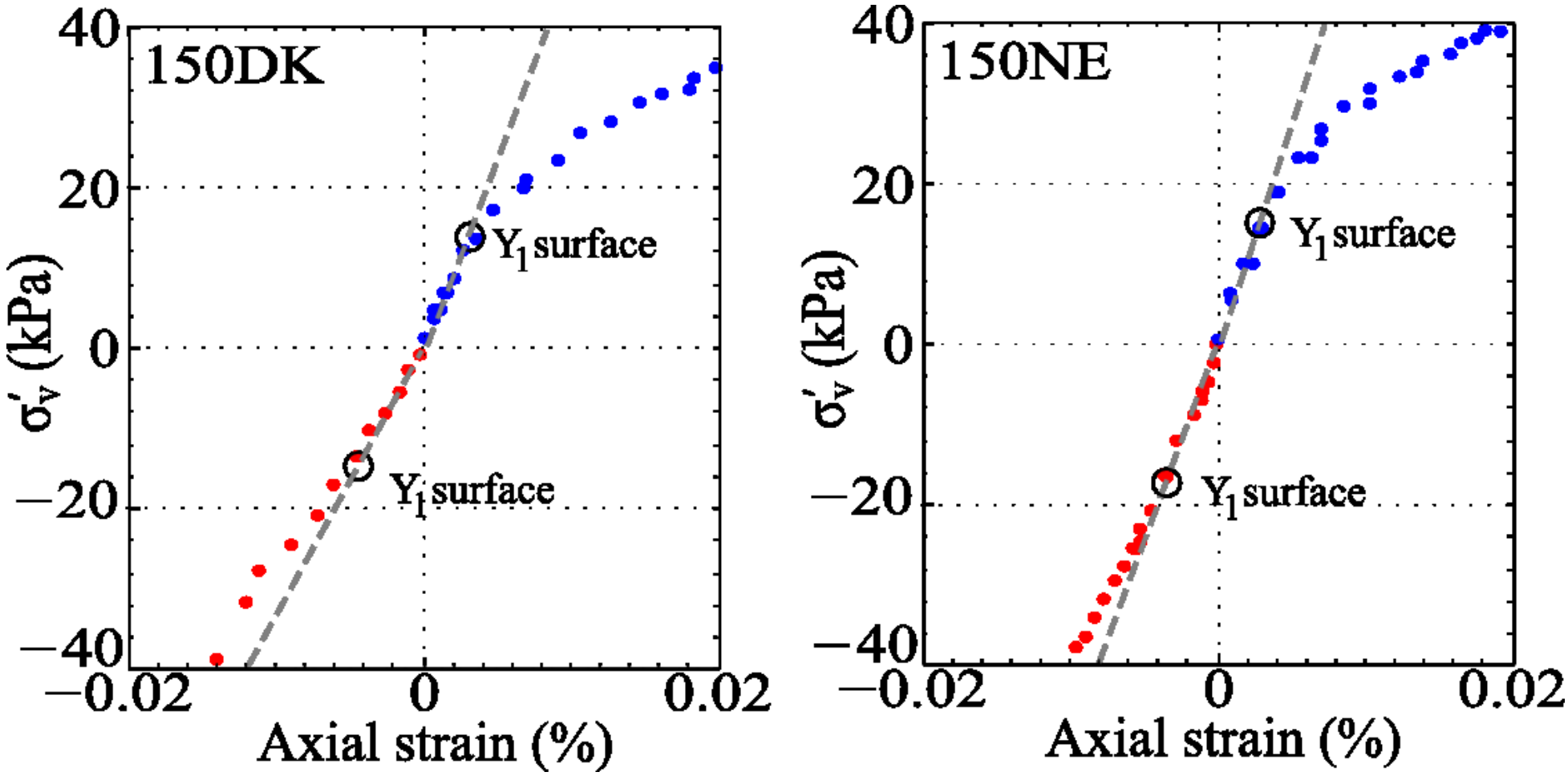


Figure 5-13a Axial stress-strain probing to locate Y_1 boundary for K_0 drained -p'_0=150kPa

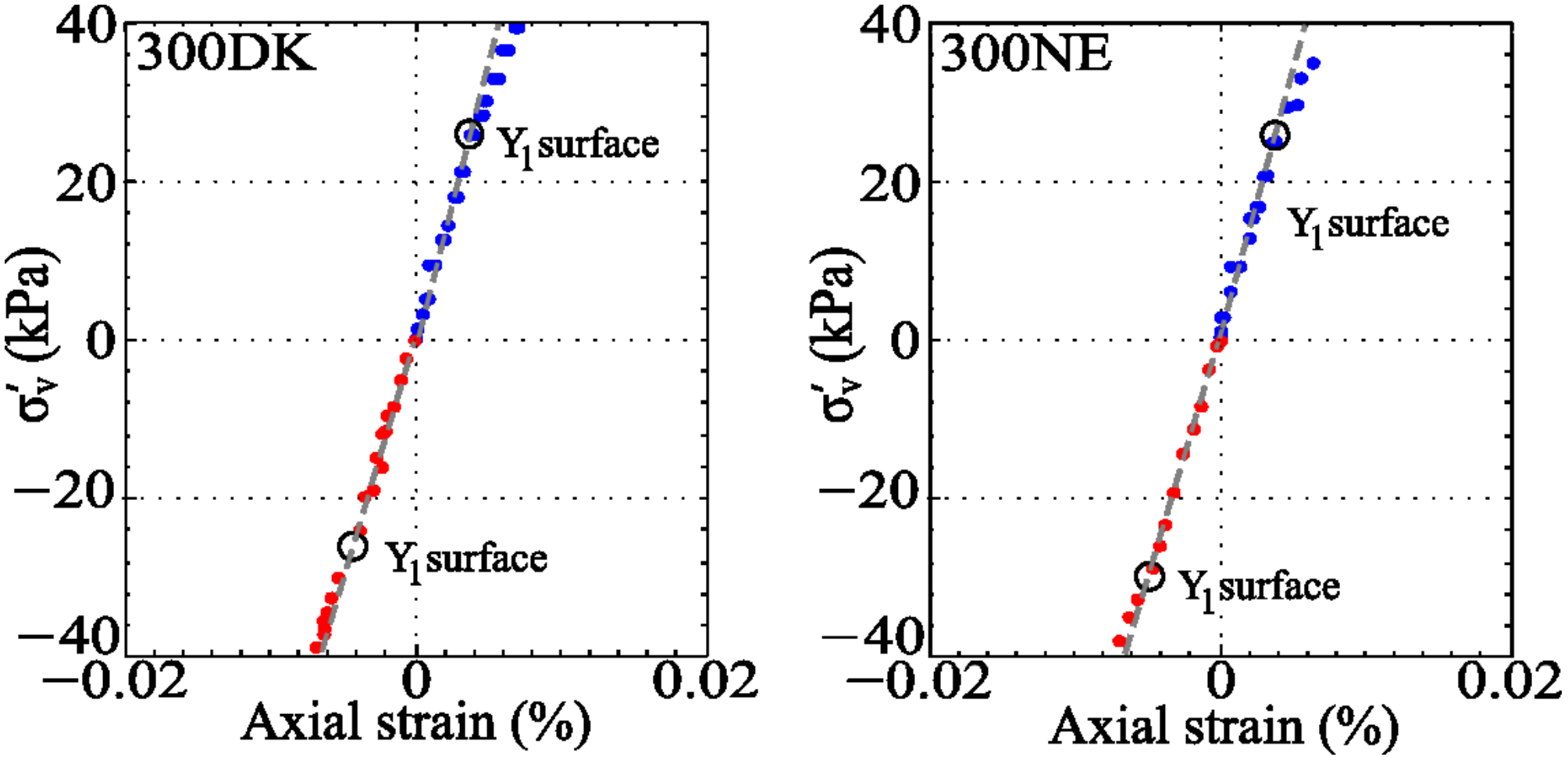


Figure 5-13b Axial stress-strain probing to locate Y_1 boundary for K_0 drained-p'_0=300kPa

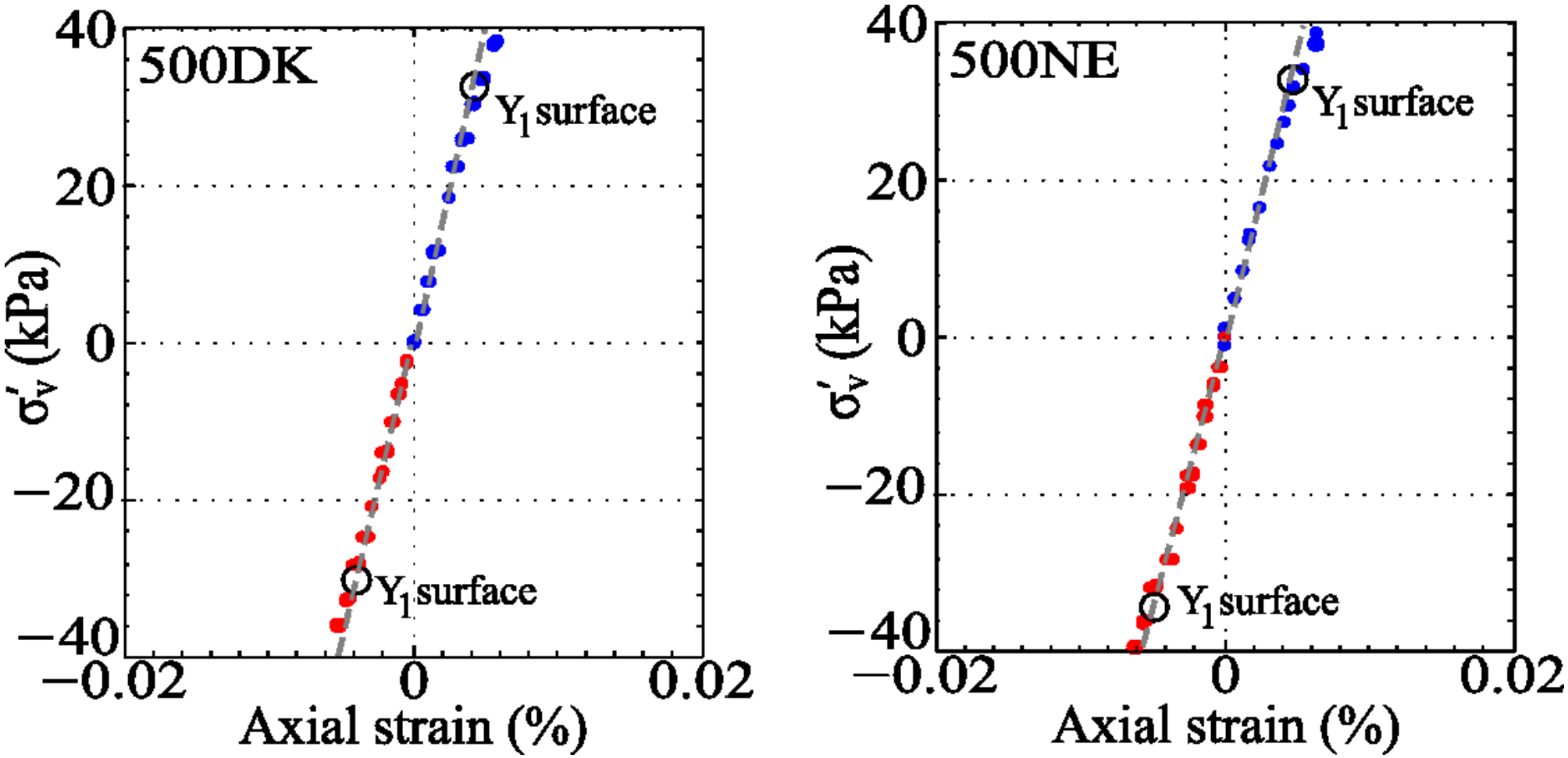


Figure 5-13c Axial stress-strain probing to locate Y_1 boundary for K_0 drained-p'_0=5

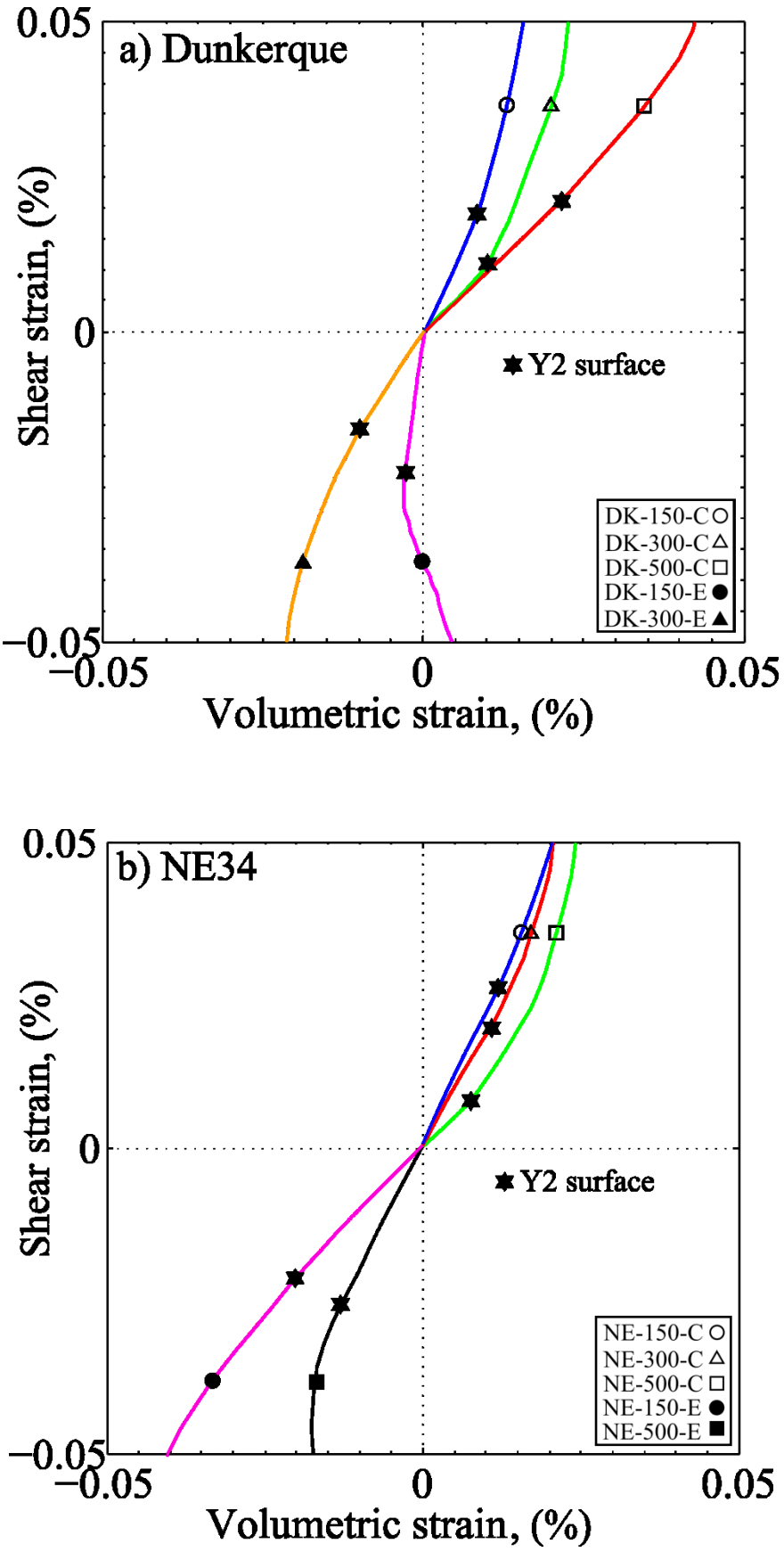


Figure 5-14 Locating the Y_2 surface in ε_v- ε_s space for K_0 drained tests on a) Dunkerque, b) NE34. e_0=0.64.

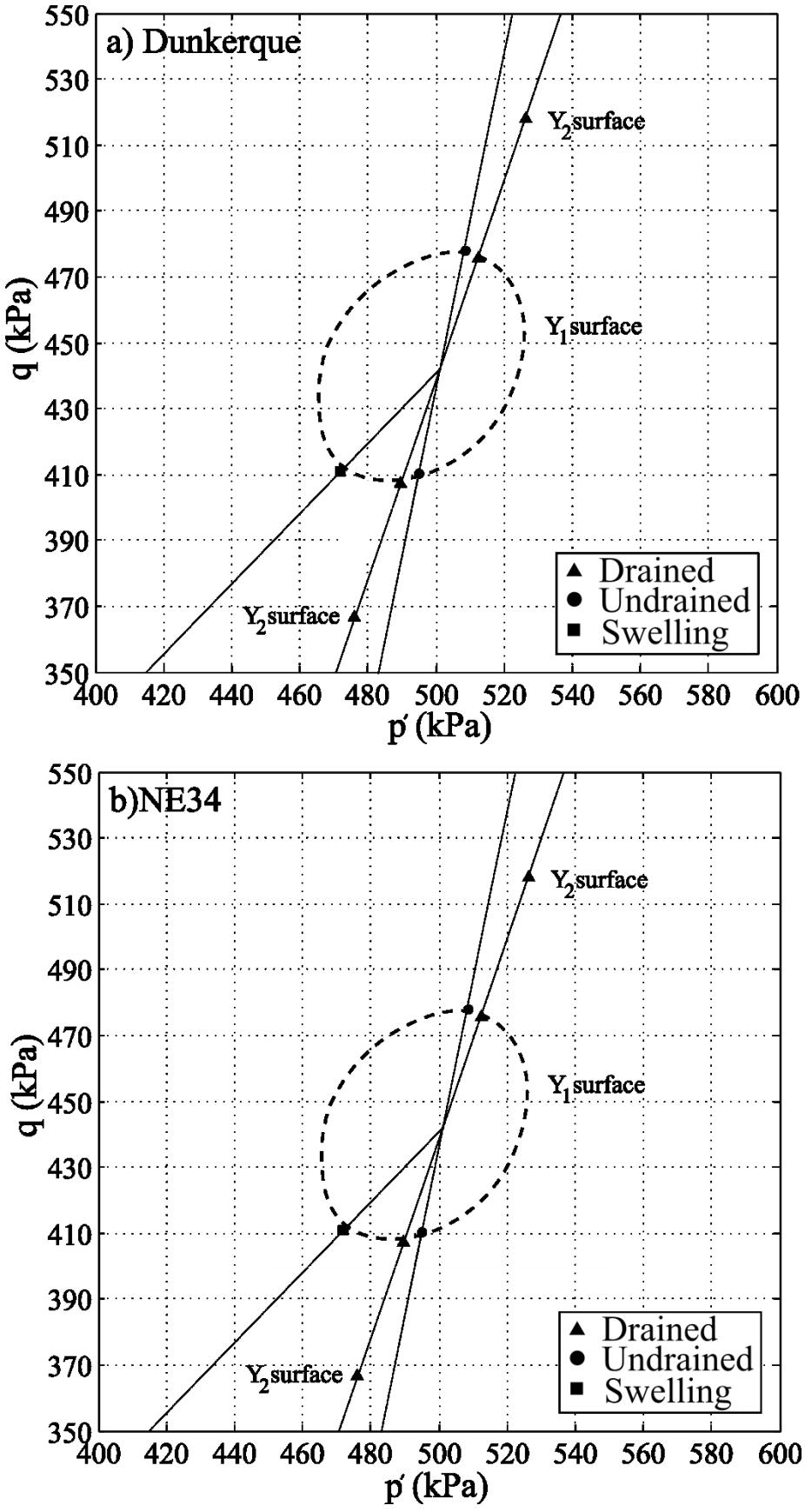


Figure 5-15 Locating the kinematic boundaries obtained from drained and undrained tests and comparison with ones reported by Kuwano & Jardine (2007).

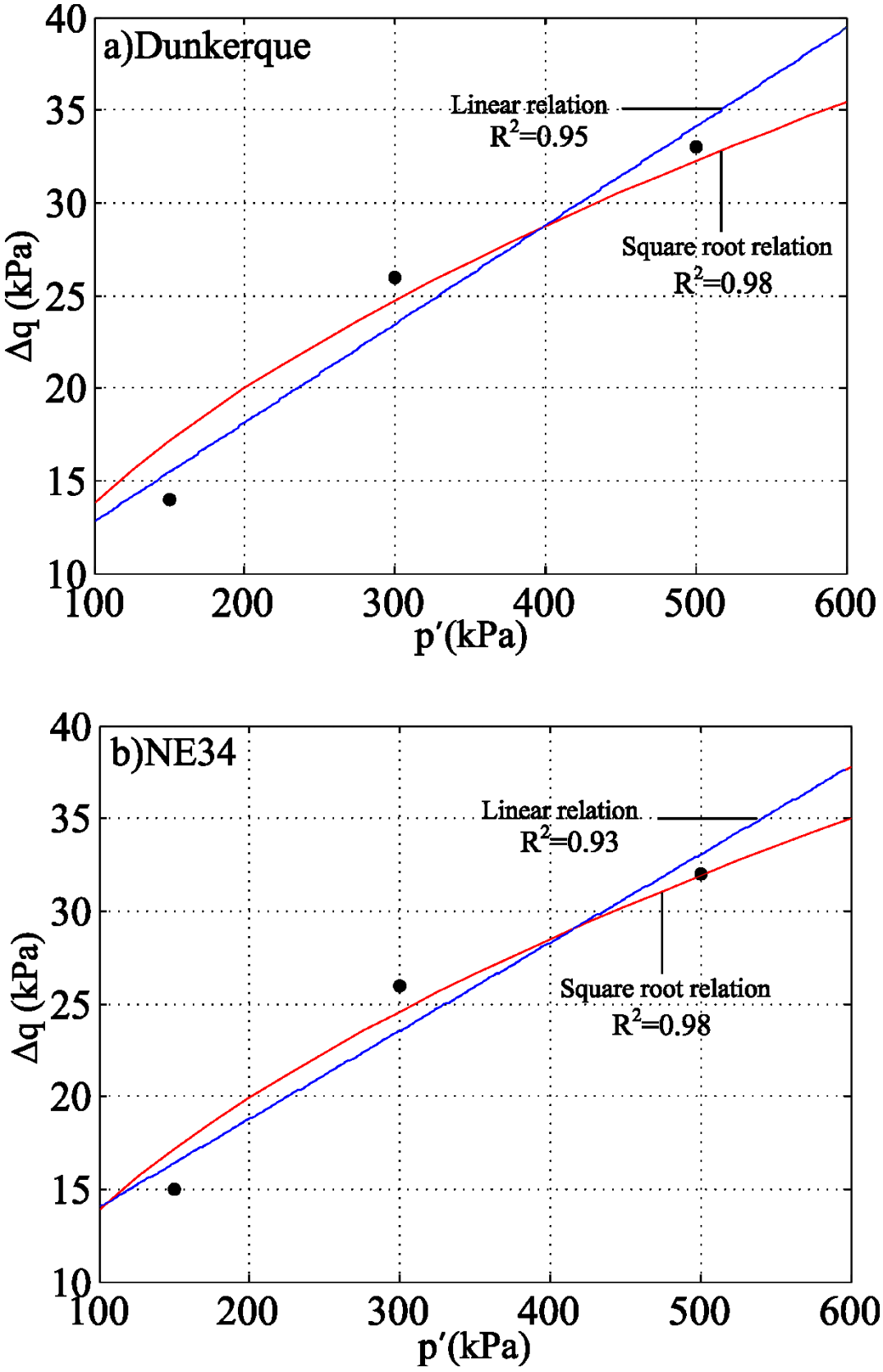


Figure 5-16 Evolution of the Y_1 surface size in relation with the p'_0 in K_0 consolidated drained tests.

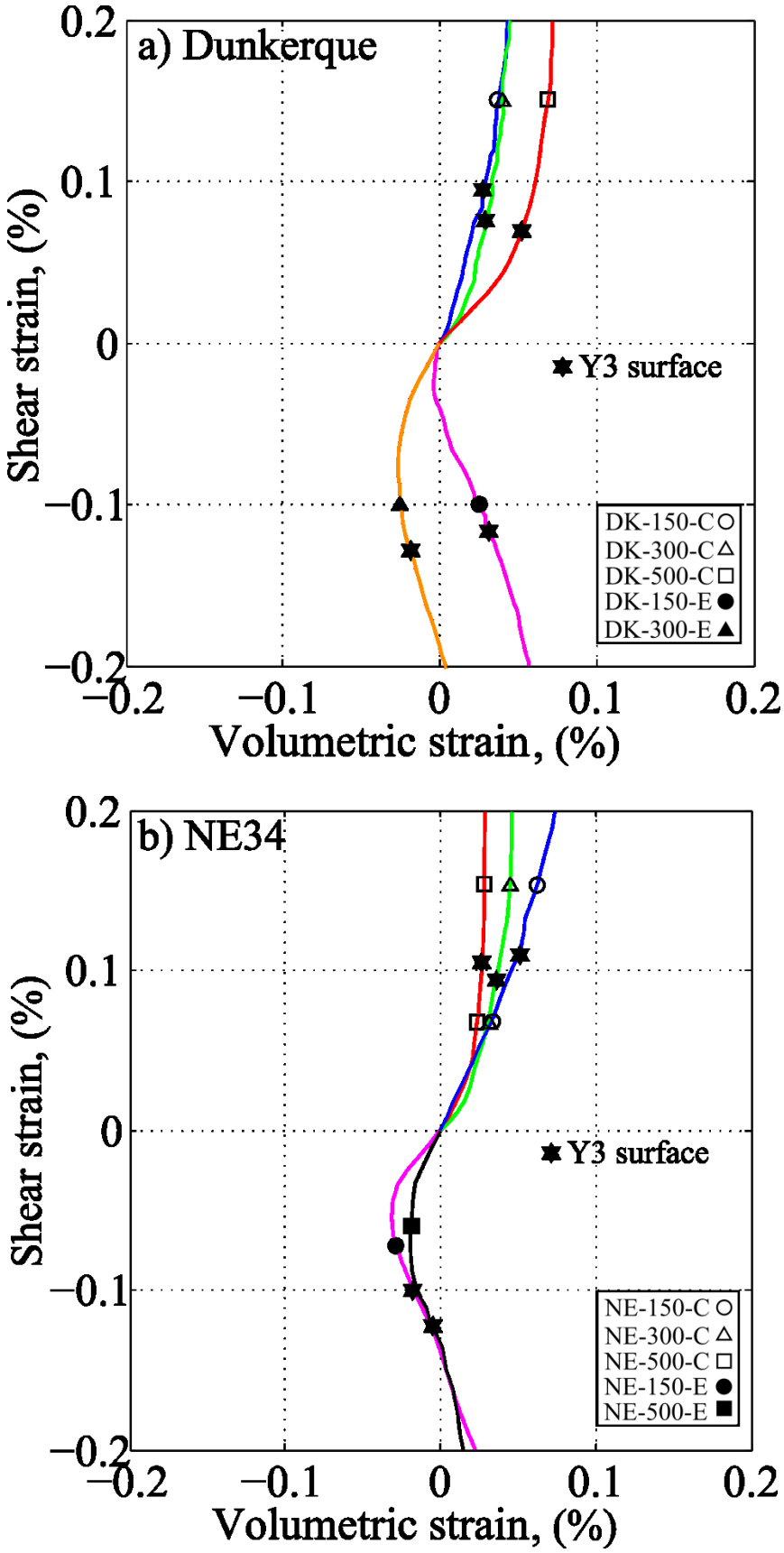


Figure 5-17 Locating Y_3 surface in ε_v- ε_s space for K_0 drained tests on a) Dunkerque, b) NE34. e_0=0.64.

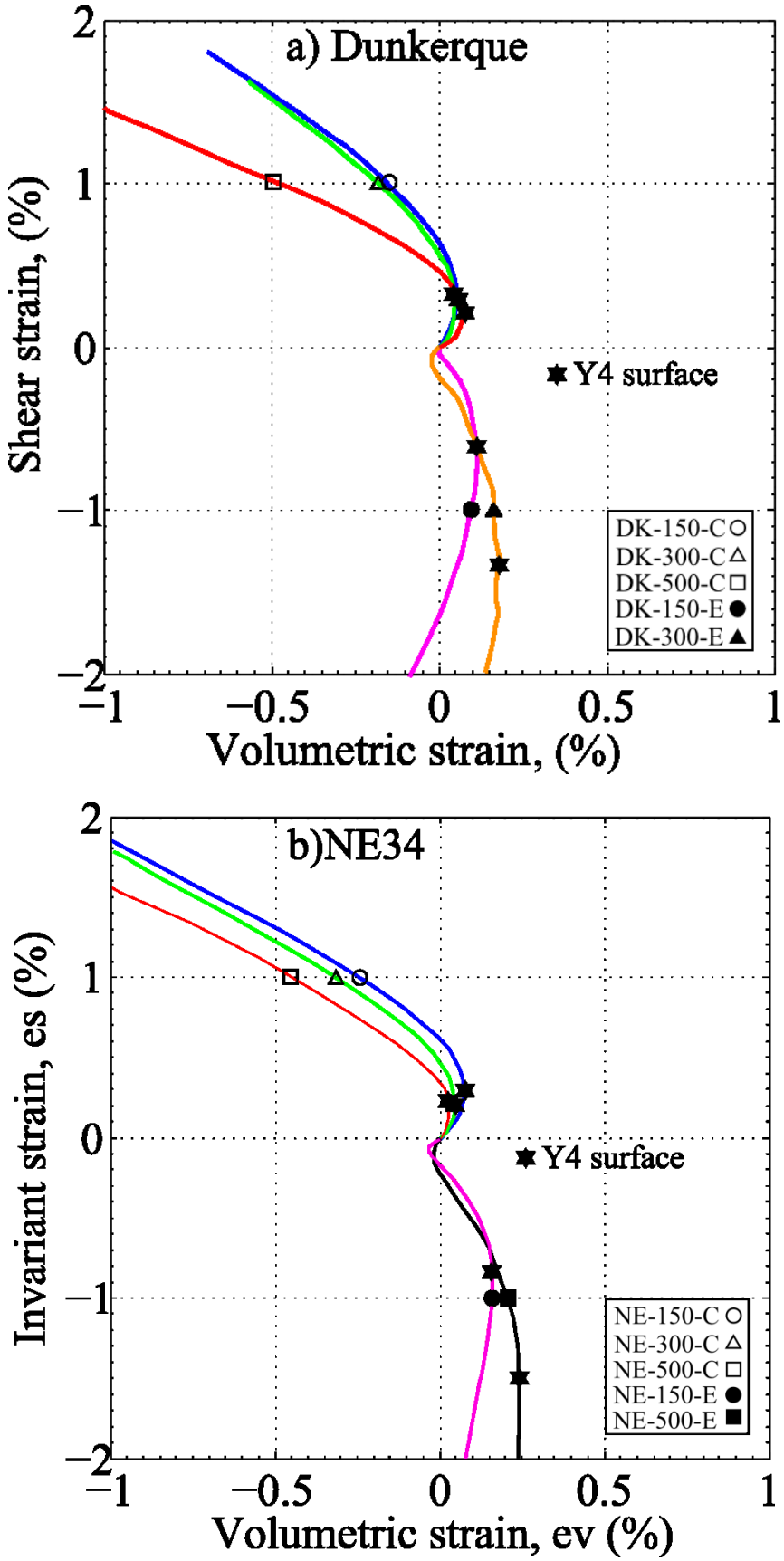


Figure 5-18 Locating Y_4 surface in ε_v- ε_s for K_0 drained tests on a) Dunkerque, b) NE34. e_0=0.64.

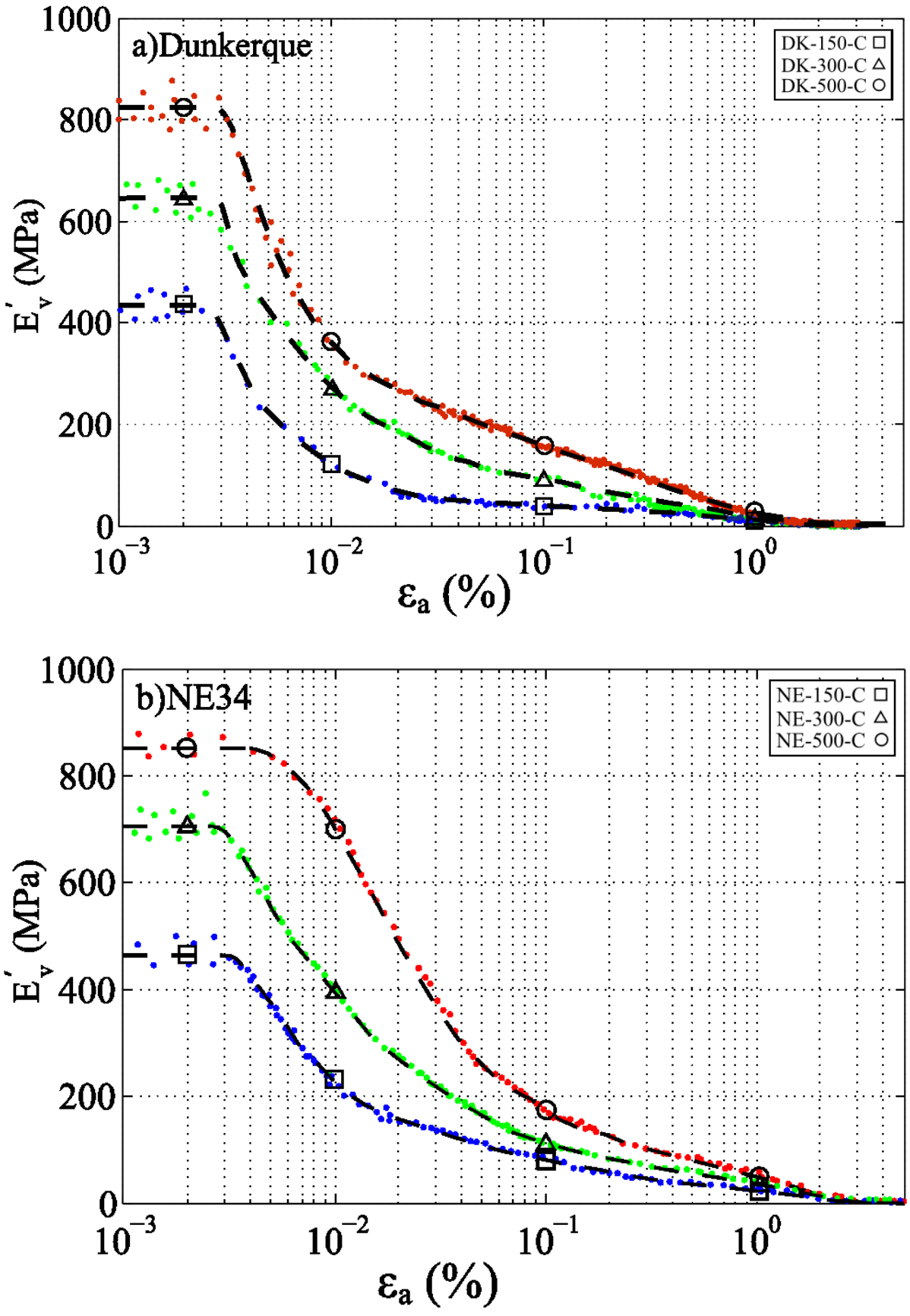


Figure 5-19 Tangent stiffness degradation curves from drained K_0 compression tests on a) Dunkerque, b) NE34. e_0=0.64.

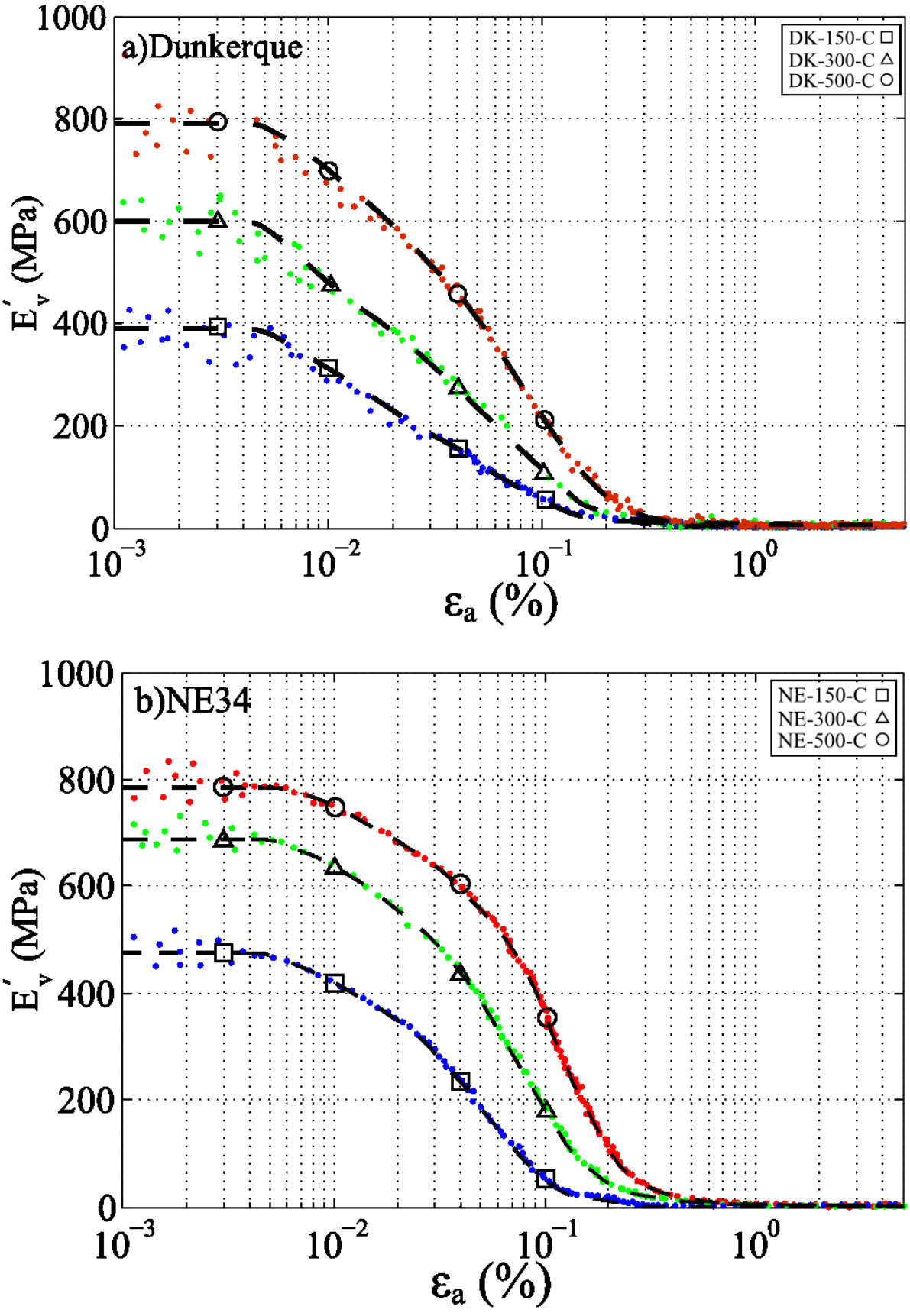


Figure 5-20 Tangent stiffness degradation curves from drained K_0 extension tests on a) Dunkerque, b) NE34. e_0=0.64

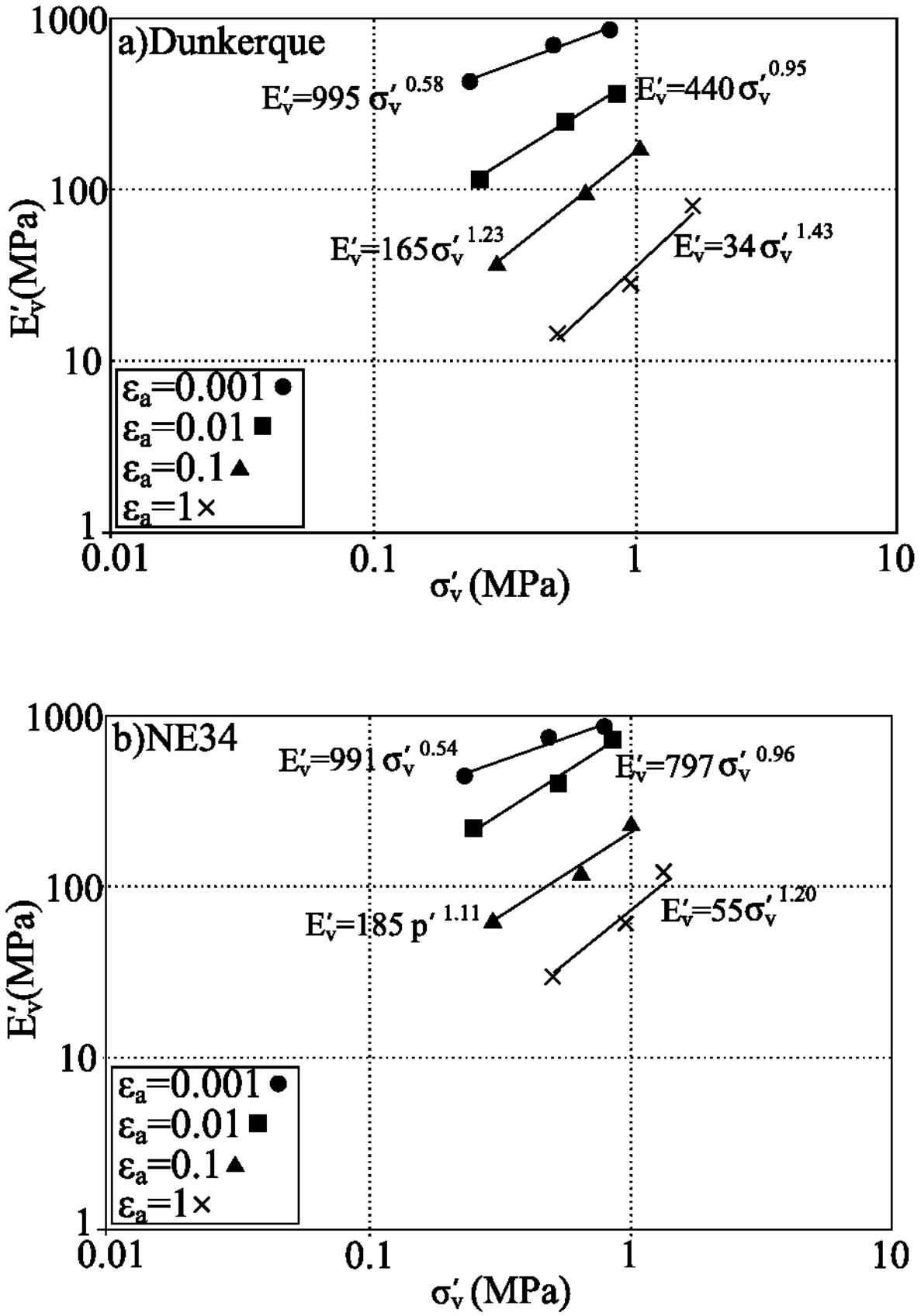


Figure 5-21 Relation between E'_v and p′from from drained K_0 compression tests on a) Dunkerque, b) NE34. e_0=0.64

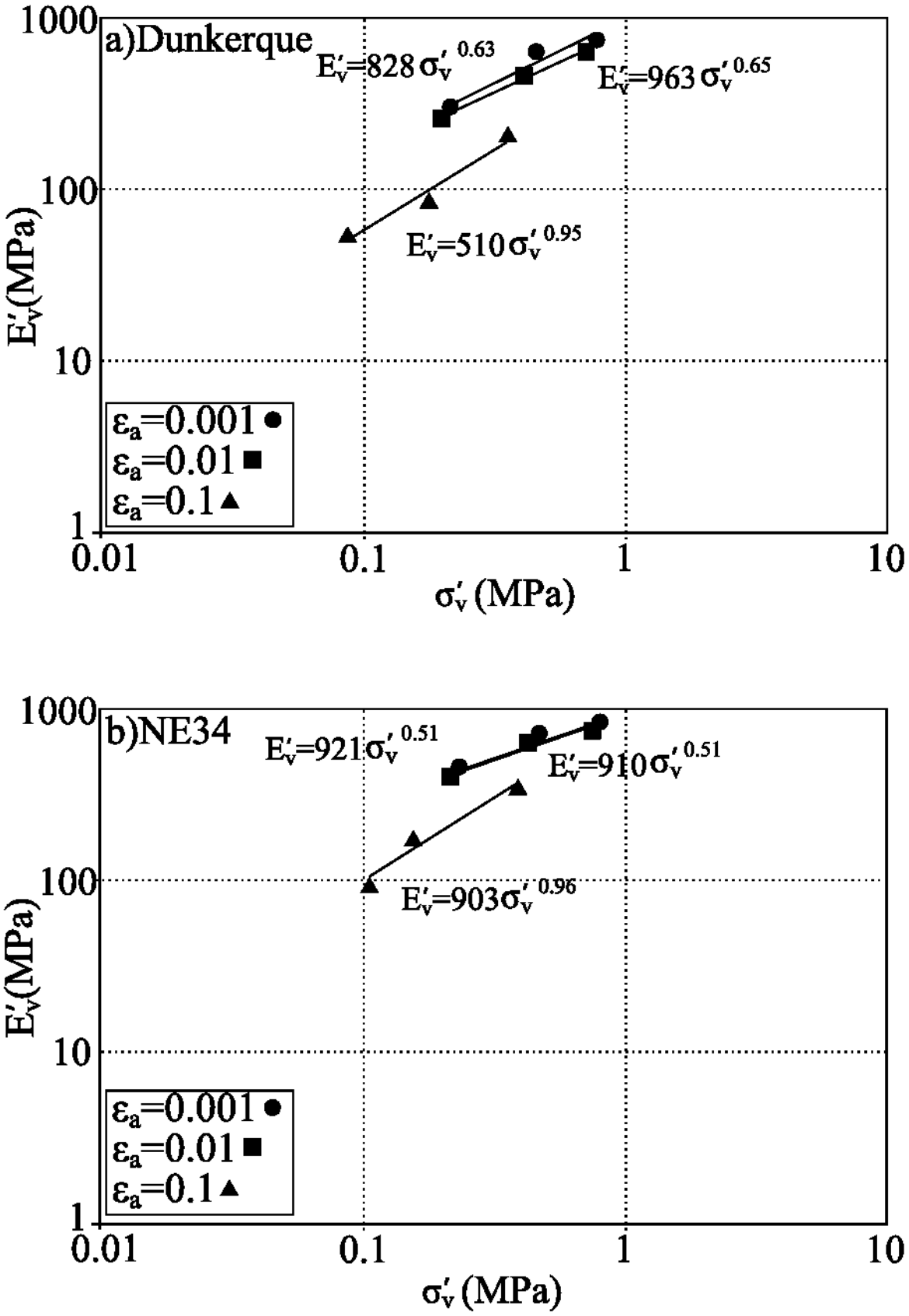


Figure 5-22 Relation between E'_v and p′from from drained K_0 extension tests on a) Dunkerque, b) NE34. e_0=0.64

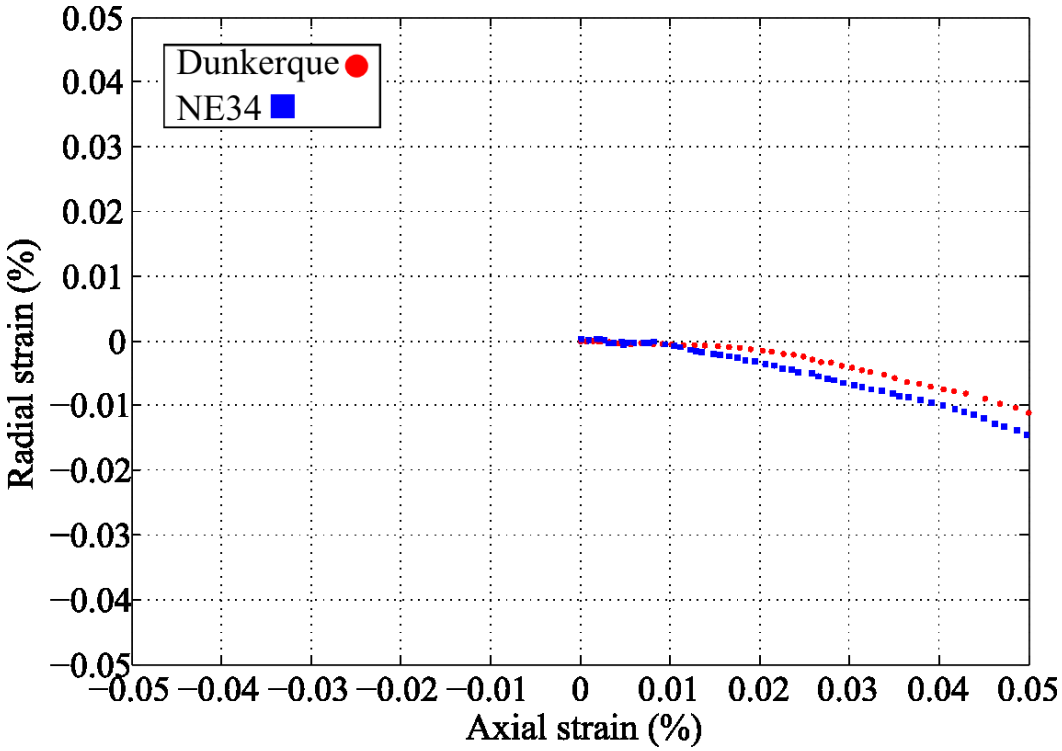


Figure 5-23 Radial strain vs axial strain under drained K_0 shearing to measure Poisson's ratio

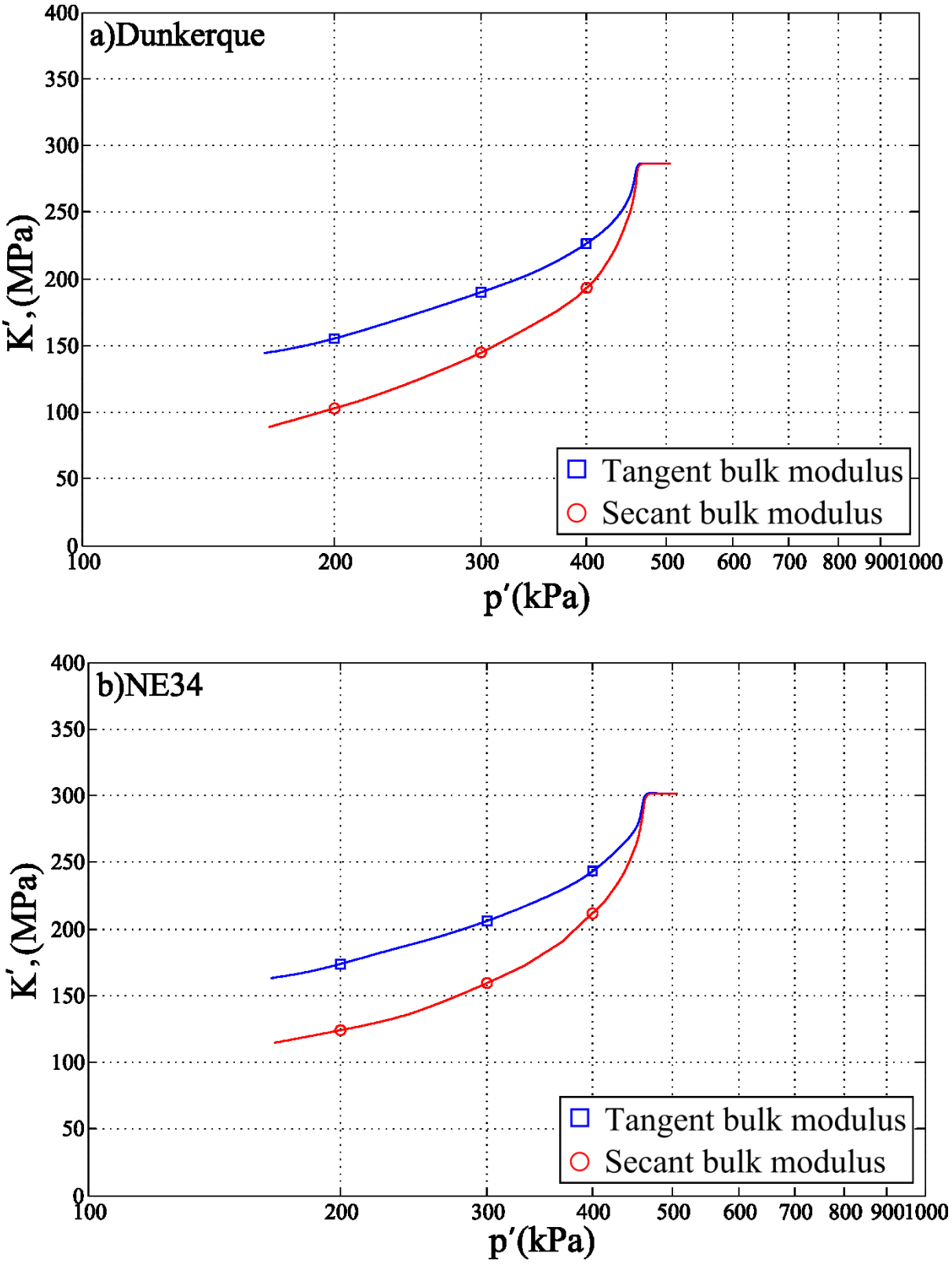


Figure 5-24 Calculation of the bulk modulus for Dunkerque and NE34 sands using swelling stage data. e_0=0.64.

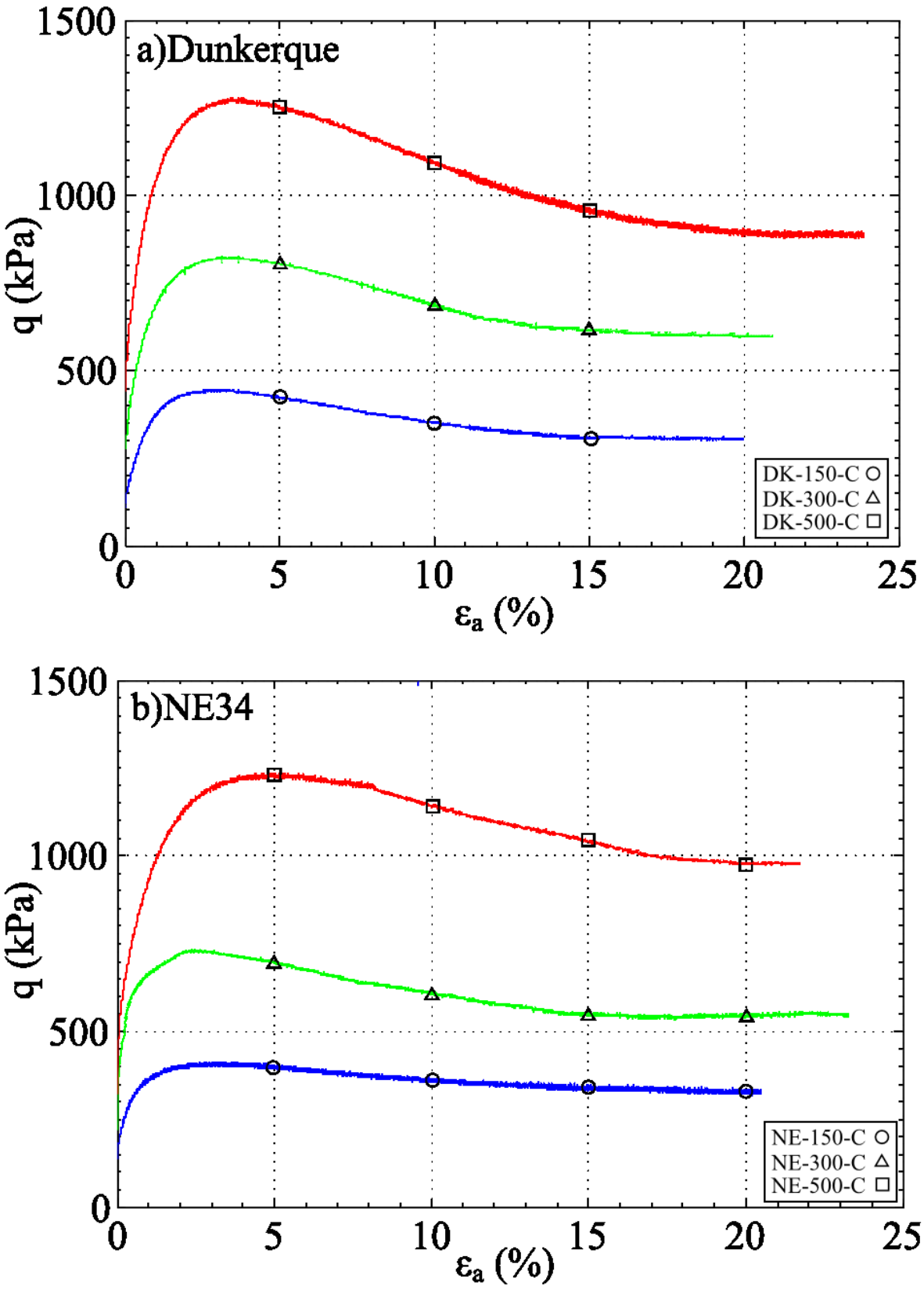


Figure 5-25 q-ε_a trends from drained K_0 compression tests on a) Dunkerque, b) NE34. e_0=0.64

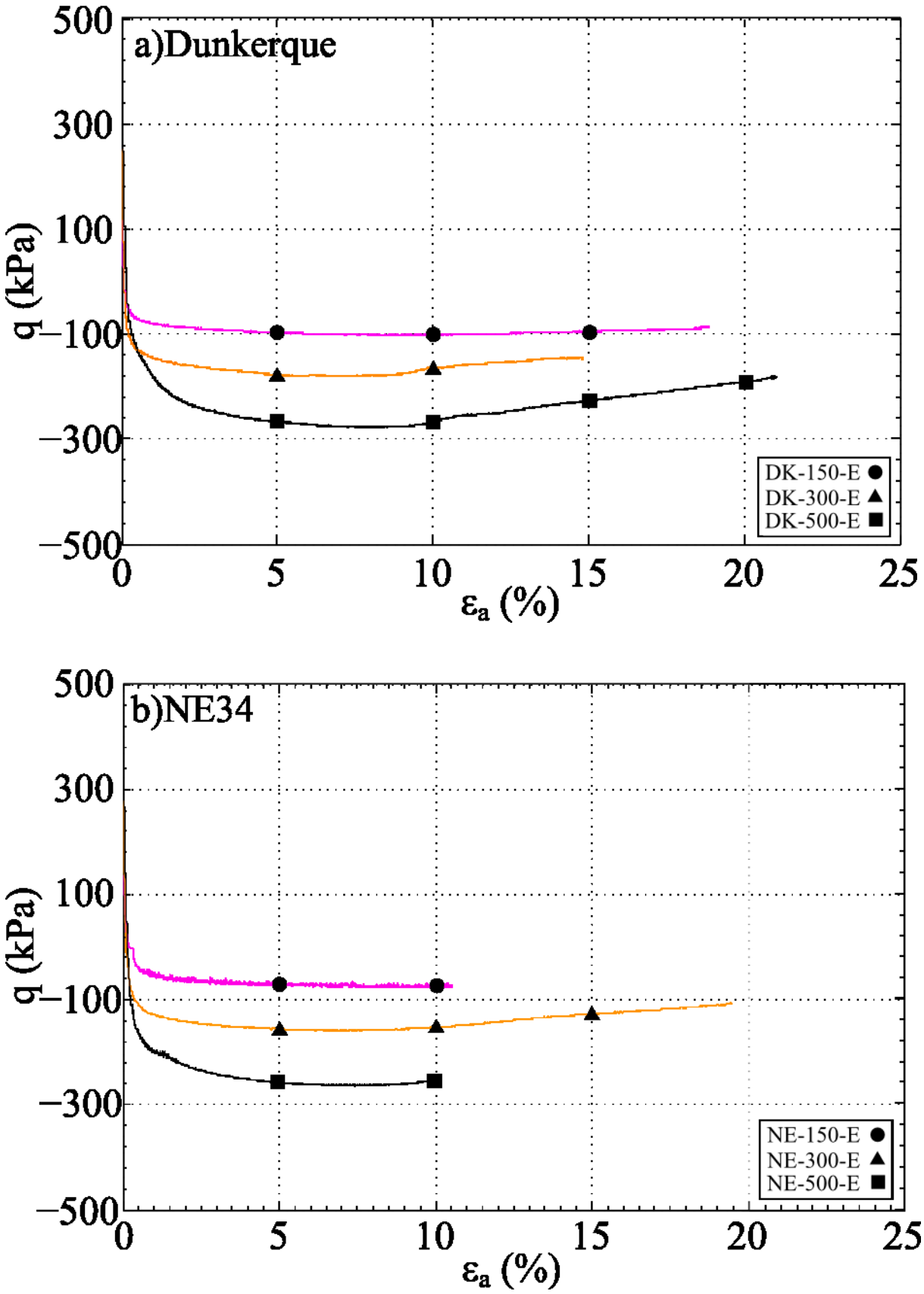


Figure 5-26 q-ε_a trends from drained K_0 extension tests on a) Dunkerque, b) NE34. e_0=0.64

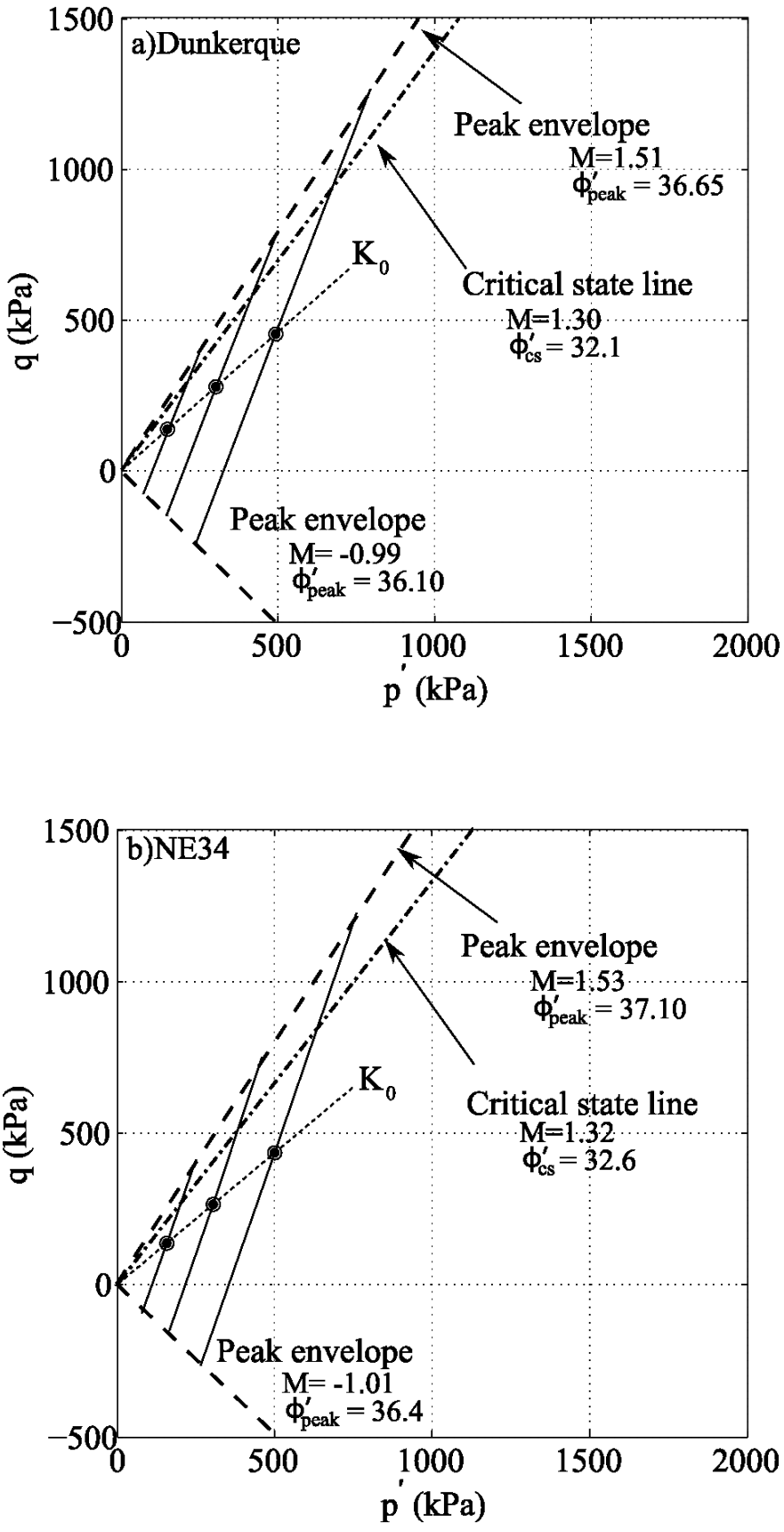


Figure 5-27 Stress paths in q-p′ space from drained K_0 tests, a) Dunkerque, b) NE34. e_0=0.64

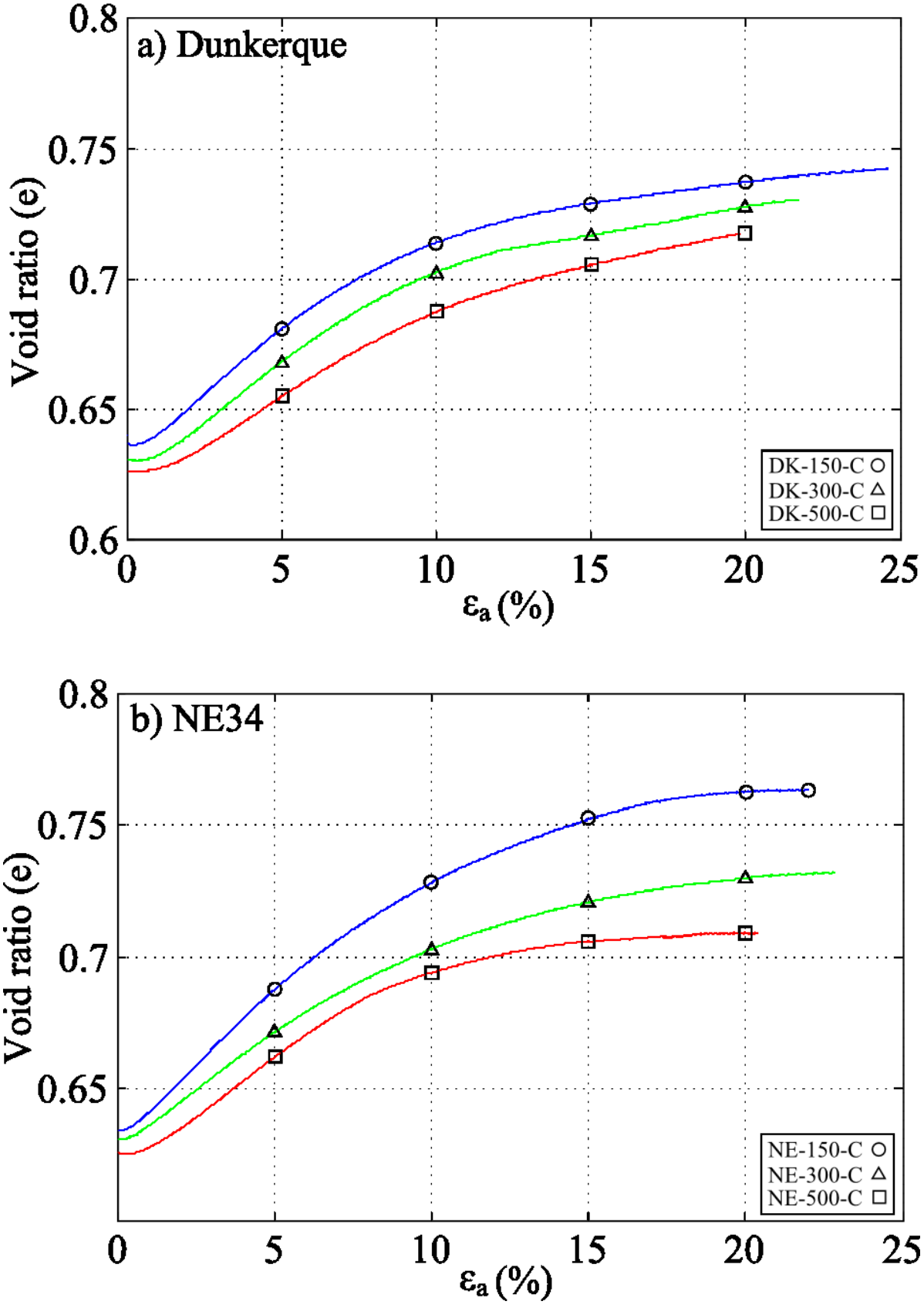


Figure 5-28 Void ratio changes from drained K_0 compression tests, a) Dunkerque, b) NE34. e_0=0.64

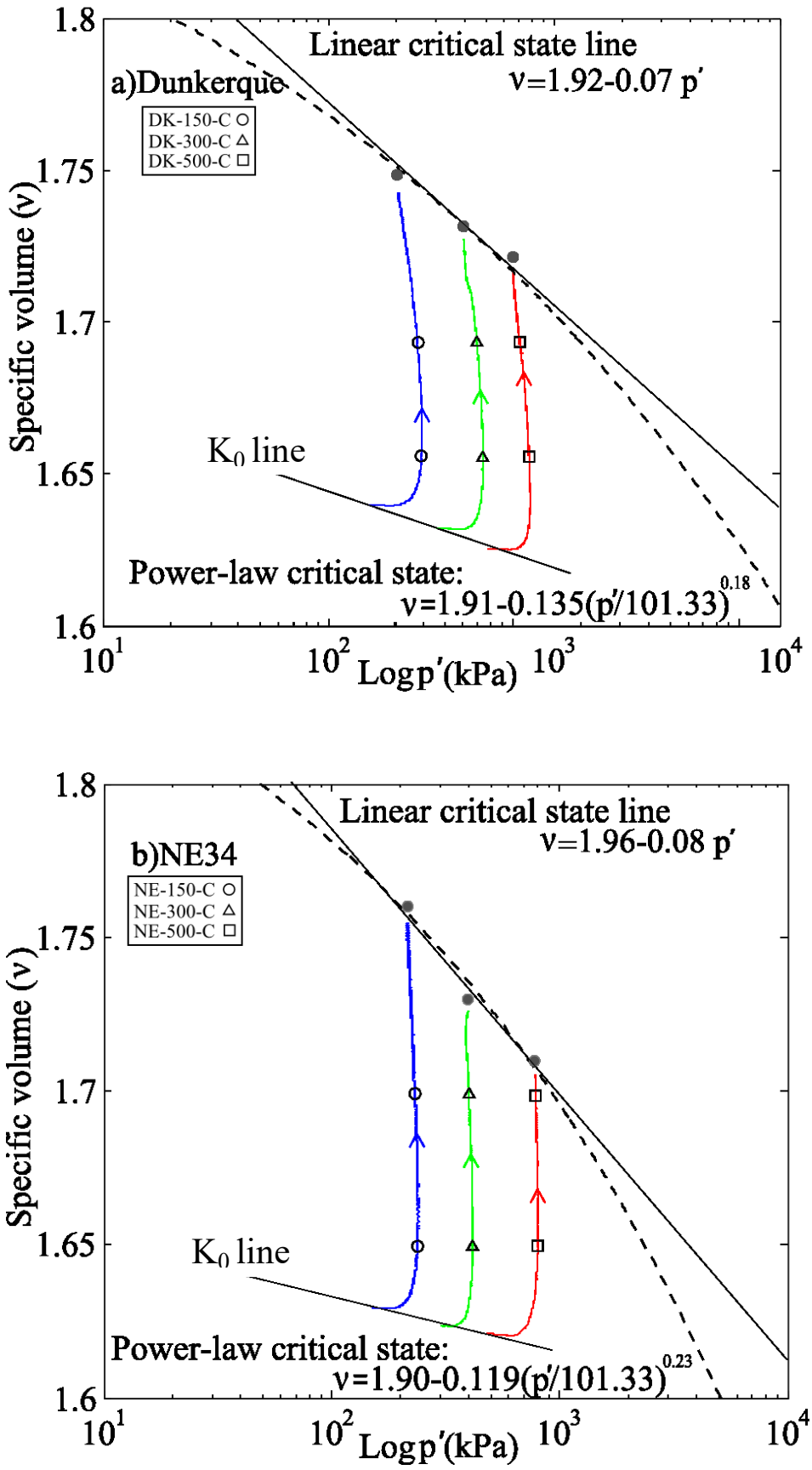


Figure 5-29 Locating the critical state line in e-logp′space, a) Dunkerque, b) NE34. e_0=0.64

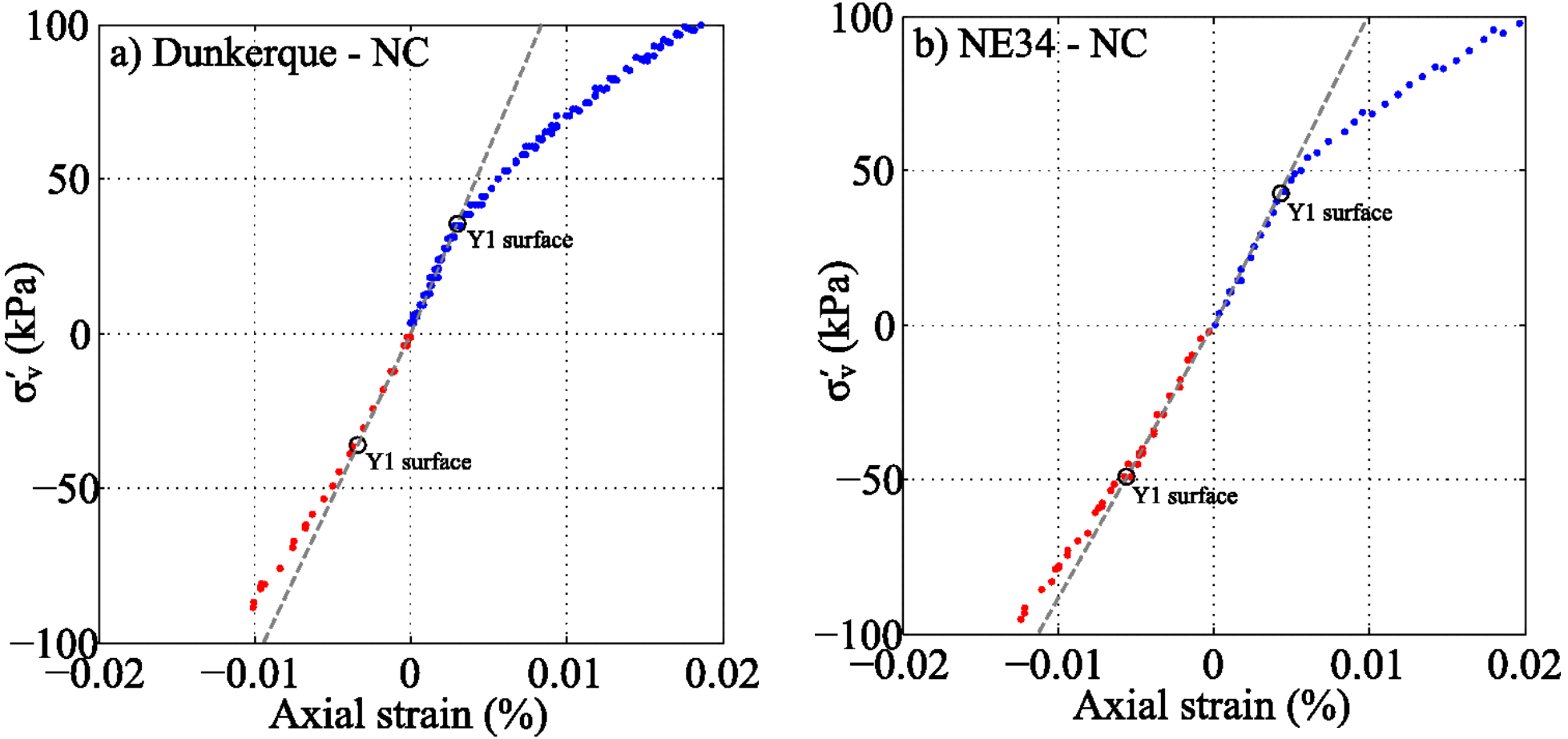


Figure 5-30 Axial stress-strain probing to locate Y_1 boundary for undrained normally consolidated Dunkerque and NE34 sands. e_0=0.64

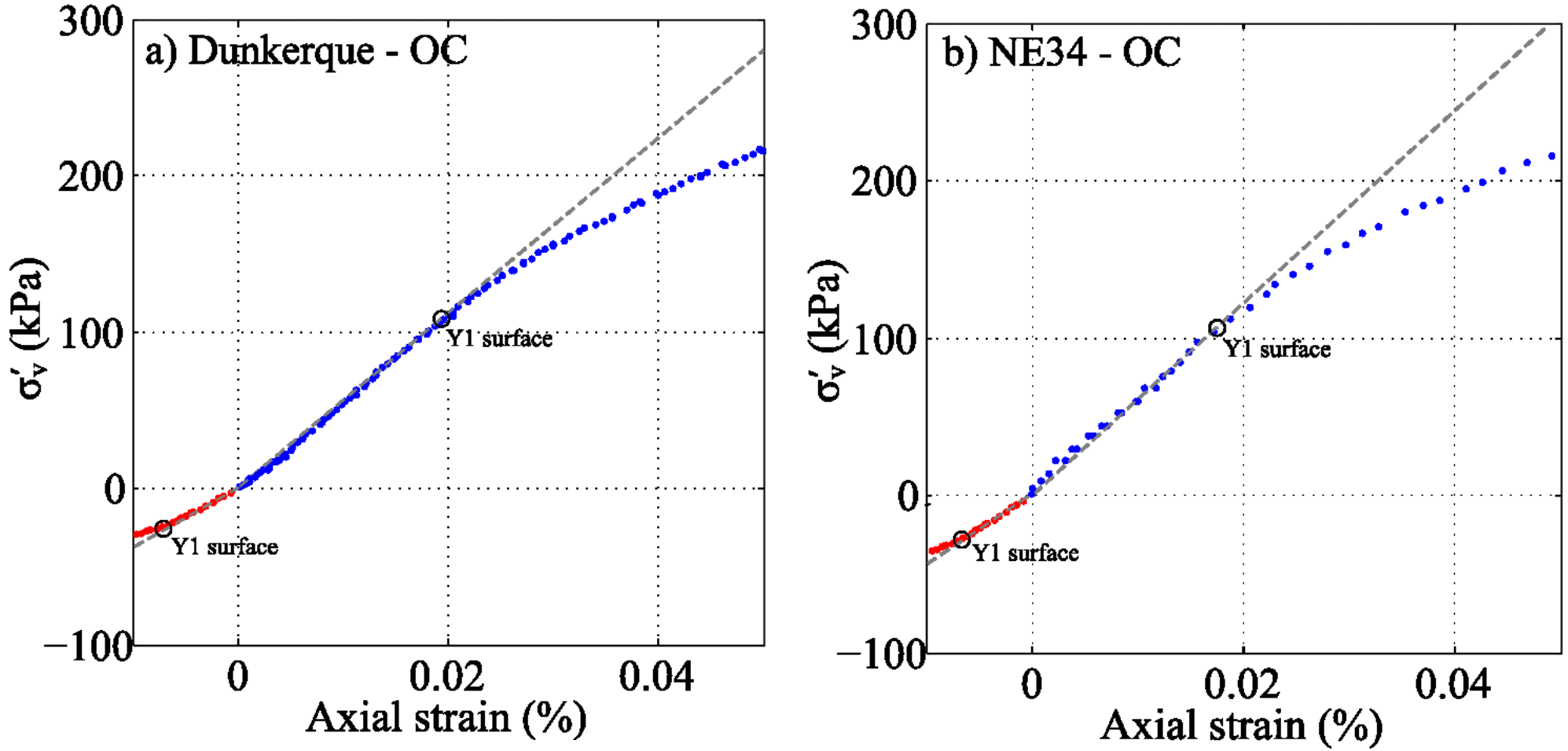


Figure 5-31 Axial stress-strain probing to locate Y_1 boundary for undrained over-consolidated Dunkerque and NE34 sands. e_0=0.64

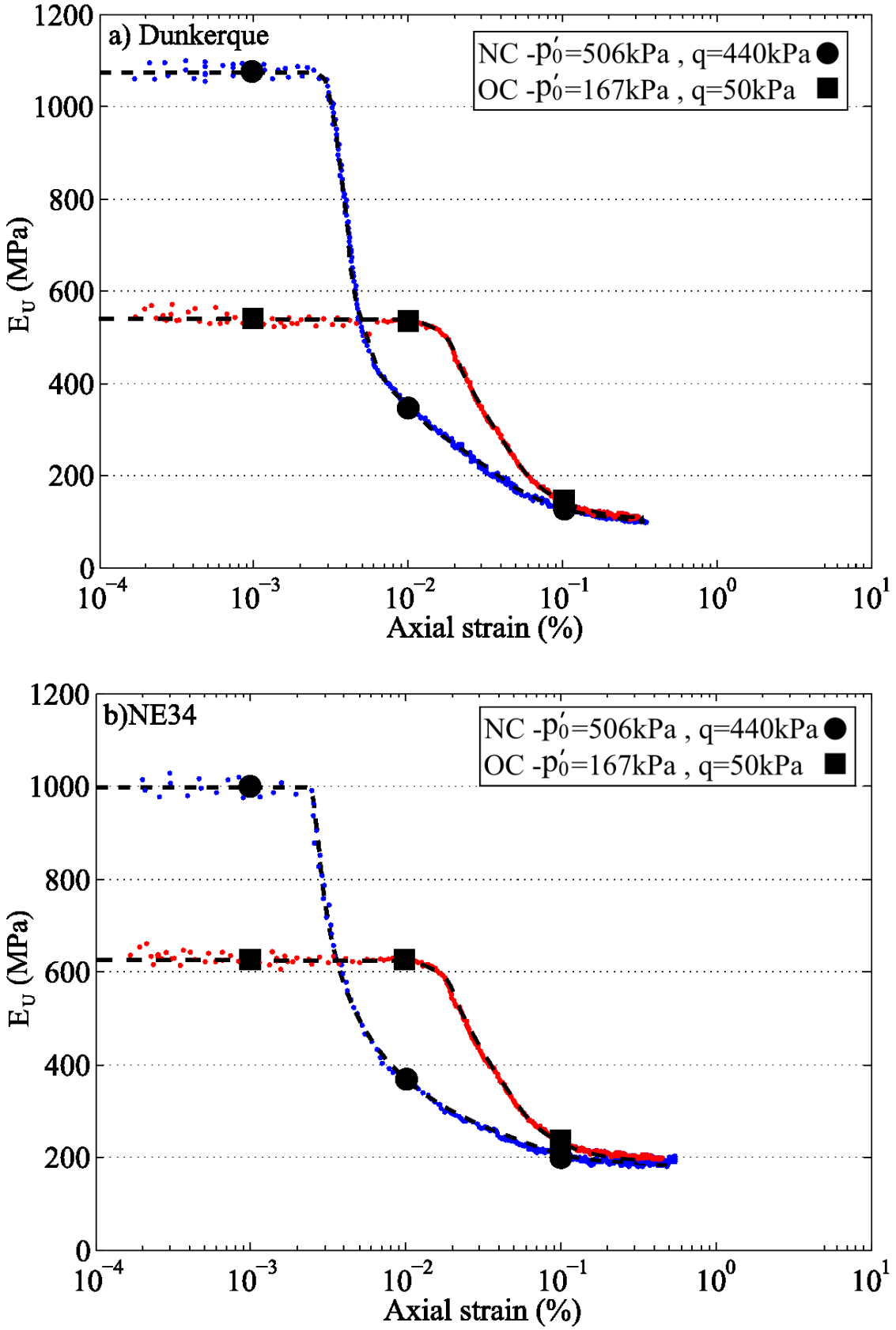


Figure 5-32 Undrained vertical E_U degradation from normally and over consolidated specimens under compression.

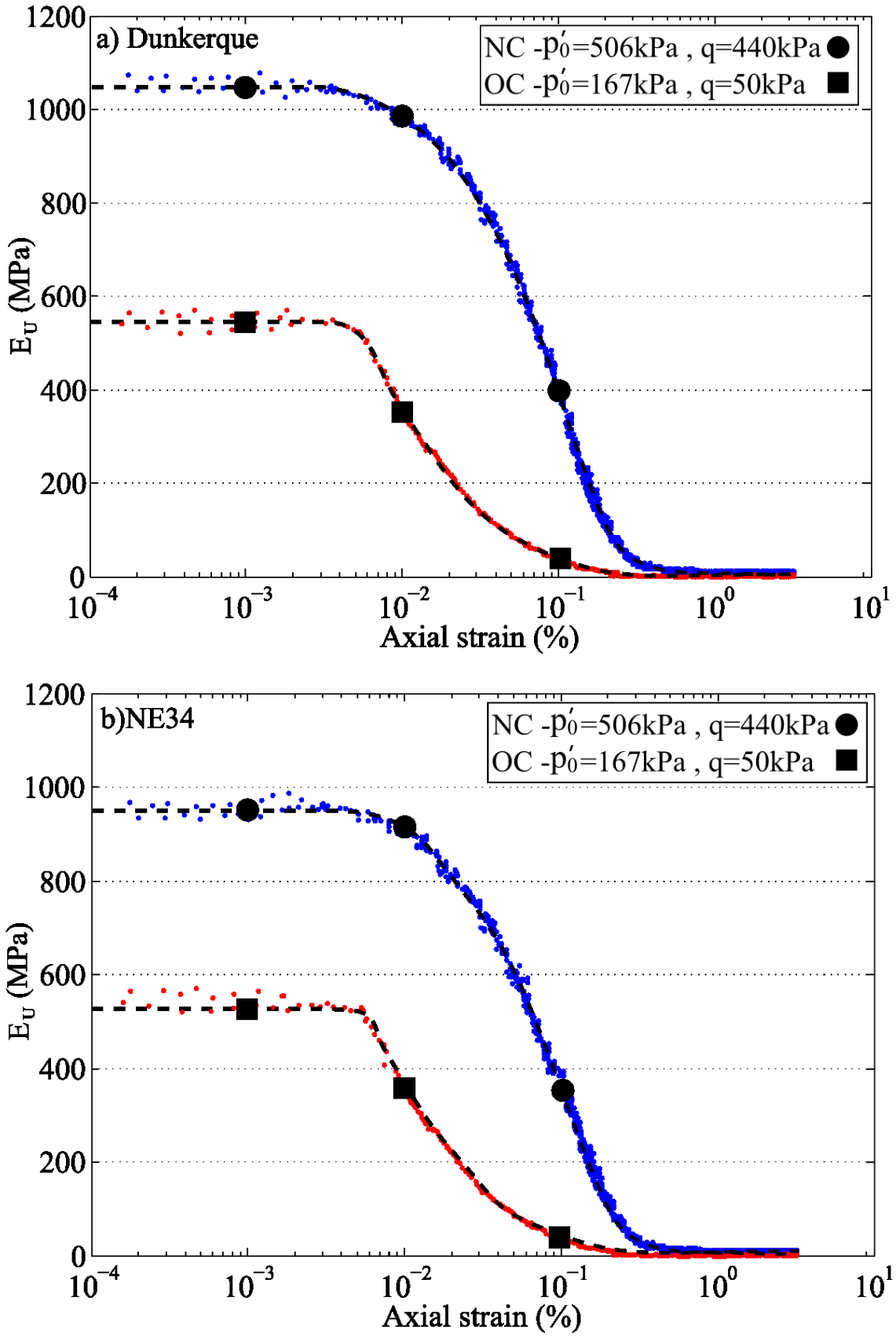


Figure 5-33 Undrained vertical E_U degradation from normally and over consolidated specimens under extension.

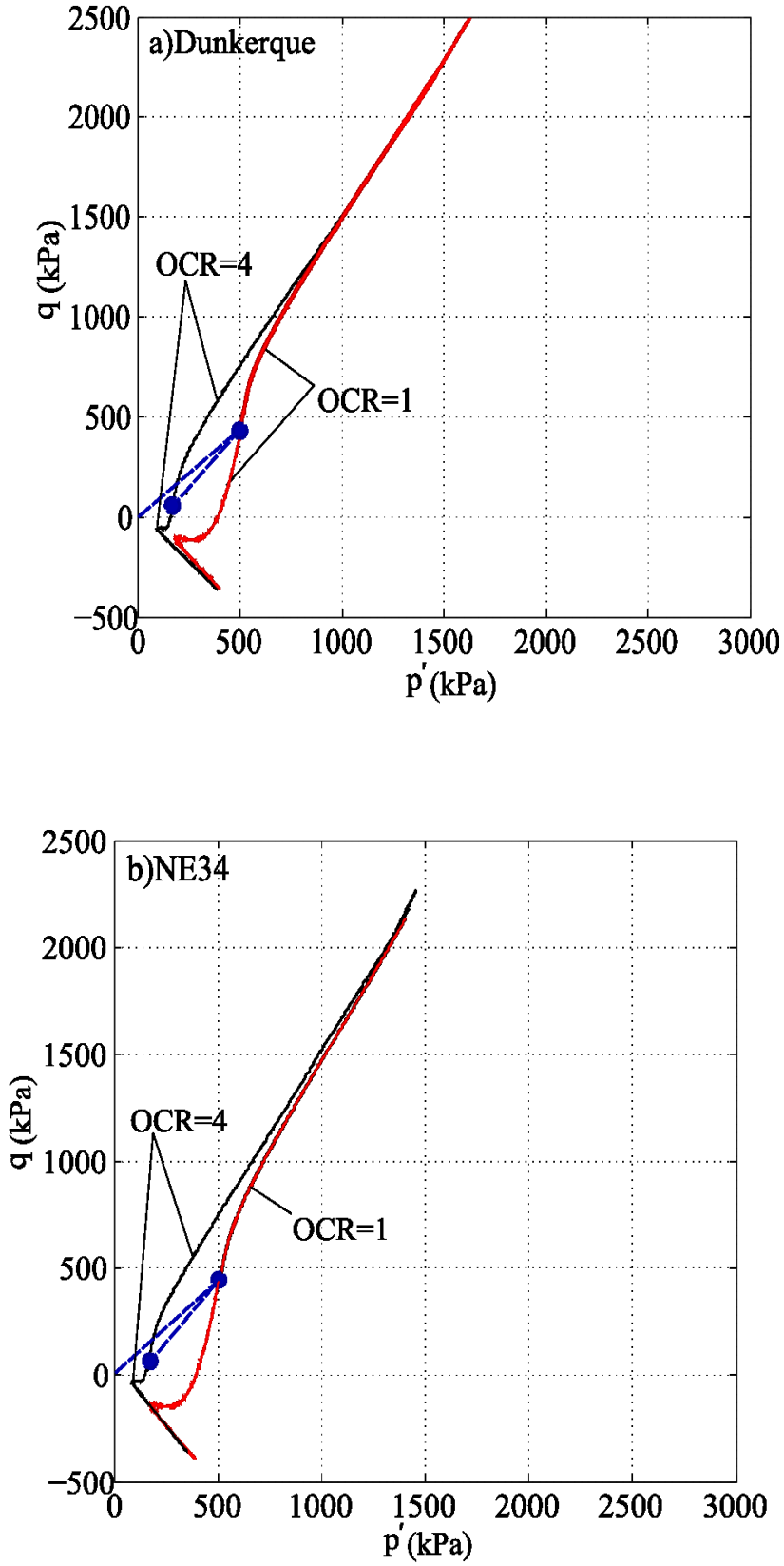


Figure 5-34 Stress paths in q-p′ space from undrained normally consolidated and over-consolidated tests, a) Dunkerque, b) NE34.

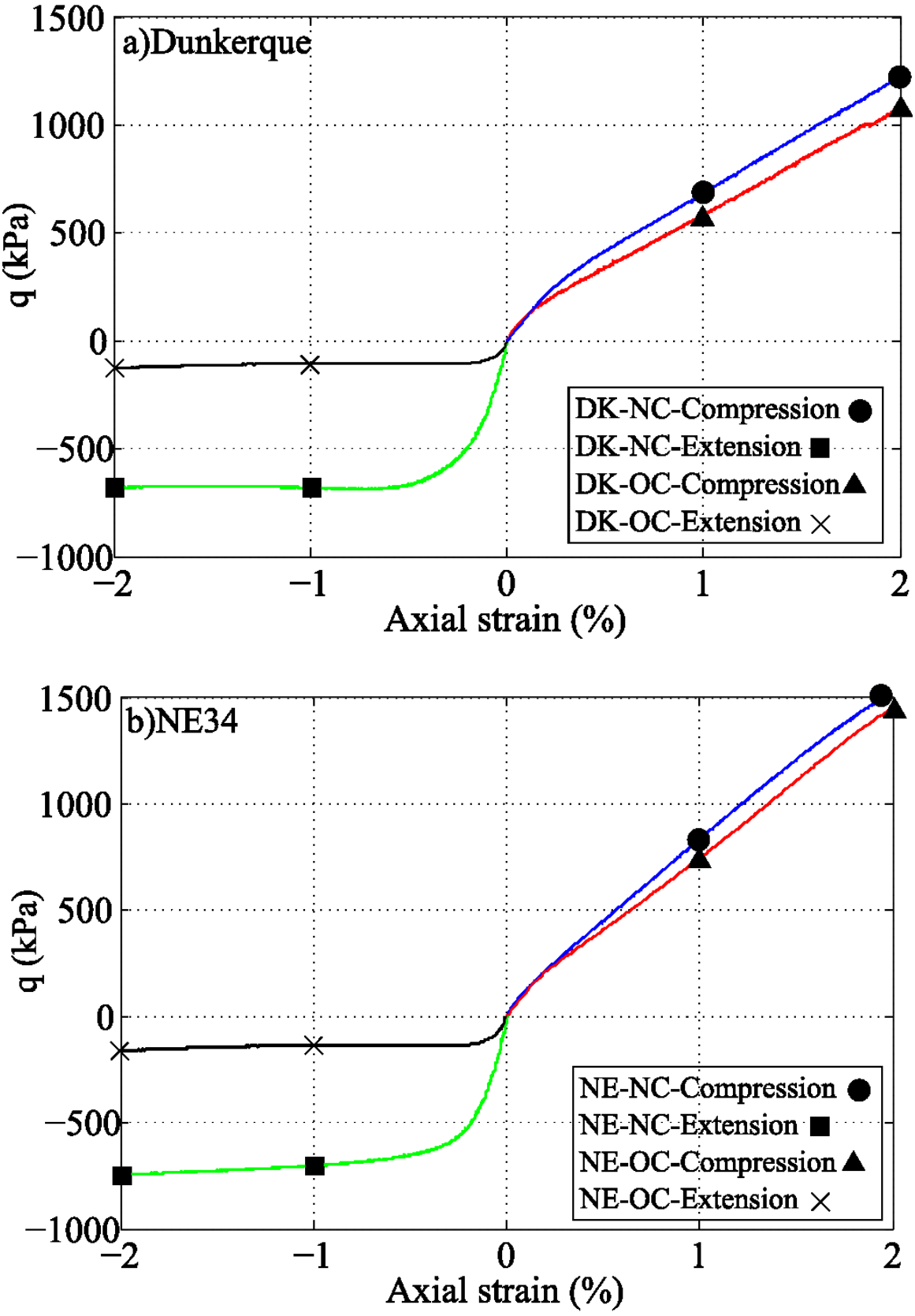


Figure 5-35 q-ε_a trends from undrained normally consolidated and over-consolidated tests, a) Dunkerque, b) NE34.

CHAPTER 6
Design of the “standard” testing procedure

Introduction

The experiments reported in Chapter 2, 3 and 5 demonstrated that experimental boundary conditions specimen formation details and testing stress histories have an important impact on the static and cyclic loading responses of sands. It follows that the same aspects must be considered carefully when designing features of a single element tests to model the behaviour of soil adjacent to a pile experiencing axial cycling. This chapter uses results from instrumented model and field pile tests to consider which key features need to be addressed to obtain representative measurements. The effects of several parameters on cyclic response are assessed using carefully designed suites of cyclic triaxial tests. The investigation described led to a standard testing procedure for modelling the boundary conditions and stress histories experienced by soil elements adjacent to driven piles. This “standard” approach was carried forwards and applied in the wider range of cyclic triaxial and HCA tests described in Chapters 7 and 8.

6.1 Field conditions

In order to design cyclic tests that model the soil element conditions adjacent to a pile subjected to cyclic loads, one must understand and capture the kinematic element conditions and stress histories experienced during the installation and ageing periods that precede any cyclic loading. To do this, we draw on the main outcomes from previous research, especially the conclusions made from highly instrumented model and field pile tests performed by Lehanne *et al.* (1993), Chow (1997), Jardine & Standing (2012) and Tsuha *et al.* (2012) which were summarised in Chapter 3.

6.1.1 Soil element stress regime and failure mechanism

Model and field instrumented pile tests by Lehanne *et al.* (1993), Chow (1997), Jardine & Standing (2000, 2012) and Tsuha *et al.* (2012) demonstrated how cyclic axial pile head loads induce cyclic shear stresses (τ_{rz}) over the pile shaft. In most cases the base loads remain relatively unaffected until the shaft capacity was largely mobilised. The onset of axial cyclic failure is often controlled by the shaft's cyclic capacity. Pile tests reported by Lehanne *et al.* (1993), Chow (1997) and Jardine *et al.* (2013a) showed that the local shaft failure is governed by the Coulomb failure criterion applying to the shaft σ'_r and τ_{rz} values through an interface angle of friction (δ'), which depends on the size and shape of the sand grains and the roughness and hardiness of the pile surface (See section 3.1.2 for more detailed discussion). In order to reach local failure under a maximum cyclic shear stress $[\tau_{rz}]_{max}$, the local shaft radial effective stresses must fall from their initial (equilibrium) values to $[\tau_{rz}]_{max}$ / tan δ'. Such failure patterns were observed with special surface stress transducers that traced the local effective stress patterns followed in *Stable*, *Metastable* and *Unstable* tests involving mini-ICP piles as reported by Tsuha *et al.* (2012) and Rimoy (2013) as reviewed earlier in Figure 3-17.

The kinematic conditions under which such patterns develop can be understood by considering a soil element adjacent to a relatively incompressible pile as shown in Figure 3-21. Under axial loading, the circumferential strains (ε_θ) are very small due to symmetry. The vertical strains (ε_z) are negligible until slip occurs and therefore, the only possible normal strain is radial strain (ε_r). Under these conditions any radial straining provoked by changing shaft shear stresses will cause changes in σ'_r in the surrounding sand mass. Assuming a simple elastic soil response allows local dilation or contraction (Δr) in the interface shear zone to be related to $\Delta\sigma'_r$ changes by cavity expansion theory (Boulon & Foray, 1986):

$$\Delta\sigma'_r / \delta_r = 2G / R = K_{CNS} \qquad \text{Equation 6-1}$$

Where G is the sand shear stiffness and R is pile radius. Equation 6-1 predicts that elastic soils experience Constant Normal Stiffness (CNS) boundary conditions with CNS=K_{CNS}. In principle, CNS laboratory tests can simulate this condition with a mechanism such as that shown in Figure 3-22. However, due to the non-linear, stress dependent and anisotropic nature of sand stiffness (see Chapters 2 and 5), it is not possible to choose a single correct K_{CNS}. Moreover, the K_{CNS} parameter depends on pile radius, making the results hard to apply under general conditions. A simple conservative solution to this problem is to assume that all volume changes are suppressed, implying that K_{CNS} is infinite. This condition can be modelled in undrained element tests on fully saturated samples.

Constant volume Direct Simple Shear (DSS) tests can model these conditions. However, as discussed in section 3.4.2 they cannot provide a complete description of specimen's stress state and also inherit stress non-uniformity in specimen under shearing. These issues can be overcome by performing simple shear tests using Hollow Cylinder Apparatus (HCA) or by performing cyclic triaxial tests. The pile shaft shear stresses can be considered analogous to triaxial deviatoric stress changes (q) and the variations in mean effective stress (p′) developed

under undrained cycling taken as indicators of how σ'_r may change close to pile under cyclic loading.

In this research constant volume (undrained) cyclic triaxial tests were chosen to first assess the effects of different aspects of specimen pre-conditioning on the subsequent cyclic response and so establish a standard testing procedure. Results from these tests are presented in this chapter. The results from triaxial and HCA cyclic tests performed with the established "standard" testing procedure with the stress path triaxial and HCA are presented in subsequent Chapters 7 and 8.

6.1.2 Soil element stress history adjacent to pile

The soil element's stress history should be considered in conjunction with the effects on cyclic response of the kinematic conditions. As discussed in detail in section 3.1.2, field and model ICP pile tests by Lehanne *et al.* (1993), Chow (1997), Yang *et al.* (2010) and Jardine *et al.* (2013) showed that at any given depth below ground level, the radial effective stresses developed at particular depths in the soil mass rise dramatically around the pile axis as the tip approaches from above, and then decay rapidly towards "equilibrium" values as the tip passes that particular fixed depth (see Figure 3-6). Radial effective stress maxima of $q_c/3$ may develop in the sand close to the tip and fall to values about 20 times lower when stresses relax as the tip penetrates to many pile diameters below the fixed depth. Regarding the fabric of the sand, a highly crushed and densified shear band adheres to the pile surface, with moderate breakage developing further from the pile surface as discussed in section 3.1.2 and shown in Figure 3-10. Installation by driving or multi-stroke jacking also imposes high-level cyclic loading that involves full downwards shaft failure and a tension rebound with each cycle. The sand around the pile is left at the end of installation in a heavily pre-sheared state with the degree of "over-consolidation" diminishing with radial distance from the shaft.

In single element testing, over-consolidated conditions can be modelled during the consolidation stage by taking the effective stresses to higher than finally desired levels and then swelling back to lower effective stresses. A specific consolidation-swelling stage was designed and tested for this purpose. The cyclic effects of driving or multi-stroke jacking were also modelled by imposing large cycles of shear stress during the pre-conditioning stage.

6.1.3 Cyclic loads

As discussed in section 3.2, cyclic loads experienced by foundations comprise a series of non-uniform irregular amplitude load cycles. Simplified cyclic analysis for design usually involves transforming the true loading series expected in extreme design events into idealised suites of uniform cycles with fixed cyclic amplitude and average load. (See for example Jardine *et al.* (2012)).

Axial sinusoidal cyclic loads under constant radial stresses were chosen for the cyclic triaxial tests. The equation imposed using the TRIAX control software is:

$$q = q_{mean} + q_{cyc}\sin(\frac{2\,\pi\,time}{T}) \qquad \text{Equation 6-2}$$

Where q_{mean} is the average deviatoric stress, q_{cyc} is the deviatoric stress amplitude and T is the cycle period as defined in Figure 6-1.

The amplitude of the cyclic loads was described using a Cyclic Stress Ratio (CSR) parameter defined here as:

$$CSR = \frac{q_{cyc}}{p'_0} \qquad \text{Equation 6-3}$$

6.2 Cyclic tests

Separate suites of tests were performed to assess the effect on the cyclic response of sand by three key pre-conditioning parameters:

1- Matching the pile installation stress history of mean stress build-up followed by relaxation.

2- Applying large pre-loading cycles to match those experienced during pile driving.

3- Allowing extended creep and ageing pauses prior to applying cycling.

6.2.1 Effect of stress history on cyclic response

The effects of the stress history imposed during the pile installation phase on cyclic response were assessed in two series of cyclic tests involving similar undrained cyclic loads (with q_{cyc} and q_{mean} set to give CSR=0.25), but with the alternative (A-C or A-B-C) stress histories defined in Figure 6-2. Their key parameters are listed in Table 6-1 and Figure 6-2.

Table 6-1 List of triaxial tests that assessed the effect of stress history. Stress history patterns are defined in Figure 6-2.

Sand	Test code	Stress history	CSR	e_0
Dunkerque	DK-NC	A-C	0.25	0.641
	DK-OC	A-B-C	0.25	0.642
NE34	NE-NC	A-C	0.25	0.638
	NE-OC	A-B-C	0.25	0.639

The pre-conditioning procedures for these suites were as follows:

Standard tests: DK-OC and NE-OC specimens were consolidated and swelled prior to applying cyclic loading. Noting from Jardine *et al.* (2013b) that the most extreme stress variations apply to elements initially positioned on the pile axis and that a highly densified interface shear zone develops close to the shaft, an OCR of 4 was chosen to represent conditions applying to soil elements positioned within 2 pile radii (R) of the axis. Altuhafi & Jardine (2011) explored a wider range of conditions in special high pressure triaxial tests, However, practical considerations relating to system limitations also influenced the choice made for the Author's cyclic triaxial tests, as discussed in chapter 4.

The "over-consolidated" conditions were modelled by applying effective stress paths shown in Figure 6-2. After sample set-up and saturation (as explained in section 4.3), the "standard" loading path progressed at a rate $d\sigma'_r/dt$= of 60 kPa/hr from initially isotropic set-up conditions at point A (with p'= 20 kPa) towards constant $K = \sigma'_r/\sigma'_z = 0.45$ paths at Point B that broadly match the $[K0]_{NC}$ ranges given by Kuwano (1999) and Gaudin *et al.* (2005) for Dunkerque and NE34 Fontainebleau sands. On arriving at point B, the stress state was held constant for 48 hours to allow creep strains to stabilise. After this, the sample was unloaded along path B-C at the same rate of $d\sigma'_r/dt$= 60 kPa/hr.

The 'over-consolidated' K_{OCR} value was chosen to be 0.75, which is lower than the K_0 values (≈ 0.98) indicated by Mayne & Kulhawy (1982) at OCR = 4 for the two sands. The ratio was chosen to reduce the scatter that could be experienced in low-level cyclic tests centred on the isotropic axis. Moreover, this ratio located the initial stress point sufficiently far from the failure envelope to allow cyclic tests with high numbers of cycles. A further 48 hours creep stage was allowed at point C prior to starting undrained cyclic loading. It should be noted that in field conditions, the unloading phase is accompanied by possible rotation of direction of principal stresses (i.e changes in α). However, in this research this effect is not considered in pre-conditioning procedure. This can be done using advanced HCA tests with separate control of inner and outer cell pressures.

Reference tests: In a second series of "normally consolidated" tests, samples DK-NC and NE-NC were consolidated directly from Point A to Point C (Figure 6-2) and at Point C, 48 hours of creep was allowed prior to applying undrained cyclic loading.

6.2.1.1 Tests results

Pre-conditioning: The void ratio changes developed during the consolidation stages of both series of tests are shown in Figure 6-3. As shown, the final void ratio values obtained from two different pre-conditioning procedures are only 0.002 and 0.001 apart for the Dunkerque

and NE34 sands, respectively. However, as the undrained tests reported in Chapter 5 showed, over-consolidation leads to markedly different stress-strain behaviour from small to large strains. In particular, the OCR=4 samples' internal fabric could be expected to be far more resistant to low level cycling.

Effective stress drifts: Once the final creep stages at Point C were completed, undrained cyclic loading with CSR = 0.25 and 1 cycle/min (T=1/60 s) was applied to all samples. The normalised p′drifts recorded at the mid-cycle q = 50 kPa points are shown in Figure 6-4 and the cyclic effective stress paths followed are shown in Figure 6-5. The "standard" over-consolidated specimens of Dunkerque and NE34 consistently showed gentler increases in p′ over their 4500 cycles (with final $\Delta p'/p'_0$ ratios of 10% and 15%, respectively), while the normally consolidated "reference" specimens developed negative trends and marked final $\Delta p'/p'_0$ losses of 58% and 40%, respectively. These results are in agreement with Ovando&Shelley (1986) and Qadimi & Coop (2006) who report that over-consolidated specimens show higher resistance to cyclic loading (section 2.3.2.2).

The results also suggest that the Y_2 boundary, or the threshold cyclic loading condition (as introduced by Dobry *et al.*, 1982) below which cycling has little or no effect, is likely to be strongly influenced by the stress history. The boundary to the Y_2 kinematic region is stress history dependent, as was shown by Kuwano & Jardine (2007) and also emphasised in Chapter 5.

Strain accumulation: The trends for the accumulation of permanent vertical strains at the mid-cycle (q = 50 kPa) stages of all tests are shown in Figure 6-6. As expected, the over-consolidated "standard" samples generated far smaller permanent vertical strains than the "reference" OCR=1 tests.

Stiffness degradation: Secant undrained cyclic vertical stiffness values were calculated for each cycle as the slope of a line connecting the maximum and minimum deviatoric stress points in q-ε_a space as:

$$E_U = \frac{[q_{max}]_n - [q_{min}]_n}{[\varepsilon_{a\,max}]_n - [\varepsilon_{a\,min}]_n} \qquad \text{Equation 6-4}$$

The stiffness degradation curves from "standard" and "reference" tests are shown in Figure 6-7. As shown, the initial E^u_v trends are similar in all tests. But as cycling continued, the "reference" tests showed more stiffness degradation than the "standard" over-consolidated tests.

6.2.1.2 Procedure chosen for "standard" procedure

It is clearly important to model the effective stress build-up and relaxation that accompanies pile installation in single element tests designed to predict the undrained cyclic response under cyclic loads. The A-B-C path was therefore chosen as "standard" procedure for all subsequent tests.

6.2.2 Effect of pre-cycling

The effects of extreme shaft loading cycles during pile driving or jacking were explored by imposing large pre-cycles in a second suite of triaxial cyclic tests. The Dunkerque field piles were driven with around 100 to 150 blows/metre (Jardine & Standing, 2012) in which each blow involved a full scale of downward failure and partial re-bound. The calibration chamber mini-ICP model tests (Tsuha *et al.,* 2012) also applied 50 to 100 full load-unload cycles to achieve their single metre of penetration. Jardine *et al.* (2013a) showed that the interface angle of shearing resistance (δ′) was fully mobilised in each downward jack stroke and that the interface shear zone, which consists of crushed and densified sand material, gradually increased in thickness due to abrasion between the sand and the pile surface.

The potentially significant effects of pre-cycling, such as that imposed by driving, on the subsequent cyclic response were also emphasised by Andersen (2009) who noted that such conditioning may improve cyclic shear strengths, allowing the sands' micro-structure and contact distributions to carry subsequent cyclic loads more effectively.

To study this, a series of tests were performed as discussed in the following paragraphs:

6.2.2.1 Effect of pre-cycling on low-medium CSR undrained cyclic tests

The Effects of pre-cycling on the response to low-medium CSR undrained cycling were investigated in the test series performed on both sands outlined in Table 6-2:

Table 6-2 List of triaxial tests that assessed the effect of pre-cycling on undrained cyclic behaviour with low to medium CSR's

Sand	Test Code	Pre-conditioning path *	$CSR_{pre\text{-}cyc}$ at Point C	CSR at Point D	Creep time at Point D	e_0
Dunkerque	DK-P0-05	A-B-D	0	0.05	48 hrs	0.644
	DK-P0-25	A-B-D	0	0.25	48 hrs	0.637
	DK-P50-05	A-B-C-D	0.5	0.05	48 hrs	0.642
	DK-P50-25	A-B-C-D	0.5	0.25	48 hrs	0.642
NE34	NE-P0-05	A-B-D	0	0.05	48 hrs	0.642
	NE-P0-25	A-B-D	0	0.25	48 hrs	0.645
	NE-P50-05	A-B-C-D	0.5	0.05	48 hrs	0.640
	NE-P50-25	A-B-C-D	0.5	0.25	48 hrs	0.641

* See Figure 6-8

All specimens experienced the "standard" consolidation-swelling stress path outlined in previous section. In addition, four specimens (DK-P0-05, DK-P0-25, NE-P0-05, NE-P0-25) experienced relatively high-level drained sinusoidal cycling at Point C (see Figure 6-8) as part of their pre-conditioning stress histories. It should be noted that similar to main suites of cyclic loads, installation pre-conditioning pre-cycles would better be replicated in tests under undrained conditions. However, application of such large pre-cycles under undrained conditions will lead to large losses in effective stresses or might even cause full sample failure. Moreover, although all samples are prepared with similar procedures and have almost

identical initial void ratios, their small inner fabric differences might lead to different levels of effective stress losses. This will lead to non-unique pre-conditioning stress paths which will have an impact on the subsequent cyclic response and will make the comparison of results difficult. Therefore, pre-cycles are applied under drained conditions which will have an impact on evolution of the inner fabric of the specimens.

The adopted conditioning cyclic amplitude (q_{cyc} = 112.5 kPa) and mean cyclic deviatoric stress level (q_{mean} = 225 kPa) were chosen to give a Cyclic Stress Ratio ($CSR_{pre\text{-}cyclic}= q_{cyc}/p'_0$) = 0.5. This choice led a peak maximum principal stress ratio $\sigma'_z/\sigma'_r = \tan^2(45 - \phi'_{mob}/2)=0.45$ which in turn required ϕ' to be mobilised to 23°. The latter angle reflected the mobilised τ_{rz}/σ'_r ratio expected at 2 pile radii from axis under installation conditions (Jardine *et al.*, 2013a). The number of conditioning cycles imposed (30) was chosen after considering the cyclic shear and volumetric strain development seen in trial tests. The cyclic period (T) (2 mins) was chosen to ensure good control over the applied cycles which followed the ideal sinusoidal path accurately.

Pre-conditioning: The void ratio against p′trends seen over the full pre-conditioning stages of the tests listed in Table 6.2 are plotted in Figure 6-9. As in the earlier tests, compressibility during consolidation loading is p′dependent and the creep stages that follow are compressive. The swelling paths follow a lower slope, (with $C_s < C_c$ as expected) and the creeping observed after swelling is dilative.

Samples that experienced drained pre-cycling at Point C showed a contractile response (decrease in void ratio) but these changes in void ratio were relatively small (less than 0.001) in both sands. More important than the final void ratio difference between the “standard” pre-cycled and “reference” (non-cycled) tests was the sand fabric resulting from the pre-cycling.

The internal fabrics of the "standard" tests were more resistant to the undrained cycles that were applied subsequently at Point D (see Figure 6-8).

The accumulation of shear and volumetric strains during pre-cycling are illustrated in Figure 6-10, tracking the mid-cycle (q = 116.7 kPa) conditions. The patterns of straining tended to stabilise at N > 25, indicating that around 30 such cycles could be applied in the "standard" tests to keep compatibility with the typical number of high-level jack strokes applied in the field and model pile tests. Below, we explore the "standard" and "reference" sample's responses to subsequent undrained cycling applied after 48 hours of creep and ageing.

Effective stress drifts: Figure 6-11 shows the mid-level (q = 50 kPa) p′drifts as developed in low to medium CSR undrained cyclic tests conducted from Point D. As shown, all four specimens showed increases in p′under such cyclic loading levels. However, the samples that had experienced pre-cycling showed more up to 5% growth in p′after 4500 cycles under the same CSR values. As noted earlier, the p′changes developed under undrained cycling can be taken as indicator of how σ_r' may change close to the pile under cyclic loading. Gains in shaft capacity could be expected to match the growth of local σ_r' or p′.

Strain accumulation: The permanent vertical strains accumulated in all four tests amounted to less than 0.005% in all tests and no meaningful difference could be defined at this level between the "standard" and "reference" tests, due to the scattering effects of minor temperature fluctuations and the limitations of the strain and transducers resolutions.

Stiffness degradation: The cyclic E_U values established during the first undrained cycle and after 4500 cycles at Point D are given in Table 6-3. The stiffnesses were practically constant in the CSR=0.05 tests, with no meaningful difference seen between the "standard" and

"reference" tests. All CSR = 0.25 tests showed modest (<5%) stiffness degradation over their first 500 cycles, reaching a steady state at higher numbers of cycles, but still without any clear effect of pre-cycling.

Table 6-3 E_U values at N=1 and 4500 from tests with low to medium CSRs that assessed the effect of pre-cycling

Sand	Test Code	E_U at N=1 (MPa)	E_U at N=4500 (MPa)
Dunkerque	DK-P0-05	410	405
	DK-P0-25	390	380
	DK-P50-05	405	405
	DK-P50-25	385	380
NE34	NE-P0-05	415	410
	NE-P0-25	400	385
	NE-P50-05	415	405
	NE-P50-25	390	380

6.2.2.2 Effect of pre-cycling on high level undrained cyclic loads

The Effects of pre-cycling at Point C on the undrained response under subsequent high CSR cycling at Point D was investigated with three tests on Dunkerque sand that applied $CSR_{pre\text{-}cyc}$ ratios of 0, 0.25 and 0.5 at Point C. Details from these tests are given in Table 6-4:

Table 6-4 List of triaxial tests that assessed the effect of pre-cycling on undrained cyclic behaviour with high CSR

Sand	Test Code	Pre-conditioning path *	$CSR_{pre\text{-}cyc}$ at Point C	CSR at Point D	Creep time at Point D	e_0
Dunkerque	DK-P0-45	A-B-D	0	0.45	48 hrs	0.643
	DK-P25-45	A-B-C-D	0.25	0.45	48 hrs	0.645
	DK-P50-45	A-B-C-D	0.5	0.45	48 hrs	0.644

* See Figure 6-8

Pre-conditioning: Figure 6-12 shows the changes in void ratio against p′ during the pre-conditioning stages of all three tests. The accumulation of shear and volumetric straining during drained pre-cycling is shown in Figure 6-13 and Figure 6-14, tracking the mid-cycle (q = 116.7 kPa) conditions. As expected, the specimen cycled with $CSR_{pre\text{-}cyc}$ = 0.5 showed higher levels of strain accumulation compared to that pre-cycled under $CSR_{pre\text{-}cyc}$ = 0.25, but both tests stabilised at N>25.

Effective stress drifts: The impact of the variable drained pre-cycling on the subsequent undrained cyclic response at Point D can be seen in the mean effective stress drifts tracked at mid-cycle (q = 50 kPa) conditions in Figure 6-15. The specimen that had experienced no pre-cycling reached cyclic failure rapidly at N_f (number of cycles to failure) = 160, while the specimen pre-cycled with $CSR_{pre\text{-}cycling}$=0.5 endured until N_f=590. The third specimen which had experienced pre-cycling with $CSR_{pre\text{-}cycling}$=0.25 reached failure at an intermediate stage with N_f= 440. As noted earlier, drained pre-cycling improves the cyclic strength.

Strain accumulation: The permanent vertical strains accumulated at the mid-cycle (q = 50 kPa) points are shown in Figure 6-16. The plots show how the tests developed increases sharp increases in strain rates towards the full cyclic failures outlined above.

Stiffness degradation: Stiffness degradation plots from the three tests are given in Figure 6-17., showing how E_U reduced progressively as the elements moved towards full cyclic failure upon which stiffness dropped towards zero.

6.2.2.3 Procedure chosen for "standard" procedure

It is clear that drained pre-cycling impacts on the response of sand samples to subsequent undrained cycling, particularly that imposed at high CSRs, where higher cyclic resistances and delayed failure resulted. Pre-cycling stage involving 30 drained pre-cycles with $CSR_{pre\text{-}cyc}$ = 0.5 at Point C were therefore added to the "standard" test procedure.

6.2.3 Effects of ageing

The sand masses positioned around pile shafts invariably experiences ageing between the end of installation and any subsequent load-test or storm loading event. *Stable* creep straining, which could continue for days or months, generally promotes more advantageous particle and contact arrangements and can also contribute to large gains in shaft capacity with time (Jardine, 2013). Kuwano (1999) and Kuwano & Jardine (2002) report on the creep strains

developed by dense Dunkerque sand under various triaxial conditions and the Authors' research included an assessment of the potential effects of such creep on the subsequent cyclic response. The assessment was made by contrasting the effects of imposing either 12 or 48 hour drained creep periods at Points B and D, as identified in Figure 6-8. The experiments, which are summarised in Table 6-5, all followed the "standard" load-unload conditioning effective stress paths shown in Figure 6-8. To simplify the interpretation, no pre-cycling was included. Both Dunkerque and NE34 samples were tested; the only difference in procedure was that half the specimens experienced 12 hour creep periods while the others had 48 hours creep times at Points B and D before being subjected to undrained cycling at CSRs of 0.05 and 0.25.

Table 6-5 List of triaxial tests that assessed the effect of creep time on undrained cyclic response

Sand	Test Code	Pre-conditioning path *	$CSR_{pre\text{-}cyc}$ at Point C	CSR at Point D	Creep time at Point D
Dunkerque	DK-P0-05-12	A-B-D	0	0.05	12hrs
	DK-P0-25-12	A-B-D	0	0.25	12hrs
	DK-P0-05-48	A-B-D	0	0.05	48 hrs
	DK-P0-25-48	A-B-D	0	0.25	48 hrs
NE34	NE-P0-05-12	A-B-D	0	0.05	12hrs
	NE-P0-25-12	A-B-D	0	0.25	12hrs
	NE-P0-05-48	A-B-D	0	0.05	48 hrs
	NE-P0-25-48	A-B-D	0	0.25	48 hrs

6.2.3.1 Outcomes

The observation of drained creep straining after arriving at Point D showed that creep rates remained significant (0.011%/day) after 12 hours and dropped to rates three times lower after 48 hours of creep.

Effective stress drifts: The p′ drifts recorded over the first 1500 cycles are presented in Figure 6-18, considering both Dunkerque and NE34 specimens under CSRs of 0.05 and 0.25.

Strongly negative p′ drift rates were observed in tests performed after 12 hour creep periods. However, the drift rates were all positive in the tests that adopted 48 hour creep periods.

These results suggest that the Y_2 (or threshold boundary proposed by Dobry *et al.* (1982)) depend strongly on the ageing history as well as the OCR of the specimens. The 48 hour aged specimens appear able to have remained within their Y_2 kinematic yield surfaces, while specimens aged for just 12 hours showed significant losses in p′that would imply pile shaft capacity losses in comparable pile loading tests.

6.2.3.2 Procedure chosen for "standard" regime

A simple, approximate, way to relate the cyclic responses of field and model piles and the above triaxial cyclic tests is to assume that the triaxial tests' $\Delta p'/p'_0$ trends are direct indicators of the corresponding changes in pile shaft capacity under cycling. The field and model pile tests summarized in Figure 3-15 and 3-19 showed no negative effect under cyclic loading at modest CSRs, comparable to those considered in Table 6-5. The negative $\Delta p'/p'_0$ trends seen in tests involving shorter (12 hour) ageing periods of 12 hours are incompatible with the results with field and model pile tests. Considering that the, 48 hour "creep time" tests were fully compatible with the field trends, the latter period was chosen and applied in the "standard" procedure. A more detailed comparison between field and model pile tests with single element tests will be presented in Chapters 7 and 8.

6.3 Standard test procedure

The Author's standard test procedure, which was applied in all subsequent test series, accounted for three key important features of the conditions experienced by a soil element adjacent to driven pile that might otherwise be neglected. The three features were:

- A load-unload stress path that model the stress build-up and relaxation followed in-situ during pile installation.

- A pre-cycling stage that models the large cycles imposed during pile driving or cyclic jacking.
- An ageing period that allowed creep strain rates to fall to negligible levels prior starting of cycling.

All three of these steps were shown to have potentially major impacts on the rates of $\Delta p'/p'_0$ drift, permanent straining and stiffness degradation experienced under subsequent constant volume (undrained) cycling. Failure to include any of the three steps would be likely to lead to over-conservative assessments of the potential impact of field cyclic loading on piles driven in sands.

6.4 Conclusion and remarks

The goal in Chapter was to design a testing procedure that captures and models the key features of the kinematic conditions and stress history experienced by soil elements adjacent to a driven pile subjected to axial cyclic loading. The test programme drew from the results from research by Lehanne *et al.* (1993), Jardine & Standing (2012), Tsuha *et al.* (2012) and Rimoy (2013) on highly instrumented model and field piles that were summarised in earlier Chapters and assessed each key factors' importance and influence on the two test sands' undrained cyclic behaviour. The results obtained led to the "standard" testing procedure followed in the Author's main research programme.

The key conclusions made are:

1- Single element triaxial and HCA tests can be designed to match key aspects of the conditions applying close to the shafts of piles driven in sands.
2- While Constant Normal Stiffness (CNS) tests can be proposed to model the kinematic boundary conditions adjacent to driven pile under axial loading, choosing a unique

fully representative K_{CNS} is not possible due to the anisotropic, stress dependent nature of sand stiffness and the effect of pile radius on the K_{CNS} values.

3- A simple conservative solution to this problem is to assume that volume changes are negligible in the sand mass, meaning that K_{CNS} is infinite. Constant volume (undrained) single element tests on saturated specimens can be used to achieve these conditions readily.

4- The effective stress histories (OCRs and ageing) applied to sand elements have a major impact on their subsequent undrained cyclic triaxial response. It is vital in tests designed to match pile loading to capture the considerable local "over-consolidation" that results from installing displacement piles in silica sands.

5- Pile installation by driving or cyclic jacking imposes conditioning pre-cycling that stiffens the sand and improves its subsequent cyclic resistance. This facet of behaviour must also be modelled when attempting to replicate field or model test behaviour.

6- Any on-going creep affects the undrained cyclic response of sands by generating excess pore pressure and reductions in p′. Allowing sufficient time for creep strains to stabilise under drained conditions at points of stress path reversal and prior to the undrained cyclic stage is therefore vital. Two day (48 hour) periods were found to be sufficient with the sands tested.

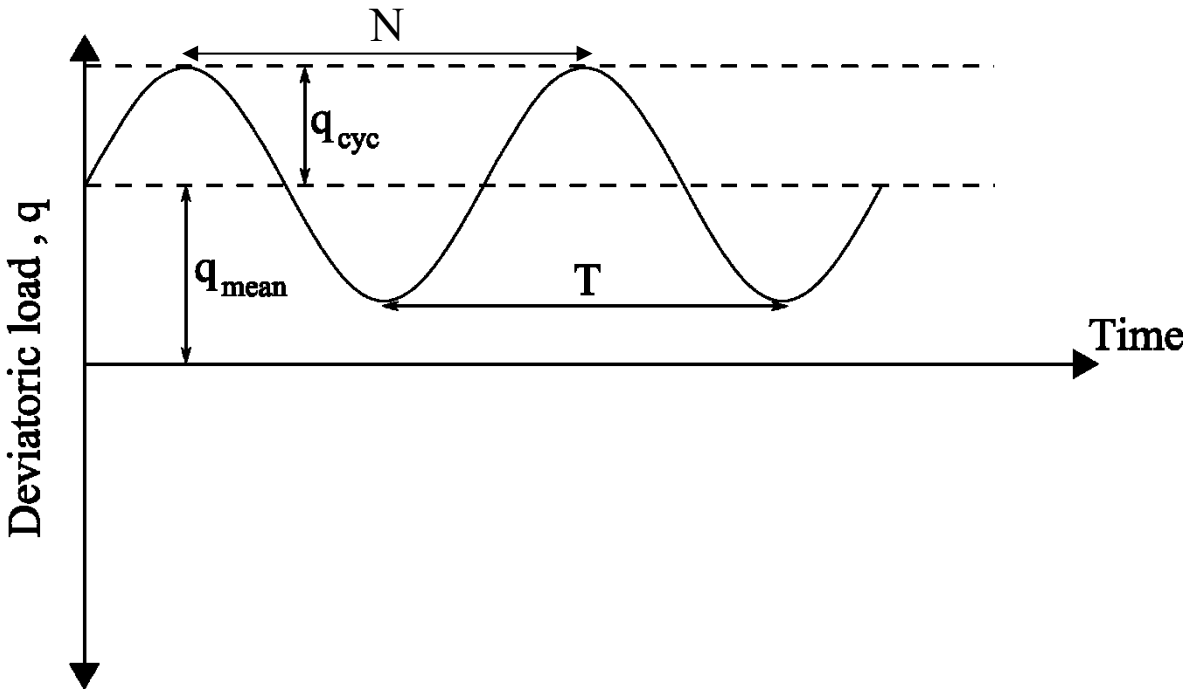


Figure 6-1Schematic illustration of cyclic triaxial loading shearing definition of q_{mean}, q_{cyc}, T (period) and N (number of cycles).

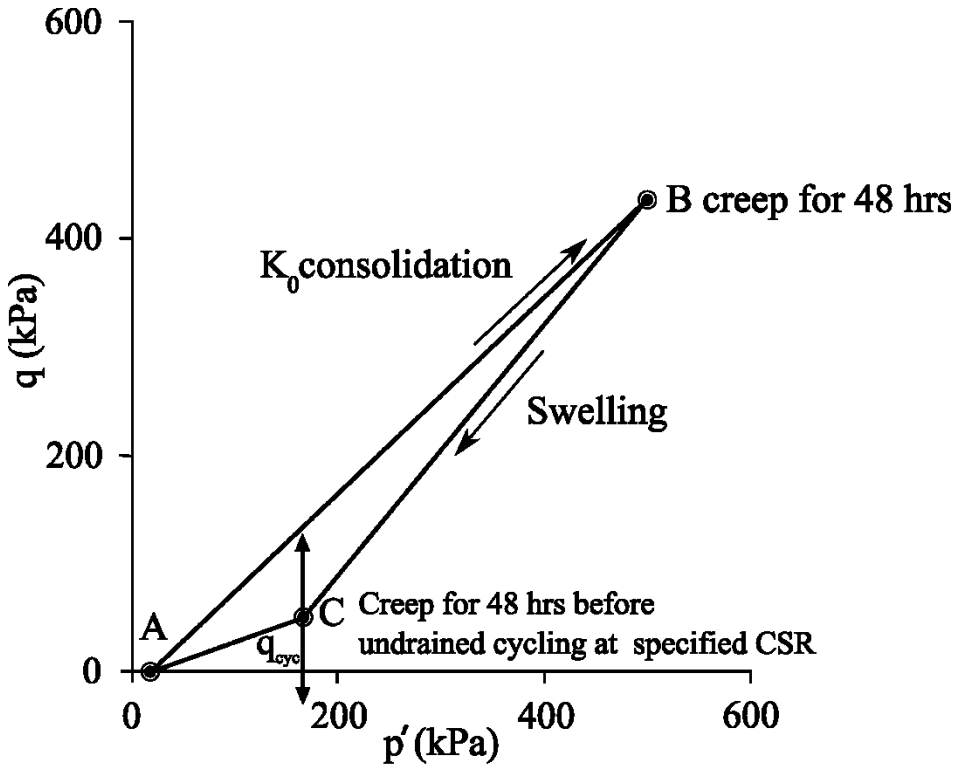


Figure 6-2 Pre-conditioning consolidation effective stress paths applied in tests that assessed the effect of stress history on undrained cyclic response. A-C for normally consolidated specimens and A-B-C for over-consolidated specimens.

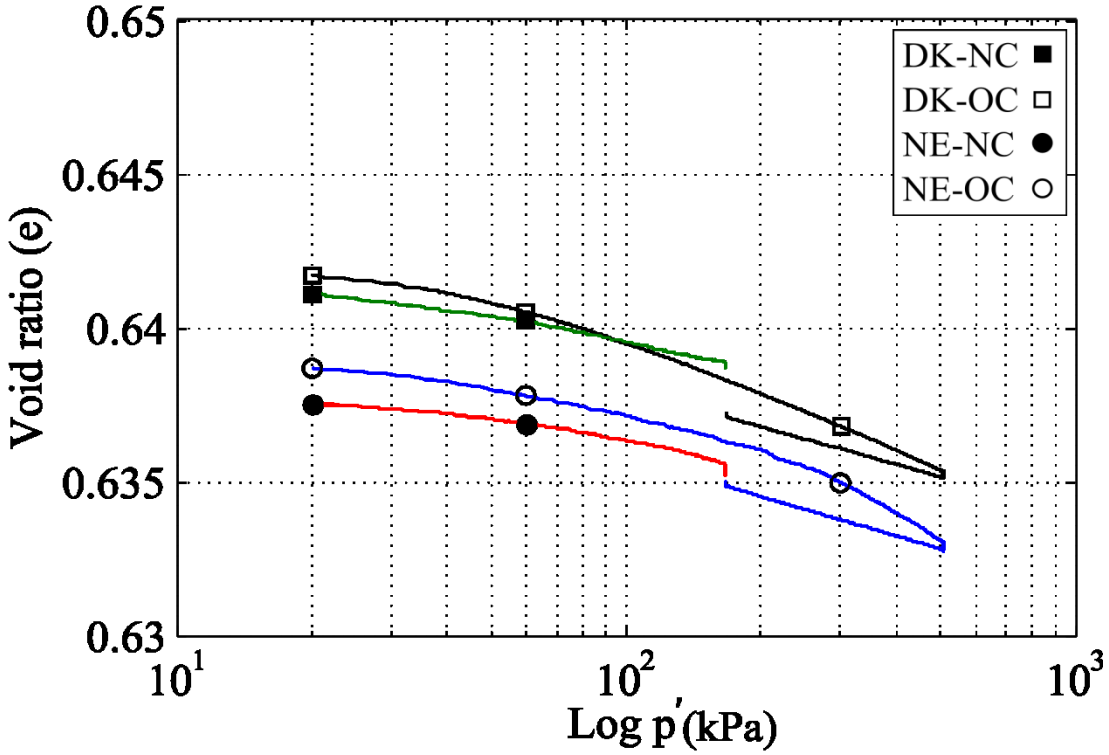


Figure 6-3 Void-ratio changes during the pre-conditioning stages for normally-consolidated and over-consolidated specimens that assessed the effect of stress history on undrained cyclic response.

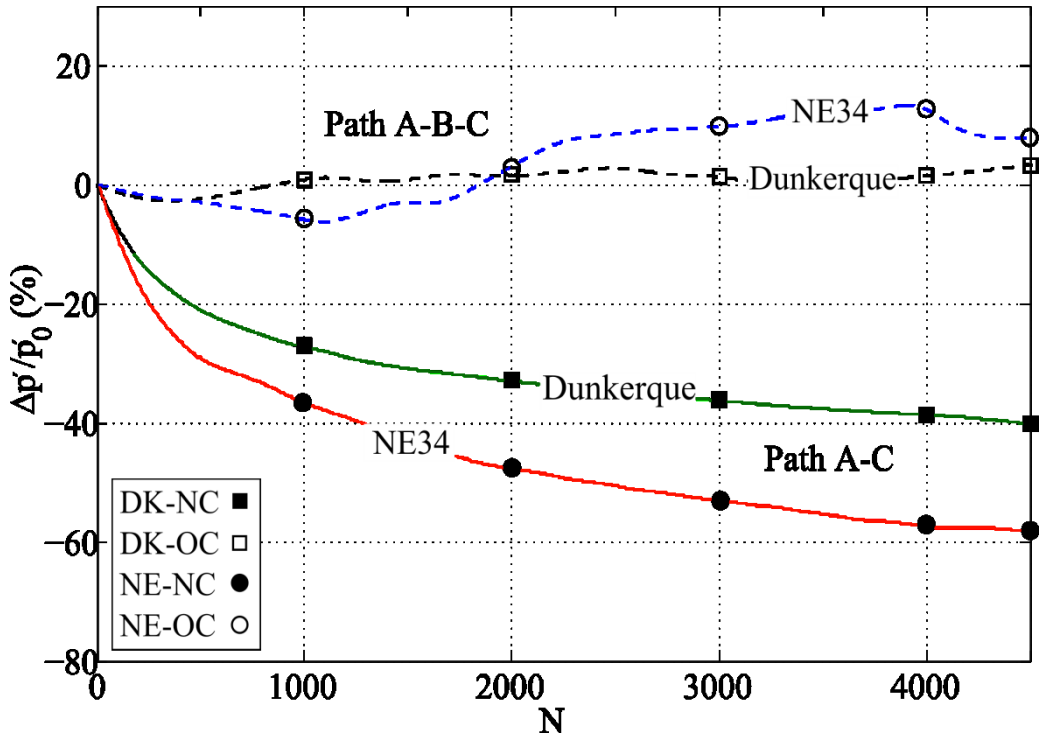


Figure 6-4 Effect of consolidation stress history on p′drifts observed in undrained cyclic tests with CSR=0.25. Plot shows the p′ drift at mid-cycle (q = 50kPa) points versus number of cycles.

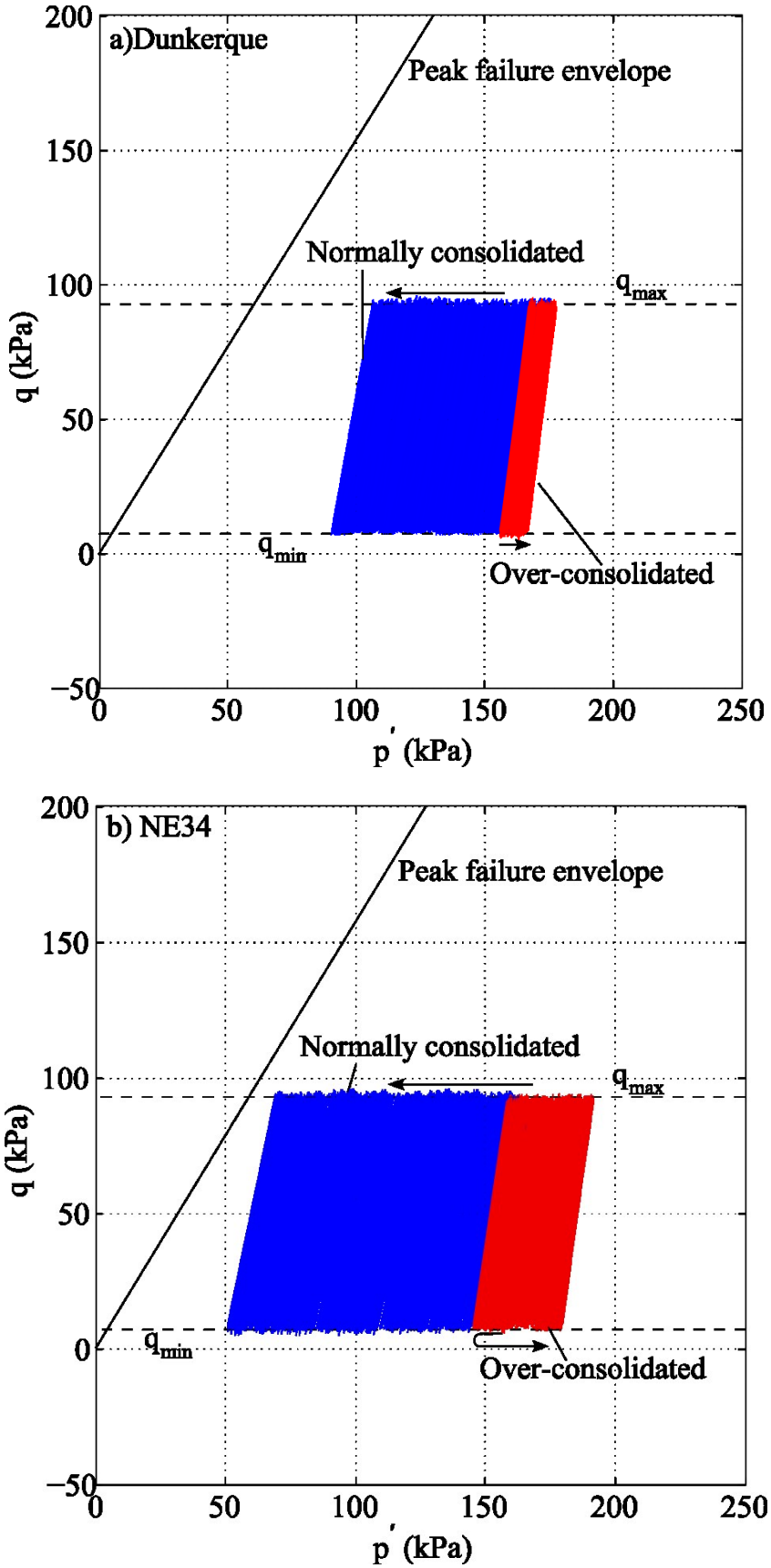


Figure 6-5 Effect of consolidation stress history on p′drifts observed in undrained cyclic tests with CSR = 0.25. Plot shows the stress paths followed in q-p′ space under undrained cyclic loading.

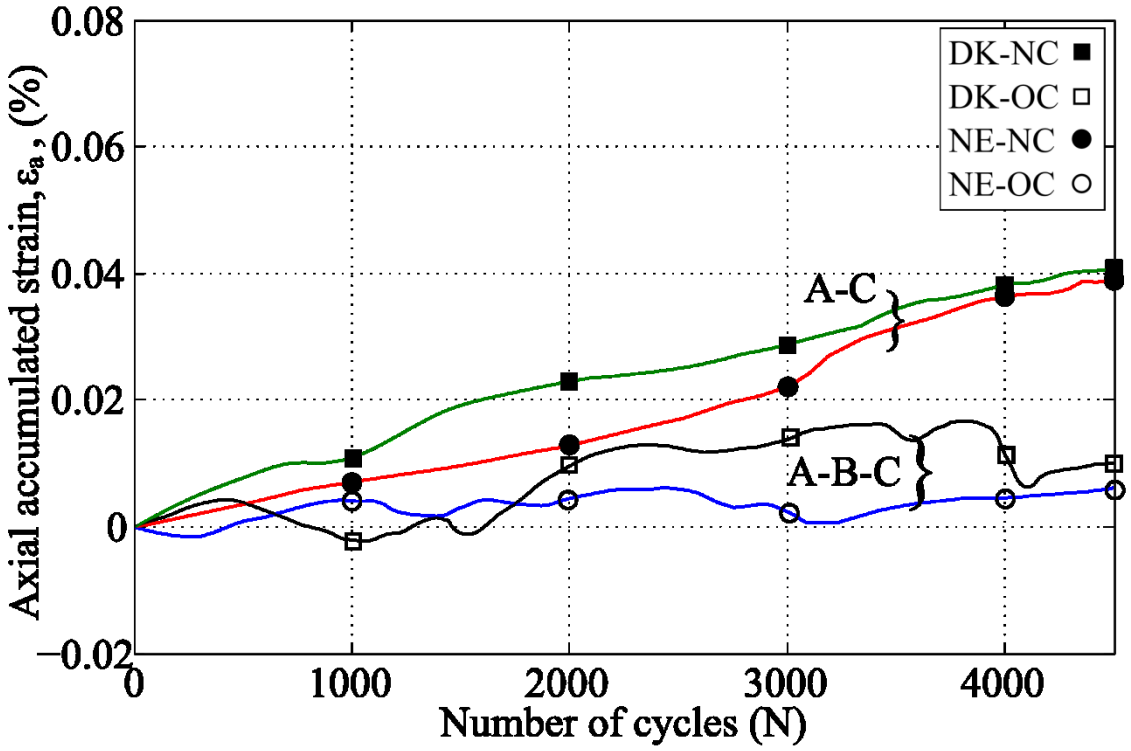


Figure 6-6 Effect of consolidation stress history on accumulation of permanent axial strains at mid-cycle (q = 50kPa) points observed in undrained cyclic tests with CSR = 0.25. Note NC=normally consolidated, OC=over-consolidated, DK=Dunkerque and NE=NE34 sand

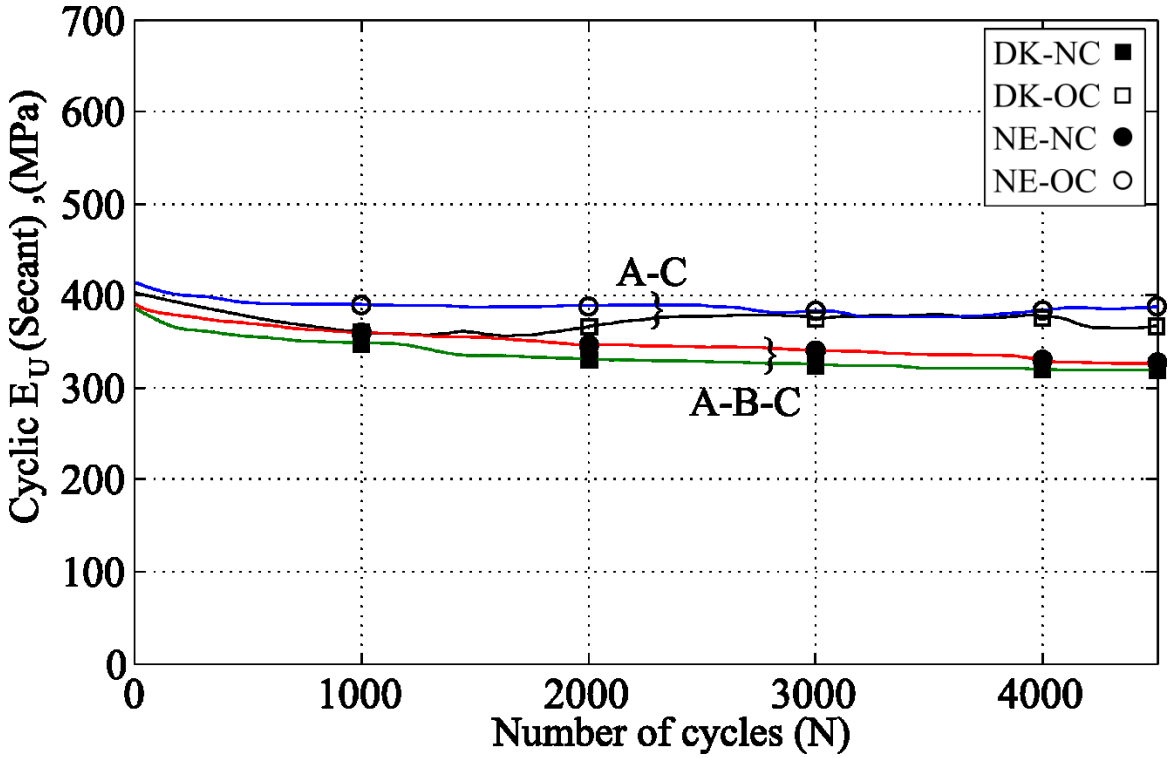


Figure 6-7 Effect of consolidation stress history on secant undrained stiffness under undrained cyclic tests with CSR = 0.25. Note NC=normally consolidated, OC=over-consolidated, DK=Dunkerque and NE=NE34 sand

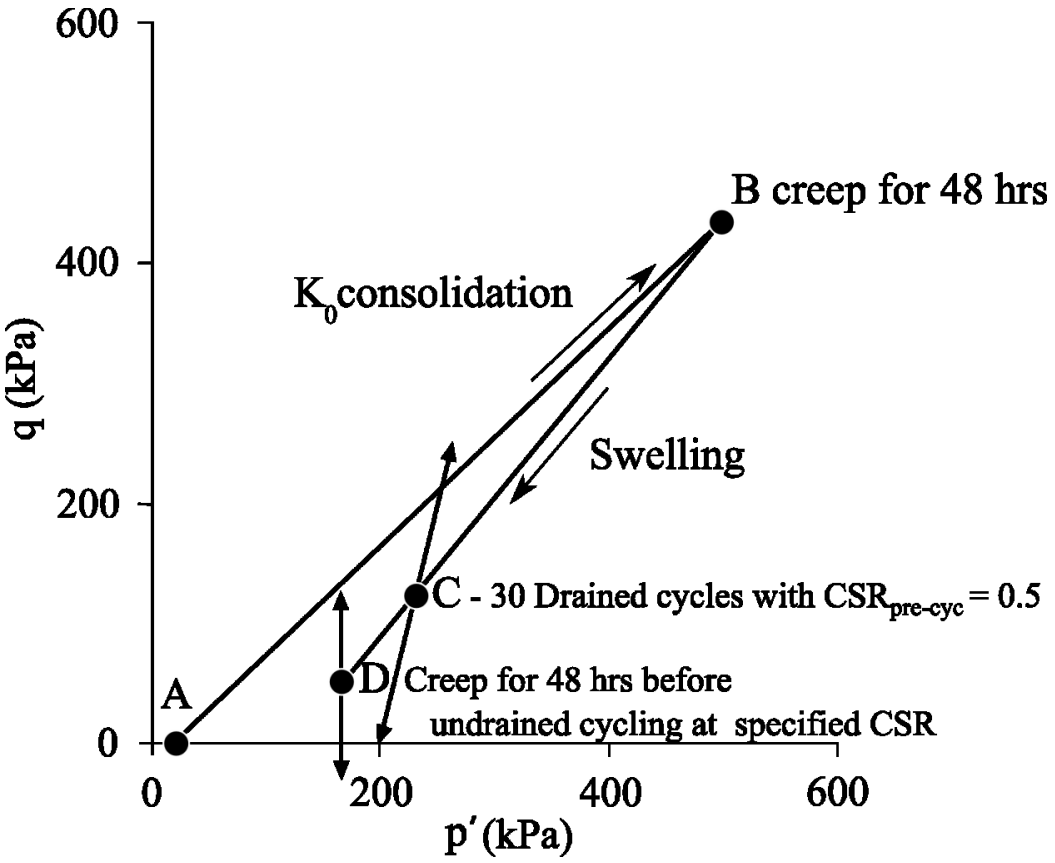


Figure 6-8 Pre-conditioning consolidation effective stress paths applied in tests that assessed the effect of pre-cycling by 30 drained cycles at Point C.

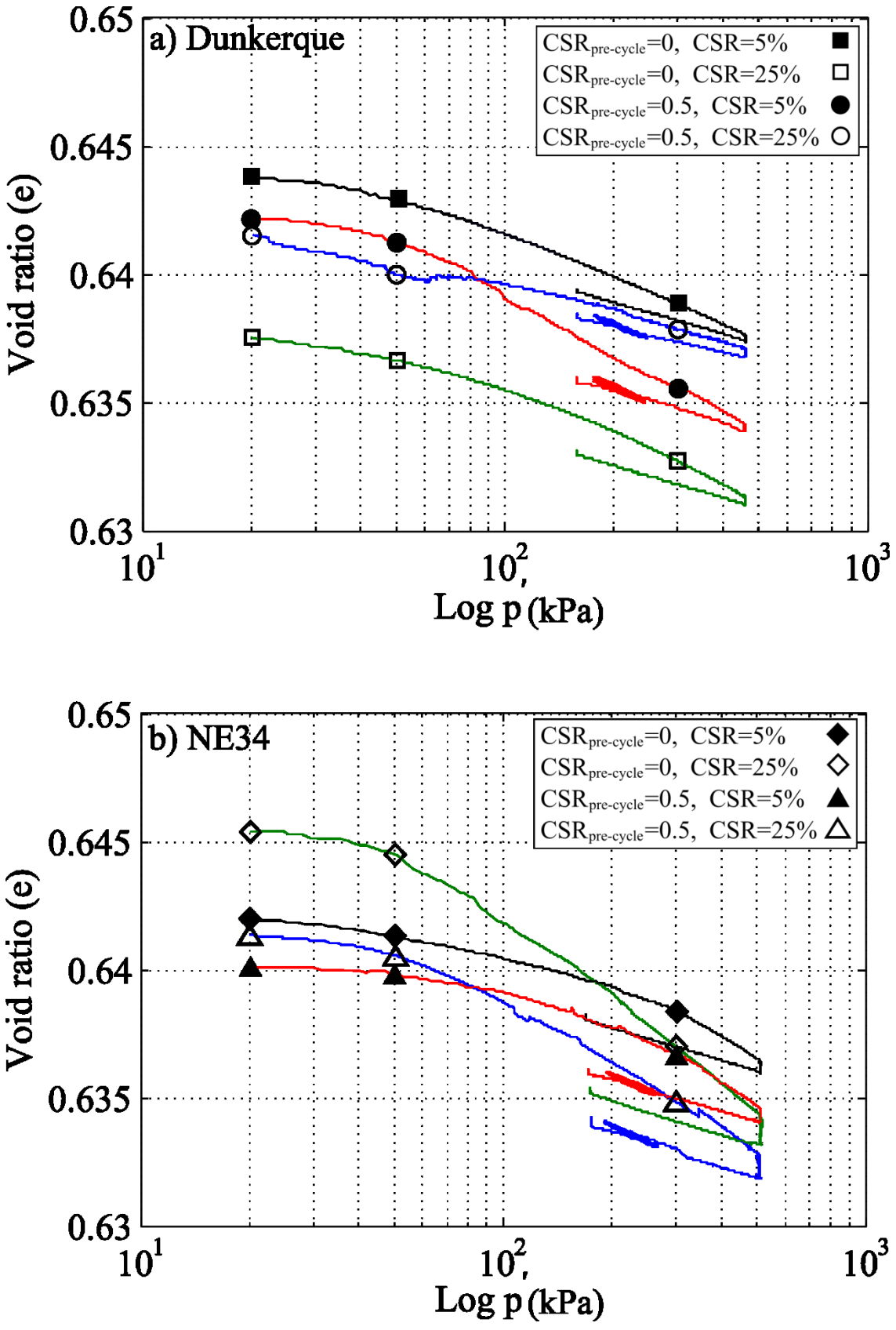


Figure 6-9 Void ratio changes during the pre-conditioning stages of tests on a) Dunkerque and b) NE34 specimens that assessed the pre-cycling (at Point C) on undrained cyclic behaviour (at Point D) with low to medium CSRs.

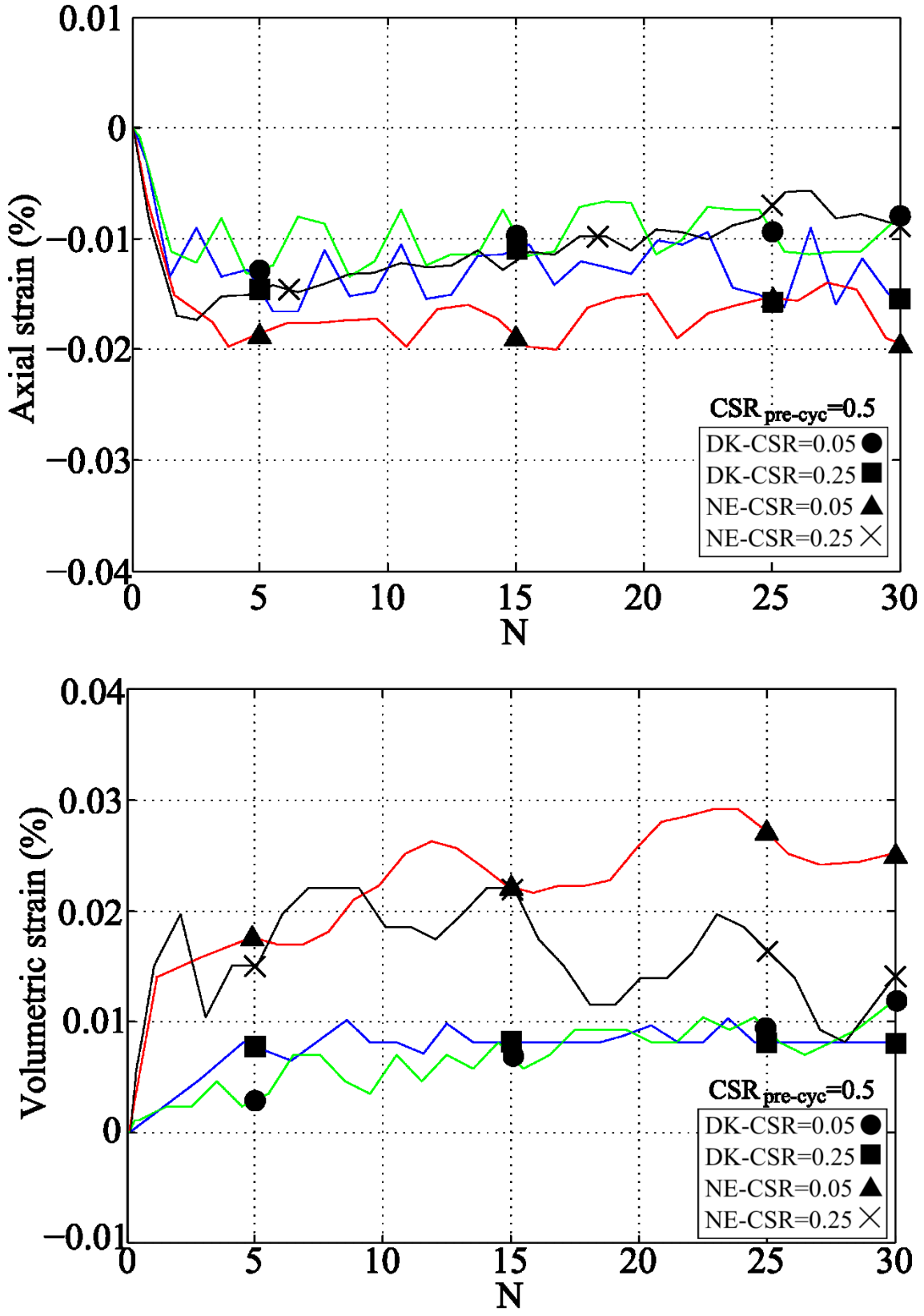


Figure 6-10 Accumulation of a) axial and b) volumetric strains under drained pre-cycling stage with CSR = 0.5 from tests that assessed the effect of pre-cycling on undrained cyclic response with low to medium CSRs.

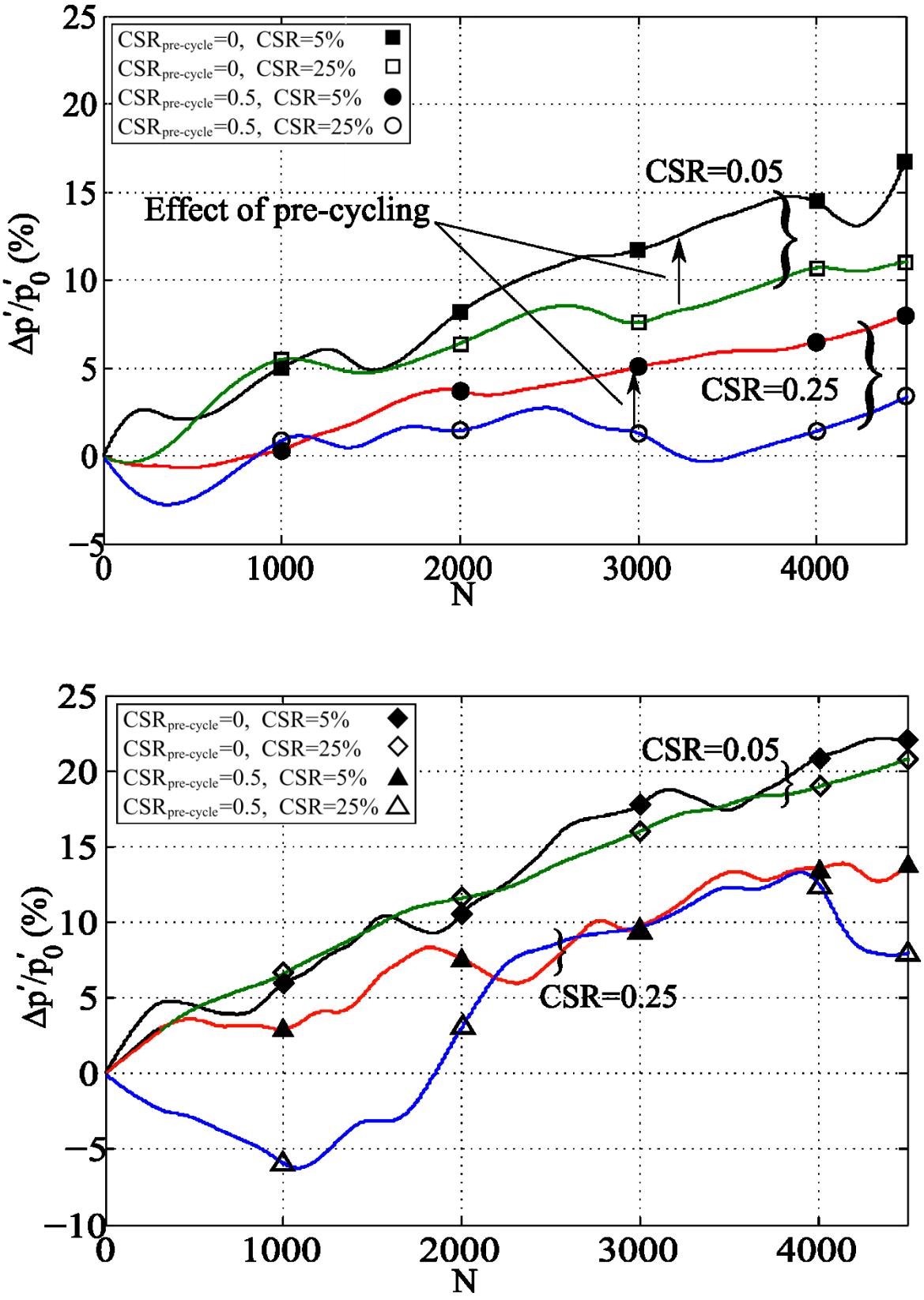


Figure 6-11 Effect of pre-cycling at point C (30 drained cycles with CSR = 0.5) on p′ drifts in undrained cyclic tests with low to medium CSRs.

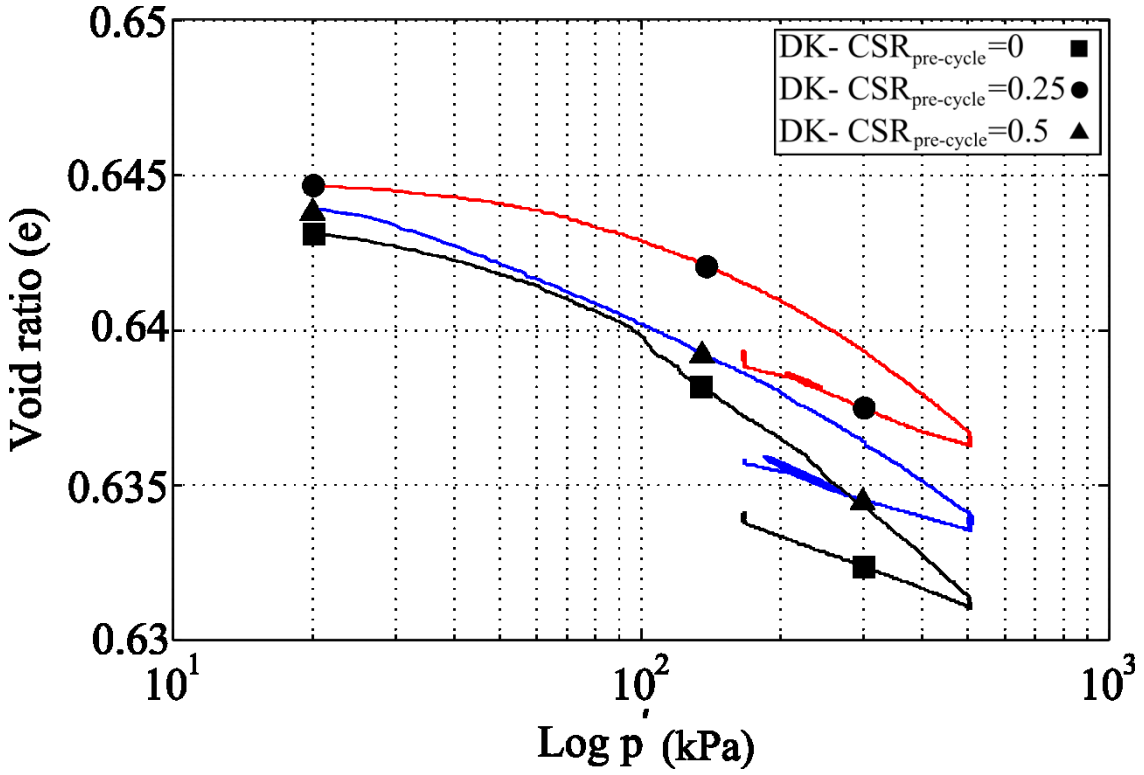


Figure 6-12 Void ratio changes during the pre-conditioning stage of Dunkerque tests that assessed the pre-cycling effect at point C with $CSR_{pre-cyc}$=0, 0.25 and 0.5 on undrained cyclic behaviour with high CSR=0.45.

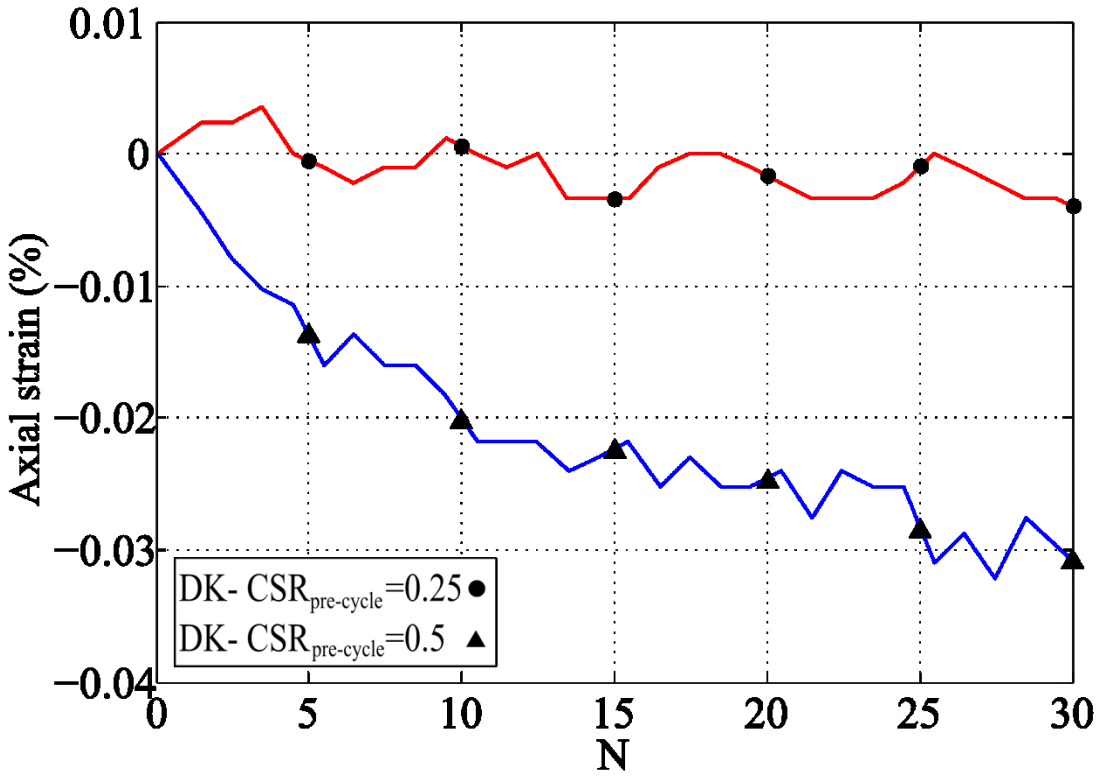


Figure 6-13 Accumulation of axial strains under 30 drained cycles at point C during the pre-cycling stage with $CSR_{pre-cyc}$=0.25 and 0.5 from tests that assessed the effect of pre-cycling on undrained cyclic response with high CSR=0.45.

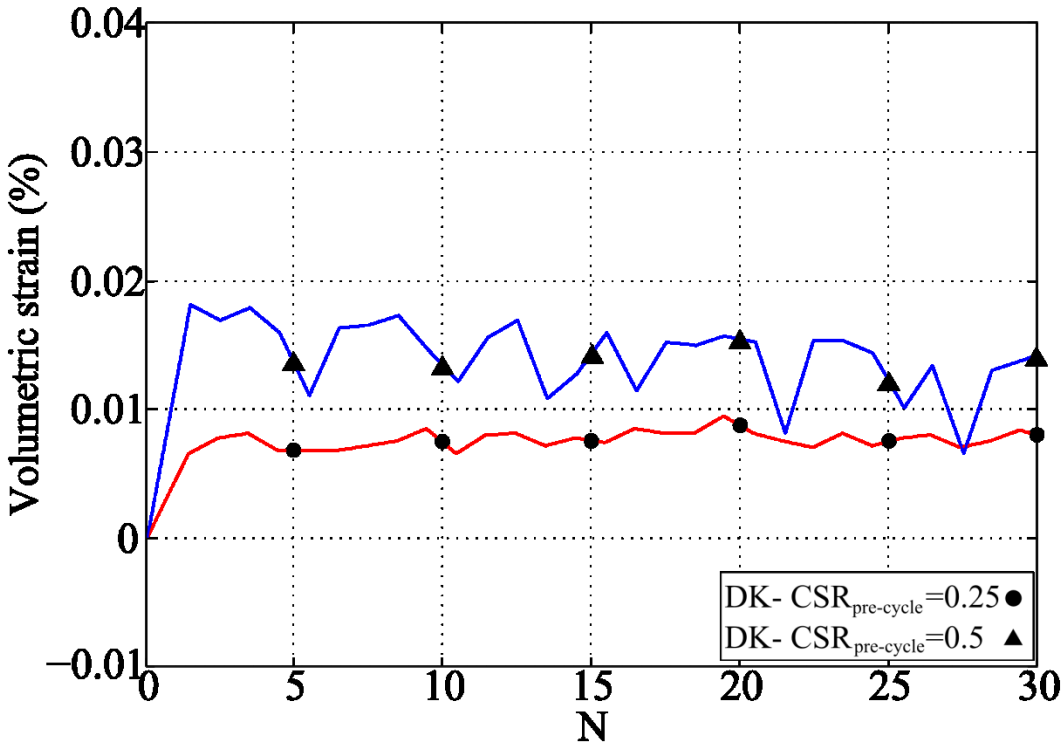


Figure 6-14 Accumulation of volumetric strains under 30 drained cycles at point C during the pre-cycling stage with $CSR_{pre-cyc}$=0.25 and 0.5 from tests that assessed the effect of pre-cycling on undrained cyclic response with high CSR=0.45.

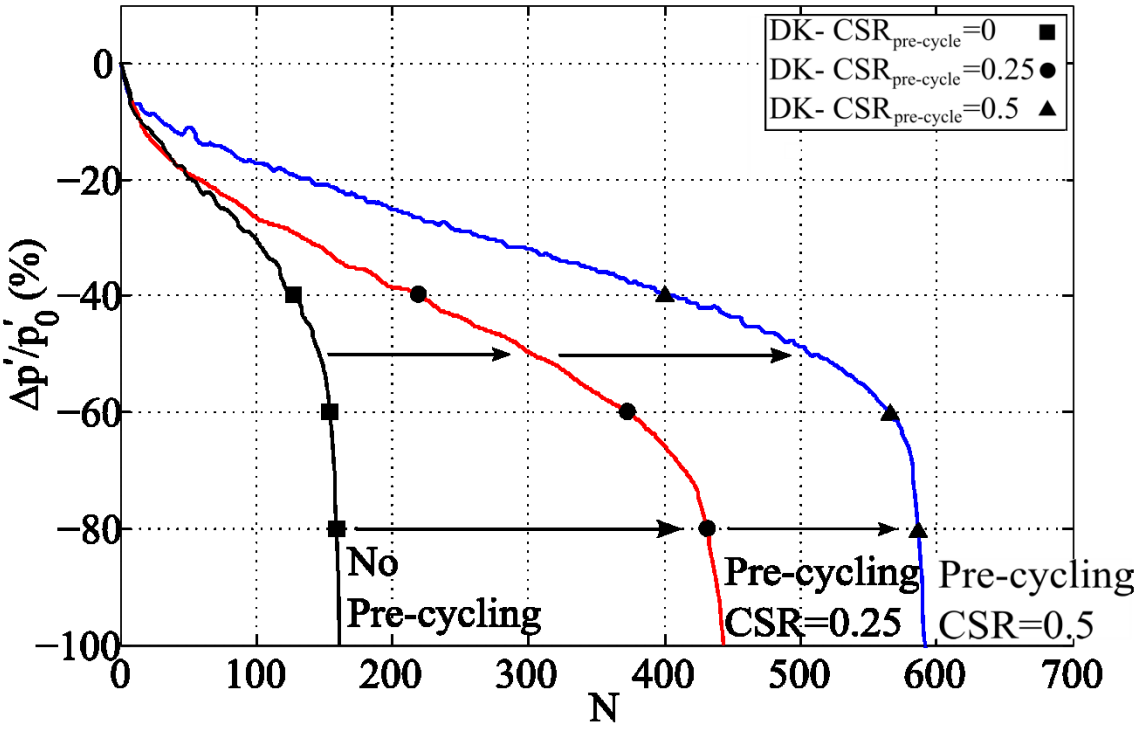


Figure 6-15 Effect of pre-cycling at point C (30 drained cycles with CSR=0, 0.25 and 0.5) on p′drifts observed under high CSR = 0.45 at mid-cycle (q = 50 kPa) points.

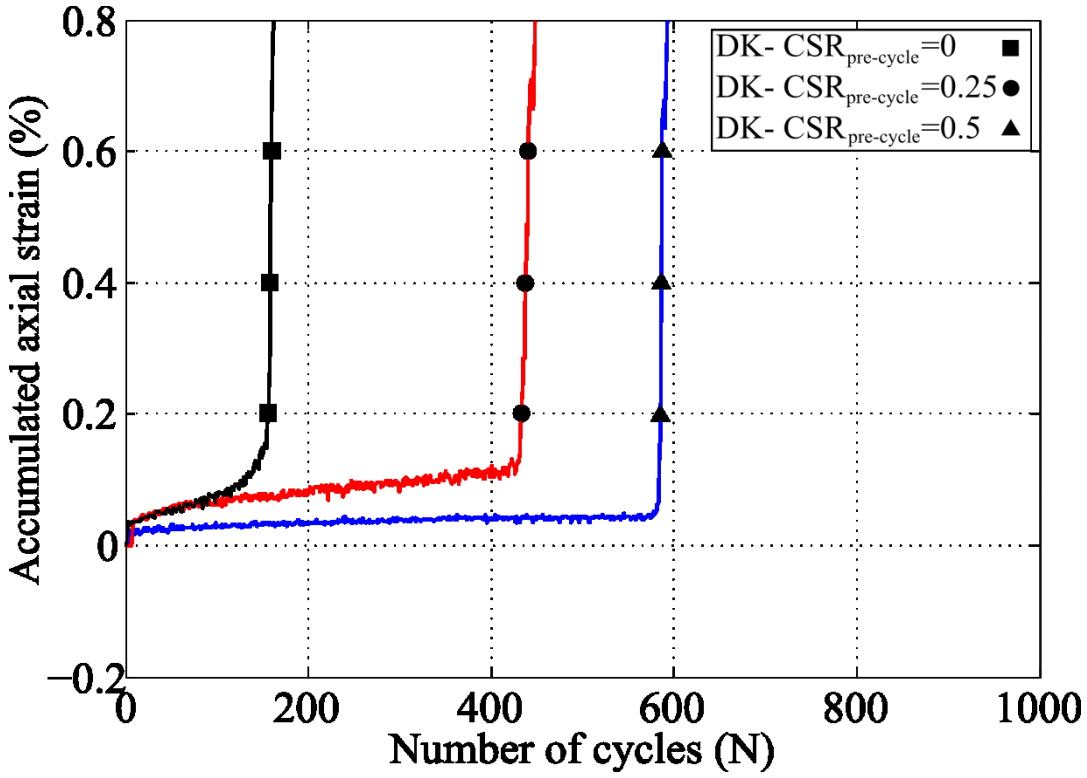


Figure 6-16 Effect of pre-cycling at point C (30 drained cycles with CSR = 0, 0.25 and 0.5) on accumulation of axial strains observed under high CSR = 0.45 at mid-cycle (q = 50 kPa) points.

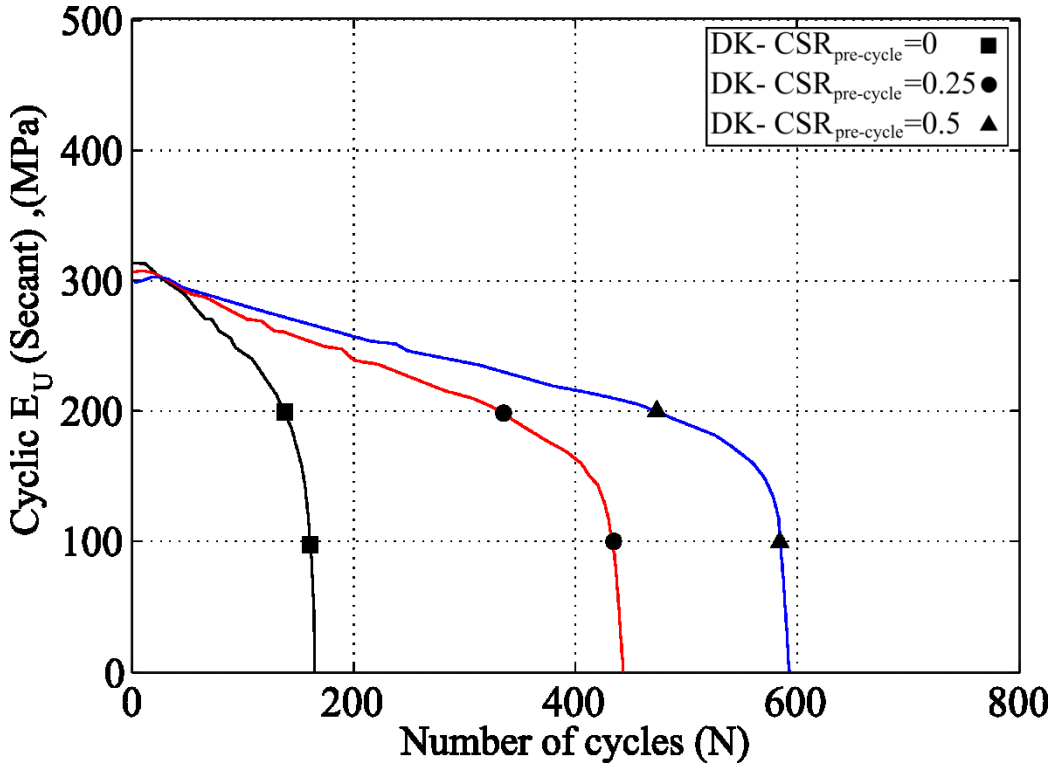


Figure 6-17 Effect of pre-cycling at point C (30 drained cycles with CSR = 0, 0.25 and 0.5) on undrained secant cyclic stiffness observed under high CSR = 0.45 at mid-cycle (q = 50 kPa) points.

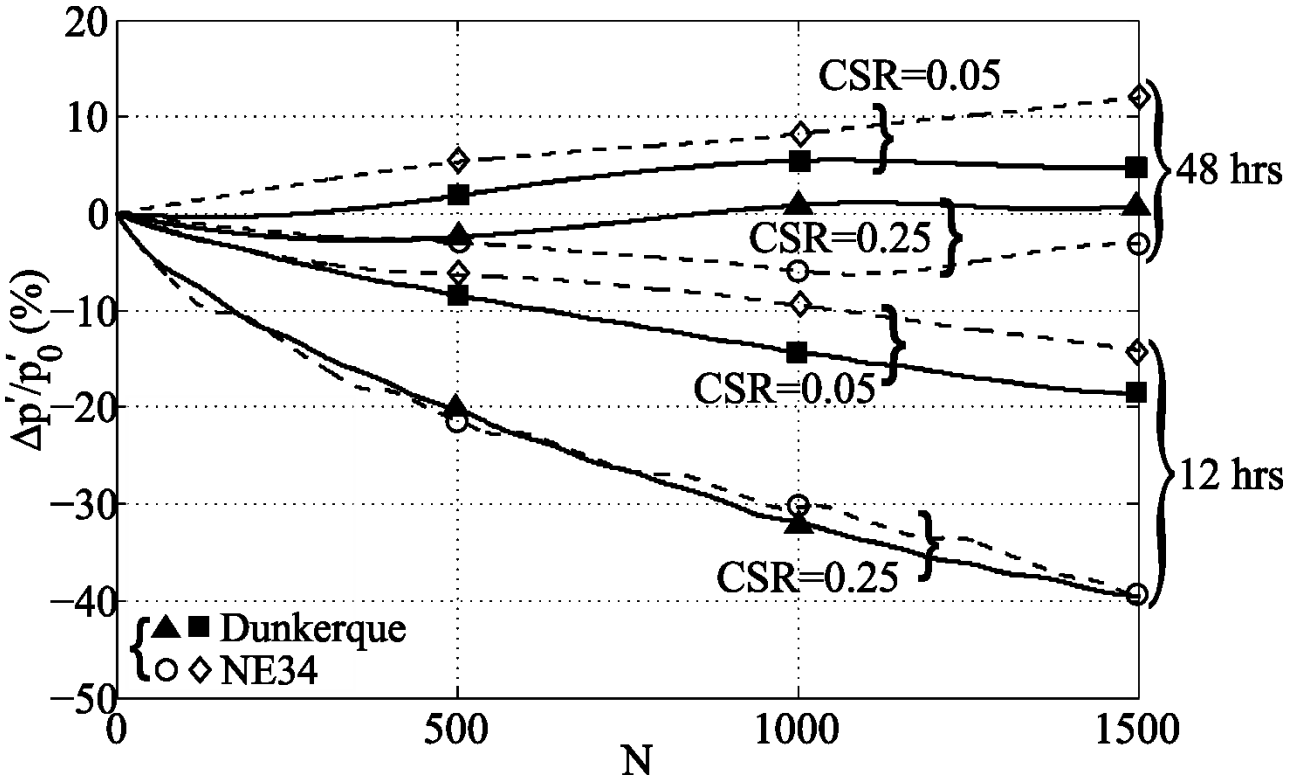


Figure 6-18 Effect of ageing time at points A and D on p′drifts under undrained cyclic loading at point D with low to medium CSRs.

CHAPTER 7

Main triaxial cyclic series to evaluate the axial cyclic response of piles

Introduction

This chapter presents the main results from the triaxial tests series designed to evaluate the axial cyclic responses of displacement piles in Dunkerque and NE34 sands. The following sections outline the mean effective stress degradation, accumulation of permanent strains, and cyclic stiffness degradation seen under undrained cyclic loading covering a wide range of cyclic amplitudes (q_{cyc}) and specified initial void ratios. All the tests followed the "standard" triaxial testing procedure whose development was outlined in chapter 6. Drained cyclic tests are also reported that investigated the shear and volumetric strain accumulation trends developed in triaxial tests that employed the same pre-conditioning procedure as the "standard" undrained tests.

7.1 Undrained "standard" cyclic tests

The standard testing procedure developed in chapter 6 was applied in dual series of triaxial cyclic tests on both sands each of which employed seven undrained CSR values as outlined in Table 7-1. As described earlier, the target initial void ratios were chosen to replicate the field conditions of field pile tests at Dunkerque (Jardine & Standing; 2000, 2012) and laboratory calibration chamber model pile tests on NE34 sand in Grenoble (Tsuha *et al.*, 2012). Samples

were prepared using the sample preparation technique explained in Chapter 4 and Table 7-1 lists initial void ratios of each test as established after sample set-up.

Table 7-1 List of undrained triaxial tests performed after "standard" pre-conditioning procedure.

Sand	Test Code	Pre-conditioning	CSR	e_0
Dunkerque	DK-S-05	Standard*	5	0.650
	DK-S-15	Standard	15	0.647
	DK-S-25	Standard	25	0.636
	DK-S-35	Standard	35	0.642
	DK-S-40	Standard	40	0.649
	DK-S-45	Standard	45	0.642
	DK-S-50	Standard	50	0.642
NE34	NE-S-05	Standard	5	0.639
	NE-S-15	Standard	15	0.640
	NE-S-25	Standard	25	0.642
	NE-S-35	Standard	35	0.643
	NE-S-45	Standard	45	0.643
	NE-S-55	Standard	55	0.637
	NE-S-65	Standard	65	0.646

* See chapter 6 for detailed description of the procedure

Results from pre-conditioning and cyclic stages are presented in the following sections.

7.1.1 Pre-conditioning

The “standard” consolidation-swelling path was applied in all tests with creep stages lasting for 48 hours after each stress path segment as shown in Figure 6-2. Specimens also experienced 30 drained pre-cycles with $CSR_{pre\text{-}cyc}$=0.5 at Point C in the swelling path before reaching to their final “equilibrium” pre-cycling state at Point D.

7.1.1.1 Consolidation and ageing stages

Figure 7-1 shows the samples’ void ratio changes developed during pre-conditioning in e:log(p′) space. Creeping involved contractive straining at Point B and a dilative response at Point D. The accumulations of vertical strains during these creep periods are shown in Figure 7-2 and Figure 7-3. As with the simpler “monotonic” tests discussed in Chapter 4, the

creep rates followed power-law relationships with time and, dropped to below 0.001%/hr for Dunkerque sand and 0.0002%/hr for NE34 sand after 48 hours of creep at Point B, and fell below to 0.0001%/hr for both sands after 48 hours of creep. As noted earlier, Dunkerque specimens develop higher creep rates than NE34 under similar conditions, probably due to the effects of $CaCO_3$ shell fragments that are absent from the clean processed NE34 sand.

7.1.1.2 Drained pre-cycles

All specimens experienced 30 large amplitude (CSR=0.5) drained cycles at Point C (Figure 6-8) as part of the "standard" pre-conditioning procedure to account for large installation cycles experienced by an element adjacent to a driven pile.

The volumetric (ε_v) and shear (ε_s) shear strains developed during pre-cycling are shown in Figure 7-4 and Figure 7-5, tracking the mid-cycle (q = 116.7kPa) points. As discussed in the last chapter, the straining tends to stabilise at N > 25. Both sands showed cotractant volumetric behaviour under the relatively large cycles applied but axial strains in direction of cycles were dilative.

7.1.2 Undrained cyclic response

The Undrained cyclic loading experiments conducted at seven CSR levels revealed three main styles of response in both sands: *Stable*, *Metastable* and *Unstable*. Each type of behaviour is discussed in the following paragraphs:

7.1.2.1 *Stable* response

Mean effective stress drifts: All Dunkerque and NE34 specimens cycled at CSR $\leq$ 0.25 showed gentle rises in their p′ values over 4500 cycles applied with cyclic stress paths shifting towards the right in q-p′as shown in Figure 7-6a. Figure **7-7** tracks the drift in p′ observed at mid-cycle (q = 50kPa) points and shows that specimens with CSR = 0.05 generated the largest increases in p′(of about 20%) for both sands, while specimens that experienced CSR = 0.25 showed the least p′gain (around 10%) over 4500 applied cycles. The

Stable tests' effective stress paths indicate that cyclic loading at CSR≤0.25 was beneficial and involved no degradation of the sands' load carrying capacity.

Accumulation of permanent strains:, The vertical strains plotted at the mid-cycle points shown in Figure 7-8 present insignificant permanent straining under the *Stable* load levels (CSR < 0.25) applied to both sands.

Accumulation of permanent strains under cycling can be understood using the kinematic multi-yield surface framework. As discussed in Chapter 5, cyclic load levels that keep the effective stress path inside the Y_2 locus do not generate considerable permanent strains even if they engage the linear Y_1 boundary surface. Using the axial effective stress against axial strain plots from cyclic tests with CSR=0.15 at first cycle (N=1), the Y_1 surfaces were located for both test sands as shown in Figure 7-12. Results show that while in CSR=0.05 tests stress and strain levels were kept inside the Y_1 surface, at higher CSR=0.15 and 0.25 they clearly passed the Y_1 range but since they stayed inside the Y_2 surface, no permanent strains were accumulated under cycling. Therefore the Y_2 surface can estimated to locate between CSR=0.25 and CSR=0.35 which was the first cyclic test that generated permanent strains as shown in Figure 7-13. Complete shape of the Y_1 and Y_2 surfaces can be found with more probe testing at different directions in the q-p′space.

Cyclic stiffness degradation: The associated trends for undrained cyclic secant stiffness E_U show insignificant degradation in cyclic stiffness values over 4500 cycles in *Stable* tests. The recorded strains are very small, close to the instrument's resolution, leading to some fluctuations in the E_U trends at low CSR ratios. The initial E_U values depend on the CSR levels imposed as all tests but the CSR=0.05 tests engaged the Y_1 surface leading to non-linear strain response under cyclic loading.

7.1.2.2 *Metastable* response

Metastable behaviour was generally observed in tests that applied CSRs between the lower limit of the *Stable* margin and an upper limit around that applied in the conditioning cycles imposed at Point C (0.5). The *Metastable* range was 0.30 < CSR < 0.45 for Dunkerque specimens and slightly greater, 0.30 < CSR < 0.55 for NE34 sand. These *Metastable* tests showed gradual decreases (<35%) in p′, which increased systematically with CSR, over their 4500 cycles, but did not develop full cyclic failure before tests terminated.

It should be noted that definition of *Metastable* response in laboratory tests and field and model pile tests presented in Chapter 3 have some differences. While in pile tests *Metastable* behaviour was referred to tests that showed modest rates of axial strain displacement which led to failure after between 100 to 1000 cycles, in triaxial (and later HCA) tests *Metastable* response defines cyclic tests that generated losses in p′and cyclic stiffness and also showed permanent accumulated strains but did not reach failure up to 4500 cycles applied. The reason for this difference in behaviour (beyond the *Stable* zone) is due to the different friction angles that control the failure envelope location. While in pile tests failure is controlled by the interface friction angle, δ′, (see Section 3.1.2) in laboratory single element tests failure is controlled by the peak friction angle, $\phi'_{peak,}$ as discussed in Section 2.3.2.1. Therefore, laboratory single element tests show higher resistance to cycling under similar load levels by reaching failure after higher number of cycles applied.

Mean effective stress drifts: The stress paths in q-p′space started to move towards the left during the first few cycles but tended to relatively modest rates of change at higher N values, as shown in Figure7-6b.The mid-cycle (q = 50 kPa) point p′ drifts shown in Figure **7-7** indicate direct links between the $\Delta p'/p'_0$ drifts and CSR for both sands.

Accumulation of permanent strains: The accumulation of vertical permanent strains with N shown in Figure 7-8 show the sharply rising impact of cycling at CSR > 0.40 levels that approaching the pre-conditioning $CSR_{pre\text{-}cyc}$=0.5 cyclic loading level.

Accumulations of permanent strains growth show that the cyclic stress paths (Figure 7-10) engaged and displaced the Y_2 surface under *Metastable* cycling. Therefore, as was discussed earlier, the initial location of Y_2 surface places between highest amplitude *Stable* (CSR=0.25) test and lowest amplitude *Metastable* (CSR=0.35) test as shown in Figure 7-13.

Cyclic stiffness degradation: The E_U degradation trends, shown in Figure 7-14, indicate only marginal decreases in the tests non-linear stiffness with N over the first 1000 cycles and steady conditions at higher N values. As in monotonic tests, the Dunkerque specimens showed lower cyclic stiffnesses than the equivalent NE34 experiments.

7.1.2.3 *Unstable* response

Fully *Unstable* conditions were achieved when CSR > 0.5 and > 0.6 for Dunkerque and NE34 specimens respectively, with cyclic failures developing within 1000 or fewer cycles.

Similar to *Metastable* behaviour, definition of *Unstable* response in laboratory tests is slightly different with field and model pile's *Unstable* response definition. Although in both cases cycling leads to failure, but in *Unstable* pile tests failure is reached within 100 cycles while in *Unstable* triaxial tests failure is reached up to around 1000 cycles. The higher resistance observed in laboratory tests is as discussed earlier due to different failure criterions.

Mean effective stress drifts: Under these conditions, the stress paths followed in q-p′ space (Figure 7-6c) shifted rapidly towards the left without stabilising until they reached the full failure by hitting the peak failure envelope measured from monotonic tests. Further cycles led to a butterfly-shaped "cyclic-mobility" effective stress path, moving along the failure envelope. The specimens that developed cyclic-mobility failures were able to hold the loads

applied under further cycling, which distinguish this pattern of failure from that of looser specimens that can liquefy.

Accumulation of permanent strains: The specimens experienced rapidly growing compressive vertical permanent strains until the point of failure, as shown in Figure 7-8.

The stress-strain loops from specified n^{th} cycles, shown in Figure 7-11, illustrate fully non-linear behaviour with completely open load-unload loops under the high CSR levels imposed. The effective stress paths clearly engaged Y_2 surface at an early stage in their first cycles as shown in Figure 7-13.

Cyclic stiffness degradation: The cyclic E_U trends (Figure 7-14) show very sharp falls as cycling continued, which eventually led to complete loss of stiffness when the cyclic-mobility failures were reached. The initial E_U values fell with increasing CSR values indicating the progression of the non-linear response under the growing cyclic loading levels applied.

Comparison of cyclic response between two test sands: Comparison between cyclic responses of two test sands show that their behaviour at low level cycling was almost identical with both sands giving the threshold for the *Stable-Metastable* response at CSR levels between 0.25 and 0.35. However, under intermediate and high level cycling Dunkerque sand showed lower cyclic resistance with *Metastable* tests showing higher levels of effective stress degradation and *Unstable* tests reaching failure at lower N_f values. This is particularly interesting since small strain stiffness and large strain strength characteristics of both tests sands were very similar as was found in monotonic tests reported in Chapter 5. However, as was found in high pressure oedometer tests reported in Figure 5-12, Dunkerque sand shows higher levels of crushing under high level loading. This might be the reason for Dunkerque sand's lower cyclic resistance at higher cyclic loading levels. This idea can be further investigated by comparing the particle size grading of the specimens prior and after testing

using high quality QicPic laser-based apparatus. Result can determine whether there is a correlation between cyclic resistance and crushing levels of the specimens.

7.2 Undrained "standard" cyclic tests at other void ratios

To study the effect of initial sand state on cyclic resistance, experiments were undertaken with looser (D_r = 50%) and denser (D_r = 90%) specimens and their responses compared to standard samples prepared at D_r=72% and 75%. All other aspects of the tests followed the "standard" pre-conditioning procedure. The initial states of the three types of sample and their location relative to the critical state lines obtained from monotonic tests (Chapter5) are shown in e:log(p′) space in Figure 7-15.

Table 7-2 presents a list of tests performed with loose and dense initial relative densities:

Table 7-2 List of undrained triaxial tests performed with "standard" pre-conditioning

Sand	Test Code	Pre-conditioning	CSR	e_0
Dunkerque	DK-D-35	Standard*	0.35	0.617
	DK-L-35	Standard	0.35	0.735
NE34	NE-D-35	Standard	0.35	0.582
	NE-L-35	Standard	0.35	0.725

* See chapter 6 for detailed description of the procedure

Results from these tests are presented in the following paragraphs:

7.2.1 Pre-conditioning

The void ratio changes during the "standard" pre-conditioning procedure are shown in e:log(p′) space for all specimens in Figure 7-16. The looser samples showed higher compressibility in comparison with the denser samples for both sands. Dunkerque specimens again showed greater compressibility than their NE34 equivalents probably due to their shell fragment fractions. As presented in Table 7-3, the compressibility, λ, of the specimens increases with p′and e reflecting their current states.

Table 7-3 Coefficients of compressibility and swelling achieved at different void ratio and p′ values.

Sand	Density	e_0	λ		
			20-100	100-300	300-500
Dunkerque	Loose	0.73	6.7×10^{-4}	1.3×10^{-3}	1.7×10^{-3}
	Standard	0.64	6.1×10^{-4}	9.3×10^{-4}	1.2×10^{-3}
	Dense	0.61	6.0×10^{-4}	9.2×10^{-4}	1.0×10^{-3}
NE34	Loose	0.72	6.5×10^{-4}	1.1×10^{-3}	1.4×10^{-3}
	Standard	0.64	6.3×10^{-4}	9.0×10^{-4}	1.1×10^{-3}
	Dense	0.58	6.2×10^{-4}	9.0×10^{-4}	1.0×10^{-3}

As part of the "standard" pre-conditioning, 48 hours of creep was allowed after consolidation and swelling stages. The accumulations of axial strain during creeping at Point B (see Figure 6-8) are shown in Figure 7-17. As in previous tests, the creep strain rates were reduced markedly with time. Loose samples showed more creep straining than dense and NE34 specimens less than equivalent Dunkerque specimens. As noted earlier, the power-law equation (Equation 5-2) proposed by Kuwano (1999) can match the behaviour and the best fitting parameters obtained for different density states are presented in Table 7-4.

Table 7-4 Constants obtained from power-law fitting to creep trends at different void ratios

Sand	Initial D_r	e_0	A_{cre}	B_{cre}
Dunkerque	Loose	0.73	0.0007	-0.49
	Standard	0.64	0.0009	-0.64
	Dense	0.61	0.0011	-0.76
NE34	Loose	0.72	0.0004	-0.55
	Standard	0.64	0.0009	-0.70
	Dense	0.58	0.0009	-0.75

The swelling creep at Point D (Figure 6-2) also extended for 48 hours. The creep rates over this stage were far smaller than at Point B and were hard to measure reliably with the systems deployed.

7.2.2 Undrained cyclic response

After applying the "standard" pre-conditioning procedure, all specimens were cycled undrained with constant CSR = 0.35 up to maximum 4500 cycles, maintaining a cyclic period of 1 cycles/min.

Mean effective stress drifts: The q-p′stress paths followed and mean effective stress trends at mid-cycle points (q = 50 kPa) points are shown in Figure 7-18 and Figure 7-19. The dense specimens manifested greater resistances to cycling than the "standard" density specimens, showing smaller p′ reductions with Dunkerque sand and generating even small positive p′ changes in NE34 specimen. However, loose specimens manifested markedly poorer cyclic behaviour. The Dunkerque and NE34 specimens both showed rapid reductions in p′with their effective stress paths moving toward the failure line rapidly and developing full triaxial cyclic failures after 1460 cycles and 1695 cycles in the NE34 and Dunkerque specimens respectively. Cycling applied after the onset of cyclic-mobility led to butterfly shaped effective stress paths in q-p′space, similar to those seen in standard tests.

Accumulation of permanent strains: The accumulation of axial strains during the cycling stages are shown in Figure 7-20. The dense NE34 specimen that generated positive p′trends developed small tensile axial strains while the dense Dunkerque specimen that showed negative p′trends showed limited compressive axial strains. The loose specimens that reached failure after 1460 and 1695 cycles showed large rates of accumulated compressive straining as they moved towards their cyclic failure conditions.

These supplementary tests indicate the critical importance of sand state (that is distance from critical state line) on its cyclic resistance, as emphasised by Seed & Lee (1966), Ishihara (1975) and Tatsouka *et al.* (1986). The effects of reducing the initial density were more

marked than those of void ratio reductions. The boundary of the Y_2 surface (or "no effect" threshold) is highly influenced by state as well as stress history and ageing.

Cyclic stiffness degradation: The variations of secant undrained stiffness, E_U, developed during cyclic stages are shown in Figure 7-21. The dense Dunkerque specimen's stiffness dropped by ≈15% over the first 500 cycles, reaching a steady state afterwards, while the corresponding NE34 specimen showed almost no reduction in stiffness. The stiffnesses of the loose specimens dropped rapidly as they moved towards failure.

7.3 Drained cyclic tests with "standard" pre-conditioning

As discussed in Chapter 6, the "standard" procedure involving undrained cyclic tests was designed to model the boundary conditions of a soil element adjacent to a driven pile subjected to axial loading. The constant volume undrained testing was chosen as a conservative approach by assuming infinite K_{CNS} in place of any failure constant normal stiffness (CNS). Results from these tests provided information regarding the p′drifts under cycling which are correlated later with the σ'_r changes that can be expected around the pile under cyclic loading (see Chapter 9). Permanent strain accumulation and undrained cyclic stiffness degradation trends were also obtained. However, the data from undrained tests can only provide information about one strain invariant under constant volume conditions. In order to obtain more information about straining under cyclic loading additional drained tests were performed that could evolution of both volume and shear straining under cyclic loading.

To achieve this, six cyclic drained tests were performed after applying the "standard" pre-conditioning procedures. Table 7-5 presents the initial and final void ratios obtained and the cyclic parameters applied in each test. The CSR=0.05 and 0.25 tests had cyclic periods= 1cycle/min while the CSR=0.45 tests were cycled at 0.67cycle/min.

Table 7-5 Details from drained cyclic tests with "standard" pre-conditioning procedure

Sand	Test code	Pre-conditioning	CSR	e_0	e_c*
Dunkerque	DK-D-05	Standard	5	0.642	0.640
	DK-D-25	Standard	25	0.638	0.636
	DK-D-45	Standard	45	0.641	0.638
NE34	NE-D-05	Standard	5	0.646	0.642
	NE-D-25	Standard	25	0.640	0.637
	NE-D-45	Standard	45	0.636	0.633

* After end of pre-conditioning

Accumulation of permanent strains: The axial, radial, shear and volumetric permanent strains at mid-cycle (q = 50 kPa) points are shown in Figure 7-22, 7-23, 7-24 and 7-25 from all tests. Both NE34 and Dunkerque specimens showed almost no accumulation of axial or radial strains under CSR=0.05, with strains remaining below 0.005% over 3 days of cycling up to 4500 cycles. The stress-strain loops (Figure 7-26a&b) indicate that the stress states remained within the initial Y_2 locus. The CSR= 0.25 tests accumulated relatively small tensile axial and compressive radial strains, suggesting that the stress-strain loops (Figure 7-26c&d) were just engaging the Y_2 surface..

The two specimens subjected to the larger CSR = 0.45 cyclic amplitudes showed markedly greater straining with tensile axial and compressive radial strains of up to -0.11% and 0.12% respectively under 4500 cycles leading to significant compressive volume straining. The rates of strain accumulation reduced as cycling continued. The stress-strain loops (Figure 7-26e&f) had clearly engaged the Y_2 surfaces leading to a marked change in the patterns of cyclic straining, that is compatible by the reducing mean effective stress response seen in equivalent undrained tests.

Cyclic stiffness degradation: Secant cyclic vertical stiffnesses, E'_v, were calculated for each cycle by finding the slope between the maximum and minimum stress points in σ'_v:ε_1 space. Figure 7-27 shows how E'_v varied with N for all the drained tests showing modest reductions

(≈10%) over the first 500 cycles before reaching steady states, even in the high amplitude (CSR=0.45) tests.

7.4 Comparison between drained and undrained tests

Results from both drained and undrained tests showed that a cyclic strain threshold exists below which no volumetric strain is accumulated in drained tests and no mean effective stress drift is generated in undrained tests. In both cases this strain threshold correlated with the Y_2 surface from the multi-yield kinematic surface model obtained from monotonic tests (which were reported in chapter 5).

For CSR levels above the Y_2 'no effect' threshold, undrained specimens generated negative mean effective stress drifts, which correlates with a net tendency for contraction as was observed in drained tests. Closer inspection of the stress paths followed in q-p′ space from undrained tests shows that during loading, p′increases indicating a tendency for dilation under compressive loading and reductions on unloading (or extension) when the sands show their tendency to contract. However, the drops in p′on the unloading (extension) section outweigh the increases observed during loading, leading to a net drift towards contraction.

7.5 Conclusions and remarks

This chapter presents the behaviour seen in a wide range of undrained triaxial experiments that followed the "standard" procedure developed in Chapter 6. Mean effective stress drifts, accumulation of permanent strain and cyclic stiffness drifts were tracked in tests that applied with different CSR and initial void ratios. The outcomes from additional series of drained triaxial tests following "standard" pre-conditioning and initial void ratios were presented. The accumulations of axial, radial, shear strain invariant and volumetric strains were presented as were the effective stiffness degradations under different CSR levels.

The following conclusions were made:

1- The Undrained cyclic responses of "standard" pre-conditioned Dunkerque and NE 34 sand specimens were broadly comparable, sharing similar sensitives to the CSR values applied.

2- Tests conducted with q_{mean}/p'_0 = 0.3 and CSR up to 0.3 were fully *Stable* and could show mild increases in p′ and no drift in permanent displacements, inferring matching improvements in pile shaft capacity. However, tests with CSRs exceeding 0.5 to 0.6 for Dunkerque and NE34 respectively could be rapidly *Unstable*. *Metastable* conditions applied between these limits in cases where hundreds of cycles could be applied without failure occurring, but with some cyclic damage and permanent displacement growth. The two sands' cyclic stiffnesses improved marginally under *Stable* conditions, degraded rapidly in *Unstable* tests but showed only marginal losses under *Metastable* cycling.

3- The main sets of triaxial specimens were prepared with relative densities of 72% and 79% for the NE34 and Dunkerque sands respectively. Additional tests mild improvement in cyclic response with increased initial relative density. However, samples prepared at significantly lower D_r values showed far greater cyclic degradation. The sands' initial relative densities (or state parameters) are highly influential and must be matched to in-situ values to achieve meaningful results.

4- The drained cycling on "standard" pre-conditioned specimens showed that low to moderate (CSR = 0.05 to 0.25) cyclic loading led to either immeasurably small strains or dilative volumetric drifts at higher CSRs or The amount of permanent strains were directly related to the CSR values applied and strain accumulation rates dropped as cycling continued.

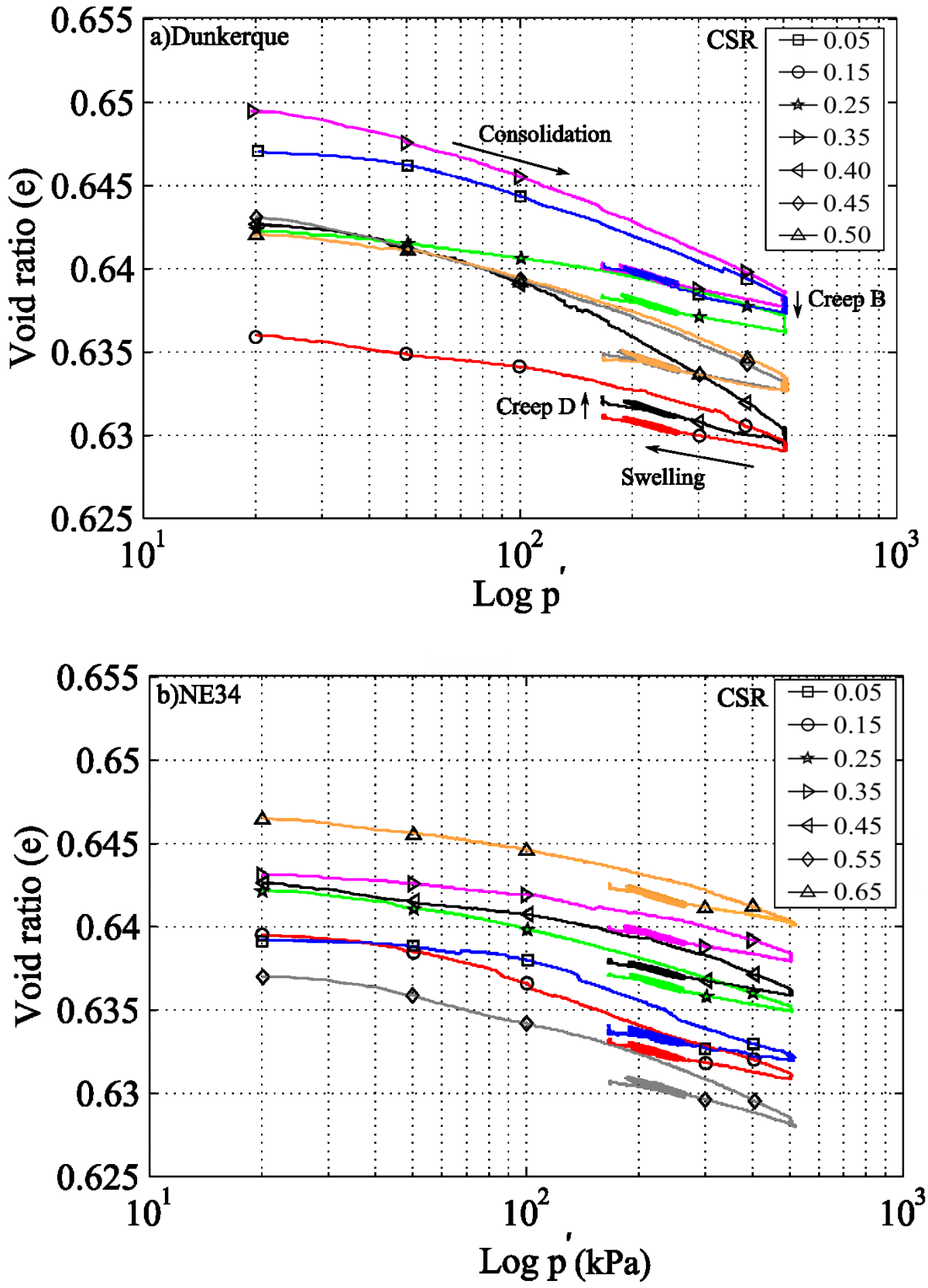


Figure 7-1 Void ratio changes during the "standard" pre-conditioning procedure on a) Dunkerque and b) NE34 sands prior to applying Undrained cyclic loads at different CSR values. e_0 target=0.64.

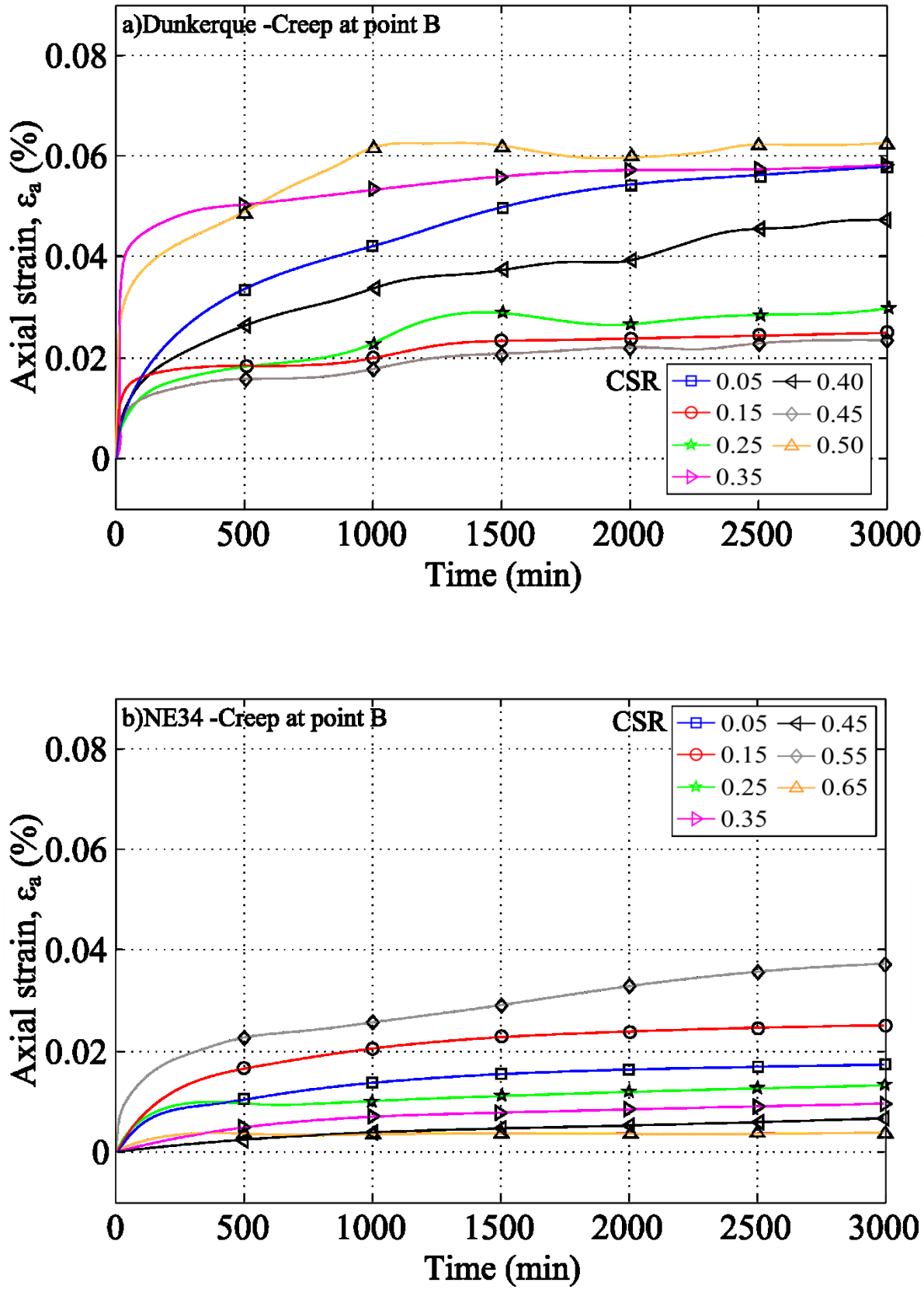


Figure 7-2 Axial straining during 48 hours of creep at point B after consolidation on a) Dunkerque and b) NE34 as part of the "standard" pre-conditioning procedure prior to applying Undrained cyclic loads at different CSR values. e_0=0.64.

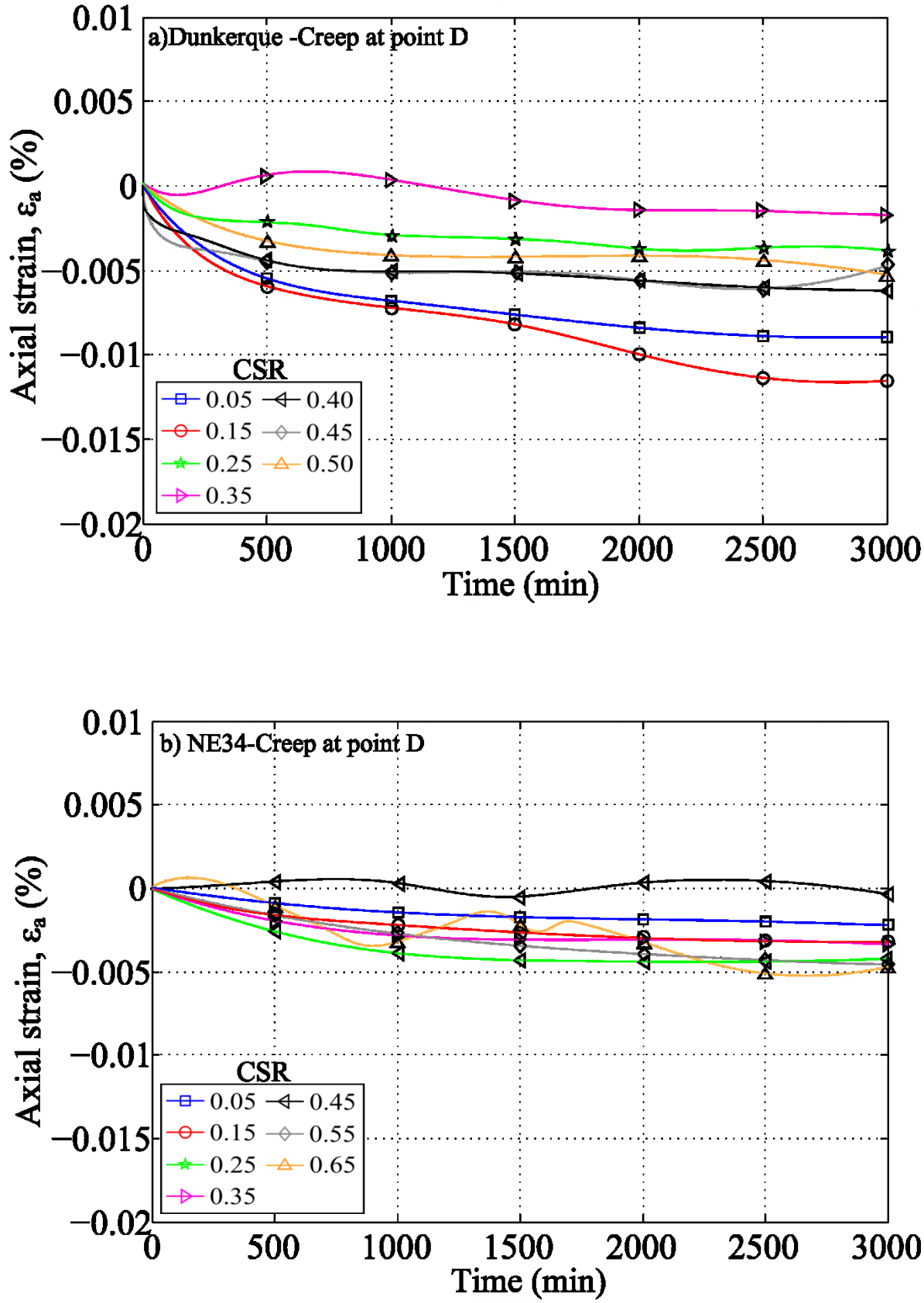


Figure 7-3 Axial straining during 48 hours of creep at point D after swelling on a) Dunkerque and b) NE34 as part of the "standard" pre-conditioning procedure prior to applying Undrained cyclic loads at different CSR values. e_0=0.64.

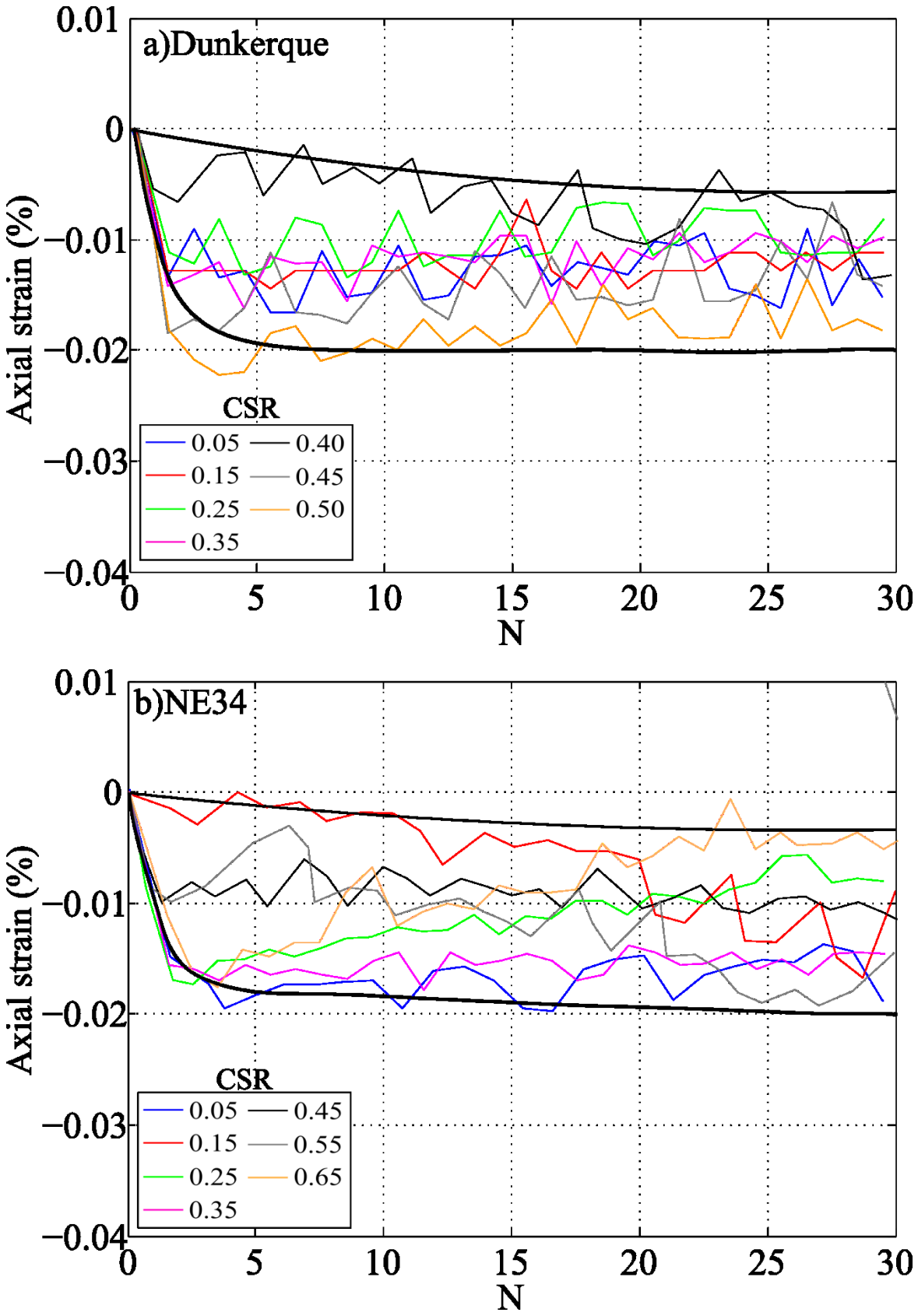


Figure 7-4 Accumulation of axial strains under drained pre-cycling at point C on a) Dunkerque and b) NE34 as part of the "standard" pre-conditioning procedure prior to applying Undrained cyclic loads at different CSR values. e_0 =0.64. $CSR_{pre\text{-}cycle}$=0.5

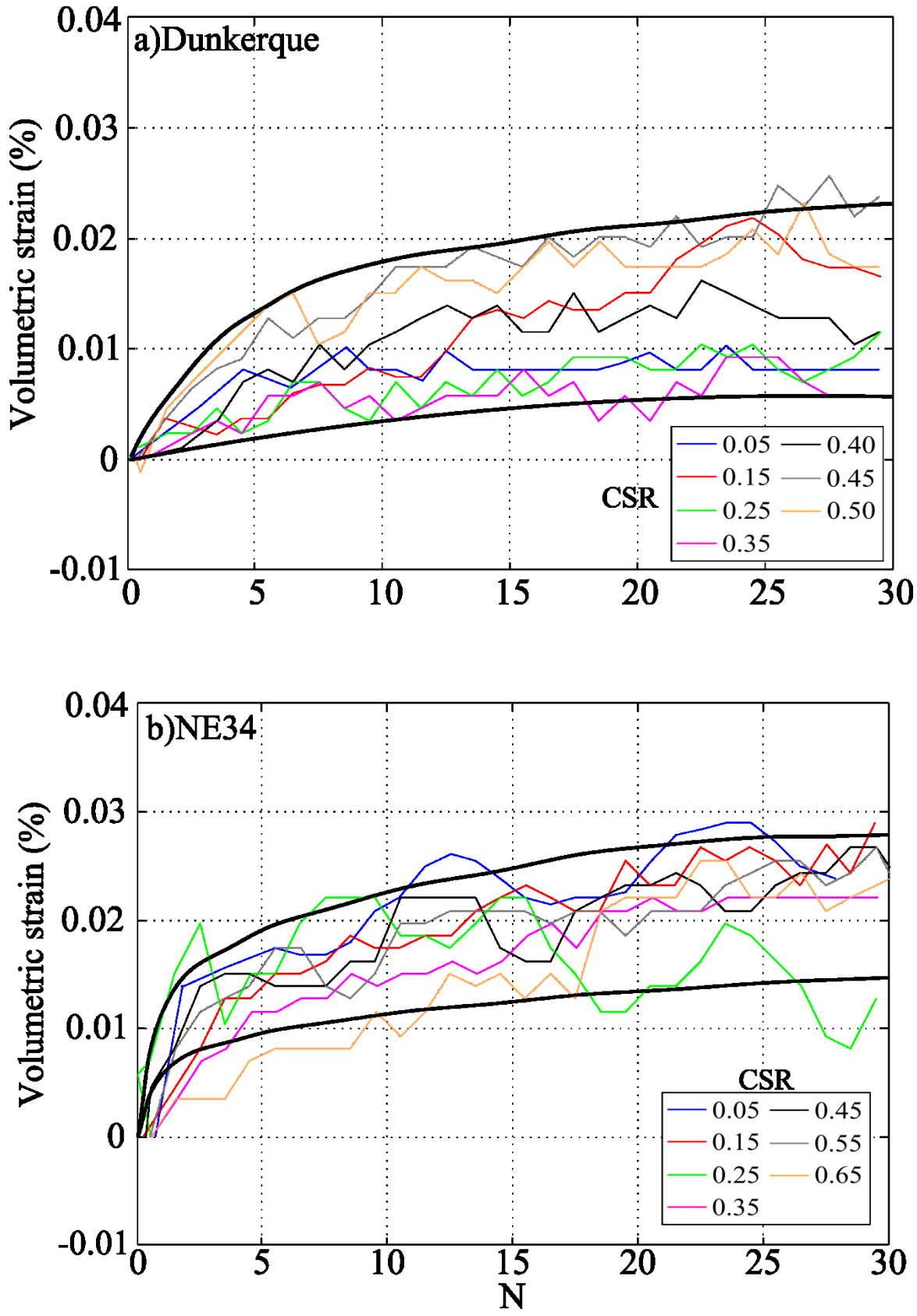


Figure 7-5 Accumulation of volumetric strains under drained pre-cycling at point C on a) Dunkerque and b) NE34 as part of the "standard" pre-conditioning procedure prior to applying Undrained cyclic loads at different CSR values. e_0=0.64. $CSR_{pre\text{-}cycle}$=0.5.

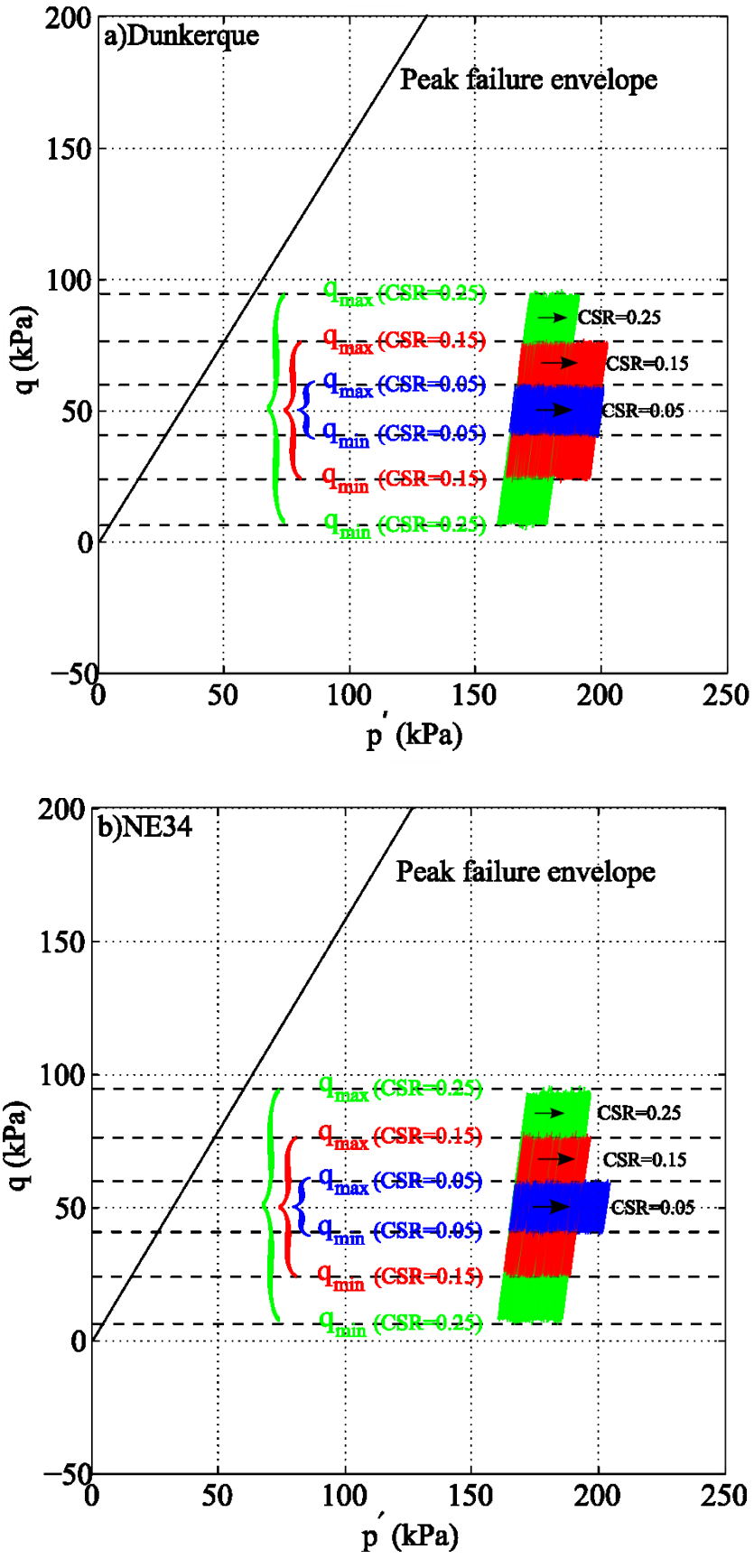


Figure 7-6a Stress paths followed in "*Stable*" tests in q-p′ space from "standard" pre-conditioned a) Dunkerque and b) NE34 sands at CSR levels up to 0.25.

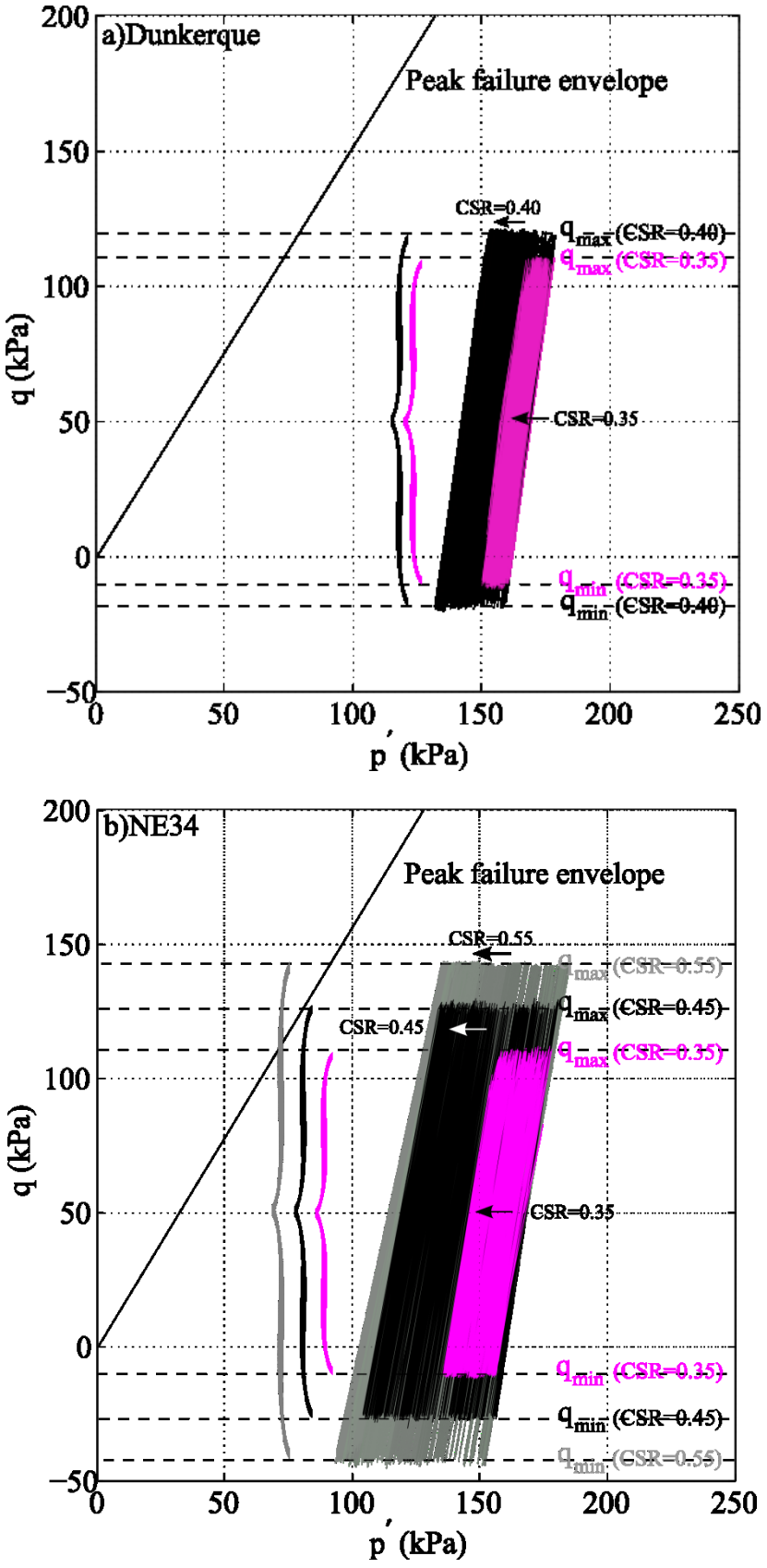


Figure 7-6b Stress paths followed in *Metastable* tests in q-p′space from "standard" pre-conditioned a) Dunkerque and b) NE34 sands at CSR levels up to 0.40 for Dunkerque and 0.55 for NE34 specimens.

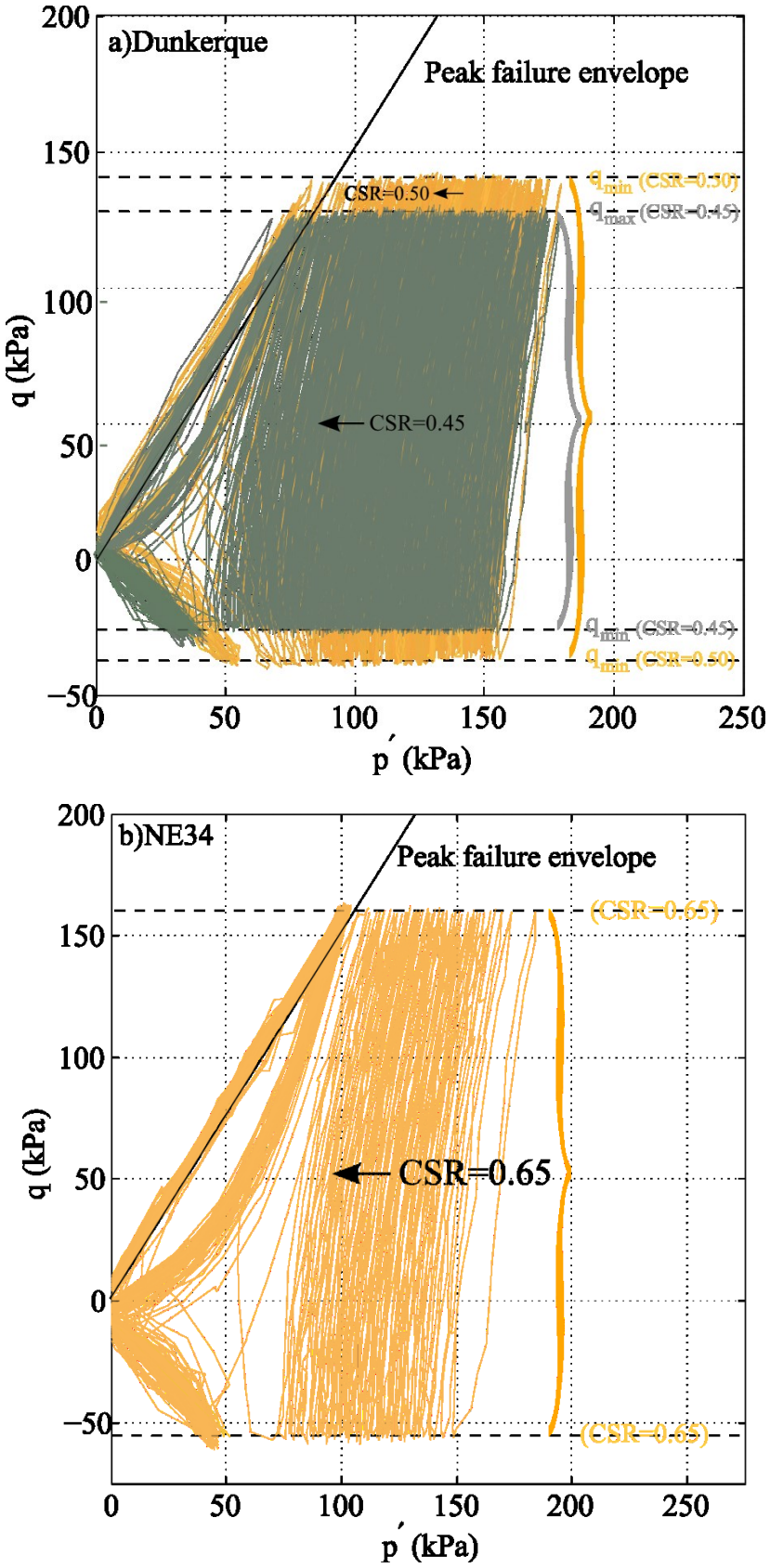


Figure 7-6c Stress paths followed in *Unstable* tests in q-p′space from "standard" pre-conditioned a) Dunkerque and b) NE34 sands at CSR levels above 0.40 for Dunkerque and 0.55 for NE34 specimens.

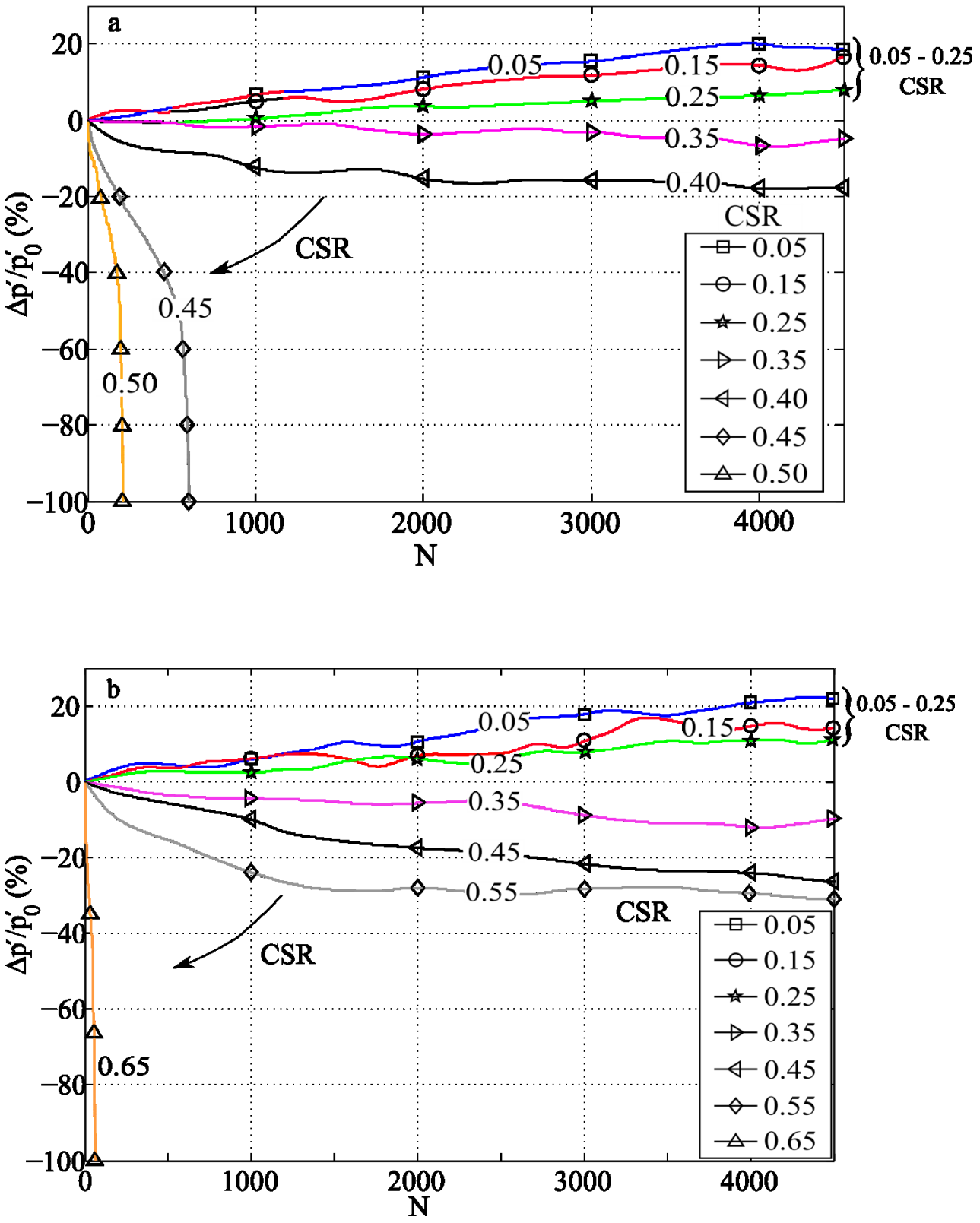


Figure 7-7 Effect of CSR on mean effective stress drifts under undrained cycling at Point D for a) Dunkerque and b) NE34 specimens after standard consolidation, conditioning cycles and ageing stages. All samples prepared to e_0=0.64

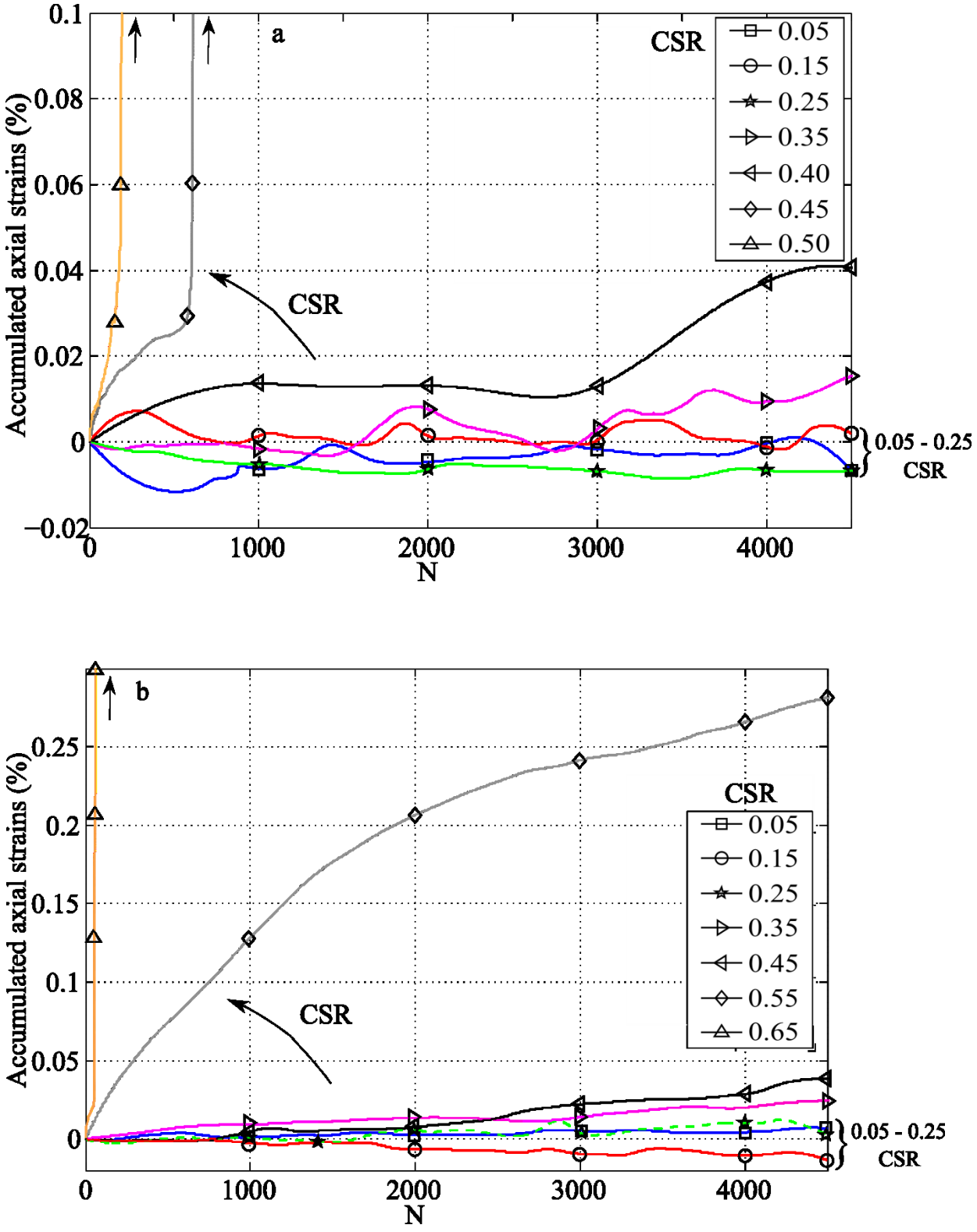


Figure 7-8 Effect of CSR on strain accumulation under undrained cycling at Point D for a) Dunkerque and b) NE34 specimens after standard consolidation, conditioning cycles and ageing stages. All samples prepared to e0=0.64

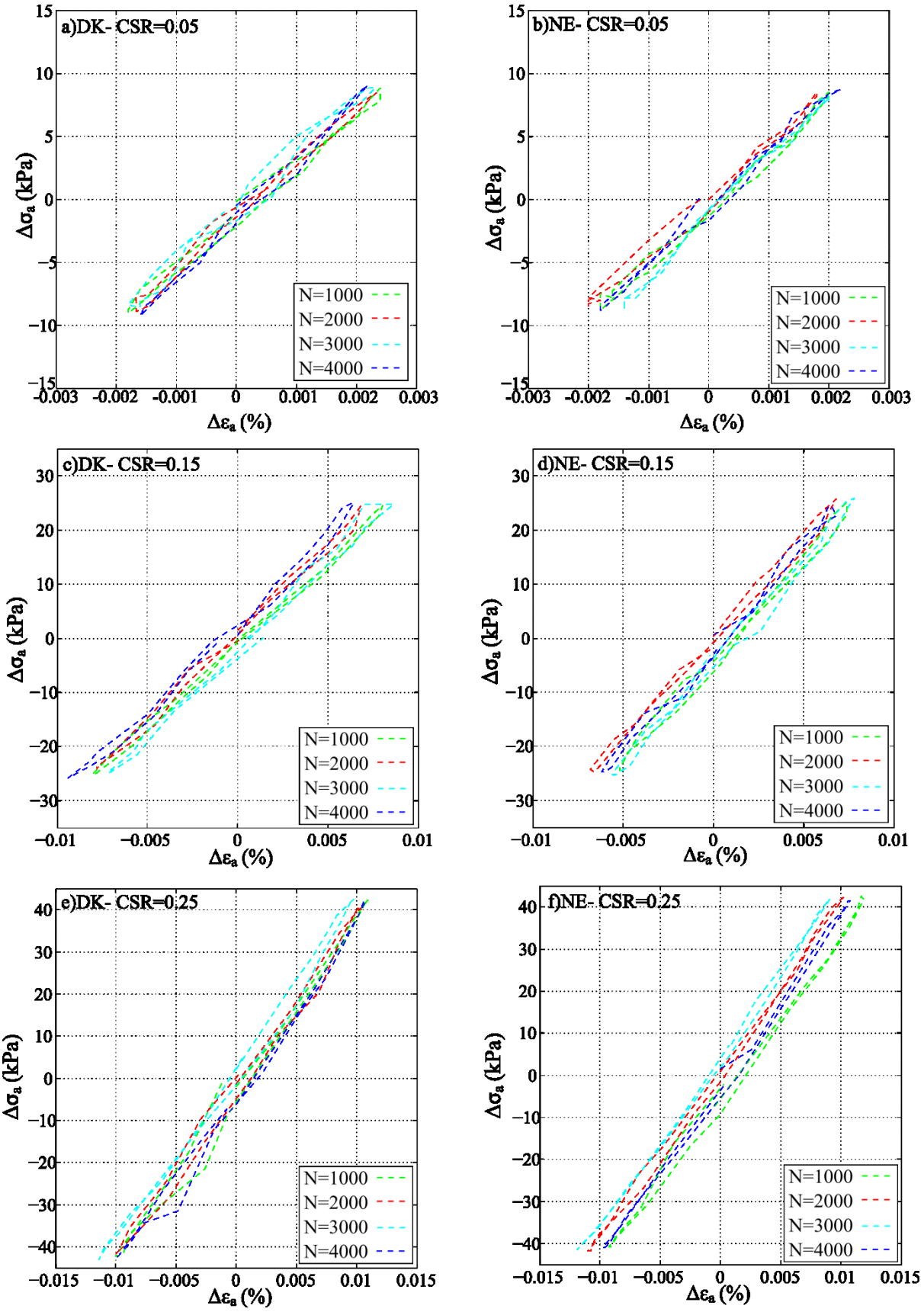


Figure 7-9 Stress-strain loops of specified nth cycles from undrained tests with "standard" pre-conditioning and *Stable* response.

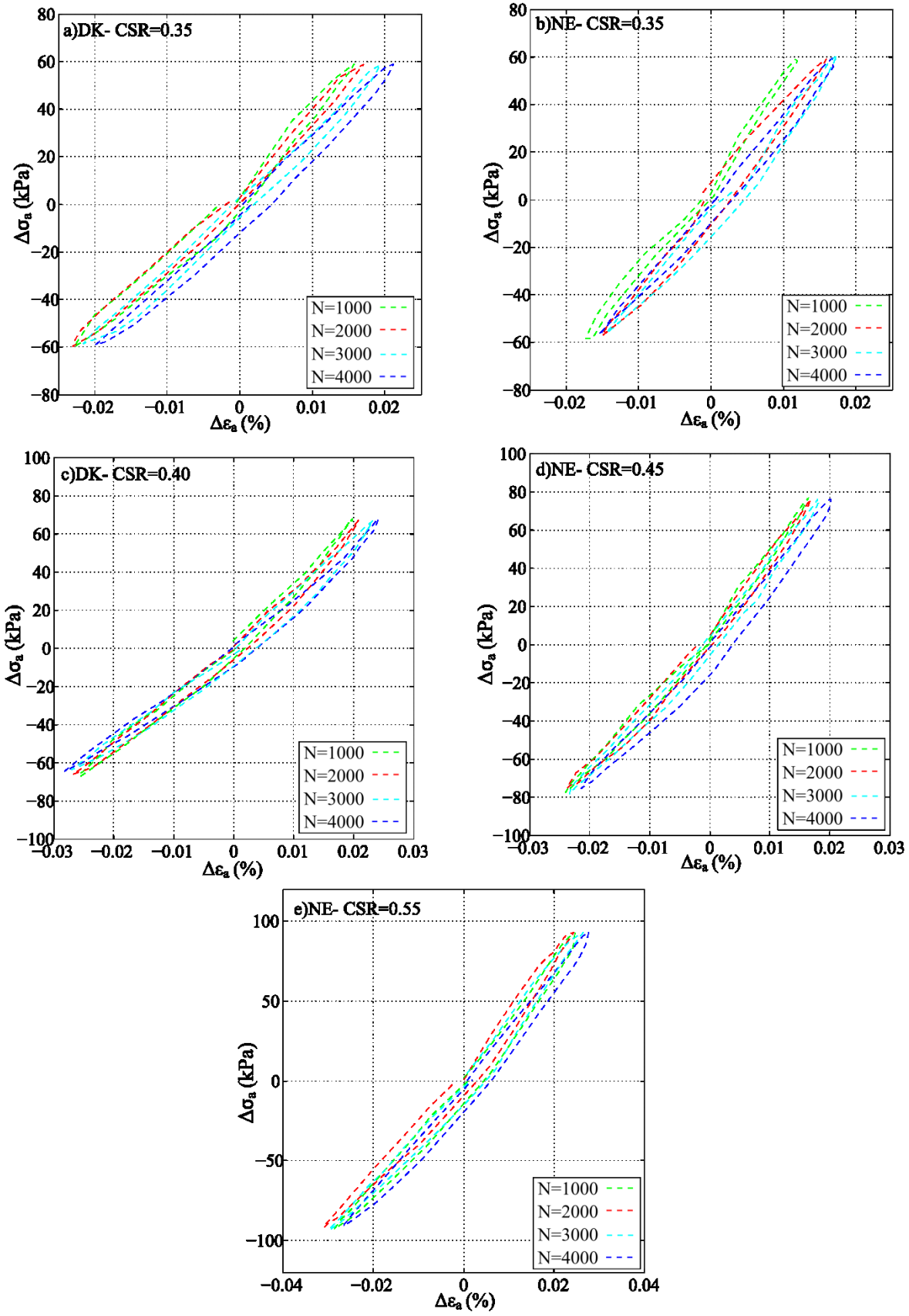


Figure 7-10 Stress-strain loops of specified nth cycles from undrained tests with "standard" pre-conditioning and *Metastable* response.

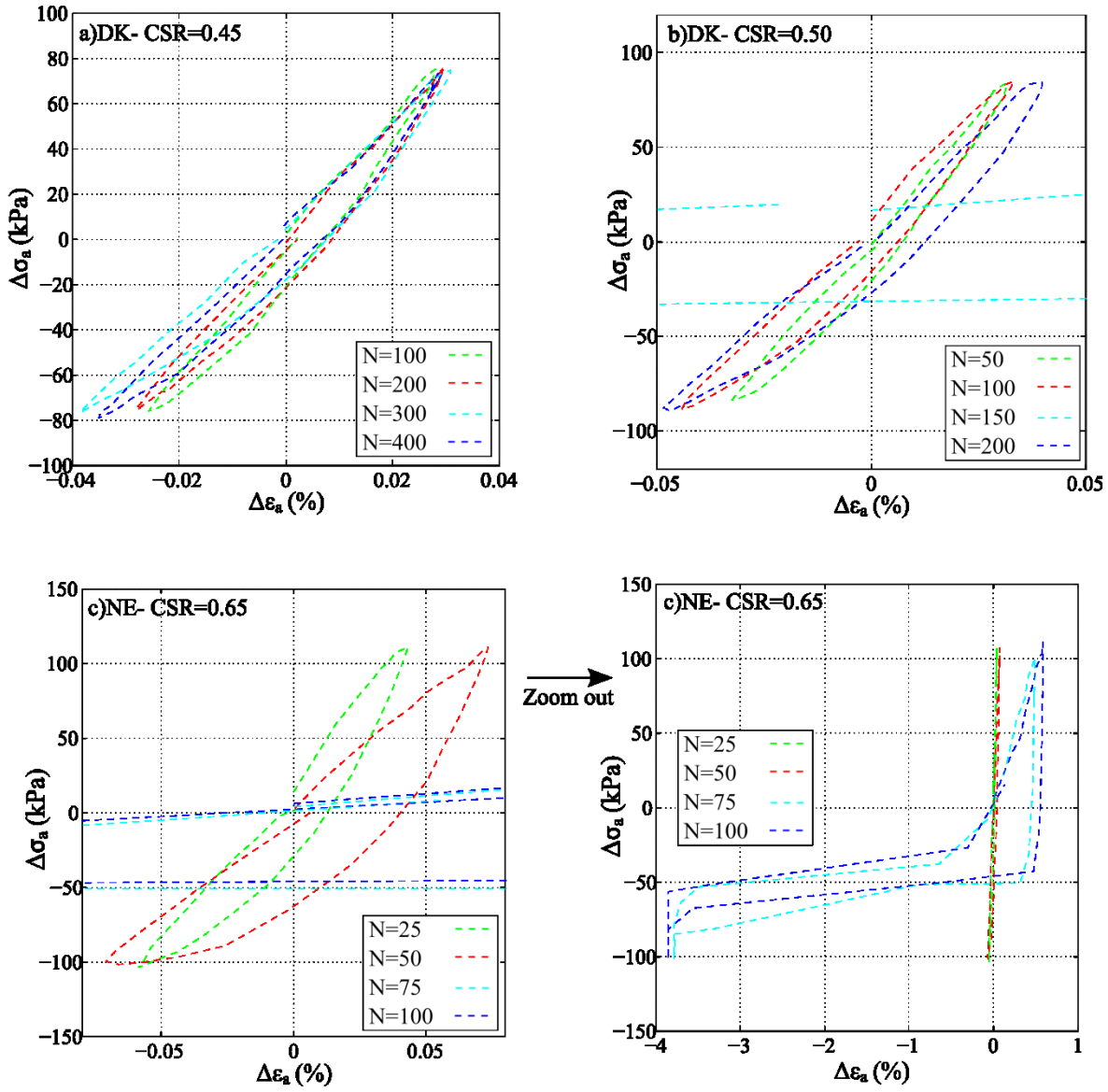


Figure 7-11 Stress-strain loops of specified nth cycles from undrained tests with "standard" pre-conditioning and *Unstable* response.

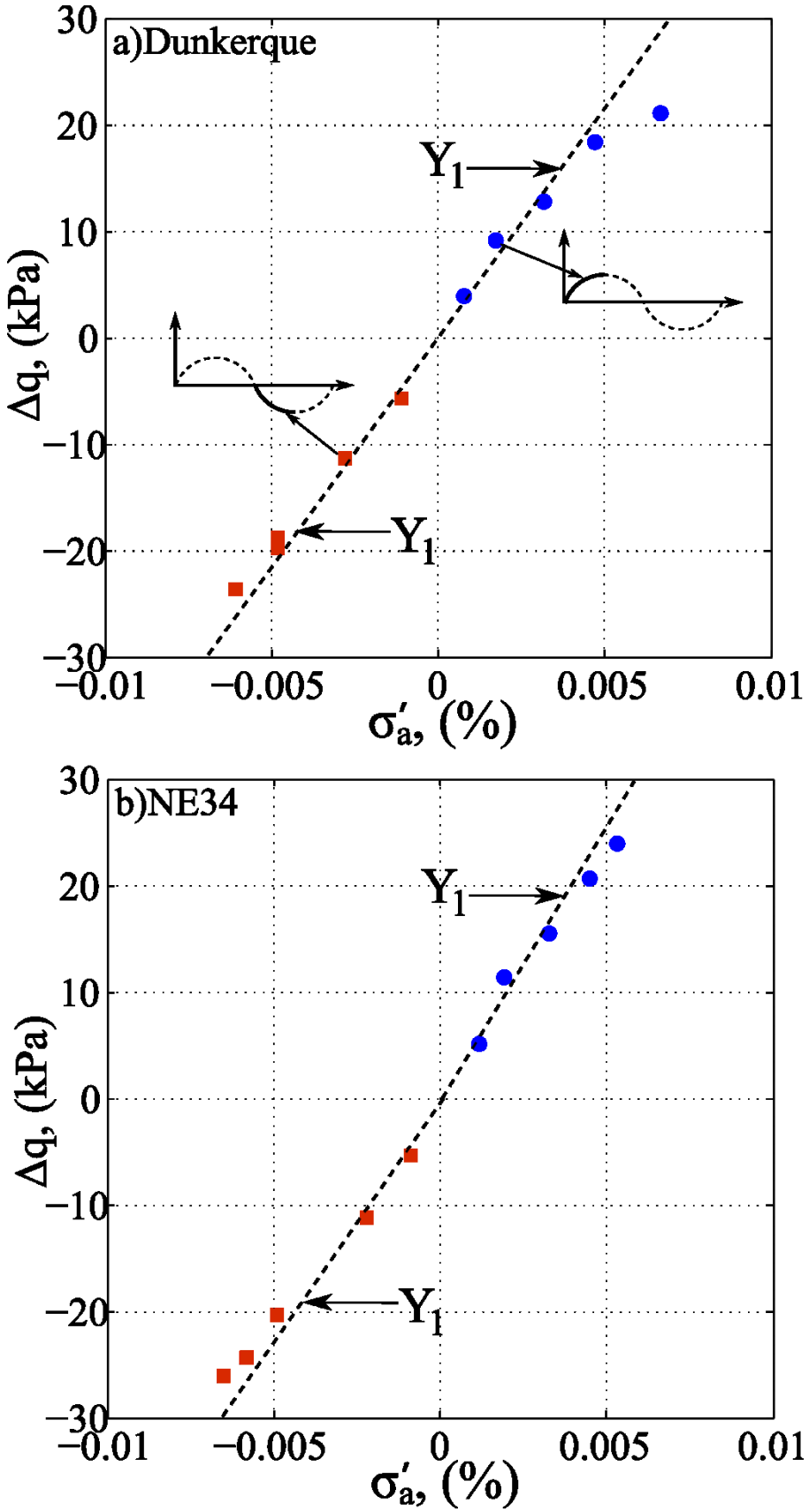


Figure 7-12 Locating the Y_1 surface using the CSR=0.15 cyclic tests stress-strain data for a)Dunkerque and b)NE34 sands

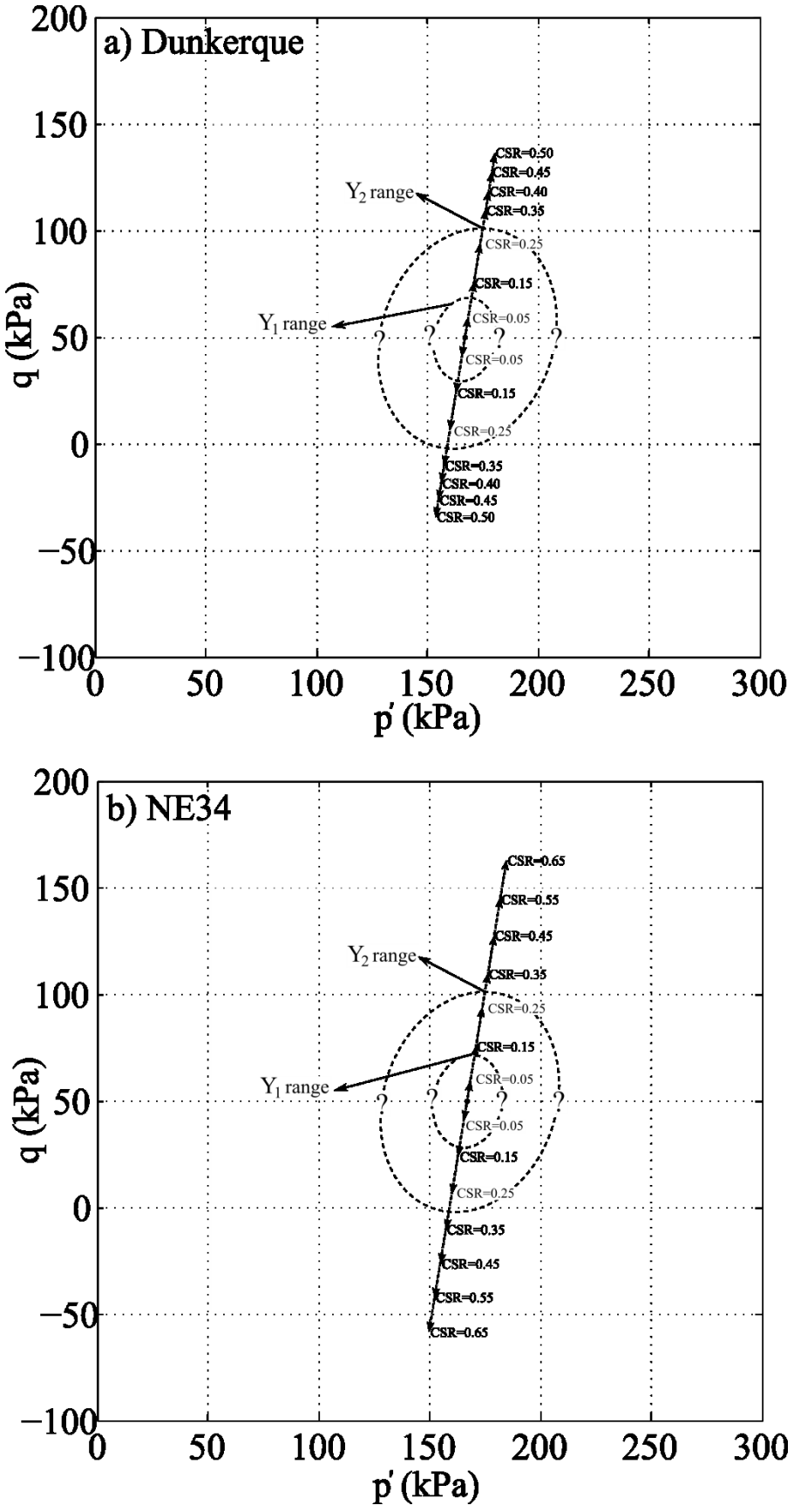


Figure 7-13 Location of maximum effective stress points achieved in each undrained cyclic test with standard pre-conditioning and location of Y_1 surface from monotonic undrained test with OCR=4 and estimation of the Y_2 surface based on cyclic results.

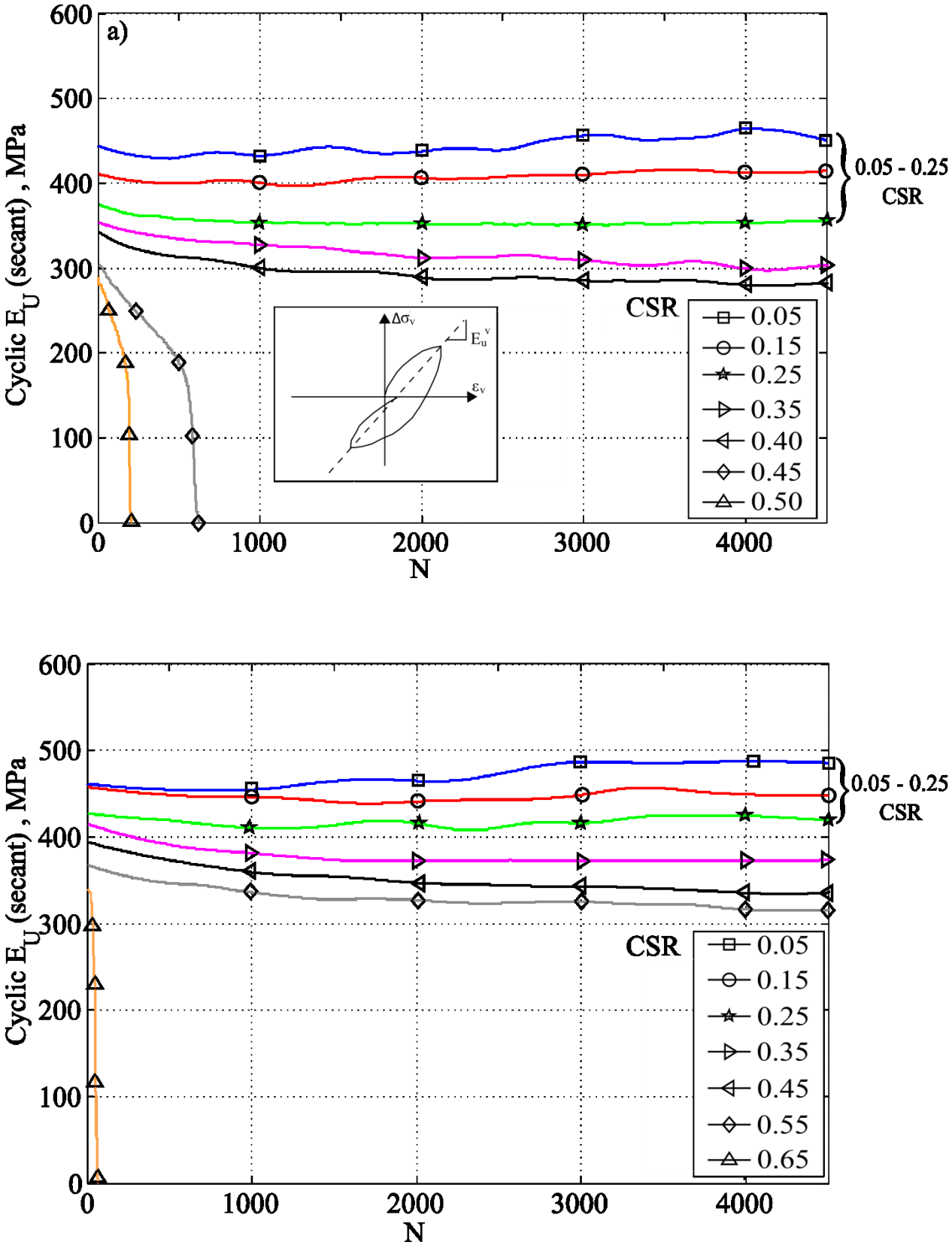


Figure 7-14 Effect of CSR on undrained stiffness response under undrained cycling at Point D for a) Dunekrque and b) NE34 specimens after standard consolidation, conditioning cycles and ageing stages. All samples prepared to e0=0.64

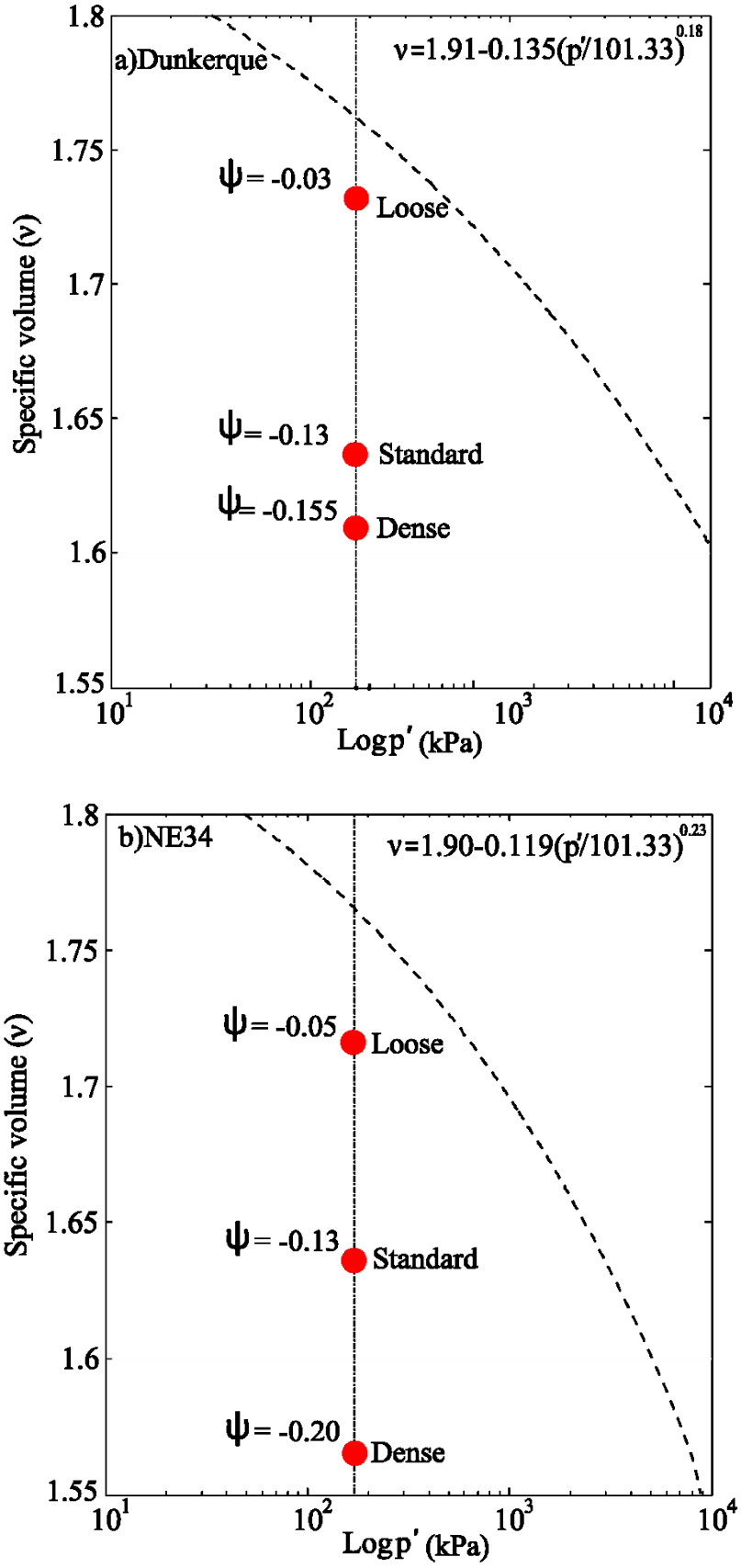


Figure 7-15 Initial target void ratio of dense and loose specimens and their location relative to the critical state line obtained from monotonic tests.

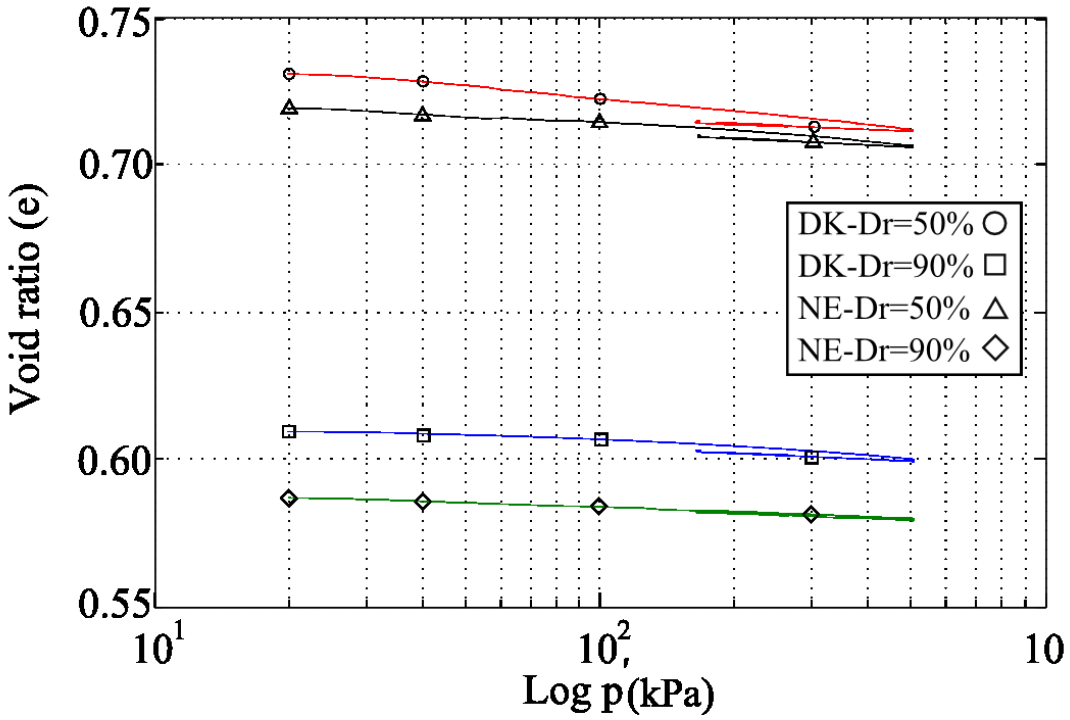


Figure 7-16 Void ratio changes during the "standard" pre-conditioning procedure for dense (D_r=90%) and loose (D_r=50%) Dunkerque and NE34 specimens prior to applying undrained cyclic loads with CSR=0.35.

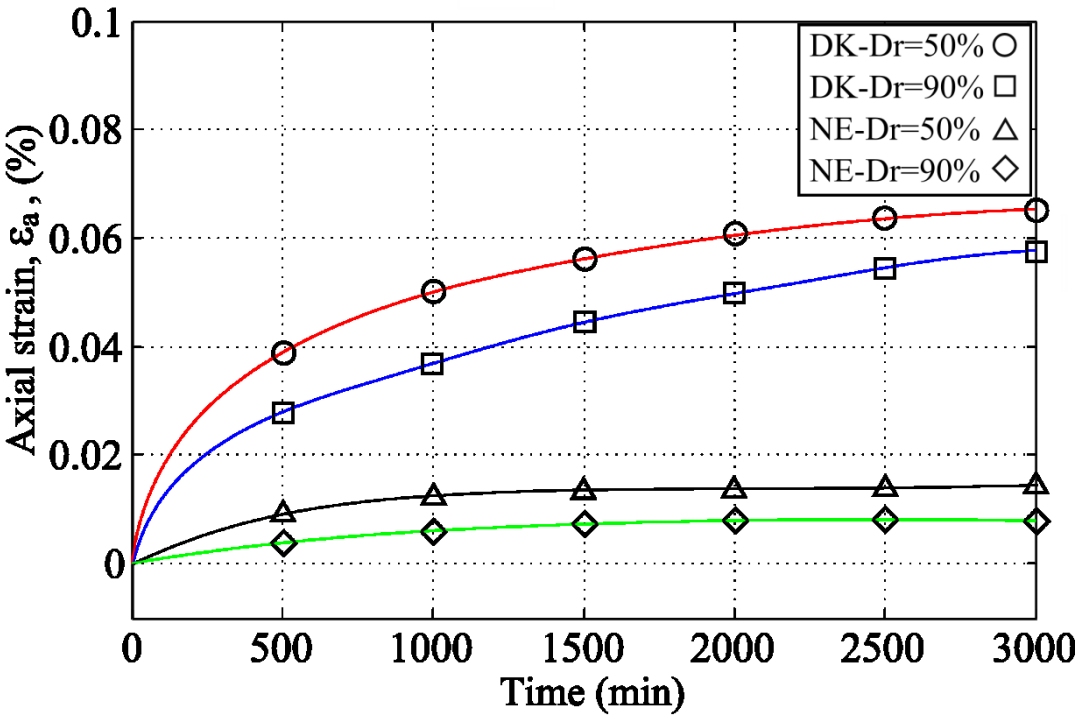


Figure 7-17 Accumulation of axial strains during 48 hours of creep on dense and loose specimens after consolidation at point B as part of the "standard" pre-conditioning to applying undrained cyclic loads with CSR=0.35.

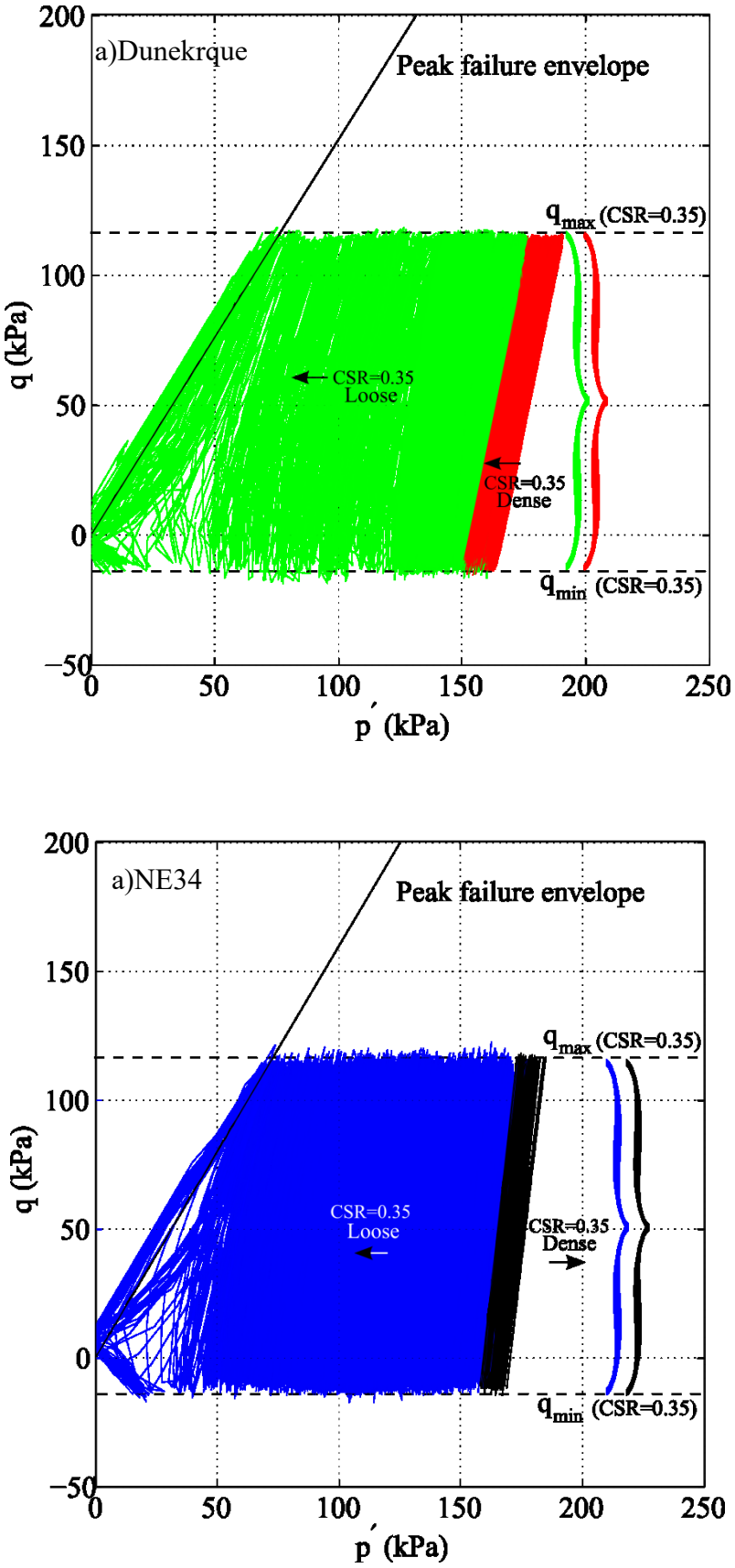


Figure 7-18 Stress paths followed under undrained cycling after "standard" pre-conditioning procedure at point D for a) Dunkerque and b) NE34 specimens with CSR=0.35

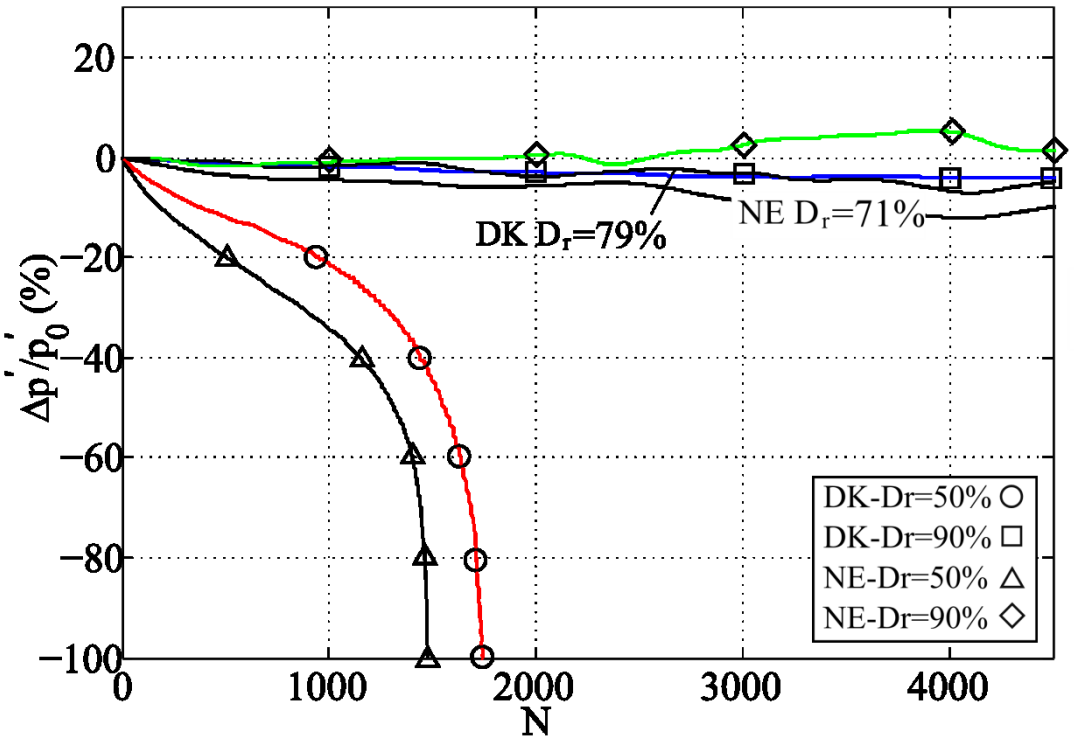


Figure 7-19 Effect of relative density on p′drift under undrained cycling on "standard" pre-conditioned Dunkerque and NE34 specimens. CSR=0.35.

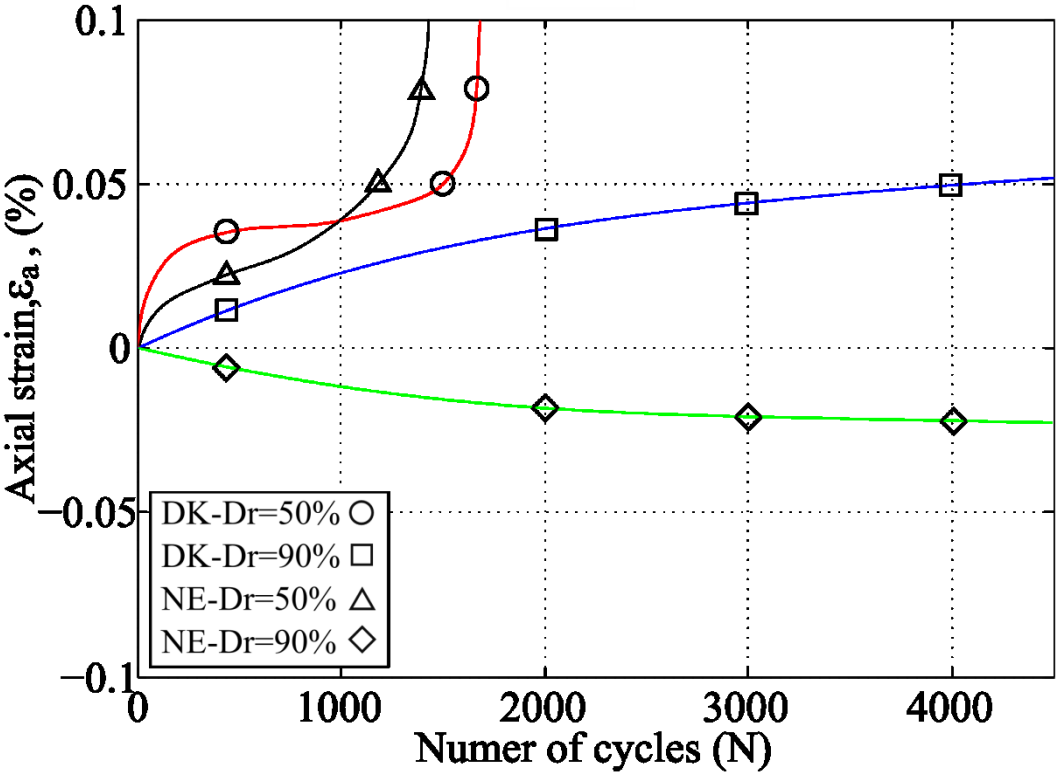


Figure 7-20 Effect of relative density on strain accumulation under undrained cycling on "standard" pre-conditioned Dunkerque and NE34 specimens. CSR=0.35.

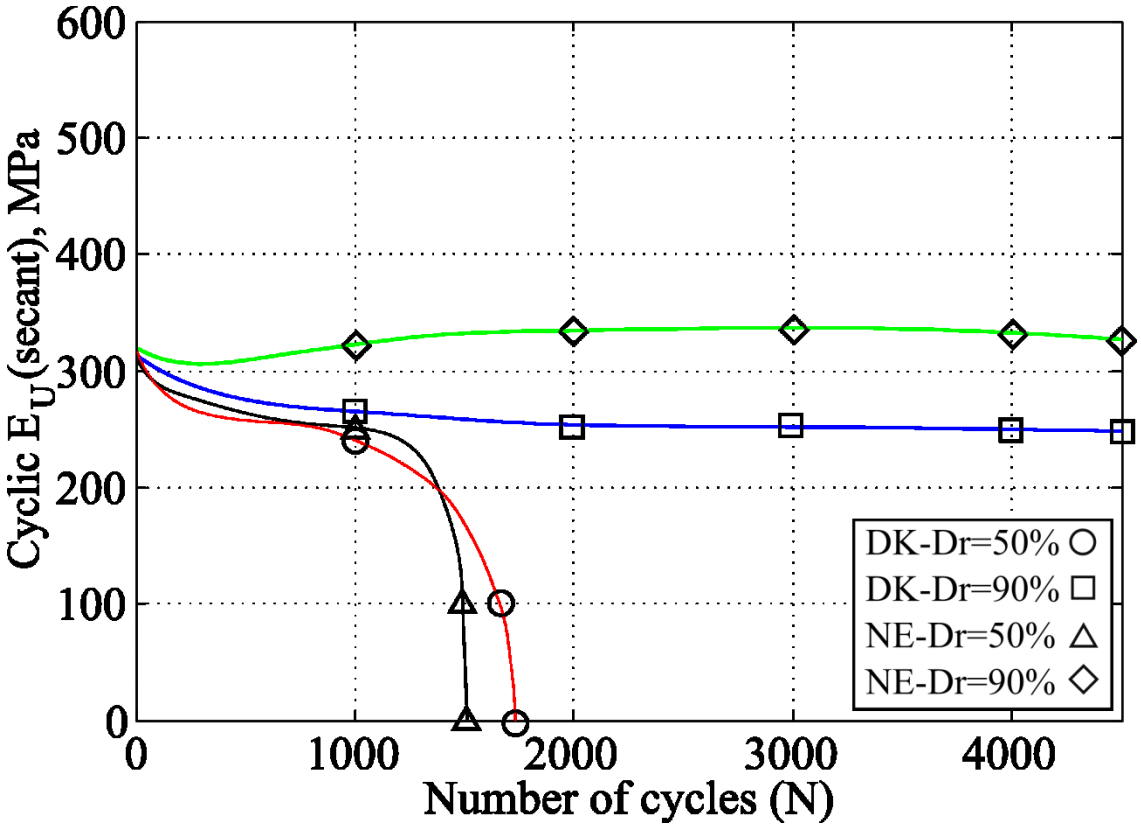


Figure 7-21 Effect of relative density on undrained stiffness response under undrained cycling on "standard" pre-conditioned Dunkerque and NE34 specimens. CSR=0.35.

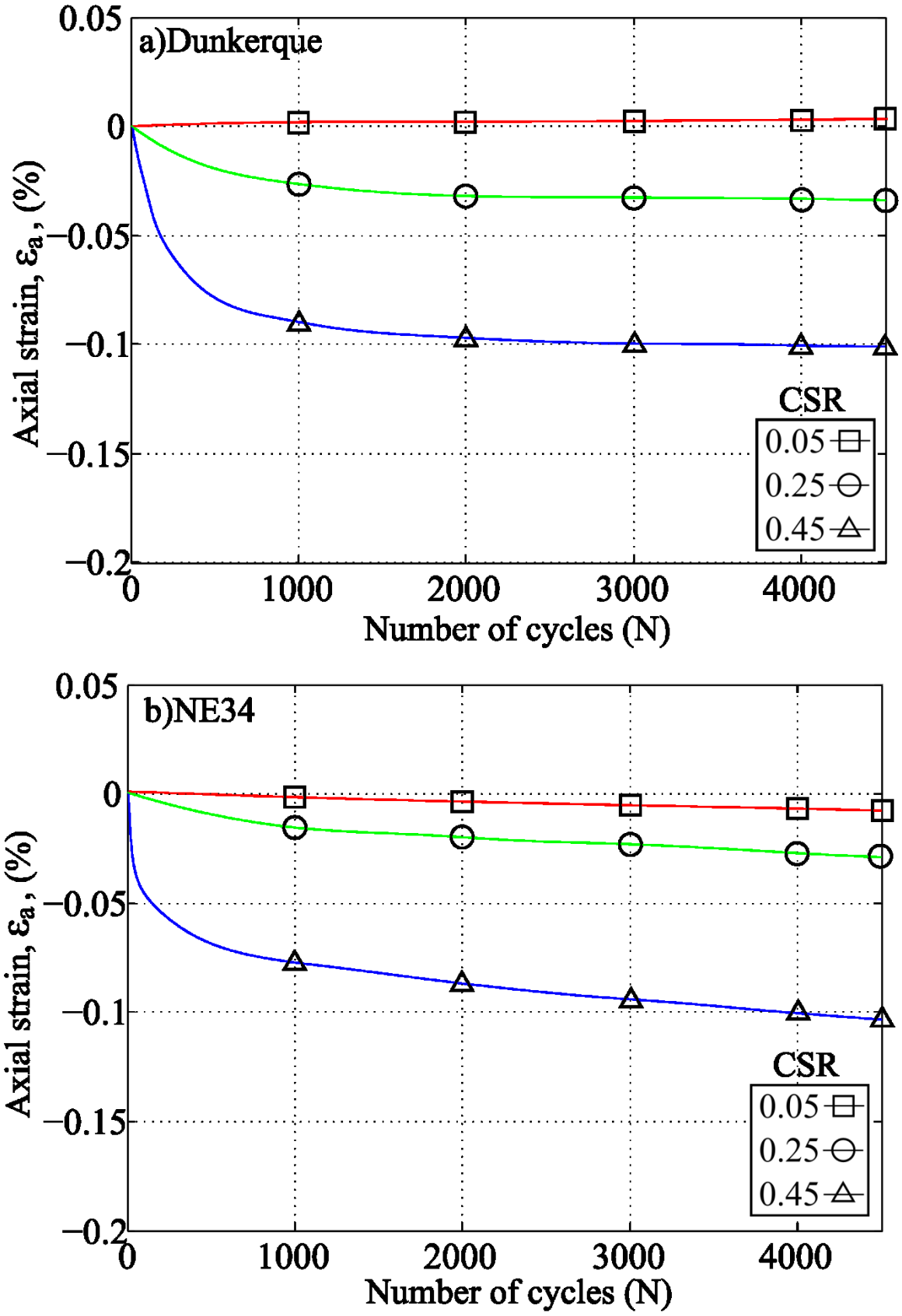


Figure 7-22 Accumulation of axial strains under drained cyclic loading on "standard" pre-conditioned a) Dunkerque and b) NE34 specimens.

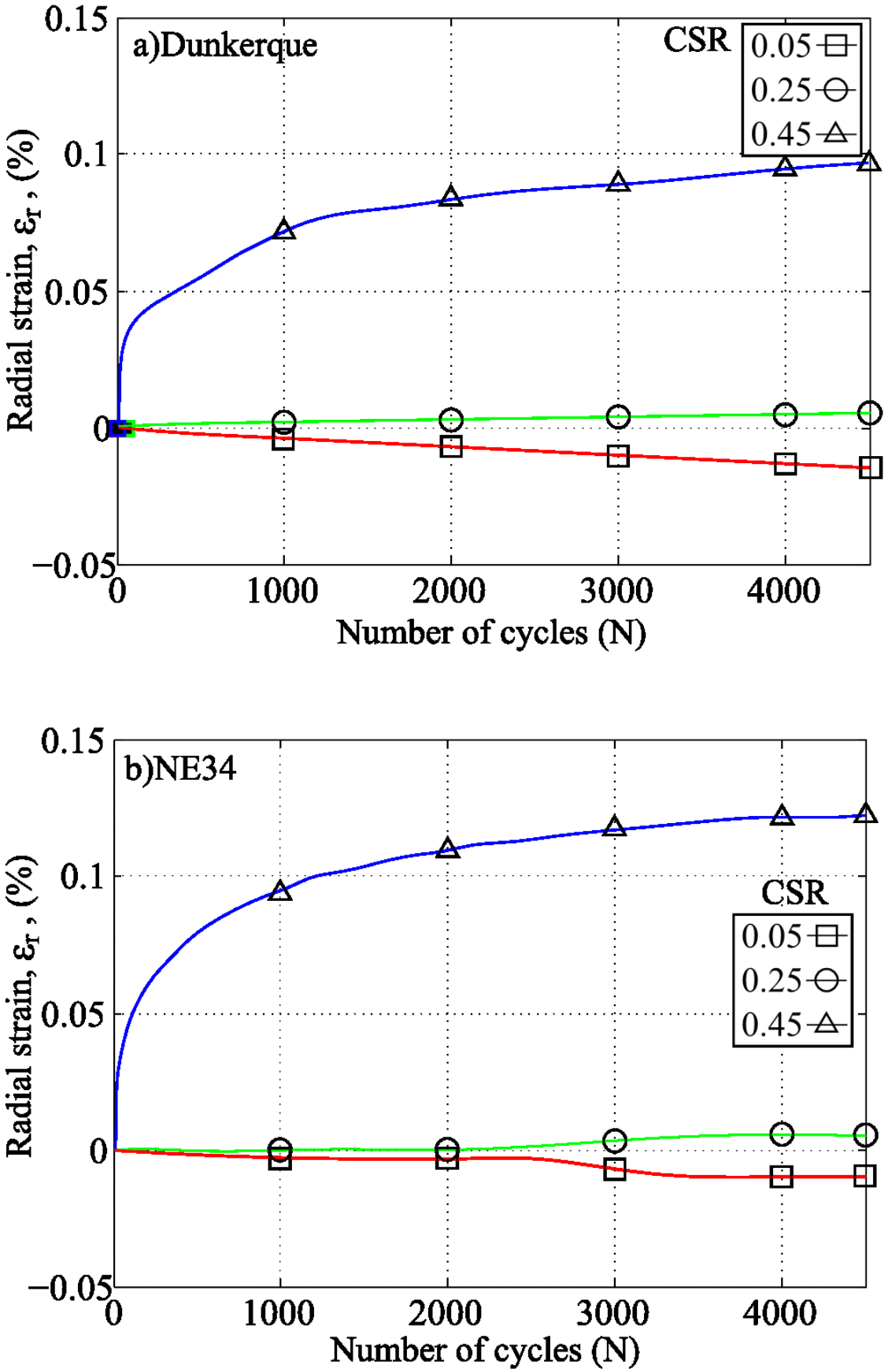


Figure 7-23 Accumulation of radial strains under drained cyclic tests on "standard" pre-conditioned a) Dunkerque and b) NE34 specimens.

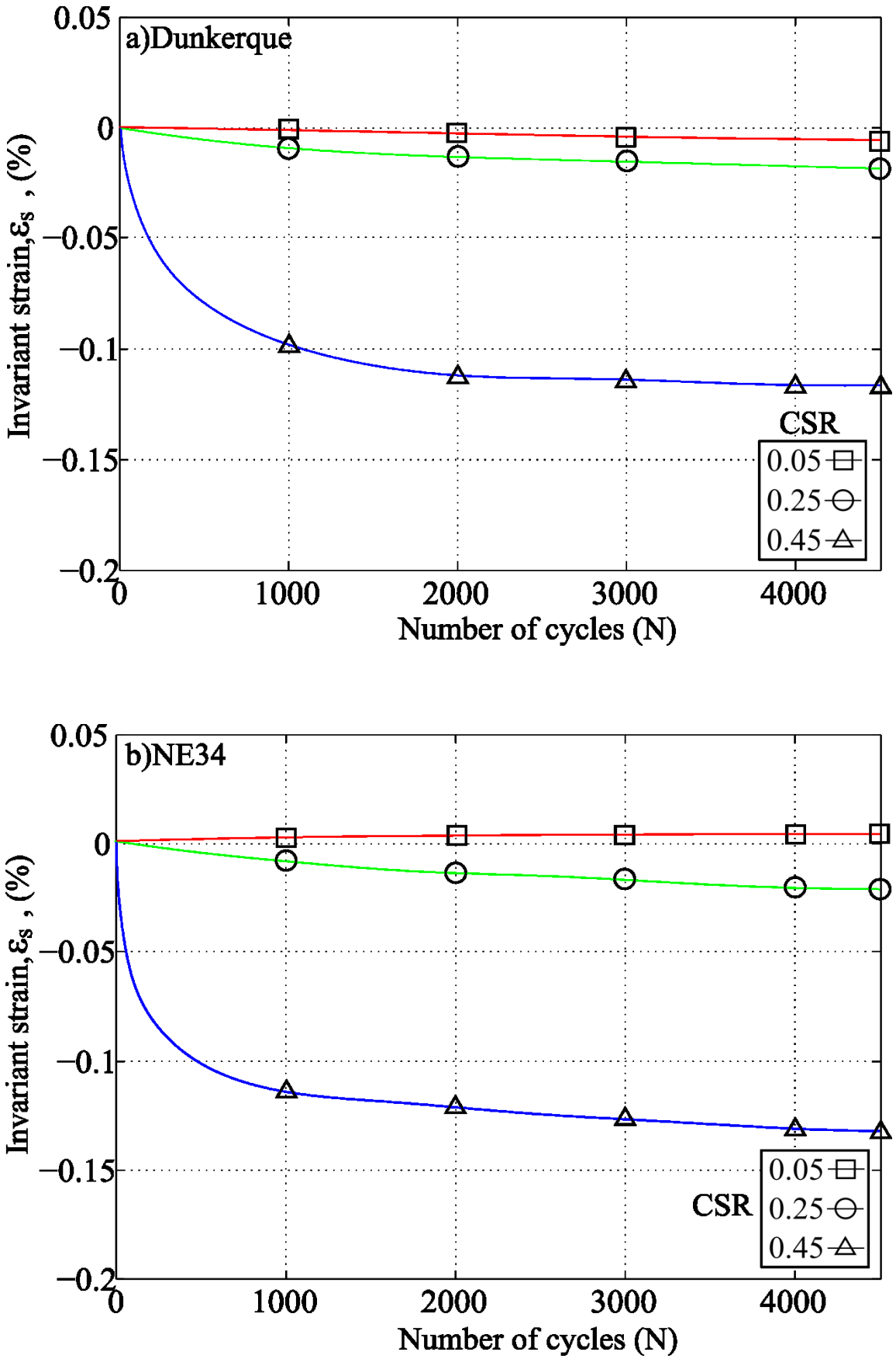


Figure 7-24 Accumulation of shear strains under drained cyclic tests on "standard" pre-conditioned a) Dunkerque and b) NE34 specimens.

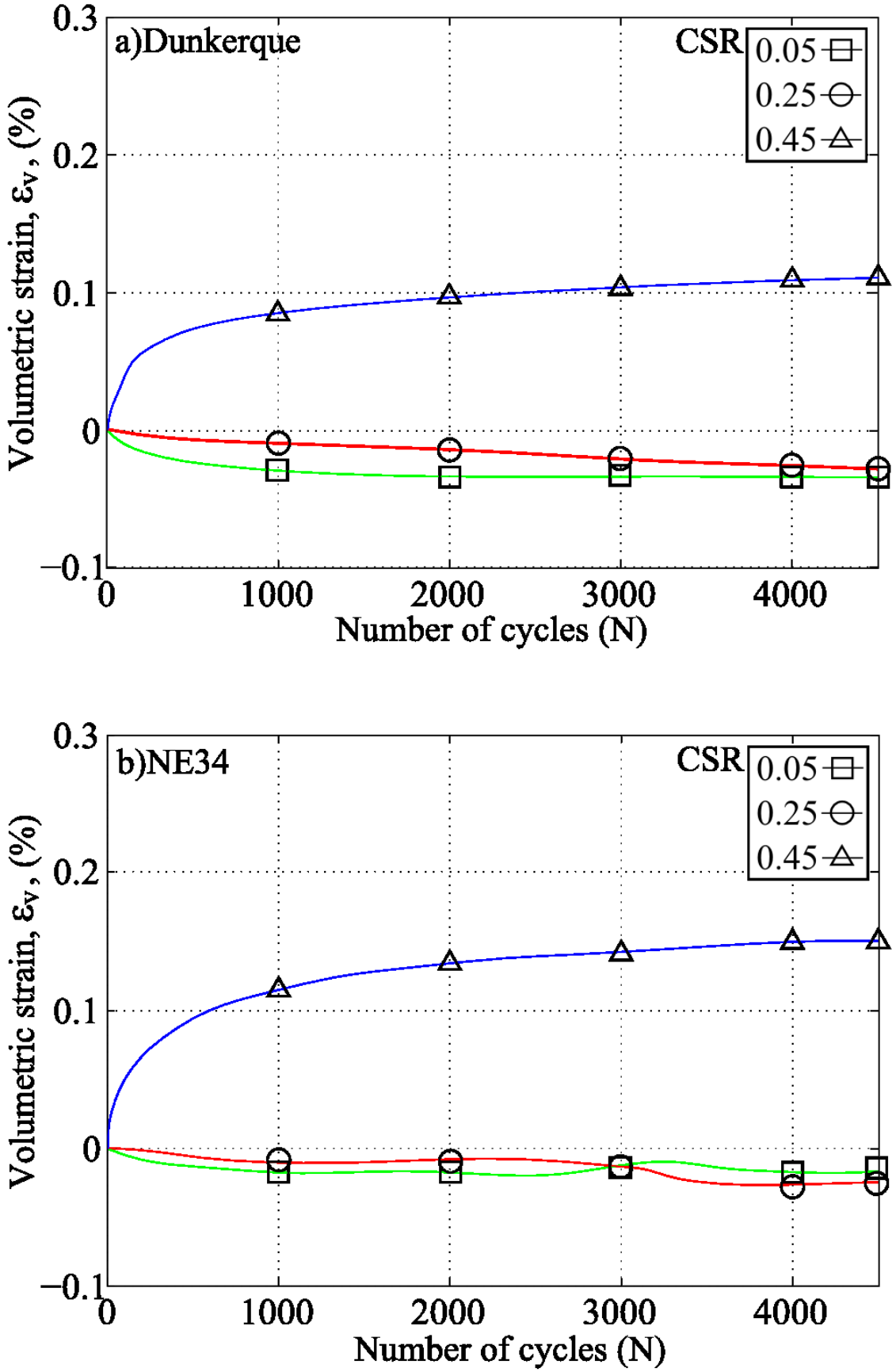


Figure 7-25 Accumulation of volumetric strains under drained cyclic tests on "standard" pre-conditioned a) Dunkerque and b) NE34 specimens.

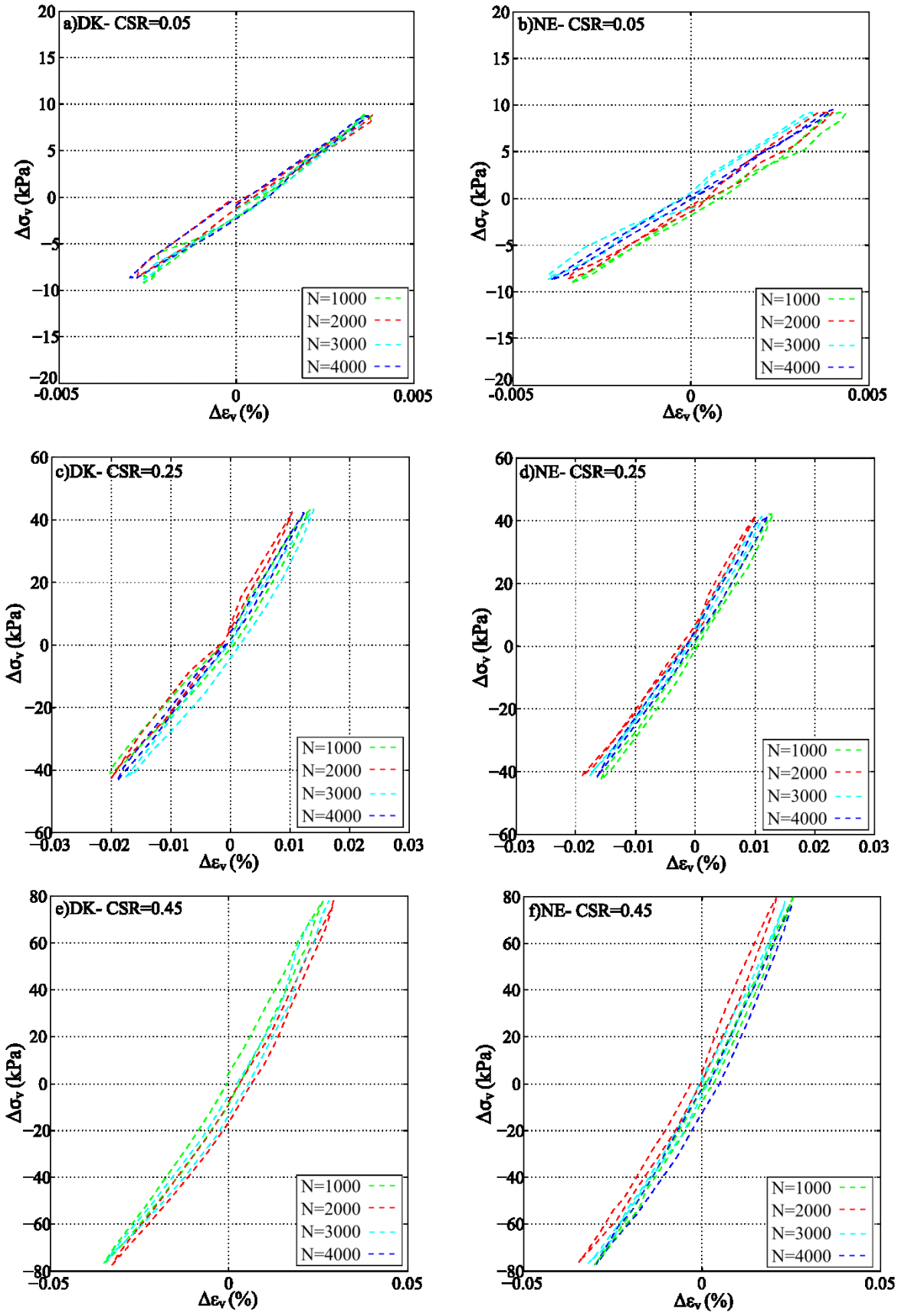


Figure 7-26 Stress-strain loops of specified nth cycles from drained tests with "standard" pre-conditioning.

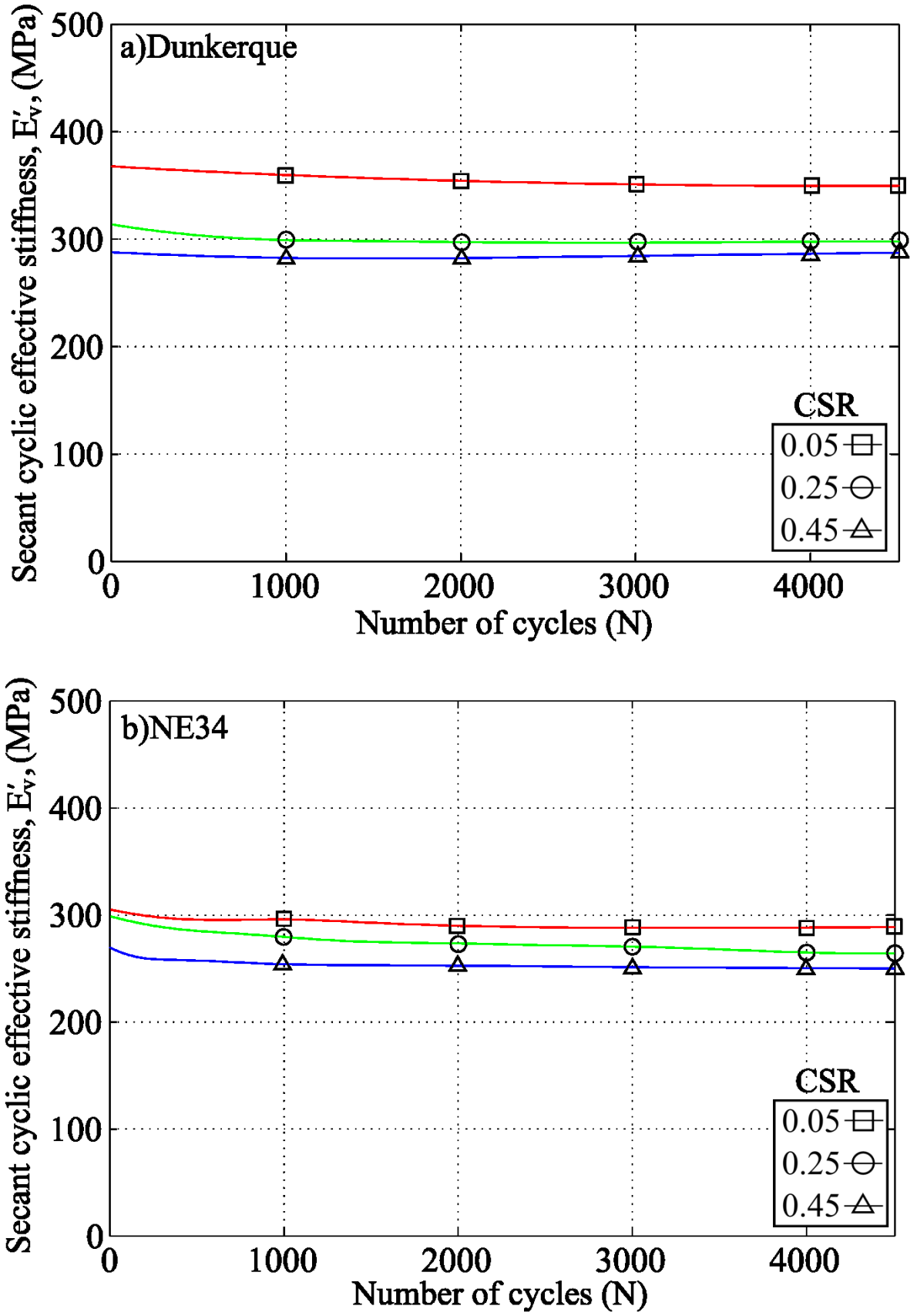


Figure 7-27 Degradation of Secant cyclic vertical effective stiffnesses under drained cyclic loading with "standard" pre-conditioned specimens.

CHAPTER 8

HCA undrained tests using the "standard" test procedure

Introduction

As discussed in chapter 3, the simple shear test's configuration models key aspects of the kinematic and stress boundary conditions applying to soil elements adjacent to piles under axial loading. Among the methods available for performing simple shear experiments, HCA simple shear testing is the most capable due to (i) its ability to give information on the complete stress tensor and (ii) its lower degree of sample non-uniformity compared to other simple shear apparatus. This chapter presents results from a series of cyclic simple shear tests in which a range of cyclic amplitudes (τ_{cyc}) was applied after following the "standard" testing and pre-conditioning approaches outlined in chapter 6. In addition, results are presented from two monotonic "standard" pre-conditioned simple shear tests which add to the understanding of the stiffness and strength behaviour of the test sands under simple shear conditions and also provide small strain data that aids the interpretation of the cyclic tests.

8.1 Modelling the simple shear conditions adjacent to pile in HCA tests

As was discussed in Section 3.4, the loading conditions of a single element of soil adjacent to pile experiencing axial load are analogous to simple shear laboratory test conditions. Simple shear tests can be undertaken in the laboratory using DSS and HCA apparatuses. As discussed in Section 3.4.2, that HCA apparatus offers the best available option due to its ability to give information on the complete stress tensor (with four non-zero terms; σ'_z, σ'_θ, σ'_r, $\tau_{z\theta}$) while conventional DSS tests only track σ'_z and $\tau_{z\theta}$. Also the HCA tests generate a lower degree of sample and internal stress non-uniformity than routine DSS apparatus.

Figure 8-1 shows how HCA tests model simple shear conditions. As shown, the HCA vertical effective stress, σ'_z is analagous the radial effective stress acting on the pile shaft and the HCA's $\tau_{z\theta}$ represents the shearing stresses τ_{rz} acting at the soil-pile interface. This analogy allows results from laboratory tests to be linked to pile behaviour.

8.2 "Standard" test procedure for HCA tests

The "standard" triaxial test procedure designed to model (for this study) driven pile shaft boundary conditions and stress history with triaxial tests was outlined in Chapter 6. Some modifications were required in order to apply the same approach to HCA simple shear tests. These modifications are discussed in the following paragraphs:

8.2.1 Consolidation-swelling

The consolidation-swelling effective stress paths chosen for HCA tests were similar to triaxial tests as shown in Figure 8-2 in q-p′space. As mentioned earlier in Chapter 4, for HCA tests a more complete definition of the deviatoric stress, q, is appropriate because unlike triaxial tests, the intermediate effective stress is not necessarily equal to the major or minor principal stresses ($\sigma'_2 \neq \sigma'_1$ or σ'_3). The following definitions of q and p′are used in this chapter:

$$q = \sqrt{\frac{(\sigma'_1-\sigma'_3)^2+(\sigma'_1-\sigma'_2)^2+(\sigma'_2-\sigma'_3)^2}{2}}$$ Equation 8-1

$$p' = \frac{\sigma'_1+\sigma'_2+\sigma'_3}{3}$$ Equation 8-2

Applying Equation 8-1 simplifies the comparison of triaxial and HCA tests because when $\sigma'_2 = \sigma'_1$ or σ'_3, above equations simplify to $q=\sigma'_1-\sigma'_3$ as in the triaxial tests.

The stress history proposed in Figure 8-2 aims to model the stress build-up and relaxation experienced by soil elements near the shaft during pile installation. However the maximum cell pressure achievable in the HCA was constrained to 600kPa for safety reasons. The back pressure that could be applied at the end of saturation in tests that progressed to maximum horizontal effective stresses $\sigma'_r=\sigma'_\theta$=420kPa was limited to 180kPa, which was insufficent to ensure full saturation and high B values. Final saturation was therefore delayed until after reaching the consolidation stress maxima and was applied over the swelling path section by increasing the back pressure at 60kPa/hr while the inner and outer cell pressures were kept constant as the vertical stress reduced. This contrasts with the standard triaxial test procedure where the back pressure was kept constant and the cell pressure was reduced (see Chapter 4) during the swelling phase. The same rate of radial stress change ($d\sigma'_r/dt$=60kPa/hr) was applied in both the consolidation and swelling phases.

8.2.2 Creep and ageing

In triaxial "standard" tests two creep periods, each lasting 48 hours, were allowed after the ends of consolidation and swelling. Similar creep stages were allowed in the HCA tests at Points B and D in Figure 8-2. The HCA specimens had 6.15 times more sand mass than the triaxial equivalents and it was found necessary to extend to 72 hours the drained creep times imposed prior to start of shearing (at Point D) to ensure that creep rates had reduced

sufficiently to not affect the subsequent undrained cyclic simple shear response. Perhaps surprisingly, it appears that creep rates depend on the specimen's dimensions.

8.2.3 Pre-cycling

The pre-cycling stage designed for "standard" triaxial tests involved 30 drained deviatoric cycles applied with amplitude q_{cyc}=111.7kPa and fixed q_{mean}=116.7kPa and p' = 225kPa. Since the cyclic shearing mode was torsional in HCA tests, the pre-cycling stage had to be redesigned. The aim was to have comparable pre-cycling stages to those imposed in the triaxial tests. Among different options available, the decision was made to match the q_{max}/p' values between triaxial and HCA tests. In triaxial tests q_{max}=228.4kPa ($q_{mean}+q_{cyc}$=116.7+111.7) was chosen to give a q_{max}/p'=0.87 and $CSR_{pre\text{-}cyc}$=0.5 which led to mobilised ϕ'=23° and reflected the mobilised τ_{rz}/σ'_r ratio expected at 2 pile radii from the axis under installation conditions. The Author chose to apply, symmetrical cycles around $\tau_{z\theta}$=0 with amplitudes (τ_{cyc}=79kPa) that led to q_{max}/p'_0=0.87 and $CSR_{\tau\ pre\text{-}cyc}=\tau_{cyc}/p'_0$=0.35. These cycles imposed a maximum mobilised δ'=15° in the τ_{rz} plane and matched the τ_{rz} levels expected at a radial distance r/R=3 from the pile axis. An alternative choice would have been to apply the same mobilised δ' by increasing τ_{cyc}=128.5kPa. The latter option would have led to a greater resistance to renewed cyclic loading and would have been less conservative. Table 8-1 summarizes the parameters used in the triaxial and HCA pre-cycling stages, Figure 8-3 shows the stress paths followed in q-p'space and Table 8-2 gives the values for all 4 stress invariants in Points A-D.

Table 8-1 Comparison between properties of applied pre-cycles in triaxial and HCA tests

Apparatus	Number of cycles	q_{cyc} (kPa)	τ_{rz} (kPa)	q_{max}/p'	CSR	
HCA	30	79.7	79	0.87	0.35	δ'=15°* in $\tau_{z\theta}$ plane
Triaxial	30	111.7	-	0.87	0.50	ϕ'=23°

* 79/302.8=0.26 → arctan(0.26)=15°

The maximum mobilised $\delta \doteq 15°$ in $\tau_{z\theta}$ plane can be compared to the interface friction angle recorded in pile or interface shear tests which, was $\delta \doteq 27$. Matching the conditions applying 2 pile radii away from pile surface is constant with the consolidation load-unload path and OCR=4 value chosen for the triaxial and HCA tests, as described in Section 6.1.

Table 8-2 Details of stresses applied at Points A-D during pre-conditioning procedure.

Point	σ'_θ (kPa)	σ'_r (kPa)	σ'_z (kPa)	$\tau_{z\theta}$ (kPa)	p′(kPa)	q (kPa)
A	20	20	20	0	20	0
B	360	360	800	0	506	440
C_{mean}	186.1	186.1	302.8	0	225	116.7
C_{max}	186.1	186.1	302.8	79	225	195.7
D	150	150	200	0	167	50

8.2.4 Main cycling stage

As discussed in Chapter 3, it has been argued that axial cyclic loading conditions adjacent to a driven pile can be modelled by CNS simple shear tests. It was later discussed in Section 6.1 that using constant volume conditions (CNS=infinity) can eliminate the uncertainties involved in choosing an appropriate CNS value in a conservative manner. Considering these points, constant volume cyclic simple shear conditions were imposed for the main stage of cyclic testing after the end of the second creep stage at point D.

Simple shear involves applying shear stresses parallel to the specimen boundaries under plane strain conditions. To achieve this, the inner HCA cell was isolated to give constant inner cell volume. Constant height was also imposed by a rigid bar connected to the axial shaft. The TRIAX software also allowed for second order axial compliance effects by further checking the axial displacement transducer readings and adjusting the axial load incrementally, if required to maintain constant height. This dual system kept the axial straining below 2×10^{-3}% in all tests. Finally, the drainage lines were closed to prevent any specimen volume change. Assuming that the specimen deforms as a twisting cylinder (see Section 4.2.3), keeping the

height and the inner circumference constant leads to a constant outer circumference under undrained conditions and therefore no radial straining.

8.3 Monotonic simple shear tests with "standard" pre-conditioning

To obtain a better understanding of the monotonic behaviour of test sands under simple shear loading, two static simple shear tests were performed on specimens that had been "consolidated" following the "standard" pre-conditioning procedures starting from q=50kPa and p'_0=167kPa and with a rate of$\gamma_{z\theta}$=0.1%/hr. The details of both tests are presented in Table 8-3.

Table 8-3 Details from monotonic "standard" pre-conditioned simple shear tests

Sand	Test code	Pre-conditioning	Ageing time at Point B	Ageing time at Point D	e_0
Dunkerque	H-DK-S	Standard*	48 hours	72 hours	0.641
NE34	H-NE-S	Standard	48 hours	72 hours	0.637

* See Figure 8-2

8.3.1 Small strain behaviour

The stiffness and extent of the linear Y_1 range was studied by plotting $\tau_{z\theta}$ against $\gamma_{z\theta}$ as shown in Figure 8-4 which showed, with these "pre-conditioned" samples to extended linear responses up to 0.014% and 0.018% for Dunkerque and NE34 specimens respectively. The extents of the Y_1 linear ranges are large compared to those observed in drained normally consolidated triaxial tests (see Section 5.2). However, as was observed in "standard" pre-conditioned monotonic undrained triaxial tests (Section 5.7); application of consolidation-swelling and large pre-cycling stages prior to shearing, extends the size and the orientation of the Y_1 and Y_2 surface considerably. Therefore, it is more appropriate to compare the Y_1 ranges achieved from these tests with ones from triaxial tests with "standard" pre-conditioning ($\varepsilon_a \approx 0.02\%$ for both Dunkerque and NE34 sands in compression direction). Once

the Y_1 surfaces were engaged behaviour became progressively less linear as the stress paths moved towards their final peak conditions.

8.3.2 Stiffness measurements

The maximum tangent shear stiffness, $G_{z\theta}$, as measured within the Y_1 linear range and rapid falls of tangent stiffness seen once the Y_1 surfaces were engaged are shown in Figure 8-5. A similar technique to that applied to the triaxial tests was used to derive tangent stiffness trends by fitting polynomial equations to small sections of each $\tau_{z\theta}$ versus $\gamma_{z\theta}$ curve and differentiating the equations. The initial monotonic shear stiffnesses obtained from the Dunkerque test was slightly lower than that for NE34 and lower than might be expected from the triaxial test equivalents (see Section5.2). This will be discussed later when the static tests values are compared with secant cyclic $G_{z\theta}$ values.

The maximum $G_{z\theta}$ stiffness values were also measured at effective stress Points B and D (defined in Figure 8-2) using the Resonant Column (RC) equipment described in Section 4.3. Results from both RC and monotonic tests are presented in Table 8-4.

Table 8-4 Comparison between maximum $G_{z\theta}$ values obtained from static and RC tests.

Soil	Location	p′(kPa)	$G_{z\theta}$ – RC (MPa)	$G_{z\theta}$ – Monotonic (MPa)	Difference (%)
Dunkerque	Point B	506	259	-	-
Dunkerque	Point D	167	124	113	9.7
NE34	Point B	506	265	-	-
NE34	Point D	167	139	129	7.7

As shown the maximum monotonic $G_{z\theta}$ values were significantly lower than the equivalent RC measurements at Point D. Brosse (2012) and Nishimura (2006) have reported similar patterns in their tests on stiff clays; Brosse reported offsets of around 20% and Nishimura

reported differences of 10-30%. Nishimura (2006) suggested possible causes for this consistent trend:

1- Non-uniformities in $\tau_{z\theta}$ and $\gamma_{z\theta}$ may lead to some errors in stiffness measurement.
2- For higher strain rates are applied in RC tests (which resonated at around 250Hz) which may lead to higher shear stiffnesses developing under dynamic conditions.
3- Inherent errors may apply in the visco-elastic model used for deriving shear stiffness in RC tests.
4- Possible shear compliance errors in the static tests, which effectively define the shear strains from platen to platen measurements. There is a possibility of imperfect shear coupling between the sands and the platens that might reduce the stiffness values measured in monotonic tests.

8.3.3 Behaviour moving towards the critical state line

Both tests showed dilative (positive dq/dp′) behaviour from the beginning of their shearing stages and no phase transformation point, Y_4, was identified. This behaviour is similar to what was obtained from "standard" pre-conditioned undrained triaxial tests and, as was discussed in Section 5.2.2.1, is due to existence of initial deviatoric loads (q=50kPa) and the dense initial state of the specimens. The effective stress paths followed in the $\tau_{z\theta}$-$(\sigma'_z - \sigma'_\theta)/2$ and $(\sigma'_z - \sigma'_\theta)/2$-p′planes are shown in Figure 8-6 and Figure 8-7. Shearing led to initial increase in $(\sigma'_z-\sigma'_\theta)/2$ values that reversed after p′had climbed to 400kPa and then reduced continuously as $\tau_{z\theta}$ and p′progressed to their maximum values. The effective stress paths are also shown in q-p′ space in Figure 8-8 and are compared with those developed in equivalent undrained triaxial tests that manifest similar tests as they moved towards the critical state conditions, except that the with HCA stress paths move more vertically over the early stages of shearing. The maxima for the ϕ'_{max} values achieved may be calculated using the following equation:

$$\varphi' = \sin^{-1}\left(\frac{t}{s'}\right)$$ Equation 8-3

Using this equation indicates ϕ'_{max}=37.3 and 36.6 for Dunkerque and NE34 sands respectively. However, critical state values could not be achieved. The dilative response under shearing led to continuous reductions in pore pressures and the system cavitated well before reaching ultimate critical state points. Higher pressure apparatus would be required to reach critical states under undrained conditions. The $\tau_{z\theta}$ versus $\gamma_{z\theta}$ plots from both tests are shown in Figure 8-9. As shown, $\tau_{z\theta}$ values continuously increase with a relatively steady slope after 0.2% torsional strain levels.

8.4 "Standard" HCA cyclic tests

A series of cyclic tests using the "standard" procedure described earlier was performed on both test sands covering a range of $CSR_\tau = \tau_{z\theta\ cyc}/p'_0$ values. Table 8-5 presents the initial void ratio values after set-up and the cyclic parameters for each test:

Table 8-5 Details from cyclic "standard" pre-conditioned simple shear tests

Sand	Test Code	Pre-conditioning	CSR_τ	e_0
Dunkerque	HDK-S-05	Standard*	5	0.638
	HDK-S-15	Standard	15	0.646
	HDK-S-25	Standard	25	0.642
	HDK-S-35	Standard	35	0.641
	HDK-S-45	Standard	45	0.633
NE34	HNE-S-05	Standard	5	0.642
	HNE-S-15	Standard	15	0.645
	HNE-S-25	Standard	25	0.642
	HNE-S-35	Standard	35	0.637
	HNE-S-45	Standard	45	0.651

* See Figure 8-1

The following paragraphs present the results from the pre-conditioning and main cyclic stages.

8.4.1 Pre-conditioning

8.4.1.1 Consolidation and swelling from Point A to B and B to D

The void ratio changes developed during the pre-conditioning stages of all relevant HCA tests are shown in Figure 8-10. As in the triaxial tests, the coefficients of compressibility were pressure dependent, leading to λ values that grow with pressure as shown in Table 8-6. Along with values obtained in similar triaxial test stages, the HCA and triaxial values match closely giving a good indication that the flows of water in and out of the specimens were representative of fully saturated conditions, despite the lower than ideal initial back pressures and possibly lower degrees of saturation.

Table 8-6 Compressibility values obtained from different pressure ranges in HCA tests and comparison with values obtained from triaxial tests

Material	Test	λ		
		20-100kPa	**100-300kPa**	**300-500kPa**
Dunkerque	Triaxial	6.1×10^{-4}	9.3×10^{-4}	1.2×10^{-3}
Dunkerque	HCA	6.3×10^{-4}	9.5×10^{-4}	1.3×10^{-3}
NE34	Triaxial	6.3×10^{-4}	9.0×10^{-4}	1.1×10^{-3}
NE34	HCA	6.4×10^{-4}	9.3×10^{-4}	1.2×10^{-3}

8.4.1.2 Creep and ageing at Point B and D

The creep periods imposed after consolidation and swelling stages showed similar styles of response to the triaxial tests. Axial creep straining was compressive after consolidation and rebounded after swelling, with strain rates reducing considerably over time.

Figure 8-11 shows the creep behaviour observed at Point B (after the end of consolidation) for all specimens. As shown, the axial strain rates drop considerably after 48 hours, falling below 0.005 and 0.002%/day for Dunkerque and NE34 sands respectively. Comparison between the two sands show that, as with triaxial tests, Dunkerque sand generated higher creep rates at any given time, under similar p' and e_0 conditions. As discussed in Section 5.2.1.1, this is probably due to existence of shell fragments in Dunkerque sand. Variations in broken shell content could also explain why the Dunkerque specimens' creep trends varied

more widely between tests conducted under similar conditions while NE34 specimens showed almost identical trends in all tests.

The second creep stage at Point D (prior to main cycling) showed axial strains rebounding over 72 hours of creep. However, since the strain changes were very small and, given the finite resolution of the axial external transducer, the strain: time trends are less systematic than with the locally instrumented triaxial tests. Nevertheless, the measurements showed that the final axial creep strain rates fell below 0.001%/day in all cases for both test sands.

8.4.1.3 Pre-cycling at Point C (with τ_{cyc}=79kPa)

"Standard" pre-cycling stages (designed in Section 8.1.3) were applied at Point C to all specimens as outlined in Section 8.1.3. The axial and volumetric shear strains developed are shown in Figure 8-12 and Figure 8-13, tracking the mid-cycle ($\tau_{z\theta}$=0kPa) points. As in the triaxial tests, both sands showed compressive accumulated volumetric strains although the values were approximately 0.01% higher than those achieved in the triaxial tests. The Dunkerque triaxial and HCA ε_{vol} ranges were 0.005-0.02% and 0.04-0.09% respectively, while those for NE34 were 0.015-0.03% and 0.07-0.13%. However, in contrast with triaxial tests, the axial strains were compressive at Point C. The two test types followed different stress paths in q-p′-b-α space (See Figure 8-3) and the principal stress axis rotations affected the patterns of plastic straining.

8.4.2 Undrained simple shear cycling at Point D

Similar to triaxial tests, three types of behaviour were observed at different CSR_τ levels. In the following paragraphs each of these various types of behaviour is discussed. For each type of behaviour, the results are presented first in $\tau_{z\theta}$-σ'_z space. As discussed earlier, these results correlate with the τ_{rz}-σ'_r stress regime adjacent to a driven pile's surface and therefore can be related to the cyclic response of piles. Moreover, since the HCA apparatus is able to measure

the complete stress tensor, effective stress degradation trends can also be presented in the full q-p′-b-α space.

8.4.2.1 *Stable* response; CSR_τ up to 0.15

Response in $\tau_{z\theta}$-σ'_z space: Specimens of both sands cycled at CSR_τ=0.05 showed gentle rises in their σ'_z values over 4500 cycles as shown in Figure 8-14a-b and Figure 8-15, and those cycled at CSR_τ=0.15 showed almost no change in σ'_z, as shown in Figure 8-14c-d and Figure 8-15. These tests are therefore categorized as *Stable* tests which correlate with the *Stable* response observed in triaxial tests with CSR<0.25 where p′showed no reduction under cycling. In terms of pile response, the HCA results predict that low level cyclic loading under CNS=infinity conditions will lead to gentle rises in σ'_r acting on pile surface, as was discussed in Chapter 3. This outcome matches the behaviour seen in the instrumented model pile tests by Tsuha *et al.* (2012)

Response in invariant effective stress space: HCA tests can show how all stress components vary during simple shear testing. Using the equations provided in Section 4.2.3.3, the σ'_1, σ'_2 and σ'_3 stresses were calculated at mid-cycle and maximum points in each cycle. Figure 8-16 illustrates the scheme of the Mohr circles developed at mid-cycle and maximum points in all tests. As shown, at mid-cycle points where $\tau_{z\theta}$=0kPa, the minor and intermediate principal stresses were equal ($\sigma'_r = \sigma'_\theta$, $\sigma'_2 = \sigma'_3$ and b=0) with $\sigma'_1 = \sigma'_z$ and this condition applied in all tests, even those at higher amplitudes that reached cyclic failure eventually. However, once the shear stresses were applied, the major principal stress, σ'_1, exceeded σ'_z and its axis rotated by an angle α while the minor principal stress, σ'_3, decreased leading to b values greater than 0, as shown in Figure 8-16.

Figure 8-17 and Figure 8-18a-d show the principal stresses at the mid-cycle and maximum points in *all* tests. As shown, cycling in *Stable* tests with CSR_τ=0.05 led to gradual increases

of all these principal effective stresses (at similar rates) at both the mid-cycle and maximum points while in tests with CSR_τ=0.15, cycling led to relatively minor drops in the principal stresses at the mid-cycle points and caused small drops in σ'_1 values at N>1000 cycles.

The effective stress paths followed can also be studied in the general q-p′-b-α space. Figure 8-19a-d show the complete stress paths followed in q-p′ space and Figure 8-20 shows the trends at the mid-cycle points. As shown, cycling led to gentle shifts towards the right (increase in mean p′ values with constant mean q values) in tests with CSR_τ=0.05 and led to almost no movement in tests with CSR_τ=0.15 with only slight negative shifts in q and p′. The response can be studied by tracking the p′ values at mid-cycle (τ=0kPa) points as shown in Figure 8-21 and also tracking the q values at mid-cycle and maximum points in each cycle as shown in Figure 8-22 and Figure 8-23.

Figure 8-24 shows the b values obtained at the maximum points in each cycle. As shown, tests with CSR_τ=0.05, kept almost constant up to 4500 cycles applied, while b increased slightly after the first 1000 cycles applied at CSR_τ=0.15. Figure 8-25 shows the maximum α value from each cycle; showing slight α increases after the first 1000 cycles in all *Stable* tests which were more evident in tests with CSR_τ=0.15.

Stress-Strain response: Figure 8-26a-d show the complete $\tau_{z\theta}$ vs $\gamma_{z\theta}$ load-unload loops developed over the N=1000, 2000, 3000 and 4000 cycles. Comparison between the maximum $\gamma_{z\theta}$ values reached in *Stable* tests with the Y_1 thresholds obtained from the monotonic simple shear tests show that while in tests with CSR_τ=0.05 stress paths remained inside the Y_1 threshold, while tests with CSR_τ=0.15 engaged the Y_1 surface during each cycle. This can be confirmed by the $\tau_{z\theta}$:$\gamma_{z\theta}$ curves of the first cycle of CSR_τ=0.15 tests as shown in Figure 8-27. The curves show clearly the levels where behaviour became non-linear on both the positive and negative $\tau_{z\theta}$ sections. The stress-strain levels applying to the cyclic Y_1 limits are

comparable with those from monotonic tests albeit with some difference which can be attributed to rates effects. The strain rate in monotonic tests was $\gamma_{z\theta}$=0.1%/hr and it took about 10 minutes to reach the Y_1 limit, while in cyclic tests with CSR_τ=0.15 the cyclic period was 1min/cycle leading to a 15 seconds 'rise time' to go from $\tau_{z\theta}$=0 to the maximum point of each cycle. Therefore, the Y_1 limit was reached about 50 times faster than under monotonic testing. For the same reason, far fewer number of "small strain" data points could be recorded in cyclic tests, making it more difficult to locate the Y_1 point reliably.

Since CSR_τ=0.15 tests showed only very slight degradations after large N in effective stresses, it can be assumed that they were close to engaging the "no effect" threshold (Y_2 surface) at their maximum points. The Y_2 surfaces have been estimated as being very close to the maximum stress points in these tests, as shown in Figure 8-28 for which $\gamma_{z\theta}$=0.02% in both sands. The estimated locations of the HCA tests Y_1 and Y_2 surfaces are very similar to those obtained from triaxial tests, which were shown in Figure 7.13 in q-p′space.

Accumulation of permanent strains: Since the cyclic loads applied were symmetrical around the τ=0kPa stress point, little permanent straining might be expected during testing. However, due to the imperfect geometry of the specimens and probable non uniformities in the load transmitting system and proximity transducers, a level of permanent strain accumulation was recorded in all tests, although the direction of strain accumulation was random. Table 8-7 shows the maximum levels of permanent strain reached in all tests, which grew with applied CSR_τ. Once permanent straining started, in either direction of rotation, it grew with loading level.

Table 8-7 Maximum permanent strains reached after 4500 cycles in standard pre-conditioned cyclic simple shear tests.

CSR_τ	Soil	Max permanent $\gamma_{z\theta,}$ (%)	Soil	Max permanent $\gamma_{z\theta}$, (%)
0.05	Dunkerque	0.012	NE34	0.001
0.15		0.030		0.009
0.25		0.120		0.091
0.35		0.985		0.812
0.45		0.817		0.883

Cyclic stiffness degradation: The cyclic secant shear stiffness, G_{cyc}, was calculated as the slope of a line connecting the maximum and minimum $\tau_{z\theta}$ points at every cycle:

$$G_{z\theta\ cyc} = \frac{\tau_{z\theta\ max} - \tau_{z\theta\ min}}{\gamma_{z\theta\ max} - \gamma_{z\theta\ min}} \qquad \text{Equation 8-1}$$

As shown in Figure 8-29, *Stable* tests showed almost no significant stiffness degradation up to 4500 cycles. Comparison of $G_{z\theta\ cyc}$ with $G_{z\theta\ max}$ values obtained from static tests show that the NE34 tests' static values matched the $G_{z\theta\ cyc}$ values in CSR_τ=0.05 tests while the Dunkerque static $G_{z\theta}$ fell below the sand's cyclic stiffness. As discussed earlier the Dunkerque static test may have under measured the stiffness.

Note also that the definition for fully *Stable* behaviour adopted for the Author's element tests is more severe than that applied by Tsuha *et al.* (2012) and Jardine & Standing (2012) to their cyclic pile tests, who considered the absence of shaft failure within 1000 cycles as proving stability, while in this thesis the lack of any reduction in p' or σ'_z is taken as the definition of stability.

8.4.2.2 *Metastable* response

Response in $\tau_{z\theta}$-σ'_z space: *Metastable* behaviour was observed in tests that showed gradual decrease in σ'_z values but did not reach failure within the 4500 cycles applied. This behaviour observed in both sands at CSR_τ=0.25 and the NE34 specimen cycled at CSR_τ=0.15 was on the borderline between the *Stable* and *Metastable* categories. As shown in Figure 8-15 the

latter NE34 test experienced slight increases in σ'_z up to N=300 and fell slowly thereafter to reach a final reduction of 3% by the final applied cycle at N=4500. In terms of pile response, the results predict that intermediate level cyclic loading leads to gentle drops in σ'_r acting on the pile surface similar to those observed in model pile tests by Tsuha *et al.* (2012), and discussed in Chapter 3. Again, it should be noted that the definition of *Metastable* behaviour in the Author's triaxial and HCA tests is different to that applied in the pile and model pile tests. The pile tests were defined *Metastable* if the developed shaft failure after between 100 and 1000 cycles. However, in making this comparison it should become in mind that the single element tests reached failure when they engaged their continuum failure ϕ' envelopes, while failure was controlled in pile tests by the interface friction angle, δ, which generally cuts in well before continuum failure leading, under similar loading conditions ,to pile shaft failure at lower N than in element tests. The links between single element and pile shaft behaviour are further discussed in next chapter.

Response in general stress space: Tracking the vertical and principal effective stresses at the mid-cycle and maximum cyclic points (in Figure 8-17 and Figure 8-18) reveals gradual drops in σ'_1, σ'_2 and σ'_3 with growing N under *Metastable* cycling, with σ'_1, showing the fastest degradation. The complete stress paths presented in q-p′ space in Figure 8-19f and Figure 8-20 show effective stress paths that initially moved in the up-left direction and then changed after around 100 cycles to move towards the origin. The initial increases seen in q may reflect Airey's (1992) CNS direct shear cyclic tests observation of the normal stresses increasing over the first few cycles before dropping quickly after (See Figure 3-24). Drifts in q and p′ values are also plotted against the number of cycles at mid-cycle and maximum points in Figure 8-21to Figure 8-23.

Figure 8-24 shows the b values applying at the maximum $\tau_{z\theta}$ points of each cycle. The b values were almost constant under *Metastable* conditions in the first 100 cycles, but then started to increase after that. The corresponding maximum α values generally showed increases as cycling continued; see Figure 8-25.

Stress-Strain response: Figure 8-26f shows the complete $\tau_{z\theta}$ vs $\gamma_{z\theta}$ load-unload loops for every 1000th cycle of the CSR_τ=0.25 test and Figure 8-28 shows the location of the maximum effective stresses reached compared to the Y_1 and Y_2 surfaces developed earlier. As predicted, the effective stress path fully engages the Y_2 surface before achieving the cyclic maxima, which explains the drops in effective stresses under cycling.

Cyclic stiffness degradation: The degradation of cyclic stiffness continued through the 4500 cycles applied without reaching any steady state, as may be seen in Figure 8-29.

8.4.2.3 *Unstable* response; CSR_τ>0.25

Response in $\tau_{z\theta}$-σ'_z space: *Unstable* conditions were observed at CSR_τ >0.25 for Dunkerque and NE34 sands respectively where cycling led to failure in less than 1000 cycles. The failure was associated with initial increases in σ'_z which were quickly followed by continuous drops until the failure envelope was reached (see Figure 8-15). Once continuum failure was engaged, a butterfly-shaped effective stress paths formed as the effective stress paths followed the cyclic mobility patterns displayed in Figure 8-14.

As with *Metasable* conditions, the definition of *Unstable* is differs between the single element laboratory and pile and model pile tests. While in single element laboratory tests *Unstable* means reaching failure after up to about 1000 cycles, behaviour was only identified as *Unstable* if pile failure developed after less than 100 cycles. The difference in definition is due, as explained earlier, to different failure criteria applying, as will be further discussed in the next chapter.

Response in invariant effective stress space: The *Unstable* effective stress paths followed in q-p′space are broadly similar to those from *Metastable* tests with initial movement towards up-left and subsequent movement toward the origin after. These changes correspond to the Mohr circle initially increasing in diameter and then shrinking as it moves towards the origin.

Figure 8-24 shows the b values developed at the maximum points in each cycle. As shown, for *Unstable* conditions, the b values were almost constant in the first 10 cycles but then increased towards b=0.5 at failure. The Maximum α values developed over each cycle showed continuous increases up to 45° at failure, as shown in Figure 8-25.

Stress-Strain response: The complete stress-strain loops developed at three N values are shown in Figure 8-26f-j. The stiffnesses corresponding to the slopes of the loops rapidly degraded as cycling continued towards failure. Figure 8-28 shows that the tests engaged the Y_2 limits during the early stages of cycling, leading to rapid degradation of effective stresses and cyclic stiffness.

Cyclic stiffness degradation: The G_{cyc} trends show sharp falls as cycling continued which eventually led to complete loss of stiffness as failure was reached. The initial $G_{cyc\ cyc}$ values fell with increasing CSR, indicating the progress of the non-linear response under the increasing load levels applied (Figure 8-29).

Comparison of cyclic response between two test sands: Similar to triaxial tests, comparison between the cyclic response of two test sands show that under low level cycling both sands showed almost identical response and the thresholds between *Stable* and *Metastable* zones were located at $0.15<CSR_\tau<0.25$ in both cases. However, under intermediate and high level cycling Dunkerque sand showed lower cyclic resistance. This, as was discussed in Chapter 7, might be due to Dunkerque's higher level of crushing under higher cyclic loads. Further research is needed to assess this possibility.

8.5 Relation between σ'_r and p′degradation

In Chapter 6, it was argued that (i) the shearing mode developed under pile axial loading could be modelled reasonably as constant volume simple shear, and that (ii) the mean effective stress (p′) developed under undrained triaxial cycling could be taken as an indicator of how σ'_r may change close to a pile shaft under cyclic loading. The results from this chapter can be used to establish the relation between the rates of σ'_r and p′ degradation which can be used to relate the triaxial tests results presented in Chapter 7 to this chapter's HCA tests and also the field and model pile tests. To aid this comparison, the $\Delta\sigma'_r/\Delta p'$ratios developed in the HCA tests are plotted against the number of cycles in Figure 8-30. The ratio is close to 1 initially but drops with the degree of effective stress degradation towards an ultimate ratio of 0.835. This finding will be used in next chapter to relate the triaxial test results to the pile experiments.

8.6 Conclusions and remarks

This Chapter presents results from monotonic and cyclic simple shear HCA tests involving the Author's "standard" pre-conditioning procedures. Monotonic tests provided reference information on the small strain behaviour and stiffness data along with the sand's peak shear strengths. It was not possible to measure in these tests the sands' critical state parameters; high pressure apparatuses are required for this purpose. The programme of cyclic simple shear tests identified the key trends for mean effective stress drifts, degradations of q, cyclic stiffness and other parameters, covering a wide range of CSR_τ values. The following conclusions can be drawn:

1- The monotonic tests show that the limit for the linear response Y_1 is extended by the pre-conditioning effective stress path imposed, including the ageing periods.

2- Similar to triaxial tests, three different modes of behaviour were observed at different CSR_τ levels. *Stable* responses were observed in tests with CSR_τ=0.05 and 0.15 where simple shear cycling led to marginal gains in p′ and no clear cyclic stiffness and deviatoric stress degradation were observed. *Unstable* tests at CSR_τ>0.25 levels showed rapid drops in p′ accompanied by degradation of cyclic stiffness and the deviatoric stress within 1000 cycles. *Metastable* behaviour was observed at Intermediate CSR_τ levels were cyclic loading led to p′, q and cyclic stiffness degradation, but not full continuum failure within 1000 cycles.

3- Assessment of full cyclic stress-strain loops showed that in *Stable* tests the stress paths were kept inside the Y_2 kinematic yield surface even in cases where they had engaged the linear elastic Y_1 linear limit. However, the Y_2 limits were engaged in *Metastable* and *Unstable* tests which led to loss of effective stress and cyclic stiffness, but at moderately different rates.

4- Under similar loading conditions single element specimens can sustain higher cyclic loading levels than field or model pile shafts without failure. This is due to triaxial and HCA single element tests' failure being controlled by the continuum failure envelope, while in pile and model pile tests' failure are controlled by the soil-pile interface friction angle enevelope with $\delta' < \phi'$.

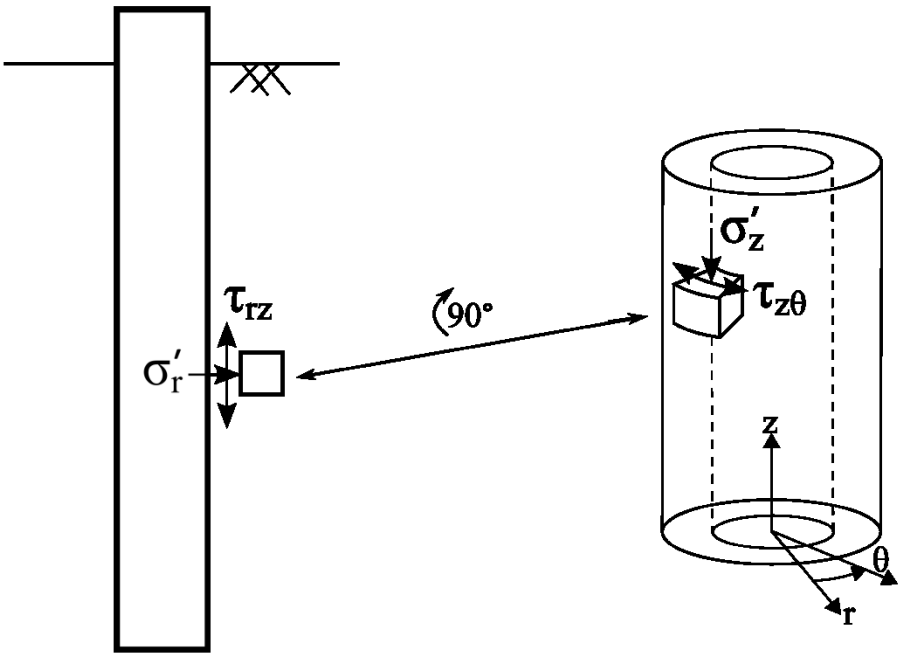


Figure 8-1 Analogy for modelling the stress conditions adjacent to pile surface under axial loading in HCA apparatus.

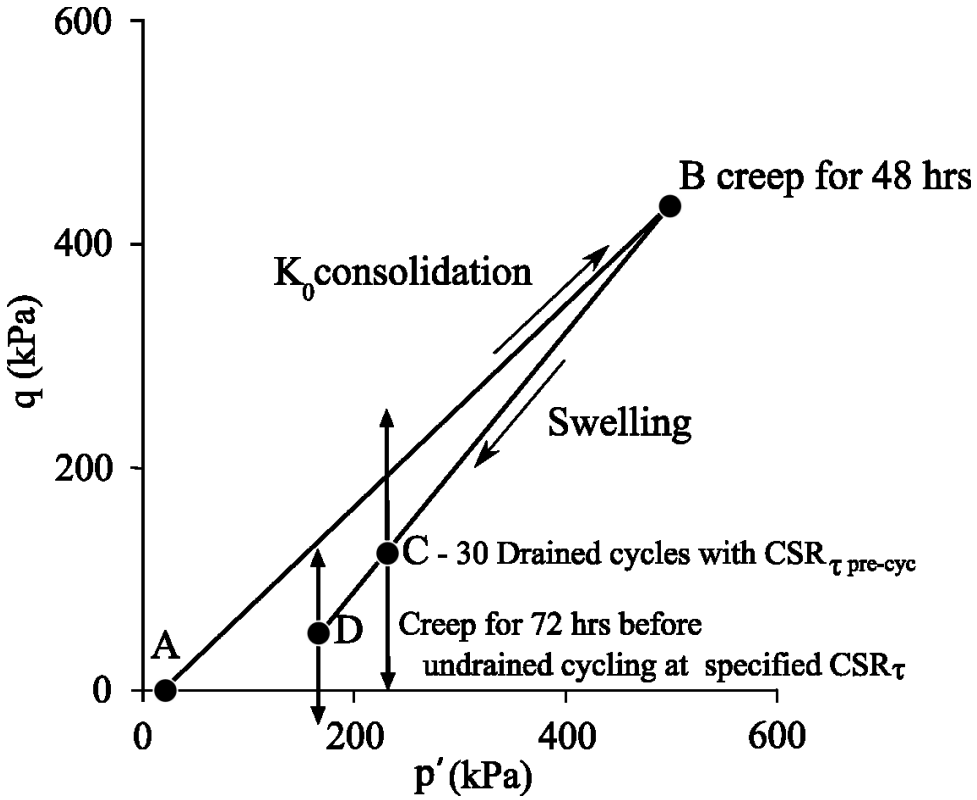


Figure 8-2 The "standard" pre-conditioning procedure applied for monotonic and cyclic simple shear tests.

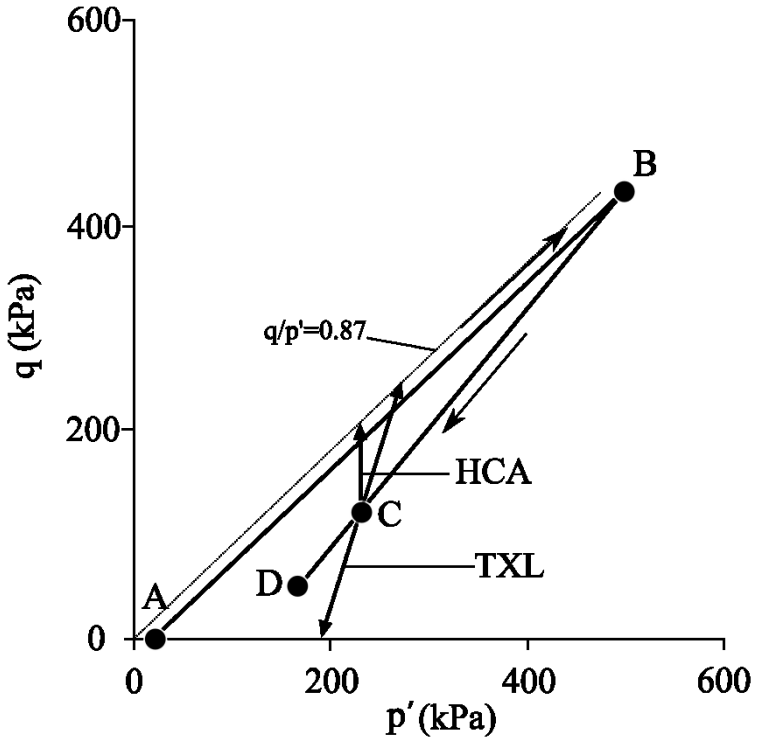


Figure 8-3 Comparison between stress paths followed in HCA and triaxial tests during the pre-cycling stage

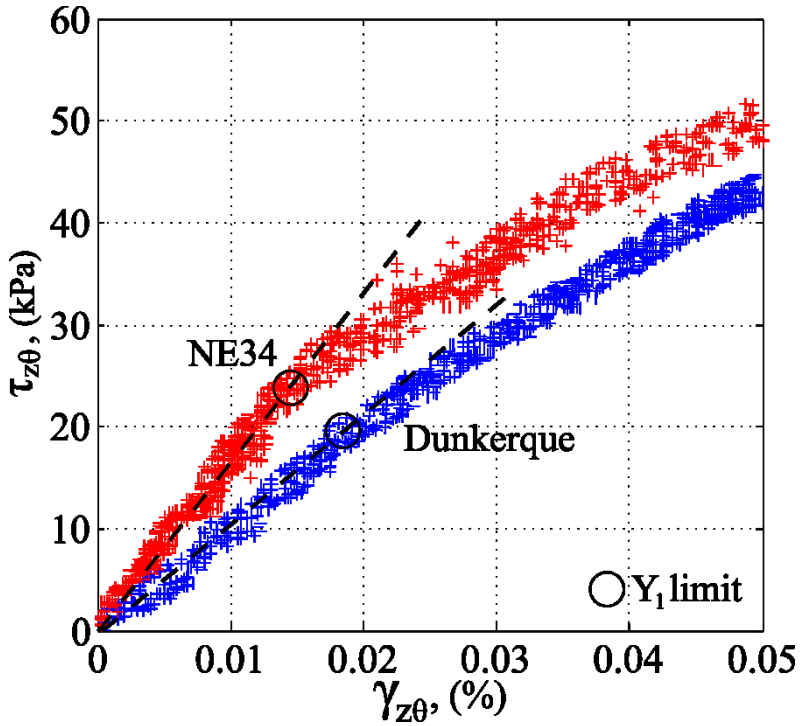


Figure 8-4 Torsional stress-strain probing to locate Y_1 boundary for "standard" pre-conditioned Dunkerque and NE34 sands. e_0=0.64.

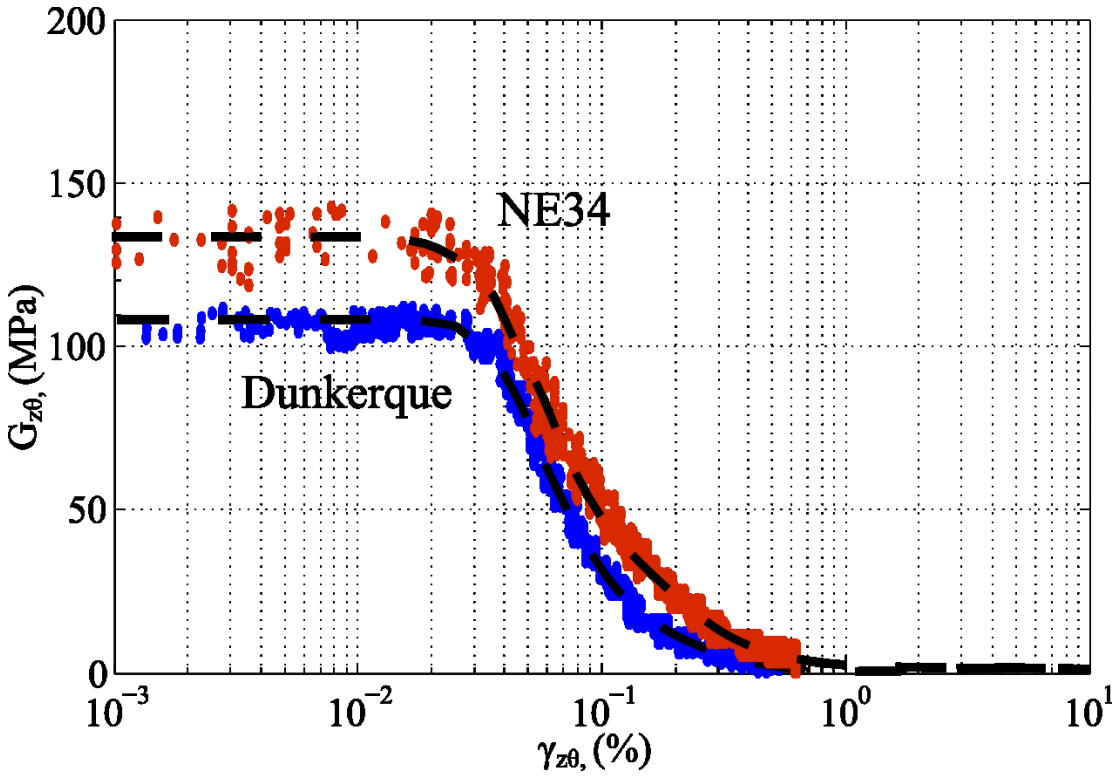


Figure 8-5 $G_{z\theta}$ tangent degradation of "standard" pre-conditioned Dunkerque and NE34 sands. e_0=0.64.

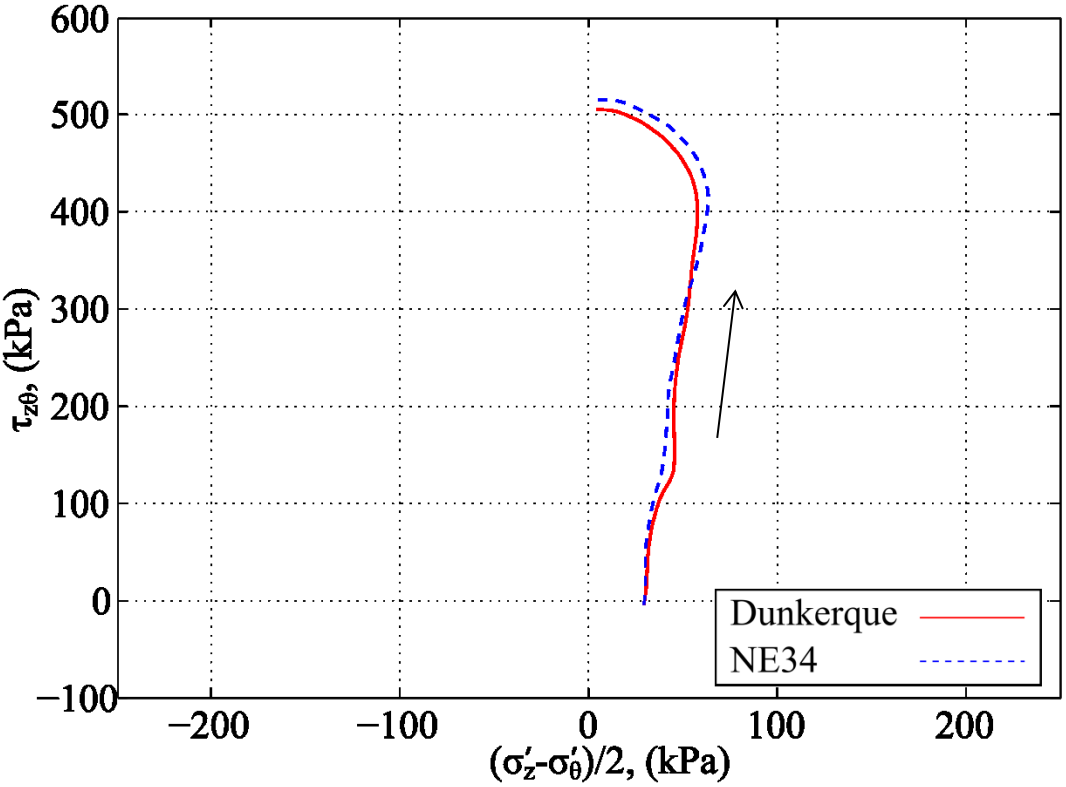


Figure 8-6 Effective stress paths followed in $\tau_{z\theta}$-(σ'_z- σ'_θ)/2 space in monotonic simple shear tests in HCA with in "standard" pre-conditioning.

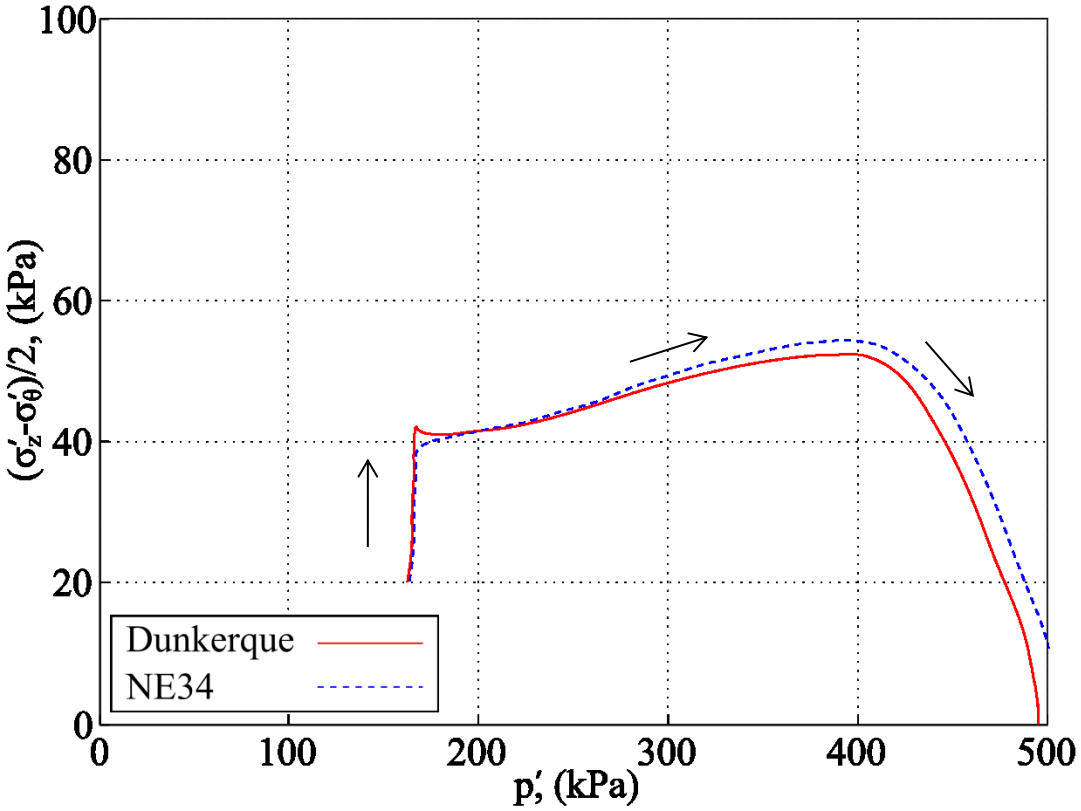


Figure 8-7 Stress paths followed in (σ'_z- σ'_θ)/2 – p′space in monotonic simple shear tests in HCA with in "standard" pre-conditioning.

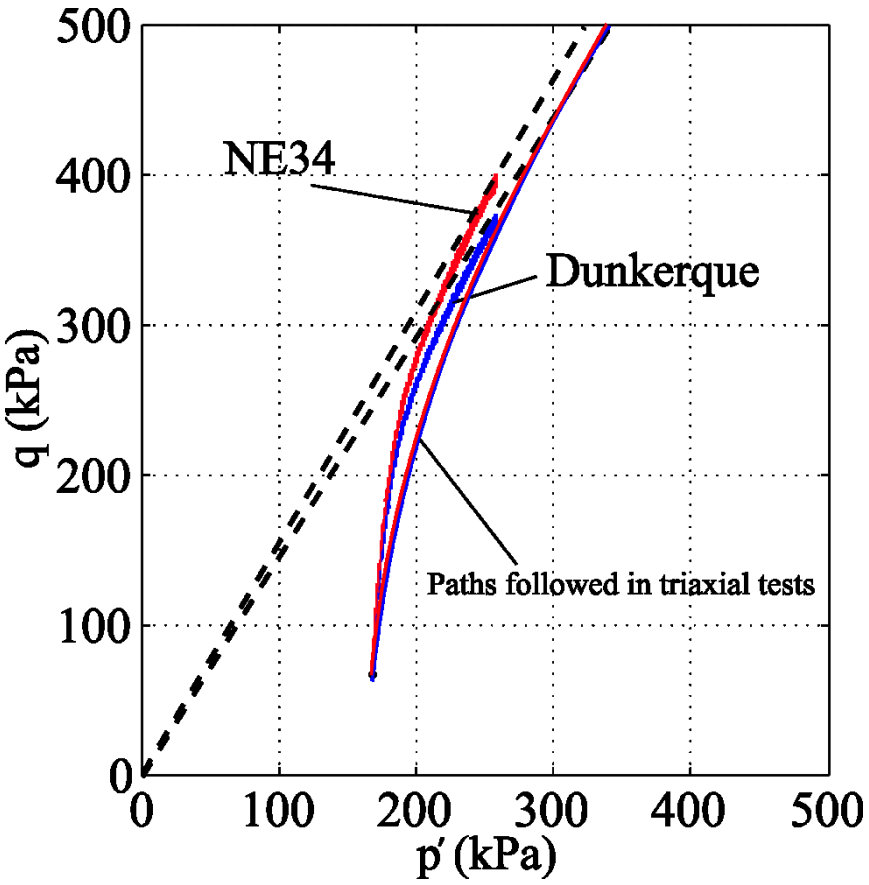


Figure 8-8 The q-p′stress paths followed in HCA simple shear tests with "standard" pre-conditioning and comparison with stress paths followed in triaxial undrained tests. e_0=0.64.

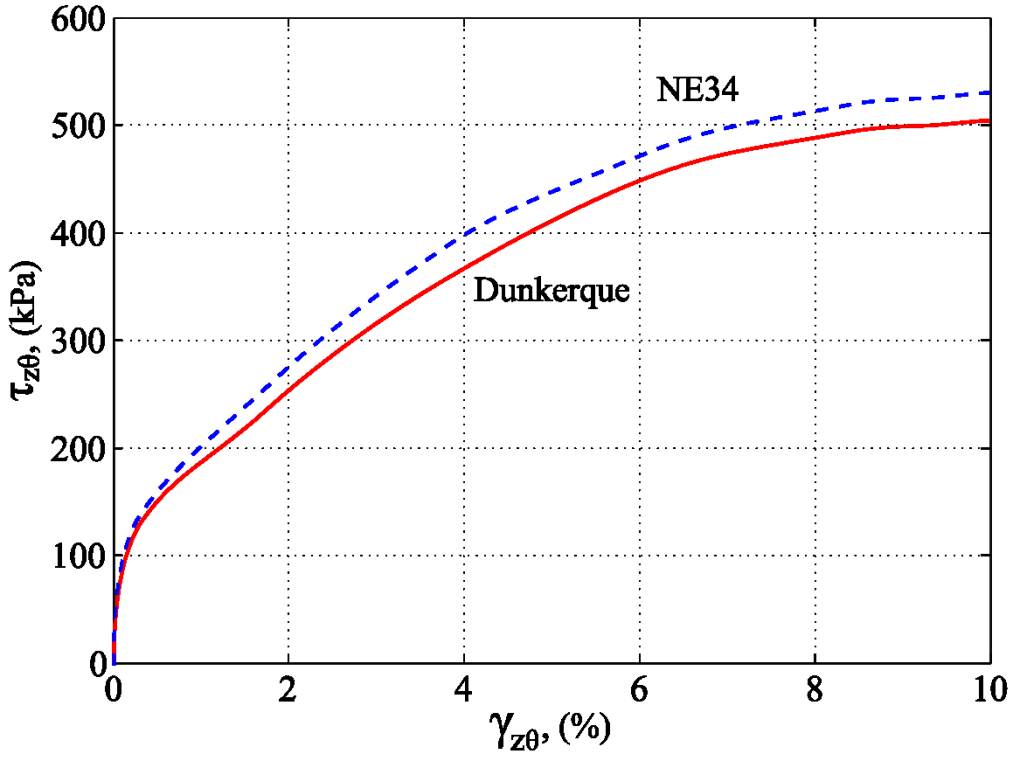


Figure 8-9 $\tau_{z\theta}$-$\gamma_{z\theta}$ trends from simple shear tests with "standard" preconditioning e_0=0.64

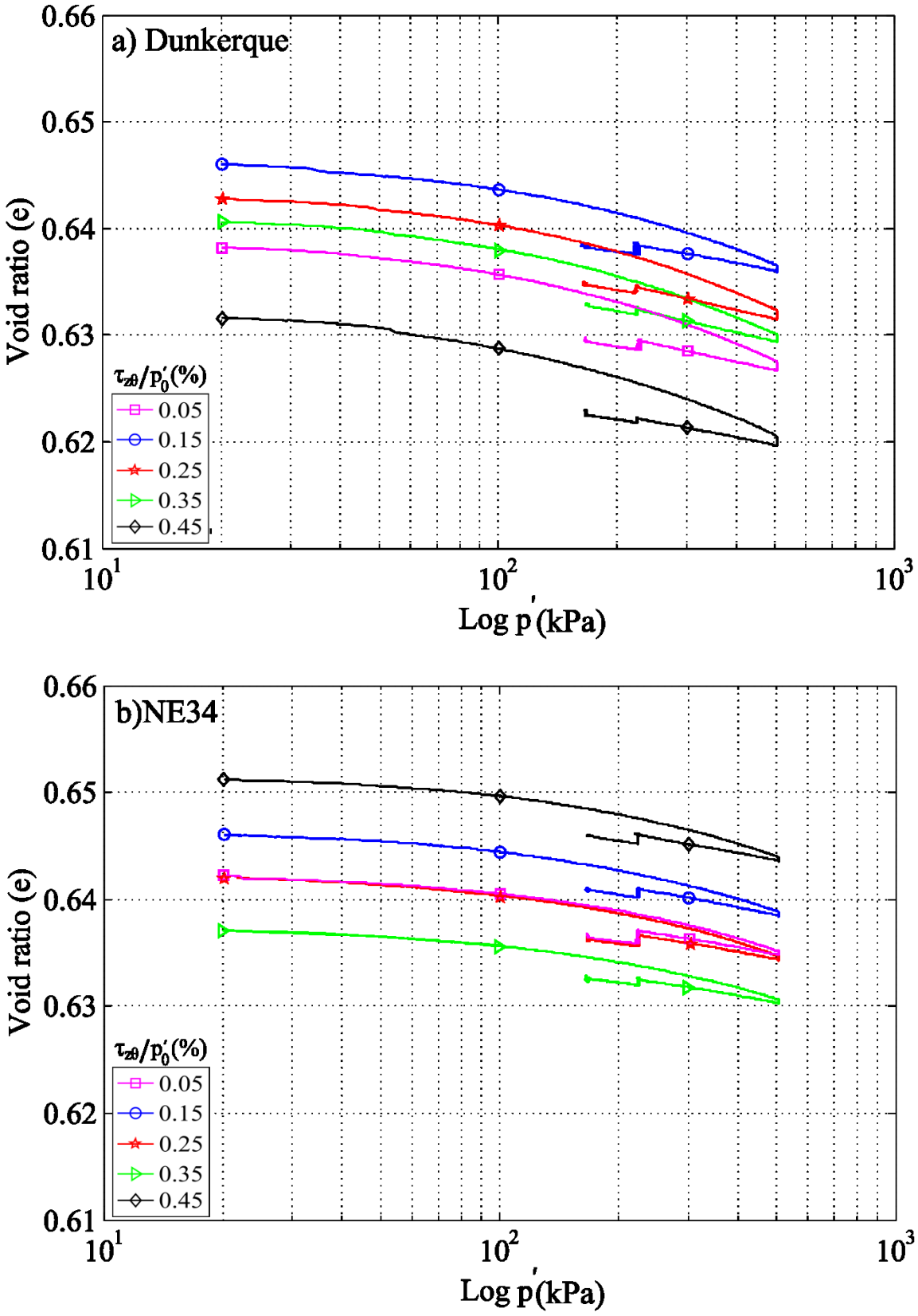


Figure 8-10 Void ratio changes during the "standard" pre-conditioning procedure on a) Dunkerque and b) NE34 sands prior to applying simple shear cyclic loads at different CSR_τ values. e_0 target=0.64.

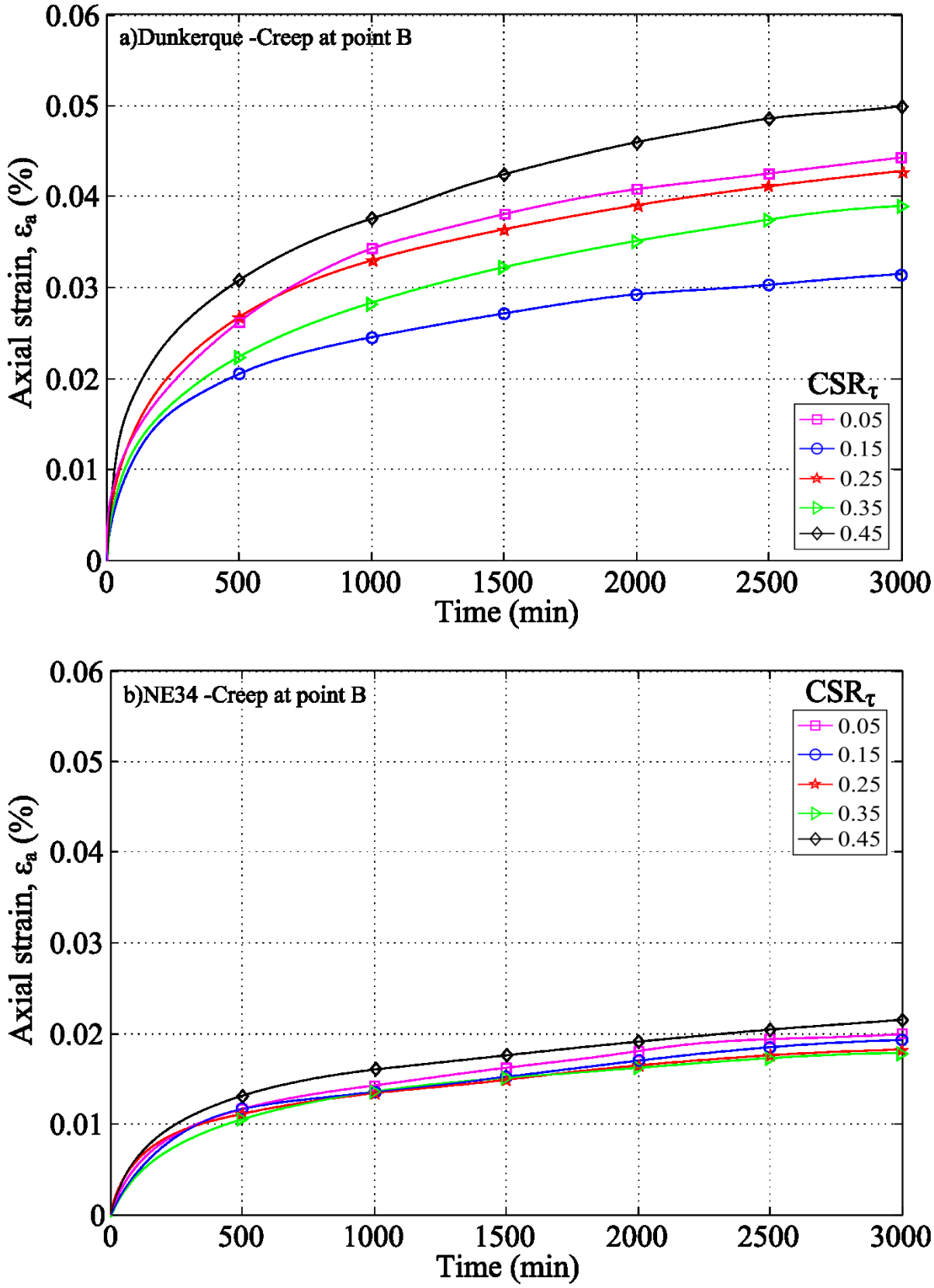


Figure 8-11 Axial straining during 48 hours of creep at point B after consolidation on a) Dunkerque and b) NE34 as part of the "standard" pre-conditioning procedure prior to applying simple shear cyclic loads at different CSR_τ values. e_0=0.64.

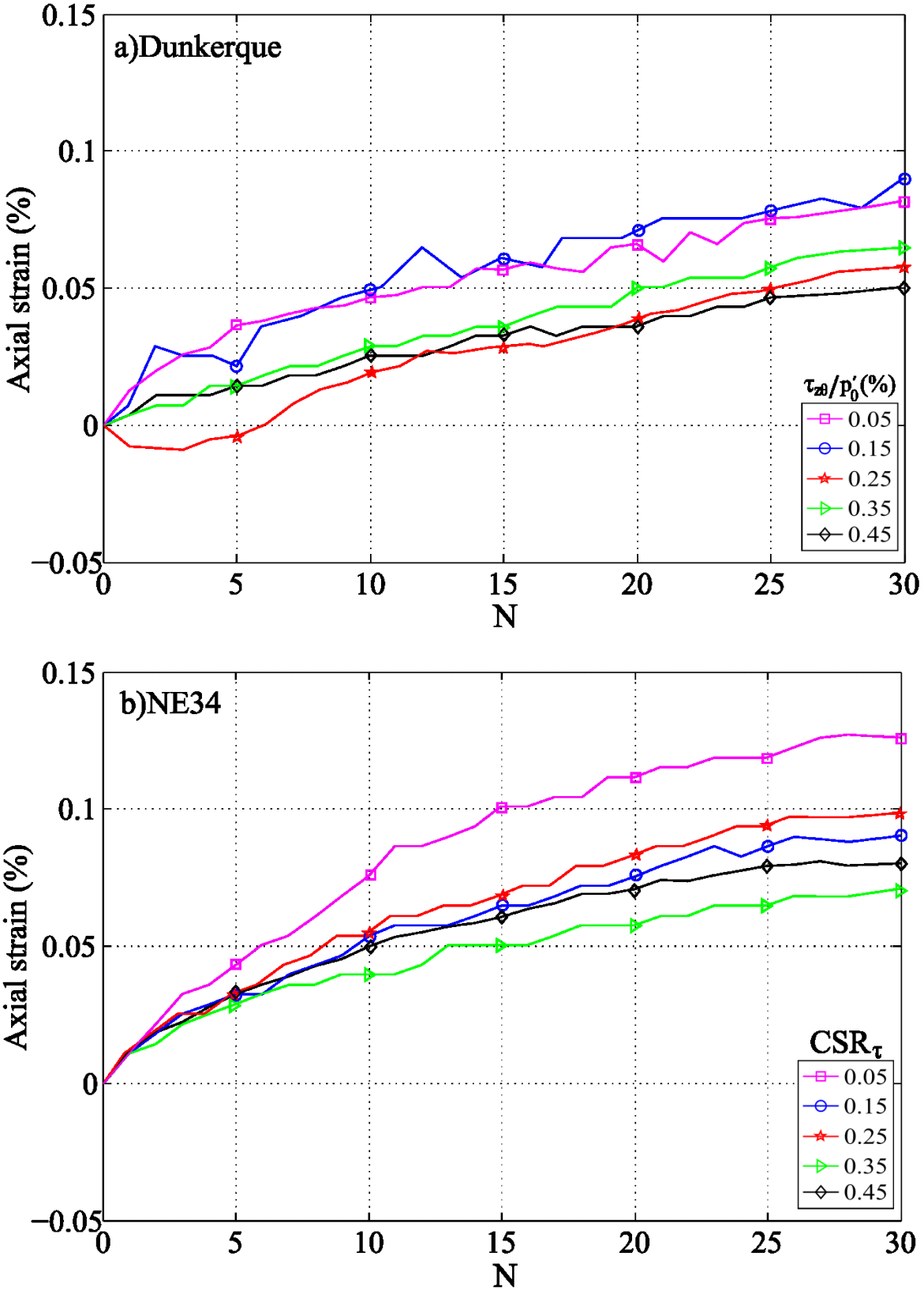


Figure 8-12 Accumulation of axial strains under drained pre-cycling at point C on a) Dunkerque and b) NE34 as part of the "standard" pre-conditioning procedure prior to applying simple shear cyclic loads at different CSR_τ values. e_0 =0.64. $CSR_{\tau precycle}$=0.47

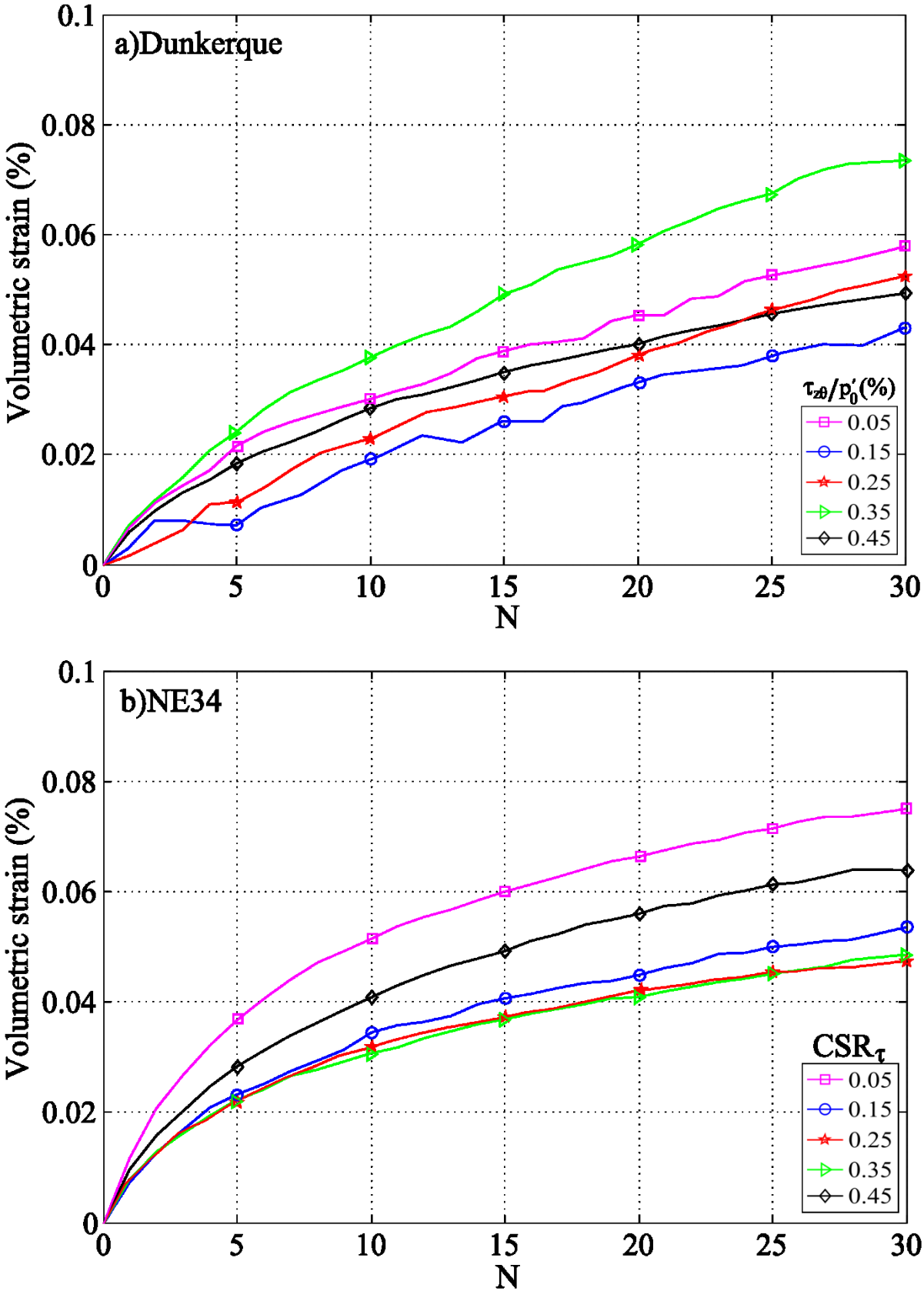


Figure 8-13 Accumulation of volumetric strains under drained pre-cycling at point C on a) Dunkerque and b) NE34 as part of the "standard" pre-conditioning procedure prior to applying simple shear cyclic loads at different CSR_τ values. e_0 =0.64. $CSR_{\tau precycle}$=0.47

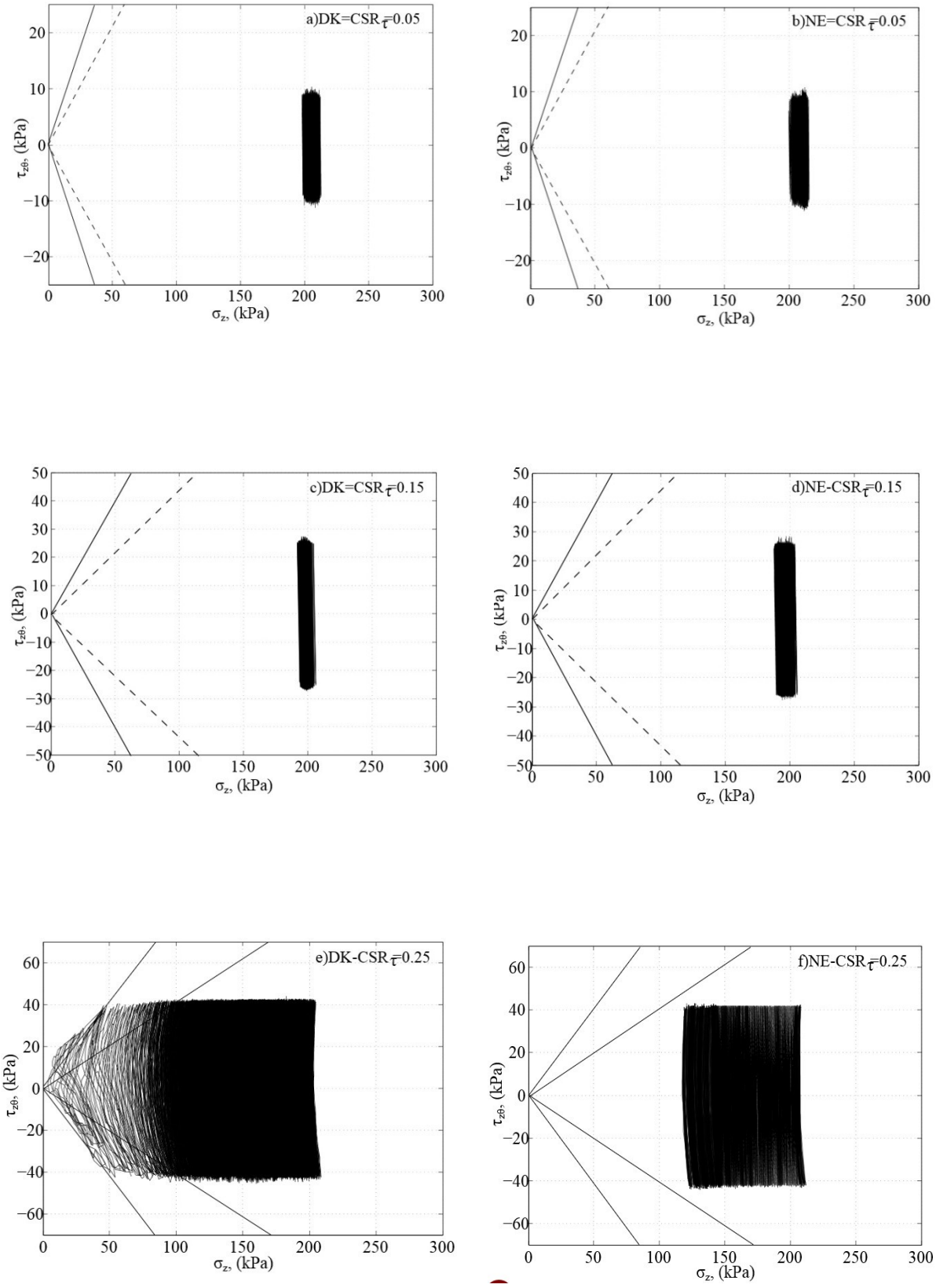


Figure 8-14a-f $\tau_{z\theta}$-σ'_z stress paths following under simple shear cycling in tests with "standard" pre-conditioning. e_0=0.64

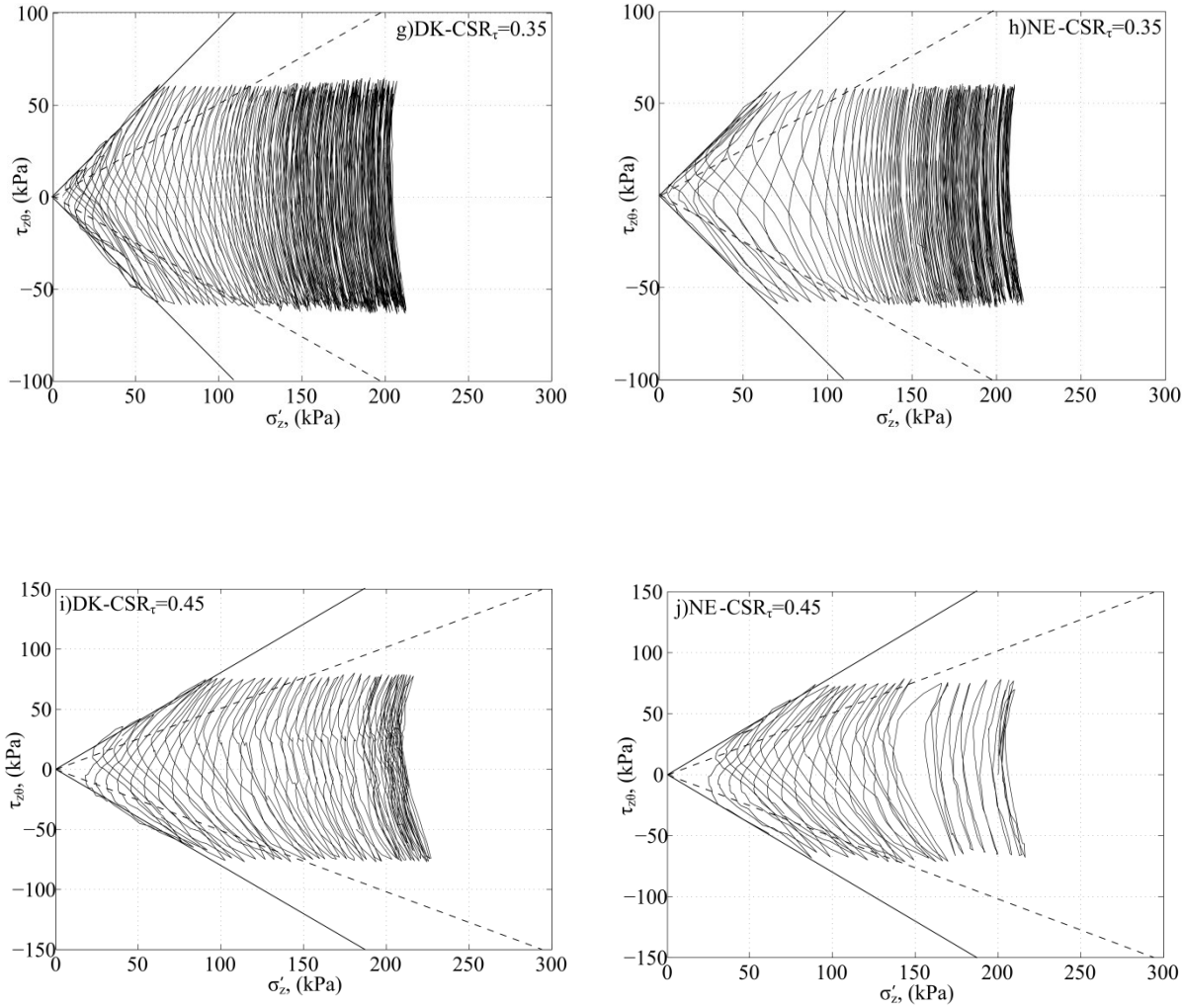


Figure 8-14 g-j $\tau_{z\theta}$-σ'_z stress paths following under simple shear cycling in tests with "standard" pre-conditioning. e_0=0.64

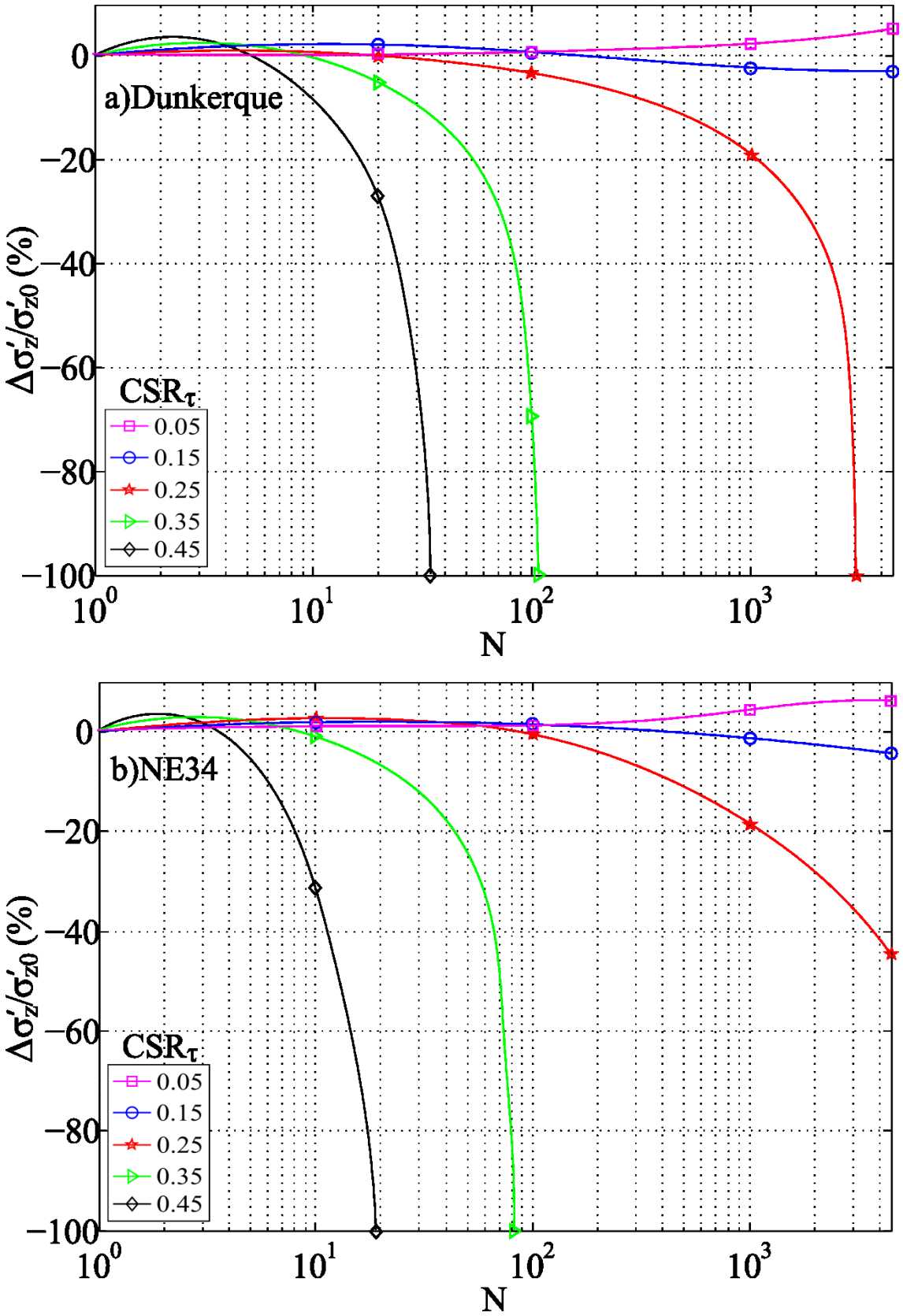


Figure 8-15 Effect of CSR_τ on degradation of σ'_z at mid cycle point (τ=0kPa) under simple shear cycling at Point D for a)Dunkerque and b)NE34 specimens after standard consolidation, conditioning cycles and ageing stages. All samples prepared at e_0=0.64.

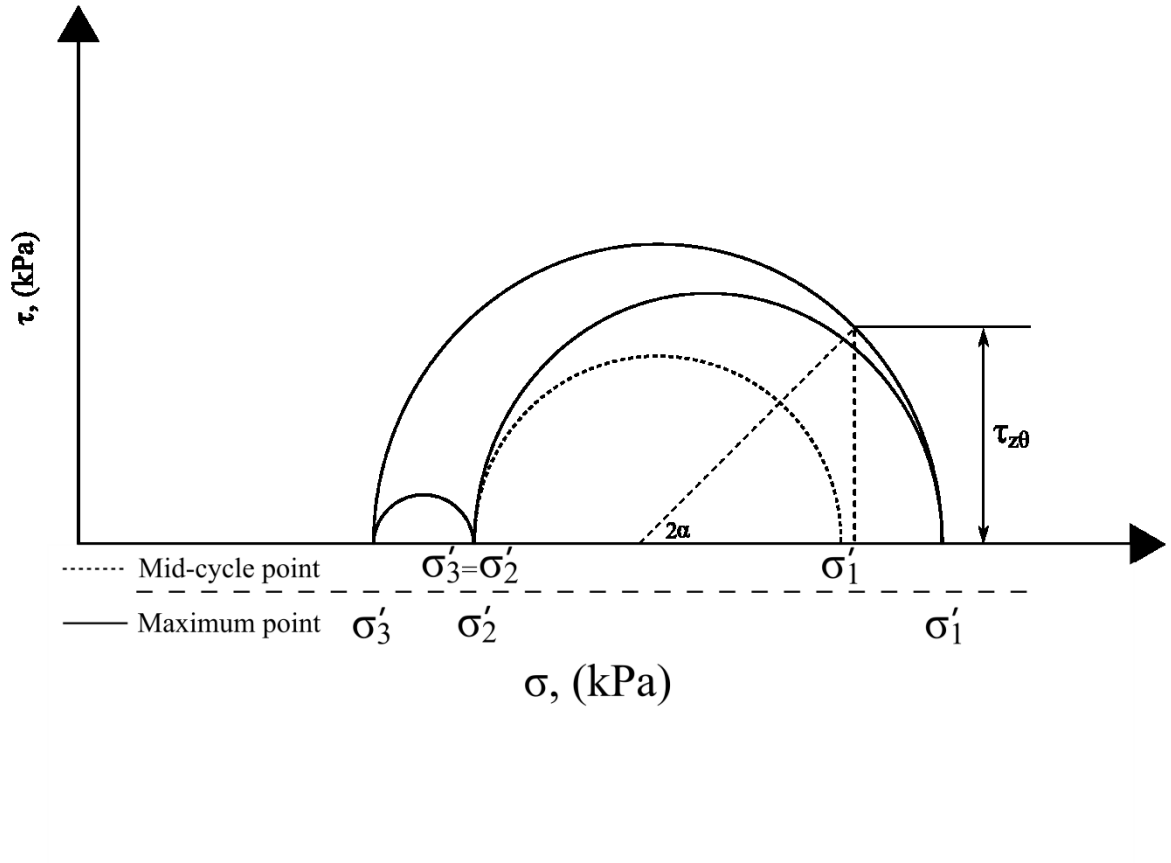


Figure 8-16 Illustration of Mohr circles at mid-cycle and maximum points in simple shear HCA tests

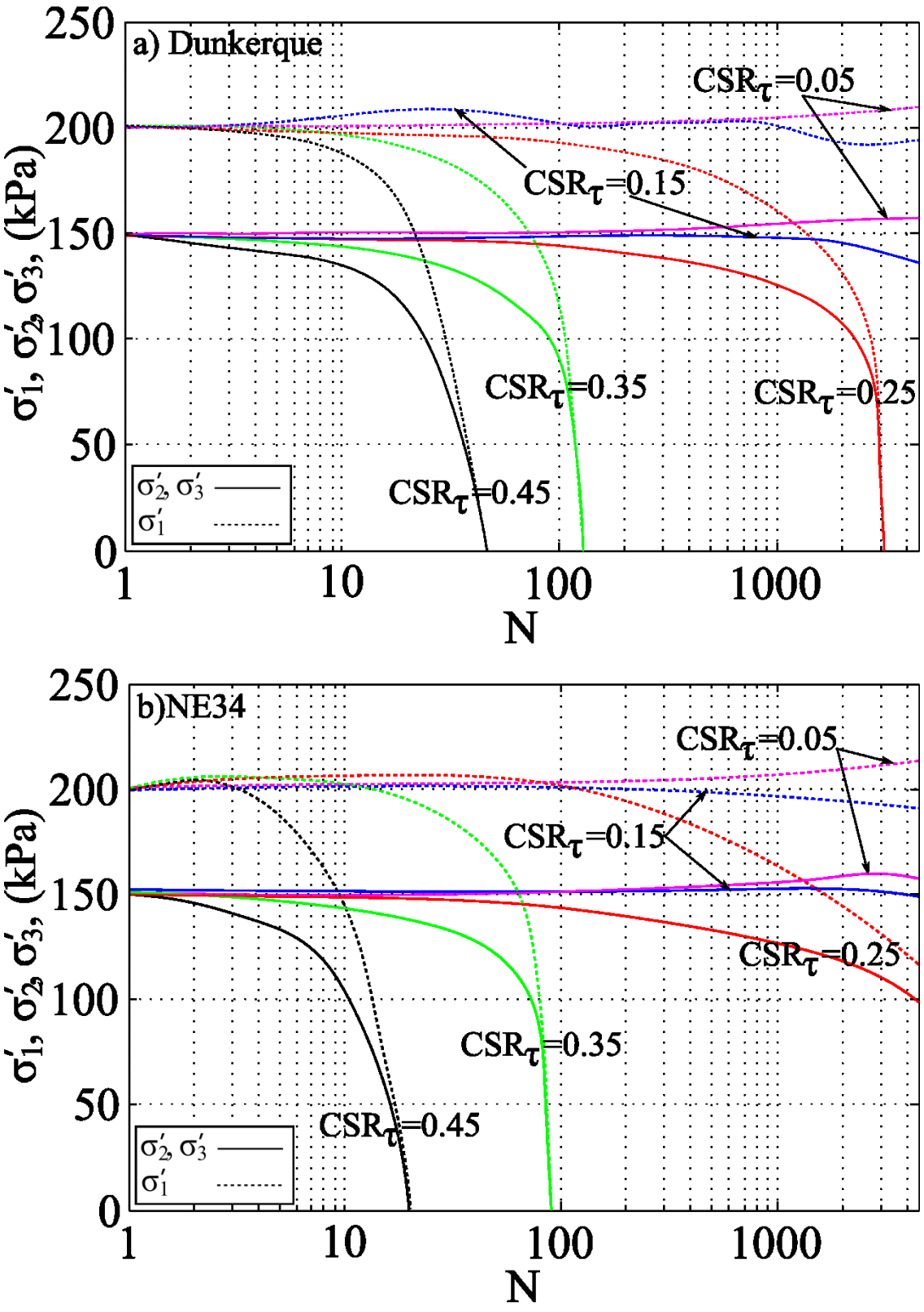


Figure 8-17 Effect of CSRτ on degradation of σ'_r, σ'_z and σ'_θ at mid cyclic point ($\tau=\tau_{cyc}$) under simple shear cycling at Point D for a)Dunkerque and b)NE34 specimens after standard consolidation, conditioning cycles and ageing stages. All samples prepared at e0=0.64.

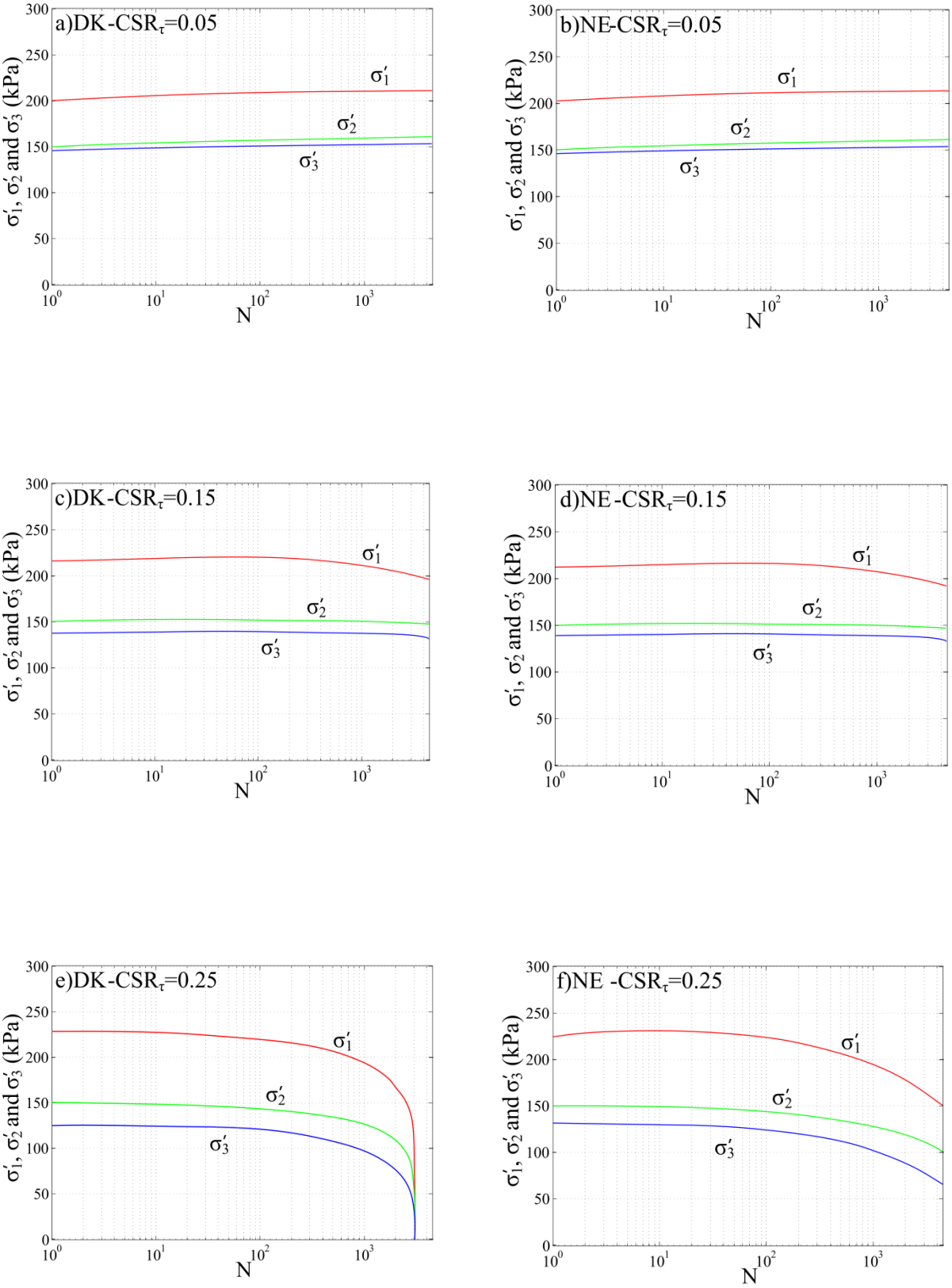


Figure 8-18a-f Degradation of σ'_1, σ'_2 and σ'_3 at maximum cyclic point under simple shear cycling at Point D after standard consolidation, conditioning cycles and ageing stages. All samples prepared at e_0=0.64

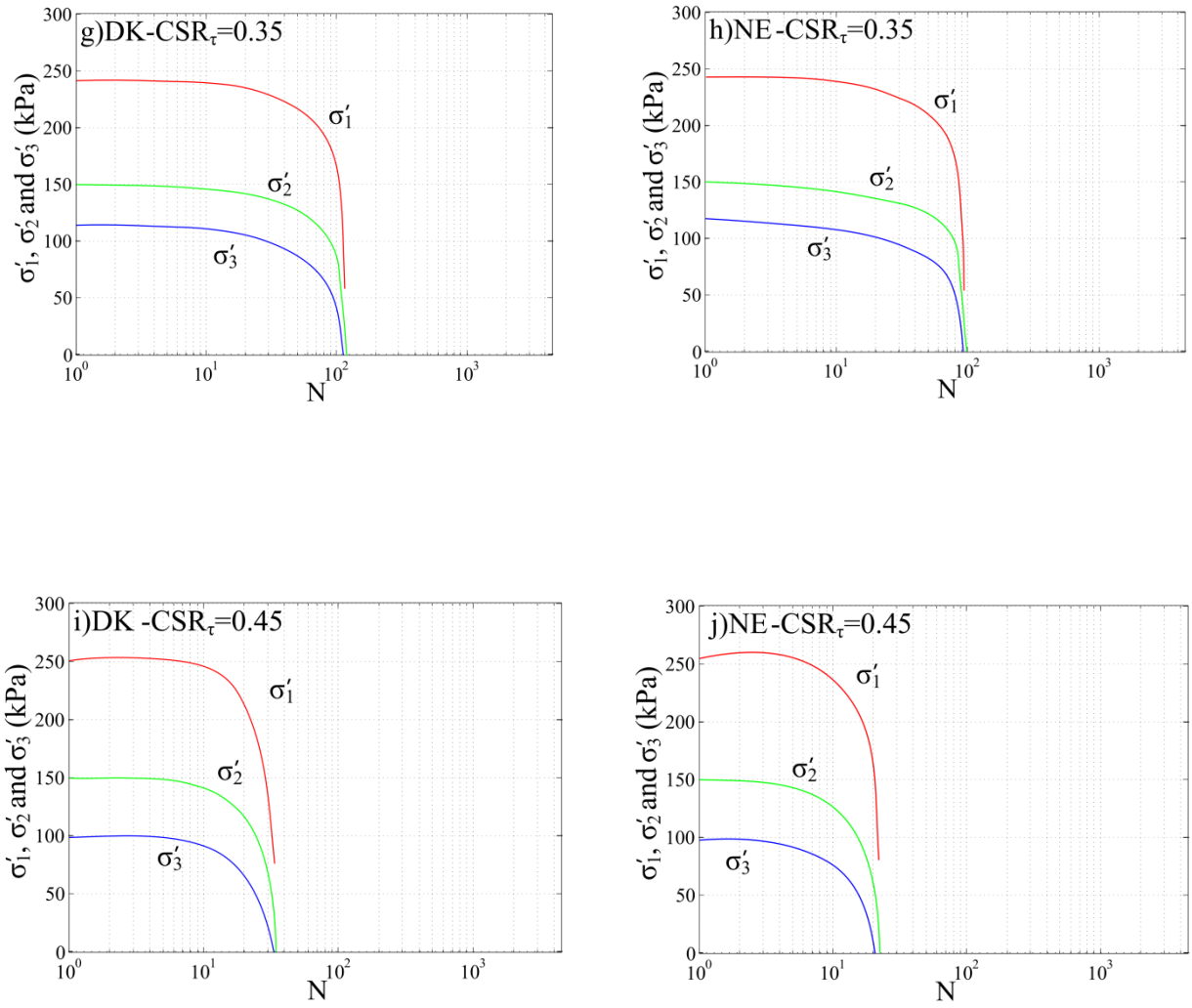


Figure 8-18g-j Degradation of σ'_1, σ'_2 and σ'_3 at maximum cyclic point under simple shear cycling at Point D after standard consolidation, conditioning cycles and ageing stages. All samples prepared at e_0=0.64.

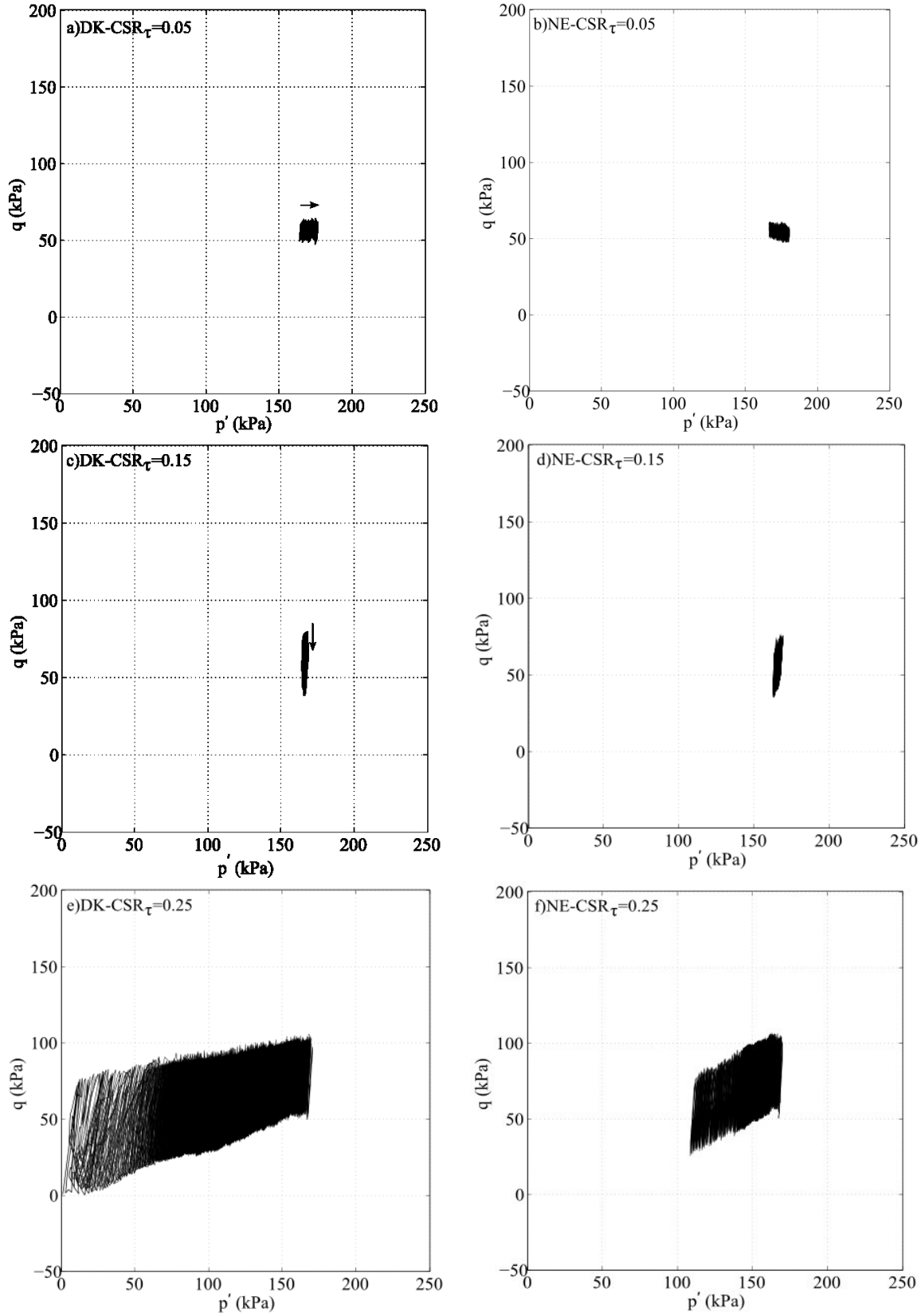


Figure 8-19 a-f stress paths followed in q-p′in cyclic simple shear tests with "standard" pre-conditioning at different CSR_τ levels. e_0=0.64

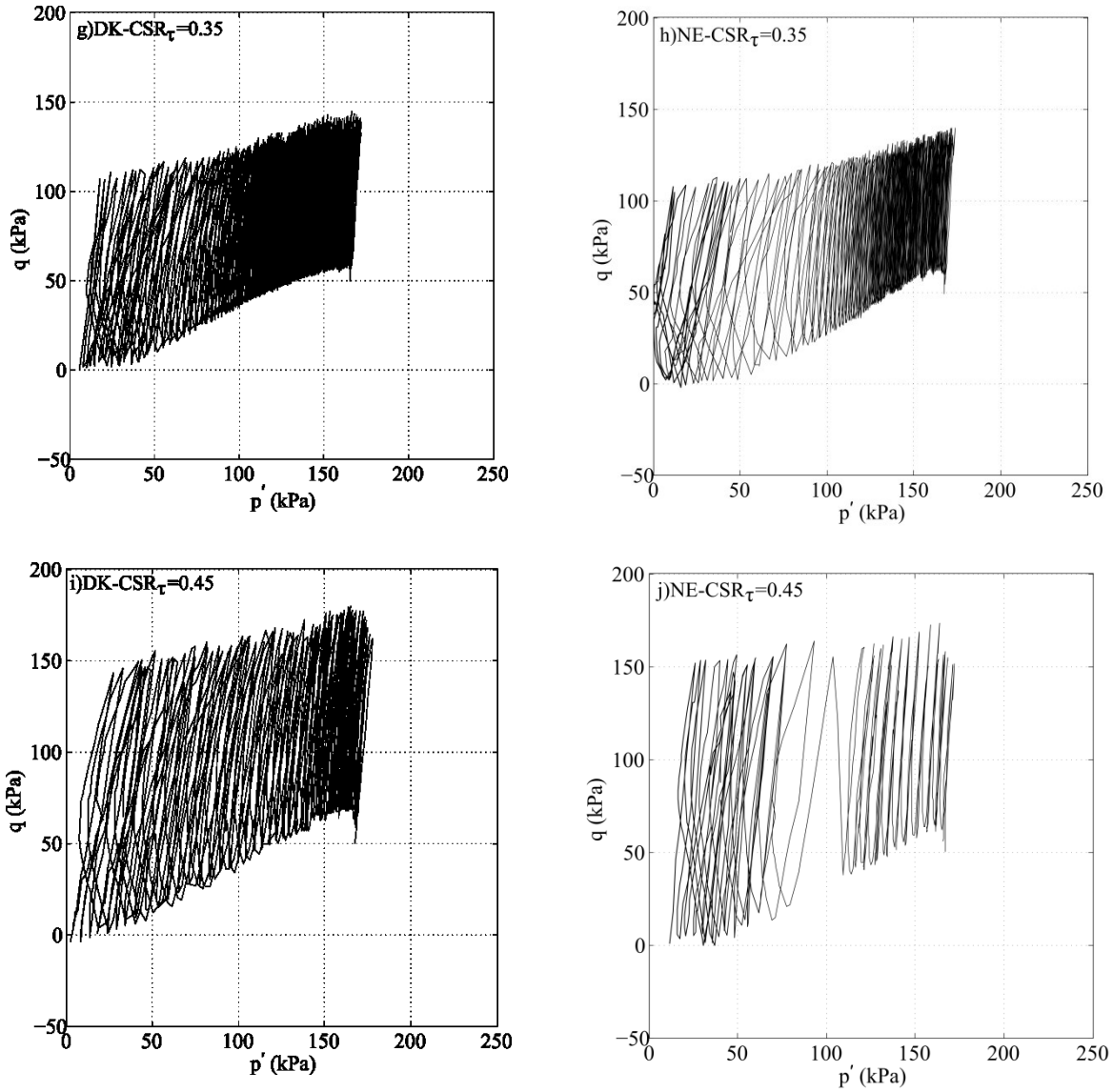


Figure 8-19 g-j stress paths followed in q-p′in cyclic simple shear tests with "standard" pre-conditioning at different CSR_τ levels. e_0=0.64

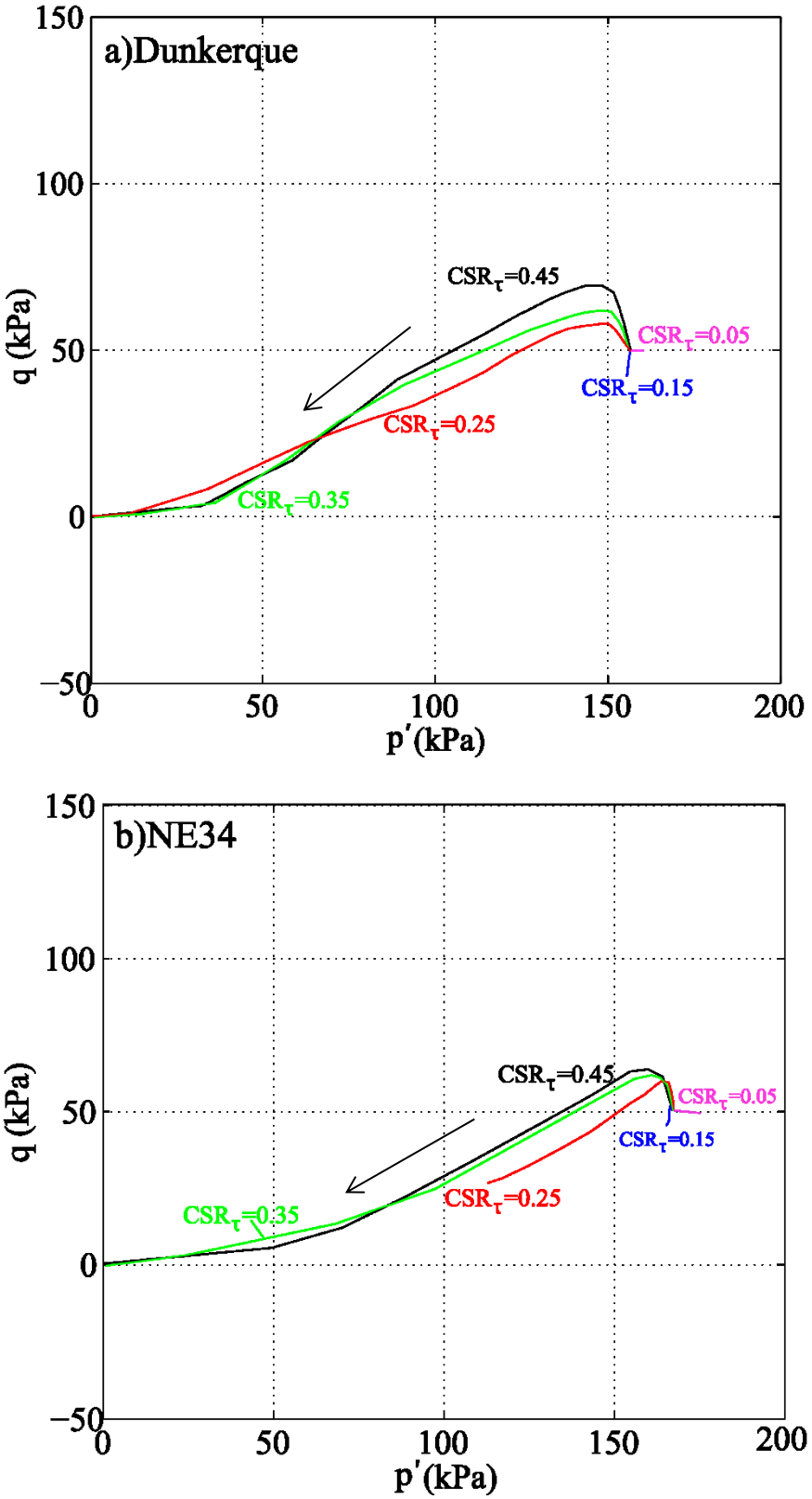


Figure 8-20 Stress paths followed in cyclic simple shear tests in q-p′space from "standard" pre-conditioned tests on a)Dunkerque and b)NE34 sands at mid cycle points (τ=0kPa). All samples prepared at e_0=0.64.

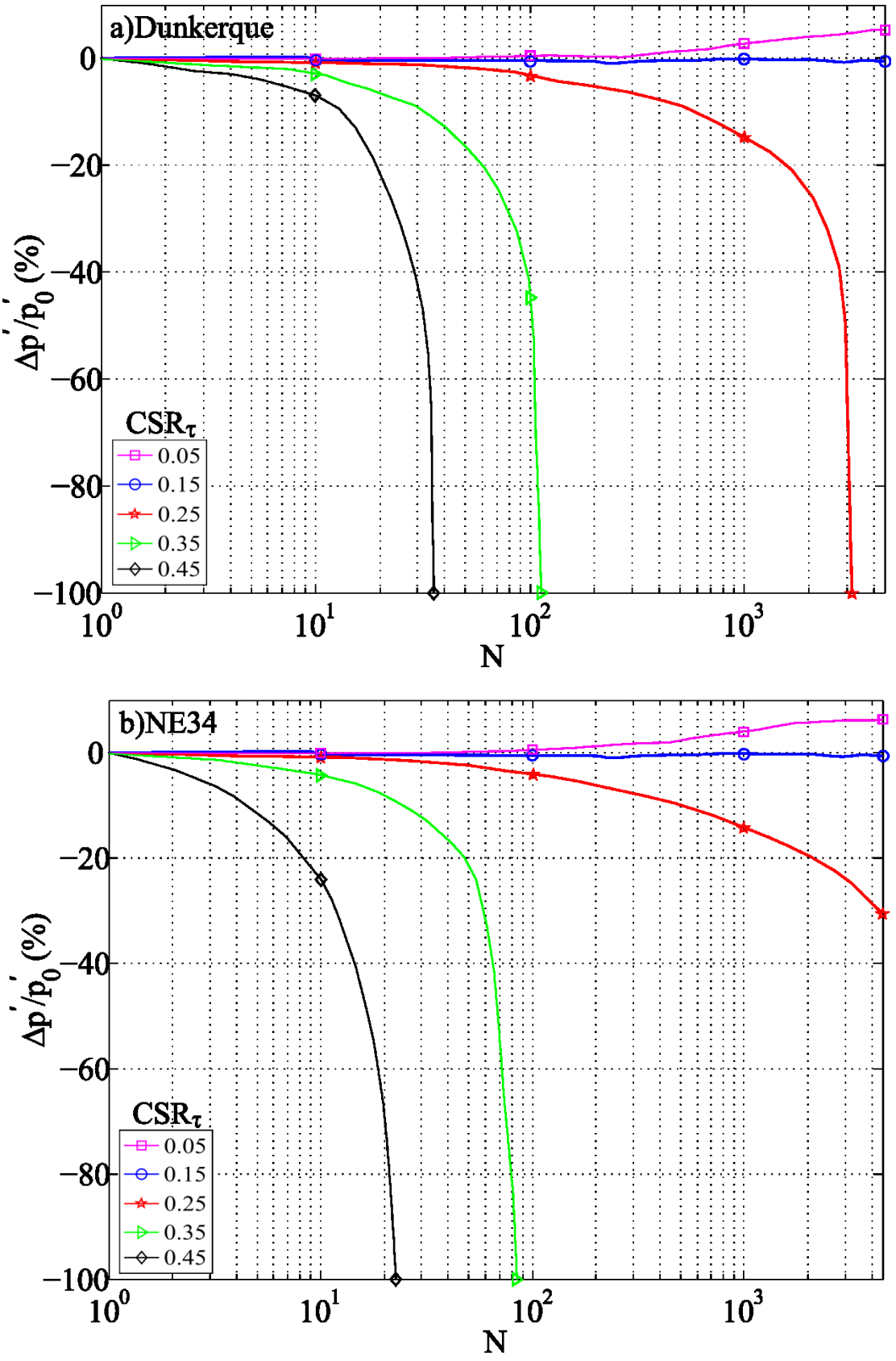


Figure 8-21 Effect of CSR_τ on degradation of mean effective stresses at mid cycle point (τ=0kPa) under simple shear cycling at Point D for a)Dunkerque and b)NE34 specimens after standard consolidation, conditioning cycles and ageing stages. All samples prepared at e_0=0.64.

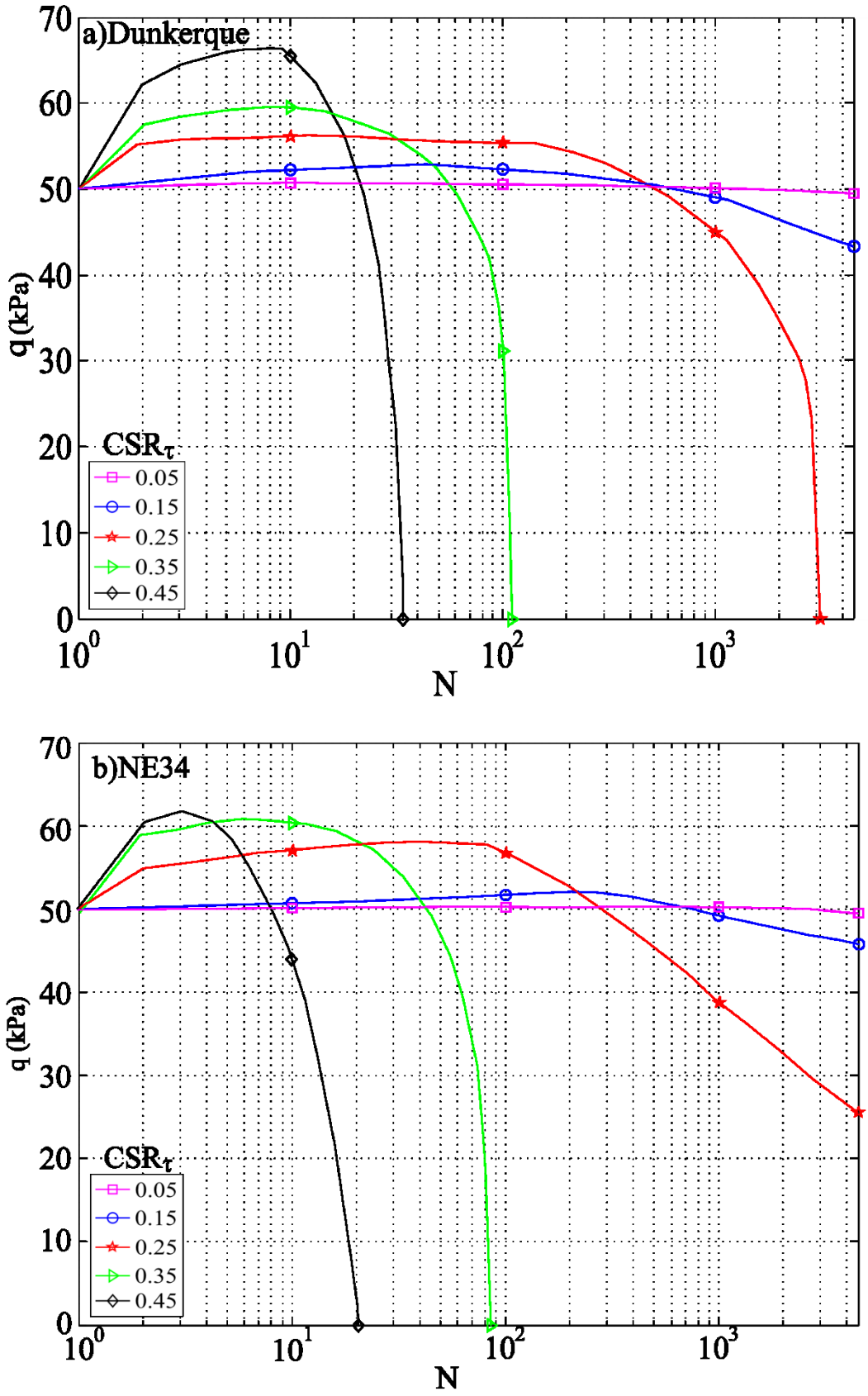


Figure 8-22 Effect of CSR_τ on degradation of deviatoric stresses at mid cycle point (τ=0kPa) under simple shear cycling at Point D for a)Dunkerque and b)NE34 specimens after standard consolidation, conditioning cycles and ageing stages. All samples prepared at e_0=0.64.

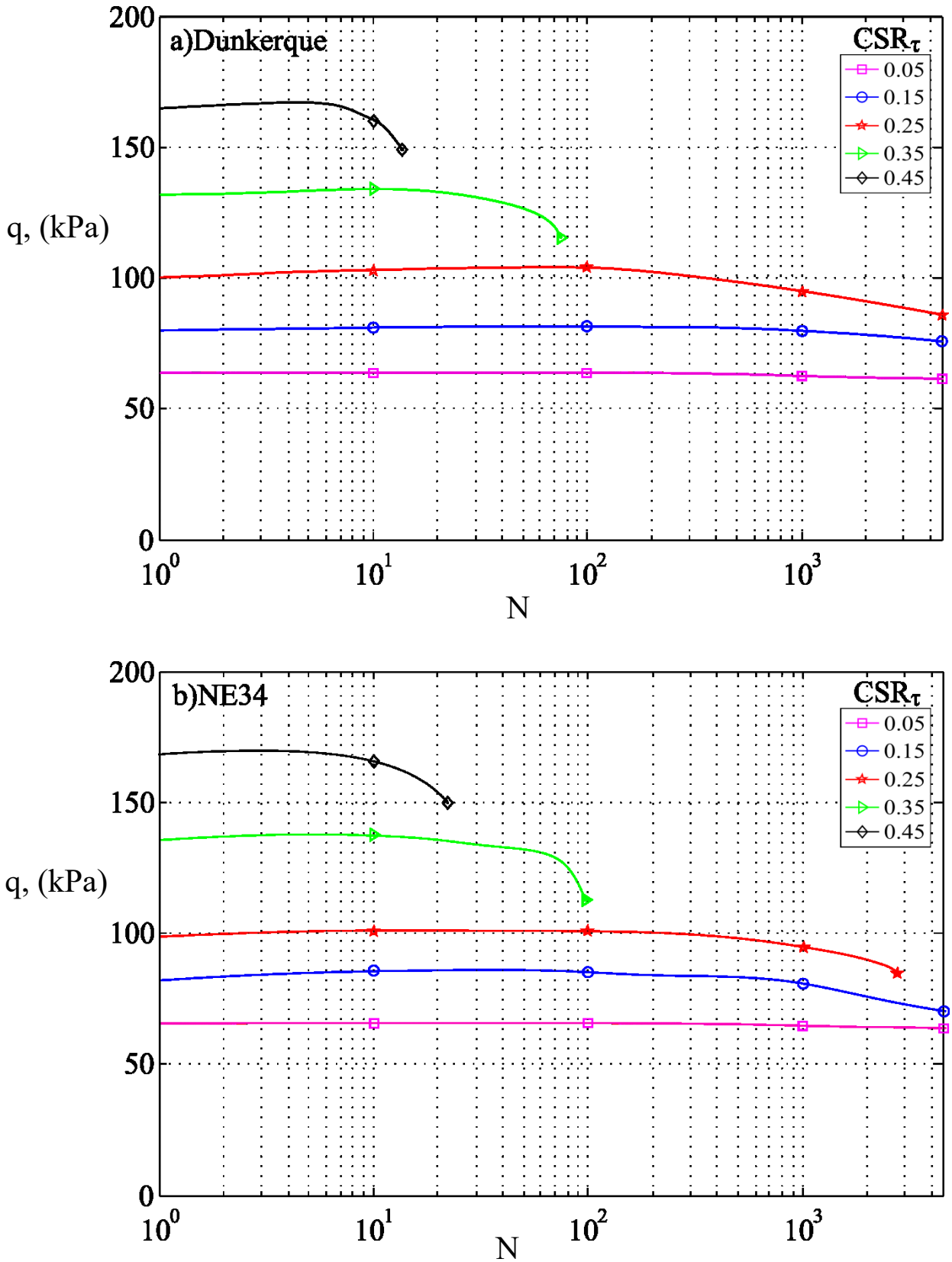


Figure 8-23 Effect of CSR_τ on degradation of deviatoric stresses at maximum cyclic point ($\tau=\tau_{cyc}$) under simple shear cycling at Point D for a)Dunkerque and b)NE34 specimens after standard consolidation, conditioning cycles and ageing stages. All samples prepared at e_0=0.64

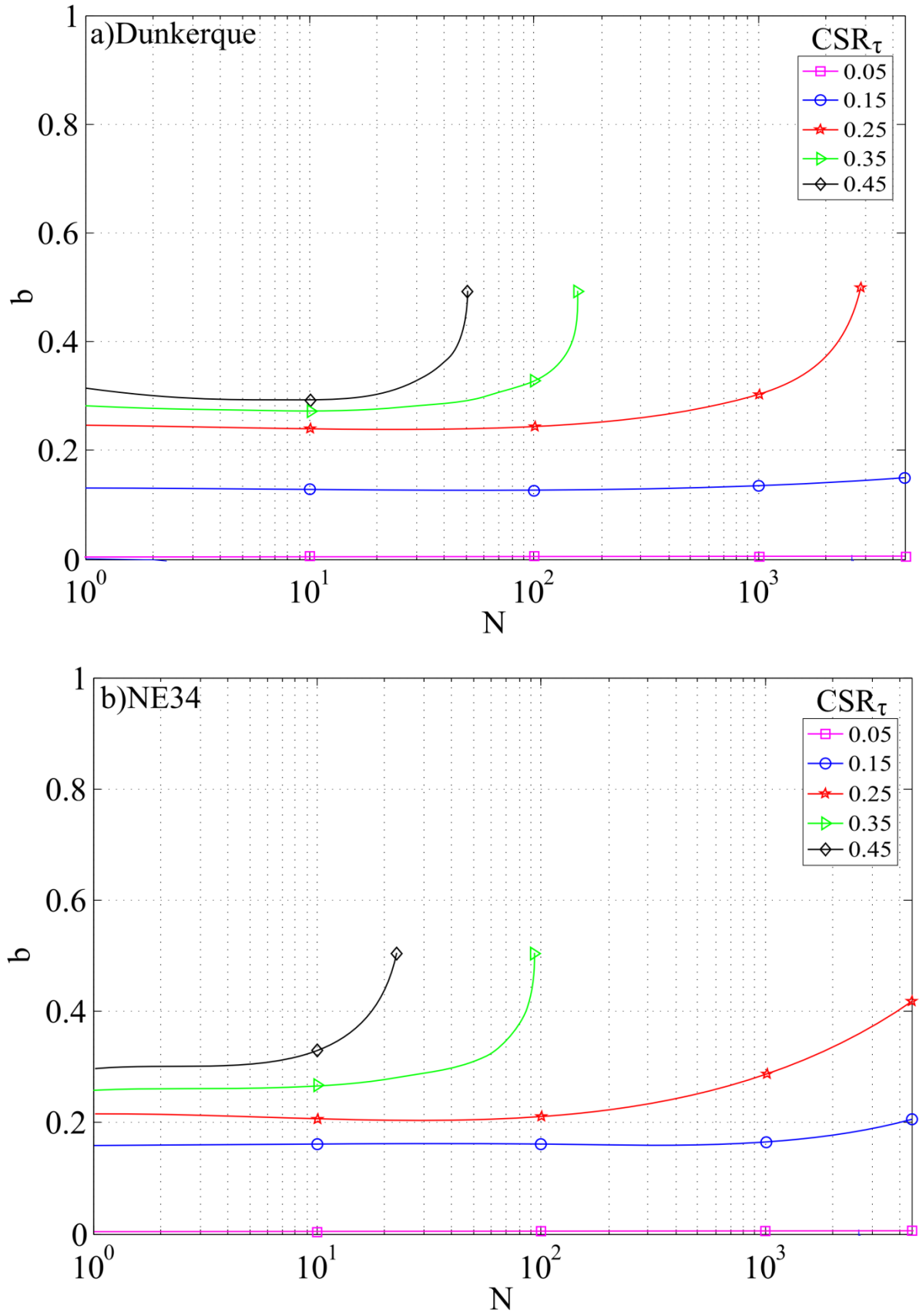


Figure 8-24 Value of b at maximum point in each cycle in "standard" pre-conditioned tests on a)Dunkerque and b)NE34 sands at maximum cycle points ($\tau = \tau_{cyc}$ kPa). All samples prepared at e_0=0.64.

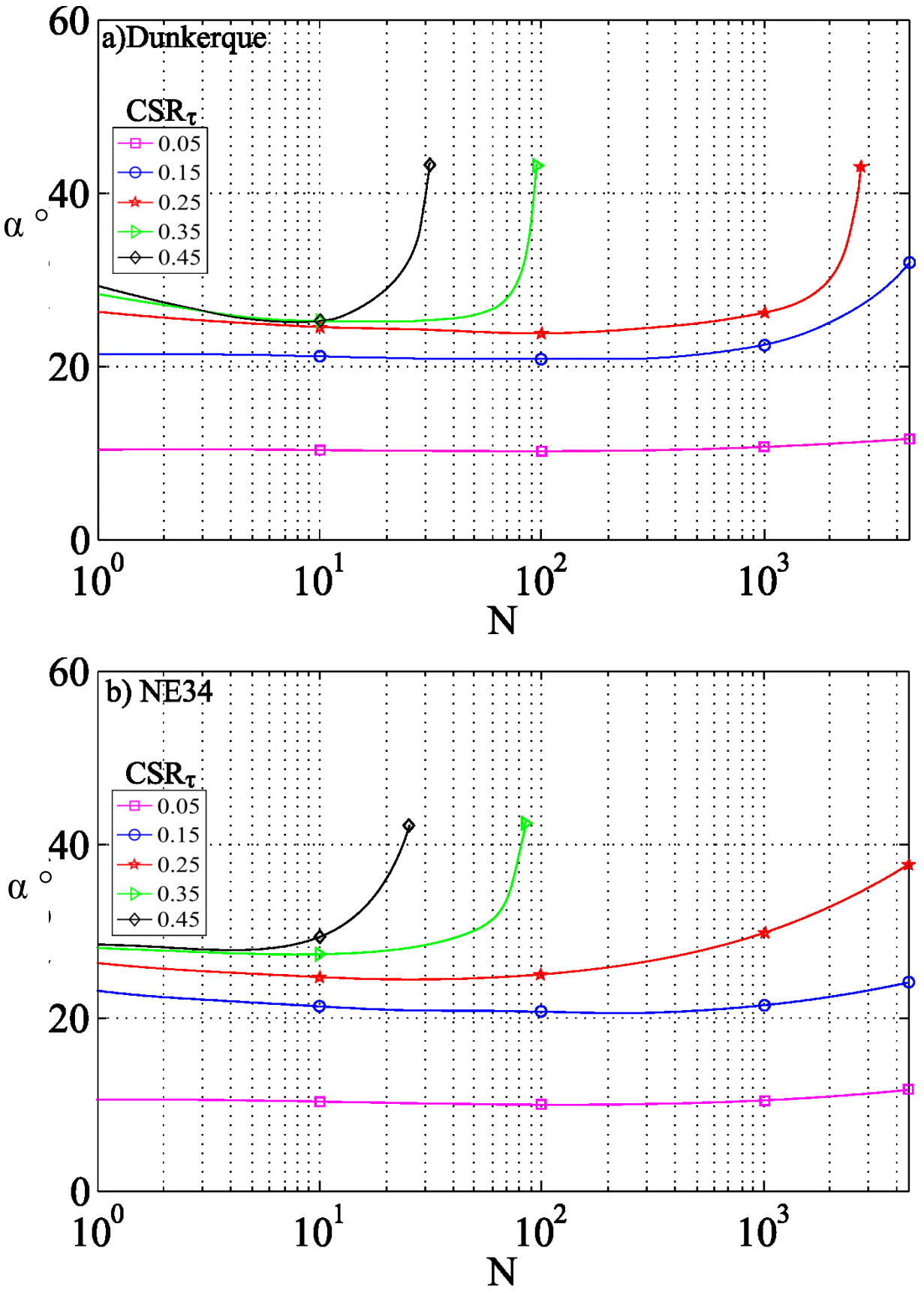


Figure 8-25 Maximum degree of rotation of principle stresses in each cycle in "standard" pre-conditioned tests on a)Dunkerque and b)NE34 sands at maximum cycle points ($\tau = \tau_{cyc}$ kPa). All samples prepared at e_0=0.64.

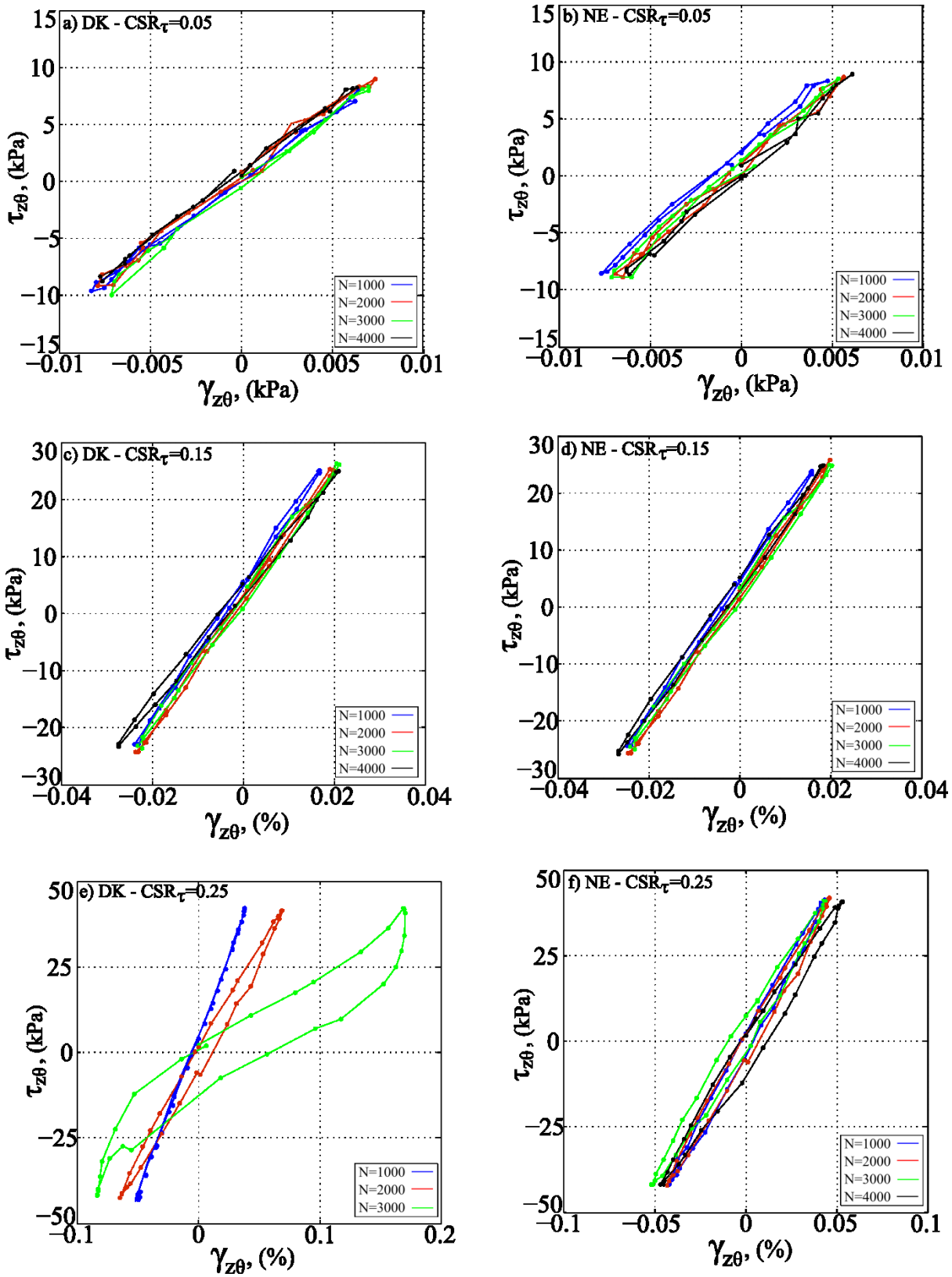


Figure 8-26a-f Stress-strain loops of specified nth cycles from cyclic simple shear tests with "standard" pre-conditioning procedures.

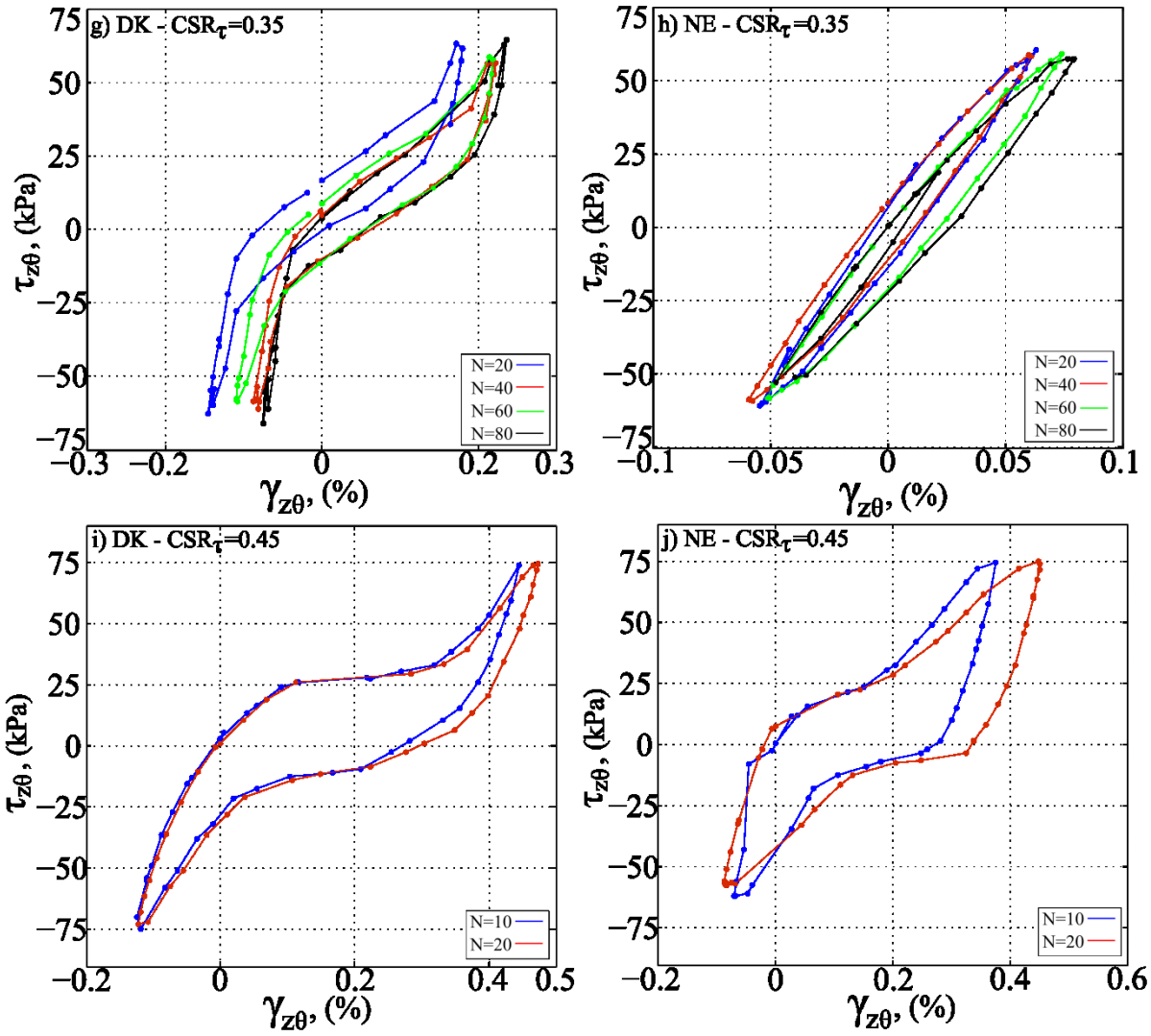


Figure 8-26g-j Stress-strain loops of specified nth cycles from cyclic simple shear tests with "standard" pre-conditioning procedures.

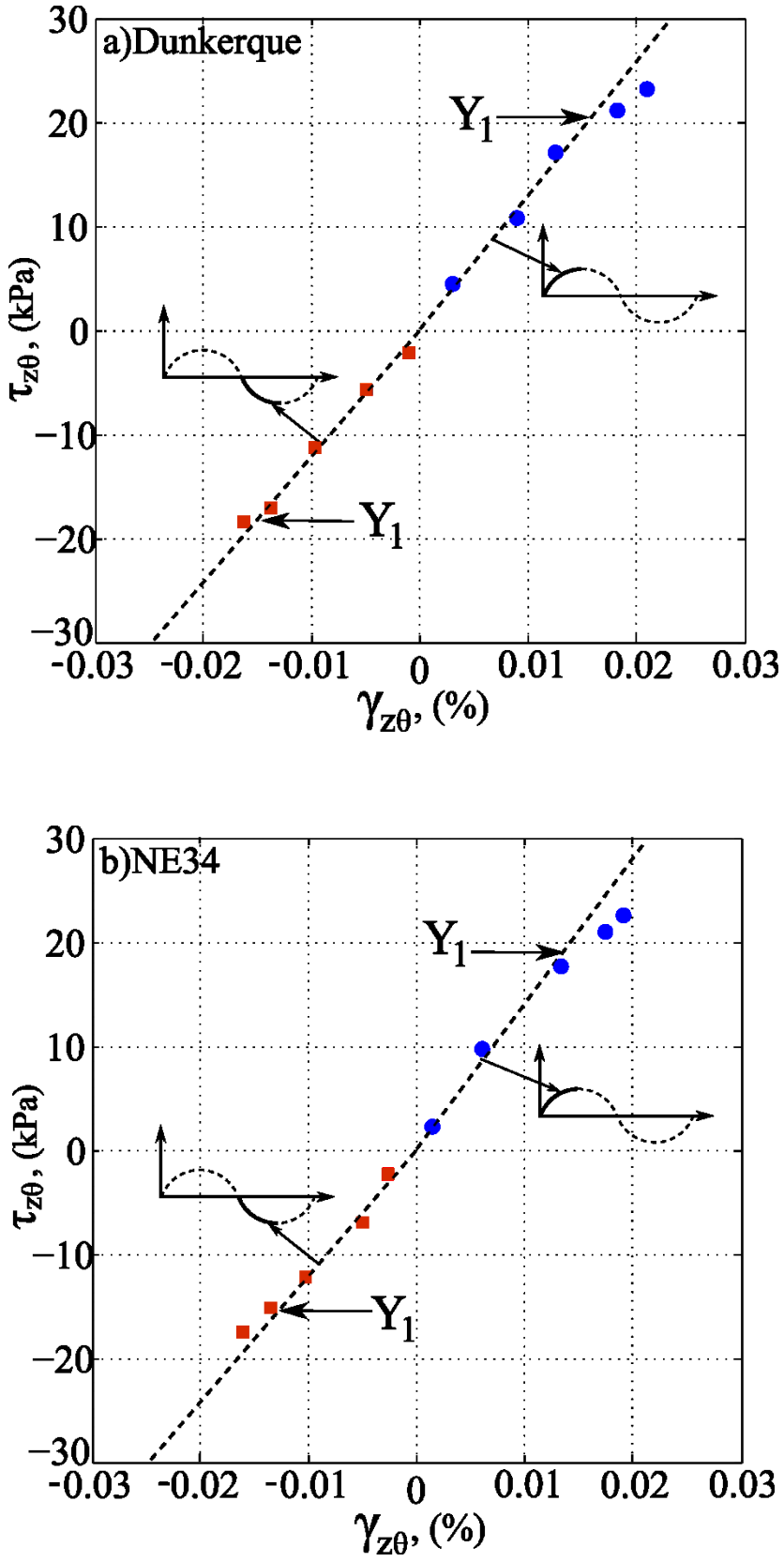
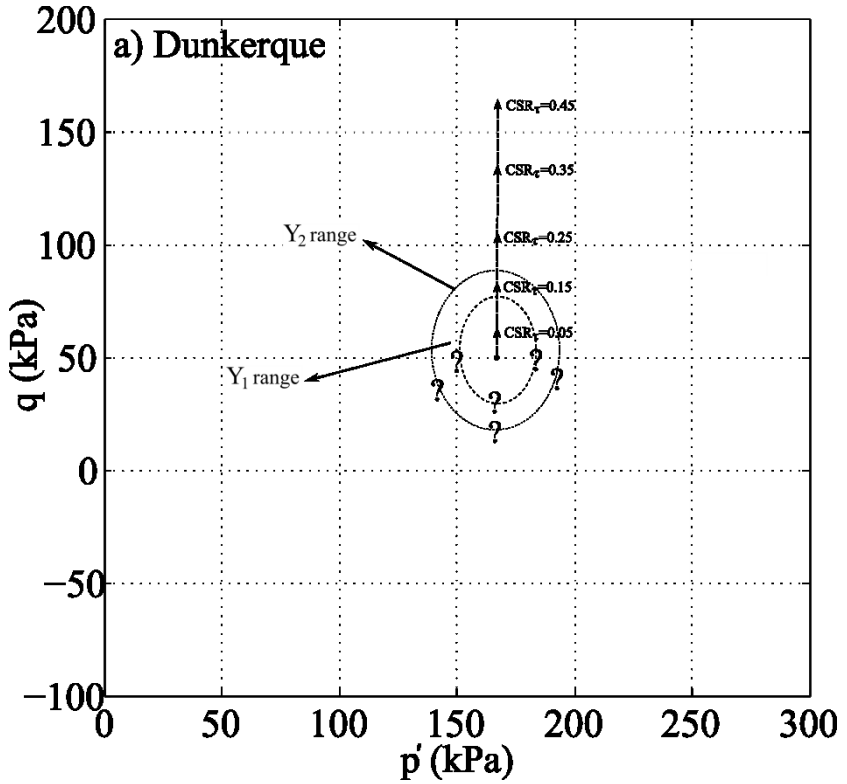


Figure 8-27 Locating the Y_1 limit using the stress-strain loop from tests with CSRτ=0.15.



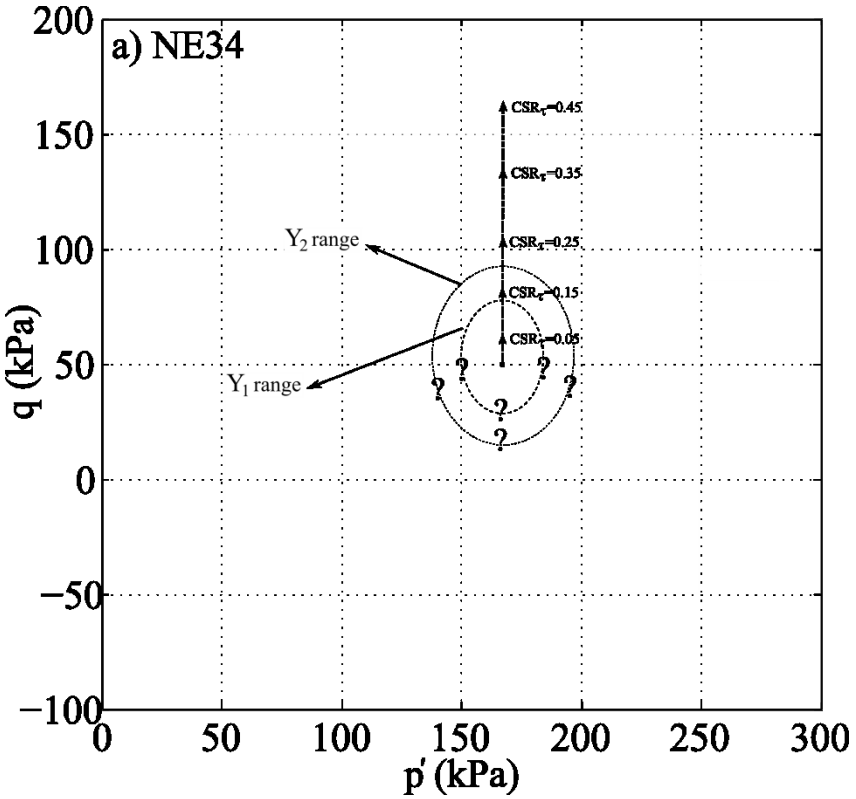


Figure 8-28 Location of maximum q levels reached in each cyclic test compared to the Y_1 limits obtained from monotonic simple shear tests with similar pre-conditioning procedure.

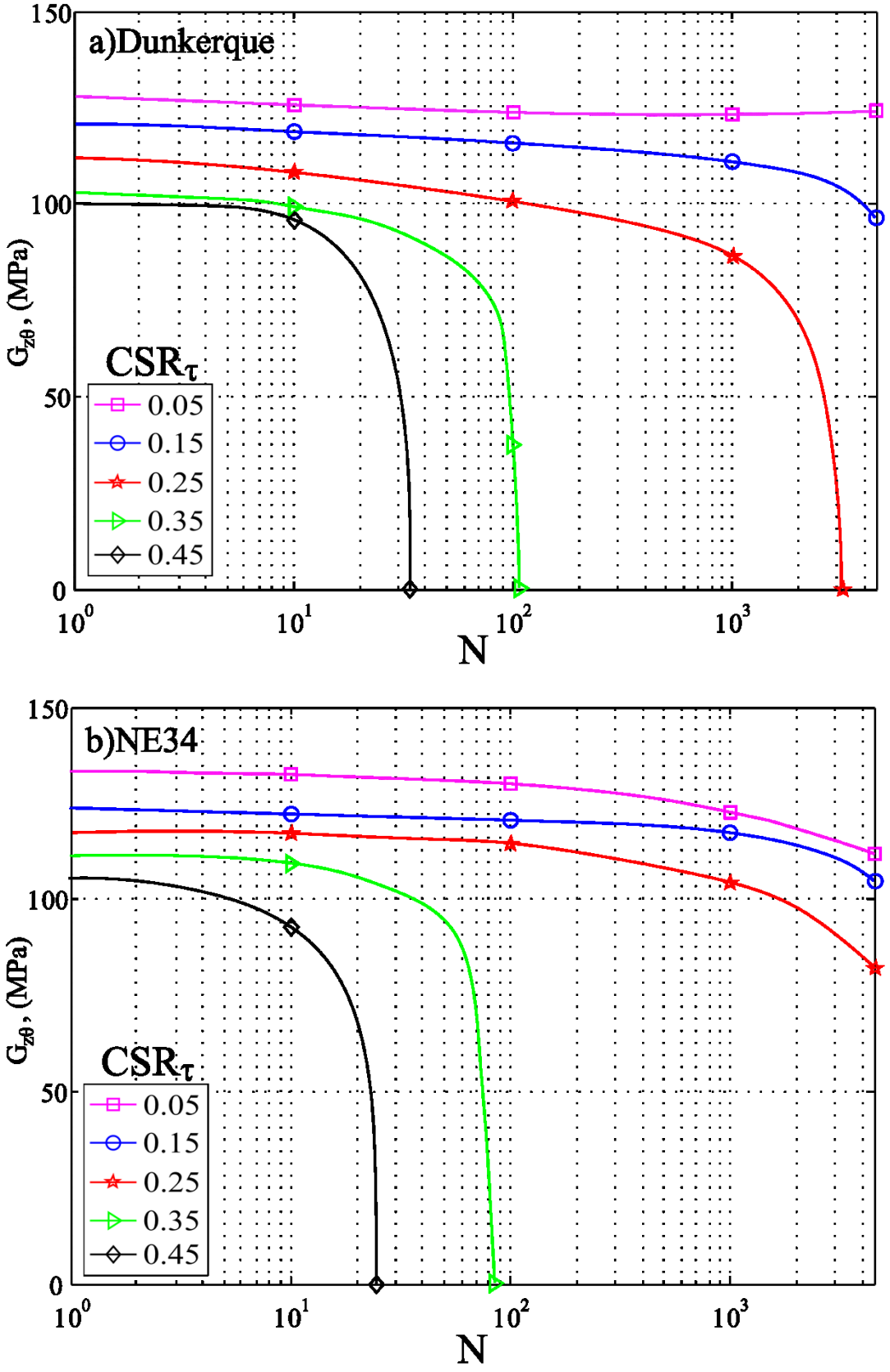


Figure 8-29 Effect of CSR_τ on undrained cyclic stiffness under simple shear cycling at Point D for a)Dunkerque and b)NE34 specimens after standard consolidation, conditioning cycles and ageing stages. All samples prepared at e_0=0.64.

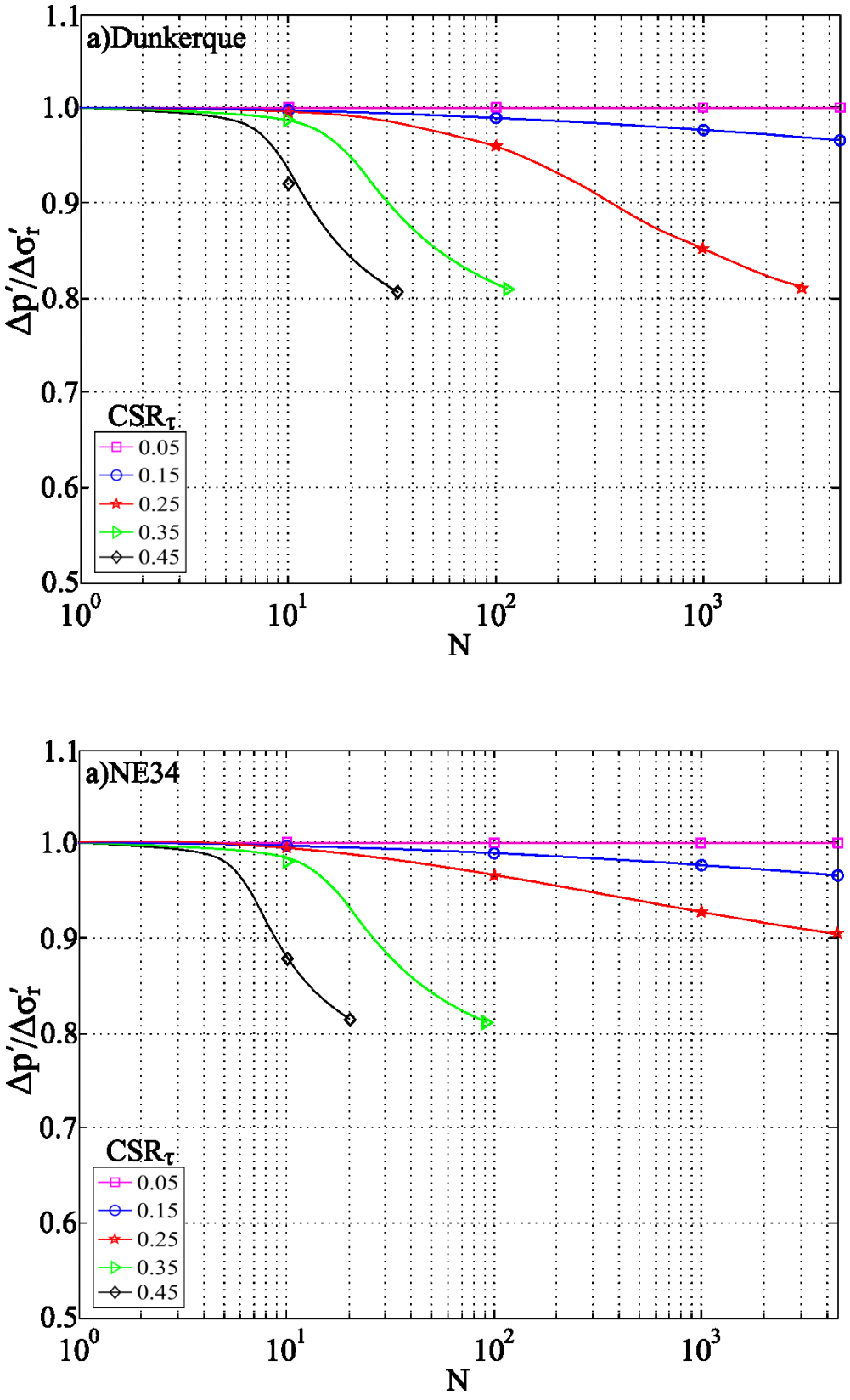


Figure 8-30 Evolution of the $\Delta\sigma'_r/\Delta p'$ ratio under cyclic simple shear in "standard" pre-conditioned tests with different CSR_τ levels.

CHAPTER 9

Comparison of stress path testing results with field and model pile tests

Introduction

The cyclic triaxial and HCA tests that the Author conducted using the "standard" test procedure revealed important features regarding the cyclic response of the two test sands. In this chapter, attempts will be made to compare the soil element tests' behaviour with the cyclic field pile tests reported by Jardine & Standing (2000, 2012) and the model pile tests of Tsuha *et al.* (2012). The aim is to assess the applicability of the laboratory stress path element tests predicting the cyclic behaviour of piles.

9.1 Outcomes of single element testing programme

Pre-conditioning effects: The extensive series of cyclic triaxial experiments reported in Chapter 6 showed the importance of pre-conditioning on the subsequent cyclic response of the sand test specimens. It was clear by inspection that the single element tests could only be applicable if they matched the over-consolidation, ageing and pre-cycling episodes experienced by soil element, adjacent to the pile shafts during installation and equalisation after driving.

The importance of matching those installation effects is reinforced by noting the sharply different responses of driven and bored continuous Flight Auger (CFA) piles noted by Puech (2012) and Benzaria *et al.* (2012). Pile driving at Dunkerque induced highly over-consolidated, and heavily pre-cycled conditions around the pile shaft and the interface friction angles, δ', developed in the shear zone of crushed soil were likely to have fallen below the peak angle of shearing resistance, ϕ'. These features led to high resistances under cyclic loading and a *Stable* response under low amplitude cycles. In contrast, the soil layers positioned adjacent to piles bored in nearly similar Dunkerque sands for a parallel set of cyclic tests conducted as part of the French national SOLCYP programme at Loon-Plage, (Puech, 2012) had no previous exposure to cyclic loading during their installation, which the near shaft effective radial stresses reacting front the flight auger boring process and then pressurised concrete placement. However, the interface friction angles, δ', developed against the rough shafts of the 8m long 420m diameter concrete bored CFA piles were likely to have been higher than those developed on the steel piles, and under loading to failure their shearing response is likely to have been more dilative. These contrasting conditions led to very low resistances under cyclic loading developing in the CFA piles tested in dense sand at Loon-Plage, as reported by Benzaria *et al.* (2012) For example, compression cycling on a virgin pile with $Q_{mean}/Q_{us}=0.36$ and $Q_{cyc}/Q_{us}=0.27$ led to large permanent displacements accumulating and full failure within only 14 cycles as shown in Figure 9-1a (CC1), while the driven Dunkerque piles could be expected to sustain hundreds of cycles at this loading level (Jardine & Standing, 2012). A drastic reduction of the maximum cyclic load to $Q_{cyc}/Q_{us}=0.13$ was insufficient to stabilise the pile; 500 cycles at this level generated more than 15mm of additional displacement (CC2). The cyclic interaction diagram constructed by Puech (2012) for the CFA piles (Figure 9-1b) showed considerably lower levels for the *Stable-Metastable* and *Metastable-Unstable* thresholds than those reported for the driven pile tests by Jardine &

Standing (2012) (see Figure 3-15), verifying the crucial importance of the pre-conditioning imposed by driven pile installation.

Modes of behaviour: As shown in Chapter 7 and 8, the "standard" triaxial and HCA cyclic tests showed three separate modes of behaviour under a wide range of cyclic amplitudes.

In both triaxial and HCA cyclic tests a threshold was found below which constant volume (undrained) cyclic loading had a positive or null impact on the effective stress state. The samples showed practically negligible permanent strain development and little or no degradation in cyclic stiffness in either test sands. The existence of a similarly *Stable* mode of pile behaviour has been observed in both full scale field (Jardine & Standing, 2000 and 2012, Puech, 2012) and laboratory model tests on displacement piles (Tsuha *et al.,* 2012). However, it should be noted that that the more complete measurements that could be made in the Author's element tests allowed a more rigorous definition of stability to be adopted than that applied by Tsuha *et al.* (2012) and Jardine & Standing (2012) to their pile experiments, for which the absence of shaft failure within 1000 cycles was taken as proving stability, while the lack of any reduction in p′was adopted to define stability the element tests described in this thesis. Tsuha *et al.* (2012) argued that shaft capacity gains could be due to marginal changes in the sand near the interface creating an optimal soil fabric that led to enhanced dilatancy tendencies under later static loading. This can be associated with the tendency for samples to dilate under low level cycling in undrained triaxial and HCA tests and develop to gains in mean effective stress. Small volumetric dilations were also recorded in drained "standard" triaxial tests (see Figure 7-24).

Metastable responses were observed in both standard cyclic triaxial and HCA tests once the CSR and CSR_τ levels passed the *Stable* (Y_2) threshold. In these tests cyclic loading led to moderate rates of mean effective loss and led to failure in no fewer than 1000 cycles. The

effective stress degradation was associated with accumulation of axial strains in triaxial tests and drops in axial effective stress in HCA tests and degradation of cyclic stiffness in both triaxial and HCA tests. In contrast, Jardine & Standing (2012) and Tsuha *et al.* (2012) defined *Metastable* pile behaviour as that developed under cycling that led to failure after between 100 to 1000 cycles. As discussed in Chapter 8, the single element cyclic loading failures were controlled by the continuum failure ϕ' envelope. While, in pile tests the shaft failure is controlled by the interface friction angle, δ, which is generally significantly lower than the peak friction angle with driven piles.

Triaxial and HCA experiments that reached full failure under cyclic loading after less than 1000 cycles were identified as having *Unstable* behaviour. In these tests, cyclic loading led to rapid losses in mean effective stress values which were accompanied by steady strain accumulation rates and matched reductions in effective stresses, along with falling cyclic stiffnesses. The field and model piles that reached failure in less than 100 cycles were classed as *Unstable* and these tests showed rapid rates of axial displacement accumulation and substantial cyclic stiffness degradation from their early cycles onwards. As with the *Stable* and *Metastable* cases, the definition of instability was more severe in the laboratory tests than in the pile cases.

The following section aims to link the triaxial, HCA results, field and model pile trends quantitatively and examine the scope for using the laboratory tests to predict pile behaviour in the field.

9.2 Interpretation of pile behaviour based on laboratory tests

As discussed in Chapter 3, Jardine *et al.* (2012) proposed a flow chart scheme for designing piles under axial cyclic loading as shown in Figure 9-2. According to this approach, degradation laws can be obtained using either the a) In-situ testing procedures (PMTc,

CPTc), b) Laboratory element (HCA, TXL, CSS) tests or c) pile experiments (involving field or model pile tests). Degradation relationships can then be estimated for regular cycling by one of the following methods:

a) *Local T-Z type soil-pile analysis* using numerical codes such as that employed in codes such as, RATZ (Randolph, 1994), PAXCY (Karlsrud *et al.*, 1986), PAX2 (Nadim & Dahlberg, 1996) or the substructured software described by Atkins (2000) that employed local version of the "A, B, C" procedure suggested in the ICP-05 (Jardine *et al.,* 2005).
b) *Rigorous FE analysis that specify complete cyclic soil and interface behavioural laws* including constitutive approaches such as that reported by Witchmann (2005) (See Section 2.4).
c) *Global pile analyses* using the design methods that employ physically reasonable failure mechanisms and parameters calibrated from field pile tests such as the Jardine *et al.* (2005) "A, B, C" procedure.

The results from the Author's cyclic triaxial and HCA tests reported in Chapter 7 and 8 can be implemented by various means into in the local soil-pile analyses codes or finite element codes to design for axial cyclic loading. In this section, single element results will be analysed and a global pile analyses approach based on ICP-05 method. The following paragraphs explain this procedure:

Failure mechanism in piles: As discussed in Section 3.1.2, Lehane *et al.* (1993), Chow (1997) and Jardine *et al.* (2005) demonstrated that the ultimate shaft shear stress developed against the shaft of field displacement piles can be described by the simple Coulomb failure criterion (Figure 9-3):

$$\tau_{rzf} = \sigma'_{rf} \tan(\delta'_f) \qquad \text{Equation 9-1}$$

The failure value of σ'_{rf} differs from σ'_{rc} which is the stationary radial effective stress acting on the pile surface after installation, due to several factors, including interface dilation and principal stress axis rotation under load. The failure value can be written as $\sigma'_{rf} = (\sigma'_{rc} + \Delta\sigma'_{rd})$ in compression and $\sigma'_{rf} = (0.8\sigma'_{rc} + \Delta\sigma'_{rd})$ for closed ended piles in tension. The σ'_{rc} term can be calculated from q_c, σ'_{v0} and h/R* using the experimental power-law equation (Equation 3-9) proposed by Chow (1997). The $\Delta\sigma'_{rd}$ term describes the change occurring in radial effective stresses under loading and is generated by effective stresses changes in the sand caused by principal stress axis rotation and the constrained dilation induced by interface shearing. The dilatancy component of radial effective stress is inversely proportional to pile radius R and under compression loading, large piles will tend towards the lower limit of $\tau_{rzf} = \sigma'_{rc} \tan(\delta'_f)$. And $0.8\ \sigma'_{rc} \tan(\delta'_f)$ in tension. A further ≈10% reduction applies to σ'_r in tension cases involving open-ended piles to simulate Poisson effects in the pile shaft and other factors.

The $(\sigma'_{rf}/\sigma'_{rc})_{static}$ ratios applying under static tension failure conditions to the 19.3m long 457mm diameter open-ended steel piles used in tension cyclic tests at Dunkerque by Jardine & Standing (2000, 2012) can be estimated by applying the ICP procedure. Jardine (2015) found that the typical ratio applying at failure at the mid-point on the capacity-depth curve was ≈0.85. Meanwhile, Rimoy (2013) reported $(\sigma'_{rf}/\sigma'_{rc})_{static} \approx 1.20$ in his calibration chamber tension tests using the 36mm × 0.99mm 60° conical-tip ended ICP model pile in the calibration chamber on NE34 sand. While it is often convenient when designing cyclic element tests to assume $(\sigma'_{rf}/\sigma'_{rc})_{static} = 1$, these above ratios are applied below to link the single element tests to the cyclic field pile tests at Dunkerque and the cyclic model pile tests in NE34 sand. Implementing these ratios to Equation 9-1 gives for static loading:

Dunkerque: $\tau_{max\ static} = 0.85\ \sigma'_{rc} \tan(\delta'_f)$ Equation 9-2a

NE34: $\tau_{max\ static} = 1.20\ \sigma'_{rc} \tan(\delta'_f)$ Equation 9-2b

Pile failure mechanism under cyclic loading is shown in Figure 9-3. Tsuha *et al.* (2012) showed that local shaft cyclic failure initiates when the peak of the cyclic effective stress paths engage the interface failure δ'_f. Under regular cycling with constant τ_{mean}, this gives:

$$\sigma'_{rf} = \frac{\tau_{max}}{\tan(\delta'_f)}$$ Equation 9-3

By similar triangles:

$$\left(\frac{\sigma'_{rf}}{\sigma'_{rc}}\right)_{cyclic} = \frac{\tau_{max}}{\sigma'_{rc} \tan(\delta'_f)}$$ Equation 9-4

Substituting $\sigma'_{rf} = \sigma'_{rc} - \Delta\sigma'_r$ into Equation 9-4 gives:

$$\left(\frac{\Delta\sigma'_r}{\sigma'_{rc}}\right)_{cyclic} = \frac{\sigma'_{rc} - \sigma'_{rf}}{\sigma'_{rc}} = 1 - \frac{\tau_{max}}{\sigma'_{rc} \tan(\delta'_f)}$$ Equation 9-5

Which we can expand to:

$$\left(\frac{\Delta\sigma'_r}{\sigma'_{rc}}\right)_{cyclic} = \frac{\sigma'_{rf} - \sigma'_{rc}}{\sigma'_{rc}} = 1 - \left[\frac{\tau_{mean}}{\sigma'_{rc} \tan(\delta'_f)} + \frac{\tau_{cyc}}{\sigma'_{rc} \tan(\delta'_f)}\right]$$ Equation 9-6

Substituting $\tau_{max\ static}$ from Equation 9-2 into Equation 9-6 gives:

Dunkerque: $\left(\frac{\Delta\sigma'_r}{\sigma'_{rc}}\right)_{cyclic} = 1 - 0.85\left[\frac{\tau_{mean}}{\tau_{max\ static}} + \frac{\tau_{cyc}}{\tau_{max\ static}}\right]$ Equation 9-7a

NE34: $\left(\frac{\Delta\sigma'_r}{\sigma'_{rc}}\right)_{cyclic} = 1 - 1.20\left[\frac{\tau_{mean}}{\tau_{max\ static}} + \frac{\tau_{cyc}}{\tau_{max\ static}}\right]$ Equation 9-7b

These cyclic equations allow the use of single element laboratory tests to predict the local shaft cyclic failure of piles by linking the effective stress degradation to $\Delta\sigma'_r/\sigma'_{rc}$ as will be discussed in the following paragraphs:

9.2.1 Cyclic HCA tests

As discussed in Section 3.4 and Chapter 5, simple shear HCA tests are able to replicate key aspects of the shearing mode applying at the pile-soil interface. The horizontal plane on which cyclic shear stresses are applied in the laboratory models the vertical soil-pile interface surface and the laboratory axial effective stresses acting represent the radial effective stresses acting in the ground. Therefore:

$$\left[\frac{\sigma'_r}{\sigma'_{r0}}\right]_{HCA} = \left[\frac{\sigma'_z}{\sigma'_{z0}}\right]_{pile} \quad \text{Equation 9-8}$$

Construction of N_f lines: Considering first the HCA tests, their results can be used to find the N_f, values that can be expected at a range of different applied τ_{cyc} / $\tau_{max\ static}$ ratios. This can be assessed directly for the τ_{mean}/ $\tau_{max\ static}$ =0 case. However, for other cases it is necessary to either conduct additional HCA tests employing $\tau_{ave}\neq 0$ or to assume that the Author's tests can be stretched to cover other cases by assuming:

$$\Delta\sigma'_z/\sigma'_{z0} = f(\tau_{cyc} / \tau_{max\ static}, N) \neq f(\tau_{mean}/\tau_{static\ max}) \quad \text{Equation 9-9}$$

Substituting Equation 9-8 into Equation 9-7 and rewriting it as below will give values of τ_{mean}/ $\tau_{max\ static}$ that give failure after specified N (=10, 50, 100, 1000) cycles for fixed τ_{cyc} / $\tau_{max\ static}$ values.

Dunkerque: $$\frac{\tau_{mean}}{\tau_{max\ static}} = \frac{1}{0.85}\left[1 - \left(\frac{\Delta\sigma'_z}{\sigma'_{zc}}\right)_{cyclic}\right] - \frac{\tau_{cyc}}{\tau_{max\ static}} \quad \text{Equation 9-10a}$$

NE34: $$\frac{\tau_{mean}}{\tau_{max\ static}} = \frac{1}{1.20}\left[1 - \left(\frac{\Delta\sigma'_z}{\sigma'_{zc}}\right)_{cyclic}\right] - \frac{\tau_{cyc}}{\tau_{max\ static}} \quad \text{Equation 9-10b}$$

Where τ_{cyc} /$\tau_{max\ static}$ defines test curve and $(\Delta\sigma'_z/\ \Delta\sigma'_{zc})_{cyclic}$ ratios are taken from the appropriate ($\tau_{cyc}/\tau_{static\ max}$) curve for each N from Figure 9-4.

To construct N_f lines in the τ_{cyc} / $\tau_{max\ static}$: τ_{mean}/ $\tau_{max\ static}$ space, it is useful to find the interception of each N_f line with the vertical axis where τ_{mean}/ $\tau_{max\ static}$ =0. To do this,

$\tau_{cyc}/\tau_{maxstatic}$: N_f curves can be plotted from Equation 9-9 by substituting $\tau_{mean}/\ \tau_{max\ static}$ =0. This gives:

Dunkerque: $\frac{\tau_{cyc}}{\tau_{max\ static}} = \frac{1}{0.85}\left[1 - \frac{\Delta\sigma'_z}{\sigma'_{zc}}\right]$ Equation 9-11a

NE34: $\frac{\tau_{cyc}}{\tau_{max\ static}} = \frac{1}{1.20}\left[1 - \frac{\Delta\sigma'_z}{\sigma'_{zc}}\right]$ Equation 9-11b

Using the curves obtained shown in Figure 9-5, $\tau_{cyc}/\ \tau_{max\ static}$ values for N=10, 50, 100 and 1000 can be obtained.

Using the points obtained, N_f lines are drawn in $\tau_{mean}/\ \tau_{max\ static}$: $\tau_{cyc}\ /\ \tau_{max\ static}$ space as shown in Figure 9-6. According to the pile test definitions, the boundaries for the *Stable-Metastable* and *Metastable-Unstable* regions are located at N_f=100 and 1000 respectively. The locations of these zones are indicated in Figure 9-7 and compared with the global pile and model pile trends for the Dunkerque and NE34 tests. The results show a generally good match between the laboratory predictions. The agreement is very good for NE34 tests, while the Dunkerque field test trends appear to indicate marginally less favourable global performance than indicated from the laboratory element tests. This could be due to multiple factors including the more progressive failure of the pile tests, the lack of HCA tests with τ_{mean}>0, pre-conditioning procedures and possible differences in initial density state. In addition, it should be noted that while in field conditions, cyclic loads are applied parallel to the pile interface and therefore perpendicular to the direction of the sand deposition, in laboratory they are applied parallel with specimen deposition layers. This difference might also have an impact on the cyclic response sand specimens. However, the degree of agreement between soil element and full pile behaviour is highly encouraging.

9.2.2 Cyclic Triaxial tests

As discussed in Section 6.1.1, triaxial tests cannot apply the pile-soil interface conditions as well as HCA experiments. However, the tests are far more practical to conduct and it is important to assess whether, they can be used to assess pile cyclic behaviour. This may be approached by considering the pile shaft shear stresses to be analogous to triaxial deviatoric stress changes (Δq) and taking the variations in mean effective stress (p') as indicators of how σ'_r may change close to pile under cyclic loading.

Under triaxial conditions, $q_{cyc}= (\sigma'_1-\sigma'_3)_{cyc}=2t_{cyc}$ while under simple shear conditions $\tau_{zh\ cyc}$ remains approximately equal to t_{cyc} (see Figure 8-18) throughout the experiments. The q_{cyc} and q_{mean} relationships can therefore be expressed as equivalent HCA simple shear tests by equating:

$$\frac{\tau_{cyc}}{\tau_{max\ static}} = \frac{(q_{cyc})/2}{\tau_{max\ static}} \qquad \text{Equation 9-12a}$$

$$\frac{\tau_{mean}}{\tau_{max\ static}} = \frac{(q_{mean})/2}{\tau_{max\ static}} \qquad \text{Equation 9-12b}$$

To relate the pile loading and triaxial tests, the $[\delta p'/p'_0]/[\delta\sigma'_z/\sigma'_{z0}]$ relationship between the p' and σ'_{z0} drift characteristics must be known. The HCA experiments (Figure 8-30) showed that the ratio is initially equal to 1 over the early stages of cycling but reduces continuously as degradation progresses and reaches an ultimate value of 0.835 at failure. A Correction Factor can be defined as:

$$\frac{\Delta p'}{p'_0} = (CF)\frac{\Delta\sigma'_z}{\sigma'_{zc}} \qquad \text{Equation 9-13}$$

CF can be read from Figure 8-30 at any degradation level in each test. However, if HCA results are not available, the CF factor can be assumed to be nearly equal to 1, which is a reasonable estimation based given that the average value for CF=0.92±0.08.

Construction of N_f lines: Substituting Equations 9-12 and 9-13 into Equation 9-10 gives:

Dunkerque: $\frac{(q_{mean})/2}{\tau_{max\ static}} = \frac{1}{0.85}\left[1 - \frac{\Delta p'}{p'_0}\left(\frac{1}{CF}\right)\right] - \frac{(q_{cyc})/2}{\tau_{max\ static}}$ Equation 9-14a

NE34: $\frac{(q_{mean})/2}{\tau_{max\ static}} = \frac{1}{1.20}\left[1 - \frac{\Delta p'}{p'_0}\left(\frac{1}{CF}\right)\right] - \frac{(q_{cyc})/2}{\tau_{max\ static}}$ Equation 9-14b

Where the $(q_{cyc})/2\tau_{static\ max}$ ($=\tau_{cyc}/\tau_{max\ static}$) ratio defines each test curve and $\Delta p'/p'_0$ values are taken from given curve for each N from Figure 9-8.

As with the HCA tests, it is helpful when constructing N_f lines in the $\tau_{cyc}/\tau_{max\ static}$: $\tau_{mean}/\tau_{max\ static}$ space to find the interception of each N_f line with the vertical axis where $(q_{mean})/2\tau_{static\ max}$ ($=\tau_{mean}/\tau_{max\ static}$)=0. This can be done by substituting $(q_{mean})/2\ \tau_{static\ max}$=0 in Equation 9-14:

Dunkerque: $\frac{(q_{cyc})/2}{\tau_{max\ static}} = \frac{1}{0.85}\left[1 - \frac{\Delta p'}{p'_0}\left(\frac{1}{CF}\right)\right]$ Equation 9-15a

NE34: $\frac{(q_{cyc})/2}{\tau_{max\ static}} = \frac{1}{1.20}\left[1 - \frac{\Delta p'}{p'_0}\left(\frac{1}{CF}\right)\right]$ Equation 9-15b

Using the curves plotted in Figure 9-9 $(q_{cyc})/2\ \tau_{static\ max} = \tau_{cyc}/\ \tau_{max\ static}$ values for N=10, 50, 100 and 1000 can be obtained.

Using the points obtained, N_f lines are drawn in $\tau_{mean}/\ \tau_{max\ static}$: $\tau_{cyc}/\ \tau_{max\ static}$ space as shown in Figure 9-10. The Boundaries between *Stable-Metastable* (N_f=1000) and *Metastable-Unstable* (N_f=100) regions obtained are also compared to the global trends from the field and model pile tests in Figure 9-11. The Results show a generally good match between the triaxial tests predictions with the field and model pile tests, although the latter predicts a generally narrower *Metastable* zone.

9.2.3 Shaft friction degradation relation with N

As discussed in Section 3.3, based on pile test results, Jardine *et al.* (2005) proposed two alternative approximate expressions to relate σ'_r changes developed on the pile shaft to τ_{cyc} and N that could be used to estimate the pile responses to particular packets of regular cycles. Adding an "equivalent number of cycles" memory parameter allows this approach to be extended to consider batches of dissimilar cycles and so be employed in assessing design conditions; Meritt *et al.* (2012); Jardine *et al.* (2015):

$$\Delta\sigma'_r/\sigma'_{rc} = A\,(B + \tau_{cyclic}/\tau_{max\ static})\,N^C \qquad \text{Equation 9-16a}$$

$$\Delta\sigma'_r/\sigma'_{rc} = A\,(B + \tau_{cyclic}/\tau_{max\ static})\,\text{Log } N \qquad \text{Equation 9-16b}$$

The material dependent A, B and C parameters can be obtained from instrumented pile, triaxial or HCA cyclic tests such as those discussed earlier. The applicability of the implicit power expression to the Author's tests was examined by considering the $[\Delta\sigma'_z/\sigma'_{z0}]_n$ and $[\Delta p'/p'_0]_n$ trends from HCA and triaxial tests normalised with their value at a specific N=100 in each test giving:

$$\frac{[\,\Delta\sigma'_z\,]_n}{[\,\Delta\sigma'_z\,]_{20}} = \frac{A\left(B+\frac{\tau_{cyc}}{\tau_{max\,static}}\right)N^C}{A\left(B+\frac{\tau_{cyc}}{\tau_{max\,static}}\right)20^C} = \left(\frac{N}{20}\right)^C \qquad \text{Equation 9-17}$$

The results from the normalised HCA test trends are shown in Figure 9-12 and the normalised triaxial trends shown in Figure 9-13 suggested that the expression are not appropriate for modelling either *Unstable* or *Stable* tests in either laboratory test series on either sand. However, the *Metastable* tests followed trends that followed the power-law equation with nearly linear lines in log-log space in both triaxial and HCA tests indicating a narrow range of exponents C. Based on the results obtained, the following A, B and C values were calculated from the triaxial and HCA tests on both test sands. The proposed parameters

are broadly in the range proposed by Jardine & Standing (2012), but show higher values for C.

Table 9-1 A, B and C parameters calculated from laboratory and pile tests

Sand type	Test type	A	B	C
Dunkerque	Pile tests (Jardine & Standing (2012)	-0.126	-0.10	0.45
	HCA	-	-	0.61
	Triaxial	-0.05	-0.31	0.51
NE34	HCA	-	-	0.47
	Triaxial	-0.03	-0.18	0.57

9.3 Conclusions

This chapter presented an approach to compare the Author's laboratory triaxial and HCA cyclic tests with earlier field and model axial cyclic loading pile tests. A general comparison between different modes of behaviour obtained was given in the first section. Later, laboratory and pile tests were compared using the general approach introduced. The following conclusions may be drawn:

1- Pre-conditioning has major impact on the subsequent cyclic response and must vary to account for pile installation processes and their effects. The results from the "standard" tests performed in this thesis can only be applied to driven piles.

2- Both laboratory and pile tests identify three distinct modes of behaviour that show similar characteristics under different levels of cycling. The laboratory tests provide scope for adopting slightly more severe definitions of stability.

3- Using a local pile analysis approach, the results from laboratory tests were reinterpreted to predict local pile shaft cyclic responses. The latter were shown to be showing generally consistent between HCA and triaxial experiments.

4- The local pile analysis predictions were shown to give broadly good predictions for the global responses seen in filed and model pile tests. The HCA predictions appear to be marginally non-conservative and potential reasons for this trend were discussed.

5- The “A,B,C” approach for assessing local radial effective stress degradation and the pile shaft under cycling can provide a reasonable approach for *Metastable* conditions and can be combined with an “equivalent number of cycles” approach to consider batches of dissimilar cycles (see Meritt *et al.,* 2012). However, the parameters developed to match *Metastable* conditions are not applicable to *Unstable* conditions. Further development is required to consider such cases. Provided that *Stable* conditions can be identified, then there is no need to model their “no detrimental effect” response to cycling.

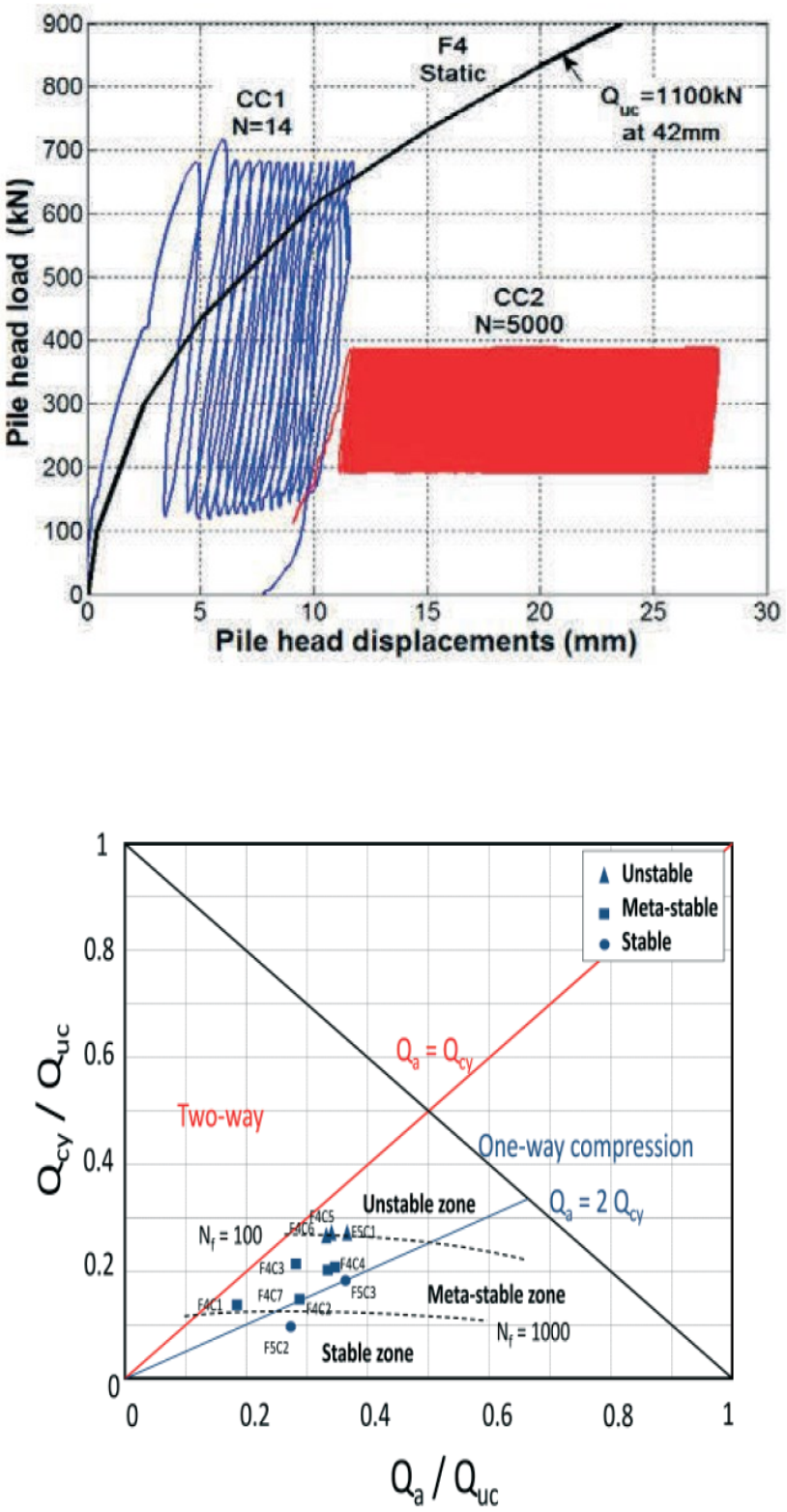


Figure 9-1 Loong-Plage field bored pile tests. a) Pile head load-displacement graph under one-way compression. b) Cyclic interaction diagram constructed based on bored-pile cyclic tests.

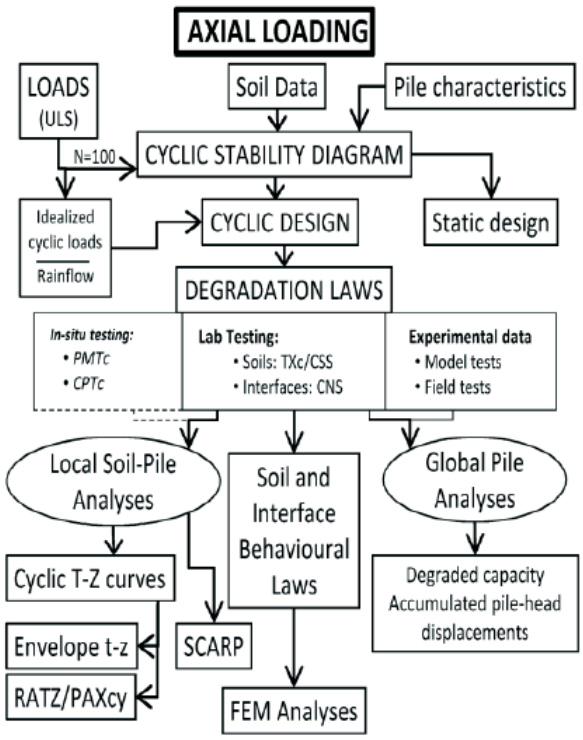


Figure 9-2 SOLCYP flow chart for designing under axial cyclic loading (Jardine *et al.* (2012).

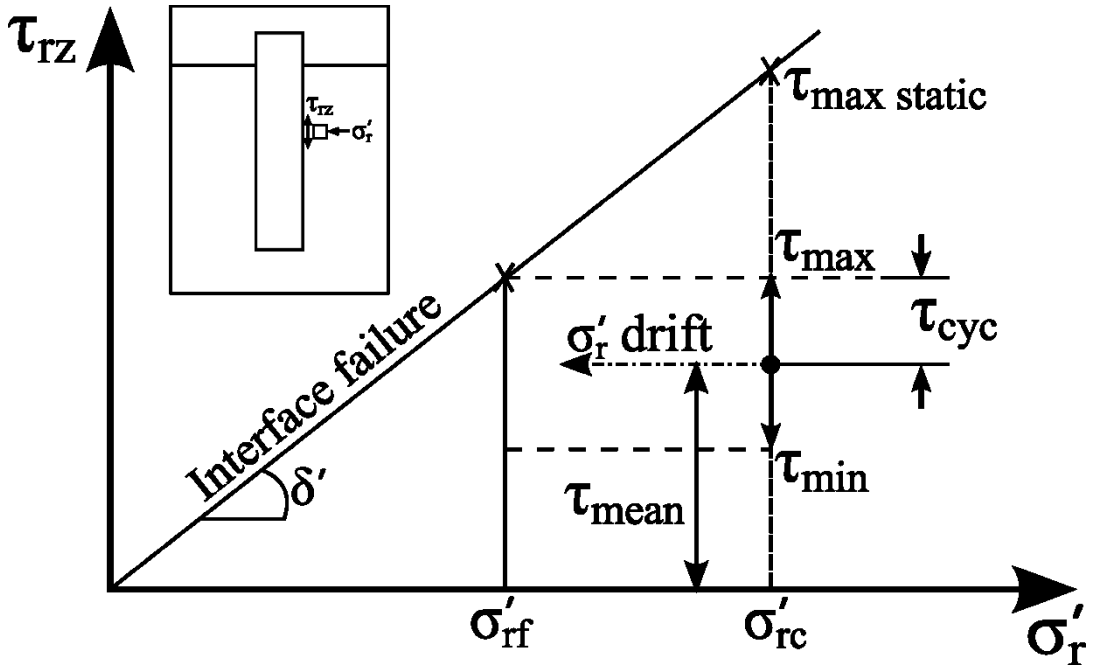


Figure 9-3 Failure mechanism and evolution of σ'_r and τ_{rz} of soil element adjacent to pile surface.

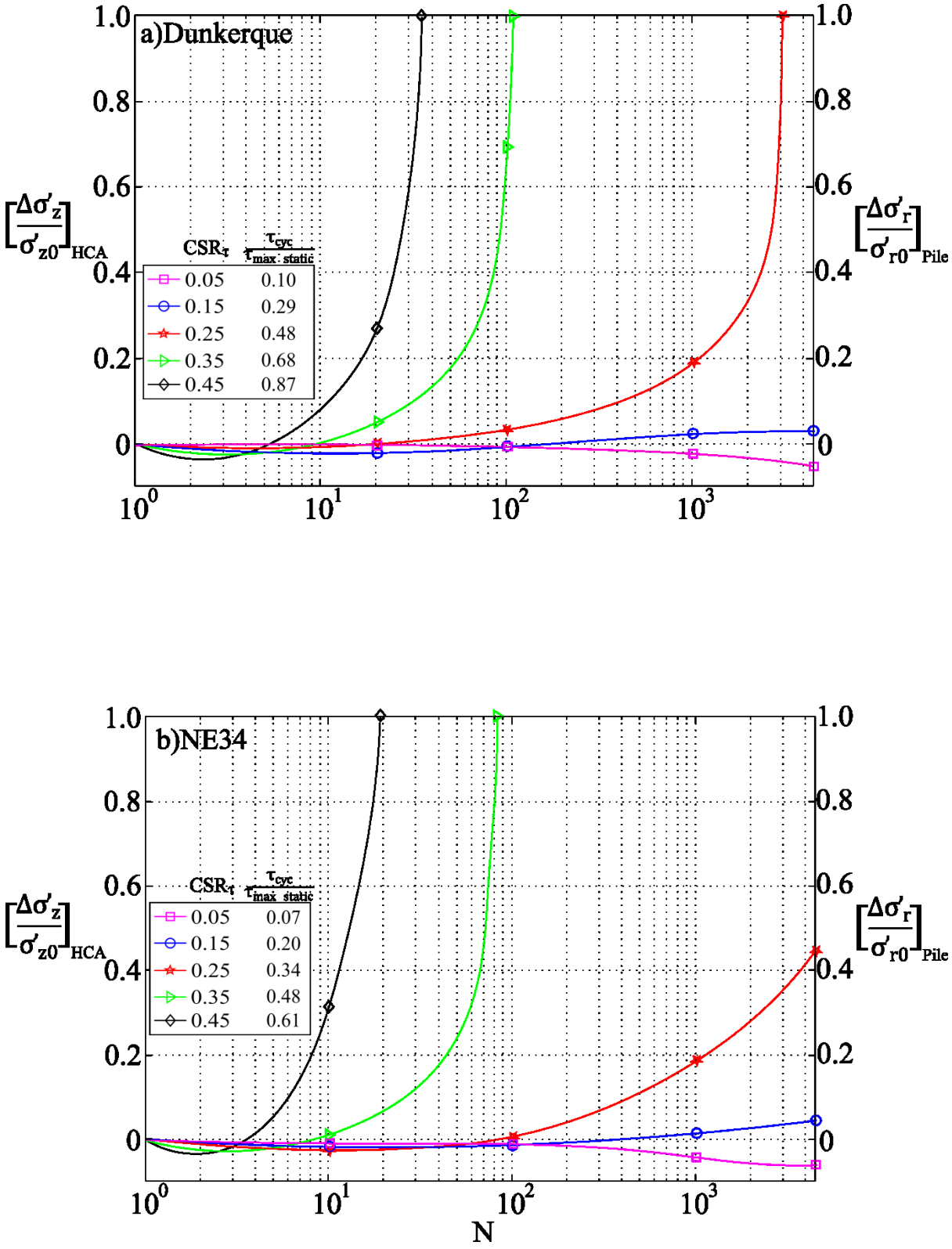


Figure 9-4 $\Delta\sigma'_z/\sigma'_{z0}$ curves from HCA cyclic tests for calculation of pile failure parameters for a)Dunkerque and b)NE34 specimens.

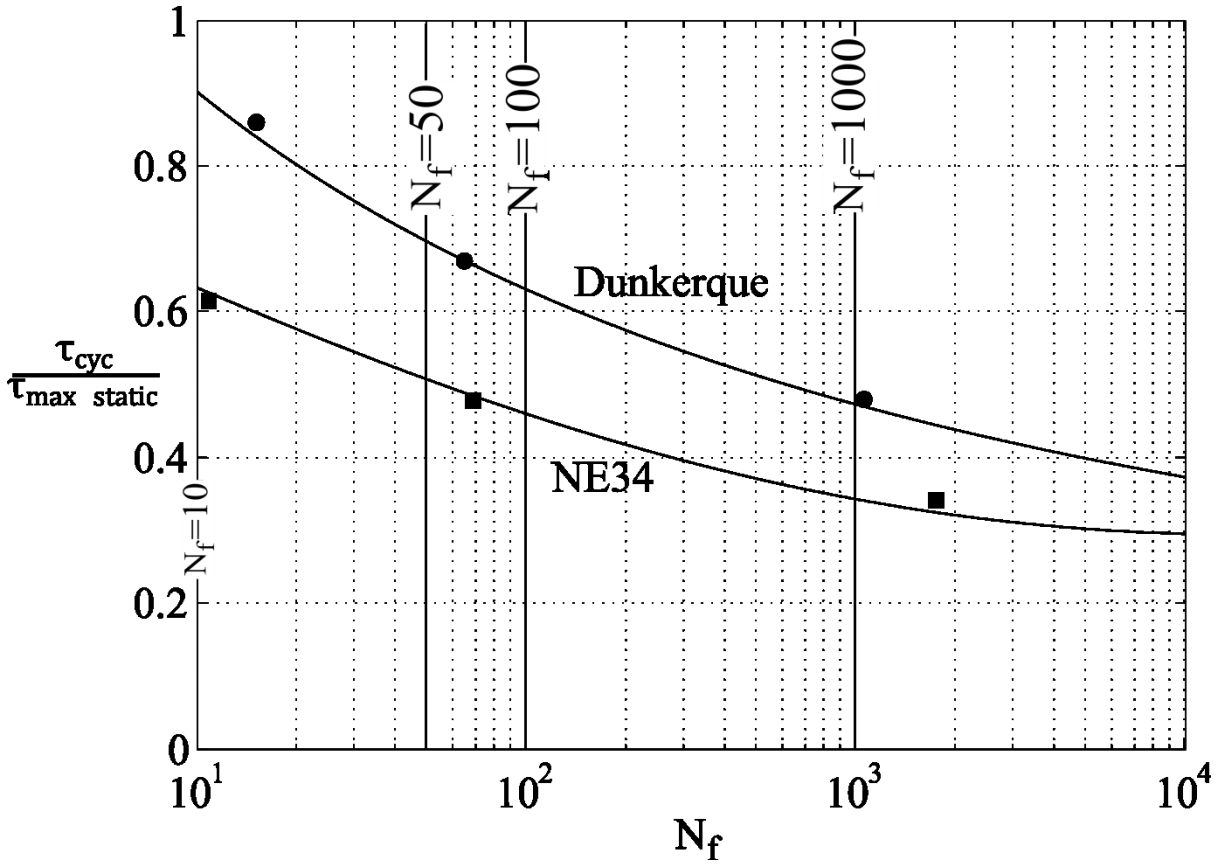


Figure 9-5 $\tau_{cyc}/\tau_{max\ static}$ against N_f graph obtained from cyclic simple shear HCA tests at $\tau_{mean}/\tau_{max\ static}$ =0 for a)Dunkerque and b)NE34 specimens.

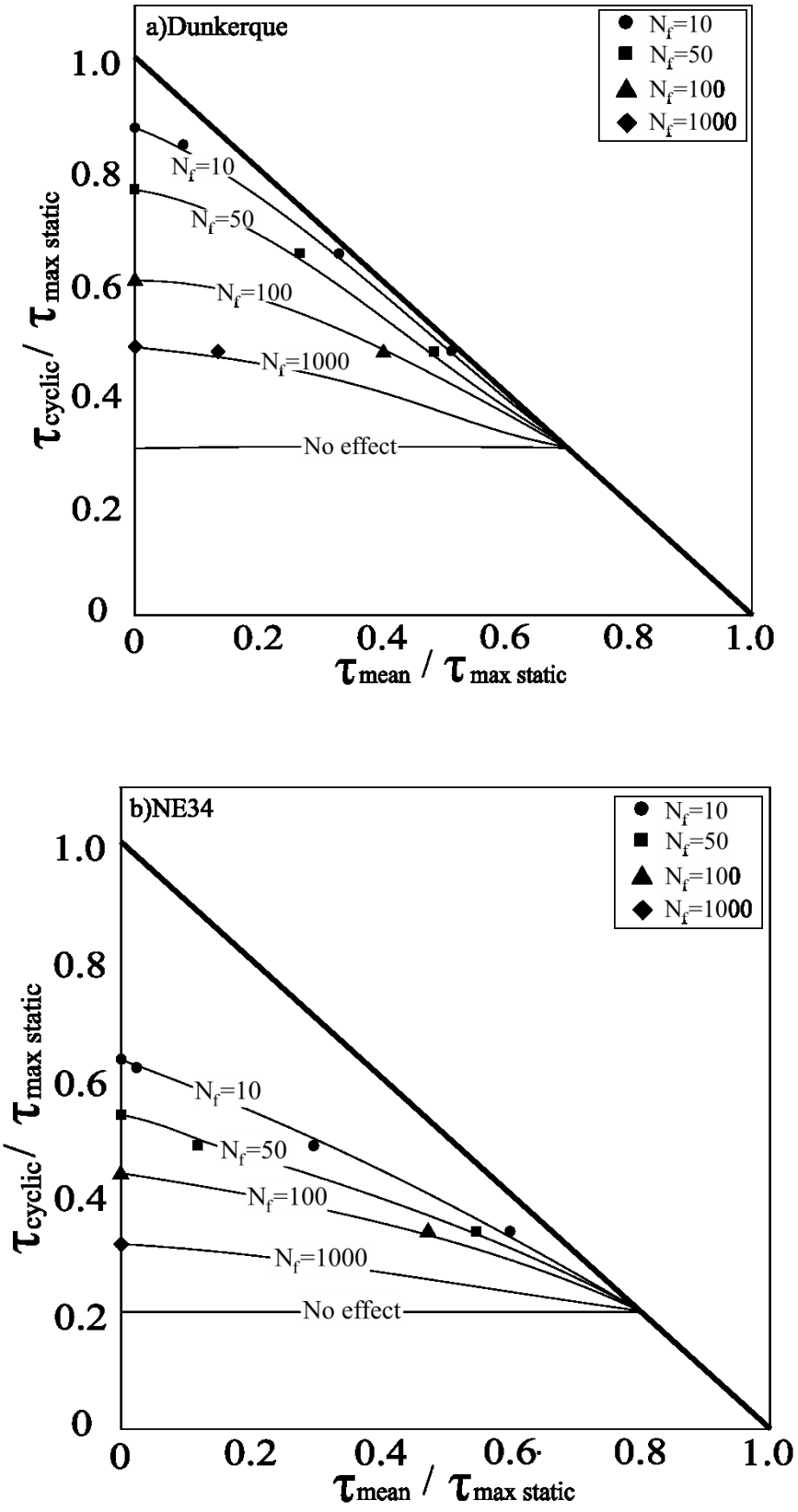


Figure 9-6 Contours of number of cycles required to reach failure plotted on the interaction diagram for a)Dunkerque and b)NE 34 specimens obtained from HCA tests

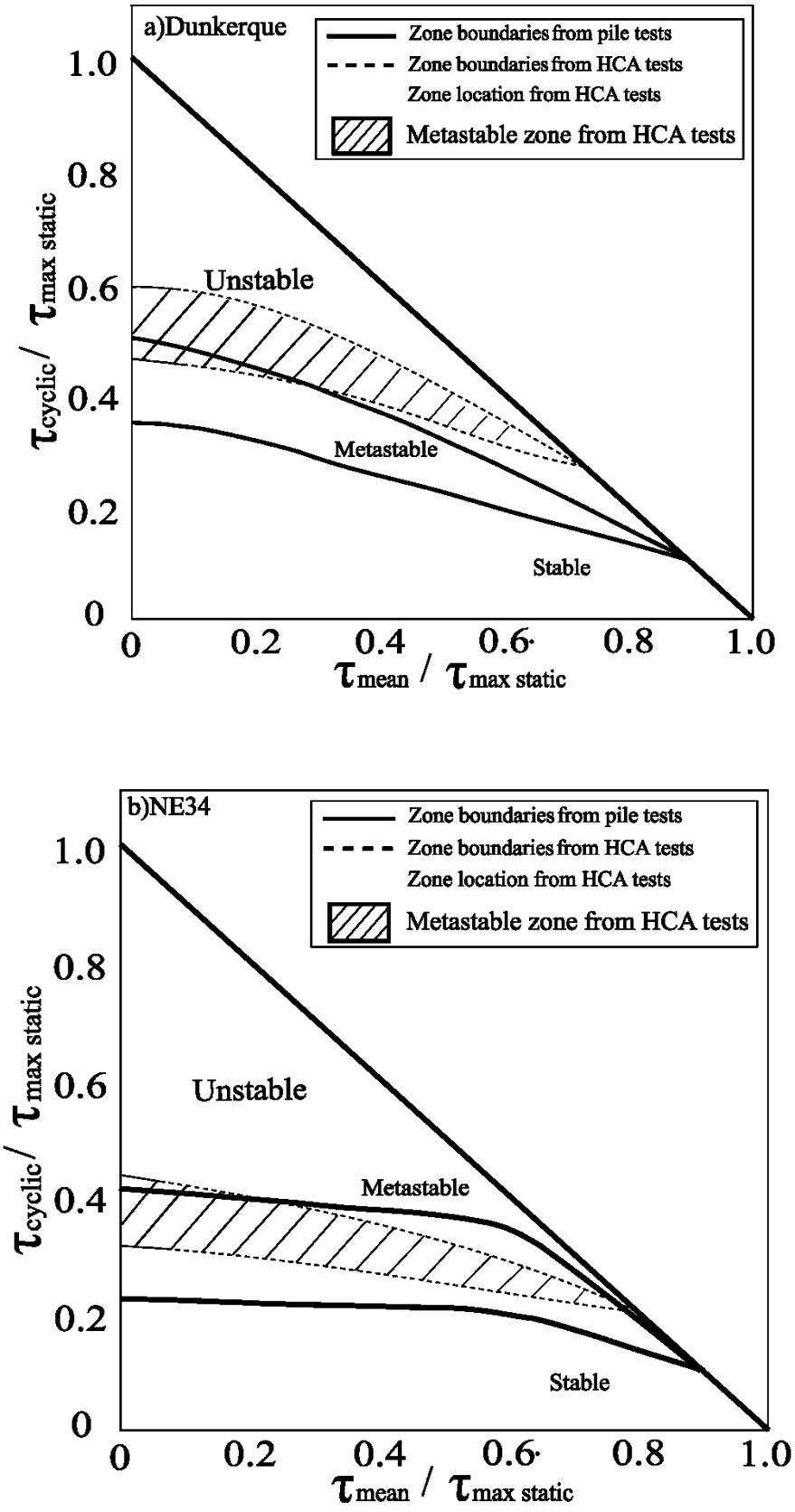


Figure 9-7 Comparison between different zones of behaviour obtained from HCA tests with a) in-situ Dunkerque and b)model NE34 pile tests .

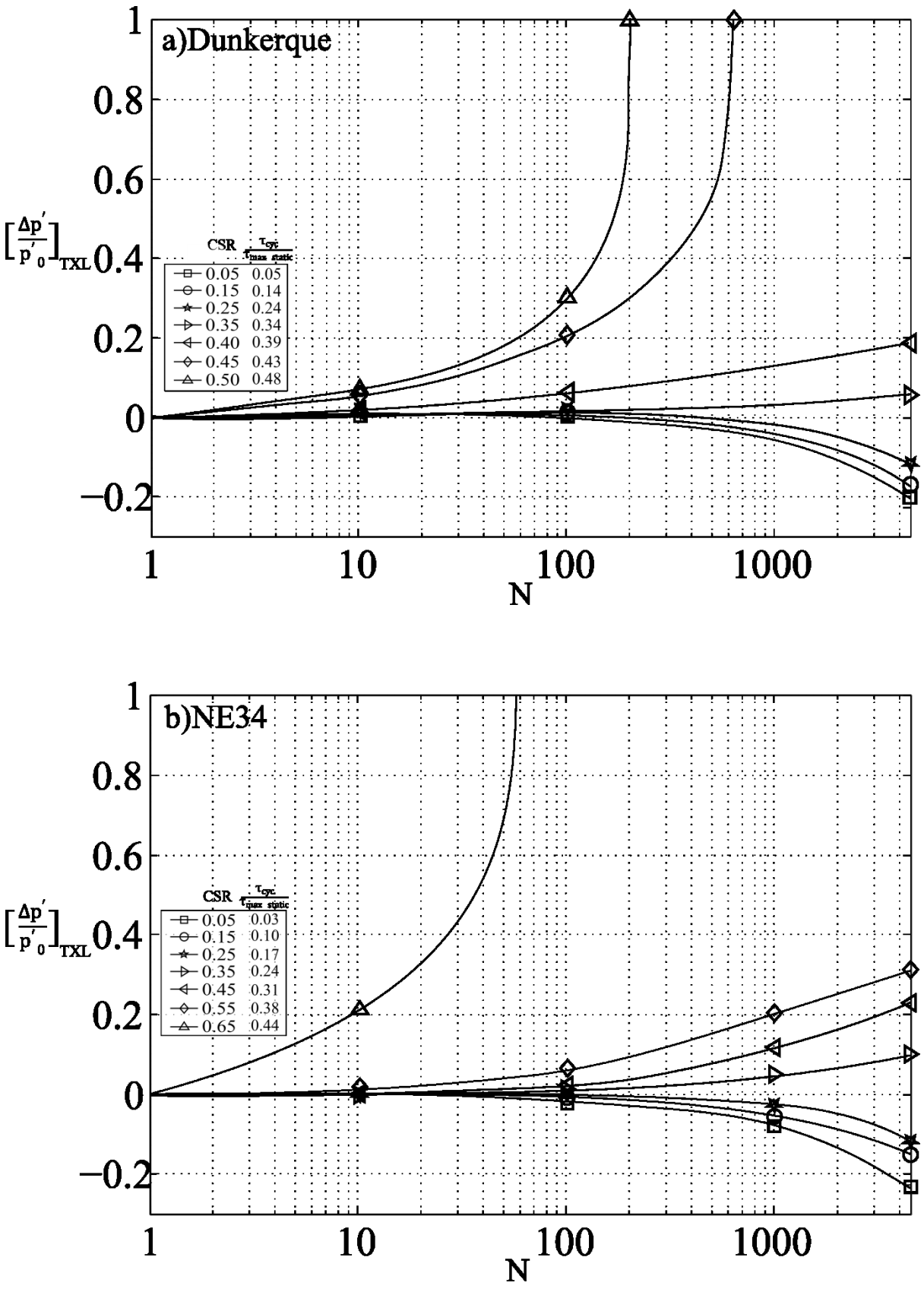


Figure 9-8 $\Delta p'/p'_0$ curves from triaxial cyclic tests for calculation of pile failure parameters for a)Dunkerque and b)NE34 specimens.

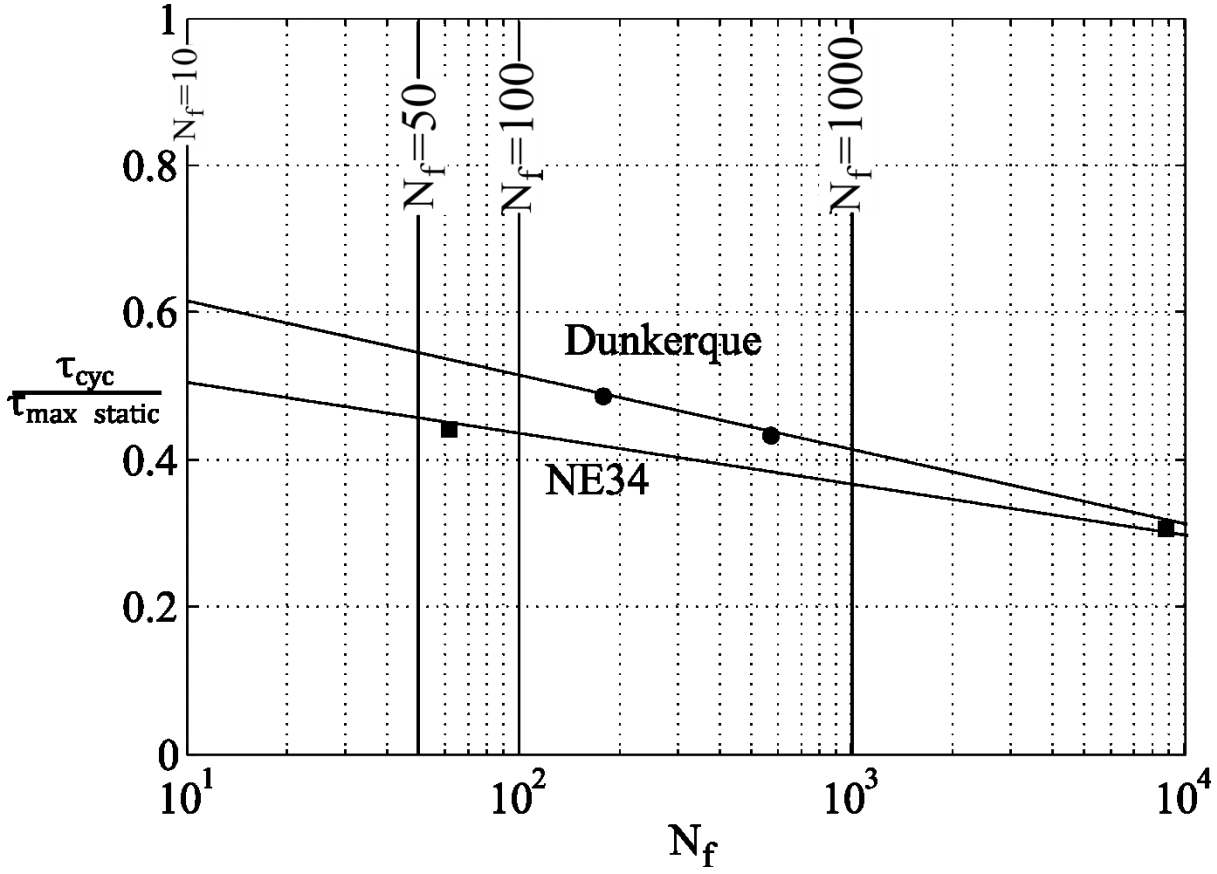


Figure 9-9 $\tau_{cyc}/\tau_{max\ static}$ against N_f graph obtained from cyclic triaxial tests at $\tau_{mean}/\tau_{max\ static}$ =0 for a)Dunkerque and b)NE34 specimens.

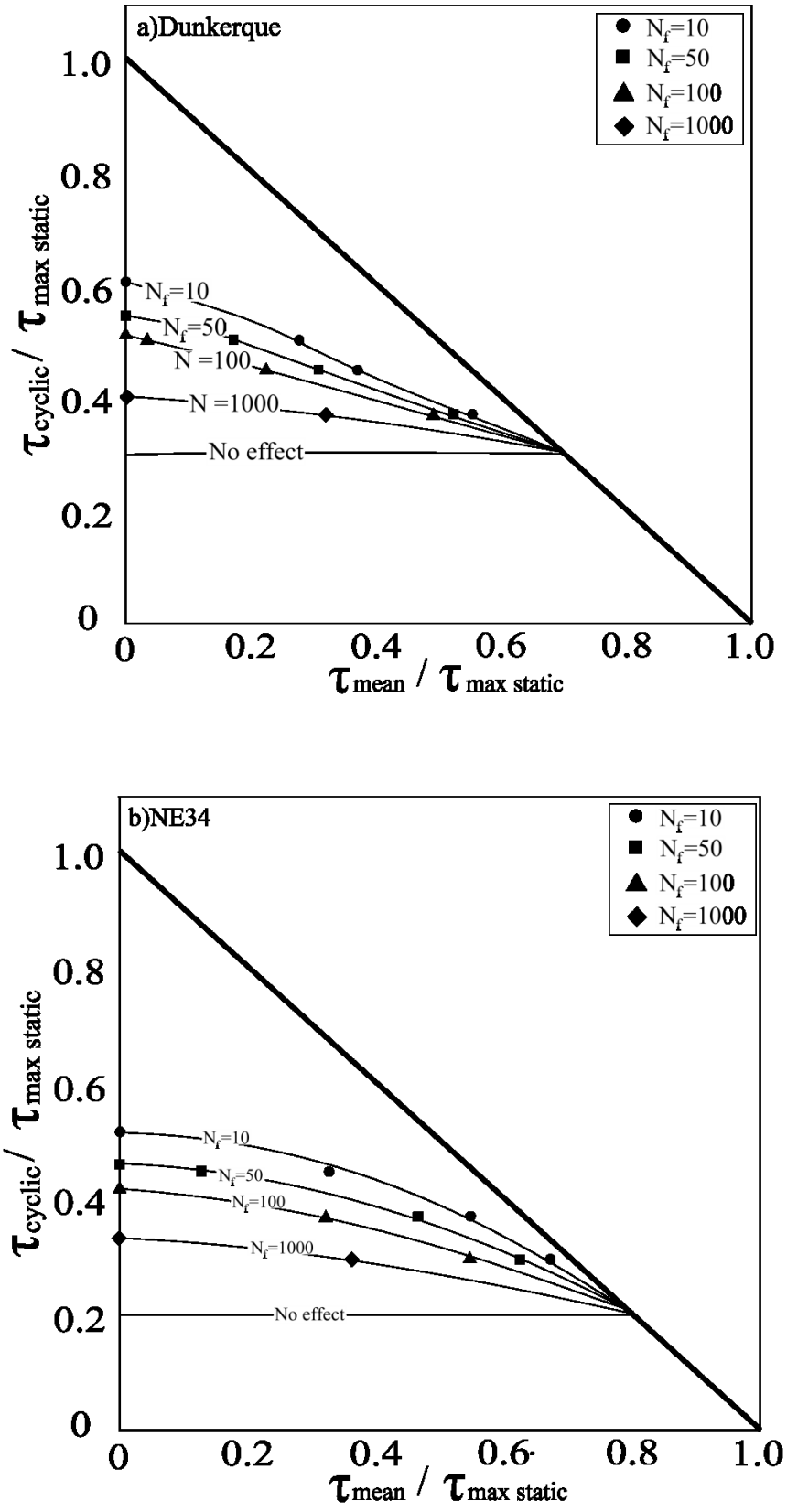


Figure 9-10 Contours of number of cycles required to reach failure plotted on the interaction diagram for a)Dunkerque and b)NE 34 specimens from triaxial tests obtained from triaxial tests.

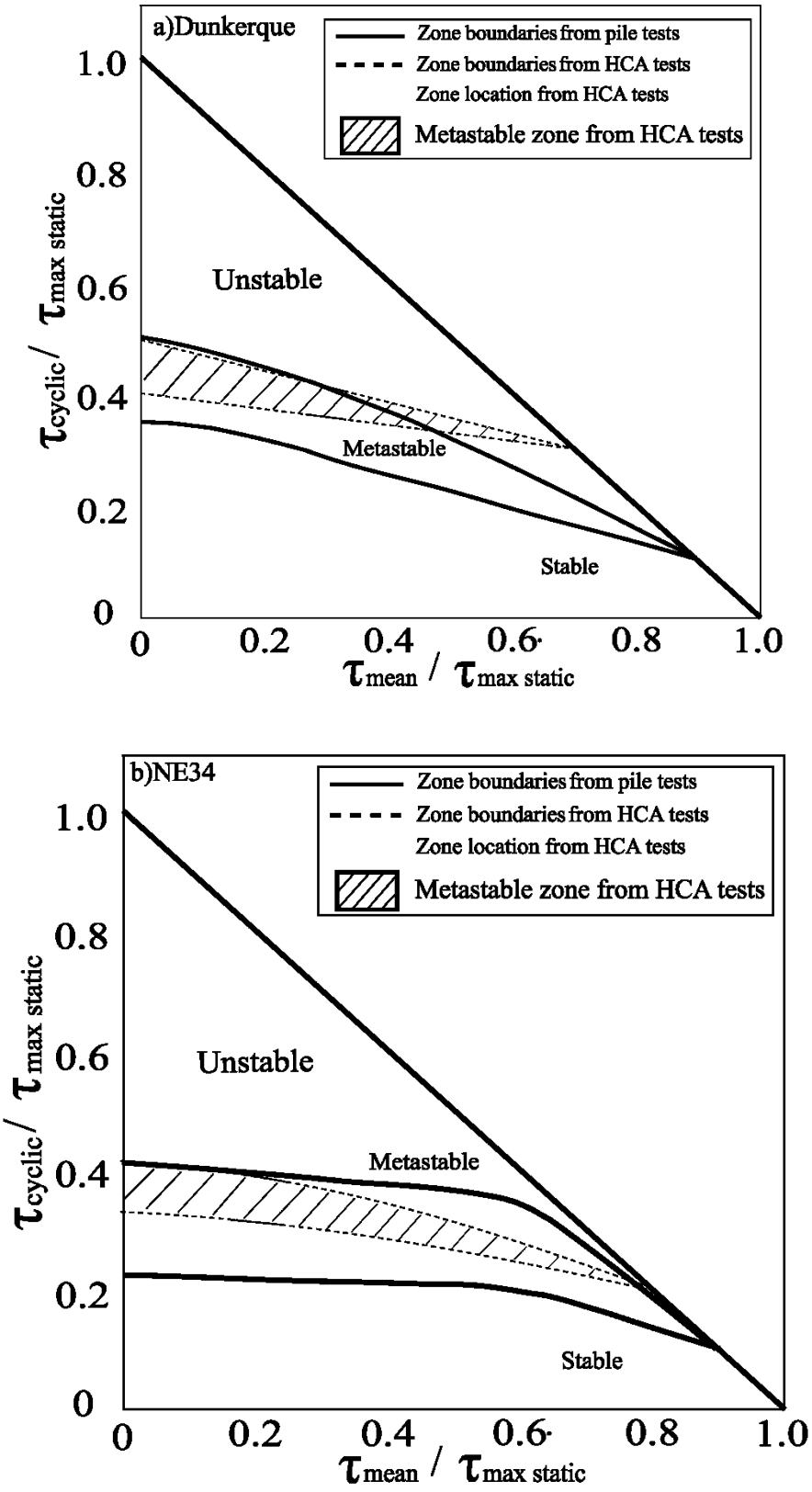


Figure 9-11 Comparison between different zones of behaviour obtained from triaxial tests with a) in-situ Dunkerque and b)model NE34 pile tests

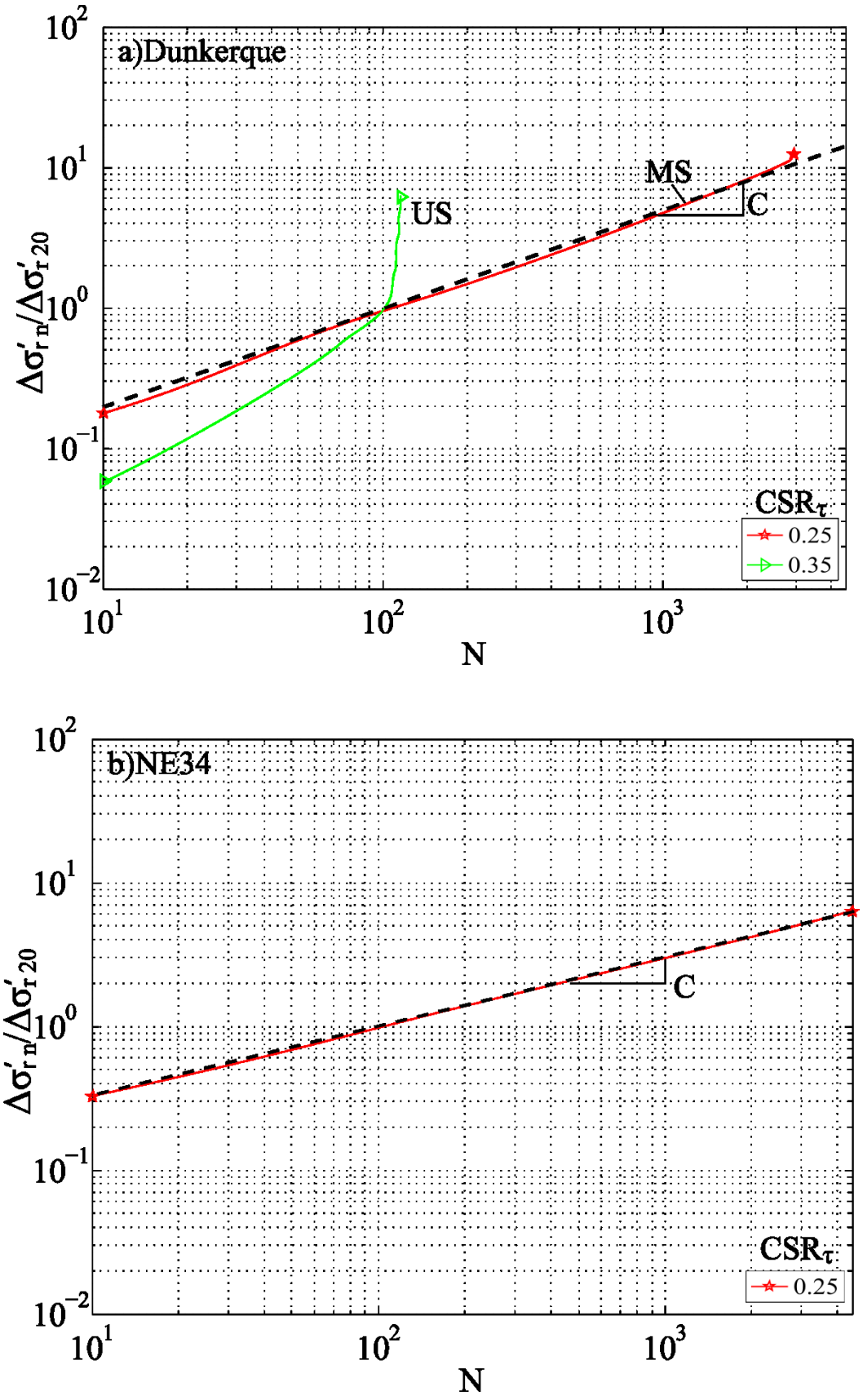


Figure 9-12 Assessment of the A,B C approach (Jardine et al., 2005) applicability for pile shaft degradation under cycling in laboratory HCA tests in a)Dunkerque and b)NE34 tests.

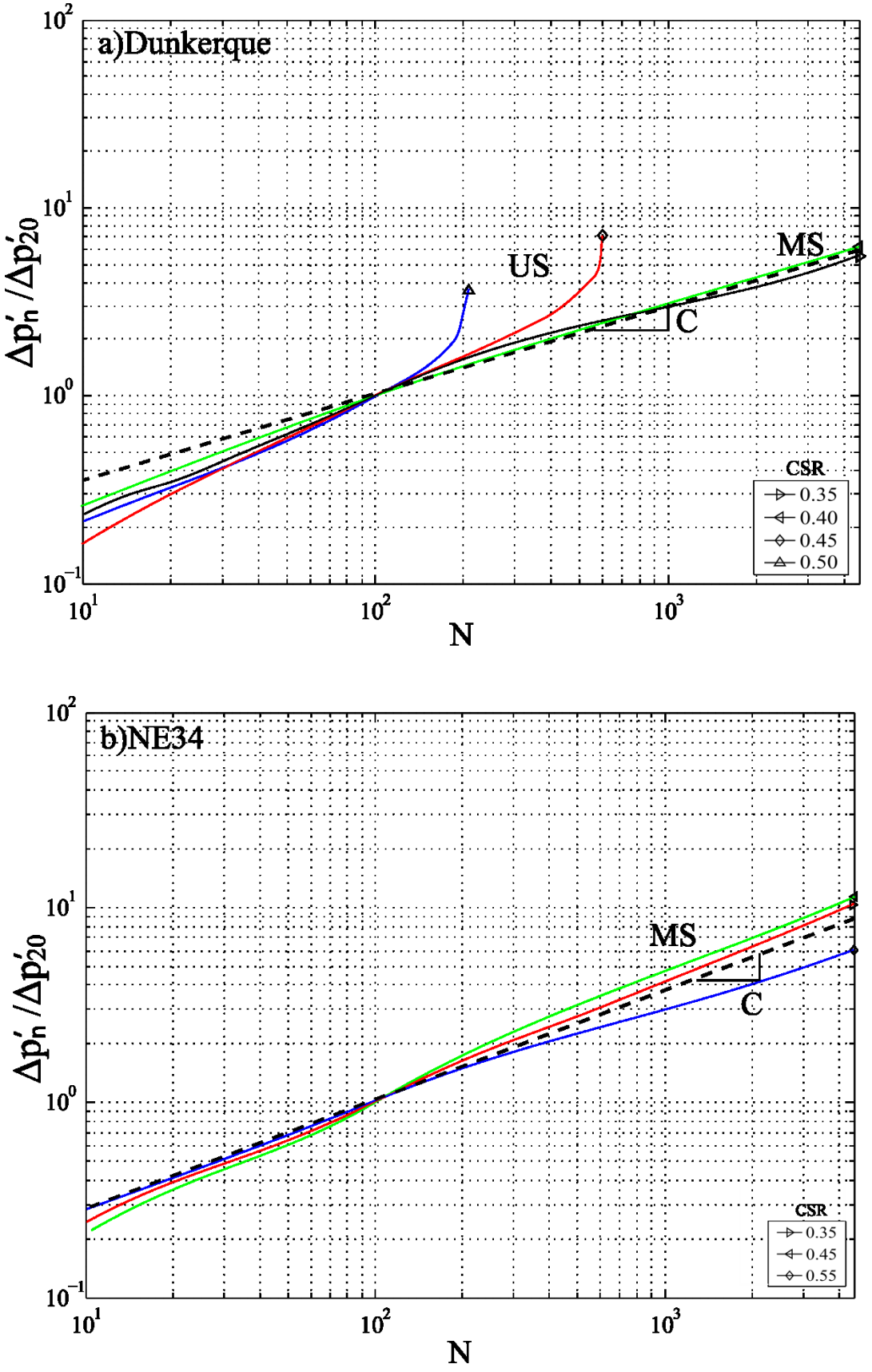


Figure 9-13 Assessment of the A,B C approach (Jardine et al., 2005) applicability for pile shaft degradation under cycling in laboratory triaxial tests in a)Dunkerque and b)NE34 tests.

CHAPTER 10

Conclusions, remarks and recommendations for future work

This thesis has considered how laboratory triaxial and HCA stress path tests might be employed to predict the cyclic shaft response of piles driven in sands by replicating as closely as possible the effective stress history and kinematic conditions of single elements of soil positioned adjacent to pile shafts that experience axial cyclic loading. The main conclusions and outcomes of this study are as follows:

10.1 Apparatus and sample set-up

Monotonic and cyclic triaxial and HCA stress path experiments can provide relevant and useful information provided that due attention is given to a considerable list of testing details. The Author's tests on two sands were prepared using a water pluviation technique, which was able to produce medium-dense to dense samples with an internal fabric similar to marine sand deposits. The technique proved to be highly efficient in producing repeatable samples with initial void ratios close to the targeted values. In principle, simple shear HCA tests were best able to model the shearing mode near the pile shaft. However, triaxial tests were also able to consider similar conditions by monitoring the mean effective stress changes developed as a key indicator of how radial effective stress may change close to a pile shaft under cyclic

loading. Both test types also showed how cyclic stiffnesses might vary and the degree to which permanent strains would develop under cycling

Prior to performing the main series of cyclic loading tests, the abilities of both apparatus to apply relatively fast and accurate cyclic loading over long durations was assessed. The modified Bishop & Wesley (1975) triaxial setup employed was able to apply cycles at rates of up to one per minute for q_{cyc} up to 60 kPa and 0.75 cycle/min for higher amplitudes to 38mm diameter, 76mm high specimens, while maintaining accurate sine-wave axial cyclic load forms. Assessments made with the ICRCHCA showed that the torque transmitting system and controlling software could not initially conduct the cycling as desired with the 72mm outside diameter 190 high HCA specimens. Modifications were made to the torque system to achieve the necessary performance and the control software was updated to operate on the windows based TRIAX 5.2 (Toll, 1993).

10.2 Test sands and their monotonic behaviour

Dunkerque and Fontainebleau NE34 sands were chosen to provide an experimental soil element dataset that could be compared with the field pile tests reported by Jardine & Standing (2000, 2012) on Dunkerque and the model pile tests described by Tsuha *et al.* (2012) on NE34 sand. Both are fine predominantly silica sands with Dunkerque sand having ≈ 10% $CaCO_3$ shell fragments while NE34 is almost pure silica.

Several series of static triaxial and simple shear HCA tests were performed to obtain the mechanical characteristics of the test sands. The small strain behaviours of the test sands were interpreted within a kinematic multi-yield surface framework. Drained K_0 normally-consolidated compression and extension tests performed from different p'_0 levels located the linear Y_1 surface along with Y_2 and Y_3 surfaces. Comparison of the results obtained at different pressures showed that Y_1 to Y_3 surfaces increase almost linearly in size with p'_0. The

large strain critical state (e-lnp) parameters of the test sands were also assessed from drained normally-consolidated compression tests, which also gave sands' peak and critical state angles of shearing resistance.

Undrained tests were also performed on both normally consolidated and over consolidated triaxial specimens. These provided information on how overconsolidation increases the size of the Y_1 and Y_2 regions. They also confirmed that critical states could not be reached under the pressures or strains that could be mobilised under undrained conditions with apparatus available.

Normally consolidated and over consolidated monotonic undrained simple shear HCA tests were also performed on both test sands. The small strain results showed that, as in triaxial tests, overconsolidation extended the Y_1 limits. Similar to the triaxial tests, critical state conditions were not reached.

10.3 Development of the "standard" testing procedure

Field and model instrumented pile tests have shown that soil elements adjacent to displacement pile experience extreme loading conditions during driving, prior to equalisation rest periods and later cyclic working loads. Comparisons with field cyclic tests on CFA piles show that installation stress history has a major impact on the driven piles subsequent cyclic response. It was concluded that the stress histories and boundary conditions of a single element adjacent to pile shafts surface must be matched closley in laboratory tests if they are to achieve comparable cyclic behaviour to that developed in the pile tests. The key features identified were:

Effect of stress history on cyclic response: Triaxial undrained cyclic tests on normally consolidated and overconsolidated specimens with similar initial void ratios, effective stresses and cyclic load levels showed that overconsolidation improves the subsequent cyclic

resistance considerably. Based on the results obtained, it was concluded that the over-consolidation implicit in pile driving must be matched in the pre-conditioning procedure of cyclic tests that aim to replicate the results obtained from driven field and jacked model pile tests.

Effect of pre-cycling: Each blow or jack stroke imported to displacement piles involves a full cycle of downward shaft failure followed by partial re-bound. Numerous researchers have reported that applying large pre-cycles improve the subsequent cyclic response of soils. To assess this, two series of triaxial tests with similar stress history, ageing and cyclic loads but with different levels of pre-cycling were performed. The results showed that pre-cycling greatly improved the subsequent cyclic response of both test sands. Using the outcomes, a representative pre-cycling stages was added to the "standard" pre-conditioning procedure.

Effect of ageing: The sand positioned around the pile shaft experiences ageing between installation and any load-test or storm loading event. Ageing was found to have a significant impact on the subsequent cyclic resistance Based on the results obtained it was decided that the pre-conditioning should involve 48 hours of ageing after each consolidation and swelling phase.

The main stages of cyclic loading were performed maintaining constant volume conditions that effectively provided Constant Normal Stiffness (CNS) tests with K_{CNS}=infinity. Adopting this upper limit avoided the ambiguity of choosing a representative K_{CNS} value that is in practice dependent on variable pile radius and non-linear soil shear stiffness.

10.4 "Standard" triaxial and HCA cyclic results

An extensive series of cyclic triaxial and HCA tests was performed on "standard" pre-conditioned specimens. The results led to the identification of *Stable*, *Metastable* and *Unstable* modes of behaviour that were encountered under different cyclic loading levels.

These types are behaviour are generally similar to those seen in pile tests, although their limits were defined herein in slightly different ways. The key features of these modes are:

Stable behaviour: Triaxial and HCA specimens cycled at low cyclic amplitudes showed either no change, or gentle rises, in their p′ values over 4500 cycles. *Stable* triaxial tests showed almost no permanent strain accumulation. Similarly, no deviatoric stress degradation was observed in the *Stable* cyclic HCA SS tests. Cyclic stiffness also remained steady in both types of tests. According to the kinematic multi-yield surface framework, the threshold for this "no deleterious effect" *Stable* zone is the Y_2 surface. The initial locations of the Y_2 surfaces, were estimated from the recorded stress-strain cycles.

Metastable behaviour: This behaviour was observed in triaxial and HCA cyclic tests that were cycled at intermediate cyclic loading levels. Cycling in these tests led to p′degradations but with no failure within 1000 cycles. The p′ degradation was associated with axial strain accumulation cyclic stiffness degradation in both triaxial and HCA tests. Degradation of effective stresses and accumulation of permanent strains in these tests indicate that the stress paths engaged and relocated the Y_2 surfaces in each cycle of *Metastable* loading.

Unstable behaviour: Triaxial and HCA tests that reached failure after less than 1000 cycles were categorised as *Unstable*. Under these cyclic levels marked losses of p′ values were accompanied by matching permanent strain accumulations and sharp drops of cyclic stiffness.

Comparison of cyclic responses between two test sands showed that their behaviour is almost identical under low level cycling but Dunkerque sand showed less resistance under intermediate and high level cyclic loads. It was argued that this could be due to higher level of particle crushing at these cyclic levels. Further study is needed to assess this idea.

The main series of "standard" triaxial tests were performed with initial density states close to the average seen in the field and model pile tests in an attempt to achieve comparable results. Additional tests at different density states showed that the sands' cyclic behaviours were only mildly sensitive to increases in initial relative density above the ratios of 75% for the main test programme. However, samples prepared at significantly lower D_r values showed far more marked cyclic degradation. It is clear that sands' initial relative densities (or state parameters) are highly influential and must be matched to achieve meaningful results.

Drained triaxial tests were also performed to give information about the development of the principal strains under cycling. The drained tests also manifested a cyclic Y_2 threshold below which accumulated permanent strains were negligible.

10.5Comparison with pile tests

Along with in-situ testing procedures and pile experiments, laboratory tests can be employed to obtain cyclic degradation laws which can be implemented in *local soil-pile analysis*, *rigorous FEM modelling* or *global soil-pile analysis* methods to obtain pile cyclic degradation for regular cycling as proposed by Jardine *et al.* (2012).

A simplified pile analysis approach was set out and applied in Chapter 9 to relate the laboratory tests to pile behaviour by predicting the cyclic capacity trends expected in displacement pile tests conducted on the two test sands. The inter-relationships between single element and field pile conditions were considered carefully to develop appropriate rules for applying the laboratory test data. Comparison between the predictions and failure trends observed in field and model pile tests showed a generally good match with HCA tests slightly over-predicting the cyclic resistance and triaxial tests showing a narrower *Metastable* zone than in the field. Such relatively minor discrepancies could be due to multiple factors including the more progressive failure of the pile tests, the details of the pre-conditioning procedures, the absence of more tests with higher τ_{mean} and q_{mean} values, or possible

differences in initial density state. There was no evidence that it is overly conservative to conduct the laboratory experiments under constant volume ($K_{CNS}=\infty$) conditions. More detailed predictions of the piles' cyclic response can be made from the laboratory tests using local pile T-Z analyses software or FEM methods such as those described in Chapter 2. The results presented in Chapter 7 and 8 can be used as the key inputs for the calibration of such numerical methods.

Applicability of the "A,B,C" approach proposed by Jardine *et al.* (2005) to relate σ'_r changes developed on the pile shaft to τ_{cyc} and N was examined using normalised trends from laboratory tests. Results suggested that method can provide reasonable predictions for *Metastable* conditions and can be combined with an "equivalent number of cycles" approach to consider batches of dissimilar cycles. However, the parameters developed to match *Metastable* conditions were not applicable to *Unstable* conditions which moved more rapidly to failure than expected. Further development is required to consider such cases. Provided that *Stable* conditions can be identified from the element tests as described, then there is no need to model their "no detrimental effect" response to cycling.

10.6 Recommendations for future work

The Author is aware on completing his study that several challenges remain to be addressed by further research. These include:

Idealisation of storms into regular cycles: As was discussed in Section 3.2, the cyclic loads experienced by foundations under critical storm conditions comprise a series of non-uniform irregular amplitude load cycles. It was discussed that in practice these time-histories are usually transformed into idealized suites of uniform cycles with each suite having a fixed load amplitude (Q_{cyc}) and average load (Q_{avg}) and specific number of cycles. It is often assumed that the cumulative effect of these cycles can be calculated using the equivalent

number of cycles approach (described in Section 2.3.3). The ability of this approach to account for irregular cyclic loading can be tested using multistage laboratory cyclic tests, extending the experimental approach outlined in this thesis.

Implementation of laboratory results into design methods: Section 9.2 discussed different approaches for employing laboratory derived degradation laws into pile axial cyclic design. Among the techniques proposed (local, global and FEM) this thesis could only offer global comparisons (Chapter 9). Further checking and development is required to allow laboratory tests results to be implemented into local pile analyses and FEM analyses methods and to extend the approach to consider local permanent strain development and cyclic stiffness changes. The results from the predictions made by these approaches can then be compared with field and model pile test results to assess each calculation method's accuracy.

Accuracy of results obtained from Cyclic Simple Shear tests (CSS): As was discussed in Section 3.4, conventional simple shear tests are not ideal for cyclic testing due to their inherent stress non-uniformity and their in-ability to give information on the full stress tensor. However, these tests are more commonly used in practice than HCA simple shear tests, which are difficult to perform and are mostly employed in research laboratories. It would be highly valuable to investigate whether conventional CSS tests can give similarly useful predictions of cyclic pile response.

Further cyclic and monotonic testing: Extra testing at different OCRs, ageing times and pre-cycling loads would also be valuable to further assess the effects of pre-conditioning on the cyclic response seen in triaxial and HCA tests. Moreover, cyclic tests should be performed at different τ_{ave} and q_{mean} levels to assess the effect of mean cyclic load on cyclic response. Further monotonic testing including probing tests to capture the small strain stiffness

behaviour more comprehensively and high pressure tests to obtain critical state response would also be useful adding to the database of measurements available for the two test sands.

Study on cyclic response of other types of foundations: The cyclic tests presented in this thesis are only applicable to displacement piles. As was shown in Section 9.1, other types of deep foundations, including bored CFA piles, show a completely different response to cyclic loading in the same sand due to their different installation stress history. Different pre-conditioning procedures are applicable to such foundation types and impact of such procedures could be investigated through further experiments of the type undertaken by the Author.

Study on the lateral cyclic loading response: Piled foundations often have to carry considerable lateral and moment loading components in addition to their axial loads. Lateral failures involve a far larger mass of soil experiencing large strains than is the case under axial shaft loading. These different conditions will need to be considered in any single element tests designed to simulate lateral cyclic loading. The current PISA project (Bryne *et al.,* 2015) involves both new static and cyclic field pile tests at Dunkerque on piles of various scales. New single element experiments are being performed at Imperial College London by Mr Tingfa Liu to aid investigations into how modelling may be improved for such lateral cases.

References

1. Airey, D. W. & Fahey, M. (1991). Cyclic response of calcareous soil from the North-West Shelf of Australia. *Géotechnique*, **41**(1): 101-121.
2. Airey, D. W., Al-Douri, R. H., & Poulos, H. G. (1992). Estimation of pile friction degradation from shearbox tests. Geotechnical Testing Journal, 15, 388-388.
3. Alawneh, A.S. & Husein Malkawi, I. (2000). Estimation of post-driving residual stresses along driven piles in sand. *Geotechnical Testing Journal, ASTM*, **23**(3): 313–326.
4. AI-Douri, R. H., 1992, "Behaviour of Single Pile and Pile Groups in Calcareous Sands," forthcoming, Ph.D. thesis, University of Sydney, Australia.
5. Altuhafi, F., & Jardine, R. J. (2011). *Effect of particle breakage and strain path reversal on the properties of sands located near to driven piles*. Proceedings of the Fifth International Symposium on Deformation Characteristics of Geomaterials, IS-Seoul 2011. IOS Press. Seoul, Korea Vol. 2, 388.
6. American Petroleum Institute (1969). *Recommended Practice for Planning, Designing and Constructing Fixed Offshore Platforms (API RP2A) – 1st edition*, Washington, D.C., USA.
7. American Petroleum Institute (2014). *Recommended Practice for Planning, Designing and Constructing Fixed Offshore Platforms (API RP2A) – 22nd edition*, Washington, D.C., USA.
8. Andersen, K.H. (2009). Bearing capacity under cyclic loading-offshore, along the coast, and on land. *Canadian Geotechnical Journal*, **46**(5): 513-535.
9. Andersen, K.H., Puech, A.A. & Jardine, R.J. (2013). Cyclic resistant geotechnical design and parameter selection for offshore engineering and other applications. *Design for cyclic loading: piles and other foundations*. Presse des Ponts, Paris. 9-44
10. Anderson, K.H., Allard, M.A. & Hermstad, J. (1994). *Centrifuge model tests for a gravity platform on very dense sand*; II: Interpretation, Proc. 7th International Conference on behaviour of Offshore Structures, BOSS'94. Cambridge, Mass., vol. 1, 255-282.
11. Anh-Minh, N. (2007). *An investigation of the anisotropic stress-strain-strength characteristics of an Eocene clay*. Ph.D. thesis, Imperial College London.
12. Ashmawy, A.K. & Drnevich, V.P. (1994). General dynamic model for the resonant column/quasi-static torsional shear apparatus. *Geotechnical Testing Journal* **17**(3): 337-348.
13. Åstedt, B., Weiner, L. & Holm, G. (1992). Increase in bearing capacity with time for friction piles in silt and sand. *Proceedings of Nordic Geotechnical Meeting*: 411–416.
14. Atkins Consultants Ltd. (2000). *Cyclic degradation of offshore piles*. HSE offshore technology Report OTO 2000 013. Health and Safety Executive, London.
15. Axelsson, G. (2000). *Long term set-up of driven piles in sand*. PhD thesis, Royal Institute of Technology, Stockholm, Sweden.
15. Baxter, C.D., & Mitchell, J.K. (2004). Experimental study on the aging of sands. *Journal of Geotechnical and Geoenvironmental Engineering*, **130**(10): 1051-1062

16. Been, K. & Jefferies, M. G. (1985). A state parameter for sands. *Géotechnique*, **35**(2): 99-112
17. Been, K. & Jefferies, M.G. (1986); A state parameter for sands: Reply to Discussion, *Géotechnique*, **36** (1): 123–132.
18. Been, K., Jefferies, M.G., & Hachey, J. (1991). The critical state of sands. *Géotechnique*, **41**(3): 365-381.
19. Benzaria, A., Puech, A. & Le Kouby, A. (2013). Cyclic axial load tests on bored piles in dense sands. 18th ICSMGE, 1071-1096.
20. Bishop, A.W. & Wesley, L.D. (1975). A hydraulic triaxial apparatus for controlled stress path testing. *Géotechnique* **25**(4): 657–670.
21. Boulon, M. & Foray, P. (1986). *Physical and numerical simulation of lateral shaft friction along offshore piles in sand*. Proceedings of the 3rd International Conference on Numerical Methods in Offshore Piling, Nantes, France, 127– 147.
22. Boulon, M., Hoteit, N., & Marchina, P. (1988). A complete constitutive law for soil-structure interfaces. In *VI International Conference on Numerical Methods in Geomechanics* (pp. 311-316). Balkema Rotterdam.
23. Bowman, E.T. & Soga, K. (2005). Mechanisms of setup of displacement piles in sand: laboratory creep tests. *Canadian Geotechnical Journal*, **42**(5): 1391-1407.
24. Brosse, A. (2012). *Study of the anisotropy of three British mudrocks using a hollow cylinder apparatus*. Ph.D. thesis, Imperial College London.
25. Cai, G., Liu, S., Tong, L., & Du, G. (2008). Assessment of direct CPT and CPTU methods for predicting the ultimate bearing capacity of single piles. *Eng. Geology* **104**(3-4): 211–222.
26. Castro, G. (1975); Liquefaction and cyclic mobility of saturated sands. *Journal of Geotechnical Engineering* Division, ASCE, **101**(6): 551–569.
27. Chan, S. & Hanna, T.H. (1980). Repeated loading on single piles in sand. *Journal of the Geotechnical Engineering. Division* ASCE, **106**(2): 171-188.
28. Chow, F.C. (1997). *Investigation into Displacement Pile Behaviour for Offshore Foundations*. PhD thesis, Imperial College London, London, UK.
29. Chow, F.C., Jardine, R.J., Brucy, F. & Nauroy, J.F. (1998). Effects of time on capacity of pipe piles in dense marine sands, *Journal of Geotechnical and Geoenvironmental Engineering ASCE*, **124**(3): 254 – 264.
30. Chow, F.C., Jardine, R.J., Nauroy, J.F., & Brucy, F. (1997). Time-related increases in the shaft capacities of driven piles in sand. *Géotechnique*, **47**(2): 353-361.
31. Clausen, C.J.F., Aas, P.M. & Karlsrud, K. (2005). Bearing capacity of driven piles in sand, the NGI approach. *Proceedings of International Symposiom. on Frontiers in Offshore Geomechanics (ISFOG)*, Taylor & Francis, London: 677–681.
32. Cooling, L.F. & Smith, D.B. (1936). The shearing resistance of soils. *Journal of the ICE.* **3**(7): 333-343.
33. Coop, M.R. & Lee, I.K. (1993*). The behaviour of granular soils at elevated stresses*. C. P. Wroth Memorial Symposium. Predictive Soil Mechanics. Thomas Telford, London, pp. 186-198.
34. Cuccovillo, T. & Coop, M.R. (1997). The measurement of local axial strains in triaxial tests using LVDTs. *Géotechnique* **47**(1): 167–171.

35. Dejong, J. T., Randolph, M. F., & White, D. J. (2003). Interface load transfer degradation during cyclic loading: a microscale investigation. *Soils and foundation*, **43**(4), 81-93.
36. Dobry, R., Ladd, R., Yokel, F., Chung, R. & Powell, D. (1982). Prediction of pore water pressure build up and liquefaction of sands during earthquakes by the cyclic strain method. NBS Building Science Series 138, National Bureau of Standards, US Department of Commerce.
37. Donaghe, R. T., & Chaney, R. C. (1988). *Advanced triaxial testing of soil and rock* Vol. 977. ASTM International.
38. Drnevich, V.P. (1978). *Resonant-column testing: problems and solutions. In Dynamic Geotechnical Testing*, no. 654 in STP. American Society for Testing and Materials, Philadelphia, USA, pp. 384-398.
39. Erbrich, C. T., O'Neill, M. P., Clancy, P. and Randolph, M. F. (2010). *Axial and lateral pile design in carbonate soils*. Frontiers in Offshore Geotechnics II. Taylor & Francis Group, London, 125-154.
40. Fakharian, K., & Evgin, E. (1997). Cyclic simple-shear behavior of sand-steel interfaces under constant normal stiffness condition. *Journal of Geotechnical and Geoenvironmental Engineering ASCE*, **123**(12): 1096-1105.
41. Fleming. W.G.K., Weltman. A.J., Randolnh, M.F., & Elson, W.K. (1992). *Piling engineering*, Glasgow: Blackie (Halsted Press). 2nd edition.
42. Fugro Engineers B.V. (2004). *Axial Pile Capacity Design Method for Offshore Driven Piles in Sand*. Report P1003 presented to the American Petroleum Institute, Issue 3, 5.
43. Gaudin, C., Schnaid, F., & Garnier, J. (2005). Sand characterization by combined centrifuge and laboratory tests. *International Journal of Physical Modelling in Geotechnics*, **5**(1): 42-56.
44. Gavin, K. & O'Kelly, B. (2007). Effect of friction fatigue on piles in dense sand. *Journal of Geotechnical and Geoenvironmental Engineering ASCE*, **133**(1): 63–71.
45. Gavin, K., Igoe, D. & Kirwan, L. (2013). The effect of ageing on the axial capacity of piles in sand. *Proc. of the ICE Geotech. Eng*, **166**(2): 122-130.
46. Gavin, K.G. & Lehane, B.M. (2003). The shaft capacity of pipe piles in sand. *Canadian Geotechnical Journal* **40**(1): 36–45.
47. Gennaro, V.D., Canou, J., Dupla, J.C., & Benahmed, N. (2004). Influence of loading path on the undrained behaviour of a medium loose sand. *Canadian Geotechnical Journal*, **41**(1), 166-180.
48. Gennaro, V.D., Canou, J., Dupla, J.C., & Benahmed, N. (2004). Influence of loading path on the undrained behaviour of a medium loose sand. *Canadian Geotechnical Journal*, **41**(1): 166-180.
49. Georgiannou, V. N., Tsomokos, A., & Stavrou, K. (2008). Monotonic and cyclic behaviour of sand under torsional loading. *Géotechnique*, **58**(2), 113-124.
50. Georgiannou, V.N., & Tsomokos, A. (2008). Comparison of two fine sands under torsional loading. *Canadian Geotechnical Journal*, **45**(12): 1659-1672.
51. Gibson, R. E. (1950). Correspondence. J. Inst. Civ. Engrs, 34: 382 – 383.

52. Harder Jr, L. F., & Boulanger, R. (1997). Application of K and K correction factors. In Technical Report NCEER (Vol. 97, pp. 167-90). US National Center for Earthquake Engineering Research (NCEER).
53. Hight, D.W., Gens, A., & Symes, M.J. (1983). The development of a new hollow cylinder apparatus for investigating the effects of principal stress rotation in soils. *Géotechnique*, **33**(4): 355-383.
54. Ho, T.Y.K., Jardine, R.J., and Minh, N.A. (2011). Large displacement interface shear between steel and granular media. *Géotechnique*, **61**(3): 221–234.
55. Hsu, C.C., & Vucetic, M. (2004). Volumetric threshold shear strain for cyclic settlement. *Journal of Geotechnical and Geoenvironmental Engineering ASCE*, **130**(1): 58-70.
56. Hyodo, M., Tanimizu, H., Yasufuku, N., & Murata, H. (1994) Undrained cyclic and monotonic triaxial behaviour of saturated loose sand. *Soils and Foundations* **34**(1): 19-32.
57. Hyodo, M., Yamamoto, Y., & Fujii, T. (1998). Cyclic shear failure and strength of undisturbed marine clays. In *The Eighth International Offshore and Polar Engineering Conference*. International Society of Offshore and Polar Engineers.
58. Ishihara, K. & Towhata, I. (1983); Sand response to cyclic rotation of principal stress directions as induced by wave loads. *Soils and Foundations*, **23**(4): 11–26.
59. Ishihara, K. (1993). Liquefaction and Flow Failure during Earthquakes. *Géotechnique*, **43**(3): 351– 415.
60. Ishihara, K., Tatsuoka, F., & Yasuda S. (1975). Undrained deformation and liquefaction of sand under cyclic stresses. *Soils and Foundations*, **15**(1), 29-44.
61. Jardine, R. J., Andersen, K. and Puech, A. (2012). *Cyclic loading of offshore piles: potential effects and practical design*. In Proceedings of the 7th International Conference on Offshore Site Investigations and Geotechnics. SUT Publications, London, UK. pp. 59–100.
62. Jardine, R. J., Kuwano, R., Zdravkovic, L., & Thornton, C. (2001). Some fundamental aspects of the pre-failure behaviour of granular soils. *Pre-Failure Deformation Characteristics of Geomaterials. Edited by H. Jamiolkowski, RH Lancellota, and DCF Lo Presti. Swets and Zeitlinger, Lisse*, 1077-1111.
63. Jardine, R.J. & Standing, J.R. (2000). *Pile Load Testing Performed for HSE Cyclic Loading Study at Dunkirk*, France. Health and Safety Executive, London, Offshore Technology Report No. OTO 2000 007.
64. Jardine, R.J. (1991). The cyclic behaviour of large piles with special reference to offshore structures. *Cyclic loading of soils: From theory to design*, Blackie & Son, Glasgow.
65. Jardine, R.J. (1992). Observations on the kinematic nature of soil stiffness at small strains, *Soils and Foundations*, **32**(2): 111–124.
66. Jardine, R.J. (2013). *Advanced laboratory testing in research and practice*: the 2nd Bishop Lecture. Proceeding of 18th International Society for Soil Mechanics and Geotechnical Engineering. Paris. Presses des Ponts. Vol. 1, 35-54
67. Jardine, R.J., & Chow, F.C. (1996). *New design methods for offshore piles*. Marine Technology Directorate.

68. Jardine, R.J., & Standing, J.R. (2012). Field axial cyclic loading experiments on piles driven in sand. *Soils and Foundations.* **52(**4), 723-736.
69. Jardine, R.J., Chow, F., Overy, R., & Standing, J. (2005). *ICP design methods for driven piles in sands and clays.* London: Thomas Telford.
70. Jardine, R.J., Standing, J.R & Kovacevic, N. (2005). Lessons learned from full–scale observations and the practical application of advanced testing and modelling. Keynote paper, *Proc. Int. Symp. On Deformation Characteristics of Geomaterials*, Lyon, pub Balkema, Lisse, *2*: 201-245.
71. Jardine, R.J., Standing, J.R., & Chow, F.C. (2006). Some observations of the effects of time on the capacity of piles driven in sand. *Géotechnique*, **56**(4): 227-244.
72. Jardine, R.J., Symes, M.J. & Burland, J.B. (1984). The measurement of soil stiffness in the triaxial apparatus. *Géotechnique.* **34**(3): 323-340.
73. Jardine, R.J., Symes, M.J., & Burland, J.B. (1984). The measurement of soil stiffness in the triaxial apparatus. *Géotechnique*, **34**(3): 323-340.
74. Jardine, R.J., Zhu, B.T., Foray, P. & Yang, Z.X. (2013a). Measurement of stresses around closed-ended displacement piles in sand. *Géotechnique.* **63**(1): 1-17.
75. Jardine, R.J., Zhu, B.T., Foray, P. & Yang, Z.X. (2013b). Interpretation of stress measurements made around closed-ended displacement piles in sand. *Géotechnique.* **63**(8): 613-627.
76. Jefferies, M.G. (1993); NorSand: a simple critical state model for sand. *Géotechnique* **43(1)**, 91–103.
77. Johnston, I. W., Lam, T. S. K., & Williams, A. F. (1987). Constant normal stiffness direct shear testing for socketed pile design in weak rock. *Géotechnique*, **37**(1), 83-89.
78. Kaggwa, W. S., Booker, J. R., & Carter, J. P. (1991). Residual strains in calcareous sand due to irregular cyclic loading. *Journal of geotechnical engineering*, **117**(2), 201-218.
79. Karlsrud, K. (2014). Ultimate Shaft Friction and Load-Displacement Response of Axially Loaded Piles in Clay Based on Instrumented Pile Tests. *Journal of Geotechnical and Geoenvironmental Engineering,* **140**(12).
80. Karlsrud, K., Nadim, F. & Haugen, T. (1986). Piles in clay under cyclic axial loading: field test and computational modelling. *Proc. 3rd Int. Conf. on Numerical Methods in Offshore Piling*, Nantes Paris, France: 165–190.
81. Kelly, R. (2001). *Development of a large diameter ring shear apparatus and its use for interface testing*. PhD thesis, University of Sydney.
82. Konrad, J.M. (1988). Interpretation of flat plate dilatometer tests in sands in terms of the state parameter. *Géotechnique*, **38**(2): 263-277.
83. Konrad, J.M. (1993). Undrained response of loosely compacted sands during monotonic and cyclic compression tests. *Géotechnique*, **43**(1): 69-89.
84. Kulhawy, F.H. (1984). Limiting tip and side resistance: fact or fallacy? *Proc. of the Symp. on the Analysis and Design of pile Foundations*. ASCE, San Francisco, Calif., 80-98.
85. Kuwano, R. & Jardine, R.J. (2002). On the applicability of cross-anisotropic elasticity to granular materials at very small strains. *Géotechnique.* **52**(10): 727-749.

86. Kuwano, R. (1999). *The Stiffness and Yielding Anisotropy of Sand*. PhD thesis, Imperial College London, London, UK.
87. Kuwano, R., & Jardine, R.J. (1998). Stiffness measurements in a stress-path cell. Pre-failure deformation behaviour of geomaterials, ICE, London Thomas Telford Ltd, pp.391-94.
88. Kuwano, R., & Jardine, R.J. (2007). A triaxial investigation of kinematic yielding in sand. *Géotechnique*. **57**(7): 563-579.
89. Lehane, B.M. (1992). *Experimental Investigations of Pile Behaviour Using Instrumented Field Piles*. PhD thesis, University of London (Imperial College), UK.
90. Lehane, B.M., Jardine, R.J., Bond, A.J., & Frank, R. (1993). Mechanisms of shaft friction in sand from instrumented pile tests. *Journal of Geotechnical Engineering* **119**(1): 19-35.
91. Lehane, B.M., Schneider, J.A., & Xu, X. (2005a). The UWA-05 method for prediction of axial capacity of driven piles in sand. *Proc. 1st Int. Symp. on Frontiers in Offshore Geotechnics*. Perth, Australia: pp. 683–689.
92. Lehane, B.M., Schneider, J.A., & Xu, X. (2005b). *A review of design methods for offshore driven piles in siliceous sand*. UWA Report GEO 05358, University of Western Australia, Perth: 105pp.
93. Li, X.S. & Wang, Y. (1998). Linear representation of steady-state line for sand, *Journal of Geotechnical and Geoenvironmental Engineering*, ASCE **124**(12):1215–7.
94. Love, A.E.H. (1927). *A Treatise on the Mathematical Theory of Elasticity*. Dover Publications.
95. Mahmood, A. & Mitchell, J. (1976). Effect of specimen preparation method on grain arrangement and compressibility in sand. *ASTM special technical publication* (599): 169-192.
96. Manzari, M.T., & Dafalias, Y.F. (1997). A critical state two-surface plasticity model for sands. *Géotechnique* , **47**(2): 255-272.
97. Mayne, P.W. & Kulhawy, F.H. (1982). K_0–OCR relationships in soil. *Journal of Geotechnical and Geoenvironmental Engineering*, ASCE **108**(6): 851–872.
98. Merritt, A. S., Schroeder, F. C., Jardine, R. J., Stuyts, B., Cathie, D., and Cleverly, W. (2012). Development of pile design methodology for an offshore wind farm in the North Sea. In *Proceedings of the 7th International Conference on Offshore Site Investigations and Geotechnics*. SUT Publications, London, UK, 439-447.
99. Mortara, G. (2001). *An elastoplastic model for sand-structure interface behaviour under monotonic and cyclic loading*. Ph. D. Thesis. Technical University of Torino.
100. Mortara, G., Boulon, M., & Ghionna, V. N. (2002). A 2-D constitutive model for cyclic interface behaviour. International journal for numerical and analytical methods in geomechanics, 26(11), 1071-1096.
101. Mortara, G., Mangiola, A., & Ghionna, V. N. (2007). Cyclic shear stress degradation and post-cyclic behaviour from sand-steel interface direct shear tests. *Canadian Geotechnical Journal*, **44**(7), 739-752.
102. Mróz, Z. (1967). Graphical solution of axially symmetric problems of plastic flow. *Zeitschrift für angewandte Mathematik und Physik ZAMP*, **18**(2), 219-236.

103. Mulilis, J.P., Arulanandan, K., Mitchell, J.K., Chan, C.K., & Seed, H.B. (1977). Effects of sample preparation on sand liquefaction. *Journal of the Geotechnical Engineering Division*, **103**(2): 91-108.
104. Nadim, F., & Dahlberg, R. (1996). Numerical modelling of cyclic pile capacity in clay. In Offshore Technology Conference. Offshore Technology Conference.
105. Nishimura, S. (2006). *Laboratory study on anisotropy of natural London clay*. Ph.D. thesis, Imperial College London.
106. Oumarou, T. A., & Evgin, E. (2005). Cyclic behaviour of a sand steel plate interface. Canadian geotechnical journal, 42(6), 1695-1704.
107. Olson, R.E. & Dennis, N.D. (1982) *Review and Compilation of Pile Test Results: Axial Pile Capacity.* Final report to American Petroleum Institute on Project PRAC 81-29, University of Texas at Austin, TX, USA.
108. Ovando-Shelley, E. (1986). *Stress-strain behaviour of granular soils tested in the triaxial cell*. Imperial College London, PhD thesis.
109. Papadimitriou, A.G. & Bouckovalas, G.D. (2002). Plasticity model for sand under small and large cyclic strains: a multiaxial formulation. *Soil Dynamics and Earthquake Engineering.* **22**(3): 191-204.
110. Porovic, E. (1995). *Investigation of soil behaviour using a resonant-column torsional-shear hollow cylinder apparatus*. Ph.D. thesis, Imperial College London.
111. Poulos, H.G. (1981). Cyclic axial response of single pile. *Journal of Geotechnical and Geoenvironmental Engineering*, **107(**1) 41-58
112. Puech, A. (2013). Advances in axial cyclic pile design: contribution of the SOLCYP project. 18th International Society for Soil Mechanics and Geotechnical Engineering, 1071-1096.
113. Puzrin, A.M., & Burland, J.B. (1998). Non-linear model of small-strain behaviour of soils. *Géotechnique* , **48**(2): 217-213.
114. Qadimi A. (2005). *The cyclic response of a carbonate sand through critical state soil mechanics*. PhD thesis, Imperial College London.
115. Qadimi, A., & Coop, M.R. (2007). The undrained cyclic behaviour of a carbonate sand. *Géotechnique*. **57**(9): 739-750.
116. Randolph, M.F. (2003) Science and empiricism in pile foundation design, *Géotechnique* **53**(10): 847–875.
117. Randolph, M. F., & Wroth, C. P. (1981). Application of the failure state in undrained simple shear to the shaft capacity of driven piles. Geotechnique, 31(1), 143-157.
118. Randolph, M.F., Dolwin, J. & Beck, R. (1994). Design of driven piles in sand. *Géotechnique.* **44**(3): 427–448.
119. Rauch, A.F. (1997). *EPOLLS: An empirical method for predicting surface displacements due to liquefaction -Induced lateral spreading in earthquakes*. Virginia Polytechnic Institute and State University, PhD thesis.
120. Rimoy (2013), *Ageing and axial cyclic loading studies of displacement piles in sands.* Ph.D. thesis, Imperial College London.
121. Rimoy, S., Silva, M., Jardine, R., Yang, Z.X., Zhu, B T., & Tsuha, C.H.C. (2015). Field and model investigations into the influence of age on axial capacity of displacement piles in silica sands. *Géotechnique,* **65**(7): 576-589.

122. Rimoy, S.P., Jardine, R.J., & Standing, J.R. (2013). Displacement response to axial cycling of piles driven in sand. *Proceedings of the ICE-Geotechnical Engineering*, **166**(2): 131-146.
123. Salvati, L.A., & Anhdan, L.Q. (2008). Rate-dependent response of dense sand in cyclic triaxial tests. *Soils and Foundations*. **48**(3): 447-451.
124. Sayao, A. & Vaid, Y.P. (1991). Critical assessment of stress nonuniformities in hollow cylinder test specimens. *Soils and Foundations*, **31**(1): 60-72.
125. Schofield, A.N. & Wroth, C.P. (1968). *Critical State Soil Mechanics*. London McGraw-Hill.
126. Seed, B., & Lee, K.L. (1966). Liquefaction of saturated sands during cyclic loading. *Journal of the Soil Mechanics and Foundations Division*, **92**(6): 105-134.
127. Seed, H.B., & Idriss, I.M. (1971). Simplified procedure for evaluating soil liquefaction potential. *Journal of Soil Mechanics & Foundations Div*ision **97**(9) 1249-1273
128. Seed, H.B., Idriss, I.M., & Arango, I. (1983); Evaluation of liquefaction potential using field performance data. *Journal of Geotechnical Engineering Division, ASCE*, **109**(GT3): 458–482.
129. Shen, C. K., O'Sullivan, C., & Jardine, R. J. (2011). A micromechanical investigation of drained simple shear tests. *In Deformation Characteristics of Geomaterials: Proceedings of the Fifth International Symposium on Deformation Characteristics of Geomaterials*, 314, IS-Seoul 2011, 1-3 Seoul, Korea. IOS Press
130. Shen, C. K., (2012). *A micromechanical investigation of drained simple shear tests on dense sand using discrete element simulations*. Ph.D. thesis, Imperial College London
131. Sim, W.W., Aghakouchak, A., & Jardine, R.J. (2013). Cyclic triaxial tests to aid offshore pile analysis and design. *Proceedings of the Institution of Civil Engineers-Geotechnical Engineering* **166**(2): 111-121.
132. Skempton, A.W. (1986). Standard penetration test procedures and the effects in sands of overburden pressure, relative density, particle size, ageing and overconsolidation. *Géotechnique* , **36**(3): 425-447.
133. Taborda, D.M.G., Zdravković, L., Kontoe, S., & Potts, D.M. (2014). Computational study on the modification of a bounding surface plasticity model for sands. *Computers and Geotechnics*, **59**, 145-160.
134. Tatsuoka, F. & Shibuya, S. (1992). Deformation characteristics of soils and rocks from field and laboratory tests - Keynote lecture. In *Proc. of the 9th Asian Confrenece on Soil Mechanics and Foundation Engineering*, Bangkok, **2**, 101-170.
135. Tatsuoka, F., Ochi, K., Fujii, S., & Okamoto, M. (1986); Cyclic undrained triaxial and torsional shear strength of sands for different sample preparation methods. *Soils and Foundations*, **26**(3): 23-41.
136. Tatsuoka, F. (2011). Laboratory stress–strain tests for the development of geotechnical theories and practice, Bishop Lecture. In Proc. 5th International Conference on Deformation Characteristics of Geomaterials, Seoul, Korea. 3-50
137. Toll, D.G. (1993) *TRIAX User Manual. Version 3.3.* Geotechnical Systems Group, Durham University, Durham, UK.

138. Toll, D.G., & Ackerley, S.K. (1988). The development of two data acquisition systems for a geotechnical laboratory. In: *Proc. Int. Symposium on New Concepts in Laboratory and Field Tests in Geotechnical Engineering, Rio de Janeiro,* **2** , 453-456.
139. Tong, Z.X., Zhang, J.M., Yu, Y.L., & Zhang, G. (2010). Drained deformation behavior of anisotropic sands during cyclic rotation of principal stress axes. *Journal of Geotechnical and Geoenvironmental Engineering*, **136**(11): 1509-1518.
140. Tsuha, C.H.C., Foray, P.Y., Jardine, R.J., Yang, Z.X., Silva, M., & Rimoy, S. (2012). Behaviour of displacement piles in sand under cyclic axial loading. *Soils and Foundations* **52**(3): 393-410.
141. Uesugi, M. & Kishida, H. (1986a), Influential factors of friction between steel and dry sands, *Soils and Foundations,* **26**(2): 33–46.
142. Van Weele, A.F. (1979). Pile bearing capacity under cyclic loading compared with that under static loading. *Proc. 2nd Int. Conf. Beh. Off. Structures*, London: 475–488.
143. Vesic, A.S. (1970). Tests on instrumented piles, Ogeechee River site. *Journal of the Soil Mechanics and Foundations Division*, ASCE, **96**(2): 561–584.
144. Vucetic, M. & Dobry, R. (1988). Degradation of marine clays under cyclic loading. *Journal of Geotechnical Engineering,* **114**(2), 133-149.
145. Vucetic, M. (1994). Cyclic threshold shear strains in soils. *Journal of Geotechnical Engineering*, **120**(12): 2208-2228.
146. White, D.J. & Bolton, M.D. (2005). Comparing CPT and pile base resistance in sand. *Proceedings of the ICE-Geotechnical Engineering*, **158**(1): 3-14.
147. White, D.J. & Lehane, B.M. (2004). Friction fatigue on displacement piles in sand. *Géotechnique* , **54**(10): 645-658.
148. Wichtmann, T. & Triantafyllidis, T. (2009). Influence of the grain-size distribution curve of quartz sand on the small strain shear modulus G_{max}. *Journal of Geotechnical and Geoenvironmental Engineering*, **135**(10), 1404-1418.
149. Wichtmann, T. (2005). *Explicit accumulation model for non-cohesive soils under cyclic loading*. University of Bochum. PhD thesis.
150. Wichtmann, T., Niemunis, A. & Triantafyllidis, T. (2005). Strain accumulation in sand due to cyclic loading: drained triaxial tests. *Soil Dynamics and Earthquake Engineering*, **25**(12): 967-979.
151. Wood, D.M. & Maeda, K. (2008). Changing grading of soil: effect on critical states. *Acta Geotechnica*, **3**(1): 3-14
152. Yang, J., & Sze, H.Y. (2011). Cyclic behaviour and resistance of saturated sand under non-symmetrical loading conditions. *Géotechnique*, **61**(1): 59-73.
153. Yang, Z.X., Jardine, R.J., Zhu, B.T., Foray, P. & Tsuha, C.H.C. (2010). Sand grain crushing and interface shearing during displacement pile installation in sand. *Géotechnique* **60**(6): 469–482.
154. Zdravković, L. & Jardine, R.J. (1997). Some anisotropic stiffness characteristics of silt under general stress conditions. *Géotechnique*, **47**(3): 407-437.
155. Zdravković, L. (1996). *The stress-strain-strength anisotropy of a granular medium under general stress conditions*. Ph.D. thesis, Imperial College London.

List of Figures

Figure 2-1 Scheme for multiple yielding surface framework after Kuwano & Jardine (2007) 34
Figure 2-2 Stress-strain measurements at small strain in drained axial probing triaxial test to locate the boundary for Y1 surface (Kuwano & Jardine 2007) – HRS sand at D_r=25%, OCR=1.3 and σ'_v=243kPa.....35
Figure 2-3 a) Location of yield surfaces in dense HRS sample and b) evolution of Y2 yield surface by stress history (Kuwano & Jardine, 2007) 35
Figure 2-4 Tangent effective vertical stiffness of dense HRS sand on compression and extension tests shown in Figure 3-2 (Kuwano & Jardine , 2007). – HRS sand at D_r=25%, OCR=1.3 and σ'_v=243kPa.....36
Figure 2-5 Fitting a) multiple linear lines and b) power law equations to critical state points in e-p′space (Taborda *et al.*, 2014).....36
Figure 2-6 Comparison of behaviour as a function of state parameter for Kogyuk 350/2 and Kogyuk 350/10 sand (Jeffries & Been, 2006) 37
Figure 2-7 Cyclic parameters in triaxial conditions.....37
Figure 2-8 Schematic diagram for explaining the initiation of failure in effective stress path during cyclic loading (Hyodo *et al.*, 1994) 38
Figure 2-9 Comparison of points for initiation of instability and the monotonic stress path (De Gennaro *et al.*, 2004) 38
Figure 2-10 Undrained cyclic torsional HCA test on Fontainebleau sand a) Effective stress path b) excess PWP against time and c) shear strain against time (Georgiannou & Tsomokos, 2008) 39
Figure 2-11 Illustrative sketches showing the definition of the no effect threshold in cyclic tests 40
Figure 2-12 Schematic diagram illustrating the effect of initial stress anisotropy on the number of cycles needed for failure. (Konrad, 1993).....40
Figure 2-13 - Effect of relative density on cyclic strength (Tatsuoka *et al.*, 1986).....41
Figure 2-14 Pore pressure change for states on lines parallel to isotropic NCL line a) Initial states b) normalised PWP generated (Qadimi & Coop, 2006) 42
Figure 2-15 Undrained cyclic tests on HRS sand, samples with same initial stress state but different stress histories (Ovando-Shelley,1986).....43
Figure 2-16 - illustration of implicit and explicit models (Witchmann *et al.* 2009).....44
Figure 2-17 Accumulated strain after 10^5 cycles as a function of stress amplitude b) Development of strain amplitude with number of cycles. (Witchmann *et al.* 2009).....44

Figure 2-18 a) Accumulation of strains in tests with different relative densities b) direction of strain accumulation (Witchmann, 2005) ($\varepsilon^{acc}=\boldsymbol{\varepsilon}$, η^{av}=CSR , $q^{amp}=q_{cyc}$, $p^{av}=p'_{mean}$) 45
Figure 2-19 a) strain Accumulation curves in tests with different average pressures b) cyclic strain amplitude as a function of mean pressure (Witchmann *et al.* 2009).....45
Figure 2-20 a) Accumulation of strains in tests with different average stress ratios b) Direction of strain accumulation with different average stress ratios (Witchmann, 2005) 46
Figure 2-21Strain accumulation curves with different sequence of packets of cycles with different amplitude (Witchmann, 2005 46
Figure 3-1 Relation of cavity expansion limit pressure and end-bearing capacity (Randolph *et al.*, 1994) 83
Figure 3-2 - Effect of pile diameter on pile base resistance (Chow, 1997) 83
Figure 3-3 - Residual loads at the end of installation and their effect on base load (Alawneh & Malkawi, 2000) 84
Figure 3-4 Stationary radial effective stresses during pile installation in medium dense Dunkerque sand (Chow, 1997) 84
Figure 3-5 Comparison of shaft frictions measured during and after installation in Labenne sand with API RP2 GEO (2011) design method (Lehane, 1992 and Rimoy, 2012) 85
Figure 3-6 Effect of installation method on radial stresses at the end of each a) push; b) pause (Jardine *et al.,* 2013a) CPT1 test involved steady jacking, while CPT2 was installed by cyclic jacking with full unloading between each 20mm long jack stroke.....85
Figure 3-7 Normalisation of radial effective stresses by a) Number of cycles during installation b) h/R in 2R and 3R distances away from pile surface (Jardine *et al.,* 2013).....86
Figure 3-8 Radial, circumferential and vertical stresses at a) end of each pause and b) end of push in stationary conditions (Jardine *et al.*, 2013b) 87
Figure 3-9 Stationary a) radial and b) circumferential stress at the end final jacking stroke during installation (Jardine *et al.,* 2013b) 88
Figure 3-10 Schematic development of three zones of crushing and their stress level. (Yang *et al.,* 2013) 89
Figure 3-11 Static tension capacity-time tension capacity (Q_s) trends from tests on steel piles driven at three sand sites, normalised by ICP-05 tension capacities. (Q_s (ICP)) (Rimoy *et al.,* 2015) 90
Figure 3-12 a)chart of 600s time history for worst tensile pile during peak of 35 hour design storm in Dunkerque b) Idealised series of uniform loads. (Meritt *et al.*, 2012) 91
Figure 3-13 Schematic illustration of Q_{cyc} and Q_{mean} values (Tsuha *et al.,* 2012).....92
Figure 3-14 Illustration of potential cyclic effects; WSD, FOS=1.5 design conditions compared with Dunkerque zero damage and Haga Nf=100 contours in normalised interaction diagram 92
Figure 3-15 Interaction diagram indicating the influence of number of cycles (N) and Q_{cyc} and Q_{mean} on cyclic response with tentative *Stable*, *Metastable* and *Unstable* zones.....93
Figure 3-16 Interaction diagram based on methodology introduced by Jardine *et al.* (2005) to predict N_f in terms of Q_{cyc} and Q_{mean} 93
Figure 3-17 a) Effective stress paths recorded in ICP mini pile tests at three shaft levels (A, B, and C) and ultimate shaft failure interface envelope under *Stable*, *Metastable* and *Unstable*

axial cyclic loading tests. b) Effective stress paths developed in sand mass at 5R, h/R≈15 during each test. (After Tsuha *et al.*, 2012) 94
Figure 3-18 Effect of load cycling on tensile capacity in one-way model pile tests on NE34 sand. (Tsuha *et al.,* 2012) Q_T= Tensile capacity. 95
Figure 3-19 Interaction diagram indicating the influence of number of cycles (N) and Q_{cyc} and Q_{mean} on cyclic response with tentative *Stable*, *Metastable* and *Unstable* zones. (Tsuha *et al.,* 2012) 95
Figure 3-20 a) illustration of stiffness calculation. Normalised axial cyclic pile stiffness versus number of cycles applied in a) *Stable*, b) *Metastable* and c) *Unstable* cyclic model pile tests. (Rimoy, 2013). K= $(Q_{max}-Q_{min})/d_{cyc}$ 96
Figure 3-21 Stress and strain conditions for soil element adjacent to pile (Sim *et al.,* 2013) .97
Figure 3-22 Comparison of shear stress degradation observed in model pile tests with prediction made from cyclic CNS tests. 97
Figure 3-23 Analogy for modelling soil-pile interaction in laboratory testing (After Boulon & Foray, 1986) 98
Figure 3-24 Cyclic CNL tests on loose and dense Toyoura sand in rough and smooth surfaces (Mortara, 2001) 99
Figure 3-25 Evolution of shear and normal stresses during cyclic CNS soil-soil test (Airey 1992) 100
Figure 3-26 Two-way CNS tests on silica sand (Fakharian & Evgin, 1997) 101
Figure 3-27 a) Effect of cyclic amplitude on normal and shear stresses b) Effect of K_{CNS} on normal and shear stresses (Fakharian & Evgin, 1997) 101
Figure 3-28 Comparison between CNS tests on rough and smooth surfaces (Mortara *et al.*, 2007) 102
Figure 3-29 Interpretation of interface roughness a) rough interface b) smooth interface (Mortara *et al.*, 2007) 102
Figure 3-30 DEM analysis to simulate "Cambridge" style simple shear apparatus. a) incremental maximum deviatoric strains for frictional flat boundary specimen at 20% shear strain b) Plot of internal contact force chains and the force on the boundaries at20% shear strain from central portion (Shen ,2012) 103
Figure 3-31 Possible modes of failure in simple shear tests (Randolph & Wroth, 1981) 103
Figure 3-32 a) Shear stress vs horizontal displacements b) vertical displacement vs horizontal displacements and c) vertical position vs total horizontal displacement from cyclic tests monitored by GeoPIV image processing technique. (Dejong *et al.*, 2003) 104
Figure 4-1 Schematic diagram of the modified Bishop & Wesley (1975) triaxial apparatus used 134
Figure 4-2 Photograph of the modified Bishop & Wesley (1975) triaxial apparatus used.... 135
Figure 4-3 a) Photograph of the load cell used b) internal structure of the load cell, shearing its strain gauged shear webs. 135
Figure 4-4 Illustrative sketch showing how local transducers were installed on the surface of the triaxial specimens. 136
Figure 4-5 Effect of temperature fluctuations on local LVDT readings. 136
Figure 4-6 Different modes of sample deformation as suggested by Germaine et al (1988) 137

Figure 4-7 Deformation of a Dunkerque specimen under axial shearing to 20% axial strain as determined from digital analysis of photograph taken sequentially during compressive shearing. 137
Figure 4-8 Comparison between applied and ideal sinusoidal cyclic loads in triaxial apparatus for a) small to medium amplitudes and b) large amplitudes. 138
Figure 4-9 Schematic diagram of the ICRCHCA apparatus after Brosse (2012) 139
Figure 4-10 a) Inner cell sealing mechanism by Nishimura (2006) b) Modified inner cell mechanism by Brosse (2012) 140
Figure 4-11 Schematic illustration of the torque transmitting system in ICRCHCA 140
Figure 4-12 Schematic plan of the proximity transducers at top of the HCA specimen 141
Figure 4-13 External forces applied to the specimen in the HCA and corresponding stress state of an element of soil. 141
Figure 4-14 Stress and strain state in HCA specimen. Pp refers to pole in term of planes of stress orientation and PD in terms of stress axis direction. 142
Figure 4-15 Schematic illustration of the water changing procedure in HCA apparatus 142
Figure 4-16 Comparison of response under undrained simple shear cyclic loading between tests with different water changing procedure. p'=167kPa, $\Delta\tau_{z\theta}$=41.75kPa 143
Figure 4-17 Comparison between applied and ideal sinusoidal cyclic loads in HCA apparatus 143
Figure 4-18 Schematic illustration of the electrical set-up of the RC system 144
Figure 4-19 Schematic illustration of two possible boundary condition assumptions for HCA RC system 144
Figure 4-20 Schematic illustration of sample preparation procedure for triaxial and HCA samples. 145
Figure 4-21 Photographs of sample preparation procedure for triaxial and HCA samples. 145
Figure 5-1 Location of Dunkerque and Fontainebleau sites in France 169
Figure 5-2 Summary of geotechnical profile for Dunkerque site from Chow (1997) 169
Figure 5-3 Relative density profile in Dunkerque site reported by Chow (1997) 170
Figure 5-4 PSD graph for Dunkerque samples at surface and higher depths 170
Figure 5-5 Aspect ratio (AR), sphericity (S) and convexity (C) parameters for Dunkerque sand obtained from QicPic. 171
Figure 5-6 Microscope image of Dunkerque sand using nanotech Microsurf 3D optical profiler by Nanotech 171
Figure 5-7 PSD Graphs for NE34 and Dunkerque sand from QicPic tests 172
Figure 5-8 Aspect ratio (AR), sphericity (S) and convexity (C) parameters for NE34 sand obtained from QicPic. 172
Figure 5-9 Microscope image of NE34 sand using nanotech Microsurf 3D optical profiler by Nanotech 173
Figure 5-10 Void ratio changes during consolidation and creep stage for K_0 drained tests on a) Dunkerque, b) NE34. e_0=0.64 174
Figure 5-11 Axial strain accumulation in creep stage prior to shearing for K_0 drained tests on a) Dunkerque, b) NE34. e_0=0.64 175
Figure 5-12 void ratio changes in high-pressure Oedometer test performed on Dunkerque and NE34 sands. 176

Figure 5-13c Axial stress-strain probing to locate Y_1 boundary for K_0 drained-p'_0=5.....179
Figure 5-14 Locating the Y_2 surface in ε_v- ε_s space for K_0 drained tests on a) Dunkerque, b) NE34. e_0=0.64.....180
Figure 5-15 Locating the kinematic boundaries obtained from drained and undrained tests and comparison with ones reported by Kuwano & Jardine (2007). 181
Figure 5-16 Evolution of the Y_1 surface size in relation with the p'_0 in K_0 consolidated drained tests. 182
Figure 5-17 Locating Y_3 surface in ε_v- ε_s space for K_0 drained tests on a) Dunkerque, b) NE34. e_0=0.64.....183
Figure 5-18 Locating Y_4 surface in ε_v- ε_s for K_0 drained tests on a) Dunkerque, b) NE34. e_0=0.64. 184
Figure 5-19 Tangent stiffness degradation curves from drained K_0 compression tests on a) Dunkerque, b) NE34. e_0=0.64.....185
Figure 5-20 Tangent stiffness degradation curves from drained K_0 extension tests on a) Dunkerque, b) NE34. e_0=0.64.....186
Figure 5-21 Relation between E'_v and p' from from drained K_0 compression tests on a) Dunkerque, b) NE34. e_0=0.64.....187
Figure 5-22 Relation between E'_v and p' from from drained K_0 extension tests on a) Dunkerque, b) NE34. e_0=0.64.....188
Figure 5-23 Radial strain vs axial strain under drained K_0 shearing to measure Poisson's ratio 189
Figure 5-24 Calculation of the bulk modulus for Dunkerque and NE34 sands using swelling stage data. e_0=0.64. 190
Figure 5-25 q-ε_a trends from drained K_0 compression tests on a) Dunkerque, b) NE34. e_0=0.64 191
Figure 5-26 q-ε_a trends from drained K_0 extension tests on a) Dunkerque, b) NE34. e_0=0.64 192
Figure 5-27 Stress paths in q-p' space from drained K_0 tests, a) Dunkerque, b) NE34. e_0=0.64 193
Figure 5-28 Void ratio changes from drained K_0 compression tests, a) Dunkerque, b) NE34. e_0=0.64 194
Figure 5-29 Locating the critical state line in e-logp'space, a) Dunkerque, b) NE34. e_0=0.64 195
Figure 5-30 Axial stress-strain probing to locate Y_1 boundary for undrained normally consolidated Dunkerque and NE34 sands. e_0=0.64 196
Figure 5-31 Axial stress-strain probing to locate Y_1 boundary for undrained over-consolidated Dunkerque and NE34 sands. e_0=0.64 197
Figure 5-32 Undrained vertical E_U degradation from normally and over consolidated specimens under compression.....198
Figure 5-33 Undrained vertical E_U degradation from normally and over consolidated specimens under extension. 199
Figure 5-34 Stress paths in q-p' space from undrained normally consolidated and over-consolidated tests, a) Dunkerque, b) NE34.....200

Figure 5-35 q-ε_a trends from undrained normally consolidated and over-consolidated tests, a) Dunkerque, b) NE34. 201
Figure 6-1Schematic illustration of cyclic triaxial loading shearing definition of q_{mean}, q_{cyc}, T (period) and N (number of cycles). 220
Figure 6-2 Pre-conditioning consolidation effective stress paths applied in tests that assessed the effect of stress history on undrained cyclic response. A-C for normally consolidated specimens and A-B-C for over-consolidated specimens. 220
Figure 6-3 Void-ratio changes during the pre-conditioning stages for normally-consolidated and over-consolidated specimens that assessed the effect of stress history on undrained cyclic response.....221
Figure 6-4 Effect of consolidation stress history on p′drifts observed in undrained cyclic tests with CSR=0.25. Plot shows the p′ drift at mid-cycle (q = 50kPa) points versus number of cycles.....221
Figure 6-5 Effect of consolidation stress history on p′drifts observed in undrained cyclic tests with CSR = 0.25. Plot shows the stress paths followed in q-p′space under undrained cyclic loading.....222
Figure 6-6 Effect of consolidation stress history on accumulation of permanent axial strains at mid-cycle (q = 50kPa) points observed in undrained cyclic tests with CSR = 0.25. Note NC=normally consolidated, OC=over-consolidated, DK=Dunkerque and NE=NE34 sand.223
Figure 6-7 Effect of consolidation stress history on secant undrained stiffness under undrained cyclic tests with CSR = 0.25. Note NC=normally consolidated, OC=over-consolidated, DK=Dunkerque and NE=NE34 sand 223
Figure 6-8 Pre-conditioning consolidation effective stress paths applied in tests that assessed the effect of pre-cycling by 30 drained cycles at Point C. 224
Figure 6-9 Void ratio changes during the pre-conditioning stages of tests on a) Dunkerque and b) NE34 specimens that assessed the pre-cycling (at Point C) on undrained cyclic behaviour (at Point D) with low to medium CSRs. 225
Figure 6-10 Accumulation of a) axial and b) volumetric strains under drained pre-cycling stage with CSR = 0.5 from tests that assessed the effect of pre-cycling on undrained cyclic response with low to medium CSRs. 226
Figure 6-11 Effect of pre-cycling at point C (30 drained cycles with CSR = 0.5) on p′drifts in undrained cyclic tests with low to medium CSRs. 227
Figure 6-12 Void ratio changes during the pre-conditioning stage of Dunkerque tests that assessed the pre-cycling effect at point C with $CSR_{pre-cyc}$=0, 0.25 and 0.5 on undrained cyclic behaviour with high CSR=0.45. 228
Figure 6-13 Accumulation of axial strains under 30 drained cycles at point C during the pre-cycling stage with $CSR_{pre-cyc}$=0.25 and 0.5 from tests that assessed the effect of pre-cycling on undrained cyclic response with high CSR=0.45. 228
Figure 6-14 Accumulation of volumetric strains under 30 drained cycles at point C during the pre-cycling stage with $CSR_{pre-cyc}$=0.25 and 0.5 from tests that assessed the effect of pre-cycling on undrained cyclic response with high CSR=0.45. 229
Figure 6-15 Effect of pre-cycling at point C (30 drained cycles with CSR=0, 0.25 and 0.5) on p′drifts observed under high CSR = 0.45 at mid-cycle (q = 50 kPa) points. 229

Figure 6-16 Effect of pre-cycling at point C (30 drained cycles with CSR = 0, 0.25 and 0.5) on accumulation of axial strains observed under high CSR = 0.45 at mid-cycle (q = 50 kPa) points. 230
Figure 6-17 Effect of pre-cycling at point C (30 drained cycles with CSR = 0, 0.25 and 0.5) on undrained secant cyclic stiffness observed under high CSR = 0.45 at mid-cycle (q = 50 kPa) points. 230
Figure 6-18 Effect of ageing time at points A and D on p′ drifts under undrained cyclic loading at point D with low to medium CSRs. 231
Figure 7-1 Void ratio changes during the "standard" pre-conditioning procedure on a) Dunkerque and b) NE34 sands prior to applying Undrained cyclic loads at different CSR values. e_0 target=0.64. 246
Figure 7-2 Axial straining during 48 hours of creep at point B after consolidation on a) Dunkerque and b) NE34 as part of the "standard" pre-conditioning procedure prior to applying Undrained cyclic loads at different CSR values. e_0=0.64. 247
Figure 7-3 Axial straining during 48 hours of creep at point D after swelling on a) Dunkerque and b) NE34 as part of the "standard" pre-conditioning procedure prior to applying Undrained cyclic loads at different CSR values. e_0=0.64. 248
Figure 7-4 Accumulation of axial strains under drained pre-cycling at point C on a) Dunkerque and b) NE34 as part of the "standard" pre-conditioning procedure prior to applying Undrained cyclic loads at different CSR values. e_0 =0.64. $CSR_{pre\text{-}cycle}$=0.5 249
Figure 7-5 Accumulation of volumetric strains under drained pre-cycling at point C on a) Dunkerque and b) NE34 as part of the "standard" pre-conditioning procedure prior to applying Undrained cyclic loads at different CSR values. e_0=0.64. $CSR_{pre\text{-}cycle}$=0.5. 250
Figure 7-6a Stress paths followed in "*Stable*" tests in q-p′ space from "standard" pre-conditioned a) Dunkerque and b) NE34 sands at CSR levels up to 0.25 251
Figure 7-7 Effect of CSR on mean effective stress drifts under undrained cycling at Point D for a) Dunkerque and b) NE34 specimens after standard consolidation, conditioning cycles and ageing stages. All samples prepared to e_0=0.64 254
Figure 7-8 Effect of CSR on strain accumulation under undrained cycling at Point D for a) Dunkerque and b) NE34 specimens after standard consolidation, conditioning cycles and ageing stages. All samples prepared to e0=0.64 255
Figure 7-9 Stress-strain loops of specified nth cycles from undrained tests with "standard" pre-conditioning and *Stable* response. 256
Figure 7-10 Stress-strain loops of specified nth cycles from undrained tests with "standard" pre-conditioning and *Metastable* response. 257
Figure 7-11 Stress-strain loops of specified nth cycles from undrained tests with "standard" pre-conditioning and *Unstable* response. 258
Figure 7-12 Locating the Y_1 surface using the CSR=0.15 cyclic tests stress-strain data for a)Dunkerque and b)NE34 sands 259
Figure 7-13 Location of maximum effective stress points achieved in each undrained cyclic test with standard pre-conditioning and location of Y_1 surface from monotonic undrained test with OCR=4 and estimation of the Y_2 surface based on cyclic results. 260

Figure 7-14 Effect of CSR on undrained stiffness response under undrained cycling at Point D for a) Dunekrque and b) NE34 specimens after standard consolidation, conditioning cycles and ageing stages. All samples prepared to e0=0.64 261
Figure 7-15 Initial target void ratio of dense and loose specimens and their location relative to the critical state line obtained from monotonic tests. 262
Figure 7-16 Void ratio changes during the “standard” pre-conditioning procedure for dense (D_r=90%) and loose (D_r=50%) Dunkerque and NE34 specimens prior to applying undrained cyclic loads with CSR=0.35.....263
Figure 7-17 Accumulation of axial strains during 48 hours of creep on dense and loose specimens after consolidation at point B as part of the “standard” pre-conditioning to applying undrained cyclic loads with CSR=0.35.....263
Figure 7-18 Stress paths followed under undrained cycling after "standard" pre-conditioning procedure at point D for a) Dunkerque and b) NE34 specimens with CSR=0.35 264
Figure 7-19 Effect of relative density on p′drift under undrained cycling on "standard" pre-conditioned Dunkerque and NE34 specimens. CSR=0.35. 265
Figure 7-20 Effect of relative density on strain accumulation under undrained cycling on "standard" pre-conditioned Dunkerque and NE34 specimens. CSR=0.35. 265
Figure 7-21 Effect of relative density on undrained stiffness response under undrained cycling on "standard" pre-conditioned Dunkerque and NE34 specimens. CSR=0.35. 266
Figure 7-22 Accumulation of axial strains under drained cyclic loading on "standard" pre-conditioned a) Dunkerque and b) NE34 specimens.....267
Figure 7-23 Accumulation of radial strains under drained cyclic tests on "standard" pre-conditioned a) Dunkerque and b) NE34 specimens.....268
Figure 7-24 Accumulation of shear strains under drained cyclic tests on "standard" pre-conditioned a) Dunkerque and b) NE34 specimens.....269
Figure 7-25 Accumulation of volumetric strains under drained cyclic tests on "standard" pre-conditioned a) Dunkerque and b) NE34 specimens.....270
Figure 7-26 Stress-strain loops of specified nth cycles from drained tests with “standard” pre-conditioning. 271
Figure 7-27 Degradation of Secant cyclic vertical effective stiffnesses under drained cyclic loading with “standard” pre-conditioned specimens. 272
Figure 8-1 Analogy for modelling the stress conditions adjacent to pile surface under axial loading in HCA apparatus.....293
Figure 8-2 The "standard" pre-conditioning procedure applied for monotonic and cyclic simple shear tests. 293
Figure 8-3 Comparison between stress paths followed in HCA and triaxial tests during the pre-cycling stage 294
Figure 8-4 Torsional stress-strain probing to locate Y_1 boundary for “standard” pre-conditioned Dunkerque and NE34 sands. e_0=0.64. 295
Figure 8-5 $G_{z\theta}$ tangent degradation of “standard” pre-conditioned Dunkerque and NE34 sands. e_0=0.64. 295
Figure 8-6 Effective stress paths followed in $\tau_{z\theta}$-(σ'_z- σ'_θ)/2 space in monotonic simple shear tests in HCA with in “standard” pre-conditioning. 296

Figure 8-7 Stress paths followed in (σ'_z- σ'_θ)/2 – p′space in monotonic simple shear tests in HCA with in "standard" pre-conditioning. 296
Figure 8-8 The q-p′ stress paths followed in HCA simple shear tests with "standard" pre-conditioning and comparison with stress paths followed in triaxial undrained tests. e_0=0.64. 297
Figure 8-9 $\tau_{z\theta}$-$\gamma_{z\theta}$ trends from simple shear tests with "standard" preconditioning e_0=0.64 .297
Figure 8-10 Void ratio changes during the "standard" pre-conditioning procedure on a) Dunkerque and b) NE34 sands prior to applying simple shear cyclic loads at different CSR_τ values. e_0 target=0.64. 298
Figure 8-11 Axial straining during 48 hours of creep at point B after consolidation on a) Dunkerque and b) NE34 as part of the "standard" pre-conditioning procedure prior to applying simple shear cyclic loads at different CSR_τ values. e_0=0.64.....299
Figure 8-12 Accumulation of axial strains under drained pre-cycling at point C on a) Dunkerque and b) NE34 as part of the "standard" pre-conditioning procedure prior to applying simple shear cyclic loads at different CSR_τ values. e_0 =0.64. $CSR_{\tau precycle}$=0.47.....300
Figure 8-13 Accumulation of volumetric strains under drained pre-cycling at point C on a) Dunkerque and b) NE34 as part of the "standard" pre-conditioning procedure prior to applying simple shear cyclic loads at different CSR_τ values. e_0 =0.64. $CSR_{\tau precycle}$=0.47.....301
Figure 8-14a-f $\tau_{z\theta}$-σ'_z stress paths following under simple shear cycling in tests with "standard" pre-conditioning. e_0=0.64 302
Figure 8-15 Effect of CSR_τ on degradation of σ'_z at mid cycle point (τ=0kPa) under simple shear cycling at Point D for a)Dunkerque and b)NE34 specimens after standard consolidation, conditioning cycles and ageing stages. All samples prepared at e_0=0.64. 304
Figure 8-16 Illustration of Mohr circles at mid-cycle and maximum points in simple shear HCA tests 305
Figure 8-17 Effect of CSRτ on degradation of σ'_r, σ'_z and σ'_θ at mid cyclic point (τ=τ_{cyc}) under simple shear cycling at Point D for a)Dunkerque and b)NE34 specimens after standard consolidation, conditioning cycles and ageing stages. All samples prepared at e0=0.64.....306
Figure 8-18a-f Degradation of σ'_1, σ'_2 and σ'_3 at maximum cyclic point under simple shear cycling at Point D after standard consolidation, conditioning cycles and ageing stages. All samples prepared at e_0=0.64 307
Figure 8-19 a-f stress paths followed in q-p′in cyclic simple shear tests with "standard" pre-conditioning at different CSR_τ levels. e_0=0.64.....309
Figure 8-20 Stress paths followed in cyclic simple shear tests in q-p′space from "standard" pre-conditioned tests on a)Dunkerque and b)NE34 sands at mid cycle points (τ=0kPa). All samples prepared at e_0=0.64. 311
Figure 8-21 Effect of CSR_τ on degradation of mean effective stresses at mid cycle point (τ=0kPa) under simple shear cycling at Point D for a)Dunkerque and b)NE34 specimens after standard consolidation, conditioning cycles and ageing stages. All samples prepared at e_0=0.64. 312
Figure 8-22 Effect of CSR_τ on degradation of deviatoric stresses at mid cycle point (τ=0kPa) under simple shear cycling at Point D for a)Dunkerque and b)NE34 specimens after standard consolidation, conditioning cycles and ageing stages. All samples prepared at e_0=0.64. 313

Figure 8-23 Effect of CSR_τ on degradation of deviatoric stresses at maximum cyclic point ($\tau=\tau_{cyc}$) under simple shear cycling at Point D for a)Dunkerque and b)NE34 specimens after standard consolidation, conditioning cycles and ageing stages. All samples prepared at e_0=0.64 314
Figure 8-24 Value of b at maximum point in each cycle in "standard" pre-conditioned tests on a)Dunkerque and b)NE34 sands at maximum cycle points ($\tau= \tau_{cyc}$ kPa). All samples prepared at e_0=0.64. 315
Figure 8-25 Maximum degree of rotation of principle stresses in each cycle in "standard" pre-conditioned tests on a)Dunkerque and b)NE34 sands at maximum cycle points ($\tau= \tau_{cyc}$ kPa). All samples prepared at e_0=0.64. 316
Figure 8-26a-f Stress-strain loops of specified nth cycles from cyclic simple shear tests with "standard" pre-conditioning procedures. 317
Figure 8-27 Locating the Y_1 limit using the stress-strain loop from tests with CSRτ=0.15..319
Figure 8-28 Location of maximum q levels reached in each cyclic test compared to the Y_1 limits obtained from monotonic simple shear tests with similar pre-conditioning procedure. 320
Figure 8-29 Effect of CSR_τ on undrained cyclic stiffness under simple shear cycling at Point D for a)Dunkerque and b)NE34 specimens after standard consolidation, conditioning cycles and ageing stages. All samples prepared at e_0=0.64. 321
Figure 8-30 Evolution of the $\Delta\sigma_r'/\Delta p'$ ratio under cyclic simple shear in "standard" pre-conditioned tests with different CSR_τ levels.....322
Figure 9-1 Loong-Plage field bored pile tests. a) Pile head load-displacement graph under one-way compression. b) Cyclic interaction diagram constructed based on bored-pile cyclic tests. 337
Figure 9-2 SOLCYP flow chart for designing under axial cyclic loading (Jardine *et al.* (2012).....338
Figure 9-3 Failure mechanism and evolution of σ_r' and τ_{rz} of soil element adjacent to pile surface. 338
Figure 9-4 $\Delta\sigma_z'/\sigma_{z0}'$ curves from HCA cyclic tests for calculation of pile failure parameters for a)Dunkerque and b)NE34 specimens.....339
Figure 9-5 $\tau_{cyc}/\tau_{max\ static}$ against N_f graph obtained from cyclic simple shear HCA tests at $\tau_{mean}/\tau_{max\ static}$ =0 for a)Dunkerque and b)NE34 specimens. 340
Figure 9-6 Contours of number of cycles required to reach failure plotted on the interaction diagram for a)Dunkerque and b)NE 34 specimens obtained from HCA tests.....341
Figure 9-7 Comparison between different zones of behaviour obtained from HCA tests with a) in-situ Dunkerque and b)model NE34 pile tests 342
Figure 9-8 $\Delta p'/ p_0'$ curves from triaxial cyclic tests for calculation of pile failure parameters for a)Dunkerque and b)NE34 specimens.....343
Figure 9-9 $\tau_{cyc}/\tau_{max\ static}$ against N_f graph obtained from cyclic triaxial tests at $\tau_{mean}/\tau_{max\ static}$ =0 for a)Dunkerque and b)NE34 specimens. 344
Figure 9-10 Contours of number of cycles required to reach failure plotted on the interaction diagram for a)Dunkerque and b)NE 34 specimens from triaxial tests obtained from triaxial tests. 345

Figure 9-11 Comparison between different zones of behaviour obtained from triaxial tests with a) in-situ Dunkerque and b)model NE34 pile tests.....346
Figure 9-12 Assessment of the A,B C approach (Jardine et al., 2005) applicability for pile shaft degradation under cycling in laboratory HCA tests in a)Dunkerque and b)NE34 tests. 347
Figure 9-13 Assessment of the A,B C approach (Jardine et al., 2005) applicability for pile shaft degradation under cycling in laboratory triaxial tests in a)Dunkerque and b)NE34 tests. 348

List of Tables

Table 2-1 Modes of single element cyclic loading (After Jefferies & Been, 2006) 17
Table 2-2 Summary of functions and material constants from high cycle accumulation model by Whitchman (2005) 31
Table 3-1 API RP2 GEO (2014) recommended practice for pile base capacity design. Note: Cases for which method cannot be applied are indicated as NA. 50
Table 3-2 Indicative range of critical cyclic loads from 7 offshore platform foundation cases (Jardine *et al.*, 2012) 66
Table 4-1 Range, resolution and accuracy of transducers used for triaxial apparatus 110
Table 4-2 Accuracy of the applied cyclic loads at different cyclic amplitude ranges 113
Table 4-3 Range, resolution and accuracy of transducers used for triaxial apparatus 118
Table 5-1 Index characteristics of test sands 149
Table 5-2 Initial void ratios and radial strains accumulated in K_0 consolidation stages of static tests at OCR=1 151
Table 5-3 Compressibility values obtained from different pressure ranges 151
Table 5-4 Constants obtained from power-law fitting to creep trends at end of K_0 drained stages 153
Table 5-5 Shear, volumetric and total strains at Y_1 and Y_2 surfaces 156
Table 5-6 Shear, volumetric and total strains developed between K0 conditions points at Y3 and Y4 surfaces 157
Table 5-7 Maximum effective vertical Young's modulus from K_0 drained tests on NC samples. 158
Table 5-8 Summary of strength parameters obtained for both test sands 162
Table 5-9 initial void ratio and p'_0 and q_0 values prior to start of shearing 164
Table 5-10 Maximum shear stiffness and strain levels for reaching Y_1 – Y_3 surfaces in undrained tests 166
Table 5-11 Relation between E_U and E'_v values at close initial p'_0 values 166
Table 6-1 List of triaxial tests that assessed the effect of stress history. Stress history patterns are defined in Figure 6-2. 207
Table 6-2 List of triaxial tests that assessed the effect of pre-cycling on undrained cyclic behaviour with low to medium CSR's 211
Table 6-3 E_U values at N=1 and 4500 from tests with low to medium CSRs that assessed the effect of pre-cycling 214
Table 6-4 List of triaxial tests that assessed the effect of pre-cycling on undrained cyclic behaviour with high CSR 214
Table 6-5 List of triaxial tests that assessed the effect of creep time on undrained cyclic response 216
Table 7-1 List of undrained triaxial tests performed after "standard" pre-conditioning procedure 233
Table 7-2 List of undrained triaxial tests performed with "standard" pre-conditioning 239

Table 7-3 Coefficients of compressibility and swelling achieved at different void ratio and p′ values. 240
Table 7-4 Constants obtained from power-law fitting to creep trends at different void ratios 240
Table 7-5 Details from drained cyclic tests with “standard” pre-conditioning procedure 243
Table 8-1 Comparison between properties of applied pre-cycles in triaxial and HCA tests.276
Table 8-2 Details of stresses applied at Points A-D during pre-conditioning procedure. 277
Table 8-3 Details from monotonic "standard" pre-conditioned simple shear tests.....278
Table 8-4 Comparison between maximum $G_{z\theta}$ values obtained from static and RC tests. ...279
Table 8-5 Details from cyclic “standard” pre-conditioned simple shear tests.....281
Table 8-6 Compressibility values obtained from different pressure ranges in HCA tests and comparison with values obtained from triaxial tests.....282
Table 8-7 Maximum permanent strains reached after 4500 cycles in standard pre-conditioned cyclic simple shear tests.....287
Table 9-1 A, B and C parameters calculated from laboratory and pile tests 335